REPORT DOCUMENTATION PAGE

AFRL-SR-BL-TR-01-

0119

Public reporting burden for this collection of information is estimated to average 1 hour per response, including gathering and maintaining the data needed, and completing and reviewing the collection of information. Send c collection of information, including suggestions for reducing this burden, to Washington Headquarters Services, L Davis Highway, Suite 1204, Arlington, VA 22202-4302, and to the Office of Management and Budget, Paperwork Reduction Project (0704-0188), Washington, DC 20503.

1. AGENCY USE ONLY (Leave blank)	2. REPORT DATE	3. REPORT TYPE AND DATES COVERED
	1/10/01	Final Report 6/1/97-5/31/00

4. TITLE AND SUBTITLE
AASERT 97: Deposition of Ceramic Coatings by the Changed Liquid Beam Cluster Technique

5. FUNDING NUMBERS
F49620-97-1-0427

6. AUTHOR(S)
Professor Waltraud M. Kriven
(217) 333-5258

7. PERFORMING ORGANIZATION NAME(S) AND ADDRESS(ES)
University of Illinois
Materials Science & Engineering
1304 W. Green St.
Urbana, IL 61801

8. PERFORMING ORGANIZATION REPORT NUMBER

9. SPONSORING/MONITORING AGENCY NAME(S) AND ADDRESS(ES)
AFOSR/NA
110 Duncan Avenue, Room B115
Bolling AFB, DC 20332-8080

10. SPONSORING/MONITORING AGENCY REPORT NUMBER

20010221 000

11. SUPPLEMENTARY NOTES

12a. DISTRIBUTION/AVAILABILITY STATEMENT
No restrictions/Unlimited distribution

12b. DISTRIBUTION CODE

AIR FORCE OFFICE OF SCIENTIFIC RESEARCH (AFOSR)
NOTICE OF TRANSMITTAL DTIC. THIS TECHNICAL REPORT
HAS BEEN REVIEWED AND IS APPROVED FOR PUBLIC RELEASE
LAW AFR 190-12. DISTRIBUTION IS UNLIMITED.

13. ABSTRACT *(Maximum 200 words)*

The original aim of this work was to develop a viable, on line, coating technique for oxide fibers and weaves. The coating was to be a chemically compatible, oxide (eg. hexacelsian ($BaAl_2SiO_8$) which provided a temperature-independent, debonding mechanism based on residual stresses developed at 1590°C, due to a reconstructive phase transformation accompanied by a 5.6% volume contraction. However, the method adopted, the charged liquid beam cluster technique proved to be unfeasible at the current time. Attention was therefore focussed onto electrophoretic deposition of oxide sols (alumina, zirconia) onto carbon-coated fibers and weaves of alumina and mullite ($3Al_2O_3 \cdot 2SiO_2$). However drying of films led to extensive microcracking and this method too, was found to be unsuitable. Attention was then turned to support related AFOSR work for which intermittent funding was obtained (STTR stages I and II); viz., (i) the development of mullite and YAG fibers by amorphous crystallization from a frozen, amorphous melt; (ii) the elastic constants of single crystal, mullite and yttria fibers as measured by Brillouin spectroscopy to 1200°C; and (iii) powder synthesis of oxides for matrices or deposition as coatings.

14. SUBJECT TERMS			15. NUMBER OF PAGES
			16. PRICE CODE
17. SECURITY CLASSIFICATION OF REPORT	18. SECURITY CLASSIFICATION OF THIS PAGE	19. SECURITY CLASSIFICATION OF ABSTRACT	20. LIMITATION OF ABSTRACT

DTIC QUALITY INSPECTED 1

journal

J. Am. Ceram. Soc., 82 [8] 2049-55 (1999)

Preparation of Portland Cement Components by Poly(vinyl alcohol) Solution Polymerization

Sang-Jin Lee,* Elizabeth A. Benson,† and Waltraud M. Kriven*

Department of Materials Science and Engineering, University of Illinois at Urbana-Champaign, Urbana, Illinois 61801

The four components of portland cement—dicalcium silicate, C_2S (Ca_2SiO_4); tricalcium silicate, C_3S (Ca_3SiO_5); tricalcium aluminate, C_3A ($Ca_3Al_2O_6$); and tetracalcium aluminate iron oxide, C_4AF ($Ca_4Al_2Fe_3O_{10}$)—were formed using a solution–polymerization route based on poly(vinyl alcohol) (PVA) as the polymer carrier. The powders were characterized using X-ray diffraction techniques, BET specific surface area measurements, and scanning electron microscopy. This method produced relatively pure, synthetic cement components of submicrometer or nanometer crystallite dimensions, high specific surface areas, as well as extremely high reactivity at relatively low calcining temperatures. The PVA content and its degree of polymerization had a significant influence on the homogeneity of the final powders. Two types of degree of polymerization (DP) PVA were used. Lower crystallization temperatures and smaller particle size powders were obtained from the low-DP-type PVA at optimum content.

I. Introduction

CERAMIC processing has been using chemical synthesis routes in more recent years.[1–15] Methods based on soft-solution processing provide powders with desired properties, such as high purity and homogeneity. In particular, polymer–metal cation complexes are interesting because of their ability to produce well-characterized materials for various industrial purposes and practical uses. In recent years, a new technique has been developed in powder synthesis processing, viz., the use of a poly(vinyl alcohol) (PVA) as a polymeric carrier in a mixed metal cation solution. By using the PVA process, ceramic powders are synthesized much more easily than in other chemical synthesis routes.[1–7] Initially, Gülgün *et al.*[2,3] synthesized compounds, such as calcium aluminate, CA ($CaAl_2O_4$), and yttrium aluminate garnet, YAG ($Y_3Al_5O_{12}$), phases, using the PVA technique. Unlike the Pechini-resin process,[8,12–15] which involves chelation and polymerization, the PVA process involves primarily steric entrapment of cations into the polymer network.[3,5–7] The PVA ensures the homogenous distribution of the metal ions in its polymeric network structure and inhibits their segregation and/or precipitation from the solution.[2,3,5–7] Water is able to diffuse through the polymer and stretch it because of the acetate clusters. In the solution, the long chain polymer prevents contact between cations and limits their agglomeration and precipitation. A schematic representation of the cationic entrapment mechanism is shown in Fig. 1. The amount of polymer and its molecular length can affect the distribution of cations. The optimum amount and chain length of PVA result in a pure, highly reactive, and homogenous powder at the molecular level. It is speculated that weak hydrogen bonding promotes homogeneous entrapment between the –(OH) hydroxyl groups and cations that are solvated by water molecules. The PVA process also produces carbonaceous material that gives heat through its combustion, so that fine and single-phase powders can be formed at a relatively low external temperature.[1–7]

Some of the portland cement components have been made by other chemical synthesis routes. Kralj *et al.*[16] were able to produce C_2S (Ca_2SiO_4) in a CO_2 atmosphere at 950°C, but this required repeated firings of up to four times, with grinding in between each firing to complete the reaction. Roy *et al.*[9] also experimented with C_2S and C_3S (Ca_3SiO_5) to form the materials by a chemical process using nitrate salts and an aqueous sol of SiO_2. They used both the spray-dry technique and gel preparation methods, and obtained BET specific surface area values of 12.94 m^2/g for C_2S and 12.87 m^2/g for C_3S.

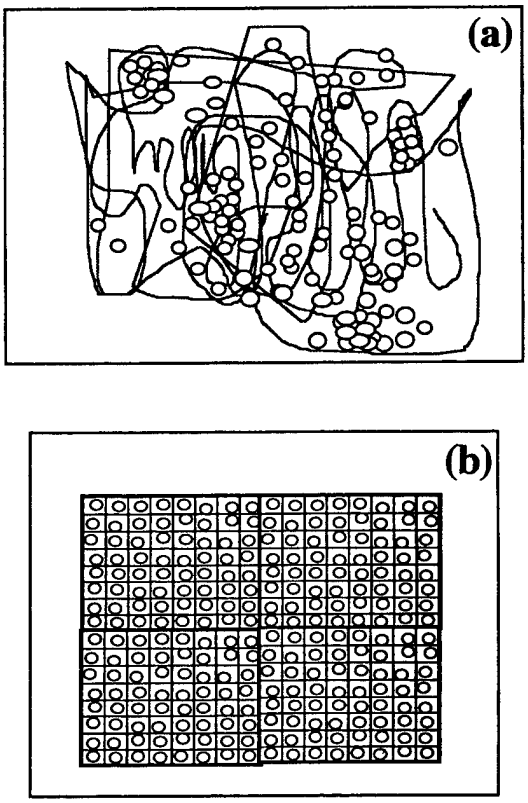


Fig. 1. Schematic representation of cationic entrapment with (a) non-optimal amount of polymer and (b) optimal amount of polymer.

G. W. Scherer—contributing editor

Manuscript No. 189964. Received August 10, 1998; approved December 28, 1998.
Funded in part by the Air Force Institute of Technology at Wright-Patterson AFB, OH, by the Graduate Studies Program at the U.S. Air Force Academy, CO, through a scholarship to the graduate school at the University of Illinois at Urbana-Champaign, and by the Air Force Office of Scientific Research AASERT Program under Grant No. F49620-97-1-0427.

*Member, American Ceramic Society.
†Now at Goodfellow AFB, TX.

In this study, the four components of portland cement—dicalcium silicate, C_2S (Ca_2SiO_4); tricalcium silicate, C_3S (Ca_3SiO_5); tricalcium aluminate, C_3A ($Ca_3Al_2O_6$); and tetracalcium aluminate iron oxide; C_4AF ($Ca_4Al_2Fe_3O_{10}$)—were made by a solution–polymerization process using PVA. By using this method, it was possible to control chemical and physical characteristics, to synthesize powders at lower temperatures, to eliminate grinding–refiring steps as mentioned above, and to produce a high powder yield.[7] Optimum synthesis conditions, such as PVA content, degree of polymerization of the PVA, and calcination temperature, were determined for each component. The powders were characterized by microstructural examination (XRD, SEM) and specific surface areas were measured by nitrogen gas adsorption (BET). The powders prepared by this new application can make pure, synthetic, cement components of nanometer or submicrometer crystallite dimensions, high specific surface area, and extremely high reactivity at relatively low calcination temperatures, in comparison with conventional methods.[17] It is then possible to explore the realm of advanced cementitious materials and composites and its interdisciplinary interface with ceramic synthesis and processing. Once the hydraulicity of each component is determined as a function of the powder characteristics, it is possible to optimize various compositions for specific applications, such as enhanced setting speed, higher strength, and other desirable characteristics.[18–20]

II. Experimental Procedure

(1) Powder Processing

The nitrate salts were in the form of cation sources, with the exception of SiO_2, which was supplied as a colloidal SiO_2 product (25% SiO_2 sol; Ludox SK, DuPont, Wilmington, DE). The chemical reagents and product manufacturers are listed in Table I. These cation sources were dissolved in stoichiometric proportions in deionized (DI) water. To improve the process of dissolving the Ludox SK, the pH of the solution was adjusted by addition of nitric acid. Once the cation sources were completely dissolved, the 5 wt% PVA (Airvol Series; Air Products and Chemicals, Inc., Allentown, PA) was dissolved in DI water and added. The degree of polymerization (DP) of the PVA was varied in these experiments. High-DP PVA was made from Airvol 540S, with a DP value of 1625 (monomers/polymer), and low-DP PVA was made with Airvol 205S with a DP of 428 (monomers/polymer). The high DP PVA had a molecular weight of 153 000, and the low DP PVA had a molecular weight of 40 000. The proportions of the PVA to cation sources in the solution were adjusted in such a way that there were 4, 8, or 12 times more positively charged valences from the cations than from the potentially negatively charged –(OH) functional groups of the polymers. The polymeric long chains have hydroxyl groups in solution. Hence, one PVA monomer, which had one hydroxyl –(OH) functional group, could be used as a unit for calculation of PVA content.

In this experiment, the effect of PVA content and its degree of polymerization on powder preparation is studied. Therefore, the exact relative amount of PVA to cations in the solution can be calculated with reference to a monomeric unit of PVA. For example, in the case of the 4:1 PVA ratio in C_2S, the total positively charged valences are eight. Thus, two PVA monomers are used per one C_2S molecule. Water is evaporated by continuous stirring during heating on a hot plate. The resulting gel-type precursors are completely dried after several hours at 100°C. The organic/inorganic precursors are then ground and kept in a dessicator because of their hydrophilic characteristics. Each of the ground precursors are calcined or crystallized at various temperatures in an air atmosphere in a box furnace. Each of the four components are calcined at a heating rate of 3°C/min. Crystallized C_3S and C_3A powders are milled using an attritor mill (Szegvari Attritor System Type B, Model 3576, Union Process, Akron, OH) to examine the effects of milling on the surface area. The powders are attritor milled at 240 rpms for 1 h. Approximately 700 g of ZrO_2 milling media 5 mm in diameter are mixed with 100 mL of methyl alcohol in a 600 mL jar.

(2) Characterization

(A) X-ray Diffraction Analysis: The crystallization behavior of each of the calcined powders was studied as a function of temperature and holding time at elevated temperatures using an X-ray diffractometer (Dmax automated powder diffractometer, Rigaku/USA, Danvers, MA) with CuK_α radiation (40 kV, 40 mA). All XRD data were obtained at room temperature, after the powder had been cooled. A scanning speed of 10°/min with a sampling interval of 0.02° over a range of 10°–70° for C_2S, C_3S, and C_3A was used. For C_4AF, the range varied from 30° to 40°.

In C_3A, the relative volume ratios of C_3A and residual CaO phases were determined by integrating the X-ray peak areas of (440) of C_3A and (200) of CaO using the equation

$$V_{C3A} = \frac{I(440)_{C3A}}{I(200)_{CaO} + I(440)_{C3A}} \times 100$$

where V_{C3A} is the volume fraction of C_3A, and $I(440)_{C3A}$ and $I(200)_{CaO}$ the 100% peak intensities of C_3A and CaO, respectively.

(B) Specific Surface Area Measurement: The specific surface area of the crystallized powders and attrition-milled powders were obtained by five-point BET analysis from nitrogen-gas adsorption (Model ASAP 2400, Micromeritics, Norcross, GA). All samples for testing were kept in a dry oven to prevent hydration of the powders.

(C) Microstructure Characterization: The morphologies of calcined, crystallized, and/or attrition-milled powders were examined by scanning electron microscopy (SEM; model

Table I. Powder Preparation and Processing Variables

Component	Chemical agents	pH adjustment	Solution color	Burnout temperature (°C)	Properties of organic/inorganic precursor
C_2S	Calcium nitrate† + Ludox SK	Nitric acid (pH 2)	Transparent	3°C/min, 1 h hold at 700°C	White precursor, fairly coarse texture, hydrophilic
C_3S	Calcium nitrate + Ludox SK	Nitric acid (pH 2)	Transparent	3°C/min, 1 h hold at 700°C	White precursor, coarse texture, hydrophilic
C_3A	Calcium nitrate + aluminum nitrate‡		Transparent	3°C/min, 1 h hold at 700°C	Yellow precursor, soft and porous texture, hydrophilic,
C_4AF	Calcium nitrate + aluminum nitrate + iron nitrate§		Transparent	3°C/min, 1 h hold at 700°C	Red/brown precursor, soft and porous texture, hydrophilic

†$Ca(NO_3)_2 \cdot 4H_2O$ (reagent grade; Aldrich Chemical Co., Milwaukee, WI). ‡$Al(NO_3)_2 \cdot 9H_2O$ (reagent grade; Aldrich Chemical Co.). §$Fe(NO_3)_3 \cdot 9H_2O$ (reagent grade; ALFA Aesor Chemical Co., Ward Hill, MA).

Table II. Crystallization Behavior from High-DP PVA

Temperature (°C)	C_2S (4:1)†	C_3S (8:1)†	C_3A (8:1)†	C_4AF (8:1)†
600	Amorphous	Amorphous	Amorphous	Amorphous
700	Amorphous + α_L'-Ca_2SiO_4	Amorphous	$Ca_3Al_2O_6$ < CaO	$Ca_4Al_2Fe_3O_{10}$
800	α_L'-Ca_2SiO_4 + CaO < β-Ca_2SiO_4	β-Ca_2SiO_4 + CaO + Ca_3SiO_5	$Ca_3Al_2O_6$ < CaO	$Ca_4Al_2Fe_3O_{10}$
900	α_L'-Ca_2SiO_4 + [CaO] < β-Ca_2SiO_4	β-Ca_2SiO_4 + CaO + Ca_3SiO_5	$Ca_3Al_2O_6$ > CaO	$Ca_4Al_2Fe_3O_{10}$
1000	β-Ca_2SiO_4 + [CaO]	Ca_3SiO_5 + CaO	$Ca_3Al_2O_6$ > CaO	$Ca_4Al_2Fe_3O_{10}$
1100	β-Ca_2SiO_4 + [CaO]	Ca_3SiO_5 + CaO	$Ca_3Al_2O_6$ + [CaO]	$Ca_4Al_2Fe_3O_{10}$
1200	β-Ca_2SiO_4	Ca_3SiO_5 + CaO	$Ca_3Al_2O_6$ + [CaO]	$Ca_4Al_2Fe_3O_{10}$
1300	γ-Ca_2SiO_4	Ca_3SiO_5 + CaO	$Ca_3Al_2O_6$	$Ca_4Al_2Fe_3O_{10}$
1400	γ-Ca_2SiO_4	Ca_3SiO_5 + [CaO]	$Ca_3Al_2O_6$	$Ca_4Al_2Fe_3O_{10}$

†( ) indicates optimum PVA content in terms of ratio of cation valences to –(OH) functional groups for lowest crystallization temperature; [ ] indicates much smaller amounts relative to other phases present.

Table III. Crystallization Behavior from Low-DP PVA

Temperature (°C)	C_2S (4:1)†	C_3S (4:1)†	C_3A (4:1)†	C_4AF (4:1)†
600	Amorphous + α_L'-Ca_2SiO_4	Amorphous	$Ca_3Al_2O_6$ < CaO	$Ca_4Al_2Fe_3O_{10}$
700	α_L'-Ca_2SiO_4 + CaO < β-Ca_2SiO_4	Ca_3SiO_5 + CaO	$Ca_3Al_2O_6$ > CaO	$Ca_4Al_2Fe_3O_{10}$
800	α_L'-Ca_2SiO_4 + [CaO] < β-Ca_2SiO_4	Ca_3SiO_5 + CaO	$Ca_3Al_2O_6$ > CaO	$Ca_4Al_2Fe_3O_{10}$
900	β-Ca_2SiO_4 + [CaO]	Ca_3SiO_5 + CaO	$Ca_3Al_2O_6$ + [CaO]	$Ca_4Al_2Fe_3O_{10}$
1000	β-Ca_2SiO_4 + [CaO]	Ca_3SiO_5 + CaO	$Ca_3Al_2O_6$ + [CaO]	$Ca_4Al_2Fe_3O_{10}$
1100	β-Ca_2SiO_4	Ca_3SiO_5 + CaO	$Ca_3Al_2O_6$	$Ca_4Al_2Fe_3O_{10}$
1200	γ-Ca_2SiO_4	Ca_3SiO_5 + CaO	$Ca_3Al_2O_6$	$Ca_4Al_2Fe_3O_{10}$
1300	γ-Ca_2SiO_4	Ca_3SiO_5 + [CaO]	$Ca_3Al_2O_6$	$Ca_4Al_2Fe_3O_{10}$
1400	γ-Ca_2SiO_4			

†( ) indicates optimum PVA content in terms of ratio of cation valences to –(OH) functional groups for lowest crystallization temperature; [ ] indicates much smaller amounts relative to other phases present.

S530, Hitachi, Tokyo, Japan). For the SEM specimens, each powder was completely dried, attached to an aluminum stub, and gold sputter coated.

III. Results and Discussion

The optimum pH values for C_2S and C_3S for forming transparent solutions and stoichiometric powders are listed in Table I. For each of the four components, the binder was completely burned out by 700°C. With respect to the characteristics of the dried precursors, both C_3A and C_4AF resembled an aerogel formed by foaming during the stirring and solution-drying process. The foam mainly resulted from elimination of NO_x gases from the $Al(NO_3)_3$ source.

(1) Crystallization Behavior

Tables II and III summarize the XRD data acquired for each of the four powders for high- and low-DP PVA, respectively. The effect of DP was particularly evident in the 700°C calcining range for C_2S and C_3S. In the high-DP route, the amorphous phase was still present, while, with the low-DP PVA, the calcined powders were crystallized. In the case of single-phase C_3A (>95 vol%), the powder prepared via low-DP PVA crystallized at 1000°C for 1 h. In comparison, 1100°C for 3 h conditions were necessary to crystallize relatively pure C_3A made by the high-DP PVA. C_4AF showed no apparent changes in its crystalline behavior.

The effect of DP of the PVA may be attributed to the following considerations. The low-DP PVA had smaller polymer chain lengths than did the high-DP PVA; therefore, it could make the range of distances between cations in the solution shorter.[5] This is especially important in the synthesis of C_3A and C_3S, because the concentration of Ca^{2+} ions is much higher than that of Al^{3+} or Si^{4+} ions, respectively. This can lead to unreacted CaO phase, even at high temperatures. For the compound to be synthesized at low temperatures, the Ca^{2+} ions and Al^{3+} or Si^{4+} ions must be homogeneously dispersed within a short range, rather than long range, of each other to promote reaction. The chain length of the lower-DP PVA is small enough for this mixing to occur in the steric entrapment mechanism. Furthermore, the higher amount of PVA (4:1 ratio) added to the solution aids in this mixing process. The low-DP PVA distributes the metal ions homogeneously, so that, after binder burnout, the network shrinks, enabling C_3A or C_3S to be formed more readily. The cations are sterically entrapped

Table IV. BET Specific Surface Area of Each Crystallized Compound at Optimum PVA Content

Conditions	C_2S	C_3S	C_3A	C_4AF
High-DP PVA method				
Crystallization temperature (°C)	900	1400	1100	700
Holding time (h)	1	2	3	1
BET specific surface area (m^2/g)	12.9	0.9	2.3	9.1
Low-DP PVA method				
Crystallization temperature (°C)	800	1400	1000	700
Holding time (h)	1	1	1	1
BET specific surface area (m^2/g)	22.1	0.8	4.2	17.1
BET specific surface area (m^2/g) (after attrition milling for 1 h)		50	18.9	

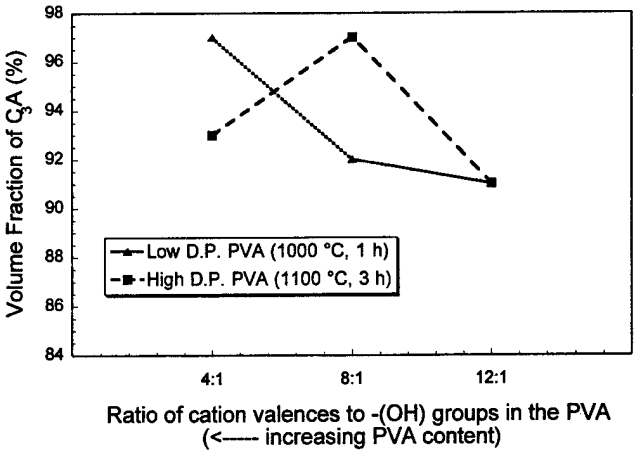


Fig. 2. Volume fraction of C_3A powder synthesized as a function of the ratio of cation valences to –(OH) groups in the PVA polymer.

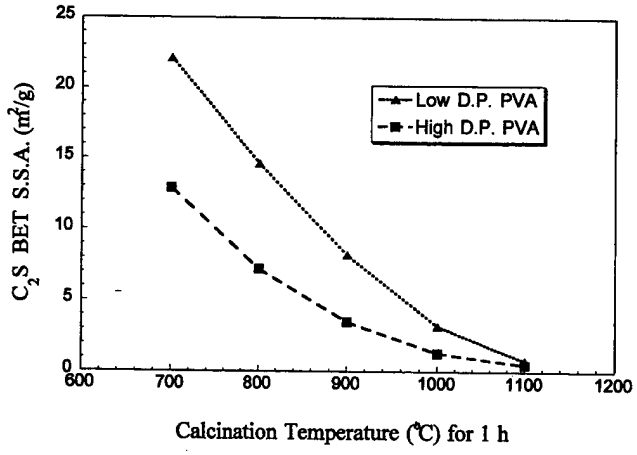


Fig. 3. Decrease in BET specific surface area for C_2S powders with increasing calcining temperature for 1 h holding time at each temperature.

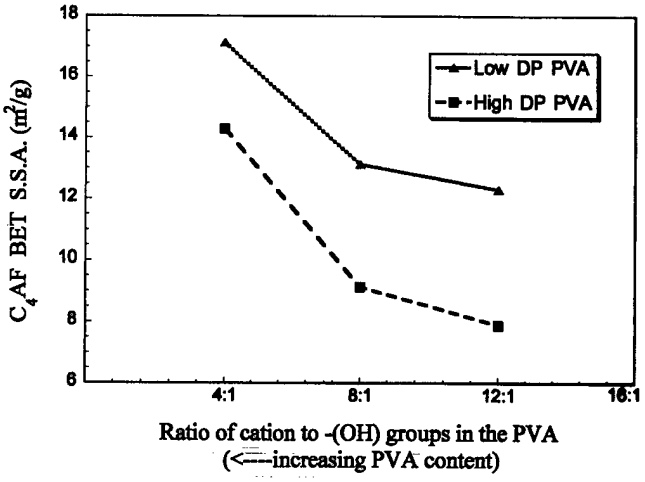


Fig. 4. Variation of BET specific surface areas for C_4AF as a function of the ratio of cation valences to –(OH) groups in the PVA polymer.

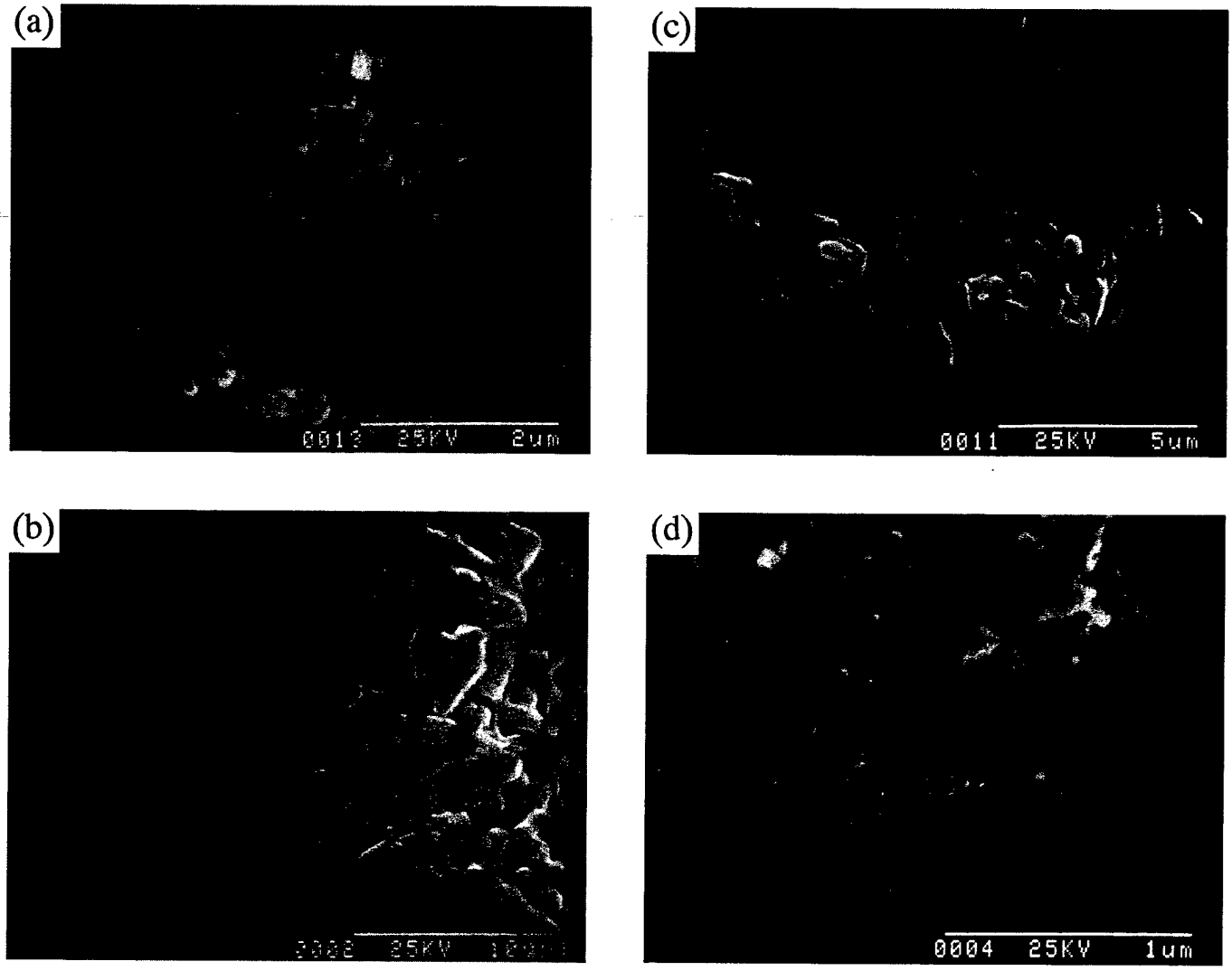


Fig. 5. Morphologies of crystalline powders for the four components of portland cement made by the high degree of polymerization PVA process at optimum PVA content (Table II): (a) C_2S powder as-calcined at 900°C for 1 h, (b) C_3S powder as-calcined at 1400°C for 2 h, (c) C_3A powder as-calcined at 1100°C for 3 h, and (d) C_4AF powder as-calcined at 700°C for 1 h.

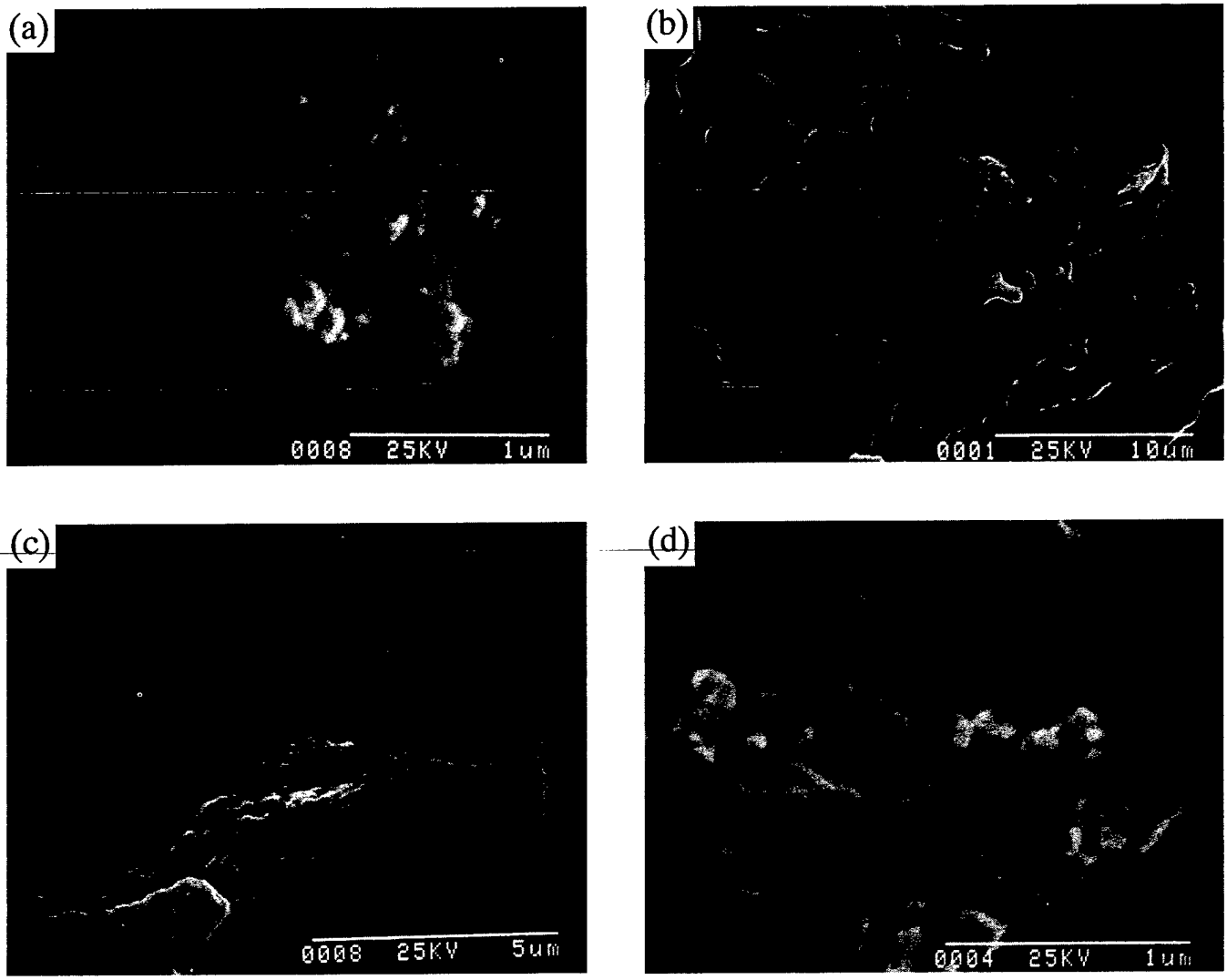


Fig. 6. Morphologies of crystalline powders for the four components of portland cement made by the low-DP PVA process at optimum PVA content (Table III): (a) C_2S powder as-calcined at 800°C for 1 h, (b) C_3S powder as-calcined at 1400°C for 1 h, (c) C_3A powder as-calcined at 1000°C for 1 h, and (d) C_4AF powder as-calcined at 700°C for 1 h.

within short range of each other and form organic precursor complexes.[3,5] Thus, as high a temperature is not required to form the compound.

Figure 2 shows the effect of PVA content on the crystallization of C_3A. The volume fraction of C_3A was determined by comparing the ratio of the integrated area of the 100% intensity peak for CaO with the 100% intensity peak for C_3A. In the low-DP PVA process, the volume fraction of C_3A increased with increased PVA. The best result was obtained with low-DP PVA in a 4:1 ratio. This implies that, in the low-DP PVA system, the higher content of PVA did not make a significant difference in the distance between cations, but rather it improved the homogeneity of the distribution of cations. In the higher-DP PVA system, the 8:1 ratio showed the highest volume fraction of C_3A. This might be attributed to the high-DP PVA chain lengths being longer than the low-DP PVA ones, so that, in the 4:1 case, the cations could not get close enough to one another to form a compound. The solution had a high viscosity with inhomogeneities caused by the entanglements of the long-chain PVA molecules in excess amount. Once this ratio was changed to 8:1, the results improved dramatically, because the metal ions could get close enough to one another to form C_3A.

Because PVA is not an expensive chemical, it may be more economical overall to use more PVA in conjunction with the lower-DP PVA, so as to achieve the best results possible, rather than calcining at 100°C higher and for 2 h longer by using the high-DP PVA. The 12:1 case is the most undesirable for both the low- and high-DP PVA, because there is simply not a high enough PVA content to make a homogeneous mixture. Agglomeration can also occur at the 12:1 PVA ratio, and, hence, the specific surface area is decreased.[5,6]

(2) BET Specific Surface Area

Table IV summarizes the BET specific surface area of each powder at the optimum crystallization conditions that have the lowest crystallization temperature. Except in the case of C_3S, the surface area increases with the use of the low-DP PVA. This may be attributed to lower crystallization and, hence, decreased sintering between particles. The higher the specific surface area, the faster the hydration, which decreases the setting time in cements.[19] Attrition milling for 1 h can also dramatically increase the specific surface area, because of the breaking up of the presintered, coarse, powder agglomerates. By attrition milling, an extra step has been added to the formation of these high-specific-surface-area powders, as well as an extra expense. However, after only 1 h of milling, the surface area is increased by >50 times in the case of C_3S and by >4 times for C_3A. C_3S is known for its ability to hydrate rapidly, to be responsible for the initial set, and to provide early

strength to portland cement.[19] These characteristics are important, because C_3S typically makes up >50% of the material.[19] Therefore, setting time can be decreased by an even greater amount, because C_3S (with a specific surface area of 50 m^2/g) hydrates faster, while providing the same strength to the cement.

A comparison is made between the low- and high-DP PVA, with reference to how the surface area changes with temperature increases. Figure 3 illustrates this behavior for C_2S, as a representative case study for each of the components of portland cement. It shows that, as the calcining temperature increases, the specific surface area decreases. This occurs in the powders made by both the low- and high-DP PVA methods. The powder made with the low-DP PVA exhibits a more negative slope than does the high-DP PVA powder. This implies that the powder made by the low-DP PVA method should have enhanced reactivity, finer particle size, and faster sintering.

Figure 4 shows the effect of PVA content on the BET specific surface area. This experiment was conducted with C_4AF calcined at 700°C, with both the low- and high-DP PVA solutions. The data remained consistent with the results from Fig. 3, in that the low-DP PVA produced powders with higher surface areas. Furthermore, Fig. 4 illustrates that the more PVA used, the higher the surface areas in the powders made from both the low- and high-DP PVA. For systems in which not enough polymer was used, agglomeration could occur. One explanation for this could be that, upon burnout, the agglomerated cation precursors lost most of the organics in the outer region. Because of the intense heat evolved from the oxidative process, organic components remained within the shell. Further application of heat caused the organics to decompose into gases and expand. The less-agglomerated particles lost most or all of the organics with the application of heat. In the case of agglomeration, during the slow decomposition of organics, the agglomerated cations were oxidized. Thus, a large powder particle-size distribution was observed. To maximize powder properties, a balance was, therefore, needed between cations and the amount of polymer.

(3) Powder Morphology

Figures 5 and 6 illustrate the morphologies of crystalline powders calcined at the lowest crystallization temperature for each compound. In the powders prepared by the high-DP PVA method (Fig. 5), particle necking resulting from sintering was observed, except in the C_4AF powder, which crystallized at low temperatures. Presintering resulted from the exceedingly high specific surface area and, hence, enhanced reactivity of the C_3A and C_3S powders, which needed a relatively high crystallization temperature to completely react all the CaO. The C_4AF powder showed a particle size distribution in the range from 50 to 400 nm.

In general, the powders derived from the low-DP PVA were more reactive than powders prepared from the high-DP PVA. For example, in the case of C_3A, the microstructure was more dense with smaller individual particle sizes (Fig. 6(c)), in comparison with the C_3A derived from the high-DP PVA (Fig. 5(c)), despite a lower crystallization temperature for the low-DP PVA method. This suggests that the low-DP PVA method was more effective in making fine and reactive powders than the high-DP PVA method. C_3S prepared from the low-DP PVA showed the same tendency as did the C_3A powder (Figs. 6(b) and 5(b)). The C_2S powder in the low-DP PVA route was crystallized before the onset of sintering. It was possible to retain a small particle size (~100 nm) without particle necking at a low crystallization temperature of 700°C (Figs. 6(a) and 5(a)). Agglomerates ~1.5 μm in size were observed. C_4AF powder derived from the low-DP PVA process exhibited nearly the same result as that obtained from the high-DP PVA system (Figs. 6(d) and 5(d)).

The morphologies of the attritor-milled C_3S and C_3A powders are seen in Fig. 7. Before attrition-milling, C_3S and C_3A powders showed quite a dense morphology because of sintering. However, attritor milling for 1 h was effective in breaking up the porous necked particles. This was clearly demonstrated for the C_3S and C_3A powders (Figs. 5(b) and 7(a) and Figs. 6(c) and 7(b), respectively). In both cases, attritor milling resulted in significant increases in specific surface area (Table IV) and, hence, reactivity.

IV. Conclusion

The four component powders of portland cement have been synthesized by the PVA solution–polymerization route. The length and amount of PVA polymer chains affected the homogeneity and distance between metal ions in the organic/inorganic precursor during the steric entrapment mechanism. More-reactive powders having higher specific surface areas were obtained by a low DP of the PVA. A ratio of 4:1 cation valences to hydroxyl functional groups produced optimum powder characteristics. The low crystallization temperature and high specific surface area of the chemically synthesized powders could economize the process of making specialty portland cement, enhance setting speed, increase strength, and lead to other desirable characteristics. The low specific surface area of the coarse, sintered powder could be improved to a higher specific surface area by an effective attrition-milling process.

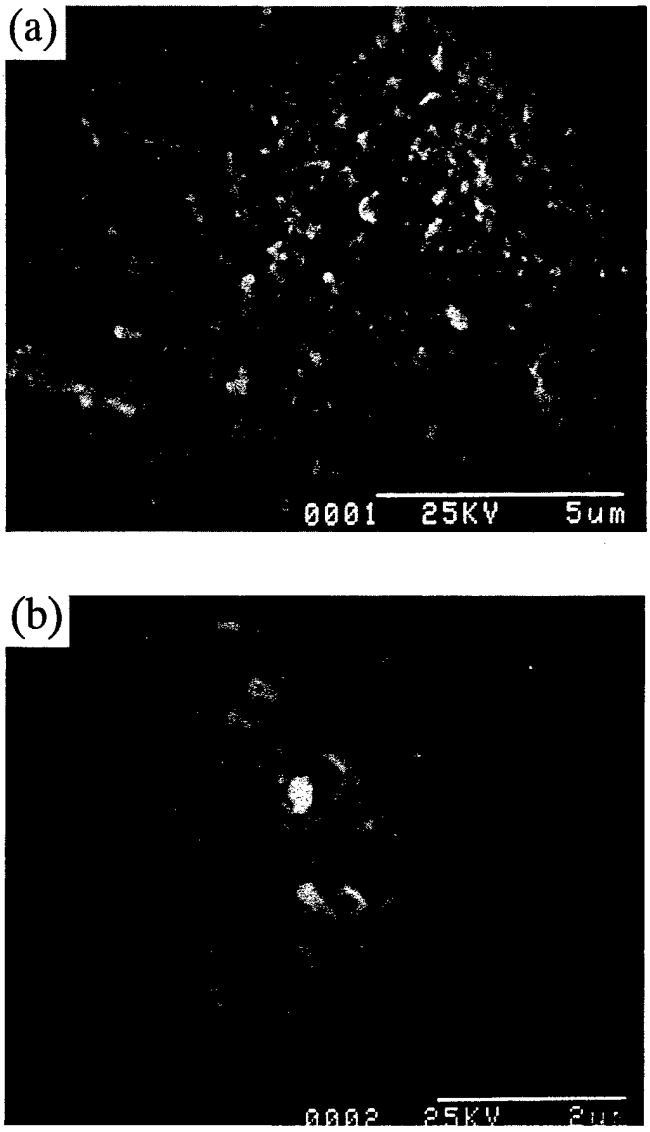


Fig. 7. Micrographs of 1 h attritor-milled crystalline powders for (a) C_3S prepared by the high-DP PVA method and (b) C_3A made by the low-DP PVA method (see also Table IV).

Acknowledgments: Use of the facilities at the Center for Advanced Cement-Based Materials at University of Illinois at Urbana-Champaign is acknowledged.

References

[1]P. Praminik and A. Pathak, "A New Chemical Route for the Preparation of Fine Particles of Mixed Oxide Systems," *Mater. Sci. Bull.*, **17** [6] 967–75 (1994).

[2]M. A. Gülgün and W. M. Kriven, "A Simple Solution–Polymerization Route for Oxide Powder Synthesis"; pp. 57–66 in Ceramic Transactions, Vol. 62, *Science, Technology, and Commercialization of Powder Synthesis and Shape Forming*. Edited by J. J. Kingsley, C. H. Schilling, and J. H. Adair. American Ceramic Society, Westerville, OH, 1995.

[3]M. A. Gülgün, M. H. Nguyen, and W. M. Kriven, "Polymerized Organic–Inorganic Synthesis of Mixed Oxides," *J. Am. Ceram. Soc.*, **82**, [3] 556–60 (1999).

[4]D. A. Fumo, M. R. Morelli, and A. M. Segadaes, "Combustion Synthesis of Calcium Aluminates," *Mater. Res. Bull.*, **31** [10] 1243–55 (1996).

[5]M. H. Nguyen, S. J. Lee, and W. M. Kriven, "Synthesis of Oxide Powders via a Polymeric Steric Entrapment Precursor Route," *J. Mater. Res.*, **14** [8] (1999), in press.

[6]M. H. Nguyen, "A New Polymer Route to the Synthesis of Mixed Oxide Ceramics"; M.S. Thesis. University of Illinois at Urbana-Champaign, IL, 1997.

[7]S. J. Lee and W. M. Kriven, "Crystallization and Densification of Nano-Size, Amorphous Cordierite Powder Prepared by a PVA Solution–Polymerication Route," *J. Am. Ceram. Soc.*, **81** [10] 2605–12 (1998).

[8]I. Nettleship, J. L. Shull, and W. M. Kriven, "Chemical Preparation and Phase Stability of Ca_2SiO_4 and Sr_2SiO_4 Powders," *J. Eur. Ceram. Soc.*, **2**, 291–98 (1993).

[9]D. M. Roy and S. O. Oyfesobi, "Preparation of Very Reactive Ca_2SiO_4 Powder," *J. Am. Ceram. Soc.*, **60**, 178–80 (1997).

[10]P. A. Lessing, "Mixed-Cation Oxide Powders via Polymeric Precursors," *Am. Ceram. Soc. Bull.*, **68** [5] 1002–1007 (1989).

[11]L.-W. Tai, H. U. Anderson, and P. A. Lessing, "Mixed-Cation Oxide Powders via Resin Intermediates Derived from a Water-Soluble Polymer," *J. Am. Ceram. Soc.*, **75** [12] 3490–94 (1992).

[12]M. A. Gülgün, O. O. Popoola, and W. M. Kriven, "Chemical Synthesis and Characterization of Calcium Aluminate Powders," *J. Am. Ceram. Soc.*, **77** [2] 531–39 (1994).

[13]M. Pechini, "Method of Preparing Lead and Alkaline-Earth Titanates and Niobates and Coating Method Using the Same to Form a Capacitor," U.S. Pat. No., 3 330 697, July 11, 1967.

[14]D. Budd and D. A. Payne, "Preparation of Strontium Titanate Ceramics and Internal Boundary Layer Capacitors by the Pechini Method," *Mater. Res. Soc. Symp. Proc.*, **32**, 239 (1984).

[15]L.-W. Tai and P. A. Lessing, "Modified Resin-Intermediate Processing of Perovskite Powders: Part I. Optimization of Polymeric Precursors," *J. Mater. Res.*, **7** [2] 502–10 (1992).

[16]D. Kralj, B. Matkovic, R. Taylor, J. F. Young, and C. J. Chan, "Preparation of Dicalcium Silicate at 950°C," *J. Am. Ceram. Soc.*, **69** [8] C-170–C-172 (1986).

[17]M. Rivera, I. Odler, and S. Abdul-Maula, "Formation of Portland Clinker—Studies on Synthetic Raw Meals," *Adv. Cem. Res.*, **1** [1] 52–57 (1987).

[18]I. Odler and H. Koster, "Investigations on the Structure of Fully Hydrated Portland Cement and Tricalcium Silicate Pastes,' *Cem. Concr. Res.*, **21** [6] 975–82 (1991).

[19]Portland Cement Association, "Portland Cement: Past and Present Characteristics," *Concr. Technol. Today*, **17** [2] 1–4 (1996).

[20]M. V. Munoz, F. G. Garcia, M. G. Rodriguez, M. C. G. Vilchez, and S. Hudson, "Influence of the Mineralogical Composition, Specific Surface Area and Strains," *Cem. Conc. Res.*, **25** [5] 1103–10 (1995). □

Journal of the European Ceramic Society 19 (1999) 2543–2550
© 1999 Elsevier Science Ltd
Printed in Great Britain. All rights reserved
PII: S0955-2219(99)00120-X
0955-2219/99/$ - see front matter

Growth and Crystallization of YAG- and Mullite-composition Glass Fibers

J. K. R. Weber,[a]* B. Cho,[a] A. D. Hixson,[a] J. G. Abadie,[a] P. C. Nordine,[a] W. M. Kriven,[b] B. R. Johnson[b] and D. Zhu[b]

[a]Containerless Research, Inc., 906 University Place, Evanston, IL 60201, USA
[b]Department of Materials Science and Engineering, University of Illinois Urbana-Champaign, Urbana, IL 61801, USA

Abstract

This paper describes a new process to synthesize crystalline oxide fibers for high temperature structural applications. Strong and chemically homogeneous precursor fibers of 5–40 μm diameter were made at rates of up to 1·6 m s^{-1} by glass fiber pulling techniques from undercooled molten oxides. The precursor fibers were heat treated at temperatures up to 1873 K to make crystalline fibers with controlled grain size and properties. Tensile strengths of the precursor fibers were up to 5–6 GPa (900 ksi) for YAG- ($Y_3Al_5O_{12}$) and mullite- ($Al_6Si_2O_{13}$) compositions. Research to optimize fiber compositions and crystallization processes, and to scale up precursor fiber production is discussed. © *1999 Elsevier Science Ltd. All rights reserved.*

Keywords: YAG, glass fibers, fibers, strength, mullite.

1 Introduction

Current technology for fiber synthesis is limited in the composition of materials from which fibers can be formed, the quality and diameters of the fibers that can be obtained, and the compatibility with coating and matrix materials that may be used in composites.[1–5] The relatively high cost of oxide fibers available for composite materials also makes research and development very expensive.[6]

It was recently shown that glass fibers can be drawn from molten oxides which are deeply undercooled to increase the melt viscosity.[7,8] By working with deeply undercooled melts, the new technique allows glass fibers to be made from materials which form 'fragile' liquids and have very low viscosity — less than 0·1 Pa s — at temperatures close to the equilibrium melting point.[9,10] Oxides of interest for high temperature structural applications such as mullite[7] ($Al_6Si_2O_{13}$) and yttrium aluminum garnet or YAG[8] ($Y_3Al_5O_{12}$) can be drawn into glass fibers in this way. Also, the high mutual solubility of many molten oxides would allow a uniform distribution of dopants or additives to be incorporated in the fibers.

Results presented later show that crystallization of mullite- and YAG-composition glass begins to occur at approximately 1200 K when the glass is heated at a rate of 2·5 K min^{-1}. The temperature at the onset of crystallization increases about 20 K when the heating rate is increased to 40 K min^{-1}. Containerless processing experiments on molten oxides achieve deep undercooling and spontaneous crystallization of the metastable liquid at somewhat higher temperatures, leading to crystal growth rates of 5–10 cm s^{-1}.[11] Since the glass fiber heating rate can be increased to several 1000 K s^{-1} by rapidly inserting the fiber into a hot furnace, crystallization can be performed over a wide range of temperatures up to the softening point of the glass fiber. The wide temperature range available for crystallization allowed control of crystal nucleation and growth rates, hence the morphology and properties of the product can be controlled and optimized.

2 Experimental

The approach to synthesis of crystalline oxide fibers comprised two steps: (i) pull glass fibers from the undercooled molten oxides, and (ii) crystallize the glass fibers by heat treatment. Table 1 presents the compositions which were investigated. Materials were synthesized from 99·999% pure elemental oxide powders (Cerac, Inc., Milwaukee, WI),

*To whom correspondence should be addressed. e-mail: weber@containerless.com

Table 1. Compositions of oxide materials investigated in fiber processing research

Aluminium oxide (mol%)	*Yttrium oxide (mol%)*	*Comment*
62·5	37·5	From crushed single crystal and mixed powders
63·5	36·5	From mixed alumina and yttria powder
62·5	36·5	+1 mol% Nd_2O_3
62·5	36·5	+1 mol% Er_2O_3
Aluminum oxide (mol%)	*Silicon dioxide (mol%)*	
60	40	From Kyoritsu mullite
58	42	From mixed alumina and silica powder
62	38	From mixed alumina and silica powder
59	40	+1 mol% Y_2O_3
55	40	+5 mol% Y_2O_3
60	39	+1 mol% TiO_2
60	35	+5 mol% TiO_2
60	39	+1 mol% ZrO_2
60	35	+5 mol% ZrO_2

Kyoritsu mullite[12] ($Al_6Si_2O_{13}$) or crushed single crystal YAG ($Y_3Al_5O_{12}$). Powder mixtures were formed into spheroids by laser hearth melting.[13] Effects of substituting cations in the mullite and YAG compositions were also investigated.

2.1 Formation of undercooled melts

In order to obtain the viscosity required to support fiber pulling, the molten oxides were undercooled below the liquidus temperature. Nucleation of the undercooled liquid was avoided by using containerless melting in an Aero-Acoustic Levitator[14] or Conical Nozzle Levitator[15] which completely eliminated contact with a solid container. In this way, the liquids could be deeply undercooled and/or cooled to form glass by reducing the heating power.

Preliminary levitation, melting and cooling experiments were performed to establish conditions under which specimens formed glass. Glass formation showed that a large increase in viscosity occurred below the melting point and that conditions which permit fiber pulling could be achieved. Material was levitated in pure argon, oxygen, or air and heated with a continuous-wave CO_2 laser beam. An automatic optical pyrometer measured the apparent temperature of the specimen at rates up to 100 Hz. Rapid cooling of the liquid was obtained by blocking the laser heating beam, and either glass formation or nucleation of crystalline materials were observed as the liquid cooled. The heat released upon nucleation and rapid crystallization of the liquid produced a rapid temperature rise (recalescence) followed by cooling of the solid material. Glass formation resulted in smooth cooling to room temperature without any discontinuity in the measured temperatures.

2.2 Fiber synthesis

The apparatus and procedure used to make most of the fibers from levitated melts is described in Ref. 8. The levitated samples were completely melted and the heating laser beam was blocked so that the drop undercooled. Fibers were pulled from the drop by rapidly introducing and withdrawing a 100 μm diameter tungsten wire stinger at a preselected temperature. Fiber pulling was performed under transient cooling conditions at pulling rates of 50–160 cm s^{-1}. Batches of 10–20 fibers up to 50 cm in length were pulled from each composition.

2.3 Crystallization

X-ray diffraction analysis confirmed that the bulk glass synthesized in the containerless experiments and the as-pulled fibers were free of detectable crystalline phases. Differential thermal analysis (DTA) experiments were performed on crushed bulk glass at heating rates from 2·5 to 40 K s^{-1} in a Netzsch STA 409 Simultaneous Thermal Analyzer.

Bulk glasses were formed from pure mullite compositions and with substituted titanium, yttrium or zirconium. The glass was annealed at 1473 K for 3 h and examined by X-ray diffraction.

Fibers were crystallized by heat treatment at temperatures above the onset temperature for crystallization and below the melting point of the crystalline solid. All of the heat treatment experiments were performed in air. Two heat treatment methods were used.

In the first method, several fibers were placed in a furnace at ambient temperature and heated at a rate of about 10 K min^{-1} to preselected maximum temperatures of 1273–1473 K. The fibers were held at the process temperature for periods of 1–4 h, and then cooled at a rate of approximately 20 K min^{-1}.

In the second method, fibers were mounted on a ceramic lance and rapidly heated by inserting the lance into a tube furnace which was preheated to temperatures of 1373–1873 K. The fibers were held in the furnace for 5–30 s and then rapidly removed and cooled to ambient temperature.

2.4 Characterization

The as-pulled glass fibers were first inspected with a 5× hand lens and their length was measured. In identifying the optimum temperature range and pulling rate for each composition, some fibers were formed that showed defects, variations in fiber diameter, and opaque regions. These fibers were not evaluated further.

Long fiber sections which showed no visible defects were identified using a video microscope

inspection technique. Fibers were mounted on a computer-controlled translation stage and scanned under the field of view of the 175× microscope. A video record of the image was reviewed to select sections of the fiber for property testing and crystallization experiments.

The strength of uniform-diameter glass fibers was measured using a fixture developed for high-modulus, single-filament materials. The fiber diameters were 5–40 μm and the gauge length was fixed at 23 mm, 580–4600 times the fiber diameter. Tests were performed in an Instron 1205 tensile testing machine equipped with a high sensitivity load cell and operated under computer control. Tensile tests were performed using a cross-head speed of 5 μm s^{-1}. Diameter measurements were obtained with an optical microscope prior to tensile testing.

Bend tests were performed on the crystalline fibers to determine the minimum bend radii at which fracture occurred.

Transmission electron microscopy (TEM) was used to examine selected fibers. A new technique for mounting small cross sections of monofilaments for TEM examination was developed. Specimens were made by bonding several 0·5 mm lengths of fiber into a zirconia disk which had an inside diameter of 140 μm and an outside diameter of 2·5 mm. Fiber sections were placed into the mount and set in epoxy resin. The resulting disks were polished and thinned to approximately 1–2 μm using a tripod polisher and diamond lapping film. Polished disks were mounted on a copper grid and thinned in a Gatan 600 Duo Mill ion mill with a liquid nitrogen cooled stage. TEM analysis was performed in Philips EM420 and CM12 microscopes.

3 Results

The following sections present the results of glass fiber synthesis experiments, characterization of the glass fibers, and investigation of crystallization of the glass fibers.

3.1 Fiber synthesis

Fibers could be pulled from mullite-composition melts in the apparent temperature range from 1600–1750 K, 425–575 K below the mullite liquidus temperature. The longest and best quality fibers were obtained at temperatures of about 1700 K. YAG-composition glass fibers were pulled in the apparent temperature range from 1600–1660 K, approximately 600 K below the equilibrium melting point of YAG.

X-ray diffraction studies of mullite-composition materials containing titanium, yttrium or zirconium showed that crystalline material was formed by annealing bulk glass at 1473 K for 3 h. Compositions containing 1–5 mol% titanium and 1 mol% yttrium or zirconium were single phase, had the mullite structure, and had unit cell dimensions that were slightly larger than the values for high purity mullite. The material with 5 mol% yttrium showed a higher background spectrum indicating the presence of amorphous phases. The material with 5 mol% zirconium contained mullite and zirconium silicate ($ZrSiO_4$).

The following guidelines were established for the fiber pulling process.

1. Material needs to be completely melted so that no residual nuclei remain in the liquid. This can be accomplished by superheating the levitated drops 50–100 K above the liquidus temperature.
2. Molten alumina–silica materials have a greater glass forming tendency in an oxygen atmosphere than in argon.
3. Molten alumina–yttria materials have a greater glass forming tendency in an argon atmosphere than in oxygen.[8]
4. Substitution of up 5 mol% yttrium for aluminum and up to 5 mol% zirconium or 1 mol% titanium for silicon in the mullite composition enhances glass formation and improves the quality of fibers pulled from the undercooled melt.
5. Addition of excess alumina or substitution of neodymium oxide for yttrium oxide in the YAG-composition enhances glass formation and improves the quality of fibers pulled from the undercooled melt.

The influence of dopants was significant at concentrations of 1 mol% and considerable at 5 mol%. Longer and more uniform diameter mullite-composition fibers could be pulled from the melts which contained substituted yttrium. Zirconium substitution decreased the temperature range for fiber pulling and increased the quality of the fibers. Fibers less than 5 cm long were obtained from these compositions. Material with 5 mol% titanium substituted for aluminum produced short and brittle fibers, with large diameter variations, which often fractured when they were bent slightly.

3.2 Glass fiber properties

Process conditions that resulted in defect-free sections of fiber with uniform diameters, smooth surfaces and no visible changes in appearance along the fiber over lengths of 5–30 cm were identified. Even the best fibers had defects near their ends, since the fiber pulling occurred in a transient process in which significant changes in the liquid temperature occurred as the fiber was pulled.

Figure 1 presents video microscope images of mullite- and YAG-composition glass fibers. Test

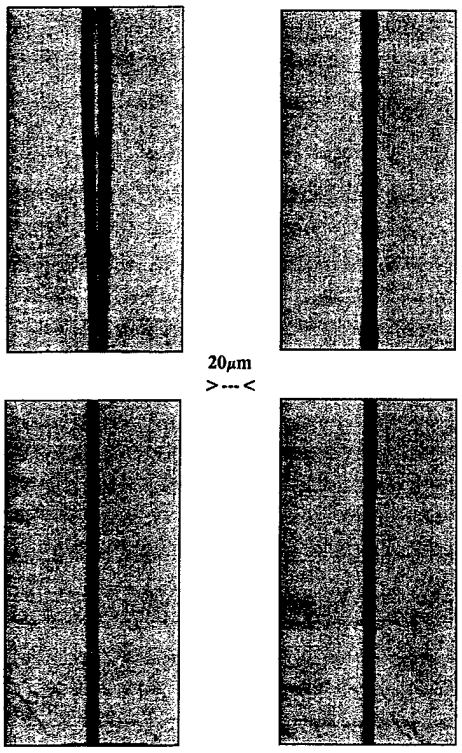


Fig. 1. Video microscope images of glass fibers. Left: mullite-composition; right: YAG-composition with 1 mol% Nd_2O_3 substituted for Y_2O_3. The top figures show characteristic defects. In mullite, regions with smoothly increasing diameter occurred along the length of the fiber. In YAG defects were localized regions where the fiber diameter changed over a distance of a few micrometers. The lower pictures show smooth sections of the fiber with uniform diameters. The scale is marked on the figure.

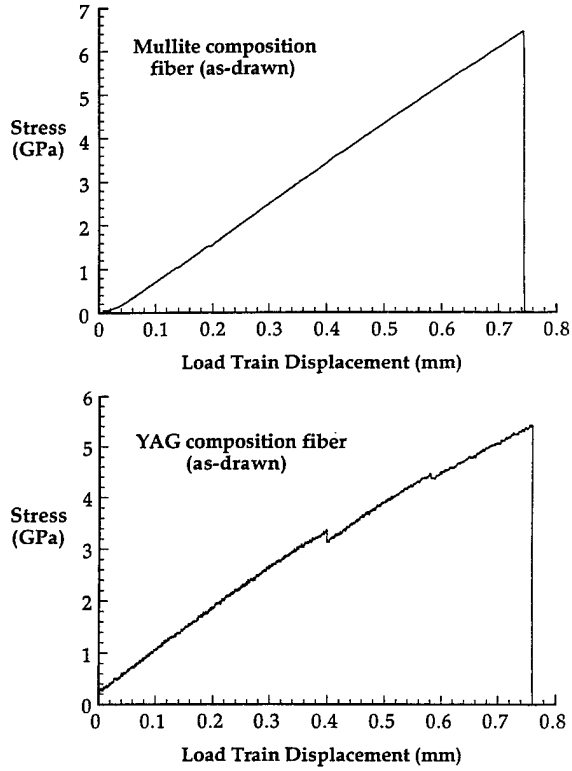


Fig. 2. Typical plots of stress versus load train displacement for selected glass fibers. Above: mullite-composition; below YAG-composition with 1 mol% neodymia substituted for yttria.

specimens were cut from uniform-diameter sections of the fibers for mechanical property testing, crystallization experiments and examination by SEM.

Figure 2 presents selected stress versus elongation plots for the glass fibers. The measurements recorded total cross-head displacement, including the load-train compliance and any movement between the fiber and the mounting, so that modulus cannot be derived from the results. Average tensile fracture strengths were $5{\cdot}6 \pm 0{\cdot}7$ GPa for the mullite-composition glass fibers and $5{\cdot}0 \pm 0{\cdot}3$ GPa for the YAG-composition fibers (with 1 mol% neodymia substituted for yttria). Both YAG- and mullite-composition glass fibers had reproducible mechanical properties. Smooth and uniform diameter mullite-composition glass fibers occasionally fractured at a stress on the order of 2 GPa. Slight movement of the fiber in the mount resulted in 'steps' in the stress-elongation plot for some fibers — see Fig. 2 for example.

3.3 Transmission electron microscopy

Figures 3 and 4 show TEM images from a mullite-composition fiber which had a tensile fracture strength of about 2 GPa, considerably less than the $5{\cdot}6 \pm 0{\cdot}7$ GPa which was obtained on other fibers. Figure 3(A) and 3(B) show regions of the fiber which contained crystallites (the dark areas) which were in the diffracting condition. The crystallites were equiaxed, had dimensions on the order of 20–50 nm, and were distributed throughout the fiber section. Figure 4(A) shows a crystallite which is approximately 75 nm across, Fig. 4(B) is the corresponding convergent beam electron diffraction pattern from this region. The diffraction pattern confirms that crystalline regions were present in the fiber. Additional TEM analysis using selected area diffraction confirmed that the crystalline material was mullite.

3.4 Crystallization

The DTA experiments performed at the slowest heating rates of 2·5 K min^{-1} indicated the onset of bulk glass crystallization at approximately 1233 K for mullite-composition glass and at 1188 K for YAG-composition glass. The data showed that the onset temperature increased with the heating rate and the rate of crystallization increased with temperature.

Rates of crystallization of the undercooled melt determined by observing recalescence were 3·5–15 cm s^{-1} at apparent temperatures of 1500–1800 K for the mullite composition and 1·4–6 cm s^{-1} at

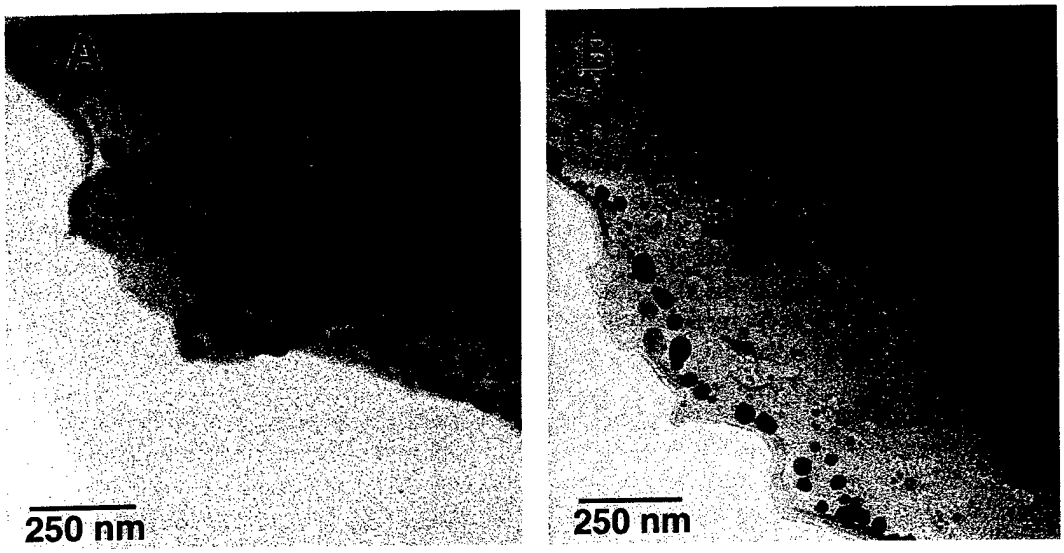


Fig. 3. (A) and (B) Bright field TEM images of an as-drawn mullite-composition glass fiber which fractured at low tensile stress. The dark areas are crystallites which were present in the fiber section.

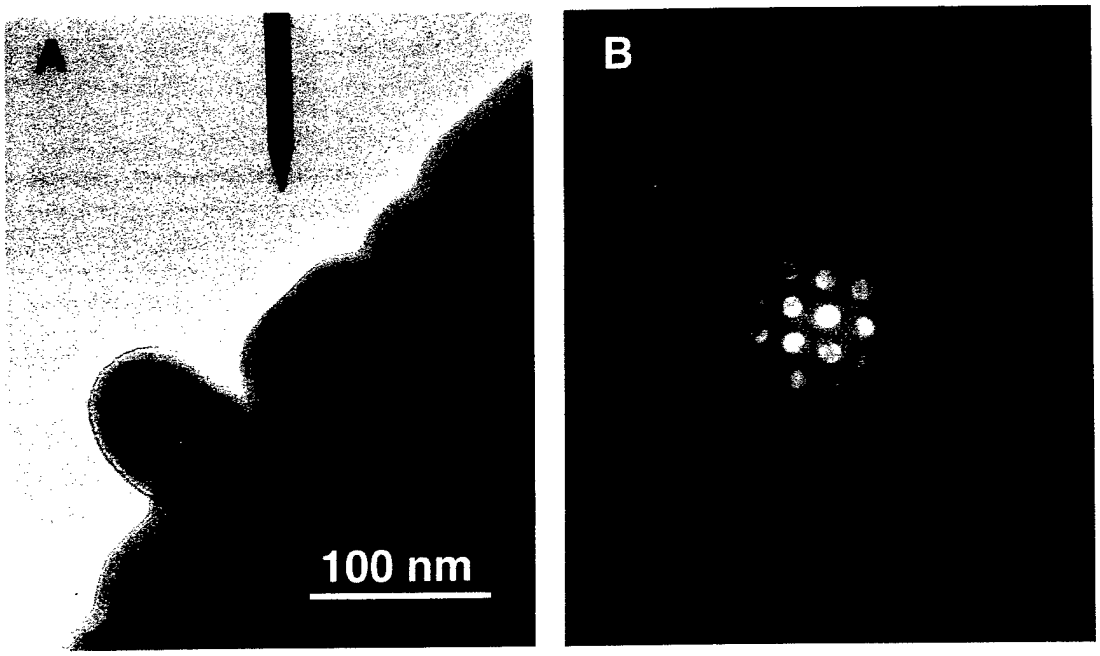


Fig. 4. (A) Bright field image of section containing a crystallite; (B) convergent beam electron diffraction image of the crystallized region.

1400–1900 K for molten YAG. The experiments with undercooled melts also demonstrated that nucleation of crystals occurs at a negligible rate in the melt at apparent temperatures above 1500 K for the mullite composition and above 1400 K for the YAG-composition.

The SEM micrographs in Figs. 5 and 6 show fibers crystallized under rapid heating conditions. Figure 5 shows longitudinal views of YAG and mullite fibers after rapid heating of the glass fibers to 1573 and 1873 K for 30 s. Figure 4 is of etched sections of mullite fibers crystallized by rapid heating to 1373 and 1673 K for 30 s followed by cooling to ambient temperature in air. The figures indicate that the grain size was rather large for the crystalline YAG fibers, on the order of 5–10 μm. Porosity is also visible in the YAG fibers. The mullite-composition glass fibers crystallized to produce dense crystalline material with grain sizes in the range 0·5–1 μm.

3.5 Properties of crystalline fibers

Crystallization of the glass fibers produced stresses that resulted in curved crystalline fibers. Some of the fibers were curled with several bends of variable radius from 2–10 mm, these were not tested.

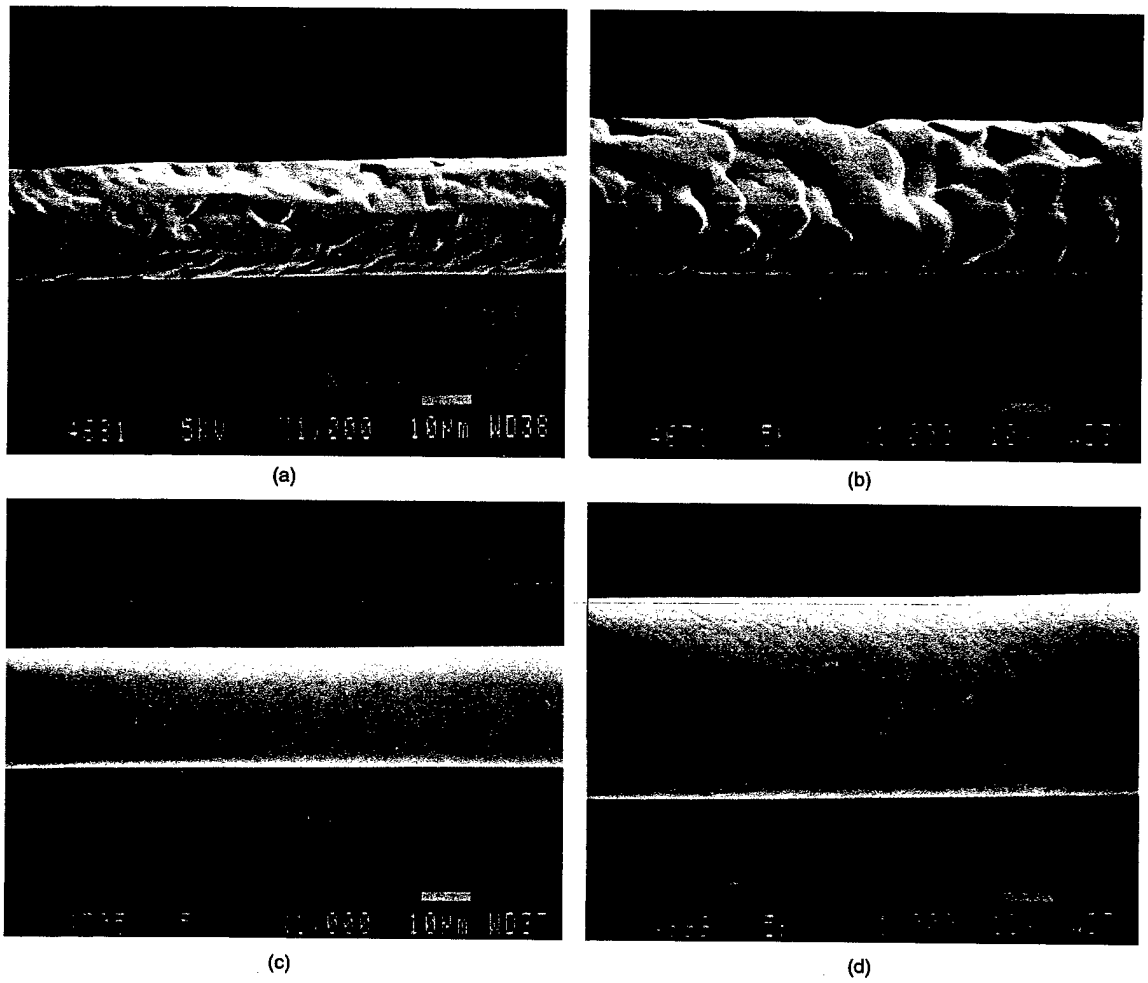


Fig. 5. SEM pictures of longitudinal views of YAG (top) and mullite (bottom) composition fibers which were crystallized by rapid heating to (left) 1573 K and (right) 1873 K and soaking for 30 s.

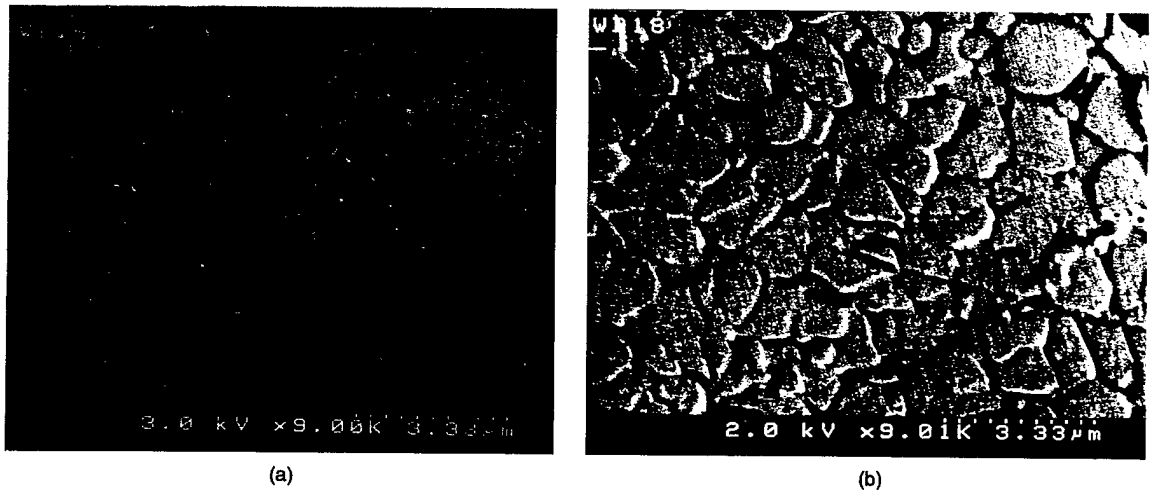


Fig. 6. SEM images of etched cross-sections of mullite fibers processed at (left) 1623 K and (right) 1873 K for 30 s.

Reproducible tensile testing of the crystallized fibers was not possible with the Instron tensile testing machine.

The tensile strength of crystallized mullite fibers was estimated by bending the fibers between the anvils of a vernier caliper. Short sections of crystallized fiber could be bent to a radius of approximately 2 mm. The minimum radius to which a fiber bent without fracture was used to calculate the tensile strain in the outer part of the curved region.

Thus for a fiber of 10 μm radius, a minimum bend radius of 2 mm corresponds to a strain of 0·5%. Using a modulus of elasticity of 360 GPa for mullite,[16] a tensile strength of 1·8 GPa is deduced.

4 Discussion

The intrinsic properties of crystalline oxides present many opportunities for application in high temperature technology. The realization of these applications would be enhanced if ceramic materials, including fibers for ceramic–ceramic composites, can be made with properties approaching the intrinsic values.

The glass fibers pulled from undercooled melts have highly reproducible properties and can be formed at high rates. The fiber pulling process creates uniform property fibers with smooth surfaces which are defined by surface tension of the liquid acting in the region where the fiber is drawn from the molten liquid. The fibers contain minimal flaws and exhibit high and reproducible values of the tensile fracture strength. TEM analysis of glass fibers which had high tensile strength indicated that they were free from crystallinity.[7] TEM analysis of mullite-composition glass fibers with decreased mechanical properties revealed that they contained nanocrystalline regions. The process by which nanocrystals are formed in some of the fibers has not been identified.

The fiber making process also allows selected additives and dopants to be added to the fibers and control of fiber diameter through changes in the fiber pulling conditions. These fibers are thus considered to be suitable precursors for investigating the production of ceramic oxide fibers by controlled crystallization of the glass.

The results demonstrate that high mechanical properties can be achieved in short sections of the crystalline fibers, as seen in the elongation results from bend tests. X-ray diffraction analysis of crystallized glass indicated that at least 1 mol% of cations can be substituted in the mullite crystal lattice and that they change the lattice parameter. Continuing work is emphasizing the study of dopant effects and control of the thermal processing on the microstructure and properties of the crystalline fibers.

The extremely rapid heat transfer that occurs from a hot ambient gas to the thin fibers allows heating rates of several thousand K s^{-1} when a fiber is inserted into a furnace. Since the levitated liquids can be formed into bulk glass at cooling rates of a few hundred K s^{-1}, it appears that the glass fibers can be heated to high temperature without nucleating crystals during the heating step. This observation explains the grain sizes observed in fibers that were rapidly heated to crystallize at high temperatures. The grain size increases with temperature, indicating that growth was enhanced relative to nucleation at the higher process temperatures.

5 Conclusions

The process of forming glass fibers from undercooled melts greatly expands the range of materials which can be made into fibers. The glass fibers have high strength, reproducible properties, and can be produced with a uniform distribution of additives. The fiber making process is inherently fast and potentially inexpensive and it can provide a source of materials for high temperature structural applications. Ongoing research is directed to scale up glass fiber production and optimize the fiber crystallization process.

Acknowledgements

This research was supported by the US Air Force Office of Scientific Research under an STTR and the US National Science Foundation. Work at University of Illinois at Urbana-Champaign (UIUC) was also supported by the AASERT Program. TEM was performed at the Center for Microanalysis of Materials in the Materials Research Laboratory at the UIUC. Earlier experiments on undercooled melts were supported by NASA. SEM photographs of rapidly crystallized fibers were taken by B.C. as part of his senior year project in Materials Science at Northwestern University under the direction of Professor Vinayak Dravid. We thank Mr William Jellison for assistance in the research.

References

1. Loewenstein, K. L., *The Manufacturing Technology of Continuous Glass Fibers*, 3rd ed. Elsevier, Amsterdam, 1993.
2. Pollock, J. T. A., Filamentary sapphire. *J. Mat. Sci.*, 1979, **7**, 787–792.
3. Haggerty, J. S., Menashi, W. P. and Wenckus, J. F., Apparatus for forming refractory fibers. US Patent 4,012,213, March 1977.
4. Sayir, A. and Farmer, S. C., Directionally solidified mullite fibers. *MRS Symp. Proc.*, 1995, **365**, 11–20.
5. Richards, E. A., Goodbrake, C. J. and Sowman, H. Z. G., Reactions and microstructure development in mullite fibers. *J. Am. Ceram. Soc.*, 1991, **74**, 2404–2409.
6. National Material Advisory Board. *Ceramic Fibers and Coatings—Advanced Materials for the Twenty-first Century*. (NMAB-494). National Academy Press, Washington, DC, 1998.
7. Kriven, W. M., Jilavi, M. H., Zhu, D., Weber, J. K. R., Cho, B., Felten, J. J. and Nordine, P. C., Synthesis and microstructure of mullite fibers grown from deeply

undercooled melts. In *Ceramic Microstructure Control at the Atomic Level*, ed. A. P. Tomsia and A. Glaeser. Plenum, New York, 1996, pp. 169–176.
8. Weber, J. K. R., Felten, J. J., Cho, B. and Nordine, P. C., Glass fibers of pure and erbium or neodymium-doped yttria-alumina compositions. *Nature*, 1998, **393**, 769–771.
9. Angell, C. A., Formation of glasses from liquids and biopolymers. *Science*, 1995, **267**, 1924–1935.
10. Debenedetti, P. G., *Metastable Liquids*. Princeton University Press, Princeton, New Jersey, 1997.
11. Weber, J. K. R., Anderson, C. D., Krishnan, S. and Nordine, P. C., Solidification behavior of undercooled liquid aluminum oxide. *J. Am. Ceram. Soc.*, 1995, **78**, 577–582.
12. Mizuno, M. and Saito, H., Preparation of highly pure fine mullite powder. *J. Am. Ceram. Soc.*, 1989, **72**, 377–382.
13. Weber, J. K. R., Felten, J. J. and Nordine, P. C., New method for high purity ceramic synthesis. *Rev. Sci. Instrum*, 1996, **67**, 522–524.
14. Weber, J. K. R., Hampton, D. S., Merkley, D. R., Rey, C. A., Zatarski, M. M. and Nordine, P. C., Aero-acoustic levitation—a method for containerless liquid-phase processing at high temperatures. *Rev. Sci. Instrum*, 1994, **65**, 456–465.
15. Weber, J. K. R. and Nordine, P. C., Containerless liquid-phase processing at high temperatures. *Microgravity Science and Technology*, 1995, **VII**, 279–282.
16. Kriven, W. M., Palko, J. W., Sinogeikin, S., Bass, J. D., Sayir, A., Brunauer, G., Boysen, H., Frey, F. and Schneider, J. High temperature single crystal properties of mullite ($3Al_2O_3{\cdot}2SiO_2$). *J. Eur. Ceram. Soc.*, 1999, **19**(13–14), this issue.

Journal of the European Ceramic Society 19 (1999) 2529–2541
© 1999 Elsevier Science Ltd
Printed in Great Britain. All rights reserved
PII: S0955-2219(99)00124-7
0955-2219/99/$ - see front matter

High Temperature Single Crystal Properties of Mullite

W. M. Kriven,[a*] J. W. Palko,[a] S. Sinogeikin,[b] J. D. Bass,[b] A. Sayir,[c] G. Brunauer,[d] H. Boysen,[d] F. Frey[d] and J. Schneider[d]

[a]Department of Materials Science and Engineering, University of Illinois at Urbana-Champaign, Urbana, IL, USA
[b]Department of Geology, University of Illinois at Urbana-Champaign, Urbana, IL, USA
[c]NASA Glenn Research Center, Cleveland, OH, USA
[d]Institut für Kristallographie und Angewandte Mineralogie, Ludwig Maximilians Universität, München, Germany

Abstract

Extensive neutron diffraction and Rietveld studies of dense, hot pressed mullite ($3Al_2O_3{\cdot}2SiO_2$) have been conducted up to 1650 °C in air, yielding a complete set of lattice parameters and axial thermal expansion coefficients. Unconstrained powders of the same stoichiometric composition were also analyzed by X-ray diffraction and Rietveld techniques up to 900 °C in air, from which lattice parameters and thermal expansion coefficients were obtained. An earlier reported structural discontinuity was confirmed by XRD to lie in the temperature range 425 to 450 °C. Single-crystalline mullite fibers of composition $2{\cdot}5Al_2O_3{\cdot}SiO_2$ were grown from the melt by a laser-heated, float zone method. A partial set of the single-crystal elastic moduli were determined from various sections of fiber, by Brillouin spectroscopy, from room temperature up to 1400 °C. They indicated a roughly 10% reduction in stiffness over that temperature range. © *1999 Elsevier Science Ltd. All rights reserved.*

Keywords: elastic modulus, fibers, X-ray methods, thermal expansion, mullite.

1 Introduction

In the design of oxidation resistant, high temperature ceramic composites, it is wise to know the intrinsic properties of the component materials, independent of their structural configuration in the composite. Detailed theoretical predictions of composite behavior, particularly at elevated temperatures, would rely heavily on a knowledge of single crystal properties. Furthermore, since the fabrication and mechanical evaluation of composites is a difficult, time consuming and costly procedure, any data on the intrinsic properties of a component material is extremely valuable in accelerating the design, modelling and development of high temperature composites.

Mullite, of nominal composition ($3Al_2O_3{\cdot}2SiO_2$), is a highly attractive candidate for oxide composites.[1] As a matrix it is a widespread 'workhorse' refractory material, having very good creep resistance and chemical stability up to 1600 °C. The current, widely accepted phase diagram indicates that the equilibrium phase grown by solid state reaction has a narrow solid solution range around the $3Al_2O_3{\cdot}2SiO_2$ (abbreviated 3:2) composition.[2] However, when grown from the melt, mullite crystallizes in $2Al_2O_3{\cdot}SiO_2$ or 2:1 composition.[2] The solid solution range can further be extended to $3Al_2O_3{\cdot}SiO_2$ or 3:1 composition by rapid cooling in a closed container, in the absence of alumina nuclei.[2,3]

Currently, steady progress is being made in the production of mullite fibers. Directionally solidified mullite fibers can be grown by a laser heated, float-zone method.[4] They appear to consist of columns of single crystals with [c] axes parallel to the fiber direction. Polycrystalline mullite–alumina fibers (Nextel 720, from 3M Company, St. Paul, MN) have also been fabricated by a sol–gel process from an 85 wt Al_2O_3–15 wt. SiO_2 composition, which subsequently converts on firing at 1350 °C to 59 vol% mullite and 41 vol% Al_2O_3.[5] The microstructure is extremely fine grained with ~0·5 μm mullite grains containing < 100 nm largely intragranular alumina grains. This microstructure is unstable above 1300 °C however, due to grain growth and drastic loss of mechanical strength from an initial 2·4 MPa.[6,7] More recently, homogeneous, aluminosilicate, glass fibers (of mullite composition) and amorphous yttrium aluminate fibers (of $Y_3Al_5O_{12}$ or 'YAG' composition) have been pulled from deeply undercooled melts via a

*To whom correspondence should be addressed. Fax: +1-217-333-2736.

containerless processing technique.[8,9] The high tensile strengths of the aluminosilicate glass fibers (~6 GPa) however, are again drastically reduced to 1 GPa at best, due to uncontrolled random crystallization to mullite or YAG, on annealing above 1100 °C. Work is therefore in progress to develop textured or single crystal fibers from the amorphous solid precursors.

1.1 Crystallographic measurements

Measurements of the thermal expansion of various mullite compositions are mainly reported for temperatures up to 900 °C and are either based on dilatometric measurements or on X-ray diffraction.[10–14] For higher temperatures reliable data are rare.[13] It has to be kept in mind that the former, i.e. the dilatometric method provides results which are always of both structural and microstructural origin and therefore, an average, which is hard to interpret on an atomic length scale. X-ray diffraction allows, at least in principle, a separation of both aspects via an evaluation of the positions of the reflections in a diffraction pattern and by a line profile analysis. The X-ray method has its limits if the sample material is coarse grained, which is sometimes unavoidable, and because of absorption effects. In particular in the high temperature regime around and above 1000 °C, the X-ray diffraction method becomes additionally tedious for experimental reasons.

An alternative diffraction method uses neutrons. In the case of mullite neutron diffraction, results are not affected by absorption and the relatively large sample volume allows for good statistics, even in the case of coarse grained samples. Moreover, the oxygens have a relatively high scattering power for neutrons so that oxygen related structural details can be studied in oxide compounds more reliably. We performed in-situ neutron diffraction experiments with the 3:2 mullite described above up to a temperature of 1650 °C. The overall aim of the investigation was a full structure refinement of mullite at high temperatures. Only the thermal expansion results of neutron diffraction measurements will be given here, since full information will be published in a forthcoming paper.[15]

1.2 Elastic constant measurements

1.2.1 Bulk properties

The bulk elastic properties of mullite have been measured on sintered compacts of relatively pure, raw materials.[16,17] More recent work on hot pressed stoichiometric 3:2 mullite, which was hydrothermally grown without any glassy phase, indicated an unusual decrease in Poisson's ratio with increasing temperature up to room temperature.[18] This was attributed to the incommensurate modulation in the mullite crystal structure. Early high temperature measurements[16] of relatively pure raw materials indicate a drop in elastic modulus for both 3:2 and 2:1 mullite above 600 °C, strongly suggesting the presence of intergranular glass. With the availability of highly textured, polycrystalline fibers,[4] it was decided to measure the elastic moduli of mullite up to temperatures of 1400 °C.

1.2.2 Single crystal properties

The complete elasticity tensor can be measured by the Brillouin light scattering technique.[19] This technique presents several advantages over other methods, the most important being that only very small samples are required, no contact is needed with the sample, and it is suitable for low-symmetry crystals. The sample size is limited only by the spot size of the laser used as the excitation source, making Brillouin scattering well-suited for measurements on the thin mullite fibers used in this study. Also, only optical access to the sample is required for Brillouin measurements, which allows much flexibility in furnace design.

Brillouin scattering involves the inelastic scattering of light from phonons in a crystal. If V is the velocity of the phonon, ϕ and ϕ' are the incident and scattered angles, respectively, and ν and ν' are the frequencies of the incident and scattered photons, respectively, then the equation relating phonon velocity to the frequency shift of the scattered photon, $\Delta\nu = \nu' - \nu$, is

$$V = \left(\frac{\Delta\nu}{\nu}\right)\left(\frac{c}{2n\sin\phi}\right) \tag{1}$$

for the case of symmetric scattering where ϕ and ϕ' are very nearly equal. c is the speed of light in vacuum and n is the refractive index for the direction of photon propagation. In this experiment we use a 'platelet geometry',[20] which allows $n\sin\phi$ to be replaced by $n_o\sin\theta_o$, where n_o is the index of the surrounding medium, and θ_o the incidence angle of the laser light. Platelet geometry allows access to all phonon directions in the plane of the sample.

The velocities of acoustic phonons are determined entirely by the elastic moduli and density of the material. The velocity in eqn (1) for plane monochromatic waves must satisfy Christoffel's equation [eqn (2)].[21]

$$\left|C_{iklm}q_iq_m - \rho V^2\delta_{kl}\right| = 0 \tag{2}$$

where q_i and q_m are unit vectors in the phonon propagation direction, ρ is the density, and C_{ijkl} is the elastic tensor.

1.3 Objective

In anticipation of the successful growth of single crystal or aligned textured fibers of mullite, the work described here was undertaken. The goal of a mullite matrix reinforced with mullite fibers coated by a suitable debonding oxide interphase would be well served by a precise knowledge of crystallographic lattice parameters as a function of temperature up to 1600 °C, as well as axial and volumetric thermal expansion coefficients. These data would enable the residual stresses arising during high temperature cycling to be estimated. Since dense mullite composites could be used as shingles to line an aircraft combustion chamber, for example, (Ref. 22 and H. Schneider, German Aerospace Center, pers. comm.) the thermal expansion of dense, hot pressed, polycrystalline mullite samples were measured, rather than of loose powders, as is customary in crystallographic measurements by X-ray or neutron diffraction. In addition, 3:2 mullite powder would be studied by X-ray diffraction up to 900 °C, and the data would be analyzed by Rietveld methods.

To complement the crystallographic data, and enable better modelling of the high temperature behavior of a mullite-containing composite, single crystal elastic moduli for orthorhombic mullite would be determined experimentally. Brillouin spectroscopic measurements would be made both at room temperature, and up to 1400 °C. Information gathered from this work would then indicate the feasibility and limits of using mullite fiber-reinforced composites in a load-bearing structural application, at high temperature in an oxidizing environment.

2 Experimental Procedures

2.1 Sample fabrication

For diffraction studies, hydrothermally grown, stoichiometric 3:2 mullite powder (Kyoritsu Ceramic Materials Co. Ltd., Tsukisan-cho 2-41, Minato-ku, Nagoya 455-91, Japan) was used as a starting material. For X-ray diffractometry, the powder of average particle size 0·3 μm was inserted into 0·3 mm diameter quartz capillaries which were kept in rotation during the measurements at all temperatures to reduce preferred orientation effects. For neutron diffraction, a polycrystalline mullite ceramic specimen was prepared by hot pressing to full density under vacuum, at 1600 °C and 34 MPa for 1 h, in a 3 inch bore graphite die with graphite spacers and plungers.[18,23]

For elastic constant measurements, mullite fibers of ~500 μm diameter were grown from starting compositions close to the 3:2 composition from high purity CERAC® pure (99·99% pure, 325 mesh) polycrystalline alumina powder (Ceralox Corp., Tucson, AZ 08576) and 99·99% pure SiO_2 from Alpha Products. The extruded mixture was made into a feeder rod in a laser heated, floating zone apparatus which was a fully automated, computer-controlled fiber processing facility at the NASA Glenn Research Center. The fiber pulling technique is fully described elsewhere.[4]

2.2 X-ray diffractometry

The X-ray powder diffraction experiments were performed on a focussing STOE-STADIP diffractometer equipped with a curved Ge(111) monochromator to produce strictly monochromatic Mo$K\alpha_1$ radiation. Data were collected using an overlapping stepscan mode of a linear position sensitive detector of about 5° acceptance angle and 0·02° channel width yielding 1500 data points in the 2θ-range from 5·5 to 35·5°. Each scan was repeated four times to monitor the stability of the intensity and the scans were then added together for better averaging. The resulting minimum half-width was 0·09° in 2θ. For measurements at elevated temperatures the computer controlled STOE furnace 0·65·1 was employed. The heating element consists of a current heated graphite tube holding the sample capillary vertically to the scattering plane. Bores in the graphite tube permitted unobstructed pathways for both the primary beam as well as for the scattered radiation. The temperature measured by a thermocouple in the graphite tube was kept constant to within 0·2°.

2.3 Neutron diffraction

The experiments were carried out at the powder diffractometer MANI at the FRM reactor facility in Munich and at the instrument D2B of the HFR/ILL in Grenoble. The diffraction patterns were recorded with a wavelength of 0·1594 nm. A mirror furnace was used which operated at ambient conditions in air. The neutron mirror furnace is based on light focussed by two rotational ellipsoids.[24] Two different experiments were carried out. The first one started with a 0·8×1×1 cm^3 sample cut from freshly hot pressed material which had a dark color. Due to a malfunction of the temperature control system at about 1100 °C, the heating procedure was interrupted. After the break, the heating sequence was continued up to 1650 °C. As a by-product we observed a colour change of the sample from dark to white. In the second experiment the 'same' (white, i.e. non-pristine) sample was used. Here an uninterrupted heating (room temperature to 1650 °C) and cooling cycle down to 650 °C was employed.

2.4 Elastic constants measurements

Three platelet-shaped samples were cut from a single mullite fiber produced by the laser-heated float zone method.[4] The platelets were ground nominally parallel to (010), (100), and (001) planes. The former two were oriented lengthwise with respect to the fiber, whereas the later was a cross section.

An Ar^+ laser at a power of < 200 mW was used for ambient temperature measurements. At high temperature, up to 400 mW were used to maximize the Brillouin signal, since sample heating was not a concern. Light scattered at 90° from the incident beam, was analyzed by a 6 pass, tandem Fabry–Perot interferometer and photomultiplier tube (PMT).[25] Figure 1 shows a representative spectrum in which Stokes and anti-Stokes Brillouin peaks occur symmetrically about the strong Rayleigh peak. The peaks labeled 'ghost' are the adjacent orders of Rayleigh scattered light which are reduced in amplitude by $> 10^3$ by the tandem interferometer. The distance from the Rayleigh peak to the Brillouin peaks is taken to be the frequency shift for that mode.

A set of elastic constants were obtained by a least-squares procedure which minimized misfit between measured velocities and those calculated from the elastic constants.[26] For the high temperature measurements, elastic moduli were calculated directly from Christoffel's equation[21] using the average velocity for each temperature and direction.

3 Results

3.1 X-ray diffraction

Rietveld refinement was performed for all data sets to extract the temperature dependence of the cell dimensions. The refinement was performed in space group *Pbam*, and published room temperature atom coordinates[27] were used as starting values. The resulting cell dimensions and the corresponding cell volumes are given in Table 1 and are shown Fig. 2(a)–(d). About 2 wt% of Al_2O_3 was detected as a minority phase, which could be neglected for the purpose of a cell parameter Rietveld refinement.

The cell dimensions of our X-ray data compared very well with previous data[14] obtained by the Guinier technique. Our cell parameters *b* and *c* deviated only by about 1 to 2 estimated standard deviations (e.s.d.s), whereas *a* deviated by about 6 e.s.d.s. The discontinuities of cell parameters *a* and *b* between 400°C and 500°C seen by Schneider *et al.*[14] were also found with this sample. The temperature range for the discontinuity could be narrowed down to between 425 and 450 °C. The discontinuity of *a* was found to be more pronounced than that of *b*, which was again in good agreement with previous literature.[14] All cell dimensions showed a marked lower thermal expansion between room temperature and 100 °C. Neglecting the (small) discontinuities around 435 °C, a linear thermal expansion may be fitted to the data from 100 up to 700 °C (presented in Table 2).

Above 700 °C, both *a* and *b* displayed a marked increase in thermal expansion and *c* showed a discontinuity. Cooling down from 900 °C to room temperature, both *a* and *b* adopted higher cell dimensions whereas *c* had a lower cell dimension, as compared to the values before the high temperature cycle.

3.2 Neutron diffraction

The measured data were analysed by the Rietveld technique using an extended version[28] of the program of Thomas and Bendall.[29] This meant that complete structure refinements were carried out for

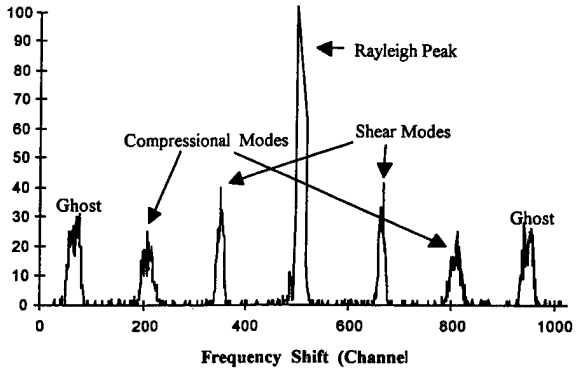


Fig. 1. A typical Brillouin spectrum, depicting the main Rayleigh peak symmetrically surrounded by Stokes and anti-Stokes peaks. The 'ghost' peaks are adjacent orders of Rayleigh scattered light which have been reduced by $> 10^3$ by the tandem Fabry–Perot interferometer.

Table 1. Cell dimensions of 3:2 Kyoritsu mullite powder as determined by X-ray diffraction and Rietvald analysis

Temperature (°C)	*a(Å)*	*b(Å)*	*c(Å)*	*Volume (Å³)*
29	7·5501(8)	7·6894(8)	2·8837	167·41
100	7·75506	7·6913	2·8845	167.51
200	7·5530	7·6958(9)	2·8858	167·74
300	7·5559	7·6995	2·8872	167·97
400	7·5579	7·7045	2·886	168·20
425	7·75588	7·7056	2·8889	168·27
450	7·5600(9)	7·7061	2·8893(3)	168·33(4)
475	7·5605	7·7073	2·8895	168·38
500	7·5613	7·7087	2·8898	168·44
600	7·5649(10)	7·7126(10)	2·8912	168·68
700	7·5668	7·7167	2·8927	168·91
800	7·5703	7·7221	2·8945	169·21
900	7·5742	7·7295(11)	2·8958	169·53
29	7·5508	7·6914	2·8830	167·43

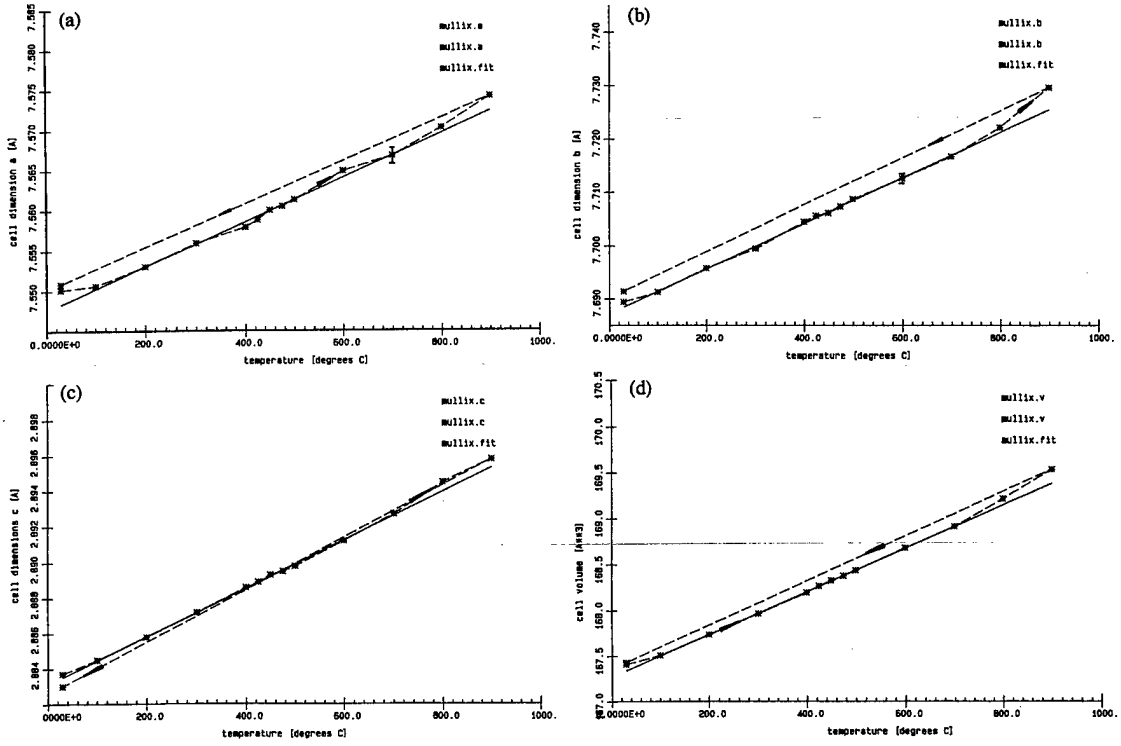


Fig. 2. Cell dimensions measured up to 900 °C by X-ray diffraction and Rietveld analysis, of stoichiometric $3Al_2O_3{\cdot}2SiO_2$ mullite powder. (a) *a*, (b) *b*, (c) *c*, (d) unit cell volume.

Table 2. Linear thermal expansion coefficients and volume expansion of 3:2 Kyoritsu mullite powder as determined by X-ray diffraction and Rietvald analysis

Cell dimensions (Å)	*Linear thermal expansion α (10⁻⁶/K) (100–700°C)*
a	3·7(2)
b	5·5(2)
c	4·7(2)
Volume = $1{\cdot}4(1)\times10^{-5}$ Å^3	

each temperature point. The refinements were carried out within the orthorhombic space group *Pbam*. It is beyond the scope of this paper to discuss the structural changes in any detail. These are the subject of the forthcoming paper.[15] The lattice constants comprised three out of 48 refinable parameters which showed, as usual, only small correlations with the set of remaining structural parameters, such as atomic positions, fractional site occupations and atomic displacement parameters, as well as instrumental parameters related to the shape of the reflections.

Results for the lattice constants are given in Tables 3 and 4, and are shown in Fig. 3(a)–(d) as a function of temperature. The lines are only a guide to the eyes and refer to the different parts of the experiment as explained in the experimental procedures (Section 2.3). The agreement factors (precisely, the weighted profile R-factors R_{wp}) between observed and fitted data were around 12%, while the goodness-of-fit values ranged between 1·2 and 1·8. Fig. 3(d) shows the behaviour of the cell volume which is simply given by the product of *a*, *b*, and *c* in the orthorhombic crystal system. From these lattice parameters, the thermal expansion coefficients may be evaluated. In our case of the point group *mmm*, we had only three independent coefficients $\alpha_{ii}(i = 1, 2, 3)$ which may be evaluated from a, b, c by $\alpha_{11} = \frac{\Delta\alpha}{(\alpha\Delta T)}$, $\alpha_{22} = \frac{\Delta\beta}{(\beta\Delta T)}$, $\alpha_{33} = \frac{\Delta c}{(c\Delta T)}$, where T denotes the temperature. These values are included in Table 3. An average lattice expansion coefficient is defined by $\alpha = \frac{(\alpha_{11}+\alpha_{22}+\alpha_{33})}{3}$ and may be compared with values determined by macroscopic methods. One should keep in mind that here *a* is a structure-related coefficient and not affected by microstructural effects which are governed by the grain-microstructure in the sample. However, structural disorder, for example, produced by vacancies, do affect the α_{ii} or α. These remarks need to be considered when comparing published data for the thermal expansion of mullite.

3.3 Elastic constants determination

Optical microscopy of the laser heated, float zone mullite fibers[4] indicated a 'bamboo-like' columnar structure with a slightly elliptical cross section,

Table 3. (a) Lattice parameters a, b, c, thermal expansion coefficients α_{ii}, and the average thermal expansion $\alpha = (\alpha_{11} + \alpha_{22} + \alpha_{33})/3$ for hot pressed, as-received (grey) 3:2 mullite, as determined by neutron diffraction

Temperature (°K)	*a (Å)*	α_{11} *(10^{-6} K^{-1})*	*b (Å)*	α_{22} *(10^{-6} K^{-1})*	*c (Å)*	α_{33} *(10^{-6} K^{-1})*	α *(10^{-6} K^{-1})*
298	7·54350(9)	4·05	7·69404(8)	5·65	2·8841(4)	5·70	5·13
723	7·55654(9)	8·14	7·71365(8)	12·41	2·89116(4)	9·81	10·12
923	7·56887(11)	2·09	7·73285(11)	1·00	2·89685(4)	3·09	2·06
1023	7·57045(8)	6·86	7·73362(8)	9·73	2·89774(3)	8·34	8·31
1123	7·57565(9)	6·12	7·74115(9)	8·55	2·90019(4)	7·87	7·51
1173	7·57796(11)	6·25	7·74446(11)	8·49	2·90133(4)	9·00	7·91
1223	7·58033(11)	6·89	7·74775(11)	9·48	2·90264(4)	9·26	8·54
1273	7·58295(10)	6·34	7·75156(9)	10·16	2·90398(4)	7·41	7·97
1373	7·58776(12)		7·75944(11)		2·90613(5)		
(b) Corresponding data after cooling to room temperature and continued heating of air-annealed, (white) 3:2 mullite specimen							
923	7·56337(29)	4·45	7·71767(25)	6·14	2·89381(10)	5·63	5·80
1373	7·57854(25)	4·47	7·73904(23)	6·48	2·90115(9)	5·86	5·60
1473	7·58193(27)	4·59	7·74406(24)	6·47	2·90285(9)	5·40	5·49
1573	7·58541(29)	4·44	7·74907(26)	6·34	2·90442(10)	4·92	5·29
1673	7·58878(23)	5·83	7·75399(20)	9·50	2·90585(8)	6·50	7·28
1773	7·59320(15)	4·83	7·76137(13)	7·45	2·90774(5)	5·49	5·92
1823	7·59504(34)	12·33	7·76426(30)	13·13	2·90854(11)	10·14	11·87
1873	7·59973(22)	3·60	7·76936(20)	10·54	2·91002(7)	3·95	6·03
1923	7·60109(42)		7·77346(38)		2·91059(14)		

Table 4. Neutron diffraction data after second heating of hot pressed, air-annealed (white) 3:2 Kyoritsu mullite specimen

Temperature (°K)	*a (Å)*	*b (Å)*	*c (Å)*
298	7·54736(13)	7·69337(12)	2·88481(5)
723	7·55767(14)	7·70975(12)	2·89021(5)
923	7·56341(14)	7·71862(13)	2·893127(5)
1273	7·57392(15)	7·73401(14)	2·89833(5)
1573	7·58386(12)	7·74743(11)	2·90361(4)
1723	7·58963(18)	7·75566(16)	2·90619(6)
1773	7·59028(19)	7·75657(17)	2·90656(6)
1823	7·59353(20)	7·76253(18)	2·90804(7)
1873	7·59682(23)	7·76810(20)	2·90937(8)
1923	7·60026(25)	7·77305(22)	2·91057(8)
1823	7·59239(21)	7·76147(19)	2·90764(7)
1773	7·58933(20)	7·75694(17)	2·90645(7)
1573	7·58085(17)	7·74428(15)	2·90238(6)
923	7·56138(14)	7·71624(12)	2·89307(5)

reminiscent of an egg shape, with a facet at the bottom of the vertical 'egg'. The fiber was for the most part optically clear, with occasional white streaks across its width, consisting of bubbles or occlusions. These white streaks often coincided with joins of the 'bamboo segments'. The fiber showed uniform extinction along its length under cross polarized light, regardless of rotation about this axis. Extinction was less uniform in cross section, indicating that the fiber was somewhat polycrystalline. Separate X-ray diffraction measurements taken on a four circle diffractometer verified that the fiber consisted of multiple crystallites oriented in very nearly the same direction along the fiber axis. The X-ray data showed that the c axis was virtually coincident with the fiber axis for all the constituent crystallites. However the crystallites had slightly varying rotations about the c axis. All the crystallites lay within 5° of each other, where of those, the majority lay within 2° of each other. Lattice parameters for the sample were calculated by fitting the major peak for each reflection (Table 5). The calculated unit cell angles deviated slightly from 90° due to the small peaks close by, but this deviation was ignored in the calculation of cell volume.

Compositional analysis was made by wavelength dispersive spectroscopy (WDS) in an electron microprobe, and it indicated a mullite composition of $2{\cdot}5Al_2O_3{\cdot}SiO_2$, with a standard deviation of $\pm 0{\cdot}10$ in the molar ratio.

Using the formula $Al_{4+2x}Si_{2-2x}O_{10-x}$ from literature[30] for unit cell composition yielded an average theoretical density of $3{\cdot}10\,g\,cm^3$ at room temperature, which lay between the 2:1 and 3:1 compositional extremes. The densities for high temperature were determined from thermal expansions calculated with a quadratic curve fit to the relative cell volume as measured by neutron diffraction presented in Section 3.2 above, using only the aged sample data.

Figures 4(a)–(c) show the ambient temperature velocities measured for the (010), (100), and (001) platelets, respectively, and velocities calculated from the fitted elastic moduli. Rotation of the sample with respect to its crystal axes was determined by optical extinction under cross-polarized light. The elastic moduli obtained are listed in Table 6. They are considered to be accurate to

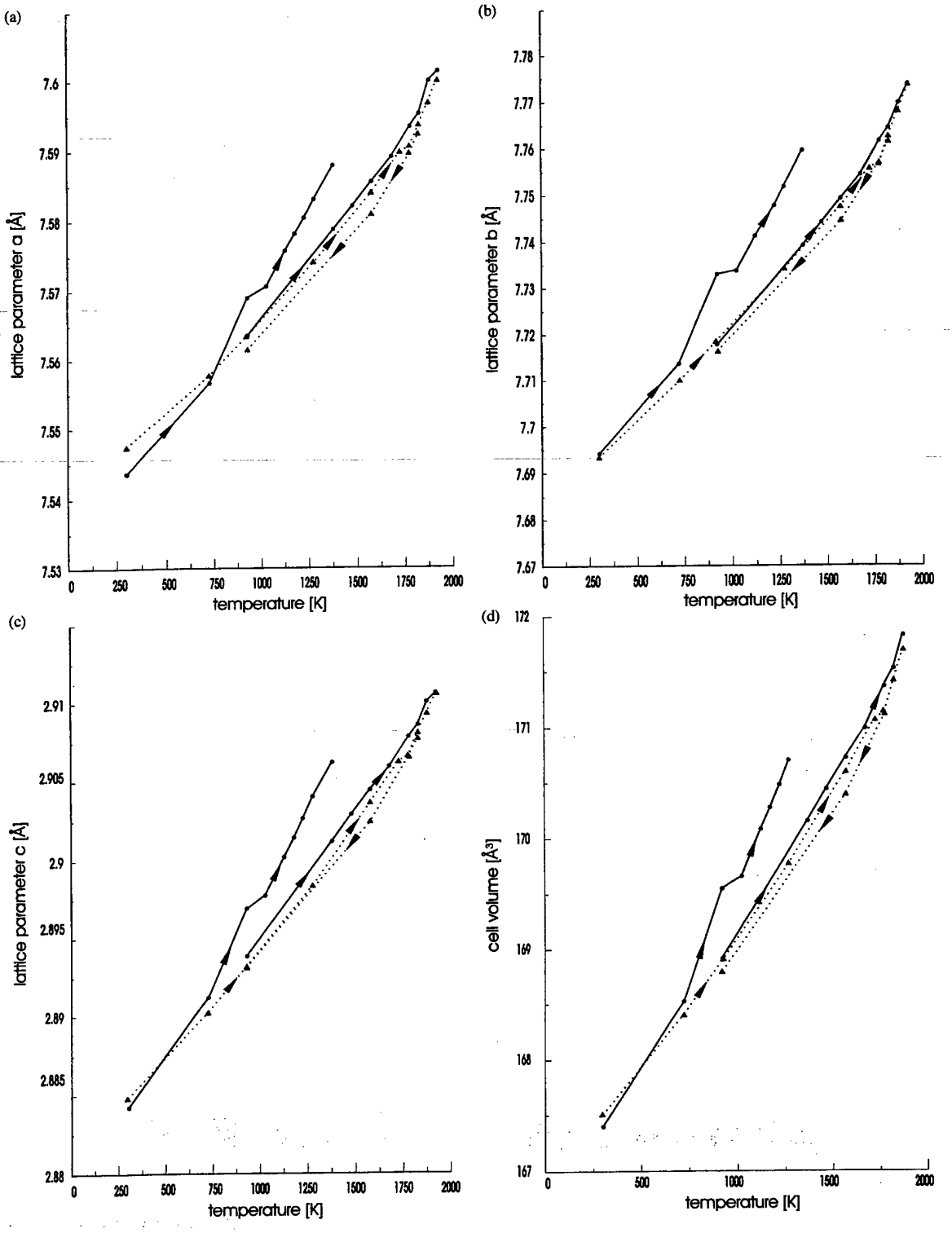


Fig. 3. Lattice parameters *a,b,c* and cell volume ($=a\times b\times c$) of mullite [(a) to (d), respectively], as a function of temperature. Full circles relate to the first experiment on grey mullite, triangles to the second experiment on annealed white mullite. Error bars are smaller than the symbols. The uncertainty of temperature was about ± 10 K. Solid and dotted lines are only guides to the eyes.

within ± 3% which accounts for uncertainty in the calculated density, as well as possible misorientation of the crystals.

Velocity measurements were made along two directions in both the *a–c* and *b–c* crystallographic planes up to 1400 °C, in increments of 200 °C [Fig. 5(a) and (b)]. In these preliminary experiments, nominal temperatures are cited as read directly from the furnace temperature controller. However, even an error of 20°C yields an ~0·2% error in the

Table 5. Lattice parameters measured by X-ray diffractometry for mullite fiber grown by the laser-heated, float-zone method

a (Å)	7·58(1)
b (Å)	7·68(1)
c (Å)	2·90(1)
Cell volume (Å^3)	169(1)
Theoretical density (g cm^{-3})	3·10

Cij's. The moduli C_{11}, C_{33}, C_{44}, and C_{55} were calculated for each temperature [Figs. 6(a) and (b)].

The orientation of the sample at high temperature in a given crystallographic plane was determined from the longitudinal to shear velocity ratio $\left(\frac{V_l}{V_s}\right)$. Uncertainties in sample orientation and the thermal expansion increased the error of the high temperature elastic constants. At this point it is difficult to assign a formal uncertainty to the high temperature measurements due to the sparse preliminary data set, but current measurements in progress will allow a more rigorous assessment in the high temperature moduli.[31]

4 Discussions

4.1 X-ray diffraction

The fact that our data also showed the discontinuities of the lattice parameters a and b around 425 °C supports the general validity of this effect in mullite. Explanations were given in terms of the complex dependencies between thermal expansion and structural arrangement of mullite and the related phases andalusite and sillimanite. A relation to domains originating from oxygen vacancies was also discussed by Schneider *et al.*[14] The somewhat larger deviation of our cell parameter a may be related to the fact that this cell direction seems to be more sensitive to sample dependent variations, possibly oxygen vacancies and their related macrostrains. These effects may also be responsible for the heating cycle induced widening and flattening of the unit cell observed with our sample but not with the sample of Schneider *et al.*[14] A full multiphase Rietveld refinement including minority phases will be performed in the future in order to extract more accurate intensities to resolve structural details at the discontinuities mentioned above.

4.2 Neutron diffraction

Figure 3 reveals a striking result in that the behavior of the lattice constants of the pristine (grey) sample material differed appreciably from that of the pre-heated sample. This difference became remarkable at temperatures of about 700 °C. Above this temperature the material exhibited a different, i.e. stronger expansion as compared to the pre-heated sample (see below). This behavior was reflected by all three lattice constants. Note that after the first heating of the sample the colour changed to white. If the hypothesis is correct that the dark colour (of the pristine material) were due to a considerable amount of oxygen vacancies, this different expansion behavior would relate to a strongly disordered mullite structure. After annihilation of these vacancies we should then have a 'normal' expansion. This is evidenced by the coincidence of the values measured in two subsequent experiments and further supported by the full structural analysis.[15] Generally the thermal expansion was most pronounced in the b-direction and the lowest values occurred along the a-axis. The mean expansion coefficient (of the non-pristine, grey sample) was around $5{\cdot}5\times10^{-6}$ (K^{-1}) for temperatures up to 1550 °C. Except for the generally different expansion of the fresh (grey) sample, we observed an additional anomaly at around 700 °C. We refrain from further discussion because this observation is based only on one single temperature measurement, and must be supported by further detailed measurements. We do mention it, however, because some 'anomalies' are reported earlier for temperatures matching this temperature regime.[14] A second 'anomaly' might be in the high temperature regime between 1550 and 1600 °C (cf. Fig. 3 and Tables 3 and 4). Once again, this effect must be substantiated by further experiments. Comparing the two different runs with the heated sample there were only small differences, and, if any, a small hysteris on completing a full heating cooling cycle (cf. Fig. 3). We are not completely sure whether these small differences or 'hysteresis' are substantial or not, because we cannot fully exclude aging effects of the sample undergoing one or more heating cycles in air.

4.3 Elastic constants

Because of fiber microstructure, the elastic moduli probably represent an average over numerous crystallites. Since the crystallites have different rotations about their c axes, this effect is most important in the (001) plane. This plane shows relatively low anisotropy in phonon velocity, which is most likely real, since velocities are averaged over a range of orientations less than 5°. The low anisotropy in the (001) plane can be correlated to the crystal structure. Mullite may be considered as cross-linked, (edge-shared) chains of Al^{3+} octahedra and tetrahedral (corner-shared) chains containing alternating Si^{4+} and Al^{3+} cations, running parallel to the c axis.[32] Longitudinal and transverse vibrations polarized in this plane represent deformations of the voids and cross-linking bonds

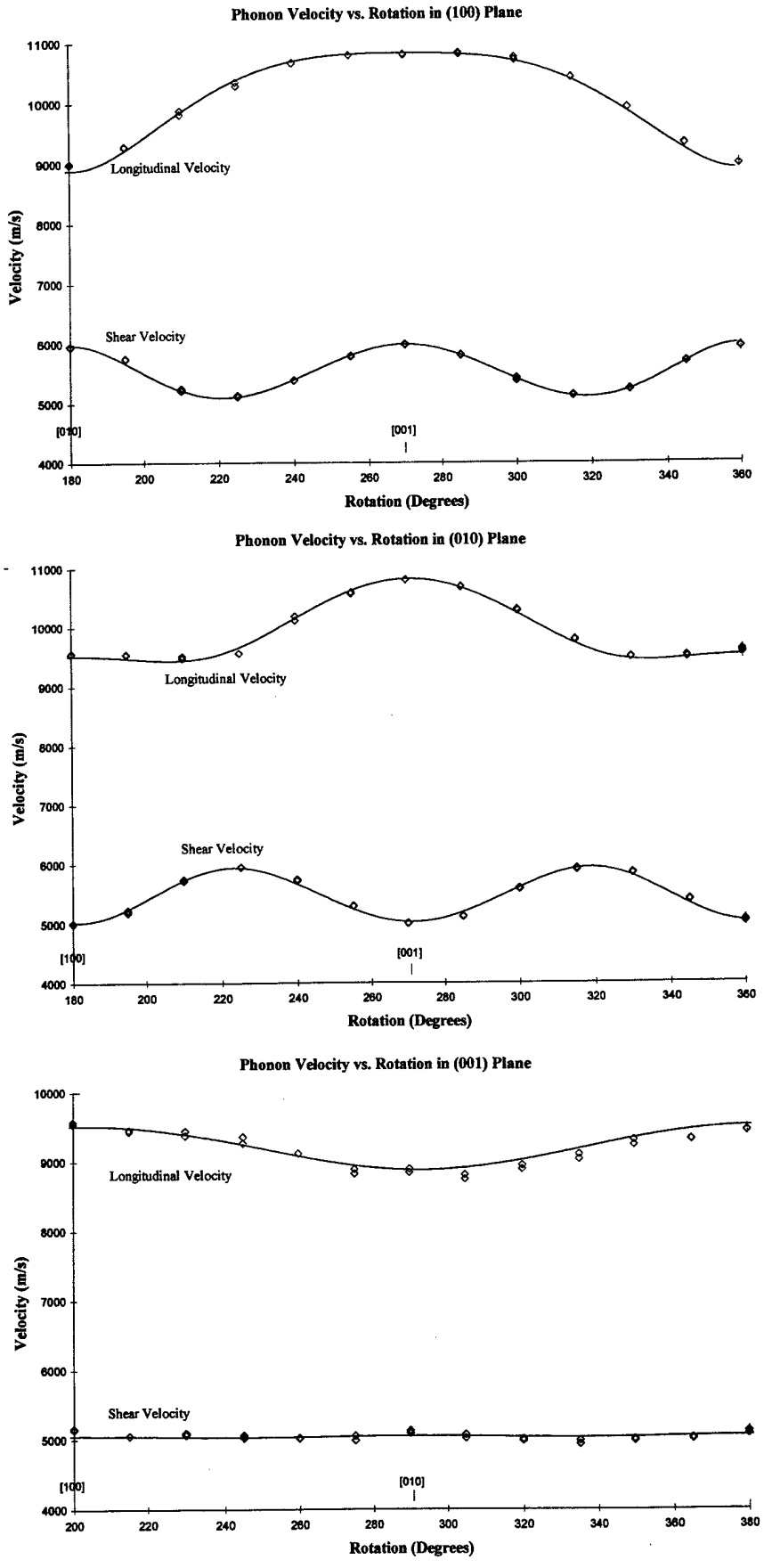


Fig. 4. Measured and fitted phonon velocities of mullite fiber in the (a) (100), (b) (010), and (c) (001) planes.

Table 6. Single crystal, room temperature, elastic moduli of mullite fiber grown by the laser heated, float-zone method

C_{11} (GPa)	280
C_{22} (GPa)	245
C_{33} (GPa)	362
C_{44} (GPa)	111
C_{55} (GPa)	78·1
C_{66} (GPa)	79·0
C_{12} (GPa)	105
C_{13} (GPa)	99·2
C_{23} (GPa)	135

between these chains regardless of directions. In the (100) and (010) planes, the nature of the deformations change from being normal to the polyhedral chains to being parallel to them, as the propagation direction approaches [001] for a longitudinal wave and vice versa for a shear wave polarized in the plane of rotation. This accounts for the higher anisotropy in these planes, since the polyhedral chains are relatively stiff along their length. This is evident from the substantially higher value of C_{33} as compared to C_{11} and C_{22}. Similar correlations have been shown for sillimanite and andalusite[33] which share structural similarities with mullite. The mullite sample measured did not contain a substantial amount of glassy phase as was thought to exist in the impure sample measured in previous work.[16,17] This accounts for the lack of marked decrease in moduli above 600 °C. Further work is in progress to completely specify the elastic tensor of mullite to 1400 °C.[31]

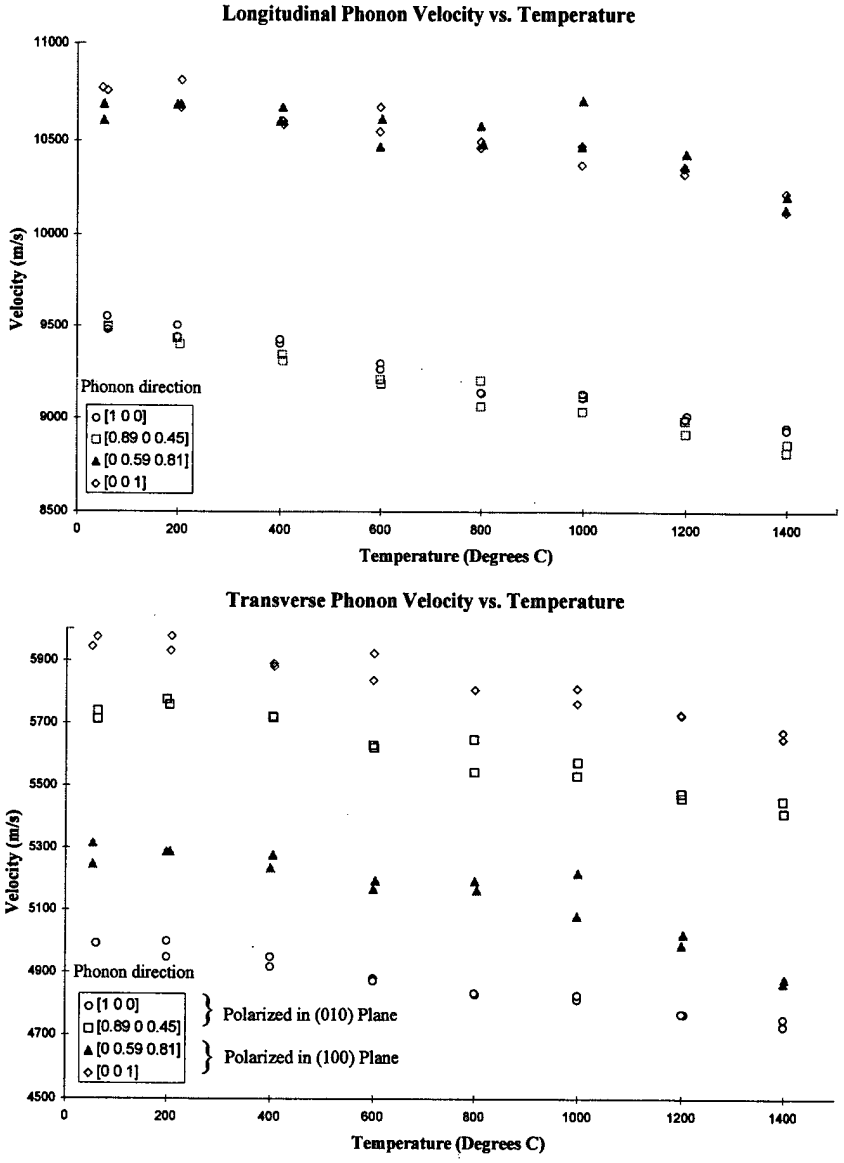


Fig. 5. Measured phonon velocities versus temperature for selected crystallographic directions. (a) longitudinal waves; (b) transverse waves.

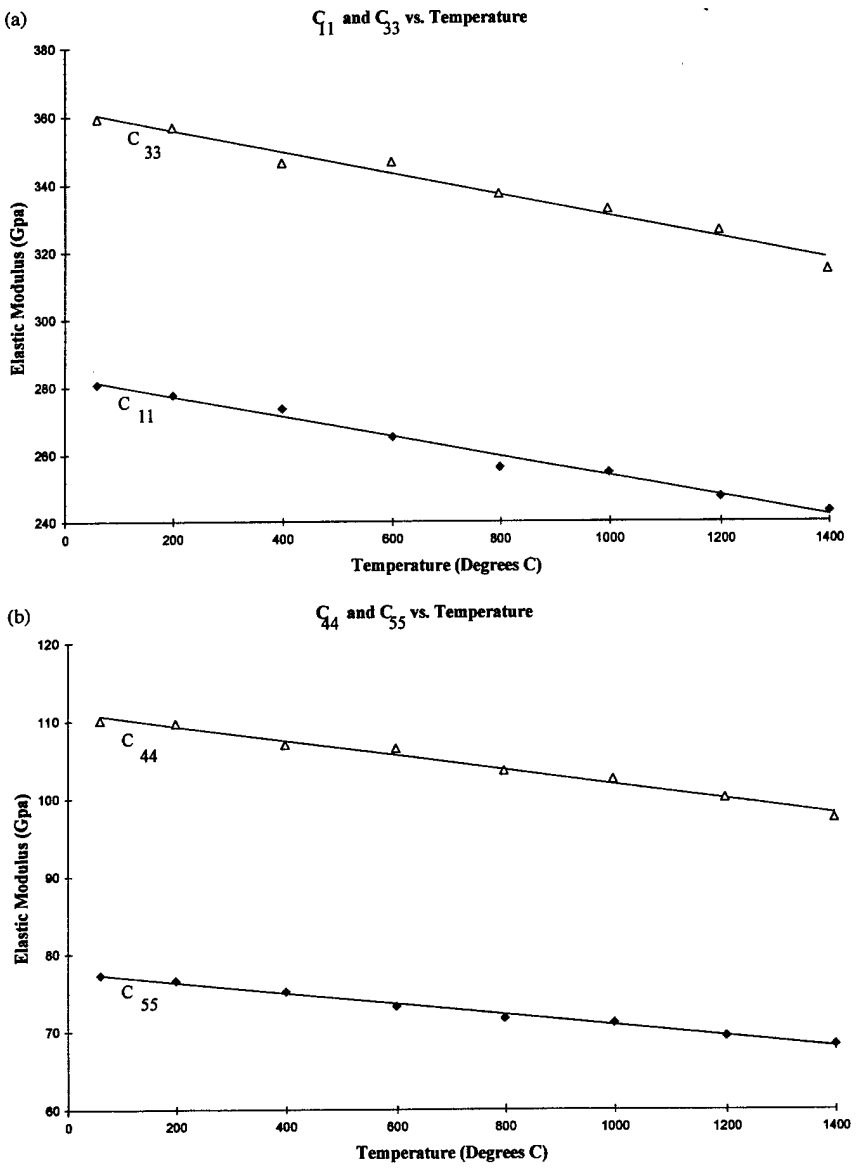


Fig. 6. Variation of selected elastic moduli with temperature.

5 Conclusions

In this work, the lattice parameters and thermal expansion coefficients for stoichiometric mullite ($3Al_2O_3{\cdot}2SiO_2$) powder were measured by X-ray diffractometry up to 900 °C. The data was analyzed by the Rietveld technique, and the strutural discontinuity reported by Schneider *et al.*[12] was confirmed. The temperature range of its occurrence was narrowed to between 425 and 450 °C.

A dense, hot pressed sample of the same mullite made from hydrothermally grown, stoichiometric $3Al_2O_3{\cdot}2SiO_2$ powder was examined by high temperature neutron diffraction and Rietveld analysis. Specimens were cycled from room temperature to 1650 °C, yielding a complete set of axial lattice parameters and thermal expansion coefficients.

In addition, the as-hot pressed, grey mullite (thought to be oxygen deficient due to hot pressing in a graphite die under vacuum) exhibited higher lattice parameters than did those of the (presumably) fully oxidized, white mullite specimen examined in subsequent heating cycles after effectively annealing in air. This observation suggests that the highly incommensurately modulated structure is highly sensitive to oxygen vacancies, and this is the subject of further ongoing work.

Cameron and others[3,33,34] define the position of satellite reflections as being determind by structural vacancies needed to accommodate composition. Thus it follows that additional vacancies will be expected to strongly impact this feature. This observation may have general ramifications in that it suggests that lattice parameters and properties of

oxygen deficient oxide ceramics may differ from those of fully oxygenated, stoichiometric oxides.

The single crystal elastic constants were measured for a melt-grown, orthorhombic, mullite fiber. The complete set of nine elastic moduli were obtained at room temperature, while incomplete measurements up to 1400 °C indicated roughly a 10% drop in stiffness at elevated temperatures.

Acknowledgements

W. M. Kriven gratefully acknowledges the Institut für Kristallographie und Angewandte Mineralogie, in München, Germany, for hosting her sabbatical leave of six months in 1997. The work of J. W. Palko was supported in the United States, by a Fannie and John Hertz Foundation graduate Fellowship. The X-ray work in conjunction with the elastic constant measurements was carried out at the Center for Microanalysis of Materials at UIUC. The WDS electron microprobe analysis was conducted by Dr. I. Steele at the University of Chicago. This work was partially supported by a United States Air Force Office of Scientific Research AASERT Grant, under Contract number F49620-97-1-0427.

References

1. Schneider, H., Okada, K. and Pask, J. A., *Mullite and Mullite Ceramics*. John Wiley, Chichester, UK, 1994.
2. Aksay, I. A. and Pask, J. A., Stable and metastable equilibria in the system SiO_2–Al_2O_3. *J. Am. Ceram. Soc.*, 1975, **58**(11–12), 507–512.
3. Kriven, W. M. and Pask, J. A., Solid solution range and microstructures of melt-grown mullite. *J. Am. Ceram. Soc.*, 1983, **66**(9), 649–654.
4. Sayir, A. and Farmer, S. C. Directionally solidified mullite fibers. In *Ceramic Matrix Composites—Advanced High Temperature Structural Materials. Mat. Res. Soc. Symp. Proc.*, Vol. 365, 1995, pp. 11–20.
5. Wilson, D. M., Lieder, S. L. and Lueneburg, D. C., Microstructure and high temperature properties of NEXTEL 720 fibers. *Cer. Eng. Sci. Proc.*, 1995, **16**, 1005–1012.
6. Göring, J. and Schneider, H., Creep and subcritical crack growth of Nextel 720 alumino silicate fibers as-received and after heat treatment at 1300°C. *Cer. Eng. Sci. Proc.*, 1997, **18**(3), 95–102.
7. Schneider, H., Göring, J., Schmücker, M. and Flucht, F., Thermal stability of Nextel 720 alumino silicate fibers. In *Ceramic Microstructure: Control at the Atomic Level*, ed. A. P. Tomsia and A. Glaeser. Plenum Press, New York, 1998, pp. 721–730.
8. Kriven, W. M., Jilavi, M. H., Zhu, D., Weber, J. K. R., Cho, B., Felten, J. and Nordine, P. C., Synthesis and microstructure of mullite fibers grown from deeply undercooled melts. In *Ceramic Microstructure: Control at the Atomic Level*, ed. A. Glaeser and A. P. Tomsia. Plenum Press, New York, 1998, pp. 169–176.
9. Weber, J. K. R., Cho, B., Hixon, A. D. Abadie, J. G., Nordine, P. C., Kriven, W. M., Johnson, B. R. and Zhu, D., Growth and crystallization of YAG and mullite-composition glass fibers. *J. Euro. Ceram. Soc.*, 1999, **19**(13–14) this issue.
10. Oehlschlegel, G., Kockel, A. and Biedl, A., Anisotrope Mischkristallbildung einiger Verbindungen des ternären Systems BaO–Al_2O_3–SiO_2. Teil II. Messungen an Strukturen mit zweidimensionaler Verknüpfung von $(Si,Al)O_4$-Tetrahederen und Modellvorstellungen von deren Wärmedehnungsanisotropie (Anisotropic mixed crystal formation of a compoundfrom the ternary system BaO–Al_2O_3–SiO_2. Part II. Measurement of structures with two dimensional joining of $(Si,Al)O_4$-tetrahedra and proposed model of their thermal expansion anisotropy). *Glastech. Ber.*, 1974, **47**, 31–41 (in German).
11. Winter, S. and Ghose, S., Thermal expansion and high-temperature crystal chemistry of Al_2SiO_5 polymorphs. *Am. Mineral*, 1979, **64**, 573–586.
12. Schneider, H. and Eberhard, E., Thermal expansion of mullite. *J. Am. Ceram. Soc.*, 1990, **73**, 2073–2076.
13. Margalit, J., Thermal expansion of mullite up to 1500 °C. Ph.D. thesis, Verlag Mainz, Wissenschaftsverlag, Aachen, Germany, 1993 (in German).
14. Schneider, H., Rodewald, K. and Eberhard, E., Thermal expansion discontinuities of mullite. *J. Amer. Ceram. Soc.*, 1993, **76**, 2896–2898.
15. Brunauer, G., Boysen, H., Frey, F., Hansen, T. and Kriven, W. M., High temperature crystal structure of a 3:2 mullite from neutron diffraction data. In preparation.
16. Fenstermacher, J. E. and Hummel, F. A., High temperature mechanical properties of ceramic materials: IV, sintered mullite bodies. *J. Am. Ceram. Soc.*, 1961, **44**(6), 284–289.
17. Davis, R. F. and Pask, J. A., Mullite. In *High Temperature Oxides*, Vol. 4., ed. A. M. Alper. Academic Press, New York, 1971, pp. 37–76.
18. Ledbetter, H., Kim, S., Crudele, S. D. and Kriven, W. M., Elastic properties of mullite. *J. Am. Ceram. Soc.*, 1998, **81**(4), 1025–1028.
19. Sanderock, J. R., Trends in Brillouin scattering: studies of opaque materials, supported films, and central modes. In *Topics in Applied Physics 51, Light Scattering in Solids III: Recent Results*, ed. G. Guntherodt, M. Cardona. Springer-Verlag, New York, 1982, pp. 173–206.
20. Zouboulis, E. S. and Grimsditch, M., Refractive index and elastic properties of MgO up to 1900 K. *J. Geophysical Res.*, 1991, **96**, 4167–4170.
21. Landau, L. D. and Lifshitz, E. M., *Theory of Elasticity. A Course of Theoretical Physics*, Vol. 7. Pergammon Press, London, 1959.
22. Proc. Int'l. Workshop on Oxide/Oxide Composites, Irsee, Bavaria, Germany, 22–24 June 1998. *J. Euro. Ceram. Soc.*, in press.
23. Crudele, S. D., Processing and characterization of alumina platelet-reinforced mullite composites. M.S. thesis, University of Illinois at Urbana-Champaign, 1989.
24. Lorenz, G., Neder, R. B., Marxreiter, J., Frey, F. and Schneider, J., A mirror furnace for neutron diffraction up to 2300 K. *J. Appl. Crystallogr.*, 1993, **26**, 632–635.
25. Sinogeikin, S. V., Bass, J. D. and Katsura, T., Sound velocities and elastic properties of Fe-bearing wadsleyite and ringwoodite. *J. Geophys. Res.*, in press.
26. Weidner, D. J. and Carleton, H. R., Elasticity of coesite. *J. Geophysical Res.*, 1977, **82**(8), 1334–1346.
27. Balzar, D. and Ledbetter, H., Crystal structure and compressibility of 3:2 mullite. *Am. Mineralogist*, 1993, **78**, 1192–1196.
28. Boysen, H., Anharmonic thermal parameters, disorder and phase transition. In *Accuracy in Powder Diffraction II*, ed. E. Prince and J. K. Stalick. NIST, Washington, DC, 1992, pp. 165–174.
29. Thomas, M. W. and Bendall, P. J., A suite of programs for total profile refinement of number of powder diffraction patterns. *Acta Crystallogr.*, 1978, **A34**, 351.

30. Rahman, S. H., Real crystal structure of mullite. In *Mullite and Mullite Ceramics*. John Wiley, Chichester, UK, 1994, pp. 4–31.
31. Palko, J. E., Kriven, W. M., Sinogeikin, S., Bass, J. D. and Sayir, A., Single crystal elastic moduli of mullite. In preparation.
32. Vaughn, M. T. and Weidner, D. J., The relationship of elasticity and crystal structure in andalusite and sillimanite. *J. Phys. Chem. Minerals*, 1978, **3**, 1–12.
33. Cameron, W. E., Composition and cell dimensions of mullite. *Ceram. Bull*, 1977, **56**(11), 1003–1007, 1011.
34. Cameron, W. E., *Amer. Miner.*, 1977, **62**, 747–755.

Reprinted from Ceramic Transactions, 108, 2000
Copyright © 2000 by The American Ceramic Society

SYNTHESIS OF OXIDE POWDERS VIA POLYMERIC STERIC ENTRAPMENT

W. M. Kriven, S. J. Lee, M. A. Gülgün, M. H. Nguyen, and D. K. Kim
Department of Materials Science and Engineering
University of Illinois at Urbana-Champaign
Urbana, IL. 61801

ABSTRACT

A new, simple, inorganic-organic polymerization method for synthesis of highly reactive, highly sinterable, oxide powders has been development in our laboratory. The method has been used to fabricate a variety of one, two and three component oxides including alumina, cristobalite, mullite, YAG, xenotime, calcium mono- and tri- aluminates, as well as mono-, di- and tri-calcium silicate, cordierite, leucite, zircon, the components of Portland cement, and various other titanates and phosphates. The polymeric carriers are polyvinyl alcohol (PVA), ethylene glycol (EG) or its polymerized form (PEG). The characteristics of such powders, e.g., specific surface areas, nanocrystallite size, and calcining vs crystallization temperatures are briefly reviewed.

INTRODUCTION

Traditionally, refractory mixed oxide powders are produced by high temperature solid state reactions. However, this route can be very cost ineffective and often leads to a final product with multiple, unwanted phases. Mixed oxide powders thus produced have low surface area and large crystallite size.[1]

Various chemical methods have been developed for the synthesis of pure, single phase mixed oxide powders with controlled powder characteristics.[2-18] Even some of these chemical routes tend to result in other phases along with the desired compound. One of the more successful techniques for single phase mixed oxide powders is the so-called Pechini process.[2] Since its invention in the 1960's, the Pechini method (and slight variations thereof) has been utilized to produce niobates, titanates, zirconates, chromites, ferrites, manganites, aluminates, cobaltites, and silicates.[2-4,11,18] The process describes utilization of hydroxycarboxylic acids (i.e. citric and lactic acids) in combination with polyhydroxyl alcohols such as ethylene glycol to form a resin through condensation reactions. The acid acts as a chelating agent which chemically binds the cations that are dissolved in the solution. The polymerization is based on the polyesterfication between the metal-chelate complexes and polyhydroxyl alcohols. Due to the chelating action of the hydroxy carboxylic acids and the polymeric network, the cations have low mobility, so that precipitation is hindered. The result is ceramic powders with better chemical homogeneity and smaller particle size.

To the extent authorized under the laws of the United States of America, all copyright interests in this publication are the property of The American Ceramic Society. Any duplication, reproduction, or republication of this publication or any part thereof, without the express written consent of The American Ceramic Society or fee paid to the Copyright Clearance Center, is prohibited.

In general, it is assumed that chelation, or chemical fixation of the cation by the organic molecule is a pre-requisite for a stable, multi-cation precursor. However, in the calcium aluminate system, our previous studies on Pechini precursors with very high metal ion to polymer end group ratios have shown that the precursors were able to support a higher amount of cations than they could chelate.[3] Thus, it is reasonable to suppose that other mechanisms of cation stabilization beside chelation are operative in these organo-metallic precursors. However, there are very few studies on the chemical synthesis of oxide powders via non-chelating organic precursors.[19-20]

In order to explore the possibility of synthesizing stable precursors from simpler molecules, polyvinyl alcohol (-[CH_2-CHOH]-$_n$, or PVA) and polyethylene glycol (H[O-CH_2-CH_2]-$_n$OH, PEG) were used as polymeric carriers. As seen in Fig. 1(a), PVA has only hydroxyl (-OH) group attached to every second C atom in the carbon backbone of a long-chain molecule. In PEG, (Fig. 1(b)) there are only two functional groups (also hydroxyl) at the two ends of the polymer. Thus, neither of the organics possesses chemical chelating capabilities. In this study, we report on the synthesis of various mixed oxides and phosphates using a relatively simple, long-chain polymer as a carrier for the ceramic precursor. By using the polymer complexation process, ceramic powders are synthesized much more easily than in other chemical synthesis routes.[21-30] The PVA ensures the homogenous distribution of the metal ions in its polymeric network structure and inhibits their segregation and/or precipitation from the solution. Water is able to diffuse through the polymer and stretch it due to the acetate clusters. In the solution, the long chain polymer prevents contact between cations and limits their agglomeration and precipitation. A schematic representation of the cationic entrapment mechanism is shown in Fig. 2. The amount of polymer and its molecular length can affect the distribution of cations. The optimum amount and chain length of PVA result in a pure, highly reactive, and homogenous powder at the molecular level. It is speculated that weak hydrogen bonding promotes homogeneous physical entrapment between the -(OH) hydroxyl groups and cations which are solvated by water molecules. The PVA process also produces carbonaceous material that gives heat through its combustion, so that fine and single phase powders can be formed at a relatively low external temperature. For systems in which not enough polymer is used, agglomeration may occur. Upon burnout, the agglomerated cation precursors lose much of their organics in the outer regions. Due to the intense heat evolved from the oxidative process, polymer and organic components remain within the shell. Further application of heat causes the organic to decompose into gases and expand, and makes oxides by combustion synthesis. The less-agglomerated particles have lost most or all of the organics with application of heat. Thus, a large powder particle size distribution is observed. To maximize the powder properties, a balance is needed between the precursors and the amount of polymer. In this study, the polymeric steric entrapment route is introduced and the oxide powders derived from this method are reviewed.

EXPERIMENTAL PROCEDURE

(1) Powder Synthesis

In the PVA process, nitrate salts were in the form of cation sources with the exception of silica which was supplied as a colloidal silica product. Diammonium hydrogen phosphate was used as the source of phosphorus. These cation sources were dissolved in stoichiometric proportions in de-ionized (DI) water. Once the cation sources were completely dissolved, the 5 wt% PVA (Air Products and Chemicals, Inc., Airvol Series, Allentown, PA) was dissolved in DI water and added.

The proportions of the PVA to cation sources in the solution were adjusted in such a way that there were 4, 8, or 12 times more positively charged valences from the cations than from the potentially negatively charged -(OH) functional groups of the polymers. The polymeric long chains have hydroxyl groups in solution. Hence, one PVA monomer, which has one hydroxyl (OH) functional group, can be used as an unit for calculation of PVA content. The exact relative amount of PVA to cations in the solution can be calculated with reference to a monomeric unit of PVA.

Water was evaporated by continuous stirring during heating on a hot plate. The resulting gel-type precursor was completely dried after several hours at 100°C. In titanium oxide compounds, titanium (IV) isopropoxide was dissolved in stoichiometric proportions in liquid-type ethylene glycol. Barium nitrite or nitrate salts were used as the source of Ba and other cations, respectively. The amount of ethylene glycol was calculated using a ratio of total weight of metal ions from cation sources to weight of ethylene glycol. The nitrite or nitrate salts were first added to the ethylene glycol and heated to 80 °C, while mixing, until it was fully dissolved. Then, the titanium (IV) isopropoxide was slowly added, while stirring. The solution was then allowed to gel for 48 h in a drying oven at 50 °C. In the case of the PEG method, a transparent sol was prepared from zirconium 2,4-pentanedionate, which is a water-insoluble chemical, and aluminum nitrate in proportions of 50:50 vol%. After dissolving these reagents in ethanol, the organic carrier, PEG (of M.W.: 2000) was added, and the mixture was stirred and heated at 80 °C. The amount of PEG was calculated using a ratio of total weight of metal ions from cation sources to weight of PEG. As the viscosity increased by evaporation of ethyl alcohol, the sol turned to a syrup-like gel. Subsequently, a vigorous exothermic reaction occurred which, with continuous heating at 80 °C, converted the gel into an expanded, porous solid.

The organic/inorganic precursors in the all cases were then ground and were calcined or crystallized at various temperatures in an air atmosphere in a box furnace. Some powders were milled using an attritor mill to examine the effects of milling on the surface area. The powders were attritor milled at 240 rpms for 1 hour using zirconia milling media (ball diameter : 5mm) and isopropyl alcohol as a solvent for milling.

(2) Characterization

(A) X-ray Diffraction Analysis : The crystallization behavior of each of the calcined powders was studied as a function of temperature and holding time at elevated temperatures, using a Rigaku X-ray diffractometer (Dmax automated powder diffractometer, Rigaku/USA, Danvers, MA) with CuK_{α} radiation (40 kV, 40 mA). All

XRD data was obtained at room temperature, after the powder had been cooled. A scanning speed of 10 °/min with a sampling interval of 0.02°.

(B) Specific Surface Area Measurement: : The specific surface area of the crystallized powders and attrition milled powders were obtained by five-point BET analysis from nitrogen gas adsorption (Model ASAP 2400, Micromeritics, Norcross, GA). All samples for testing were kept in a dry oven to prevent hydration of the powders.

(C) *Microstructure Characterization* : The morphologies of calcined, crystallized, and/or attrition-milled powders were examined by scanning electron microscopy, SEM (Model Hitachi S530, Hitachi, Japan). For the SEM specimens, each powder was completely dried, attached to an aluminum stub, and gold sputter coated.

RESULTS AND DISCUSSION

The organic-inorganic precursors derived from the PVA process resembled an aerogel and were formed by the development of foam during the stirring and solution drying process. The foam was generated during evolution of NO_x gas caused by the decomposition of the nitrates. The expansion of the gel due to the evolving NO_x gas continued until the precursors dried completely. In the EG method, the solution was pale yellow and transparent after all the chemicals were dissolved in ethylene glycol. During the drying process at 50 °C, the transparent gel turned to a yellow-colored solid gel. In PEG method, the syrup-like, precursor gel was quite flammable because of ethyl alcohol solvent and had a vigorous exothermic reaction on continuous heating. After the reaction, the gel changed to a sooty, porous solid having about a 20-fold volume expansion.

The summary of oxide powders prepared by the inorganic-organic polymerization method, and the applied methods and chemical sources for each powder were listed in Table I, and II, respectively. For the chemical sources which are insoluble to water, PVA method was substituted for PEG and EG methods. Most of cases, the calcination temperatures were below 800 °C in an air atmosphere. This means the carrier polymers were easily burnt out by the oxidation process. Once the cations are complexed and/or trapped within the polymer, heat is used to remove the polymer. For systems in which not enough polymer is used, agglomeration may occur. Upon burnout, the agglomerated cation precursors lose much of their organics in the outer regions. Due to the intense heat evolved from the oxidative process, polymer and organic components remain within the shell. Further application of heat causes the organic to decompose into gases and expand. Thus, a large powder particle size distribution is observed. The less-agglomerated particles have lost most or all of the organics with application of heat. To maximize the powder properties, a balance is needed between the precursors and the amount of polymer.[28]

The crystallization temperatures showed a difference for each case. In some powders, the crystallization temperatures were much lower than those of other powders prepared by other chemical synthesis. In particular, titanate compounds derived from the EG method showed low crystallization temperatures close to their calcination temperatures. In the case of alumina, the crystalline development was different according to the D.P. (degree of polymerization) of polymer carrier. At high D.P. of PVA, gamma phase was detected at 1100 °C. The powders prepared by the inorganic-organic polymerization method had extremely high specific surface

areas. The polymer content and its degree of polymerization affected the surface area and morphology.[27] Some powders such as cordierite, alumina and tricalcium silicate were soft agglomerated and easily break out to fine particles after attrition milling. Despite the production of nano-size particles, the calcium aluminate, barium titanate, and xenotime showed low specific surface areas of 12.0, 5.6, and 12.0 m^2/g, respectively, because the powders contained hard-agglomerated, pre-sintered particles. The SEM and TEM micrographs of the representative porous calcined powder and the nano-size powders are shown in the Fig. 3. The SEM micrograph of barium titanate powder revealed nanosized particles with a narrow particle size distribution. The particles were already presintered, suggesting that the nano-size powder was quite reactive even at low temperatures. The powders after ball milling for 1 h increased their surface area to 15 m^2/g, which resulted from breaking up of the presintered particles.

The comparison between the Pechini resin process and the PVA solution process in the cordierite powder is listed in Table III. A high yield of 59%, which is more than double in comparison with the Pechini resin process, was observed in the PVA solution process. A small weight loss was observed during calcination in the PVA solution process. This loss was consistent with the lesser amount of PVA being used in this process, as PVA has a greater effective work of polymerization. In both cases, infinitesimal residual carbon (below 0.1 wt%) was detected in the calcined powders. The powder derived from the Pechini resin had a narrower particle size distribution of 3-50 μm than did the PVA solution process. The precursor derived from the Pechini resin could be ground easily due to the larger amount of organic carrier involved. The development of crystalline phases for each case showed different behavior. In the amorphous-type cordierite derived from the Pechini resin, the α-cordierite was formed without a sequential formation of crystalline cordierite (amorphous→μ→α). However, the cordierite derived from the PVA solution revealed the intermediate μ-phase crystalline cordierite before the crystallization of α-phase. The formation of μ-cordierite was also observed in the sol-gel powder preparation process.[31] In the synthesis of cordierite, the formation of μ-phase reduced the chances of forming other silicate compounds, such as spinel and cristobalite, or the residual cordierite-type amorphous phase.[31,32]

CONCLUSIONS

A polymerized organic-inorganic complex route was successfully employed to synthesize various monophase, fine and pure, mixed oxide powders. The new technique uses simple long-chain polymers like polyvinyl alcohol (-[CH_2-CHOH]-$_n$, PVA) or polyethylene glycol (H[O-CH_2-CH_2]-$_n$OH, PEG) as the organic carrier for the pre-ceramic gel. The results show that metal ion chelation of the solution polymerization method is not the only mechanism to obtain molecularly homogeneous, stable precursors for complex mixed oxide powders. The cations of the mixed oxide are sterically entrapped in the entangled network of the organic polymers. In particular, this method had a higher powder yield than other chemical

synthesis methods and could be extended to even chemicals that decompose in water, such as titanium isopropoxide.

ACKNOWLEDGEMENT

This work was partially supported by an AFOSR AASERT Grant #F49620-97-1-0427.

REFERENCES

[1]K. Fujii, W. Kondo, and H. Ueno, "Kinetics of Hydration of Monocalcium Aluminate," *J. Am. Ceram. Soc.*, **69**[4] 361-364 (1986).

[2]M. Pechini, "Method of Preparing Lead and Alkaline-Earth Titanates and Niobates and Coating Method Using the Same to Form a Capacitor," U.S. Pat. No. 3 330 697, July 11, 1967.

[3]M.A. Gülgün, O.O. Popoola and W.M. Kriven, "Chemical Synthesis and Characterization of Calcium Aluminate Powders," *J. Am. Ceram. Soc.*, **77**[2] 531-539 (1994).

[4]M.A. Gülgün, O.O. Popoola, I. Nettleship, W.M. Kriven and J.F. Young, "Preparation and Hydration Behavior of Pure $CaAl_2O_4$," pp. 199-204 in Advanced Cementitious Systems: Mechanisms and Properties, Proceedings of the Materials Research Society Symposium (Boston, MA, December, 1992). Vol. **245**, edited by F.P. Glasser, P.L. Pratt, T.O. Mason, J.F. Young, and G.J. McCarthy. Materials Research Society, Pittsburgh, PA, (1992).

[5]L.W. Tai and P.A. Lessing, "Modified Resin-Intermediate Processing of Perovskite Powders: Part I. Optimization of Polymeric Precursors," *J. Mater. Res.*, **7**[2] 502-510 (1992).

[6]L.W. Tai and P.A. Lessing, "Modified Resin-Intermediate Processing of Perovskite Powders: Part II. Processing for Fine, Nonagglomerated Sr-Doped Lanthanum Chromite Powders," *J. Mater. Res.*, **7**[2] 511-519 (1992).

[7]S.C. Zhang, G.L. Messing, W. Huebner and M.M. Coleman, "Synthesis of $Yba_2Cu_3O_{7-X}$ Fibers from an Organic Acid," *J. Mater. Res.*, **5**[9] 1806-1812 (1990).

[8]P.A. Lessing, "Mixed-Cation Oxide Powders via Polymeric Precursors," *Am. Ceram. Soc. Bull.*, **68**[5] 1002-1007 (1989).

[9]L.W. Tai, H.U. Anderson, and P.A. Lessing, "Mixed-Cation Oxide Powders via Resin Intermediates Derived from a Water Soluble Polymer," *J. Am. Ceram. Soc.*, **75**[12] 3490-3494 (1992).

[10]H.U. Anderson, M.J. Pennell and J.P. Guha, "Polymeric Synthesis of Lead Magnesium Niobate Powders," in Advances in Ceramics, Vol. 21: *Ceramic Powders Science*, Am. Ceram. Soc., Westeville, OH (1987), p. 91.

[11]N.G. Eror and H.U. Anderson, "Polymeric Synthesis of Ceramic Materials," *Mater. Res. Soc. Symp. Proc.*, **73**, Materials Research Society, Pittburgh, PA (1986), p. 571.

[12]G. DeWith, "Preparation, Microstructure and Properties of $Y_3Al_5O_{12}$ Ceramics," *Phillips J. Res.*, **42**, 119-130 (1987).

[13]D.R. Messier and G.E. Gazza, "Synthesis of $MgAl_2O_4$ and by Thermal Decomposition of Hydrated Nitrate Mixtures," *Am. Ceram. Soc. Bull.*, **51**[9] 692-697 (1972).

[14]L.P. Morozova, E.S. Lukin, T.V. Efimovskaya, A.V. Smolya, I.F. Panteleeva, "Synthesis of Aluminum Yttrium Garnet," *Glass. Ceram.*, **35**, 158 (1978).

[15]O.J. Sordolet, M. Akinc, M. Panchula, Y. Han, M.H. Han, "Synthesis of Yttrium Aluminum Garnet Precursor Powders by Homogeneous Precipitation," *J. Euro. Ceram. Soc.*, **14**, 123-130 (1994).

[16]D.M. Roy, R.R. Neurgaonkar, T.P. O'Holleran and R. Roy, "Preparation of Fine Oxide Powders by Evaporative Decomposition of Solutions," *Am. Ceram. Soc. Bull.*, **56**[11] 1023-1024 (1977).

[17]I. Nettleship, J.L. Shull, Jr., and W.M. Kriven, "Chemical Preparation and Phase Stability of Ca_2SiO_4 and Sr_2SiO_4 Powders," *J. Euro. Ceram. Soc.*, **11**, 291-298 (1993).

[18]M. Kakihana, M. Arima, M. Yashima, M. Yoshimura, H. Mazaki, and H. Yasuoka, "Chemical Design for Functional Multi-Component Oxides by Polymerized Complex Method," *Trans. Mat. Res. Soc. Jpn.*, **14A**, *Advanced Materials '93, I/A: Ceramics, Powders, Corrosion and Advanced Processing,* edited by N. Mizutani et al., Elsevier Sci., 1994, pp. 801-806.

[19]P. Pramanik and A. Pathak, "A New Chemical Route for the Preparation of Fine Ferrite Powders," *Bull. Mater. Sci.*, **17**[6] 967-975 (1994).

[20]S. Kumar Saha, A. Pathak, and P. Pramanik, "Low-Temperature Preparation of Fine Particles of Mixed Oxide Systems," *J. Mater. Sci. Lettr.*, **14**, 35-37 (1995).

[21]P. Praminik and A. Pathak, "A New Chemical Route for the Preparation of Fine Particles of Mixed Oxide Systems," *Mater. Sci. Bull.* **17**[6] 967-975 (1994).

[22]M.A. Gülgün and W.M. Kriven, "A Simple Solution-Polymerization Route for Oxide Powder Synthesis," pp. 57-66 *Ceramic Transactions*, **62** Edited by J.J. Kingsley, C.H. Schilling and J.H. Adair. American Ceramics Society, Westerville (1995).

[23]D.A. Fumo, M.R. Morelli, and A.M. Segadaes, "Combustion Synthesis of Calcium Aluminates," *Mater. Res. Bull.*, **31**[10] 1243-1255 (1996).

[24]M.H. Nguyen, *A New Polymer Route to the Synthesis of Mixed Oxide Ceramics*, M.S. Thesis, University of Illinois at Urbana-Champaign, 1997.

[25]S.J. Lee and W.M. Kriven, "Crystallization and Densification of Nano-Size, Amorphous Cordierite Powder Prepared by a PVA Solution-Polymerization Route," *J. Am. Ceram. Soc.*, **81**[10] 2605-12 (1998).

[26]S.J. Lee and W.M. Kriven, "A Preparation of Ceramic Powders by Solution Polymerization Route Employing PVA Solution," *Ceram. Eng. & Sci. Proc.* **19**[4] 469-476 (1998).

[27]S.J. Lee, E.A. Benson, and W.M. Kriven, "Preparation of Portland Cement Components by PVA Solution Polymerization," *J. Am. Ceram. Soc.*, **82**[8] 2049-55 (1999).

[28]M.H. Nguyen, S.J. Lee, and W.M. Kriven, "Synthesis of Oxide Powders Via a Polymeric Steric Entrapment Precursor Route," in press *J. Mater. Res.*, **14**[8] (1999).

[29]S.J. Lee, M.D. Biegalski and W.M. Kriven, "Preparation and Properties of Barium Titanate and Barium Orthotitanate Powders Through Ethylene Glycol Polymerization Route," *J. Mater. Res.*, **14**[7] 3001-3006 (1999).

[30]S.J. Lee and W.M. Kriven, "A Submicron-Scale Duplex Zirconia and Alumina Composite by Polymer Complexation Processing," in press *Ceram. Eng. & Sci. Proc* (1999)

[31]H. Suzuki, K. Ota, and H. Saito, "Preparation of Cordierite Ceramics from Metal Alkoxides (Part I: Preparation and Characterization of the Powder)," *Yogyo-Kyokai-Shi*, **95** [2] 28-31 (1987).

[32]H.Y. Jang and B.C. Lim, "Effect of the Scale of Precursor Mixing on Densification Behaviors and Phase-Transformation Kinetics of Cordierite Gels," *J. Mater. Res.*, **9** [10] 2627-2633 (1994).

Table I. Summary of Oxide Powders Prepared by Inorganic-Organic Polymerization Method (Polymeric carrier : poly vinyl alcohol (PVA), poly ethylene glycol (PEG), ethylene glycol (EG)).

Compound	Heating temperature (°C)		Specific surface area (m^2/g)		Particle size (μm)	
	Calcination	Crystallization	amorphous	crystalline	as-calcined	attrition-milled
Alumina (Al_2O_3)	800	1150	83	6.2*		0.1-0.3†
β-Cristobalite (SiO_2)	800	1100	188			0.3
Mullite ($Al_6Si_2O_{13}$)	800	1300	157			0.1
Zircon ($ZrSiO_4$)	800	1100	81			0.2-0.3
Wollastonite ($CaSiO_3$)	800	800		18	0.7	0.2†
Calcium aluminate ($CaAl_2O_4$)	650	900	12		60 nm (hard aggl.)	
Belite (β-Ca_2SiO_4 or C_2S)	700	800		22.1	0.3-0.4	
Alite (Ca_3SiO_5 or C_3S)	700	1400		0.9§	3.0-5.0	0.2-0.4†
C_3A ($Ca_3Al_2O_6$)	700	1000		4.2	0.5-1.0	
C_4AF ($Ca_4Al_2Fe_2O_{10}$)	700	700		17.1	0.1-0.2	
YAG ($Y_3Al_5O_{12}$)	600	900	56	17		
Leucite ($KAlSi_2O_6$)	750	1000	50	0.2	5.0	0.5
Hexacelsian ($BaAl_2Si_2O_8$)	800	1100	79			0.5
Cordierite ($Mg_2Al_4Si_5O_{18}$)	800	1200	181 (attrition milled)			30 nm

Table I.(Cont.) Summary of Oxide Powders Prepared by Inorganic-Organic Polymerization Method (Polymeric carrier : poly vinyl alcohol (PVA), poly ethylene glycol (PEG), ethylene glycol (EG)).

Compound	Heating temperature (°C)		Specific surface area (m^2/g)		Particle size (μm)	
	Calcination	Crystallization	amorphous	crystalline	as-calcined	attrition-milled
Barium titanate ($BaTiO_3$)	700	700		5.6	0.1 (hard aggl.)	
Barium orthotitanate (Ba_2TiO_4)	700	1000				
Dysprosium titanate (Dy_2TiO_5)	800	800				0.2
Yttrium titanate (Y_2TiO_5)	850	850				
Alumina·zirconia composite ($Al_2O_3 \cdot ZrO_2$)	700	1300				0.5
Nickel aluminate ($NiAl_2O_4$)	800	1000	10	4		
Calcium phosphate (CaP_2O_6)	700	900				
Xenotime (YPO_4)	500	830	12		70 nm (hard aggl.)	
Aluminum phosphate ($AlPO_4$)	800	800	136	87	10†	0.9†
Lithium phosphate ($LiPO_4$)	700	800				

§after attrition milling for 1 h : 50 m^2/g

¥after attrition milling for 1 h : 55 m^2/g

†crystalline form

Table II. Polymerization Methods and Chemical Sources for Each Compound.

Polymer carrier	Compound	Chemical source
Polyvinyl alcohol (PVA)	Al_2O_3, SiO_2, $Al_6Si_2O_{13}$, $ZrSiO_4$, $CaAl_2O_4$, $Y_3Al_5O_{12}$, $AlPO_4$, $KAlSi_2O_6$, $BaAl_2Si_2O_8$, $NiAl_2O_4$, $Mg_2Al_4Si_5O_{18}$, CaP_2O_6, $LiPO_4$, $CaSiO_3$, Ca_2SiO_4, Ca_3SiO_5, $Ca_4Al_2Fe_2O_{10}$	nitrate salts (most cases), colloidal silica (for SiO_2), diammonium hydrogen-phosphate
Ethylene glycol (EG)	$BaTiO_3$, Ba_2TiO_4, Dy_2TiO_5, Y_2TiO_5	nitrate salts, barium nitrite, titanium isopropoxide.
Polyethylene glycol (PEG)	$Al_2O_3 \cdot ZrO_2$ composite	aluminum nitrate, zirconium 2,4-pentanedionate

Table III. Comparison between Pechini Resin Process and PVA Solution - Polymerization Process in the Synthesis of Cordierite.

Polymeric carrier	†Powder yield (%)	Residual carbon (wt%)	Particle size Distribution (μm)	Phase change
Pechini resin	27	0.07	3-50	amorphous→α
PVA solution	59	0.06	1-100	amorphous→μ →α

†Powder yield = (weight of calcined powder / weight of precursor) × 100.

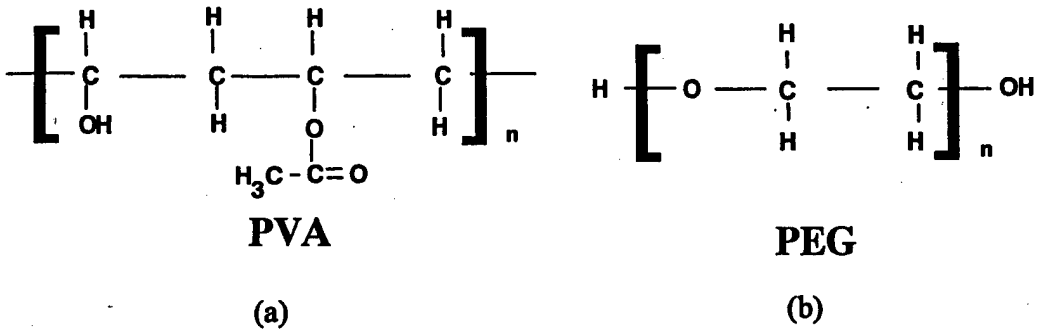


Fig. 1. Schematic formula for polyvinyl alcohol (PVA) and polyethylene glycol (PEG). (a) PVA and (b) PEG.

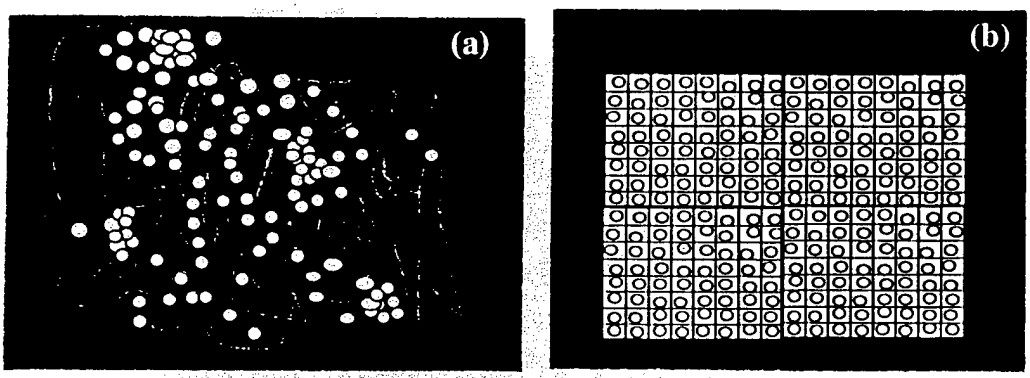


Fig. 2. Schematic of cationic entrapment with (a) small amount of polymer and (b) optimal amount of polymer.
Excess or not enough polymer results in large particle size distributions whereas the optimal amount should give a more uniform distribution.

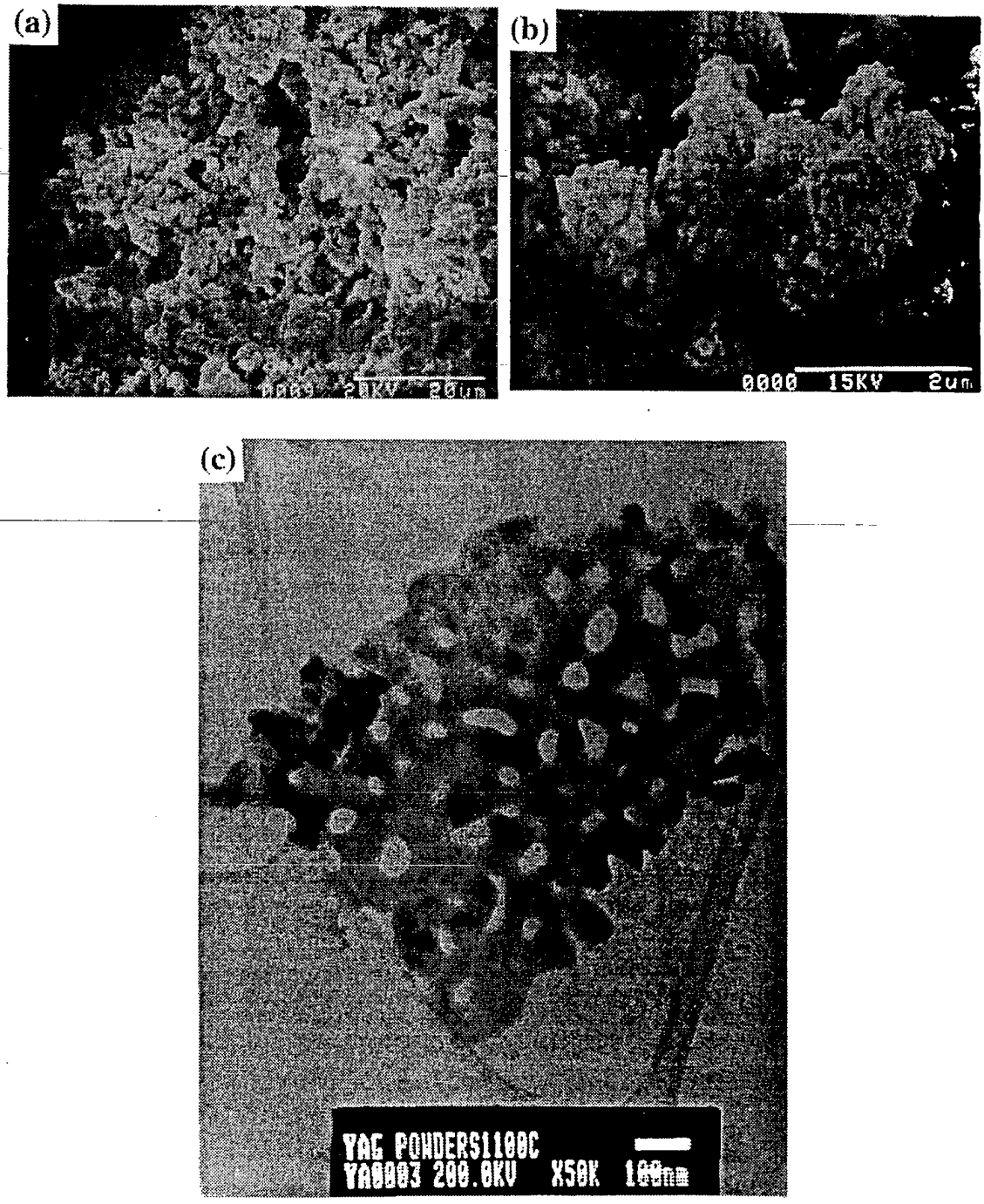


Fig. 3. SEM and TEM micrographs of calcined powders derived from polymeric steric entrapment route (a) monocalcium silicate (SEM), (b) barium titanate (SEM), and (c) YAG (TEM).

Electrosynthesis and microstructural characterization of anodic VO_x films

J.P. Schreckenbach, D. Butte, and G. Marx
Institut für Chemie, Technische Universität Chemnitz, D-09111 Chemnitz, Germany

B.R. Johnson and W.M. Kriven
Department of Materials Science and Engineering, University of Illinois at Urbana-Champaign, Urbana, Illinois 61801

(Received 30 September 1999; accepted 27 March 2000)

Anodic conversion films of vanadium oxides on vanadium were potentiodynamically generated at high voltages in an acetate electrolyte system. The microstructure of the anodic VO_x coatings was characterized by surface and solid-state techniques such as scanning electron microscopy, transmission electron microscopy, Raman spectroscopy, and x-ray photoelectron spectroscopy. An amorphous structure is proposed in which network-forming $[VO_4]$ tetrahedra in various degrees of condensation are connected by distorted $[VO_5]$ and $[VO_6]$ units. Such polyhedra lead to the formation of nanocrystalline phases of stoichiometric and substoichiometric vanadium oxides, which were observed in the amorphous phase.

I. INTRODUCTION

Anodic films on transition metals are of widespread scientific and commercial interest because of their unique physical and chemical properties. They are used in numerous high-technology areas including electronic devices, adhesive bonding, corrosion resistance, or advanced biomaterials.[1–3] Many researchers have studied the structure and growth mechanisms in anodic films, in particular porous alumina on aluminum metal.[1,4] However, the complex structure–property relationships are still not well understood. In comparison with the more widely investigated anodic film-forming metals such as tantalum or aluminum, studies of the structure of anodic conversion films on vanadium, deposited in aqueous and nonaqueous systems, have rarely been published.

There are several different ways to prepare native oxide films on vanadium metal, in addition to anodic deposition. For example, coating techniques such as sol-gel spin coating, flash evaporation, and vacuum or electron beam evaporation are increasingly used for the fabrication of vanadium oxide films, because of their potential applications such as catalysts, electrochromic devices, or high-energy density lithium microbatteries.[5–8]

The first published attempts to prepare anodic vanadium oxides in acetic acid solutions and to identify the anodic conversion films formed were reported by Keil and Salomon.[9] The films were studied by attenuated total reflectance spectra, and the results were characteristic of V_2O_4 structures. Extended investigations of the microstructure and stoichiometry of anodic films on vanadium were published by Arora and Kelly.[10] The anodic films were generated at voltages of 4 and 6 V, respectively. Reflection electron diffraction (REED) examinations of films exhibited very weak diffraction patterns of an unidentified oxide. At voltages higher than 6 V, amorphous films were produced. Hornkjoel,[11] who used chemical analysis and x-ray photoelectron spectroscopy (XPS) to show that the oxide film contained pentavalent vanadium, studied the anodic behavior of vanadium in acid electrolytes.

The reason for the different interpretations of anodic vanadium oxide films is due to the aliovalent nature of vanadium. These result in a large number of different vanadium oxide compounds, many of which have similar crystallographic structures. The most common oxidation states for vanadium are from +2 to +5, where the corresponding oxides are VO and V_2O_5, respectively. Additionally, vanadium has a tendency to polymerize through oxygen links, to form highly stable polymeric V–O–V–O–V linkages.[12] The most prevalent vanadium oxide is V_2O_5, which has an orthorhombic unit cell structure (space group *Pmmn*, No. 59). The coordination of the vanadium ions in V_2O_5 may be considered to be either distorted trigonal bipyramidal, distorted tetragonal pyramidal, or a distorted octahedron with one V–O bond of 279 pm. This structure is usually described as chains of edge-sharing $[VO_5]$ square pyramids.[7,13,14]

The present study was undertaken to characterize the surface morphology and the microstructure of anodic vanadium oxide films prepared by high electrical field anodization. Analysis of the structure and composition of noncrystalline, thin solid films requires the application of various analytical techniques to complement each other

 © 2000 Materials Research Society

and to overcome the limits of each technique. The specimens were investigated by scanning electron microscopy (SEM), transmission electron microscopy (TEM), Raman spectroscopy (RS) and XPS. On the basis of these observations, a possible constitution of the oxide film is proposed.

II. EXPERIMENTAL PROCEDURES

A. Preparation of films

Strips of vanadium metal foil (Aldrich Chemical Co., Milwaukee, WI, 99.7% pure) 0.127 mm thick and approximately 3 cm long by 0.5 cm wide were chosen for anodization. The electrolyte used to deposit anodic coatings on all of the specimens characterized in this investigation consisted of glacial acetic acid, and contained 0.02 mol/l borax ($Na_2B_4O_7$) and 1 mol/l water. Initially, various electrolyte compositions were examined to determine the optimum mixture. The concentration of water used in the electrolyte was varied, up to 5 mol/l. As the water concentration was increased, there was a decrease in the consistency of the coating quality from batch to batch. The experiments were carried out with rectangular vanadium foil as the anode, having a combined surface area of both sides up to 4 cm^2. The specimens were first cleaned in acetone, then electrochemically polished in a mixture of 80% methanol and 20% sulfuric acid for 1 min at 15 V, and finally rinsed in deionized water and dried. The cathode was platinum wire of approximately 0.5 mm in diameter. The electrochemical cell consisted of a chilled, round-bottomed, three-neck flask. The cathode and anode were placed in the outer necks of the flask. A reflux condenser was connected to the center neck and was used to prevent the escape of acetic acid vapors.

A stabilized power supply unit (Heinzinger PHN 2500-2 pos, Rosenheim, Germany), with a maximum output voltage of 2500 V direct current (dc) and a maximum current output of 2 A was used to power the electrochemical cell. All data recording and excitation of the power supply were computer controlled. The software was capable of both potentiodynamic (varying voltage) and galvanostatic (constant current) operation. The films generated in this investigation were potentiodynamically prepared at sweep rates of 0.1–1 V/s. Time, current, and voltage measurements were made at 0.6 s intervals. Anodic oxide films on vanadium were deposited at voltages up to 480 V, and corresponding current densities, up to 20 mA/cm^2. Films were formed by sweeping once at a given rate from 0 up to the specified voltage. In order to prevent excessive heating and vaporization of the electrolyte, the cell had to be thermostatically controlled to maintain a temperature of 25 °C. After the coating process was completed, the specimens were rinsed in acetone to remove adhering acetic acid residue, dried in air, and stored in inert gas atmosphere.

B. Microstructure characterization

The microstructure of the anodic coating was characterized by SEM (Jeol 840, Peabody, MA and Hitachi S4200, Tokyo, Japan) using secondary electron and backscattered electron imaging modes. Transmission electron microscopy (Philips CM 12, Eindhoven, The Netherlands) and energy dispersive spectroscopy (EDS) were used to determine the microstructure, crystallography, and microchemistry of the anodic films. Powder specimens were made by scraping the oxide coating from the metal foil and grinding the powder dispersed in acetone in an agate mortar and pestle. TEM grids were dipped into the solution and air-dried prior to examination. XPS were recorded on a SPECS SAGE 100 (Berlin, Germany) spectrometer. RS was taken with a DILOR-XY (Jobin, Yvon/Horiba, Lille, France) spectrometer equipped with a nitrogen-cooled ccd camera and an argon ion laser operated at wavelength 514.5 nm.

III. RESULTS

It was found that the water content in acetic acid-based electrolytes had a dominant influence on the growth of anodic films on vanadium. Successful anodic film formation was only possible within a small range of water concentration. When a water-free electrolyte was used, no film formation was observed. Alternatively, when a large amount of water was used (20 mol/l), there was spontaneous electrolytic dissolution of the vanadium metal into complex vanadate ions. Figure 1 shows the current density (i) versus voltage (V) curves obtained during the anodization of vanadium at various water concentrations. During the formation, the films exhibit sharp interference colors ranging from brown to gold and then purple. When using a potential of 100 V and greater, a

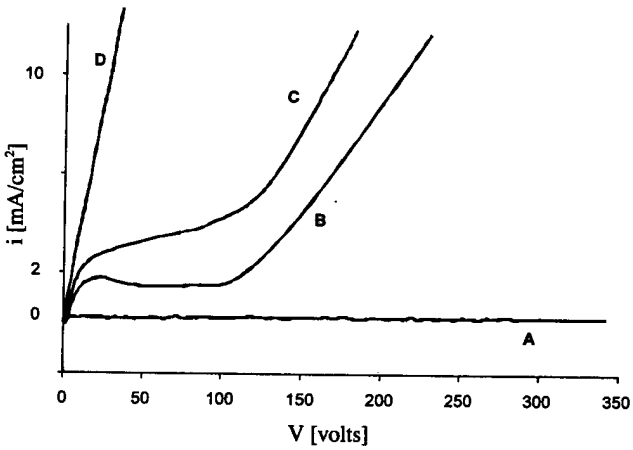


FIG. 1. Potentiodynamic voltage (V) versus current density (i) characteristics (dV/dt = 3 V/s) of the anodization of vanadium for electrolytes: (A) glacial acetic acid, (B) acetic acid + borax + 5 mol/l water, (C) acetic acid + borax + 10 mol/l water, (D) acetic acid + borax + 20 mol/l water.

greenish colored film is formed. The film thickness (d) was determined by infrared-reflectance spectroscopy according to the expression

$$d = \frac{1}{4n(\nu_{max} - \nu_{min})} \quad , \tag{1}$$

with the average refractive index $n = 2.55$ for vanadium oxide and the wave numbers (ν) of the maximum and minimum reflectance between 5000 and 25,000 cm^{-1}, respectively. The corresponding thickness for the interference colored films ranged from 120 nm to about 520 nm for greenish films formed at a voltage of 200 V.

The microstructure of anodic films generated at 80 V is shown in Fig. 2. The surface of these films had a bubbled or domed morphology with pores located in the center of most of the domes. The pore diameters ranged from 100 nm to 1 μm. The domes were thought to be formed by gas bubbles evolved from the metal surface during anodization.

The microstructure of anodic films formed at moderate voltages (150 V) is shown in the SEM micrograph of Fig. 3. An area where this film was ruptured, possibly due to electrochemical dissolution and/or mechanical stress, is seen. At higher magnifications, the surface morphology of these films was similar to those formed at lower deposition voltages.

Figure 4 is a SEM micrograph of a cross-sectioned anodic vanadium oxide film formed at 480 V, dipped in liquid N_2, and fractured. The approximately 5-μm-thick film displayed a dense oxide formation without pore connection to the underlaying metal, which was characteristic of films formed at lower voltages. The film weakly adhered to the metal substrate, and many planar cracks were observed running parallel to the interface. The microstructure was fairly homogeneous and did not possess visible grain boundaries.

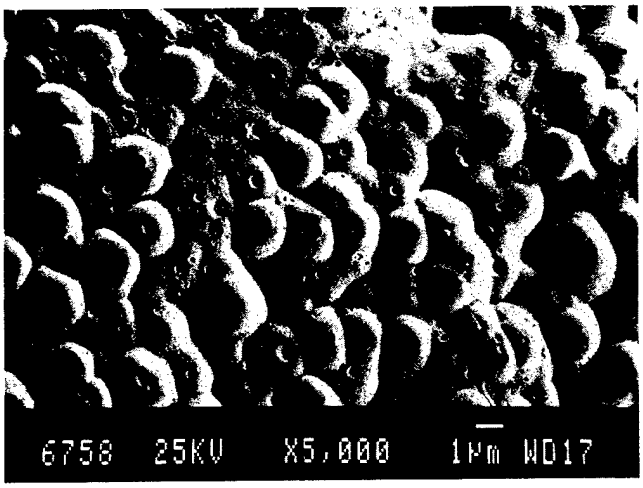


FIG. 2. SEM micrograph showing the morphology of an anodic vanadium oxide film surface deposited at 80 V.

The anodic vanadium oxide coatings were also examined by XPS to determine the oxidation state of vanadium in the coating and, hence, its chemical composition. High-resolution XPS for bare vanadium metal and two different coatings (80 and 480 V) are shown in Fig. 5. There was no significant difference in the XPS spectra for films grown at different voltages. All recorded spectra contained three intense peaks between 535 and 510 eV, corresponding to the core level binding energies of O1*s*, V2$p_{1/2}$, and V2$p_{3/2}$. The O1*s* signal had a binding energy of 530.85 eV and a full width at half-maximum (FWHM) of 1.77 eV, which corresponds to the values for thin V_2O_5 films.[7] Only a small peak asymmetry appeared at about 531.4 eV, which indicated the presence of chemisorbed water. For thin V_2O_5 films, prepared by the

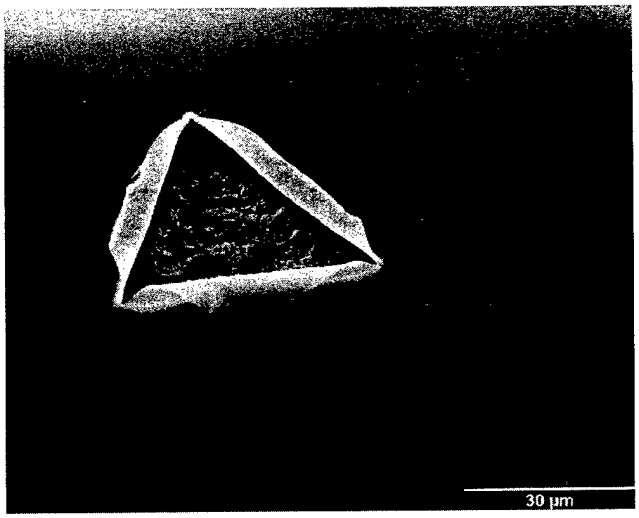


FIG. 3. SEM micrograph of a dissolved region of an outermost vanadium oxide film deposited at 150 V.

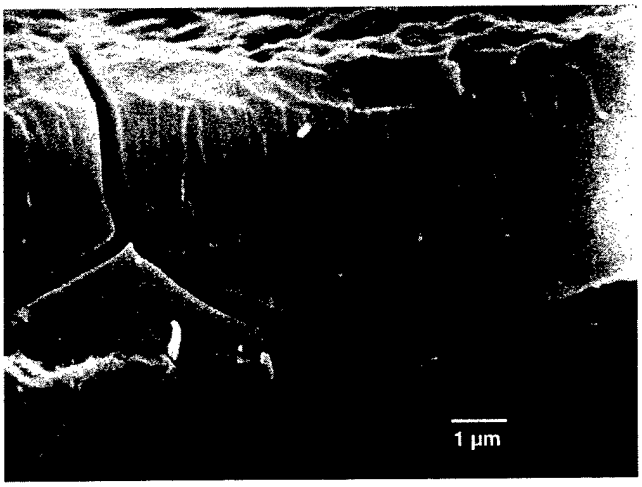


FIG. 4. SEM micrograph of a cross section of a vanadium oxide film deposited at 480 V, dipped in liquid N_2, and fractured. Cracks formed predominantly in the ceramic layer and parallel to the ceramic–metal interface.

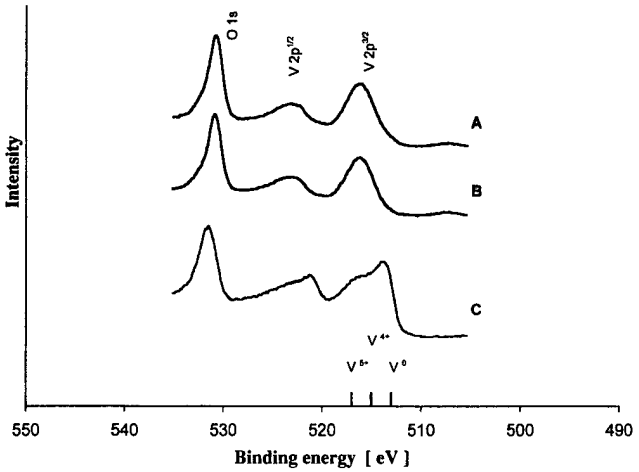


FIG. 5. High-resolution x-ray photoelectron spectra: (A) vanadium oxide film (80 V), (B) vanadium oxide film (480 V), (C) uncoated vanadium sample with transition metal/oxide.

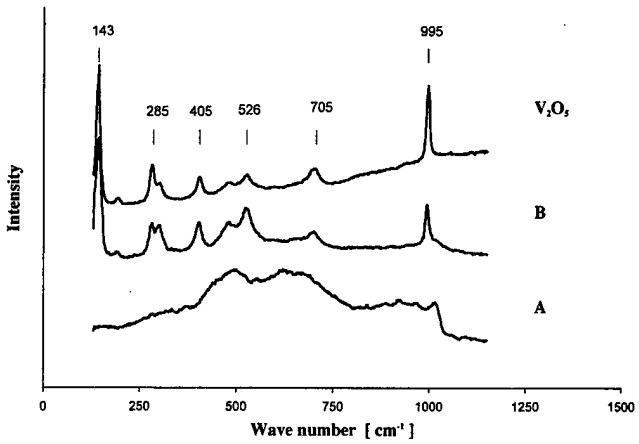


FIG. 6. Raman spectra of vanadium oxide films: (A) anodic VO_x film (4 mW), (B) anodic VO_x film (10 mW), (C) V_2O_5 (reference sample).

sol-gel technique, a peak position for V^{5+} was reported at 516.95 eV.[8] The vanadium binding energy maximum ($V2p_{3/2}$) for our anodic films was observed at 515.86 eV (which was lower than that for pure V^{5+}), and the FWHM (3.6 eV) was too high to assign this E_B value exclusively to V^{5+}. The existence of V^{4+} with E_B = 514.97 eV[8,15] or the presence of lower mixed valence vanadium suboxides could explain this broadened $V2p_{3/2}$ signal. The spectrum for the uncoated vanadium metal [Fig. 5(C)] shows a peak with a binding energy of 513.41 eV for metallic vanadium (V^0). There are also some peaks at lower binding energies, which most likely correspond to the presence of a few monolayers of the native vanadium oxide film.

Electron spin resonance (ESR) measurements on isolated anodic vanadium oxide films indicate an unpaired $3d$ electron (S = ½).[16] The low-temperature spectra (T = 130 K) exhibited a well-resolved hyperfine structure indicating an electron localization on a single vanadium site ^{51}V (nuclear spin I = 7/2). The resulting parameters of the g and A values ($g_{\|}$ = 1.936, $g_{\perp}$ = 1.981; $A_{\|}$ = 183.5, $A_{\perp}$ = 71.5) indicated a distorted $[V^{4+}O_6]$ coordination.[13,16]

RS further characterized the chemical composition of the anodic film to complement the results obtained by XPS and ESR. The Raman spectra for V_2O_5 and a film grown at 300 V are seen in Fig. 6. Two different spectra were collected from the same film at different laser energy densities. The spectrum for the anodic film using a laser power excitation of 4 mW [Fig. 6(A)] indicates an amorphous structure. The broad Raman bands between 400 and 1000 cm^{-1} correspond to V–O–V stretching and vibrational modes in disordered materials.[5,6,17] The broad Raman intensity at approximately 900 cm^{-1} indicates the existence of $[VO_4]$ tetrahedral structures,[18] and the small peak at approximately 1015 cm^{-1} corresponds to the vibration of V=O bonds in isolated $[VO_5]$ trigonal bipyramids.[19]

A drastic modification of the film was observed when the laser power was increased to 10 mW [Fig. 6(B)]. At this power level the film exhibited a well-resolved Raman spectrum characteristic of a crystalline material, and corresponded to that of V_2O_5 [Fig. 6(C)]. Laser-induced alteration of amorphous structures during RS has been previously reported.[20] It can be concluded that the increased laser energy transformed the metastable amorphous structure into microcrystalline V_2O_5 phases. The shift of the vibrational frequency from 1015 cm^{-1} [Fig. 6(A)] to a strong peak at 995 cm^{-1} [Fig. 6(B)] results from an increase of the V=O bond length and is typical for linked $[VO_5]$ units inside the network of the V_2O_5 structure. The strong band at 143 cm^{-1} was assigned to external modes due to the relative motion of long-range ordered vanadium oxide chains.[5,19] Although the spectra for this specimen only had peaks which corresponded to V_2O_5, spectra collected from other specimens[20] indicated the existence of a mixture of vanadium valences, such as was found in the XPS spectra (Fig. 5).

Crystalline phases were not detected by x-ray diffraction (XRD). This result, combined with the Raman spectra collected at low laser powers, indicated that the anodic film was essentially amorphous in nature. Transmission electron microscopy and EDS studies further substantiated and characterized the microstructure and microchemistry of the vanadium oxide films. Powder samples were made by scraping the coating off the vanadium metal and grinding it in an agate mortar and pestle. Several different techniques were tried to make cross-sectional specimens (dimpling, ion milling, tripod polishing, and ultramicrotomy), but due to the softness of the metal, and water solubility of the coating, none of the specimens proved to be satisfactory.

Figure 7(A) is a bright-field (BF) TEM image of a vanadium oxide particle, and Fig. 7(B) is the corresponding selected-area diffraction (SAD) polycrystalline ring pattern. This pattern was indexed as V_2O_5. This particle was mostly amorphous with a couple of small crystalline areas embedded in it. Qualitative EDS analysis of this particle verified that it was a vanadium oxide compound. Figure 8(A) is another SAD pattern from a powdered specimen. This pattern contained both rings and spots and was indexed as the [321] zone axis of orthorhombic V_2O_5. Qualitative EDS analysis of this particle was also performed, and the spectra confirmed it to be a vanadium oxide compound. Figure 8(B) is a SAD polycrystalline powder pattern from a crushed specimen, which contained discrete spots and diffuse rings. This type of pattern indicates a microstructure, which is a mixture of

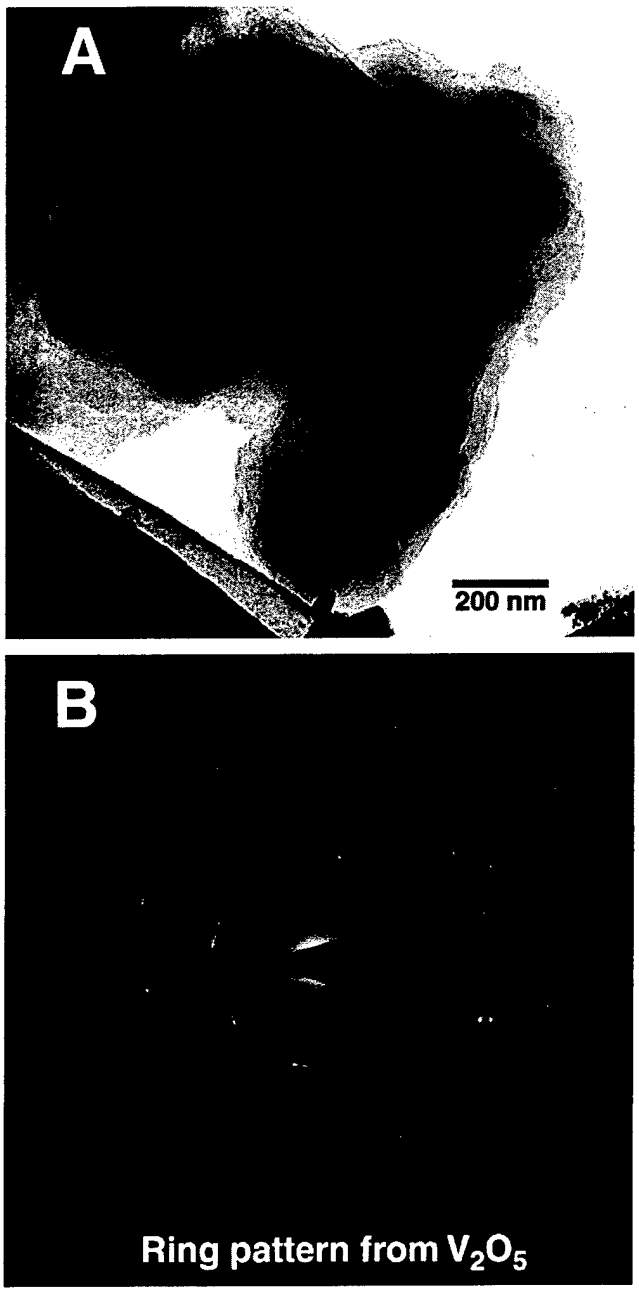


FIG. 7. TEM micrographs of anodic oxide coating on vanadium metal from a powder specimen. (A) is a bright-field TEM image of a vanadium oxide particle, and (B) is the corresponding SAD ring pattern, which identified the particle as containing V_2O_5.

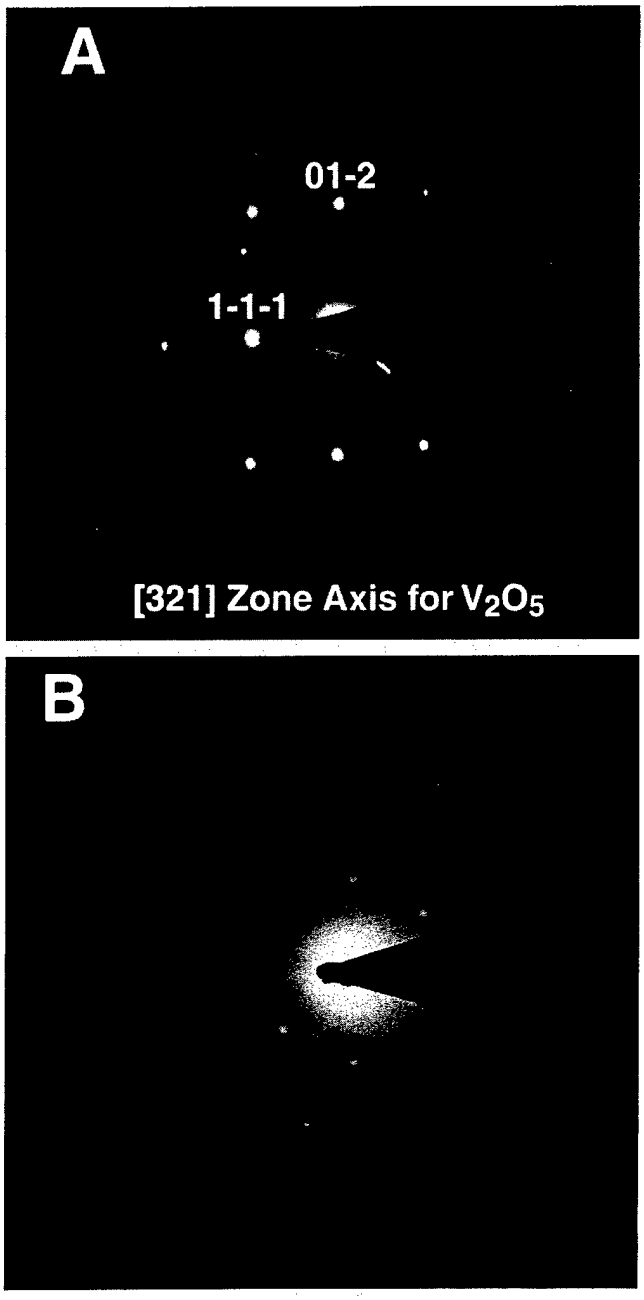


FIG. 8. SAD patterns from anodic vanadium oxide coating from powder specimens. (A) is a combined ring and spot pattern that corresponds to the [321] zone axis of V_2O_5. (B) is a SAD pattern from another region of the specimen, only this pattern contains diffuse rings and spots. This type of pattern is indicative of a mixture of amorphous and crystalline phases.

amorphous and crystalline phases. On the basis of the Raman spectroscopy investigation of the effects of laser-induced crystallization of amorphous anodic films, it is quite possible that this is also occurring under the influence of the electron beam. Crystallization effects or changes of properties during aging and storage of the films for some weeks at room temperature were not observed.

IV. DISCUSSION

Due to the complexity of mixed valence VO_x in the vanadium oxide system, multiphase formation during anodic film deposition is probable. The most common stoichiometric compositions of crystalline oxides are given by the formulae VO, V_2O_3, V_2O_4, and V_2O_5. Furthermore, a homologous series of Magnéli phases exist in the V–O system.[21] These include V_nO_{2n-1} ($4 \leq n \leq 9$) with mixed V^{3+} and V^{4+}, as well as the complex V_nO_{2n+1} phases like V_3O_7, V_4O_9, or V_6O_{13} with V^{4+} and V^{5+} species. According to the general electrochemical reaction

$$xV + yH_2O \rightarrow V_xO_y + 2yH^+ + 2ye^- \quad , \qquad (2)$$

the oxidation of vanadium to the highest valence V^{5+} state is a sequential process. The intermediate generation of low valence states is possible according to the following chemical and electrochemical reactions:

$$V + H_2O \rightarrow V(H_2O)_{ads.} \rightarrow V(OH) + H^+ + e^- \quad , \qquad (3)$$

$$V(OH) \rightarrow V(OH)^{2+} + 2e^- \quad , \qquad (4)$$

$$V(OH)^{2+} + H_3O^+ \rightarrow [V(H_2O)_2]^{3+} \quad , \qquad (5)$$

$$[V(H_2O)_2]^{3+} + H_2O \rightarrow VO^{2+} + 2H_3O^+ + e^- \quad , \qquad (6)$$

$$V(OH)^{2+} + 2H_2O \rightarrow [V(OH)_2]^{2+} + H_3O^+ + e^- \quad , \qquad (7)$$

$$[V(OH)_2]^{2+} \rightarrow VO_2 + 2H^+ \quad , \qquad (8)$$

$$2VO_2 + H_3O^+ \rightarrow V_2O_5 + 3H^+ + 2e^- \quad . \qquad (9)$$

Under the given conditions V^{3+} compounds are unstable [Eq. (6)], but the oxidation states V^{4+} and V^{5+} can generate stable oxide phases.

The following structural model for the description of anodic vanadium oxide film formation is proposed. It is believed that the primary species formed during the anodization process is a metastable amorphous VO_x phase. The vanadium ions are in tetrahedral coordination with oxygen atoms located at the distance of 175 pm from vanadium and 270 pm apart from each other.[22] These tetrahedra form chains and are connected by $[VO_5]$ square pyramids and highly distorted $[VO_6]$ octahedra, to generate a glassylike, three-dimensional network. Nanocrystalline phases of V_2O_5 units exist in this network. The lack of one-tenth of the oxygen atoms needed to form V_2O_5 during the anodic film growth leads to oxygen vacancies and to substoichiometric compositions of V_4O_9 with an orthorhombic structure.[23] Due to the transformation of corner-linked V–O octahedra into edge-linked structures by the formation of crystallographic shear planes, the V_6O_{13} phase can readily be obtained from V_2O_5.[21] In addition to vanadium oxides[14,22] other transition metal oxides such as titanium or niobium exhibit a structure derived from a translation of the unit cell such that edges or faces of polyhedra are shared instead of corners.[24] These crystallographic shear planes tend to be disordered and are associated with the mixed valence of the transition element. The films also contain paramagnetic V^{4+} ions, which are randomly distributed between the different V–O coordinations.

Figure 9 shows the proposed film architecture. It is an amorphous structure with network forming $[VO_4]$ tetrahedra of different degrees of condensation, connecting nanosize units of crystallographic phases of V_2O_5 and other vanadium suboxides.

V. CONCLUSION

Thin films of vanadium oxides have been grown on vanadium metal using an electrolytic technique at high voltages. Acetic acid with controlled amounts of water constituted the electrolyte. The films ranging from 500 to 5000 nm in thickness were characterized by several complementary techniques including SEM, TEM, EDS, and XPS. A structural chemical model is proposed which involves progressive networking of VO_x polyhedra in a metastable amorphous phase. Predominantly tetra- (V^{4+}) and pentavalent (V^{5+}) oxides are formed in the presence of laser or electron beam energy.

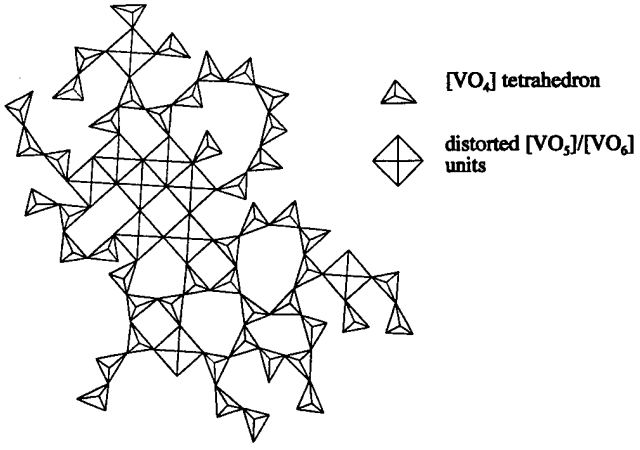


FIG. 9. Proposed chemical structural model of anodic vanadium oxide films. An amorphous $[VO_4]$ tetrahedral network surrounds nanocrystalline regions of $[VO_5]$ and $[VO_6]$ pyramids.

ACKNOWLEDGMENTS

This work was supported by the Deutsche Forschungsgemeinschaft (DFG) of Germany. Thanks are due to Dr. K. Witke for help with Raman spectroscopy. The work of B.R.J. and W.M.K. in the United States was supported by the United States Air Force Office of Scientific Research (AFOSR) under AASERT Grant No. F49620-97-1-0427.

REFERENCES

1. G.E. Thompson, Thin Solid Films **297,** 192 (1997).
2. J.P. Schreckenbach, G. Marx, F. Schlottig, M. Textor, and N.D. Spencer, J. Mater. Sci.: Mater. Med. **10,** 1 (1999).
3. J.P. Schreckenbach, F. Schlottig, G. Marx, W.M. Kriven, O.O. Popoola, M.H. Jilavi, and S.D. Brown, J. Mater. Res. **14,** 1437 (1999).
4. L. Zhang, H.S. Cho, F. Li, R.M. Metzger, and W.D. Doyle, J. Mater. Sci. Lett. **17,** 291 (1998).
5. C. Julien, G.A. Nazri, and O. Bergström, Phys. Status Solidi B **201,** 319 (1997).
6. A. Gorenstein, J.P. Khelfa, and C. Julien, in *Solid-State Ionics IV,* edited by G-A. Nazri, J-M. Tarascon, and M. Schreiber (Mater. Res. Soc. Symp. Proc. **369,** Pittsburgh, PA, 1995), p. 649.
7. V. Ramana, O.M. Hussain, B. Srinivasulu Naidu, C. Julien, and M. Balkanski, Mater. Sci. Eng. B **52,** 32 (1998).
8. Y. Chen, K. Xie, and Z.X. Liu, Appl. Surf. Sci. **133,** 221 (1998).
9. R.G. Keil and R.E. Salomon, J. Electrochem. Soc. **115,** 628 (1968).
10. M.R. Arora and R. Kelly, J. Mater. Sci. **12,** 1673 (1977).
11. S. Hornkjoel and I.M. Hornkjoel, Electrochim. Acta **36,** 577 (1991).
12. M. Privman and T. Hepel, J. Electroanal. Chem. **382,** 137 (1995).
13. M. Nabavi, C. Sanchez, and J. Livage, Philos. Mag. B **63,** 941 (1991).
14. J. Haber, M. Witko, and R. Tokarz, Appl. Catal. A **157,** 3 (1997).
15. J. Cui, D. Da, and W. Jiang, Appl. Surf. Sci. **133,** 225 (1998).
16. J.P. Schreckenbach and P. Strauch, Appl. Surf. Sci. **143,** 6 (1999).
17. J.P. Schreckenbach, K. Witke, D. Butte, and G. Marx, Fres. J. Anal. Chem. **363,** 211 (1999).
18. O. Attos, M. Massot, M. Balkanski, E. Haro-Poniatowski, and M. Asomoza, J. Non-Cryst. Solids **210,** 163 (1997).
19. C. Sanchez, J. Livage, and G. Lucazeau, J. Raman Spectrosc. **12,** 68 (1982).
20. K. Witke, D. Klaffke, A. Skopp, and J.P. Schreckenbach, J. Raman Spectrosc. **29,** 411 (1998).
21. H. Oppermann and W. Brückner, *Vanadiumoxide* (Akademie-Verlag, Berlin, Germany, 1983).
22. A. Mosset, P. Lecante, J. Galej, and J. Livage, Philos. Mag. B **46,** 137 (1982).
23. G. Grymonprez, L. Fiermans, and J. Vennik, Acta Crystallogr. A **33,** 834 (1977).
24. C.N.R. Rao and B. Raveau, *Transition Metal Oxides* (VCH Publishers, New York, 1995).

J. Appl. Physics, submitted, Sept 200

The Single-crystal Elasticity of Yttria (Y_2O_3) to High Temperature

James W. Palko and Waltraud M. Kriven

Department of Materials Science and Engineering, University of Illinois, Urbana, IL 61801

Stanislav V. Sinogeikin and Jay D. Bass

Department of Geology, University of Illinois, Urbana, IL 61801

Ali Sayir

NASA Glenn Research Center, Cleveland, OH 44135

(Recieved

The single-crystal elastic moduli of yttria have been measured by Brillouin spectroscopy up to 1200 °C. The room temperature values obtained are C_{11} = 223.6 ± 0.6 GPa, C_{44} = 74.6 ± 0.5 GPa, and C_{12} = 112.4 ± 1.0 GPa. The resulting bulk and (Voigt-Reuss-Hill) shear moduli are K = 149.5 ± 1.0 GPa and G_{VRH} = 66.3 ± 0.8 GPa, respectively. These agree much more closely with experimental values reported for polycrystalline samples than do previous single-crystal measurements. Linear least squares regressions to the variation of bulk and shear moduli with temperature result in derivatives of dK/dT = -17 ± 2 MPa/°C and dG_{VRH}/dT = -8 ± 2 MPa/°C. Elastic anisotropy was found to remain essentially constant over the temperature range studied.

PACS numbers: 62.20.Dc

I. Introduction

Yttria, or yttrium sesquioxide (Y_2O_3), is a refractory material with a cubic crystal structure.[1] Yttria, in the form of dense polycrystalline ceramics, has been considered for use in nuclear applications[2] and has gained interest relatively recently for use in infrared optics.[1,3,4] Due to yttria's optical isotropy (resulting from its cubic structure), it is possible that, in the future, optical components requiring high quality may be made from single crystals. The single-crystal elastic moduli are valuable for designing such optical components. In particular, the temperature derivatives of elastic moduli allow dimensional changes due to heating under physical constraint, as well as acoustic excitation to be determined. The single-crystal elastic moduli are also useful in understanding the fundamental physics of yttria. Single-crystal yttria fibers suitable for such elasticity measurements have recently been produced using a laser-heated, float zone technique.[5]

The elastic properties of pure and doped polycrystalline yttria have been determined by several authors[6-13] including measurements to high temperatures.[1,2,14] In addition, single-crystal measurements have been reported at room temperature.[15,16] There are, however, significant discrepancies between the bulk and shear moduli reported for dense polycrystalline materials and those calculated from the previously reported single-crystal moduli. The purpose of this study was to obtain accurate values of the single crystal elastic moduli of Y_2O_3 both at room and elevated temperatures.

Brillouin scattering offers a convenient means of measuring the complete set of elastic moduli for single crystals, especially at elevated temperatures. It requires no physical contact with the sample, is capable of measuring along numerous crystallographic directions in a single sample, and requires only small sample volumes. Brillouin scattering

arises from the inelastic scattering of photons from acoustic phonons in the sample. The scattered light is shifted in frequency with respect to the incident light by a factor that is proportional to the velocity of the acoustic waves (Eq. 1).[17]

$$V = \left(\frac{\Delta\omega}{\omega}\right)\left(\frac{c}{2\,n\sin\left(\theta/2\right)}\right) \qquad (1)$$

Here V is the velocity of an acoustic wave, $\Delta\omega$ is the frequency shift of the scattered light, ω is the frequency of the incident light, c is the speed of light, n is the index of refraction of the sample, and θ is the scattering angle. In this study, we employed a special case of symmetric scattering called platelet geometry (Figure 1), which utilizes a sample with flat, parallel faces and equal angles between the face normals and incident/scattered beam directions. The phonon propagation direction q is in the plane of the sample, and the face normals as well as the incident/scattered light rays all lie within a plane.[18] Figure 1 shows a schematic of symmetric platelet scattering. With symmetric platelet scattering geometry, the scattering angle is easily defined, and no knowledge of the index of the refraction of the sample is necessary. As seen in Figure 1, Snell's law allows the replacement of n $\sin(\theta/2)$ with $n_o\sin(\theta_o/2)$ in Eq. 1. This is particularly beneficial for high temperature studies where the variation of index of refraction with temperature is generally unknown and difficult to measure.

The elastic waves may be treated by a continuum mechanical analysis which relates their velocities along a given crystallographic direction to the adiabatic elastic moduli and density of the material via Christoffel's equation (Eq. 2).[19]

$$\left|C_{ijkl}q_jq_l - \rho V^2\delta_{ik}\right| = 0 \qquad (2)$$

C_{ijkl} is the elasticity tensor for the material, ρ is the density, and δ_{ik} is the Krönecker delta function. Since yttria has cubic symmetry, there are only three independent, nonzero components in its elasticity tensor, $C_{11}(=C_{22}=C_{33})$, $C_{12}(=C_{13}=C_{23})$, and $C_{44}(=C_{55}=C_{66})$ (in Voigt notation).[20]

II. Experiment

A. Samples

Samples for this study were taken from single-crystal fibers grown from high purity Y_2O_3 powder by a laser heated float zone (LHFZ) technique.[5,21] This containerless technique uses a scanned CO_2 laser beam (10.6 μm wavelength) that is split and focused at the tip of a polycrystalline source rod to produce a melt which is held between the source and product phases by surface tension. Temperature in the molten region was stabilized using infrared pyrometery, but absolute temperature was not determined because the emissivity of molten yttria is not known.

For preparation of the source rod, high purity (99.999% pure) polycrystalline yttria powder (Alpha Aesar) was used. Since the LHFZ technique is essentially a zone refining

process, the final purity of the yttria crystal is likely even higher. This powder was blended with 5 weight % binder (Methocel 20-231, The Dow Chemical Company, Midland, MI 48674) and glycerin was used as a plasticizer in a water based slurry. The slurry was then degassed overnight with a moderate vacuum (~$70x10^3$ Pa) to achieve a high viscosity paste. This paste was extruded with a custom-made mini-extruder, i.e. a modified hypodermic syringe. The plastic syringe wall was replaced within high wear regions to avoid contamination. At least two extrusions were made to minimize porosity in the paste. The extruded source rod was normally 250 μm in diameter and extruded lengths were 15 to 20 cm long. The rods were furnace dried in air at 200 °C for approximately 1 hour and placed in the LHFZ apparatus without any presintering.

At steady state, the source to fiber diameter ratio is inversely proportional to the square root of the feed rod to pull rod velocity ratio. The fibers used for the Brillouin work had nearly circular cross sections with average diameters slightly less than 500 μm. For fibers grown in this study, the molten zone height was kept constant at approximately one and half times the fiber diameter, and fibers were grown in air.

Octahedral cleavage was apparent in fragments broken from the fibers and showed that the fiber axis coincided closely with the <111> crystal direction. The material was clear except for occasional inclusions that appear to be bubbles. The samples were optically isotropic when examined under cross polarized light. An X-ray analysis was performed on a large fiber sample by four circle diffractometry, in order to verify the single-crystal nature and cubic symmetry of the samples. Precise values of the lattice parameter at all temperatures were calculated from the regression equation of Taylor (Eq. 3),[22]

$$a(T) = (1.06016\ \text{nm})\ (1 + 6.76\text{x}10^{-6}\ T + 1.22\text{x}10^{-9}\ T^2) \qquad (3)$$

where a(T) is the cell edge parameter at a temperature T (in °C). A value of 1.0603 nm (corresponding to 22°C) yielding a theoretical density of 5.033 g/cm^3 (which matches that reported by Tropf and Harris[1]) was used for all room temperature calculations.

Velocity measurements were performed on a single sample. It was ground into a flat plate with a thickness of ~150 μm.[23] Due to breakage during sample preparation, the usable area of the sample faces was around 250 μm x 250 μm. The ground faces corresponded closely to the {100} crystallographic plane. Orientation was accomplished by optical goniometery from cleavage planes, and measurements subsequent to grinding showed the face to be within ~2° of the {100} face.

B. Brillouin Scattering

Illumination of the sample was provided by the 514.5 nm line of an Ar^+ laser at a power of 200 mW or less for the ambient temperature measurements. For high temperature runs, a laser power of up to 400 mW was used to maximize the Brillouin signal since sample heating was not a particular concern. Higher power was necessary for high temperature experiments because of the furnace windows which reduce the intensities of both the incident and scattered beams by partial reflection and introduction of astigmatism into the focusing and collecting optical paths. Scattered light was collected through a slot with an angular acceptance of approximately 5.5° in the scattering plane to lessen broadening of Brillouin peaks. The scattered light was analyzed by a 6-pass,

tandem, Fabry-Perot interferometer. The spectrometer has been described in detail elsewhere.[24,25]

Room temperature measurements were performed with a 90° scattering angle. An Eularian cradle was used to rotate the sample around its face normal to access different phonon directions. The high temperature results of this study were obtained using a compact furnace mounted on the Eularian cradle, allowing multiple phonon directions to be collected without remounting the sample. The construction and operation of this furnace is described elsewhere.[26] An 80° scattering angle was used for the high temperature work. Velocities calculated from the measured Brillouin shifts were used in a linearized inversion algorithm[27] to solve for the elastic moduli.

III. Results and Discussion

Velocities measured at room temperature, in the plane ~(001) (outside the furnace), have a close correspondence to fits from the calculated elastic constants (solid curves Figure 2). This figure gives a sense of the anisotropy in yttria. Longitudinal velocities vary by ~ 4% in this plane, while shear velocities vary by ~ 15%.

The adiabatic elastic constants obtained are given in Table I along with those reported by Aleksandrov et al. (also measured using Brillouin spectroscopy)[15,16] Errors in Table I include contributions due to residuals of the velocity fits as well as uncertainty in sample orientation.[23] There are substantial differences between Aleksandrov's values and those obtained here (C_{11} +1.5%, C_{44} –8%, C_{12} +20%). Table II lists the bulk modulus, K, and shear modulus, G, calculated from the room temperature constants using the Voigt, Reuss, and Voigt-Reuss-Hill averaging schemes (denoted by subscripts V, R, and VRH

respectively) for both this study and for Aleksandrov et al. For comparison, values of K and G (adiabatic) reported previously by several authors for polycrystalline yttria are included in Table II. The values reported by Manning[8] are a Spriggs extrapolation to zero porosity from samples with porosity ranging from 4-22 %, whereas those of Yeheskel[13] and Tropf[1] are uncorrected, and correspond to samples of greater than 99% theoretical density. This fact may account for the differences in bulk modulus.

The values of Aleksandrov et al.[15,16] for K and G_{VRH} are 11% higher and 14% lower, respectively, than those reported here. Clearly, the current measurements agree much more closely with polycrystalline measurements than those of Aleksandrov et al. No details of the quality or properties of the sample are reported in the previous single crystal study,[15] but these aspects may partially account for some of the discrepancies. Another possible explanation is a misorientation of the sample used in the previous study. The differences decrease in the order: $|\Delta C_{12}/C_{12}| > |\Delta C_{44}/C_{44}| > |\Delta C_{11}/C_{11}|$. Ingel and Lewis derived a similar relation of relative magnitudes of deviation for misorientation in Y_2O_3 stabilized ZrO_2 along certain directions.[28] Aleksandrov et al. calculated moduli based on the longitudinal and shear (degernerate) velocities along [100] for which the reported values are 6.75 ± 0.02 km/s and 3.71 ± 0.03 km/s, respectively, as well as both shear velocities along [0.5 0.5 $1/\sqrt{2}$] which are reported as 3.43 ± 0.02 km/s and 3.69 ± 0.01 km/s.[15] Similar velocities result from Eq. 2 using the elastic moduli determined in this study, if a rotation of ~ 13° around [010] is applied to the coordinates of Aleksandrov et al. (i.e. [100] becomes [0.9744 0 0.2250], and [0.5 0.5 $1/\sqrt{2}$] becomes [0.3281 0.5 0.8015].) The resulting longitudinal and shear velocities along [0.9744 0 0.2250] are 6.726 km/s and 3.745 km/s. (The other shear mode with a velocity of 3.849 km/s is

polarized along [010]. Since the incident and scattered beams were directed along [110] and [-110] (in the original coordinate system),[15] this wave is polarized in the scattering plane and would have zero scattered intensity.[29]) The shear velocities along [0.3281 0.5 0.8015] are 3.710 km/s and 3.454 km/s. Aleksandrov et al. report the accuracy of face orientation as 3 to 5°,[15] but this degree of misorientation cannot account for the differences with the current study.

The variation of the single-crystal elastic moduli with temperature is consistent with a linear trend as shown by Figure 3. Table III lists values for the adiabatic constants determined at elevated temperatures. Errors given again include contributions from residuals in the fit as well as uncertainty in sample orientation.[23] Higher order polynomial fits to these results are not warranted, given the uncertainties in the data. The temperature derivatives of the elastic moduli from the linear fits are listed in Table IV along with those for the bulk modulus and Voigt-Reuss-Hill shear modulus. Errors in the temperature derivatives are based on the 95% confidence intervals for the slope of the linear fit. An error of $\pm$5% is given in temperature itself based on uncertainty in the gain of the amplifier used in measuring temperature. This may contribute to an absolute error in slope, but the internal temperature precision is much better (<3%).[23] Furthermore, the uncertainty in slope is dominated by errors in velocity, not in temperature.

Figures 4 and 5 show the temperature dependence of bulk and shear (Voigt-Reuss-Hill) moduli respectively. Also shown are values measured by Dickson and Anderson using a resonance technique (resulting in adiabatic moduli) on a 0.91 Y_2O_3•0.09 ThO_2 polycrystalline sample.[14] There is a slight offset in bulk modulus, but the rate of softening with temperature is similar for both materials. Linear fits to the data of Dickson and

Anderson[14] yield slopes of -15.3 MPa/ °C and -8.5 MPa/ °C for bulk and shear modulus respectively. The offset in bulk modulus may be due to composition, but no estimate of possible errors is given by Dickson and Anderson[14] so the differences may be insignificant.

Figure 6 shows the Young's modulus for yttria calculated from Eq. 4,

$$E = \frac{9KG_{VRH}}{3K + G_{VRH}} \tag{4}$$

along with the data of Price and Hubbert,[30] Dickson and Anderson,[14] a linear fit to the data of Marlowe and Wilder up to 1000 °C,[2] and a fit suggested by Tropf and Harris[1] (based on data from Price and Hubbert[30]). The fit to the data of Marlowe and Wilder[2] yields a slope of -19.5 MPa/ °C. Tropf and Harris[1] infer a pronounced softening of Y_2O_3 at high temperature and a rapid non-linear decrease in elastic modulus at temperatures greater than 1200 °C. The present results do not support such a high order variation in elastic modulus, at least not within the temperature range of this study. The constants of Dickson and Anderson[14] and Marlowe and Wilder[2] are adiabatic while those of Price and Hubbert[30] are for constant temperature.

Elastic anisotropy for a cubic crystal may be characterized by the factor, A, computed using Eq. 5.

$$A = \frac{2C_{44} + C_{12}}{C_{11}} - 1 \tag{5}$$

The elastic constants measured here yield a value for A of 0.170 ± 0.015, while those of Aleksandrov et al. yield 0.212.[15,16] For comparison the values of A for MgO, BaO, and yttrium aluminum garnet ($Y_3Al_5O_{12}$, YAG) are 0.37, -0.07 and 0.02, respectively.[16]

The anisotropy does not vary significantly over the temperature range measured. There appears to be no systematic trend, and no variations in A within the error of the measurement. This contrasts with the behavior of several other oxides which show marked changes with temperature (Table V).

It is possible that this behavior simply results from a peculiarity of the interactions of Y and O, namely that they do not change substantially with temperature, but it is also possible that the constance of anisotropy with temperature is partially tied to the structure of yttria.

To a rough approximation, the elasticity of a crystal may be described by pair potentials between neighboring atoms and 3-body terms which give a potential energy based on the angle of two bonds attached to a central atom. For the halite structure, these may be related qualitatively to the macroscopic elasticity tensor. The halite structure consists of octahedra whose points are directed along the <100> crystallographic directions.[31] Therefore, tension or compression along <100> directions (C_{11}) corresponds to a change in length of the bonds which are all directed toward the points of the octahedra (i.e. <100> directions). Shear along the <100> directions (C_{44}), however, results in the bending of 3 atom groups. Therefore, to a first approximation, a change with temperature, of only the pair potentials between atoms would result in a change in C_{11} leaving C_{44} unaffected, and vice versa for a change in the 3-body term. Though oversimplified, this analysis suggests that the halite structure would show comparable

changes in its macroscopic moduli and its fundamental atomic interactions (i.e. the relative resistance to bond stretching/compression as compared to 3-body bending).

Yttria also has 6-fold coordinated cations. It's structure (bixbyite), however, is much more complex than that of halite, with 16 formula units per cell, and the coordination polyhedra in yttria are not regular octahedra.[31] They are substantially deformed, and the structure is sometimes described as having cubic coordination for Y^{3+} with O^{2-} ions at opposite corners of the cube missing, essentially a defect fluorite structure.[22,32] Regardless of the description of the structure, the Y-O bonds point in many crystallographic directions. Therefore, unlike compounds with the halite structure, uniaxial forces along any crystallographic direction will involve both stretching/compression of bonds and 3-body bending. Therefore, a change in relative resistance of one of these as compared to the other may produce a much smaller change in the macroscopic moduli and hence the anisotropy.

This hypothesis is supported by the relatively low change in anisotropy with temperature for other crystals with a complex relationship between bond directions and the unit cell. This is seen for YAG in Table V, and applies to several other garnets such as almandine and pyrope.[16] Like yttria, garnets have a complex crystal structure with irregular coordination polyhedra. Spinel also follows this trend with a relatively low value of dA/dT.[16,33] Various III-V compounds with zinc-blende lattices, such as GaAs or GaSb, and elements with diamond cubic lattices, such as diamond and silicon, show very low changes in anisotropy with temperature as well.[16] These structures also experience a combination of bond stretching/compression and 3-body bending, for both uniaxial tension and pure shear along high symmetry directions.

IV. Conclusions

The single-crystal elastic moduli of yttria were measured using Brillouin spectroscopy at room temperature and high temperatures ranging to 1200°C. The room temperature values differed significantly from previous single-crystal measurements,[15,16] but bulk properties calculated from the present study agree much more closely with most literature values reported for polycrystalline yttria.[1,8,9,11,13] This is important since it suggests that the elasticity of polycrystalline yttria ceramics can be accounted for by the elasticity of the Y_2O_3 crystal lattice itself. No second phase or secondary effect is indicated here as may have been suggested by the previous results. Sample misorientation in the previous study is offered as a potential reason for the discrepancy.

All elastic moduli display a modest linear decrease over the temperature range studied. The variation of bulk and shear moduli with temperature correspond closely to those reported for a $91Y_2O_3 \cdot 9ThO_2$ compound.[14] Likewise, the change in Young's modulus with temperature agrees well with measurements on pure polycrystalline yttria.[2] Since accurate determinations of the temperature variation of properties for polycrystalline yttria ceramics have been made previously,[2,14] perhaps the more important addition of this study is the temperature dependence of elastic anisotropy, which was found to remain essentially constant for yttria as compared to significant changes for several other oxides with simpler cubic structures. A possible relation between the elastic anisotropy change with temperature and structure is proposed.

Acknowledgements

The work of J. W. Palko was supported by the Fannie and John Hertz Foundation graduate fellowship. X-ray work was performed by J. McMillan at the Center for Microanalysis of Materials at UIUC. Thanks to D.C. Harris for help in obtaining certain reference matter. This work was partially supported by a United States Air Force Office of Scientific Research AASERT Grant, under contract number F49620-97-1-0427 and NSF grant EAR-96-14416.

References

1 W. J. Tropf and D. C. Harris, Proc. SPIE **1112,** 9 (1989).

2 M. O. Marlowe and D. R. Wilder, J. Am. Ceram. Soc. **48,** 227 (1965).

3 R. L. Gentilman, Proc. SPIE **683,** 2 (1986).

4 W. H. Rhodes, G. C. Wei, and E. A. Trickett, Proc. SPIE **683,** 12 (1986).

5 A. Sayir, S. C. Farmer, P. O. Dikerson, and H. M. Yun, Mat. Res. Soc. Sym. Proc. **365,** 21 (1995).

6 E. K. Keler and A. B. Andreeva, Ogneupory, no.5, 224 (1963)[Refractories, no. 5, 243 (1963)].

7 W. R. Manning and J. Orville Hunter, J. Am. Ceram. Soc. **51,** 537 (1968).

8 W. R. Manning, J. O. Hunter, and J. B. R. Powell, J. Am. Ceram. Soc. **52,** 436 (1969).

9 K. K. Phani and S. K. Niyogi, J. Am. Ceram. Soc. **70,** C362 (1987).

10 G. C. Wei, C. Brecher, M. R. Pascucci, E. A. Trickett, and W. H. Rhodes, Proc. SPIE **929,** 50 (1988).

11 K. Shibata, H. Nakamura, and A. Fujii, Proc. SPIE **1326,** 48 (1990).

12 G. C. Wei, M. R. Pascucci, E. A. Trickett, S. Natansohn, and W. H. Rhodes, Proc. SPIE **1326,** 33 (1990).

13 O. Yeheskel and O. Tevet, J. Am. Ceram. Soc. **82,** 136 (1999).

14 R. W. Dickson and R. C. Anderson, J. Am. Ceram. Soc. **51,** 233 (1968).

15 V. I. Aleksandrov, V. F. Kitaeva, V. V. Osiko, N. N. Sobolev, V. M. Tatarintsev, and I. L. Chistyi, Sb. Kratk. Soobshch. Fiz. AN SSSR Fiz. Inst. P. N. Lebedeva, no. 4, 8 (1976)[Sov. Phys. Lebedev Inst. Rep., no. 4, 7 (1976)].

16 *Elastic, Piezoelectric, Pyroelectric, Piezooptic, Electrooptic Constants, and Nonlinear Dielectric Susceptibilites of Crystals*; *Vol. III/18*, edited by K.-H. Hellwege and O. Madelung (Springer-Verlag, Berlin, 1984).

17 G. B. Benedek and K. Fritsch, Phys. Rev. **149,** 647 (1966).

18 E. S. Zouboulis and M. Grimsditch, J. Appl. Phys. **70,** 772 (1991).

19 L. D. Landau and E. M. Lifshitz, *Theory of Elasticity* (Pergamon Press, London, 1959), p. 104.

20 J. F. Nye, *Physical Properties of Crystals: Their Representation by Tensors and Matrices* (Clarendon Press, Oxford, 1985), p. 114.

21 A. Sayir and S. C. Farmer, Mat. Res. Soc. Sym. Proc. **365,** 11 (1995).

22 D. Taylor, Brit. Ceram. Trans. and J. **83,** 92 (1984).

23 J. Palko, M.S. Thesis, University of Illinois, Urbana-Champaign, 2000.

24 J. D. Bass, J. Geophys. Res. **94,** 7621 (1989).

25 S. V. Sinogeikin, J. D. Bass, and T. Katsura, J. Geophys. Res. **103,** 20 (1998).

26 S. V. Sinogeikin, J. M. Jackson, B. O'Neill, J. W. Palko, and J. D. Bass, Rev. Sci. Instrum. **71,** 201 (2000).

27 D. J. Weidner and H. R. Carleton, J. Geophys. Res. **82,** 1334 (1977).

28 R. P. Ingel and D. Lewis, J. Am. Ceram. Soc. **71,** 261 (1988).

29 R. Vacher and L. Boyer, Phys. Rev. B **6,** 639 (1972).

30 M. W. Price and T. E. Hubbert, "Mechanical and Thermal Properties of Four IR Dome Materials," Southern Research Institute Report No. SRI-EAS-87-1272-6225, 1988 (unpublished see ref. 1).

31 R. W. G. Wyckoff, *Crystal Structures*, Vol. 2, 2 ed. (John Wiley & Sons, New York, 1963), p. 2.

32 M. G. Paton and E. N. Maslen, Acta Crystallogr. **19,** 307 (1965).

33 V. Askarpour, M. H. Manghnani, S. Fassbender, and A. Yoneda, Phys. Chem. Miner. **19,** 511 (1993).

Table I: Room temperature elastic constants of yttria

Modulus	This study	Aleksandrov, et al.[15,16]
C_{11} (GPa)	223.6 ± 0.6	227
C_{44} (GPa)	74.6 ± 0.5	68.6
C_{12} (GPa)	112.4 ± 1.0	138

Table II: Measured and calculated bulk properties of yttria at room conditions

K (GPa)	G_V (GPa)	G_R (GPa)	G_{VRH} (GPa)	$G_{Polycrystal}$ (GPa)	Ref.
149.5 ± 1.0	67.0 ± 0.8	65.6 ± 0.8	66.3 ± 0.8		This Study
167.7	59.0	56.4	57.7		15,16
148.9 ± 3.0				69.2 ± 2.0	13
145				67	1
146.2				69.42	8

Table III: Measured elastic constants for yttria at elevated temperatures

T (°C)	C_{11} (GPa)	C_{44} (GPa)	C_{12} (GPa)	K (GPa)	G_{VRH} (GPa)
22[a]	225.1	74.6	113.6	150.8	66.4
22[b]	222.4	73.7	110.8	148.0	66.0
200	221.1	73.4	110.6	147.5	65.5
400	216.9	72.8	108.0	144.3	64.8
600	212.2	70.4	106.7	141.8	62.7
800[a]	206.2	69.0	102.5	137.1	61.5
800[b]	205.3	67.3	103.2	137.2	60.3
1000	199.1	65.3	99.5	132.7	58.6
1200	193.6	63.7	97.9	129.8	56.8

[a] Experimental run to 800°C. Errors for this run are $\pm$0.7% for C_{11}, $\pm$3.3% for C_{44}, and $\pm$1.9% for C_{12}.

[b] Experimental run from 800°C to 1200°C. Errors for this run are $\pm$0.9% for C_{11}, $\pm$3.4% for C_{44}, and $\pm$3.5% for C_{12}.

Table IV: Fitted temperature derivatives for single-crystal and bulk elastic properties of yttria

Modulus	Temperature Derivative (MPa/ °C)
C_{11}	-26 ± 3
C_{44}	-9 ± 2
C_{12}	-13 ± 2
K	-17 ± 2
G_{VRH}	-8 ± 2

Table V: Comparison of changes in elasticity and anisotropy with temperature for several oxides

All temperature derivatives in (10^{-4}/K)	Y_2O_3 pres. study	MgO [16]	BaO [16]	$Y_3Al_5O_{12}$ (YAG) [16]
$(dC_{11}/dT)/C_{11}$	-1.14 ± 0.13	-2.0	-3.7	-0.9
$(dC_{44}/dT)/C_{44}$	-1.21 ± 0.24	-0.8	-1.16	-0.7
$(dC_{12}/dT)/C_{12}$	-1.11 ± 0.18	0.7	0	-0.52
A	0.170 ± 0.015	0.37	-0.07	0.02
dA/dT	0 ± 0.1	2.1	2.8	0.3

Figure 1: Schematic of symmetric platelet scattering geometry

Figure 2: Room temperature velocities in the {100} plane of yttria.

Figure 3: Single-crystal elastic moduli at high temperature

Figure 4: Variation of the bulk modulus of yttria with temperature

Figure 5: Variation of the shear modulus of yttria with temperature

Figure 6: Variation of the Young's modulus of yttria with temperature.

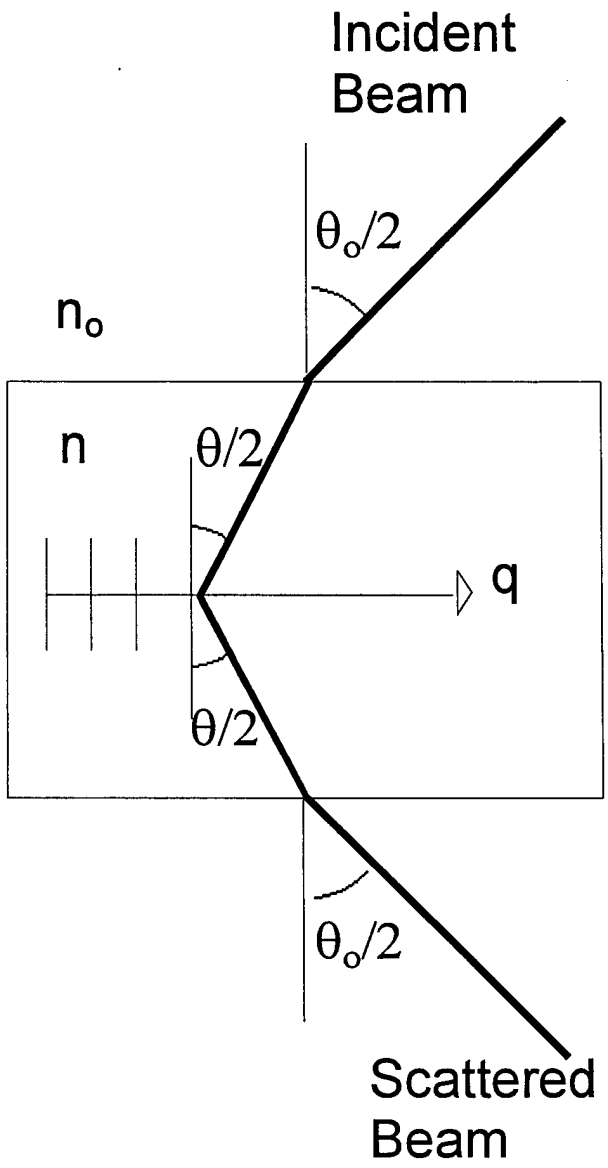


Figure 1 Palko, Kriven, Sinogeikin, Bass, Sayir (2000)

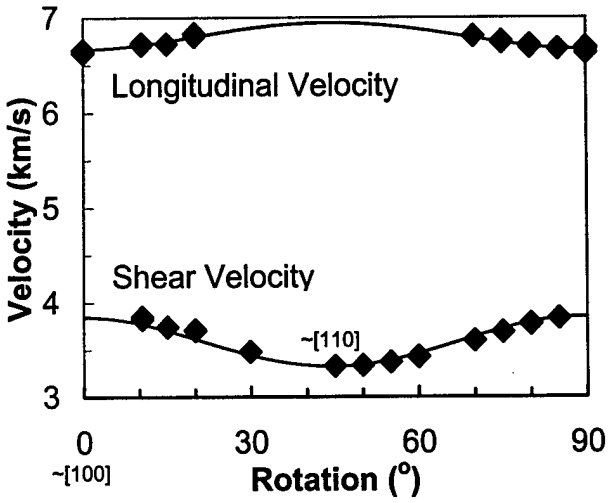


Figure 2 Palko, Kriven, Sinogeikin, Bass, Sayir (2000)

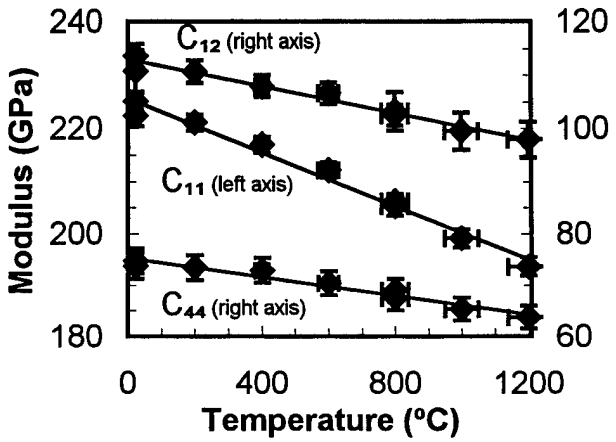


Figure 3 Palko, Kriven, Sinogeikin, Bass, Sayir (2000)

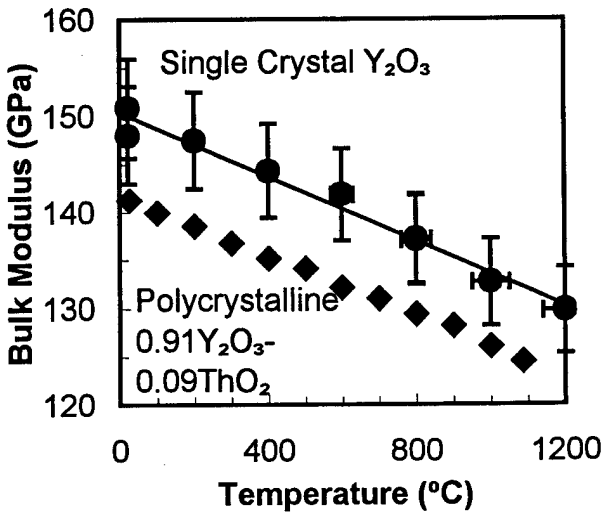


Figure 4 Palko, Kriven, Sinogeikin, Bass, Sayir (2000)

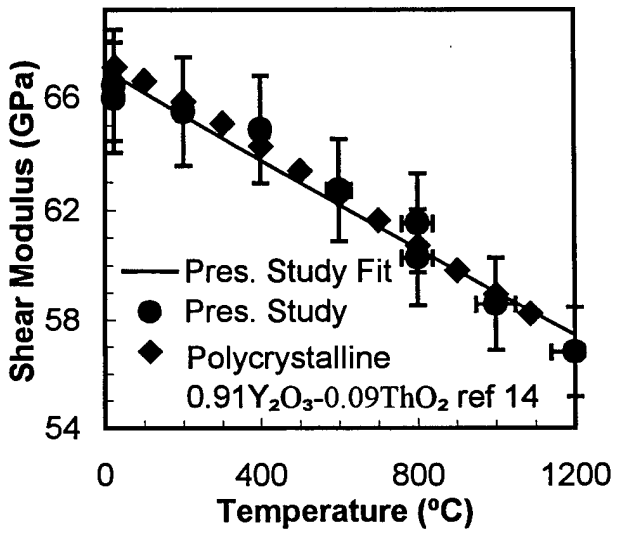


Figure 5 Palko, Kriven, Sinogeikin, Bass, Sayir (2000)

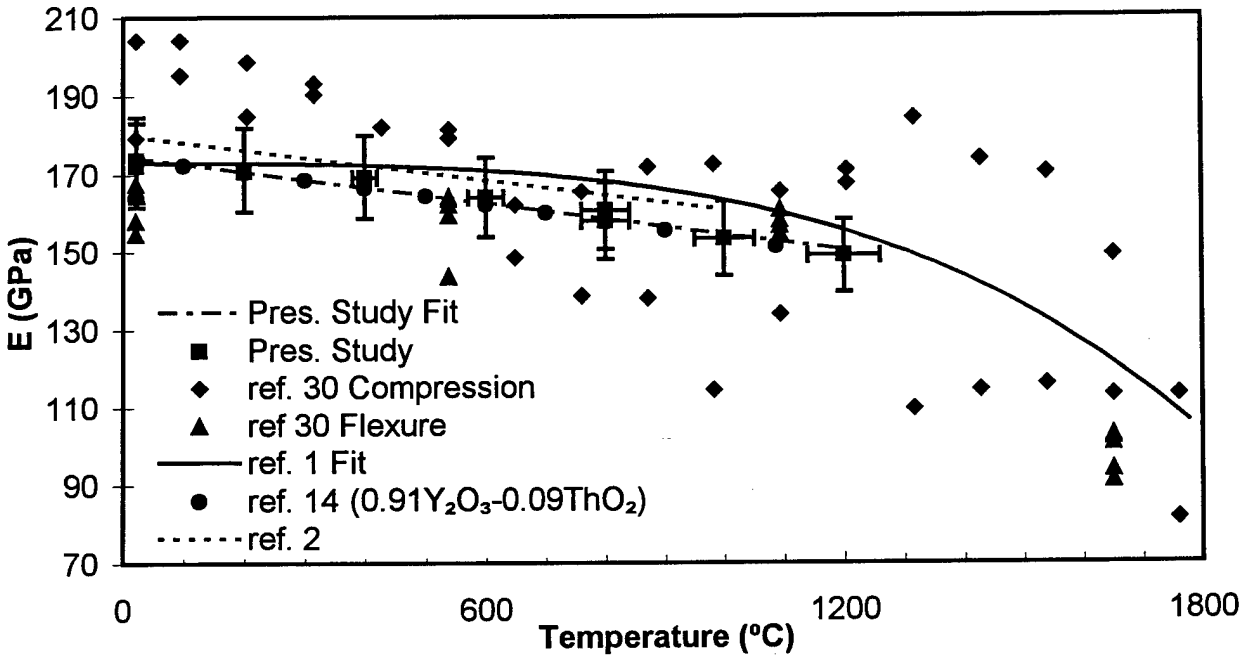


Figure 6 Palko, Kriven, Sinogeikin, Bass, Sayir (2000)

Extended Table I: Room temperature velocities for yttria

Sample Face Normal			Propagation Direction			Vl (m/s)	Vs (m/s)
0.0228	0.0007	0.9997	0.0758	0.9971	-0.0024	6671.0	3834.2
0.0228	0.0007	0.9997	0.1624	0.9867	-0.0044	6688.4	3772.8
0.0228	0.0007	0.9997	0.1624	0.9867	-0.0044	6712.7	3779.8
0.0228	0.0007	0.9997	0.2478	0.9688	-0.0063	6750.8	3689.5
0.0228	0.0007	0.9997	0.2478	0.9688	-0.0063	6735.8	3690.7
0.0228	0.0007	0.9997	0.3313	0.9435	-0.0082	6802.9	3599.3
0.0228	0.0007	0.9997	0.9355	0.3526	-0.0216	6830.0	3711.4
0.0228	0.0007	0.9997	0.9355	0.3526	-0.0216	6802.3	3703.3
0.0228	0.0007	0.9997	0.9627	0.2697	-0.0221	6724.2	3742.8
0.0228	0.0007	0.9997	0.9809	0.1933	-0.0225	6712.0	3823.7
0.0228	0.0007	0.9997	0.9809	0.1933	-0.0225	6728.2	3848.0
0.0228	0.0007	0.9997	0.4900	0.8716	-0.0118		3430.4
0.0228	0.0007	0.9997	0.4900	0.8716	-0.0118		3425.8
0.0228	0.0007	0.9997	0.5641	0.8256	-0.0134		3371.4
0.0228	0.0007	0.9997	0.6339	0.7733	-0.0150		3335.5
0.0228	0.0007	0.9997	0.6989	0.7151	-0.0164		3327.4
0.0228	0.0007	0.9997	0.8610	0.5083	-0.0200		3480.1
0.0228	0.0007	0.9997	0.9997	0.0113	-0.0228	6629.4	
0.0228	0.0007	0.9997	0.9997	0.0113	-0.0228	6658.3	
0.0228	0.0007	0.9997	-0.0113	0.9999	-0.0004	6686.1	

Extended Table I (Continued)

Sample Face Normal			Propagation Direction			Vl (m/s)	Vs (m/s)
0.0228	0.0007	0.9997	-0.0113	0.9999	-0.0004	6665.2	
0.0228	0.0007	0.9997	-0.0113	0.9999	-0.0004	6629.4	

Extended Table II: Velocities used in calculation of constants for yttria to 800 degrees Celsius

Sample Face Normal			**Propagation Direction**			**Vl (m/s)**	**Vs (m/s)**
Room temperature (~20 degrees Celsius)							
0.0228	0.0007	0.9997	0.0053	1.0000	-0.0008	6678.5	0.0
0.0228	0.0007	0.9997	0.0053	1.0000	-0.0008	6679.6	0.0
0.0228	0.0007	0.9997	0.1788	0.9839	-0.0047	6722.2	3792.3
0.0228	0.0007	0.9997	0.1788	0.9839	-0.0047	6730.1	3783.3
0.0228	0.0007	0.9997	0.3469	0.9379	-0.0085	6835.5	3619.6
0.0228	0.0007	0.9997	0.3469	0.9379	-0.0085	6806.3	3615.1
0.0228	0.0007	0.9997	0.4430	0.8965	-0.0107	0.0	3495.1
0.0228	0.0007	0.9997	0.5044	0.8634	-0.0121	0.0	3442.4
0.0228	0.0007	0.9997	0.5044	0.8634	-0.0121	0.0	3435.7
0.0228	0.0007	0.9997	0.5320	0.8466	-0.0127	0.0	3417.7
0.0228	0.0007	0.9997	0.5919	0.8059	-0.0140	0.0	3370.7
0.0228	0.0007	0.9997	0.6598	0.7512	-0.0155	0.0	3344.9
0.0228	0.0007	0.9997	0.6982	0.7157	-0.0164	0.0	3335.9
0.0228	0.0007	0.9997	0.7106	0.7034	-0.0167	0.0	3338.1
0.0228	0.0007	0.9997	0.7106	0.7034	-0.0167	0.0	3341.5
0.0228	0.0007	0.9997	0.7228	0.6909	-0.0169	0.0	3331.4
0.0228	0.0007	0.9997	0.7802	0.6252	-0.0182	0.0	3350.5
0.0228	0.0007	0.9997	0.8317	0.5548	-0.0193	0.0	3399.8

Extended Table II (Continued)

Sample Face Normal			Propagation Direction			Vl (m/s)	Vs (m/s)
Temperature = 200 degrees Celsius							
0.0228	0.0007	0.9997	0.0053	1.0000	-0.0008	6631.4	0.0
0.0228	0.0007	0.9997	0.0053	1.0000	-0.0008	6628.0	0.0
0.0228	0.0007	0.9997	0.1788	0.9839	-0.0047	6692.0	3754.1
0.0228	0.0007	0.9997	0.1788	0.9839	-0.0047	6695.3	3759.7
0.0228	0.0007	0.9997	0.3469	0.9379	-0.0085	6753.6	3614.0
0.0228	0.0007	0.9997	0.3469	0.9379	-0.0085	6760.4	3611.7
0.0228	0.0007	0.9997	0.5044	0.8634	-0.0121	0.0	3431.2
0.0228	0.0007	0.9997	0.5044	0.8634	-0.0121	0.0	3436.8
0.0228	0.0007	0.9997	0.7106	0.7034	-0.0167	0.0	3319.1
0.0228	0.0007	0.9997	0.7106	0.7034	-0.0167	0.0	3319.1
Temperature = 400 degrees Celsius							
0.0228	0.0007	0.9997	0.0053	1.0000	-0.0008	6594.4	0.0
0.0228	0.0007	0.9997	0.0053	1.0000	-0.0008	6591.0	0.0
0.0228	0.0007	0.9997	0.1788	0.9839	-0.0047	6634.8	3754.1
0.0228	0.0007	0.9997	0.1788	0.9839	-0.0047	6640.4	3760.9
0.0228	0.0007	0.9997	0.3469	0.9379	-0.0085	6720.0	3590.4
0.0228	0.0007	0.9997	0.3469	0.9379	-0.0085	6699.8	3591.5
0.0228	0.0007	0.9997	0.5044	0.8634	-0.0121	0.0	3430.1
0.0228	0.0007	0.9997	0.5044	0.8634	-0.0121	0.0	3426.7

Extended Table II (Continued)

Sample Face Normal			Propagation Direction			Vl (m/s)	Vs (m/s)
Temperature = 400 degrees Celsius							
0.0228	0.0007	0.9997	0.7106	0.7034	-0.0167	0.0	3302.3
0.0228	0.0007	0.9997	0.7106	0.7034	-0.0167	0.0	3301.1
Temperature = 600 degrees Celsius							
0.0228	0.0007	0.9997	0.0053	1.0000	-0.0008	6526.0	0.0
0.0228	0.0007	0.9997	0.0053	1.0000	-0.0008	6526.0	0.0
0.0228	0.0007	0.9997	0.1788	0.9839	-0.0047	6581.0	3695.8
0.0228	0.0007	0.9997	0.1788	0.9839	-0.0047	6579.8	3702.6
0.0228	0.0007	0.9997	0.3469	0.9379	-0.0085	6658.3	3540.0
0.0228	0.0007	0.9997	0.3469	0.9379	-0.0085	6656.1	3553.4
0.0228	0.0007	0.9997	0.5044	0.8634	-0.0121	0.0	3365.0
0.0228	0.0007	0.9997	0.5044	0.8634	-0.0121	0.0	3368.4
0.0228	0.0007	0.9997	0.7106	0.7034	-0.0167	0.0	3273.1
0.0228	0.0007	0.9997	0.7106	0.7034	-0.0167	0.0	3260.8
Temperature = 800 degrees Celsius							
0.0228	0.0007	0.9997	0.0053	1.0000	-0.0008	6456.5	0.0
0.0228	0.0007	0.9997	0.0053	1.0000	-0.0008	6457.6	0.0
0.0228	0.0007	0.9997	0.1788	0.9839	-0.0047	6494.6	3682.4
0.0228	0.0007	0.9997	0.1788	0.9839	-0.0047	6495.7	3661.1
0.0228	0.0007	0.9997	0.3469	0.9379	-0.0085	6586.6	3524.3

Extended Table II (Continued)

Sample Face Normal			Propagation Direction			Vl (m/s)	Vs (m/s)
Temperature = 800 degrees Celsius							
0.0228	0.0007	0.9997	0.3469	0.9379	-0.0085	6575.3	3510.8
0.0228	0.0007	0.9997	0.5044	0.8634	-0.0121	0.0	3358.3
0.0228	0.0007	0.9997	0.5044	0.8634	-0.0121	0.0	3358.3
0.0228	0.0007	0.9997	0.7106	0.7034	-0.0167	0.0	3238.3
0.0228	0.0007	0.9997	0.7106	0.7034	-0.0167	0.0	3238.3

Extended Table III: Velocities used in calculation of constants for yttria to 1200 degrees Celsius

Sample Face Normal			**Propagation Direction**			**Vl (m/s)**	**Vs (m/s)**
Room temperature (~20 degrees Celsius)							
0.0228	0.0007	0.9997	-0.3506	0.9365	0.0074	0.0	3598.6
0.0228	0.0007	0.9997	-0.0092	1.0000	-0.0005	6640.5	0.0
0.0228	0.0007	0.9997	-0.0092	1.0000	-0.0005	6655.0	0.0
0.0228	0.0007	0.9997	0.1645	0.9864	-0.0044	6648.3	3811.4
0.0228	0.0007	0.9997	0.1645	0.9864	-0.0044	6673.0	3815.8
0.0228	0.0007	0.9997	0.3332	0.9428	-0.0082	6776.0	3653.4
0.0228	0.0007	0.9997	0.3332	0.9428	-0.0082	6781.6	3641.1
0.0228	0.0007	0.9997	0.4141	0.9102	-0.0101	0.0	3537.0
0.0228	0.0007	0.9997	0.4919	0.8706	-0.0118	0.0	3431.7
0.0228	0.0007	0.9997	0.4919	0.8706	-0.0118	0.0	3470.9
0.0228	0.0007	0.9997	0.4919	0.8706	-0.0118	0.0	3465.3
0.0228	0.0007	0.9997	0.5658	0.8244	-0.0135	0.0	3381.3
0.0228	0.0007	0.9997	0.6355	0.7719	-0.0150	0.0	3360.0
0.0228	0.0007	0.9997	0.7004	0.7136	-0.0164	0.0	3323.0
0.0228	0.0007	0.9997	0.7004	0.7136	-0.0164	0.0	3332.0
0.0228	0.0007	0.9997	0.7599	0.6498	-0.0178	0.0	3329.8
0.0228	0.0007	0.9997	0.8136	0.5811	-0.0189	0.0	3382.4
0.0228	0.0007	0.9997	0.8611	0.5080	-0.0200	0.0	3470.9

Extended Table III (Continued)

Sample Face Normal			Propagation Direction			Vl (m/s)	Vs (m/s)
Temperature = 800 degrees Celsius							
0.0228	0.0007	0.9997	-0.0092	1.0000	-0.0005	6449.0	0.0
0.0228	0.0007	0.9997	-0.0092	1.0000	-0.0005	6434.4	0.0
0.0228	0.0007	0.9997	0.1645	0.9864	-0.0044	6455.7	3660.2
0.0228	0.0007	0.9997	0.1645	0.9864	-0.0044	6473.6	3675.8
0.0228	0.0007	0.9997	0.3332	0.9428	-0.0082	6580.0	3493.3
0.0228	0.0007	0.9997	0.3332	0.9428	-0.0082	6547.5	3485.4
0.0228	0.0007	0.9997	0.4919	0.8706	-0.0118	0.0	3334.2
0.0228	0.0007	0.9997	0.4919	0.8706	-0.0118	0.0	3344.3
0.0228	0.0007	0.9997	0.7004	0.7136	-0.0164	0.0	3215.5
0.0228	0.0007	0.9997	0.7004	0.7136	-0.0164	0.0	3218.9
Temperature = 1000 degrees Celsius							
0.0228	0.0007	0.9997	-0.0092	1.0000	-0.0005	6372.8	0.0
0.0228	0.0007	0.9997	-0.0092	1.0000	-0.0005	6356.0	0.0
0.0228	0.0007	0.9997	0.1645	0.9864	-0.0044	6399.7	3631.0
0.0228	0.0007	0.9997	0.1645	0.9864	-0.0044	6389.6	3615.4
0.0228	0.0007	0.9997	0.3332	0.9428	-0.0082	6473.6	3457.4
0.0228	0.0007	0.9997	0.3332	0.9428	-0.0082	6452.3	3459.7
0.0228	0.0007	0.9997	0.4919	0.8706	-0.0118	0.0	3292.8
0.0228	0.0007	0.9997	0.4919	0.8706	-0.0118	0.0	3287.2

Extended Table III (Continued)

Sample Face Normal			Propagation Direction			Vl (m/s)	Vs (m/s)
Temperature = 1000 degrees Celsius							
0.0228	0.0007	0.9997	0.7004	0.7136	-0.0164	0.0	3194.2
0.0228	0.0007	0.9997	0.7004	0.7136	-0.0164	0.0	3185.3
Temperature = 1200 degrees Celsius							
0.0228	0.0007	0.9997	-0.0092	1.0000	-0.0005	6311.2	0.0
0.0228	0.0007	0.9997	-0.0092	1.0000	-0.0005	6259.7	0.0
0.0228	0.0007	0.9997	0.1645	0.9864	-0.0044	6315.7	3563.8
0.0228	0.0007	0.9997	0.1645	0.9864	-0.0044	6328.0	3560.5
0.0228	0.0007	0.9997	0.3332	0.9428	-0.0082	6424.3	3404.8
0.0228	0.0007	0.9997	0.3332	0.9428	-0.0082	6394.1	3414.9
0.0228	0.0007	0.9997	0.4919	0.8706	-0.0118	0.0	3233.4
0.0228	0.0007	0.9997	0.4919	0.8706	-0.0118	0.0	3244.6
0.0228	0.0007	0.9997	0.7004	0.7136	-0.0164	0.0	3138.2
0.0228	0.0007	0.9997	0.7004	0.7136	-0.0164	0.0	3148.3

J. Am. Ceram. Soc., submitted Dec 2000

Single Crystal Elastic Moduli of Mullite (~$2.5Al_2O_3 \cdot SiO_2$) to High Temperatures by Brillouin Spectroscopy

James W. Palko[a], Ali Sayir[b], Stanislav V. Sinogeikin[c], Waltraud M. Kriven[a,**], Jay D. Bass[c]

a – Department of Materials Science and Engineering, University of Illinois, Urbana, Illinois

b – NASA Glenn Research Center, Cleveland, Ohio

c – Department of Geology, University of Illinois, Urbana, Illinois

Abstract

The complete elastic tensor of mullite has been determined by brillouin spectroscopy at room temperature and elevated temperatures up to 1200 °C. Equivalent, isotropic moduli (bulk, shear, and Young's) have been calculated. The room temperature values obtained by Voigt-Reuss-Hill averaging are (in GPa): $K_{VRH} = 173.5 \pm 6.9$, $G_{VRH} = 88.0 \pm 3.5$, $E_{VRH} = 225.9 \pm 9.0$. All moduli show relatively gradual decreases with temperature. The temperature derivatives obtained for the equivalent, isotropoic moduli are (in MPa/K): $dK_{VRH}/dT = -17.5 \pm 2.5$, $dG_{VRH}/dT = -8.8 \pm 1.4$, $dE_{VRH}/dT = -22.6 \pm 2.8$. Substantial differences between bulk properties calculated from the single crystal measurements in this study and the properties reported in literature for polycrystalline sintered mullite are identified, indicating the importance of factors such as microstructure, intergranular phases, and composition to the elasticity of mullite ceramics.

** - Fellow American Ceramic Society

I. Introduction

Mullite is found in many common ceramics. More recently it has gained favor for use in advanced materials such as structural ceramic matrix composites as both a matrix and reinforcing phase. It has such desirable qualities as high temperature stability and oxidation resistance that make it ideal for use in applications such as gas turbine engines.[1]

Because of the long-term use of mullite and its technological importance,[2] many measurements have been made of its mechanical properties, including measurements of its elastic properties at ambient and elevated temperatures.[3-9] These have all concentrated, however, on bulk polycrystalline properties, and there are great discrepancies in the measured values.

Recently, mullite has become available in single-crystal or highly textured polycrystalline fiber form by use of a laser-heated float zone technique.[10] Such samples allow measurement of the single-crystal elastic properties of mullite. These single crystal measurements provide useful property data for the design of components using large single crystals (e.g. single crystal reinforcing fibers). They also yield information as to what degree the elastic properties of mullite ceramics are a result of the intrinsic properties of the mullite crystal as compared to characteristics that may depend on processing such as microstructure and intergranular phases, which are common in sintered mullite. Therefore, a detailed understanding of the single crystal elastic properties of mullite is extremely useful for a fundamental understanding of the mechanical properties of complex, alumino-silicate ceramics. Such single crystal measurements are made in this study using Brillioun scattering.

Recently, we have reported a full single crystal elastic tensor for mullite at room temperature and selected constants (C_{11}, C_{33}, C_{44}, C_{55}) to 1400°C using brillouin spectroscopy.[11]

This work gives a more accurate room temperature tensor than the previous work (due to a refinement of the sample crystal orientations) as well as the temperature dependence of the full tensor to 1200 °C also with improved accuracy.

II. Theory

Brillouin scattering is the inelastic scattering of light from acoustic waves, allowing the determination of the wave speed. It provides an ideal probe of the elastic properties of the single crystal mullite samples available (especially at high temperatures), requiring only small sample volumes (e.g. 100 x 100 x 50 μm) and no physical contact with the sample. It is capable of measuring the phonon velocities along many propagation directions in a single sample. Brillouin scattered light is shifted in frequency with respect to the incident light by a factor that is proportional to the velocity of the acoustic waves (Eq. 1).[12]

$$V = \left(\frac{\Delta\omega}{\omega}\right)\left(\frac{c}{2\,n\sin\left(\theta/2\right)}\right) \qquad (1)$$

Here V is the velocity of the acoustic wave, $\Delta\omega$ is the frequency shift of the scattered light, ω is the frequency of the incident light, c is the speed of light, n is the index of refraction of the sample, and θ is the scattering angle.

For this study, platelet geometry is used such that the sample has flat, parallel faces, the phonon propagates in the plane of the sample, and the face normals, incident, and scattered light rays all lie within a plane[13]. Figure 1 gives a schematic of the platelet scattering geometry. With

the symmetric platelet geometry, the scattering angle is easily defined, and no knowledge of the index of the refraction of the sample is necessary. This is particularly beneficial for high temperature studies where the variation of index of refraction with temperature is generally unknown and difficult to measure.

The elastic waves probed may be treated by a continuum mechanical analysis which relates their velocities along a given crystallographic direction to the elastic moduli and density of the material via Christoffel's equation (Eq. 2)[14].

$$\left|C_{ijkl}q_jq_l - \rho V^2\delta_{ik}\right| = 0 \qquad (2)$$

C is the elasticity tensor for the material, q is a unit vector along the path of phonon propagation, ρ is the density, and δ is the Krönecker delta function. Since mullite is orthorhombic, 9 independent elastic constants (C_{11}, C_{22}, C_{33}, C_{44}, C_{55}, C_{66}, C_{12}, C_{13}, C_{23}) are required to describe its elastic tensor (in Voigt notation).

III. Experimental Procedure

(1) Brillouin Scattering System

For this study, an Ar^+ laser with a wavelength of 514.5 nm is used to illuminate the sample. Scattered light is analyzed by a 6-pass tandem Fabry-Perot interferometer. Figure 2 is a schematic of the system used to collect Brillouin spectra. The operation of the interferometer has been detailed elsewhere[15,16].

Room temperature work is performed with a 90° scattering angle. An Eularian cradle is used to rotate the sample around its face normal to access different phonon directions. The high temperature results of this study are obtained using a compact furnace mounted on the Eularian cradle, allowing multiple phonon directions to be collected without remounting the sample. The construction and operation of this furnace is described elsewhere.[17] An 80° scattering angle is used for the high temperature work.

(2) Samples

Samples are taken from a fiber grown using the laser-heated, float zone method[10]. Figure 3 shows side and cross sectional views of a representative mullite fiber. A definite growth face is apparent, forming a sawtooth pattern. X-ray analysis shows this to be the (010) face. Cleavage is occasionally observed along this plane, as is observed in natural mullite and sillimanite samples[18]. The fiber has a roughly elliptical cross section minus the growth facet. The roughness on the surface in Figure 3 (b) is due to the diamond saw cutting process. The fiber is for the most part optically clear, with occasional white streaks across its width, apparently consisting of bubbles or occlusions. These white streaks often coincide with the points of the sawtooth pattern along the fiber edge.

The fiber shows uniform extinction under cross polarized light when the polarization direction is nearly aligned or perpendicular to the fiber axis, regardless of rotation about this axis. When ground with parallel faces, some variation in interference color is noted occurring in bands across some samples. This may be a result of a slight change in index of refraction due to compositional variations (or possibly slight variations in thickness). Extinction is somewhat less uniform in cross sections of the fiber.

The composition of the mullite was determined with an electron microprobe (wavelength dispersive) by Dr. Ian Steele using natural kyanite as a standard. The average composition is listed in Table I along with unit cell parameters determined by X-ray diffraction for the mullite sample. The error quoted for composition is the standard deviation of values measured at 10 μm intervals along the length of a fiber section and 5 μm intervals across its width. Density is determined using Eq. 3 for the chemical formula of the unit cell.[19]

$$Al_2(Al_{2+2x}Si_{2-2x})O_{10-x} \qquad (3)$$

x is the average number of oxygen vacancies per unit cell. It is related to the Al_2O_3/SiO_2 molar ratio, $n(Al_2O_3/SiO_2)$ by Eq. 4.

$$x = \frac{2n(Al_2O_3/SiO_2) - 2}{2n(Al_2O_3/SiO_2) + 1} \qquad (4)$$

Initial X-ray diffraction analysis was performed by Ms. Joyce McMillian using a four-circle diffractometer. The X-ray analysis shows that the sample is actually a very highly textured polycrystal, as seen in Figure 4. This analysis verifies that the crystallites have orthorhombic symmetry with slightly varying orientations defined by small rotations about the c axis, which is coincident with the fiber axis. All the crystallites found lie within 5° of each other and the majority lie within 2°. There is no resolvable splitting in the c axis peaks. Lattice parameters for the sample are calculated by fitting the major peak for each scan. A total of six peaks are used in the calculation: $(040),(400),\ (00\bar{2}),(40\bar{2}),\ (04\bar{2}),(22\bar{2})$. The errors quoted encompass all cell

parameters calculated with five of the six peaks (i.e. the maximum and minimum values from six calculations with five peaks). The calculated unit cell angles deviate slightly from 90° (α = 90.4174°, β = 90.2971°, γ = 89.8230°), probably due to the small peaks in close proximity resulting from the highly oriented polycrystalline nature of the sample and large sample size. For the purpose of calculating the cell volume, the interaxial angles were fixed to $\alpha = \beta = \chi =$ 90°.

Separate platelets with approximate face normals of ~[0 1 0], ~[0 0 1], and ~[0.9744 0.2250 0] for velocity measurements were ground using a series of diamond and SiC abrasives ranging from 30 to 1 μm. (Normals and planes are given in an equidistant Cartesian coordinate system, not the orthorhombic lattice of mullite.) Machine grinding was used for some of the coarser steps and the finer polishing was completed by hand. Glass was placed around the sample as a sacrificial material to minimize rounding of the sample faces, which was less than 1.5° for the entire included angle of the face (usually < 1°). Nonparallelness between the faces was less than 0.5°, and the faces produced had a mirror finish with very few scratches visible at 40x magnification. Final dimensions of the samples taken lengthwise from the fiber, ~(100) and ~(010), were approximately 3 mm x 0.4 mm x 0.25 – 0.1 mm. Cross sectional samples, ~(001), had approximate diameters of 0.4 mm and thicknesses of 0.15 –0.1 mm. The orientations of the sample platelets were determined after grinding using X-ray precession photography.[20]

IV. Results

(1) Room Temperature Elasticity

158 separate velocities were measured at room temperature along 37 different crystallographic directions in three different planes(Figures 5, 6, and 7). From these velocities a full set of 9 elastic moduli, listed in Table II, have been determined using a linearized least-squares inversion procedure. This algorithm calculates velocities based on an intial set of preliminary C_{ij}'s (Eq. 2) along the same phonon propagation directions as those measured and then varies the elastic moduli so as to minimize the misfit between the calculated and measured velocities[21]. Velocities calculated from the moduli obtained appear as solid curves in Figures 5, 6, and 7. We note that the final best-fit solution is highly insensitive to the starting guess for the C_{ij}'s. Equivalent, isotropic moduli have been calculated using the Voigt, Reuss, and Voigt-Reuss-Hill averaging schemes (denoted by V, R, and VRH subscripts) and are listed in Table II.

The errors in Table II refer purely to the statistical error in the fit. Deviations from the nominal sample normals (~[0 1 0], ~[0 0 1], ~[0.9744 0.2250 0]) are less than ~4° for all samples. The higher symmetry sample normals are retained to simplify calculation of moduli and error analysis. The error resulting from misorientation of the sample (including rotation about the sample plane normal) is estimated to be less than $\pm$ 2% of the calculated moduli, and the uncertainty in density, on which the moduli are directly proportional, is $\pm$ 0.7%.

(2) High Temperature Elasticity

For high temperature moduli determinations, velocities were collected from each sample plane at 200 °C increments to 1200 °C. Figures 8, 9, and 10 show the calculated elastic longitudinal (e.g. C_{11}), shear (e.g. C_{44}), and cross (e.g. C_{12}) moduli along with best fit, least squares regression lines. High temperature constants are calculated at each temperature from 16 velocities collected along 9 directions (3 in each sample plane; one along each projection of the principle axes and one 45° between them). Linear temperature dependencies are suggested for

all single crystal moduli, with the possible exception of C_{23} which shows a large scatter with temperature. Linear decreases in E_{VRH}, G_{VRH}, and K_{VRH} are also indicated (Figures 11, 12, 13).

The high temperature constants are calculated directly from Christofel's equation assuming the same sample face normals as the room temperature calculations. C_{12} and C_{13} are determined from a weighted average of a single shear and longitudinal acoustic modes based on the sensitivity of the moduli to the specific velocity. [20] C_{23} is calculated only from the longitudinal mode due to difficulty in assigning a specific shear mode. This may account for some of the scatter in the data. A volume coefficient of thermal expansion of 15.8×10^{-6} /°C is used for the calculation of density at high temperature as obtained from the sum of linear expansion coefficients of the lattice parameters given by Schneider and Eberhard [22]. The temperature derivatives of the single crystal moduli and Voigt-Reuss-Hill average moduli are given in Table III. Errors quoted refer to the 95% confidence intervals for the slope of the linear fit.

V. Discussion

(1) Room Temperature Elasticity

The single-crystal moduli, for the most part, fall within the error bars of those previously reported.[11] The one significant discrepancy is C_{23} which was previously reported as 135 GPa based an orientation resulting from the symmetry of the velocity data itself. The current reorientation represents a change of 13° for one plane which affects C_{23}. The current value (142.3 GPa) is ~5% higher and is considered the more accurate. The other constants are clearly affected much less by this reorientation.

Sillimanite, Al_2SiO_5, which has a very similar crystal structure to mullite [23], shows similar elastic behavior. The relative magnitudes of the moduli by value is the same for both crystals, except for the exchange of C_{13} and C_{66}. Andalusite shows the same order in longitudinal constants when its a and b axes are exchanged, which is the transformation required to bring its structure into closest correspondence with mullite[23]. The bulk properties calculated for mullite and sillimanite (Table II) are similar, while andalusite has a smaller bulk modulus but larger shear and Young's moduli.

Bulk values calculated here for mullite agree well with the recent measurements of a polycrystalline mullite sample by Ledbetter et al.[9], as well as the polycrystalline Young's modulus measurements of Pentry [6]. There are, however, considerable differences among the values of elastic moduli reported for polycrystalline mullite (Table IV), and certain authors [7,8] have reported values that exceed even the Voigt bounds of the respective moduli calculated here. These should set an upper limit on the possible values for a polycrystalline aggregate of mullite. The discrepancy may be due to intergranular phases. Compositional differences may also play a role. The polycrystalline studies were performed on mullite samples with a lower alumina content ($3\ Al_2O_3 \bullet 2\ SiO_2$).

(2) High Temperature Elasticity

Comparisons with temperature derivatives of polycrystalline elastic properties given in the literature show significant differences (Table V). The derivative obtained for Young's modulus in this study is more negative than -8 MPa/°C as seen in the data of Wachtman for temperatures below 600°C[4]. (Note that the scale in Figure 11 for the literature data is twice as fine than for the current data, while in Figure 12 it is twice as coarse.) Ledbetter also reports a more gradual decrease in Young's modulus (-11 MPa/°C)[9]. These differences could result from

a glassy phase in the polycrystalline body. Silica glass is known to stiffen with temperature[24]. A similar effect may occur with an intergranular glass phase, thereby mitigating the reduction in stiffness of the mullite grains. The temperature derivative of the shear modulus from the present study, however, is much smaller than -30 MPa/°C which is suggested by a linear fit to Wygant's data.[3] This may be due to a low melting (or more rapidly softening) intergranular phase. Ledbetter reports an extremely gradual -3.3 MPa/°C temperature derivative of shear modulus as well as a bulk modulus temperature derivative of -20 MPa/°C[9]. All values from Ledbetter are for room temperature and are corrected to zero porosity. The temperature behavior of mullite ceramics is clearly affected, and possibly dominated, by properties other than those intrinsic to the crystalline mullite itself.

VI. Conclusions

The full elastic tensor of mullite has been determined at room and elevated temperatures to 1200 °C. Room temperature values show close correspondence with structural analogs, sillimanite and andalusite. Bulk elastic properties calculated from the single crystal moduli agree well with some measurements on polycrystalline mullite[6,9], but there are substantial differences with much published data. In particular some authors report values[7,8] that exceed the maximum possible limit (Voigt bound) for average moduli calculated here, suggesting that intergranular phases and composition may play a very large role in determining the elastic properties of nominally pure mullite ceramics.

High temperature measurements were made in 200 °C intervals to 1200°C. A relatively gradual linear decrease was noted in all moduli with temperature. The temperature derivatives of bulk properties calculated from the single crystal moduli do not correspond well with much of

the data in literature, again suggesting that intergranular phases are important in the elasticity of mullite ceramics. Phases having behavior at high temperature much different than mullite, such as stiffening or rapid softening with temperature, are suggested by this data.

Acknowledgments:

The work of J. W. Palko was supported by the Fannie and John Hertz Foundation graduate fellowship. X-ray work was performed by J. McMillan at the Center for Microanalysis of Materials at UIUC. Electron microprobe analysis was conducted by Dr. I. Steele at the University of Chicago. This work was partially supported by a United States Air Force Office of Scientific Research AASERT Grant, under contract number F49620-97-1-0427 and NSF grant EAR-96-14416.

References

1 U. Steinhauser, W. Braue, J. Gootring, B. Kanka, and H. Schneider, "A New Concept for Thermal Protection of All-Mullite Composites in Combustion Chambers," J. Europ. Ceram. Soc. **20** 651-658 (2000).

2 A. J. Skoog and R. E. Moore, "Refractory of the Past for the Future: Mullite and Its Use as a Bonding Phase," Am. Ceram. Soc. Bull. **67** [7] 1180-1185 (1988).

3 J. F. Wygant, "Elastic and Flow Properties of Dense, Pure Oxide Refractories," J. Am. Ceram. Soc. **34** [12] 374-380 (1951).

4 J. B. Wachtman and D. G. Lam, "Young's Modulus of Various Refractory Materials as a Function of Temperature," J. Am. Ceram. Soc. **42** [5] 254-260 (1959).

5 J. E. Fenstermacher and F. A. Hummel, "High-Temperature Mechanical Properties of Ceramic Materials: IV Sintered Mullite Bodies," J. Am. Ceram. Soc. **44** [6 June] 284-289 (1961).

6 R. A. Pentry, D. P. H. Hasselman, and R. M. Spriggs, "Young's Modulus of High-Density Polycrystalline Mullite," J. Am. Ceram. Soc. **55** 169-170 (1972).

7 M. G. M. U. Ismail, Z. Nakai, and S. Shigeyuki, "Microstructure and Mechanical Properties of Mullite Prepared by the Sol-Gel Method," Comm. Am. Ceram. Soc. **70** [1] C7-8 (1987).

8 W. H. Kelly, A. N. Palazotto, R. Ruh, J. K. Heuer, and A. Zangvil, "Thermal Shock Resistance of Mullite and Mullite-ZrO_2-SiC Whisker Composites," Ceram. Engr. & Sci. Proc. **18** [3] 195-203 (1997).

9 H. Ledbetter, S. Kim, D. Balzar, S. Crudele, and W. Kriven, "Elastic Properties of Mullite," J. Am. Ceram. Soc. **81** [4] 1025-1028 (1998).

10 A. Sayir and S. C. Farmer, "Directionally Solidified Mullite Fibers," Mat. Res. Soc. Sym. Proc. **365** 11-20 (1995).

11 W. M. Kriven, J. W. Palko, S. Sinogeikin, J. D. Bass, A. Sayir, G. Brunauer, H. Boysen, F. Frey, and J. Schneider, "High Temperature Single Crystal Properties of Mullite," J. Europ. Ceram. Soc. **19** 2529-2541 (1999).

12 G. B. Benedek and K. Fritsch, "Brillouin Scattering in Cubic Crystals," Phys. Rev. **149** [2] 647-662 (1966).

13 E. S. Zouboulis and M. Grimsditch, "Refractive Index and Elastic Properties of Single-crystal Corundum (α-Al_2O_3) up to 2100 K," J. Appl. Phys. **70** [2] 772-776 (1991).

14 L. D. Landau and E. M. Lifshitz, *Theory of Elasticity* (Pergamon Press, London, 1959), p. 104.

15 J. D. Bass, "Elasticity of Grossular and Spessartite Garnets by Brillouin Spectroscopy," J. Geophys. Res. **94** 7621-7628 (1989).

16 S. V. Sinogeikin, J. D. Bass, and T. Katsura, "Sound Velocities and Elastic Properties of Fe-bearing Wadsleyite and Ringwoodite," J. Geophys. Res. **103** [B9] 20,819-825 (1998).

17 S. V. Sinogeikin, J. M. Jackson, B. O'Neill, J. W. Palko, and J. D. Bass, "Compact High-Temperature Cell for Brillouin Scattering Measurements," Rev. Sci. Instrum. **71** [1] 201-206 (2000).

18 W. D. Nesse, *Introduction to Optical Mineralogy* (Oxford University Press, New York, 1986), p. 170-171.

19 W. M. Kriven and J. A. Pask, "Solid Solution Range and Microstructure of Melt-Grown Mullite," J. Am. Ceram. Soc. **66** [9] 649-654 (1983).

20 J. Palko, M.S. Thesis, University of Illinois, Urbana-Champaign, 2000.

21 D. J. Weidner and H. R. Carleton, "Elasticity of Coesite," J. Geophys. Res. **82** [8] 1334-1346 (1977).

22 H. Schneider and E. Eberhard, "Thermal Expansion of Mullite," J. Am. Ceram. Soc. **73** [7] 2073-2076 (1990).

23 H. Schneider, K. Okada, and J. A. Pask, *Mullite and Mullite Ceramics* (John Wiley & Sons, Chichester, 1994), p. 1-8.

24 J. D. Bass, "Elasticity of Minerals, Glasses, and Melts"; pp. 45-63 in *Mineral Physics and Crystallography: A Handbook of Physical Constants.* edited by T. J. Ahrens (American Geophysical Union, Washington, DC, 1995).

25 M. T. Vaughan and D. J. Weidner, "The Relationship of Elasticity and Crystal Structure in Andalusite and Sillimanite," Phys. Chem. Miner. **3** 1-12 (1978).

26 M. I. Osendi, B. A. Bender, and D. Lewis, III, "Microstructure and Mechanical Properties of Mullite-Silicon Carbide Composites," J. Am. Ceram. Soc. **72** [6] 1049-1054 (1989).

Figure 1: Schematic of platelet scattering geometry

Figure 2: Schematic of Brillouin scattering system.

Figure 3: Optical micrographs of mullite sample (a) lengthwise and (b) in cross section

Figure 4: X-ray scan rotating sample around fiber axis with fixed 2θ

Figure 5: Room temperature velocities versus rotation in ~(100) plane

Figure 6: Room temperature velocities versus rotation in ~(010) plane

Figure 7: Room temperature velocities versus rotation in ~(001) plane

Figure 8: Single-crystal longitudinal moduli versus temperature

Figure 9: Single-crystal shear moduli versus temperature

Figure 10: Single-crystal cross moduli versus temperature

Figure 11: Young's modulus of mullite versus temperature

Figure 12: Shear modulus of mullite versus temperature

Figure 13: Bulk modulus of mullite versus temperature

Table I: Properties of mullite sample at room temperature

a (nm)	0.758 ± 0.001
b (nm)	0.767 ± 0.001
c (nm)	0.289 ± 0.001
Cell Volume (nm^3)	0.168 ± 0.001
Molar Al_2O_3/SiO_2 ratio	2.5 ± 0.1
Theoretical Density (g/cm^3)	3.11 ± 0.02

Table II: Room temperature moduli of mullite, andalusite, and sillimanite

Constant	Mullite	Sillimanite[25]	Andalusite[25]
C_{11} (GPa)	281.9 ± 0.7	287.3	233.4
C_{22} (GPa)	244.2 ± 0.9	231.9	289.0
C_{33} (GPa)	363.6 ± 1.0	388.4	380.1
C_{44} (GPa)	111.7 ± 0.6	122.4	99.5
C_{55} (GPa)	78.2 ± 0.5	80.7	87.8
C_{66} (GPa)	79.2 ± 0.5	89.3	112.3
C_{12} (GPa)	105.1 ± 1.0	94.7	81.4
C_{13} (GPa)	100.3 ± 1.3	83.4	116.2
C_{23} (GPa)	142.3 ± 1.6	158.6	97.7
K_V (GPa)	176.1	175.1	165.9
K_R (GPa)	171.0	166.4	158.0
K_{VRH} (GPa)	173.5	170.8	162.0
G_V (GPa)	90.0	95.1	100.4
G_R (GPa)	86.1	87.8	97.7
G_{VRH} (GPa)	88.0	91.5	99.1
E_V (GPa)	230.6	241.6	250.6
E_R (GPa)	221.2	224.0	243.0
E_{VRH} (GPa)	225.9	232.8	246.8

Table III: Fitted temperature derivatives for mullite to 1200°C

Modulus	**Temperature derivative (MPa/°C)**
C_{11}	-29.2 ± 3.2
C_{22}	-29.7 ± 1.6
C_{33}	-28.6 ± 4.2
C_{44}	-7.9 ± 1.1
C_{55}	-6.5 ± 0.9
C_{66}	-10.1 ± 0.9
C_{12}	-16.1 ± 0.5
C_{13}	-6.8 ± 1.4
C_{23}	-8.1 ± 10.5
K_{VRH}	-17.5 ± 2.5
G_{VRH}	-8.8 ± 1.4
E_{VRH}	-22.6 ± 2.8

Table IV: Bulk properties of polycrystalline mullite reported in literature

E (GPa)	ν	G (GPa)	K (GPa)	Density	Ref.
225.9		88.0	173.5	3110 kg/m^3	Pres. Study (VRH Avr)
		59			3
143.0				2780 kg/m^3	4
124					5
223.4 ± 5.5				Corrected to 100% (Spriggs)	6
224.1 ± 5.5				Corrected to 100% (Hasselman)	"
246				>98% (3150 kg/m^3)	7
194	0.276	76.0	144.3	95%	26
252	0.266	99.5	179.5		8
227.5	0.280	88.9	172.4	99.6%	9
229.1	0.280	89.5	173.9	Corrected to 100%	"

Table V: Comparison of temperature derivatives with literature values

dK/dT (MPa/K)	**dG/dT(MPa/K)**	**dE/dT (MPa/K)**	**Ref.**	**Notes**
-17.5 $\pm$ 2.5	-8.8 $\pm$ 1.4	-22.6 $\pm$ 2.8	Pres. Study	VRH average
				20 – 1200 °C
		-8	4	20 – 600 °C
-20	-3.3	-11	9	
	-30		3	

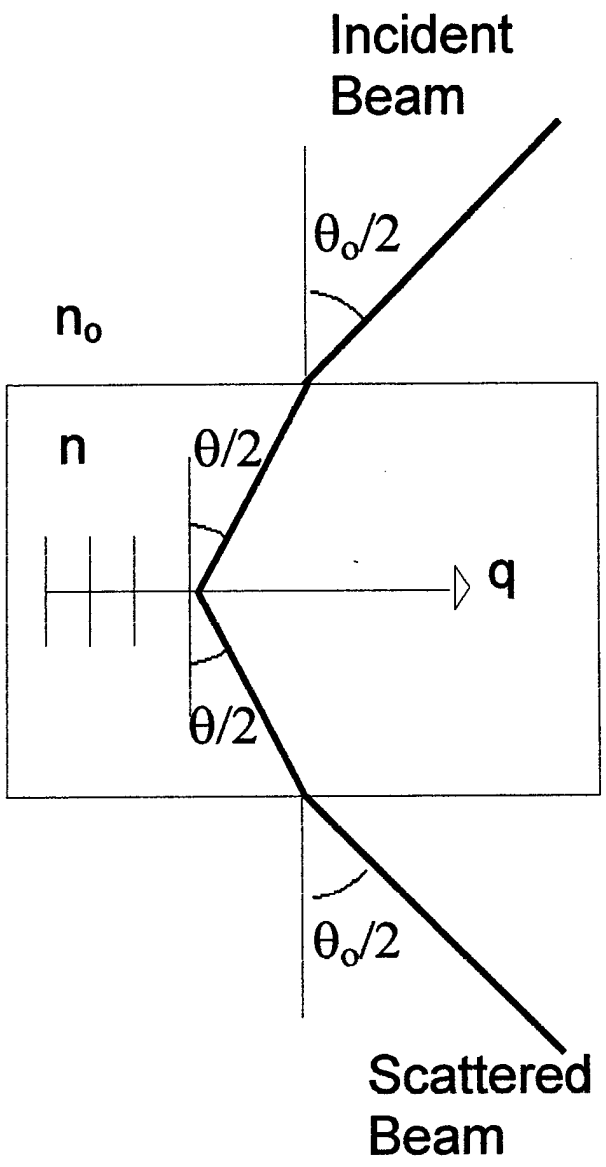


Figure 1: Schematic of platelet scattering geometry

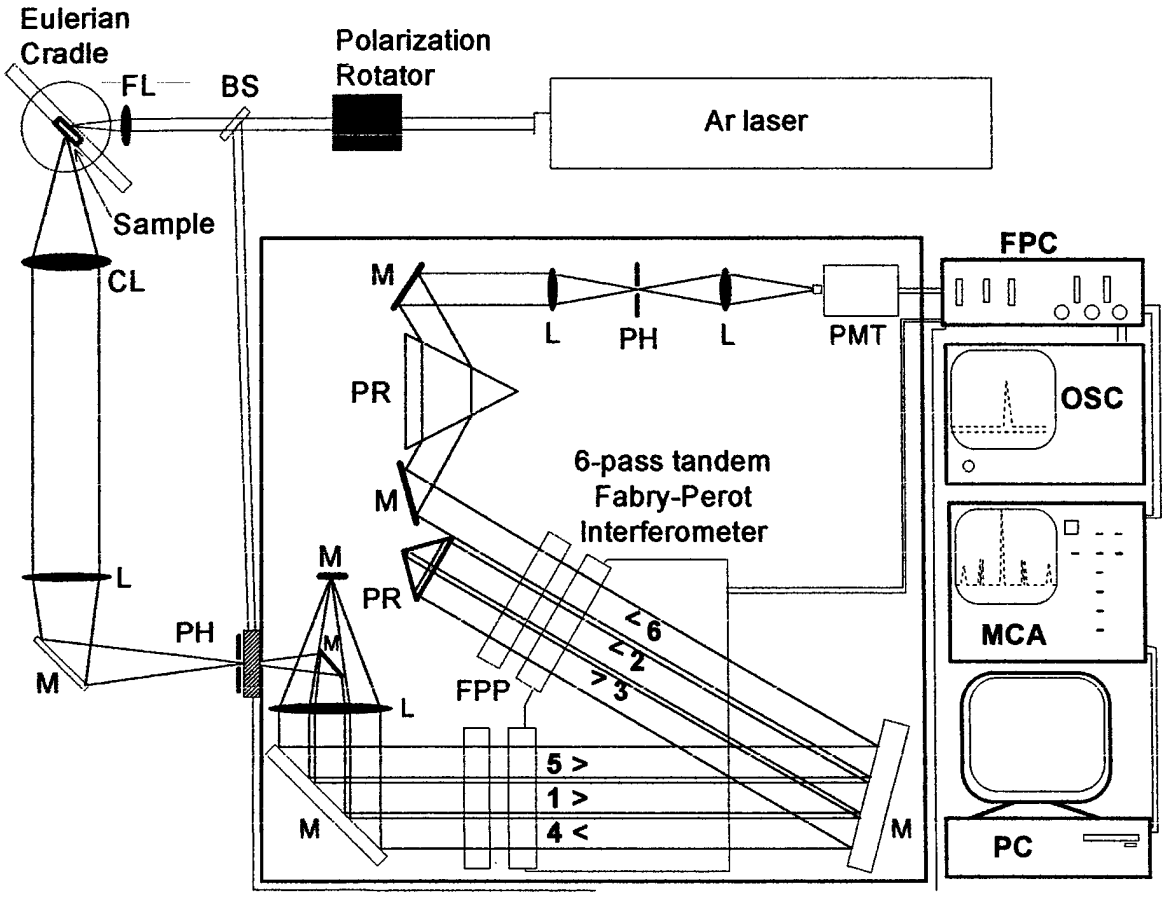
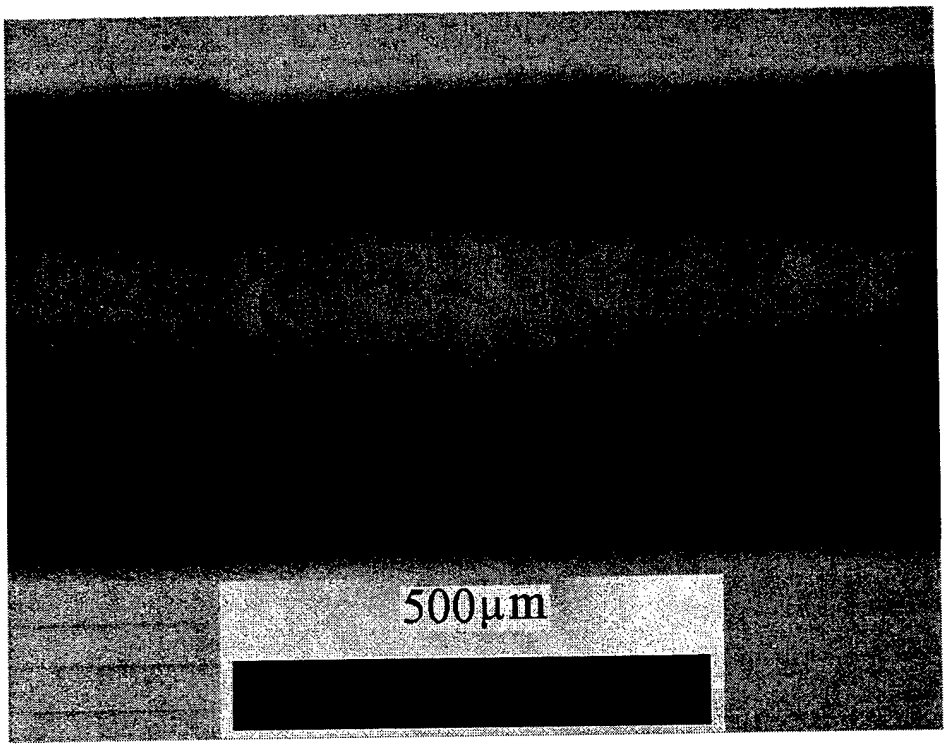
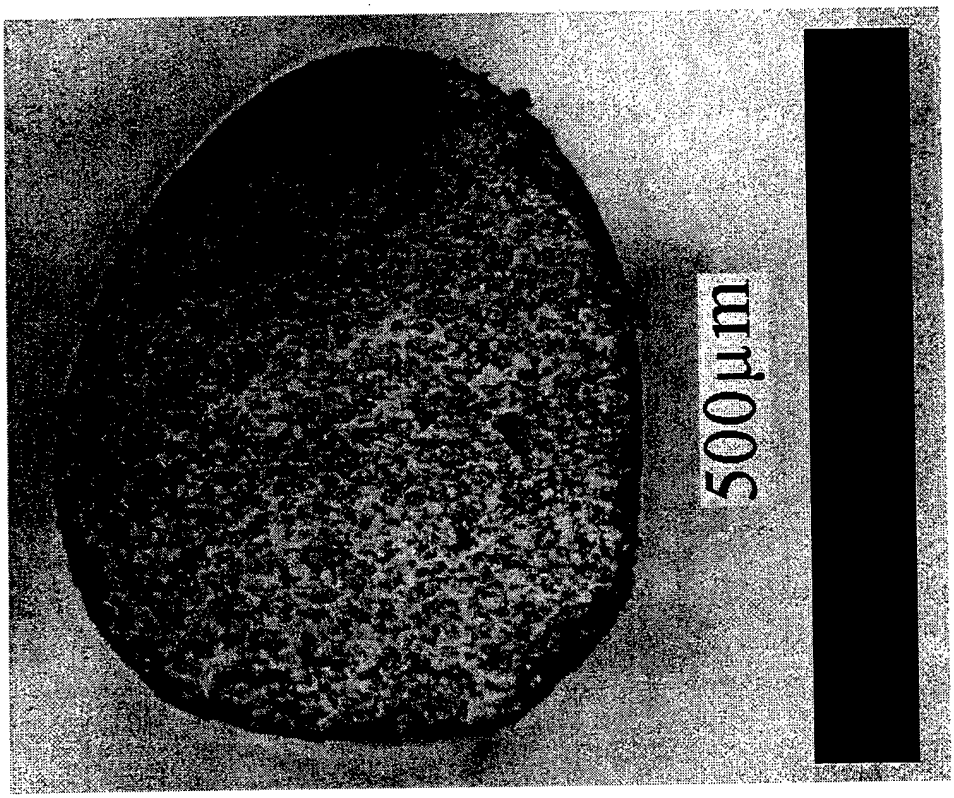


Figure 2: Schematic of the Brillouin spectroscopy system (BS = beam splitter, M = mirror, L = lens, FL = focusing lens, CL = collecting lens, PH = pinhole, PR = prism, FPC = Fabry-Perot controller, OSC = oscilloscope, MCA = multichannel analyzer, PC = Personal Computer, FPP = Fabry Perot Plates)



a)



b)

Figure 3: Optical micrographs of mullite sample (a) lengthwise and (b) in cross section

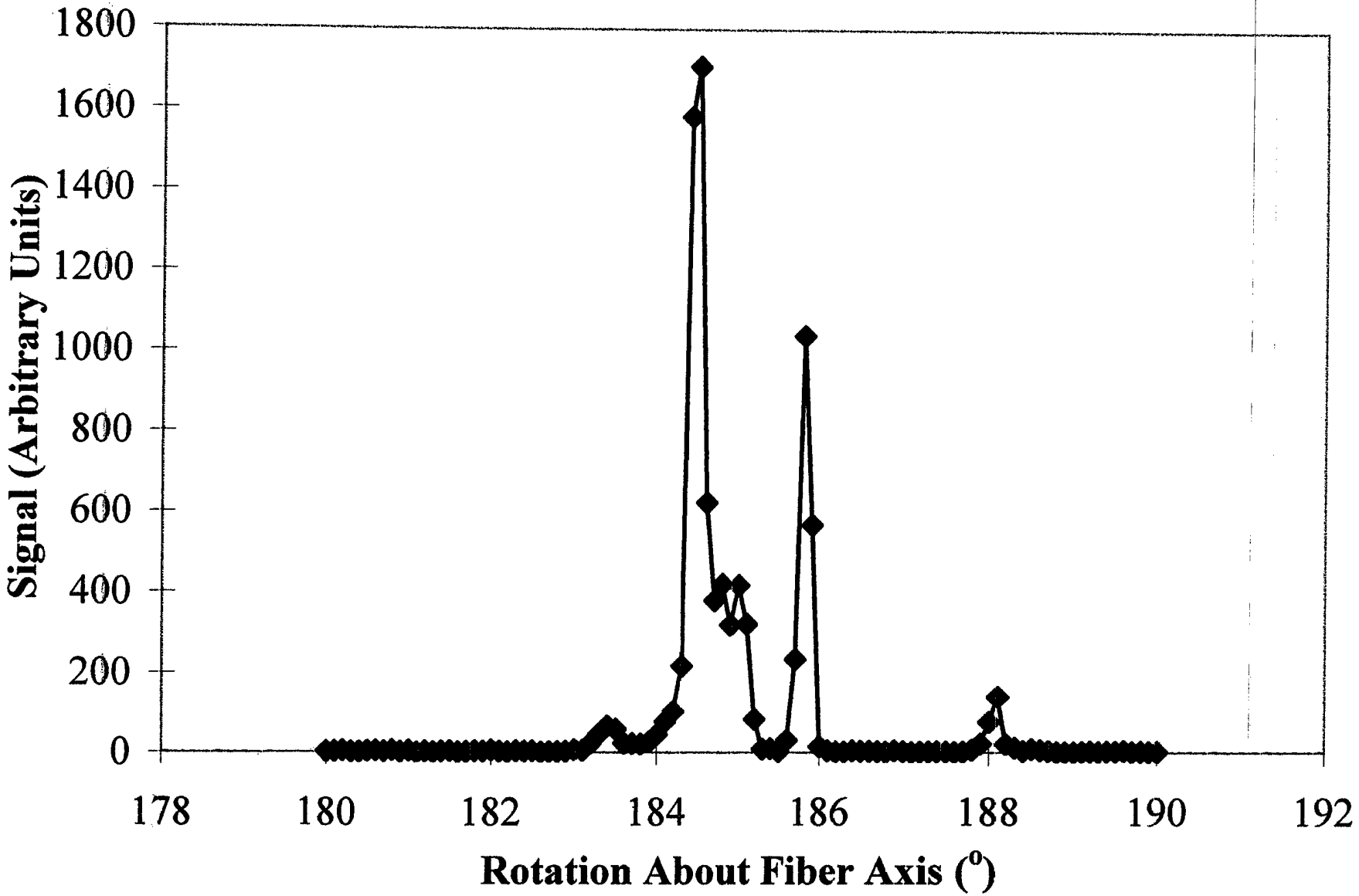


Figure 4: X-ray scan rotating sample around fiber axis with fixed 2θ

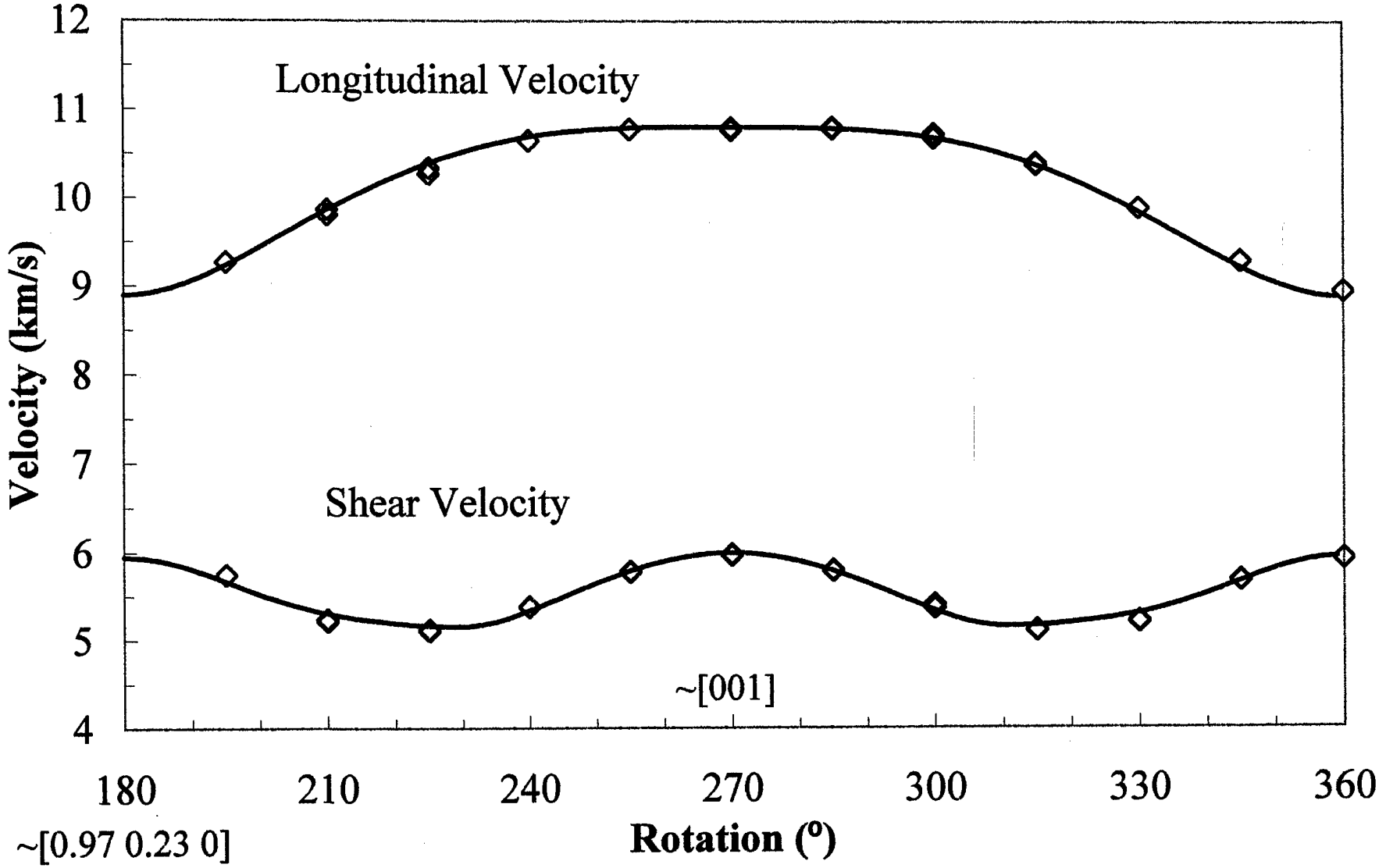


Figure 5: Room temperature velocities versus rotation in ~(100) plane

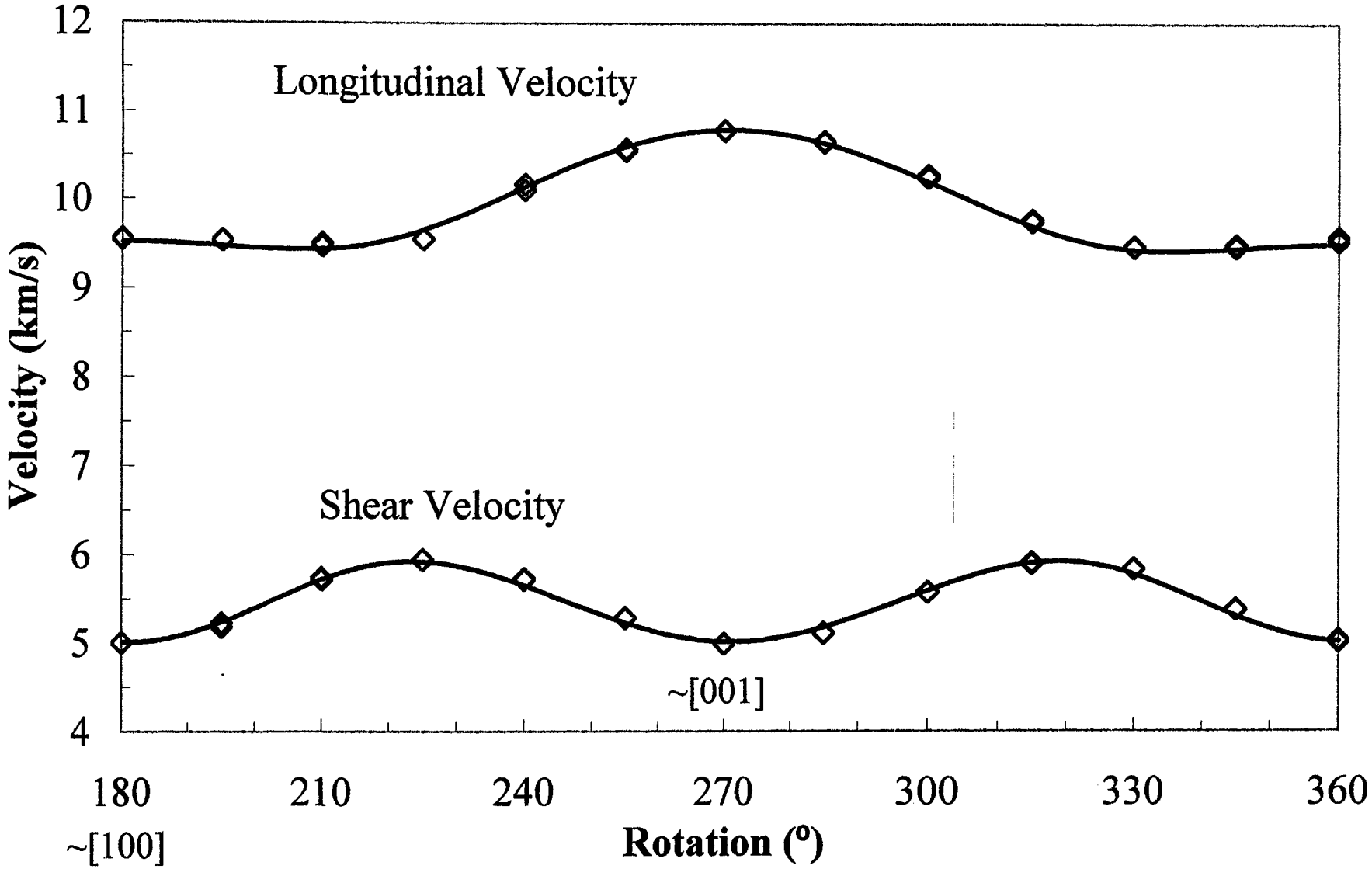


Figure 6: Room temperature velocities versus rotation in ~(010) plane

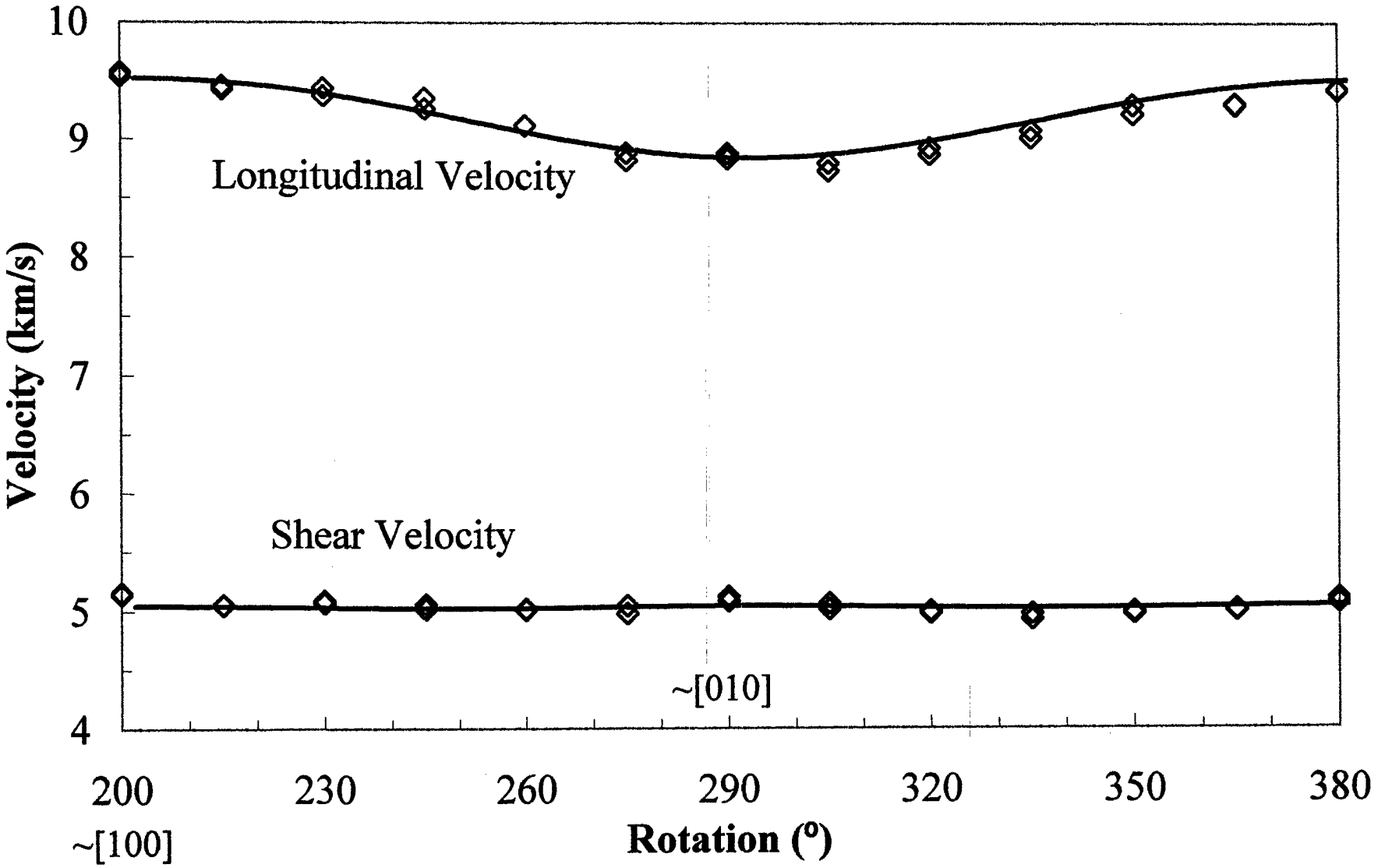


Figure 7: Room temperature velocities versus rotation in ~(001) plane

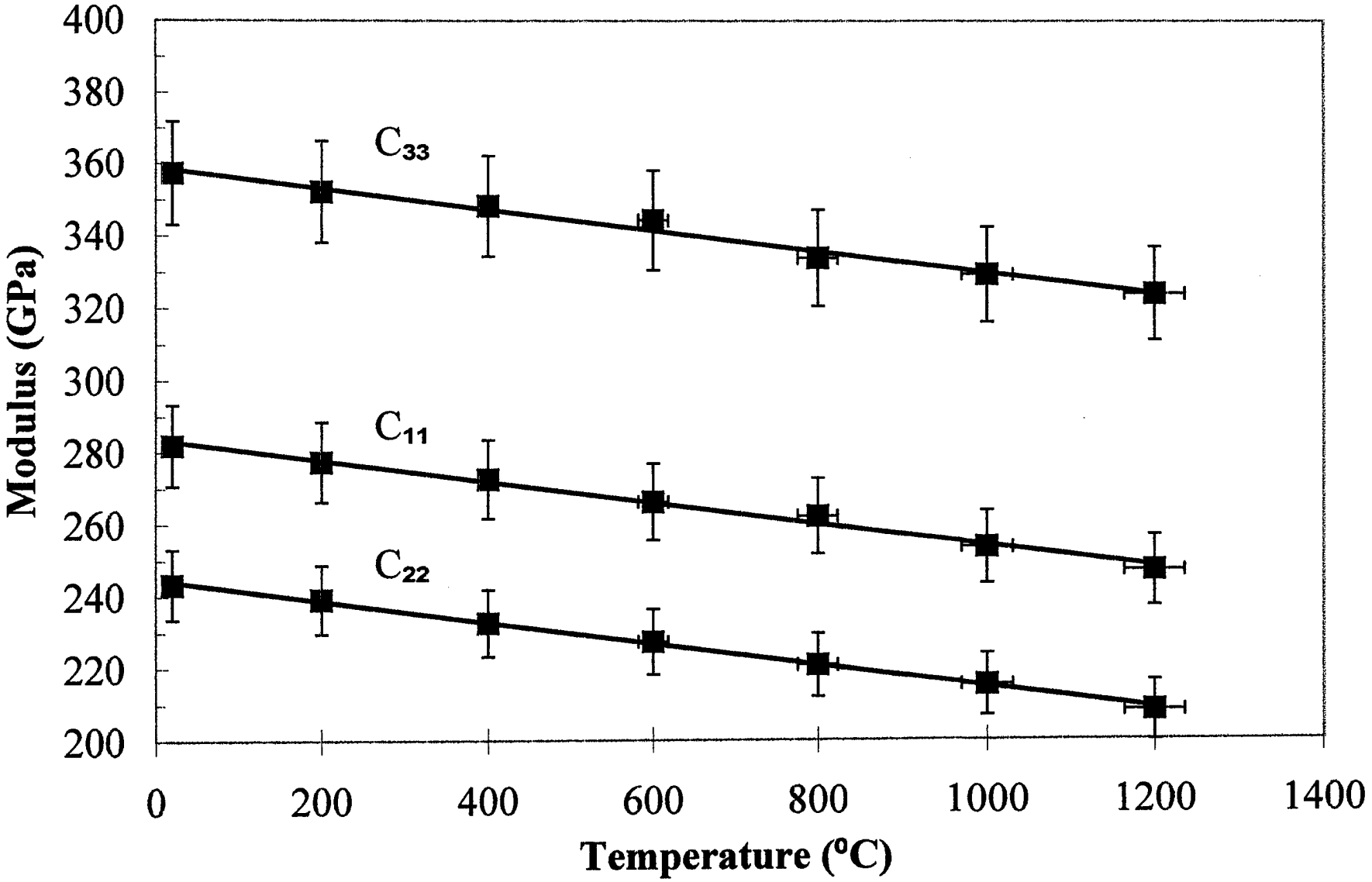


Figure 8: Single-crystal longitudinal moduli versus temperature

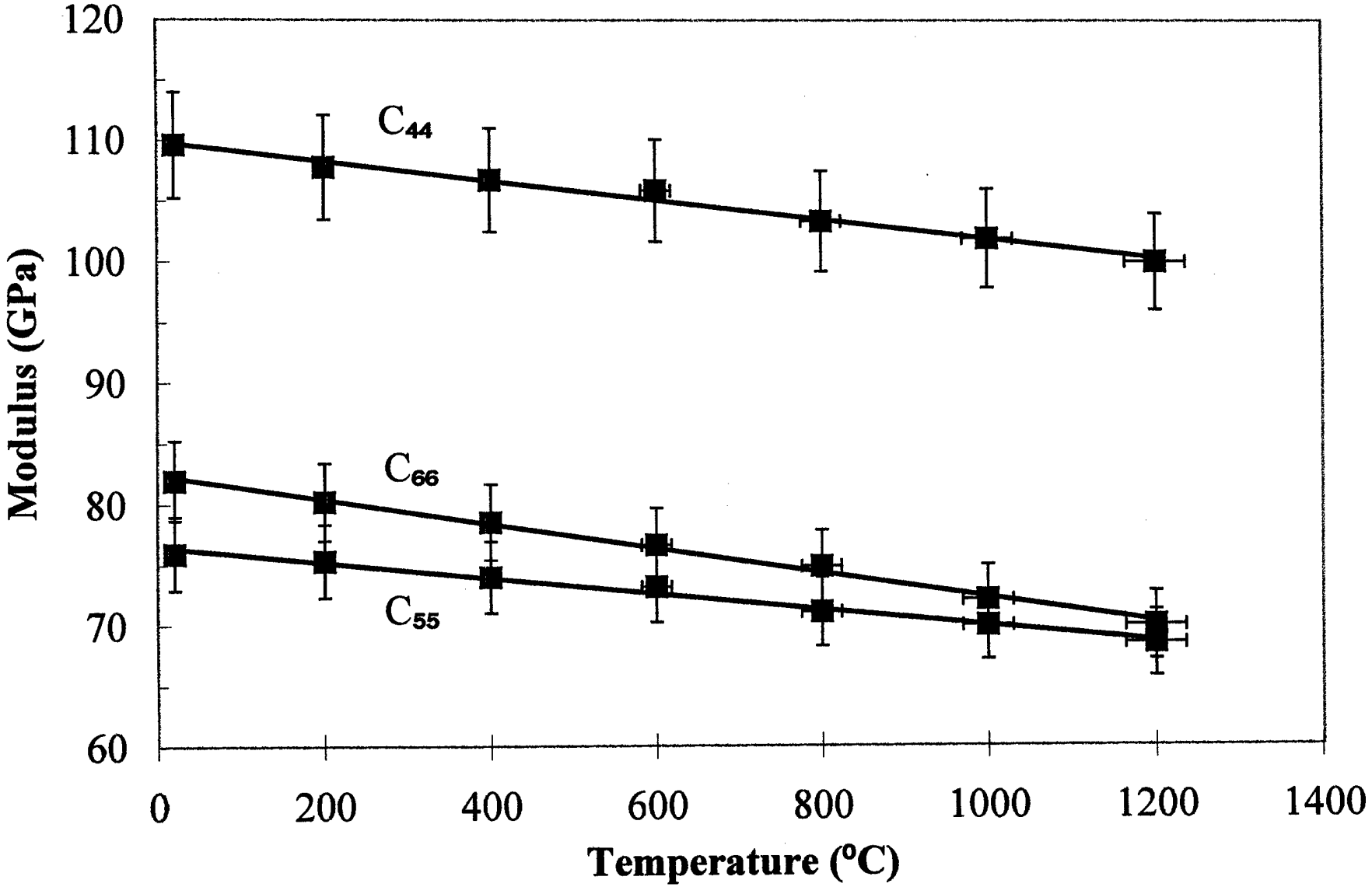


Figure 9: Single-crystal shear moduli versus temperature

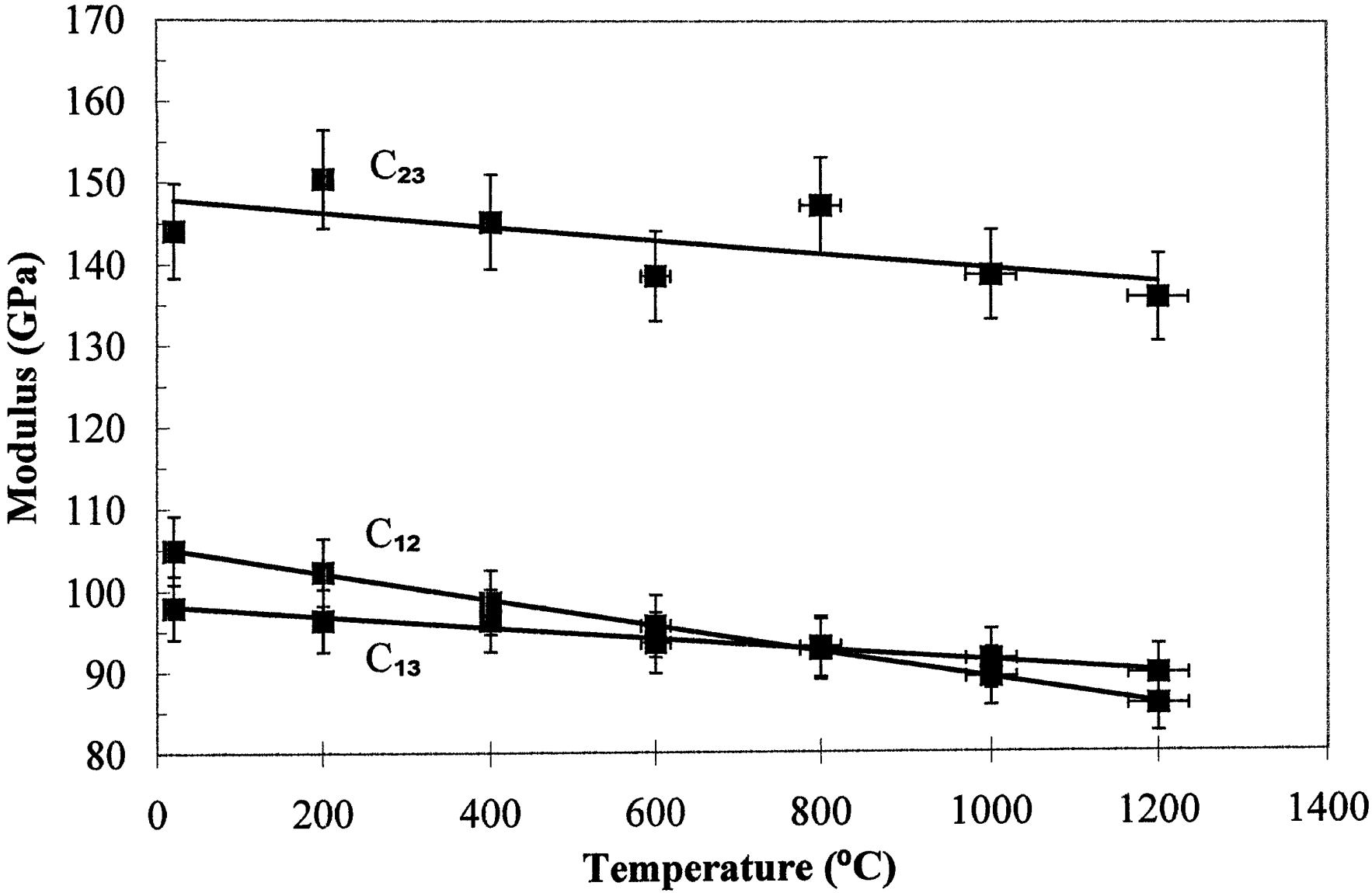


Figure 10: Single-crystal cross moduli versus temperature

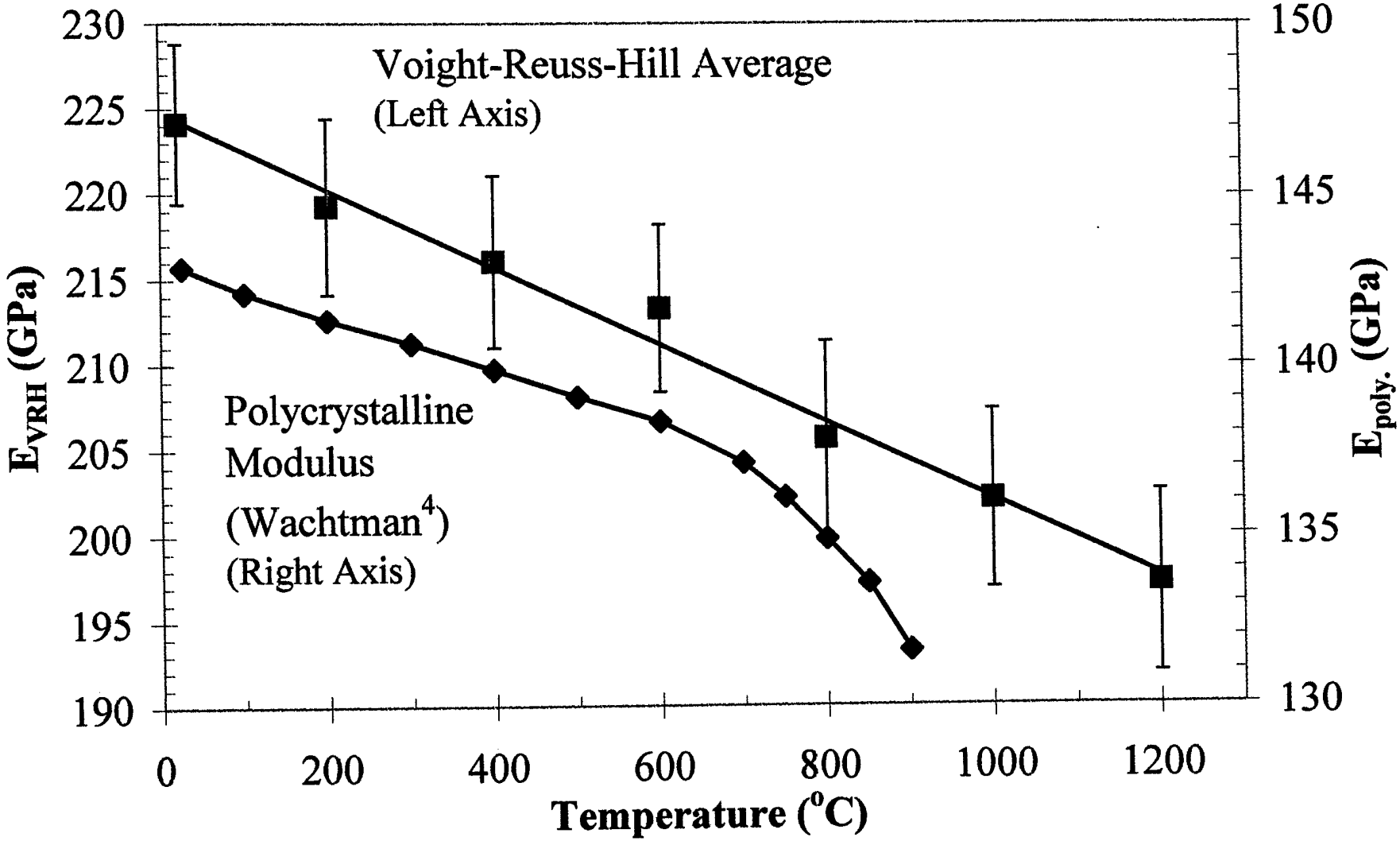


Figure 11: Young's modulus of mullite versus temperature

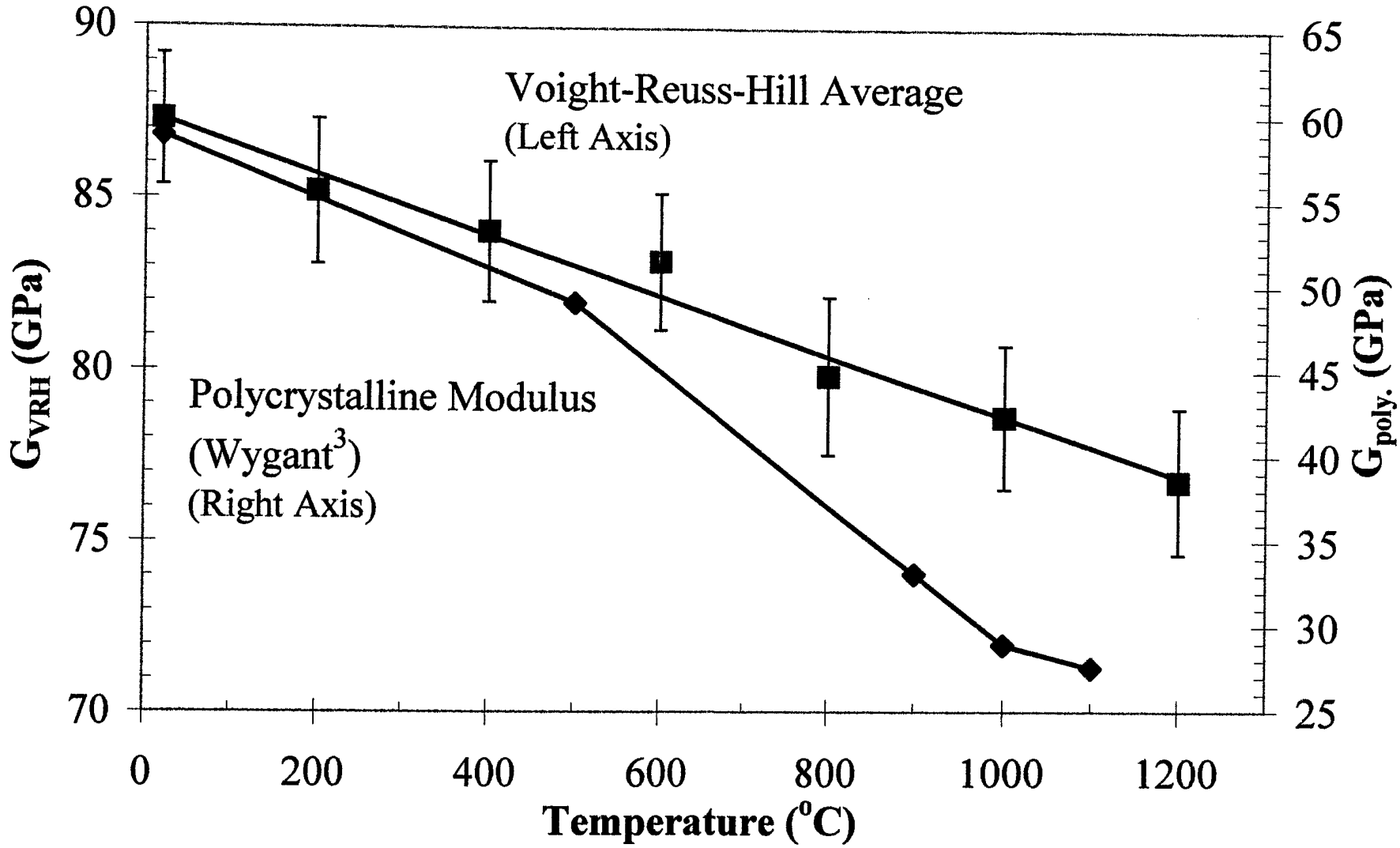


Figure 12: Shear modulus of mullite versus temperature

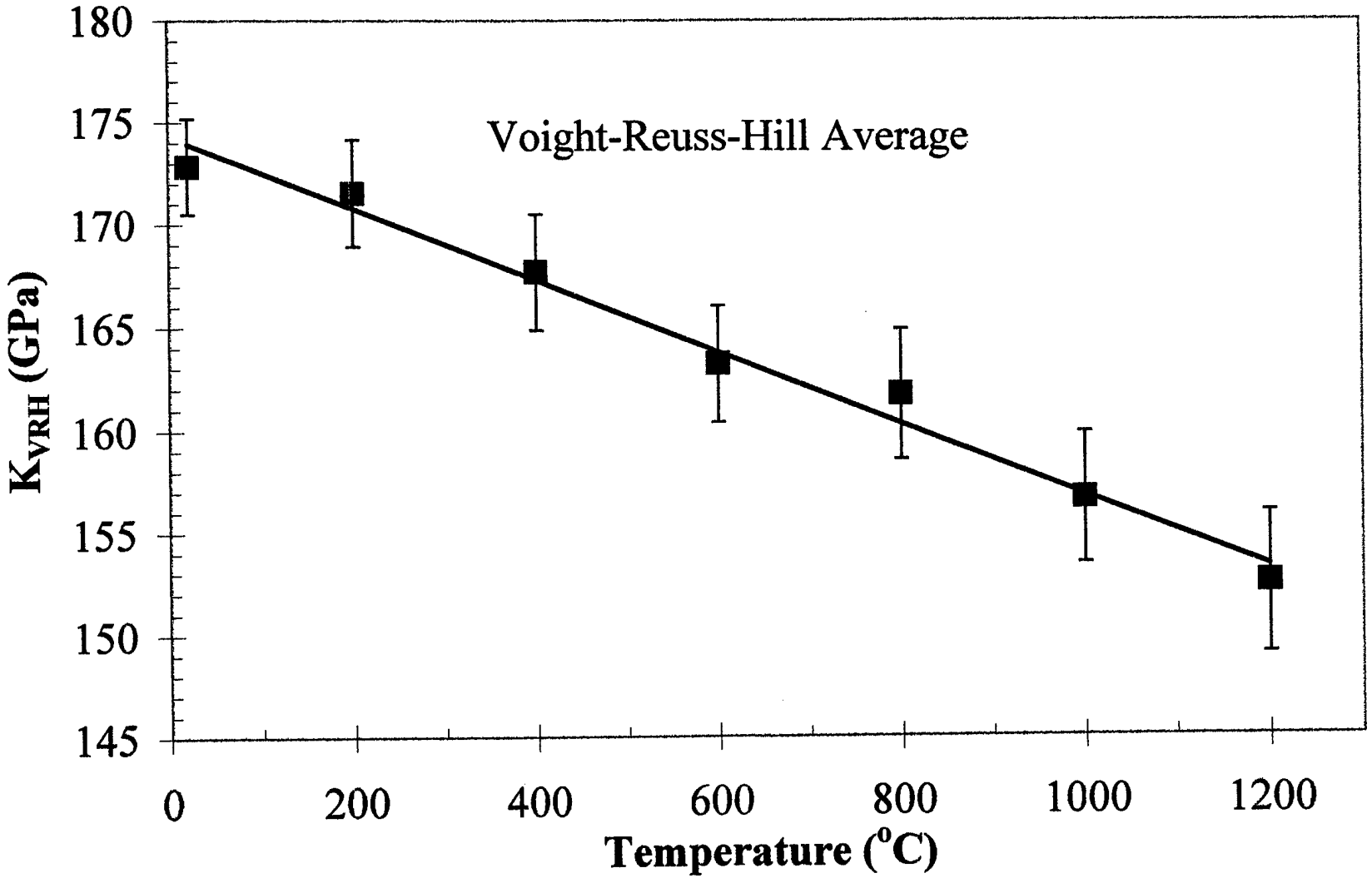


Figure 13: Bulk modulus of mullite versus temperature

J. Mat. Res., submitted, Nov 2000

Crystallization kinetics of yttrium aluminum garnet ($Y_3Al_5O_{12}$)

Bradley R. Johnson and Waltraud M. Kriven
Department of Materials Science and Engineering, University of Illinois at Urbana-Champaign, 1304 W. Green Street, Urbana, IL 61801, USA

The crystallization behavior of solid, amorphous, yttrium aluminum garnet (YAG) was studied using isothermal differential thermal analysis (DTA), X-ray diffraction (XRD) and transmission electron microscopy (TEM). The activation energy for crystallization was 437 KJ/mole and the measured Avrami exponent was 2.74, which corresponded to a three dimensional crystal growth mechanism with a constant number of nuclei. Time – temperature – transformation (T-T-T) curves were developed from the data to predict crystallization rates as a function of temperature. The crystallization pathway for YAG in this system is compared to others reported in the literature.

I. INTRODUCTION:

Yttrium aluminum garnet ($Y_3Al_5O_{12}$, "YAG") is an important ceramic material used in structural refractory applications as well as in optical applications such as laser materials (e.g. when doped with rare-earth cations, such as neodymium). Single crystal YAG is also one of the most creep resistant ceramic oxides known.[1,2] Its low creep, coupled with its very high melting temperature (1940°C[3]) makes it particularly attractive for structural applications, and it is currently under investigation for potential use as structural fibers.[4-11]

One route of structural fiber development under investigation is to use containerless methods to pull amorphous fibers from highly under-cooled melts, and to subsequently crystallize them.[4,12,13] Some of the advantages of this process are that fibers can be drawn from typically fragile, glass-forming materials, as well as from compositions which are difficult to access due to their incongruent melting behavior (e.g. mullite). To successfully crystallize such fibers with a controlled microstructure, a thorough understanding of the crystallization kinetics of quenched YAG-composition glasses is necessary.

Although YAG is a significant and well-studied engineering material, both for structural and optical applications, not much data is available concerning its crystallization kinetics. This is primarily due to the fact that YAG is a very fragile glass-forming substance, and its primary use is in its crystalline form.[14,15] Additionally crystallization studies are complicated by its very high melting temperature, making cooling studies from a molten state very difficult using standard thermal analysis techniques. Consequently, it was decided to use rapidly quenched YAG specimens to study the kinetics of crystallization from the amorphous state, and subsequently to use this information for controlled crystallization of amorphous YAG fibers.

II. EXPERIMENTAL PROCEDURES

YAG powder was chemically synthesized via a complex polymerization method as described elsewhere.[16-18] The precursors were yttrium nitrate hexahydrate,

$Y(NO_3)_3 \bullet 6H_2O$ (Alfa Aesar, Ward Hill, MA) and aluminum nitrate nonahydrate, $Al(NO_3)_3 \bullet 9H_2O$ (Aldrich, Milwaukee, WI). They were dissolved in a 5 wt% solution of 78% hydrolyzed polyvinyl alcohol PVA (Gohsenol KH-17s, MW = 106,000, Nippon Gohsei, Inc., Osaka, Japan). The chemically synthesized powders were subsequently melted in a water cooled hearth using a CO_2 laser to form a pellet.[19] The pellet was then levitated in an oxygen atmosphere with an aero-acoustic levitator, and melted again by a CO_2 laser as described in literature elsewhere.[20-23] Melt temperatures were approximately 2200°C as indicated by optical pyrometry. The suspended molten droplet was then rapidly quenched to form an amorphous YAG bead approximately 2 – 3 mm in diameter. The beads were initially crushed between two stainless steel plates to form a coarse powder. Fine grinding was done using an agate mortar and pestle. The powdered material was used for isothermal DTA experiments as well as for XRD analysis.

Isothermal DTA experiments were carried out using a Dupont 910 DTA modified by Innovative Thermal Systems (Atlanta, GA) with updated signal processing electronics and a computer controlled digital data acquisition system. The sample mass consisted of 50 mg of crushed quenched powder, while 45 mg of α-Al_2O_3 was used as the reference (to approximately match the thermal mass of the sample). Platinum crucibles were used for both sample and reference. The experiments were done with a flowing atmosphere of Ar (60 cc/min) and an initial heating rate of 40°C/min up to the desired hold temperature. The DTA thermocouples were calibrated with the melting point of gold and silver using alumina crucibles. Eight different hold temperatures were used between 840°C and 875°C at 5° increments. Hold times varied from three hours to 45 minutes, as the hold temperature was increased.

X-ray diffraction analysis was done with a DMax Automated Powder diffractometer, (Rigaku/USA, Danvers, MA) equipped with a graphite monochromator, emitting Cu K_α radiation. The operating voltage was 40 kV with a current of 40 mA and the diffractometer was operated in theta – 2-theta mode. Spectra were collected for crystallized specimens using a goniometer speed of 5° 2θ/min, with a step size of 0.01° 2θ, and summing over 5 scans. For quenched specimens, a goniometer speed of 2° 2θ/min, with a step size of 0.02° 2θ was used, and a minimum of 30 scans were summed.

Microstructural analysis of quenched YAG beads was done using a Philips CM12 (FEI company, Hillsboro, OR, USA) transmission electron microscope with a LaB_6 filament, equipped with a Gatan (Pleasanton, CA, USA) multi-scan CCD camera and an EDAX (Mahwah, NJ, USA) energy dispersive spectrometer (EDS). TEM specimens were prepared by slicing sections from the quenched beads with a diamond wafer saw (Buehler Isomet® low speed saw, Lake Bluff, IL) and mechanically thinning the sections by tripod polishing[24,25] (Model 590W, South Bay Technologies, San Clemente, CA) with diamond lapping films. Final thinning was done using an ion mill (Gatan 600 DuoMill, Pleasanton, CA, USA). The specimens were examined by bright field (BF) imaging, convergent beam electron diffraction (CBED), selected area diffraction (SAD), and energy dispersive spectroscopy (EDS). The camera length constant for the microscope was determined using a specimen of evaporated gold on a holey carbon film. The diffraction patterns for gold and the various specimen images were collected digitally and distances were measured using a free-ware image analysis software package made available by the National Institute of Standards and Testing (NIST).[26]

III. THEORETICAL ANALYSIS

Data analysis was conducted with the raw isothermal data to determine the parameters which best described the kinetics of the amorphous to crystalline transformation. Several different models were examined and tested,[27] but the model which best described the data was the Johnson – Mehls – Avrami equation[28]:

$$x = 1 - \exp\left[-(kt)^n\right] \tag{1}$$

where x is the fraction transformed, k is the reaction rate, t is time and n is the Avrami exponent which describes the geometry of the crystal growth front. The reaction rate, k, is itself an Arrhenius expression as follows:

$$k = \nu \exp\left[\frac{-E}{RT}\right] \tag{2}$$

where ν is the pre-exponential factor (in units of inverse time), E is the activation energy, R is the gas constant, and T is temperature.

Typically, the isothermal DTA or DSC data described by the JMA equation is analyzed through a series of data reduction steps and least squares fitting of Arrhenius plots. First, Eq. (1) is re-arranged as follows:

$$\ln\left(-\ln(1-x)\right) = n\ln(k) + n\ln(t) \tag{3}$$

Plots are generated of ln[-ln(1-x)] vs. ln(t) for each hold temperature and values of k and n are found from least squares fitting of the data. Next, values for the activation energy and pre-exponential factor are determined by re-arranging Equation 2 as follows:

$$\ln(k) = \ln(\nu) - \frac{E}{RT} \tag{4}$$

A plot is then generated of $\ln(k)$ vs. $1/T$ and a least squares fit is applied to the data points to determine the activation energy, E, and the pre-exponential factor ν from the slope and y-intercept of the line, respectively.

However, with the advent of digital data acquisition and sophisticated data analysis and plotting software packages[29] it is possible to analyze the raw data directly without going through the previously described data reduction processes. This is facilitated by the fact that the raw data from a DTA or DSC plot is proportional to the first derivative of the JMA equation[27] (Eq. (5)):

$$\frac{dx}{dt} = nk^n t^{n-1} \exp\left[-(kt)^n\right] \tag{5}$$

By including a proportionality constant, a curve fit can be directly applied to the raw data and numerically optimized to simultaneously determine the optimum values of n and k at each hold temperature. This was the procedure used for this analysis. This method has the advantage of being more accurate and more sensitive to subtle features

of the kinetic process. The equation used for curve fitting raw isothermal exotherms is shown in equation 6:

$$y = Ank\left[kt_0^{(n-1)}\right]\exp\left[-(kt_0)^n\right] \tag{6}$$

where A is a proportionality factor, n and k are as previously defined, and t_0 is the start time of the exotherm.

All of the pertinent variables (n, k, E and ν) for the JMA equation (Eq. 1) were thus computed from the isothermal exotherms. Time – temperature – transformation (T-T-T) curves were then calculated by re-arranging the JMA equation (Eq. 1) and analytically calculating the temperature required for a fixed fraction of conversion as a function of time:

$$T = \frac{E}{R}\left[\frac{1}{\ln(\nu t) - \frac{1}{n}\ln(-\ln(1-x))}\right] \tag{7}$$

IV. RESULTS

A. Thermal Analysis

A composite plot of isothermal DTA exotherms for the crystallization of quenched YAG beads is shown in Fig. 1. Numerical curve fitting was done to the raw data to determine the kinetic parameters of the crystallization transformation using Eq. 6. An example curve fit of the raw data and the optimized kinetic parameters (e.g. n and k) for an exotherm at a hold temperature of 855°C is shown in Fig. 2. This type of optimization was performed at each temperature and the calculated values for n and k are listed in Table I. Using the values for k and T in Table I, a plot was generated of reaction rate *vs.* temperature (Fig. 3). The equation for the reaction rate (Eq. 2) was used to fit the data and it was numerically optimized to find the best values for the pre-exponential factor, ν and the activation energy, E. The result of this curve fit for the isothermal crystallization of YAG is shown in Fig. 3.

These parameters were used in the JMA equation (Eq. 1) to calculate a T-T-T curve (Eq. 7) for the isothermal crystallization of amorphous YAG, Fig. 4. Superimposed on the plot are raw data points which show the time required for 1% and 99% crystallization. These times were measured from a plot where the integrated area under the crystallization exotherm was normalized to one.

B. X-ray Diffraction

X-ray diffraction analysis was done of the quenched YAG – composition glass powders both before and after crystallization in the DTA. A combined plot of the XRD spectra before and after crystallization with the same vertical axis is shown in Fig. 5. Figure 6 is the same two spectra in a plot normalized with respect to the 100% peak for each.

C. Microstructural Characterization

The microstructure of quenched YAG composition glass beads was examined using transmission electron microscopy (TEM). Measured d-spacings from SAD micrographs were compared to those published in the Powder Diffraction Files, PDF®, of the International Center for Diffraction Data (ICDD®, formerly known as the Joint Committee on Powder Diffraction Standards, JCPDS). Typical bright field images of a quenched YAG composition glass are shown in Figs. 7 through 10. The labeled points in Fig. 7 indicate regions where EDS analysis and microdiffraction were taken. The inset images in Fig. 7 and 8 are CBED patterns which identify the designated regions as being YAG crystals. The specimen had several dark regions. Some of these were crystalline (as noted) but not all of them. EDS spectra were taken for light regions, dark regions and crystalline regions. Standardless quantitative analysis was done using the Cliff-Lorimer approximation.[30] All regions had essentially the same composition (63 ± 1 mol % Al_2O_3 and 37 ± 1 mol % Y_2O_3. The stoichiometric composition for YAG is 62.5 mol % Al_2O_3 and 37.5 mol % Y_2O_3.

Additional analysis on other areas of the specimen showed the presence of nanocrystals being formed from the amorphous matrix. Figure 9 is a bright field image of a region with nanocrystals of YAG embedded in an amorphous matrix. The inset image is an SAD pattern corresponding to YAG which was taken from a similar area close to the BF image in Fig. 9. Figure 10 is a higher magnification BF image showing the transition from amorphous to crystalline YAG regions. Figure 11 is a TEM bright field image of the cross-section from a quenched YAG – composition fiber which was pulled from a levitated, sub-cooled liquid. Only a couple of isolated nanocrystals of YAG were found in this specimen. The darker contrast areas on the specimen were from the holey carbon support film and the glue used to hold the specimen on to the film.

V. DISCUSSION:

A. Review of YAG Synthesis

In order to put the present work in perspective and to provide better understanding of the mechanisms of crystallization in the yttrium aluminate system, a selected review is provided of YAG synthesis from chemical routes. Several different crystallization pathways and mechanisms have been proposed by other researchers who have investigated YAG synthesis via various chemical processing routes. A summary of these crystallization pathways is shown in Table II. Yamaguchi et al.[31,32] used an alkoxy-derived stoichiometric precursor for synthesizing "YAP" ($YAlO_3$), "YAM" ($Y_4Al_2O_9$) and YAG. For YAG and YAP composition precursors, the formation of an intermediate hexagonal $YAlO_3$ (PDF 16-219) phase was observed at approximately 800° - 890°C . For $Y_3Al_5O_{12}$ composition precursors, the hexagonal $YAlO_3$ phase converted to YAG and was single phase by 1050°C. For $YAlO_3$ precursors, the crystallization pathway was more complicated. Hexagonal $YAlO_3$ crystallized between 870° and 900°C and transformed into a cubic solid solution phase ($Y_3AlY(AlO_4)_3$) with a garnet structure similar to YAG (PDF 33-40) from 1000° - 1060°C. The cubic $YAlO_3$ phase (PDF 38-222) then decomposed to a YAG + YAM mixture between 1080 – 1200°C which subsequently underwent a solid state reaction to form single phase orthorhombic YAP by 1650°C. It was hypothesized that when hexagonal $YAlO_3$ was formed from $Y_3Al_5O_{12}$ precursors, the excess alumina (which must exist to maintain stoichiometry)

was accommodated into the hexagonal $YAlO_3$ structure. This conclusion was based on yttrium aluminate synthesis results over a range of compositions. Thus, Yamaguchi et al.[31,32] suggested that this phase, (hexagonal $YAlO_3$), exists in a solid solution range between 50 and 62.5 mol% Al_2O_3.

Vietch[33] used a stoichiometric mixture of aluminum and yttrium nitrates dissolved in glycerol and malonic acid as a precursor solution for YAG synthesis. The precursors were heated up and YAG formation was studied using XRD, Fourier transform infrared spectroscopy (FTIR) and DTA. Again, the hexagonal form of $YAlO_3$ (PDF 16-219) was reported to formed as an intermediate at 850°C and was eventually converted to single phase YAG by 1100°C. Since crystalline alumina was not observed by XRD when hexagonal $YAlO_3$ formed from YAG precursors, it was assumed to exist in an amorphous state.

Hay[34] studied the crystallization of YAG via an extensive TEM analysis of diphasic $Y_3Al_5O_{12}$ composition sol-gel derived films (from aluminum and yttrium isopropoxides). In this system, hydrated Y_2O_3 and Al_2O_3 particles formed first as the sol-gel films were heated, consequently mixing was not on an atomic level (as was the case in this study and some of the others mentioned). TEM analysis was done on films using a hot stage as well as by subjecting them to various heat treatments and then examining them at room temperature. XRD spectra were collected of bulk specimens heated to various temperatures to complement the study of phase evolution. It is interesting to note that the pattern for the 800°C heat treated diphasic sol had a general profile similar to what is reported here for quenched YAG composition beads.

The diphasic nature of the films (colloidal mixture of hydrated Y_2O_3 and Al_2O_3 particles) resulted in a complicated crystallization pathway with the formation of several intermediate, metastable phases (e.g. $Y_4Al_2O_9$, ϕ-Al_2O_3, and a garnet form of $YAlO_3$ (PDF 38-222)) before YAG finally crystallized. Hay[34] postulated that the nucleation of YAM ($Y_4Al_2O_9$) before YAG, was due to lower yttria mobility combined with influence of strain energy effects (due to the different volume changes associated with forming the various yttrium aluminates). The nucleation of YAG from the parent material was reported to be site saturated and crystal growth occurred by consumption of the parent phases. Crystallization was described as being a cellular transformation with spherulitic growth and with a constant number of nuclei. Crystal growth was essentially two dimensional due to very thin film thickness in comparison to spherulite size. The reported activation energy for YAG formation in this system was 280 KJ/mol. This was thought to be related to YAG-YAM boundary diffusion or surface diffusion due to the microstructural and microchemical phase composition of the parent intermediate phases.

Hess et al.[35] studied the formation of YAG, YAP and YAM via combustion synthesis of aqueous glycine-nitrate solutions with stoichiometric yttrium-to-aluminum cation ratios. This process produced X-ray amorphous powders which were crystallized by subsequent heat treatments. The general shape of the X-ray spectra for the amorphous precursors was similar to Hay's 800°C pattern[34] and to that shown here for quenched YAG-composition beads. Hess et al.[35] suggested that the two broad humps in their spectra might be due to the presence of microcrystalline Y_2O_3. Two possible crystallization pathways for YAG formation from $Y_3Al_5O_{12}$ precursors were proposed, depending on heat treatment. At temperatures of 800°C or less, YAG crystallized directly from the amorphous precursors. At higher temperatures, hexagonal YAP formed as a metastable intermediate product. Hess et al.[35] commented on the previous work of Veitch[33] and Yamaguchi[31,32] and provided evidence to show

that the transition from hexagonal $YAlO_3$ to YAG occurred by the diffusion of amorphous alumina (a separate phase, not in solid solution) into hexagonal $YAlO_3$ followed by a structural transformation into the garnet structure. It was also observed that the fuel concentration used during combustion synthesis of $Y_3Al_5O_{12}$ precursors affected the phases formed during subsequent crystallization. Specimens formed with higher fuel concentrations and subsequently crystallized produced samples containing hexagonal YAP along with YAG, whereas lower fuel concentrations produced only YAG. Since the fuel concentration could possibly affect the ultimate temperature reached during combustion synthesis, these results may be related to the metastable formation of YAP + alumina during the solidification of $Y_3Al_5O_{12}$ melts heated above 2000°C as reported by Le Floch et al.[36]

Liu et al.[37] used a metallo-organic synthesis route (based on isobutyrate) for forming YAG, and reported the direct formation of the garnet structure at 910°C with no intermediate phases. They heated up precursors to various temperatures and used Diffuse Reflectance Infrared Fourier Transform Spectroscopy (DRIFTS) and XRD to characterize phase development. The XRD spectra at 800°C appeared similar to those reported here (for quenched beads), and by Hay[34] and Hess.[35] Liu et al.[37] concluded that there was short-range order or nucleation which existed between 500° and 900°C in their system, and that the local environment was possibly YAG, but that diffusion rates were too slow at these temperatures to allow large scale crystallization. Based on similar XRD spectra profiles, and microstructural evidence by TEM of the quenched YAG specimens examined here and in sol-gel films with $Y_3Al_5O_{12}$ composition examined by Hay,[34] it is possible that there might be nanoscale YAG crystals beginning to form in the metalloorganic precursors studied by Liu.

Nguyen et al.[16,18] reported the synthesis of YAG via a polymeric solution route using metal nitrates (similar to Veitch[33]) and polyvinyl alcohol (PVA). Phase formation as a function of temperature was examined using XRD, simultaneous differential thermal analysis and thermogravimetric analysis (DTA/TGA), Fourier transform infrared spectroscopy (FTIR) and nuclear magnetic resonance (NMR). They reported the direct crystallization of YAG at 940°C, which is similar to the 910°C crystallization temperature reported by Liu[37] for the metallo-organic system they used. The XRD spectra for the PVA YAG precursors heat treated to 800° - 900°C was again similar to that reported here for quenched $Y_3Al_5O_{12}$ composition beads.

B. Thermal Analysis

The results for isothermal analysis are presented in Figs. 1 through 4. As expected, there was a decrease in duration and an increase in intensity of the crystallization exotherms as the hold temperature was increased. The best mathematical model found to characterize the data was the JMA equation (Eq. 1). The raw data from the crystallization exotherms were modeled using the first derivative of this equation, and the curve fits produced matched the experimental data very well; typical R^2-values were 0.99 or better. The overall activation energy for crystallization in the temperature range studied (840° - 875°C) was 437 KJ/mole and the value of the pre-exponential term for the reaction rate was 6.33×10^{16} (Fig. 3). The average Avrami exponent for this data set was 2.74 (Table 1). This data was used to generate a T-T-T curve (Fig. 4) to show how the rate of crystallization varied as a function of time and temperature. The exotherm observed by DTA was confirmed to be crystallization of YAG, based on TEM and XRD data. The small YAG crystals initially present in the

quenched YAG-composition beads most likely acted as sites for crystal growth, thus eliminating the activation barrier for homogeneous nucleation. The morphology of the crystals observed indicated that the geometry of crystallization was three-dimensional. Therefore, the kinetic phenomena observed by isothermal DTA was most likely three-dimensional crystal growth, with a constant number of nucleation sites (pre-existent crystals).

C. XRD

X-ray diffraction spectra of crushed quenched YAG-composition beads before and after crystallization in the DTA were consistent with SAD analysis in the TEM. The spectra for the quenched glass beads showed two diffuse humps, a pronounced one between 25° and 35° 2 theta, and a more diffuse hump between 35° and 65°. Both had several identifiable peaks super-imposed on them. The appearance of the spectra was similar to that shown by several other researchers working with chemically synthesized YAG.[18,34,35,37] The diffuse humps are considered to be due to short range ordering in the material (2.4 - 4.0 Å, and 1.4 – 2.4 Å). Most of the peaks present corresponded to YAG (PDF 33-40). Additionally, there were some peaks which corresponded to a hexagonal form of $YAlO_3$, (PDF 16-219) and an orthorhombic form of $Y_4Al_2O_9$ (PDF 14-475) as well as a few remaining peaks which could have correspond to Y_2O_3 and Al_2O_3. Several of these phases were reported by other researchers to be intermediate phases which formed during chemical synthesis of YAG.[31-35] The multi-phase nature of the quenched specimens was reasonable considering the poor glass-forming tendency of the alumina-yttria system and the slower quench rate the beads had in comparison to the fibers.

During specimen preparation, the quenched glass beads were crushed and ground to form a fine powder. Minkova et al.[38] reported results from XRD studies on highly strained YAG (e.g. ground by planetary ball milling). It was found that single-phase YAG was transformed into a mixture of the garnet phase (PDF 33-40), and a tetragonal phase $Y_3Al_5O_{12}$ (PDF 9-310).[39] Consequently, the XRD spectra for quenched YAG beads (Figs. 5 and 6) were examined for the presence of tetragonal $Y_3Al_5O_{12}$. The peak position and intensities for tetragonal $Y_3Al_5O_{12}$ did not match the data very well, and it was concluded that this phase was not present in the specimen.

The metastable formation of $YAlO_3$ + α-Al_2O_3 crystals from undercooled $Y_3Al_5O_{12}$ melts has been reported by other investigators.[3,36,40,41] Lin et al.[42] explained that this phenomenon was due to the relatively small difference in free energy of formation between YAG and $YAlO_3$ + α-Al_2O_3, (472.49 vs. 440.35 KJ/mol, respectively) and that though YAG is thermodynamically more stable, kinetic factors favor the formation of $YAlO_3$ + α-Al_2O_3.[42] Cockayne[41] offered an explanation based on the relative complexity of the respective unit cells. (YAG has 160 atoms per unit cell whereas $YAlO_3$ and Al_2O_3 have 20 atoms and 10 atoms per unit cell, respectively.) Cockayne postulated that, with increased undercooling and subsequent increased melt viscosity, it might be energetically more favorable to form $YAlO_3$ + α-Al_2O_3 instead of YAG, because of the smaller critically-sized nuclei involved.[41] Gervais et al.[40] performed high temperature DTA studies on the melting and solidification of $Y_3Al_5O_{12}$ and other rare-earth garnets. They reported the existence of a critical temperature for the molten liquid, T_{clg} (T_{clg} = 2000°C for YAG). When YAG composition liquids were heated above a critical temperature, T_{clg}, $YAlO_3$ + α-Al_2O_3 formed upon cooling, and when heated below T_{clg}, $Y_3Al_5O_{12}$ formed during solidification. Le Floch et al.[36] also studied the solidification behavior of rare-earth garnets using high temperature DTA. Additionally, they

investigated phase formation in quenched $Y_3Al_5O_{12}$ melts heated to 1980° - 2400°C using laser-heated containerless methods (a similar process as used in this study). Both the DTA studies and the containerless cooling studies of $Y_3Al_5O_{12}$ melts confirmed the existence of a critical melt temperature of 2000°C (below which YAG would crystallize, and above which $YAlO_3$ + α - Al_2O_3 formed). Based on their quench studies of containerless, laser-heated $Y_3Al_5O_{12}$ melts, they reported another molten temperature regime where solidification of $Y_3Al_5O_{12}$ melts heated above 2400°C resulted in the formation of a metastable, cubic garnet-type structure, with lattice parameters slightly larger than those of equilibrium YAG (1.2041 nm vs. 1.12010 nm).

Subsequent work by that same group (Gervais et al.[43]) refined their understanding of solidification of molten YAG. It was found that above 2000°C, the critical factor which determined the phase formed during solidification of levitated molten $Y_3Al_5O_{12}$ was the cooling rate. Starting from a temperature of 2100°C, three different solids could be formed: YAP + α-Al_2O_3, YAG or glass (in the order of increasing cooling rate). The postulated mechanisms responsible for this behavior were the combined effects of difficult YAG nucleation and varying diffusion rates in the sub-cooled liquids. At relatively low cooling rates, YAP + α-Al_2O_3 solidified at approximately 1375°C. At this cooling rate and solidification temperature, the explanation was that the homogeneous nucleation rate of YAG was extremely low while relatively high diffusion rates (due to the low melt viscosity) allowed the melt to partition into a metastable mixture of YAP + α-Al_2O_3 upon solidification. At faster cooling rates, YAG solidified from the melt at approximately 1025°C. This result was given as evidence of a high barrier to homogeneous nucleation. Gervais et al.[43] stated that the complexity of the unit cell (160 atoms) might be the reason why such high undercoolings (~920°C) were necessary for YAG crystallizaton. It was also suggested that at this temperature range (~900°C below T_{mp}), long-range diffusion in the melt would be fairly limited, possibly even comparable to the growth rate of the solid-liquid interface, thus precluding the phase separation observed at higher temperatures and lower cooling rates. At extremely fast quench rates (with over 1000°C undercooling) amorphous solid glasses formed which crystallized into single-phase YAG upon subsequent heat treatment. These results are identical to what is reported here.

Weber et al.[44] studied the structure of sub-cooled liquid $Y_3Al_5O_{12}$ using containerless methods. Though the maximum temperature for these melts was not stated, it was probably in excess of 2000°C. They reported that the primary structural units in the melt from ~ 1435° - 1900°C were AlO_4^{5-} tetrahedra and YO_6^{9-} octahedra. These units were most likely linked by corner - and edge - shared oxygen atoms in a variety of configurations in order to fulfill stoichiometry constraints. The existence of these smaller structural units in the sub-cooled liquid would seem to explain the variability of solids formed from the melt depending on the cooling rate and support the solidification model proposed by Gervais et al.[43]

With all of the above data in mind, it would seem that YAG (T_{mp} = 1940°C) nuclei can exist in the melt up to about 2000°C, thus facilitating YAG crystallization upon cooling from melts heated below that temperature (Gervais[40] and Le Floch[36]). However, it appears that above 2000°C, the majority of these nuclei are broken down into smaller embryonic units (Weber[44]). These embryonic units apparently tend to phase separate metastably into $YAlO_3$ + Al_2O_3 when the melt cools slowly and there is only a small amount of sub-cooling. At these temperatures the diffusion rates are relatively high and viscosity is low, thus facilitating phase separation. When the melt is cooled at

higher rates and solidification occurs at lower temperatures, the higher viscosity and lower diffusion rates prevent the embryonic units from phase separating. At these temperatures, the degree of undercooling (~900°C < T_{mp}) is sufficient for homogeneous YAG nucleation to be energetically favorable. At even higher cooling rates, these embryonic units are quenched into an amorphous solid with only short-range ordering. This amorphous solid is reported to have two different structural states with different densities, hardnesses and degrees of ordering, yet with the same composition.[45]

The presence of a mixture of YAG, $YAlO_3$ and Al_2O_3 crystals in the quenched beads of this study (heated to approximately 2200°C) correlates well with the data reported by Le Floch[36] and Gervais.[43] And, the presence of YAG crystals (thermodynamically more stable) explains why YAG crystallized so readily in these DTA experiments instead of $YAlO_3 + Al_2O_3$.

The XRD spectra collected after the powder was crystallized in the DTA was highly crystalline and corresponded to YAG. This confirms that the exothermic event observed by DTA was in fact a crystallization exotherm. One of the interesting differences between the XRD spectra before and after crystallization was the difference in the location of the 100% peak. For the quenched glass bead sample, the maximum in the broad diffuse hump was near 31.15° 2θ (~2.87 Å), whereas after crystallization the 100% peak (YAG) was at 33.45° 2θ (~2.68 Å).

D. Microstructure:

In TEM, Bright field (BF) and diffraction analysis (SAD and CBED) of quenched YAG-composition beads showed that the material was primarily amorphous, but that there was also a substantial number of crystals present. The crystals found could be divided into two groups by size. The larger crystals had a length scale in the micron range and the smaller crystals had a length scale in the range of tens of nanometers. The population and density of these crystals appeared to be random. In contrast, there were barely any crystals found in the amorphous YAG-composition fiber pulled from sub-cooled levitated droplets (Fig 11). The difference in microstructure was most likely a function of cooling rates. The quenched beads had an estimated cooling rate of ≥ 250°C/s while the amorphous fiber had an estimated cooling rate of ≥ 2500°C/min. The presence of crystals in the quenched beads is evidence of the poor glass-forming tendencies of YAG.

In addition to crystalline regions, there were other regions where there was enhanced contrast in the BF mode which was not due to crystallinity. Extensive EDS analysis showed no significant compositional variation between the three different regions (crystalline, light amorphous, and dark amorphous). The contrast difference observed between the two regions may be due to differences in density or thickness, or both (if the denser region had a different thinning rate then it would be thicker and also result in a darker appearance in the BF mode). There have been reports in the literature of polyamorphism in quenched YAG-composition glasses.[15,45,46] "Polyamorphism" is a term used to describe a material where there are two different amorphous phases with identical composition but different short-range order structures, with one phase typically being denser than the other.[47] The observed contrast in the amorphous regions may be the result of this phenomenon.

VI. SUMMARY

Even though rapidly quenched at approximately 250°C/s, the YAG composition glass beads were populated by crystals of YAG whose size was in the nanoscale, as well as in the micron range. These crystals most likely acted as seeds for crystal growth during subsequent studies on crystallization kinetics. In addition to crystals, there were also amorphous regions of different contrast (yet with the same composition) as observed by bright field imaging and EDS in the TEM. These regions may have been due to polyamorphism. XRD spectra of specimens heated in the DTA confirmed that the exotherm observed was for crystallization of YAG. The DTA exotherms were successfully analyzed by curve fitting the first derivative of the JMA equation to the raw data. The activation energy for crystallization was 437 KJ/mole and the Avrami exponent was 2.74. The material crystallized directly into stoichiometric YAG at temperatures as low as 840°C; no intermediate phases were observed. Crystallization most likely occurred with a constant number of sites and crystal growth was three-dimensional. Isothermal crystallization data was used to generate a TTT curve to describe crystallization as a function of time and temperature. This data set may be useful for fabricating structural YAG fibers from amorphous pre-cursors.

ACKNOWLEDGEMENTS

The authors would like to gratefully acknowledge Richard Weber and Johan Abadie from Containerless Research Inc. for supplying the quenched YAG beads used in this work. This project was funded by the U.S. Air Force Office of Scientific Research under Science and Technology Transfer Research (STTR) grants F49620 -97-1-0427 and F49620-98-C-0050. Microstructural and crystallographic characterization was performed, in part using equipment in the Center for Microanalysis of Materials (in the Materials Research Laboratory), and in the Center for Cement Composite Materials, both located at the University of Illinois at Urbana-Champaign.

REFERENCES

1. G. S. Corman, J. Mater. Sci. Lett. **12**, 379 (1993).
2. S. Karato, X. Wang, and K. Fujino, J. Mater. Sci. **29**, 6458 (1994).
3. J. L. Caslavsky and D. J. Viechnicki, J. Mater. Sci. **15**, 1709 (1980).
4. J. K. R. Weber, B. Cho, A. D. Hixson, J. G. Abadie, P. C. Nordine, W. M. Kriven, and B. R. Johnson, J. Eur. Cer. Soc. **19** (8), 2543 (1999).
5. P. A. Doleman and E. G. Butler, Key Eng. Mater. **127-131**, 193 (1997).
6. B. H. King and J. W. Halloran, J. Am. Ceram. Soc. **78** (8), 2141 (1995).
7. G. N. Morscher, K. C. Chen, and K. S. Mazdiyasni, Cer. Eng. and Sci. Proc. **15** (4), 181 (1994).
8. L. Yin, Z. Zhi-Fan, J. Halloran, and R. M. Laine, J. Am. Ceram. Soc. **81** (3), 629 (1998).
9. D. Popovich, J. L. Lombardi, and B. H. King, Cer. Eng. and Sci. Proc. **18** (3), 65 (1997).
10. W. R. Blumenthal and S. T. Taylor, Act. Mater. **45** (7), 3071 (1997).
11. W. R. Blumenthal and D. S. Phillips, J. Am. Ceram. Soc. **79** (4), 1047 (1996).

12. W. M. Kriven, M. H. Jilavi, D. Zhu, J. K. R. Weber, B. Cho, and J. Felten, in *Ceramic Microstructure: Control at the Atomic Level*, edited by A. P. Tomsia and A. Glaeser 1998), p. 169.
13. J. K. R. Weber, J. J. Felten, B. Cho, and P. C. Nordine, Nature **393**, 469 (1998).
14. C. A. Angel, Science **267**, 1924 (1995).
15. J. K. R. Weber, J. G. Abadie, A. D. Hixson, P. C. Nordine, and G. A. Jerman, J. Am. Ceram. Soc., In press (Accepted Feb 2000).
16. M. H. Nguyen, "A New Polymer Route to the Synthesis of Mixed Oxide Ceramics," MS Thesis, University of Illinois at Urbana-Champaign, 1997.
17. M. A. Gülgün, M. H. Nguyen, and W. M. Kriven, J. Am. Ceram. Soc. **82** (3), 556 (1999).
18. M. H. Nguyen, S.-J. Lee, and W. M. Kriven, J. Mater. Res. **14** (8), 3417 (1999).
19. J. K. R. Weber, J. J. Felten, and P. C. Nordine, Rev. Sci. Inst. **78**, 31 (1996).
20. S. Krishnan, J. J. Felten, J. E. Rix, and J. K. R. Weber, Rev. Sci. Inst. **68**, 3512 (1997).
21. J. K. R. Weber, C. D. Anderson, S. Krishnan, and P. C. Nordine, J. Am. Ceram. Soc. **78**, 577 (1995).
22. J. K. R. Weber, S. S. Hampton, D. R. Merkley, C. A. Rey, M. M. Zatarski, and P. C. Nordine, Rev. Sci. Inst. **65** (456-465) (1994).
23. J. K. R. Weber and P. C. Nordine, Microgravity Science and Technology **VII**, 279 (1995).
24. J. Benedict, R. Anderson, and S. J. Klepeis, in *Specimen Preparation for Transmission Electron Microscopy of Materials III*, edited by R. Anderson, B. Tracy and J. Bravman (Materials Research Society Symposium Proceedings **254**, Pittsburgh, PA, 1992), p. 121.
25. S. J. Klepeis, J. P. Benedict, and R. M. Anderson, in *Specimen Preparation for Transmission Electron Microscopy of Materials*, edited by J. C. Bravman, R. M. Anderson and M. L. McDonald (Materials Research Soceity Symposium Proceedings **115**, Pittsburgh, PA, 1988), p. 179.
26. D. S. Bright, MacLispix (National Insitute of Standards, Gaithersburg, MD, 1999).
27. A. K. Galwey and M. E. Brown, in *Handbook of Thermal Analysis and Calorimetry, Vol. 1: Principles and Practice*, edited by M. E. Brown (Elsevier Science, Amsterdam, 1998), Vol. 1, p. 147.
28. D. A. Porter and K. E. Easterling, *Phase Transformations in Metals and Alloys* (Chapman and Hall, New York, 1992).
29. Kaleidagraph (Synergy Software, Perkiomen, PA, 1998).
30. D. B. Williams and C. B. Carter, *Transmission Electron Microscopy a Textbook for Materials Science* (Plenum Press, New York, 1996).
31. O. Yamaguchi, K. Takeoka, and A. Hayashida, J. Mater. Sci. Lett. **10**, 101 (1990).
32. O. Yamaguchi, K. Takeoka, K. Hirota, H. Takano, and A. Hayashida, J. Mater. Sci. **27**, 1261 (1992).
33. C. D. Veitch, J. Mater. Sci. **26**, 6527 (1991).
34. R. S. Hay, J. Mater. Res. **8** (3), 578 (1993).
35. N. J. Hess, G. D. Maupin, L. A. Chick, D. S. Sunberg, D. E. McCreedy, and T. R. Armstrong, J. Mater. Sci. **29**, 1873 (1994).
36. S. Le Floch, J. C. Rifflet, J. Coutures, M. Gervais, and J. P. Coutures, Mater. Sci. Eng. A. **A173**, 185 (1993).
37. Y. Liu, Z.-F. Zhang, B. King, J. Halloran, and R. M. Laine, J. Am. Ceram. Soc. **79** (2), 385 (1996).

38. N. Minkova, D. Todorovsky, and G. Furdinova, Mater. Chem. Phys. **38**, 383 (1994).
39. H. S. Yoder and M. L. Kieth, Amer. Mineral. **36** (7, 8), 519 (1951).
40. M. Gervais, S. Le Floch, J. C. Rifflet, J. Coutures, and J. P. Coutures, J. Am. Ceram. Soc. **75** (11), 3166 (1992).
41. B. Cockayne, J. Less-Com. Metals **114**, 199 (1985).
42. I.-C. Lin, A. Navrotsky, J. K. R. Weber, and P. C. Nordine, J. Non-Cryst. Solids **243**, 273 (1999).
43. M. Gervais, S. Le Floch, N. Gautier, D. Massiot, and J. P. Coutures, Mater. Sci. Eng. B. **B45**, 108 (1997).
44. J. K. R. Weber, S. Krishnan, S. Ansell, A. D. Hixson, and P. C. Nordine, Phys. Rev. Let. **84** (16), 3622 (2000).
45. S. Aasland and P. F. McMillan, Nature **369** (6482), 633 (1994).
46. P. F. McMillan, C. Ho, S. Aasland, A. Yeganeh-Haeri, and R. Weber, in *Structure and Dynamics of Glasses and Glass Formers*, edited by C. A. Angell, K. L. Ngai, J. Kieffer et al. (Materials Research Society Symposium Proceedings **455**, Pittsburgh, PA, 1997), p. 377.
47. C. A. Angell, J. Shao, and M. Grabow, in *Non Equilibrium Phenomena in Supercooled Fluids, Glasses and Amorphous Materials*, edited by M. Giordano, D. Leporini and M. P. Tosi Singapore, 1996), p. 50.

LIST OF TABLES

TABLE I. List of Avrami exponent and reaction rate values as a function of temperature for isothermal crystallization of quenched YAG composition beads.

Temperature (°C)	n	k (s^{-1})
840°	2.615	1.98E-04
845°	2.616	2.45E-04
850°	2.744	3.01E-04
855°	2.653	3.88E-04
860°	2.813	4.43E-04
865°	2.909	5.14E-04
870°	2.785	7.09E-04
875°	2.780	8.27E-04
Avg.	**2.739**	

TABLE II. Crystallization pathways for YAG synthesis via different precursors.

Precursors	Pathway	
Alkoxy precursors	$YAlO_3$ (hex)→ $YAlO_3$(ortho) → YAG (800°C) (950°C) (1050°C)	Yamaguchi et al.[31,32]
Organometallic (nitrates)	$YAlO_3$ (hex) → YAG (850°C) (1100°C)	Vietch[33]
Glycine-nitrate	$YAlO_3$ (hex) → YAG (~875°C) (~1050°C)	Hess et al.[35]
Diphasic sol-gel	$\theta - Al_2O_3 + Y_2O_3 \rightarrow \theta - Al_2O_3 + YAM \rightarrow$ (500°C) (800°C) $\theta - Al_2O_3 + YAlO_3$ (garnet) → YAG (~800 – 1100°C) (900 - 1050°C)	Hay[34]
Y & Al Isobutyrate	$5Al(O_2CiPr)_3{:}3Y(O_2CiPr)_3$ → YAG (910°C)	Liu et al.[37]
PVA + Y & Al nitrates	Sterically entraped Al^{+3} and Y^{+3} cations → YAG (900°C)	Nguyen et al.[18]
Solidification of molten YAG	$YAG_L \rightarrow YAP + \alpha\text{-}Al_2O_3$: Slow cool, 1375°C [upon re-heating, melts as a metastable eutectic] $YAG_L \rightarrow$ YAG : Faster cool, 1025°C $YAG_L \rightarrow$ amorphous $Y_3Al_5O_{12}$: Quench, < 900°C	Gervais et al.[40,43] LeFloch et al.[36]
Solidification of molten YAG and re-crystallization	$YAG_L \rightarrow$ amorphous + YAG + others amorphous $Y_3Al_5O_{12}$ + mixture of phases → YAG (900°C)	This study

LIST OF FIGURES

Figure 1. Combined plot of DTA exotherms (μV vs. time for various temperatures) for isothermal crystallization of quenched YAG composition glass beads.

Figure 2. Example of an optimized curve fit directly applied to a DTA exotherm for crystallization of quenched YAG composition glass.

Figure 3. Plot of reaction rate vs. temperature with a curve fit applied to determine the optimum values for the activation energy and pre-exponential factor for crystallization of quenched YAG composition glass.

Figure 4. Time-temperature-transformation curve for isothermal crystallization of quenched YAG.

Figure 5. XRD spectra for quenched YAG composition glass, before and after crystallization in a DTA.

Figure 6. Normalized XRD spectra for quenched YAG composition glass, before and after crystallization via DTA.

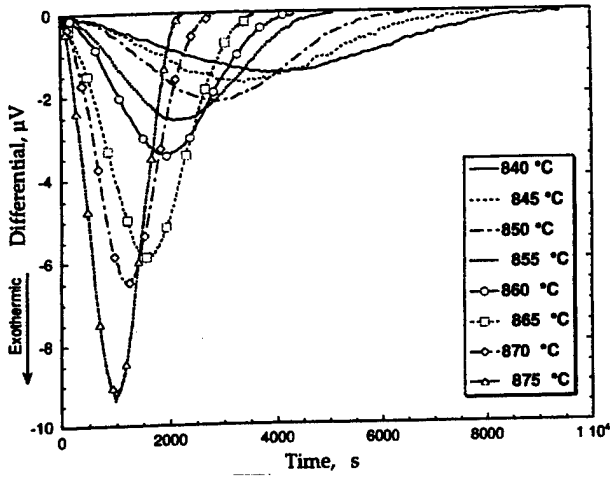
Figure 7. TEM bright field image of a quenched YAG composition glass bead. Regions 1 and 2 designate areas of EDS analysis and microdiffraction. The inset image is a CBED pattern taken from region 2 showing it crystallinity. The lighter area near region 1 was amorphous.

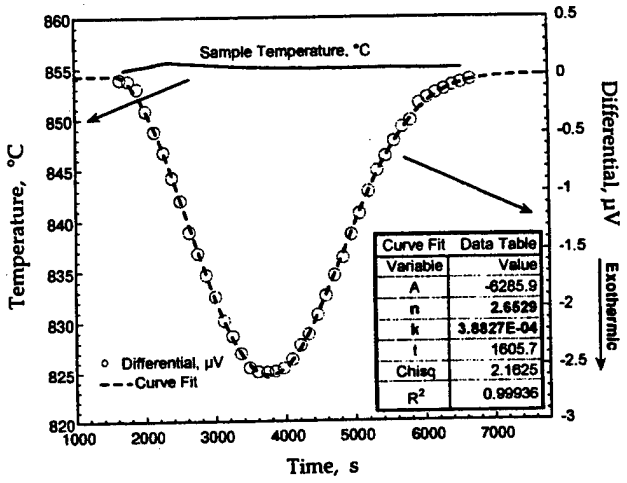
Figure 8. TEM bright field image of a diffraction YAG crystal in a quenched YAG composition glass. The adjacent region is amorphous and shows a contrast mechanism which is not due to diffraction effects. The inset image is a CBED pattern from the diffracting crystal.

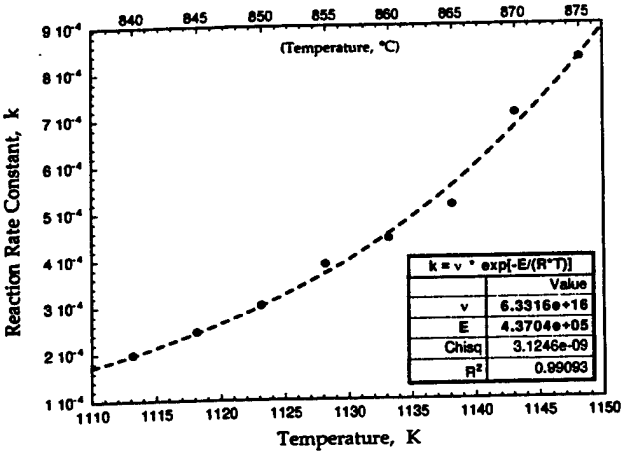
Figure 9. TEM bright field image of a quenched YAG composition glass bead showing nanocrystals of YAG. The inset image is an SAD pattern taken from similar nanocrystals in an adjacent area. The SAD pattern was indexed to be YAG.

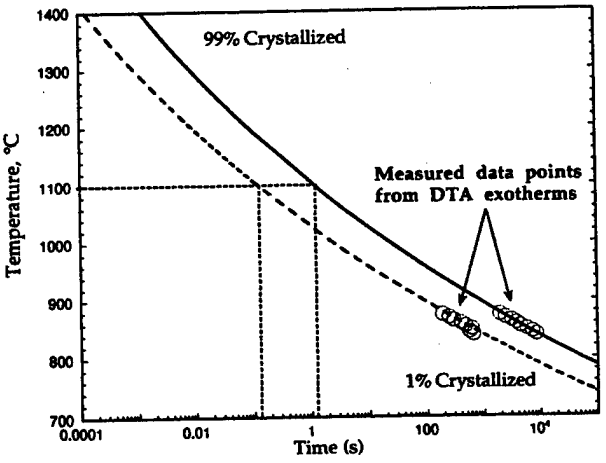
Figure 10. TEM bright field image of a quenched YAG-composition glass bead showing YAG crystals growing out of the amorphous matrix.

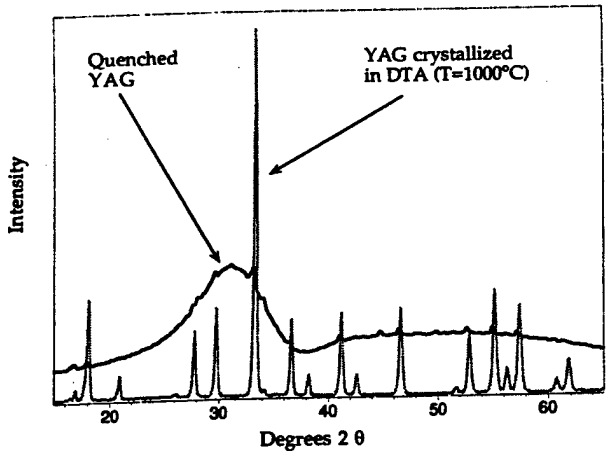
Figure 11. TEM bright field image of a cross sectioned amorphous YAG composition fiber which was pulled from a levitated, molten droplet using containerless methods. The web or lace-like features on most of the lower part of the specimen is the holey carbon film that the fiber was resting on. The dark region around the lower half of the circumference is the epoxy used to glue the fibers together.

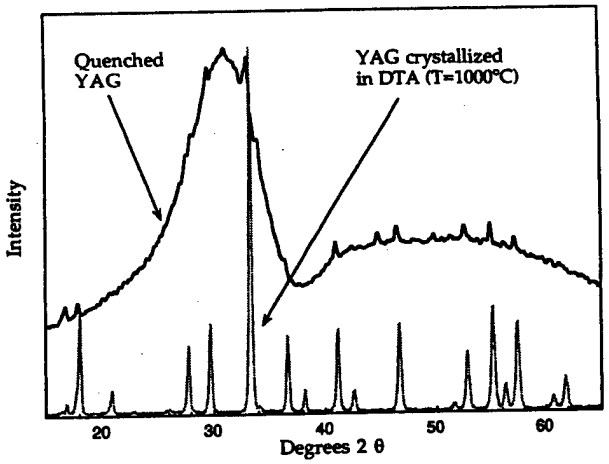

Differential, µV
Exothermic
Time, s
840 °C
845 °C
850 °C
855 °C
860 °C
865 °C
870 °C
875 °C

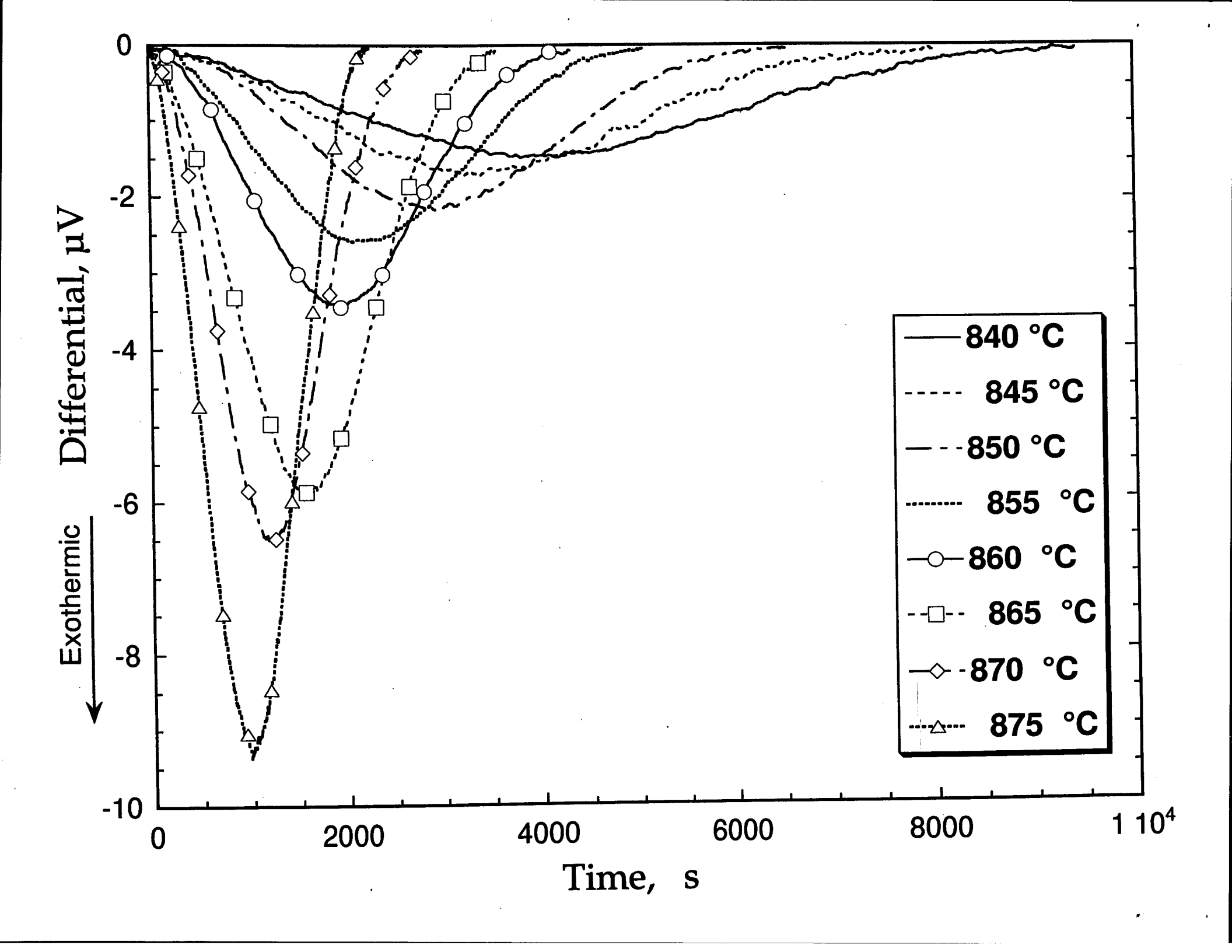

Sample Temperature, °C
Temperature, °C
Differential, µV
Exothermic
Time, s
Differential, µV
Curve Fit
Curve Fit | Data Table
Variable | Value
A | -6285.9
n | 2.6529
k | 3.8827E-04
t | 1605.7
Chisq | 2.1625
R² | 0.99936

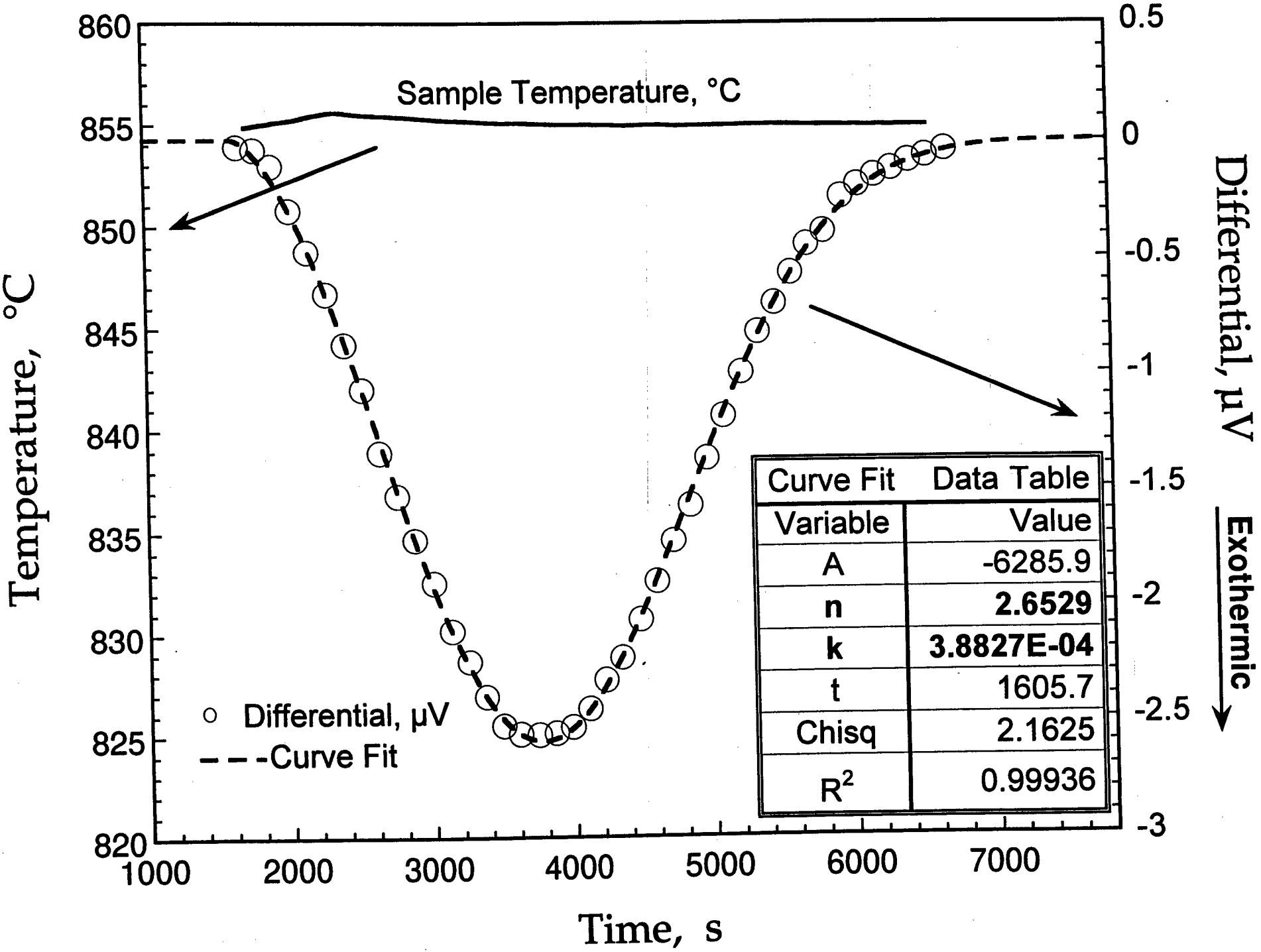

(Temperature, °C)
Reaction Rate Constant, k
Temperature, K
k = v * exp[-E/(R*T)]
Value
v | 6.3316e+16
E | 4.3704e+05
Chisq | 3.1246e-09
R² | 0.99093

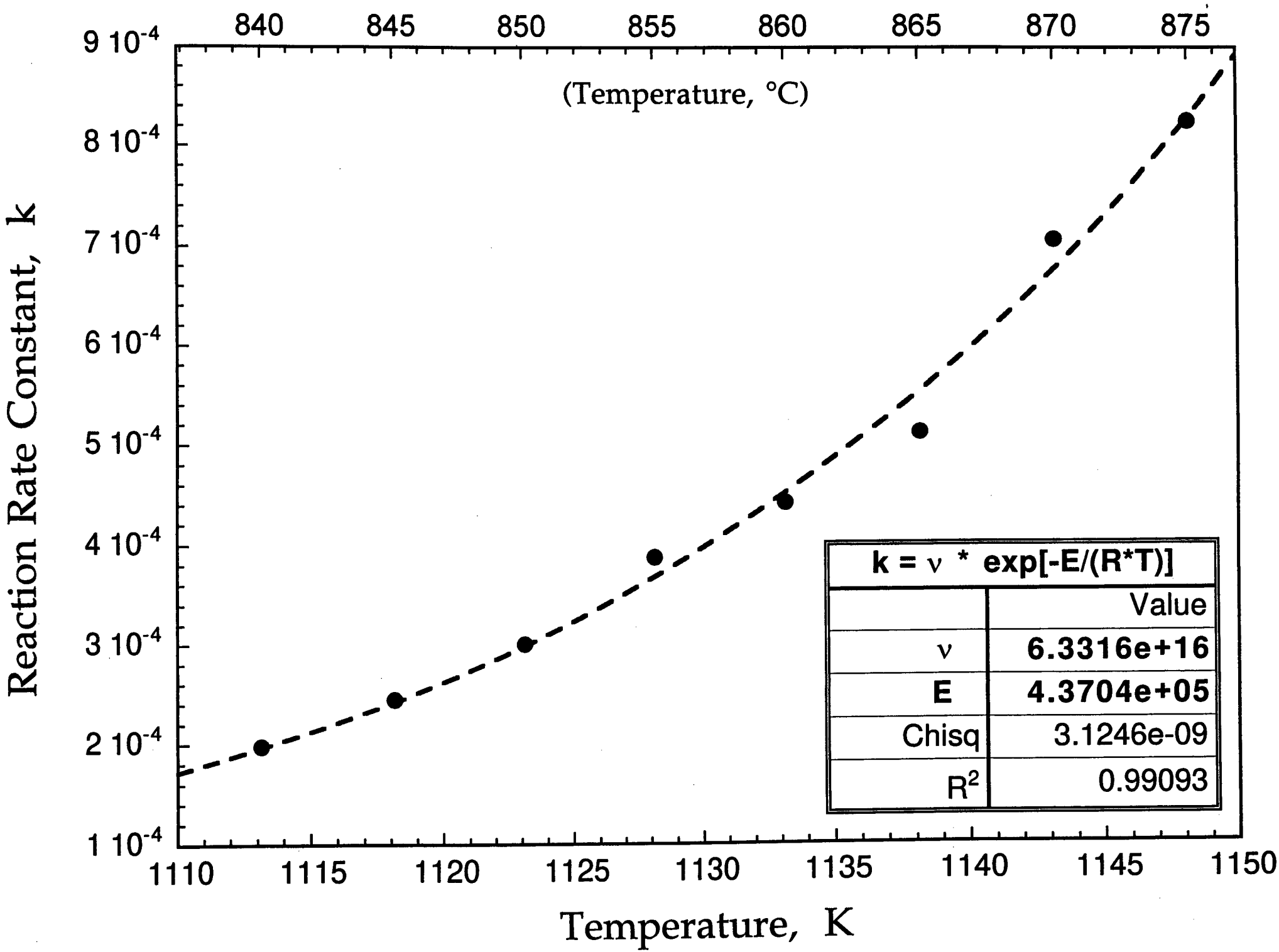

99% Crystallized
Measured data points from DTA exotherms
1% Crystallized
Temperature, °C
Time (s)

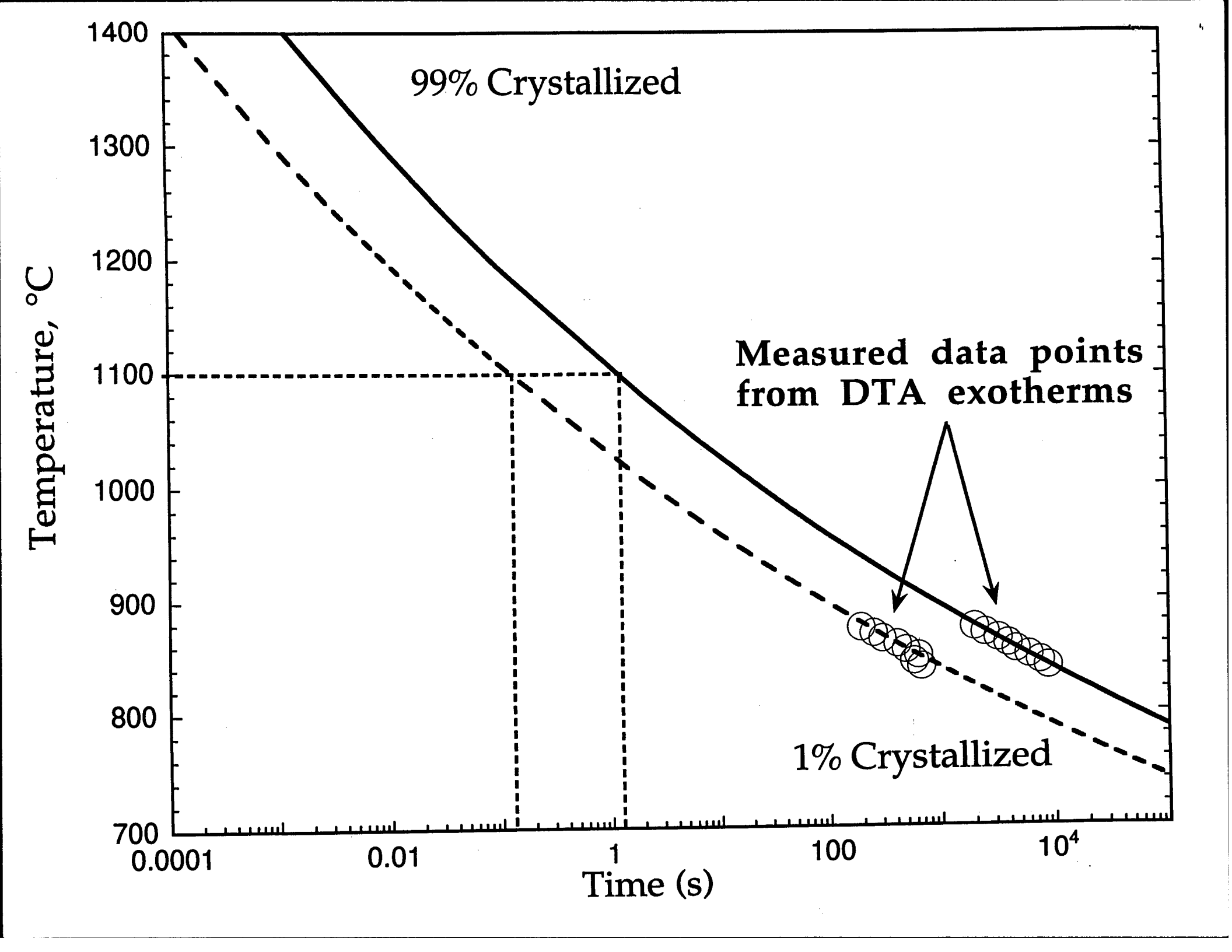

Quenched YAG
YAG crystallized in DTA (T=1000°C)
Intensity
Degrees 2 θ

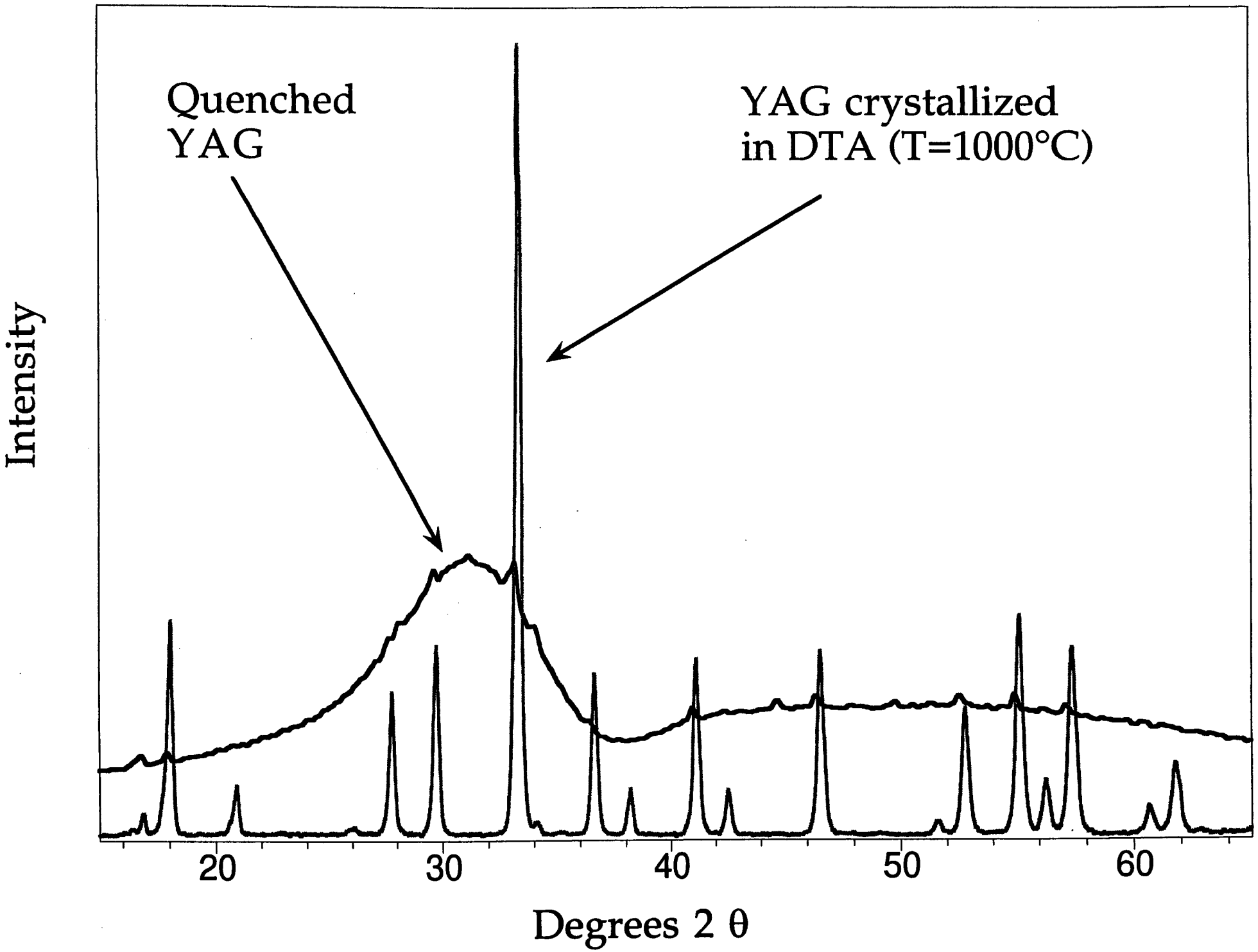

Quenched YAG
YAG crystallized in DTA (T=1000°C)
Intensity
Degrees 2 θ

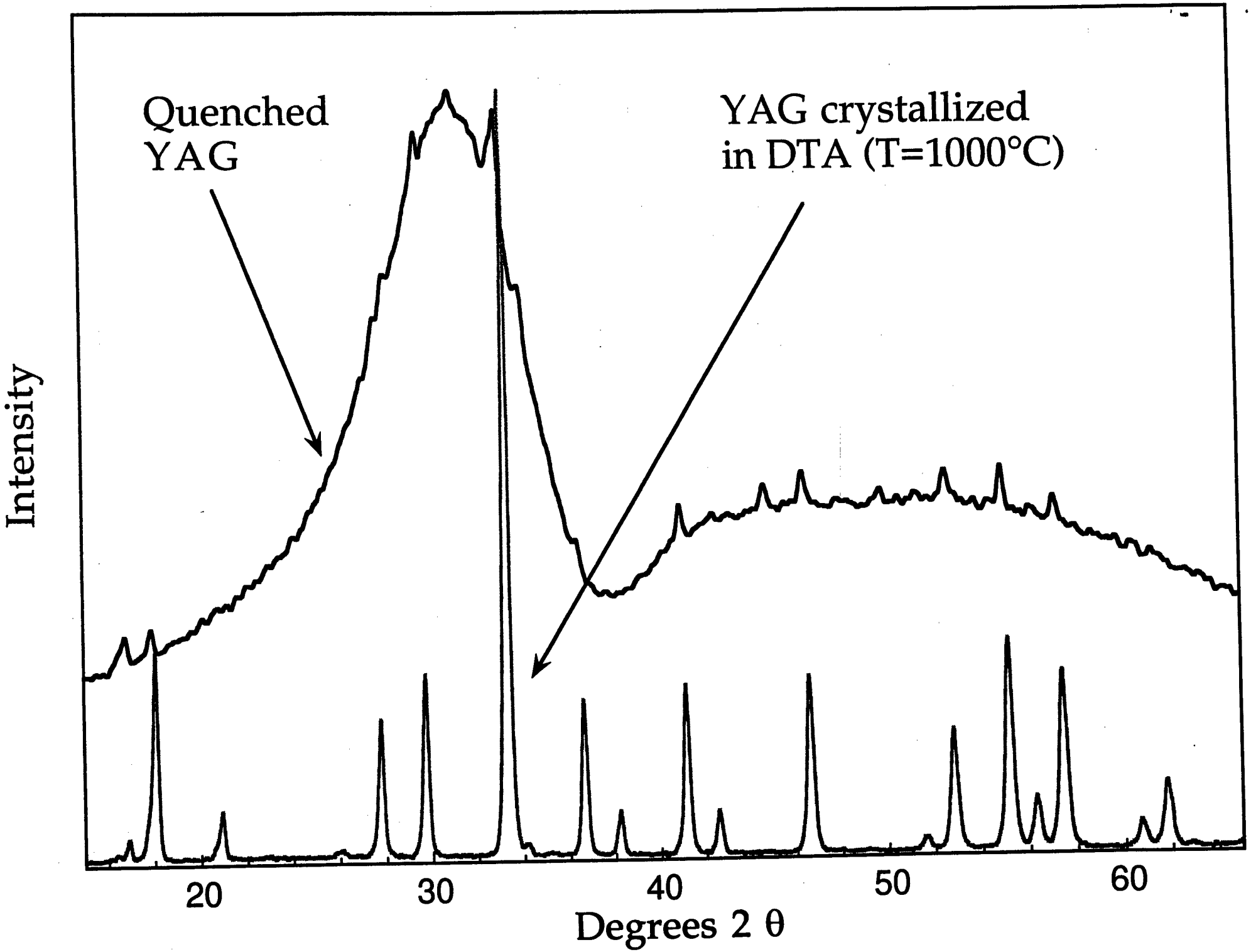

0
-2
-4
-6
-8
-10
Differential, µV
Exothermic
0
2000
4000
6000
8000
1 10^4
Time, s
840 °C
845 °C
850 °C
855 °C
860 °C
865 °C
870 °C
875 °C

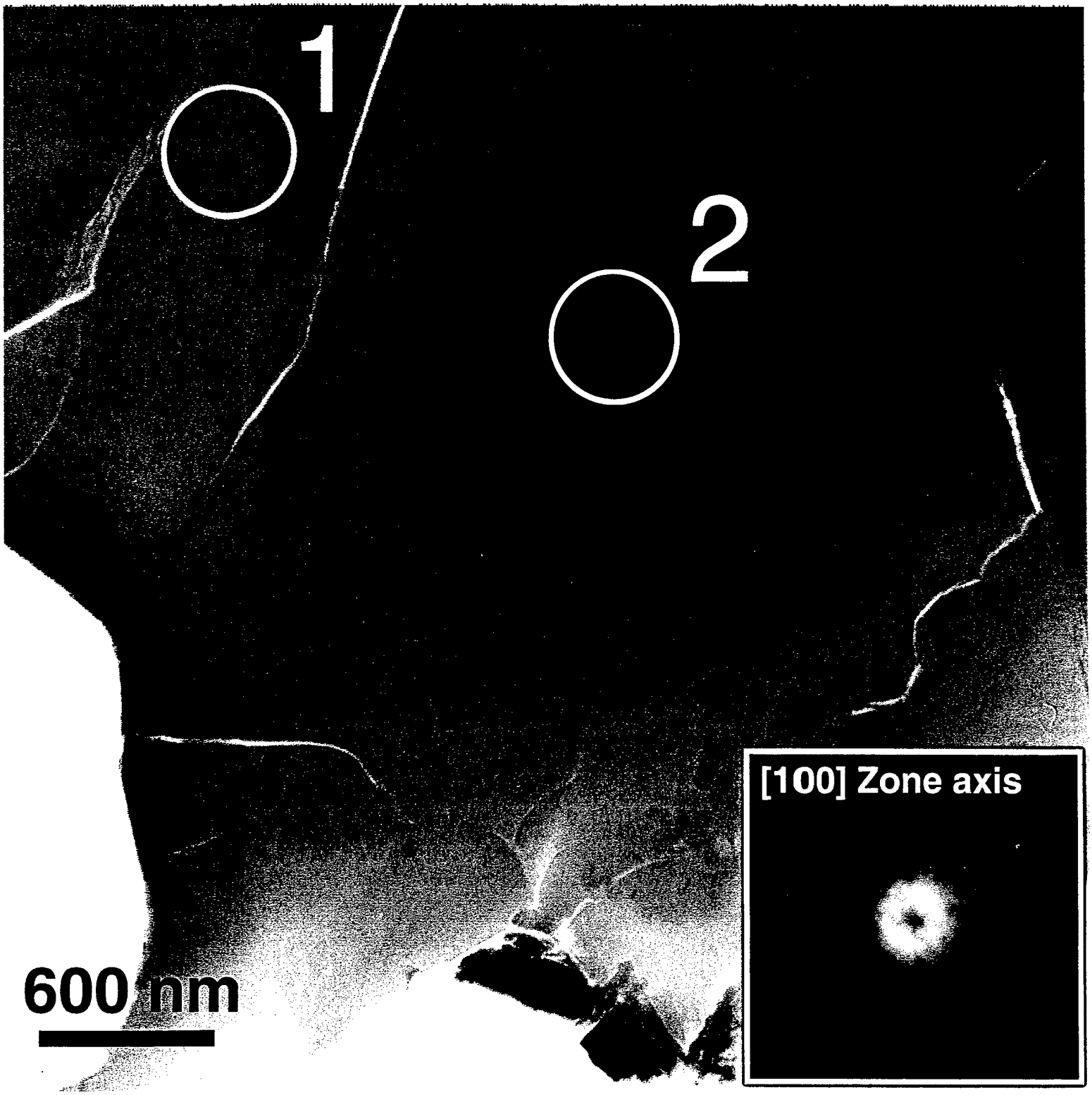

Sample Temperature, °C
Temperature, °C
Differential, µV
Exothermic
Time, s
Differential, µV
Curve Fit
860
855
850
845
840
835
830
825
820
0.5
0
-0.5
-1
-1.5
-2
-2.5
-3
1000
2000
3000
4000
5000
6000
7000
Curve Fit Data Table
Variable Value
A -6285.9
n 2.6529
k 3.8827E-04
t 1605.7
Chisq 2.1625
R2 0.99936

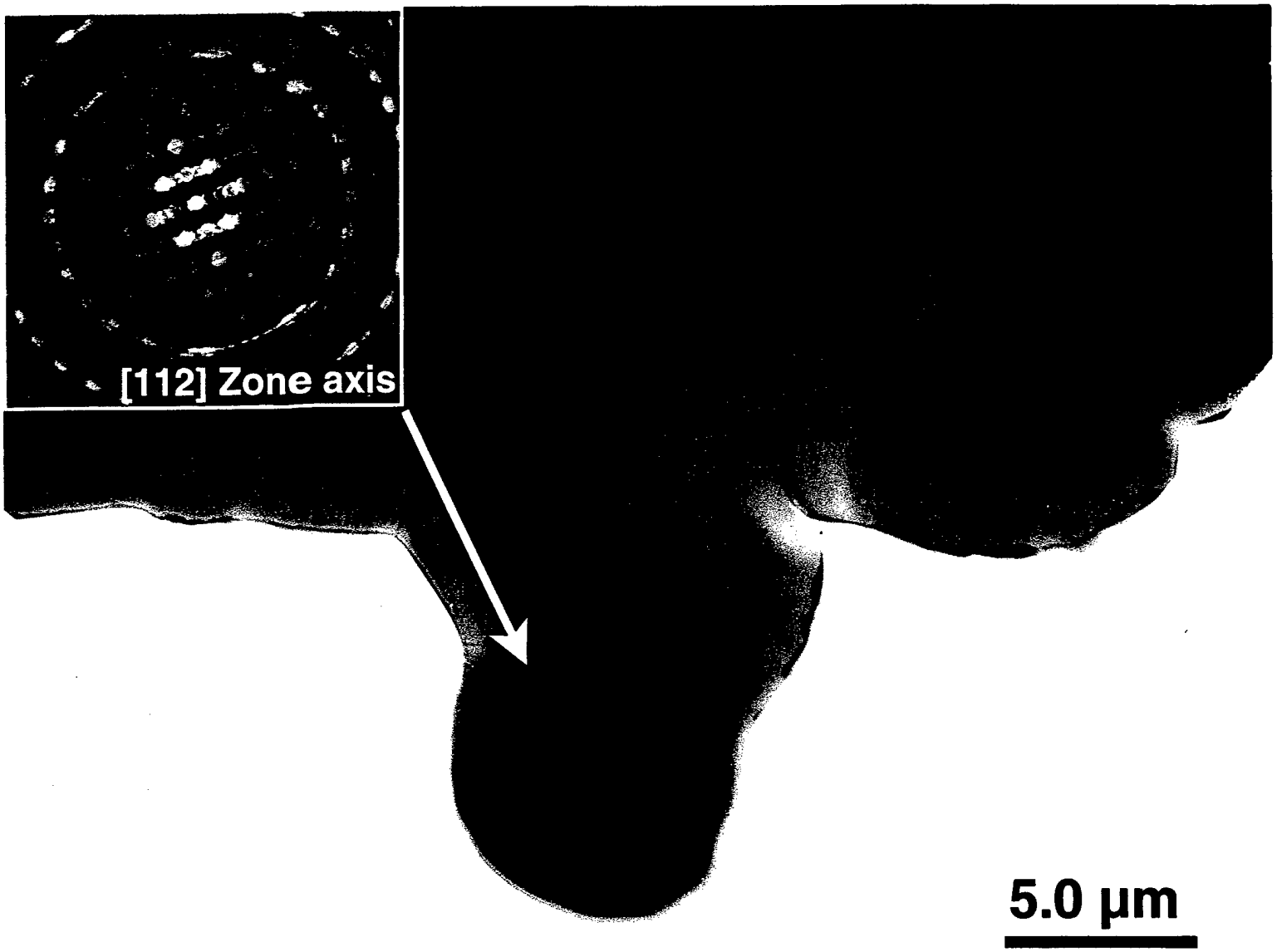

840
845
850
855
860
865
870
875
(Temperature, °C)
9 10-4
8 10-4
7 10-4
6 10-4
5 10-4
4 10-4
3 10-4
2 10-4
1 10-4
Reaction Rate Constant, k
1110
1115
1120
1125
1130
1135
1140
1145
1150
Temperature, K
k = ν * exp[-E/(R*T)]
Value
ν
6.3316e+16
E
4.3704e+05
Chisq
3.1246e-09
R2
0.99093

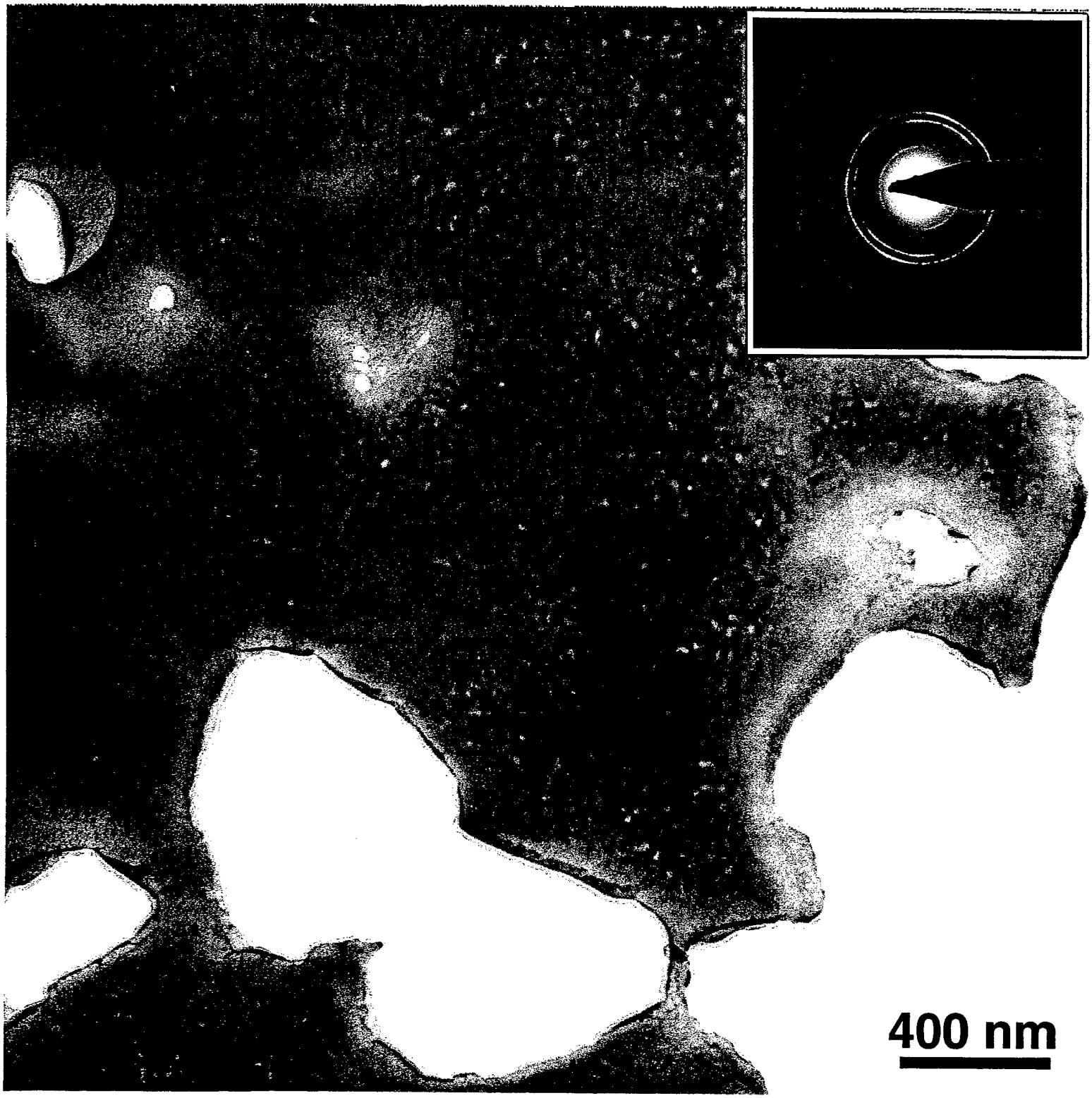

99% Crystallized
Measured data points
from DTA exotherms
1% Crystallized
Temperature, °C
Time (s)
1400
1300
1200
1100
1000
900
800
700
0.0001
0.01
1
100
10⁴

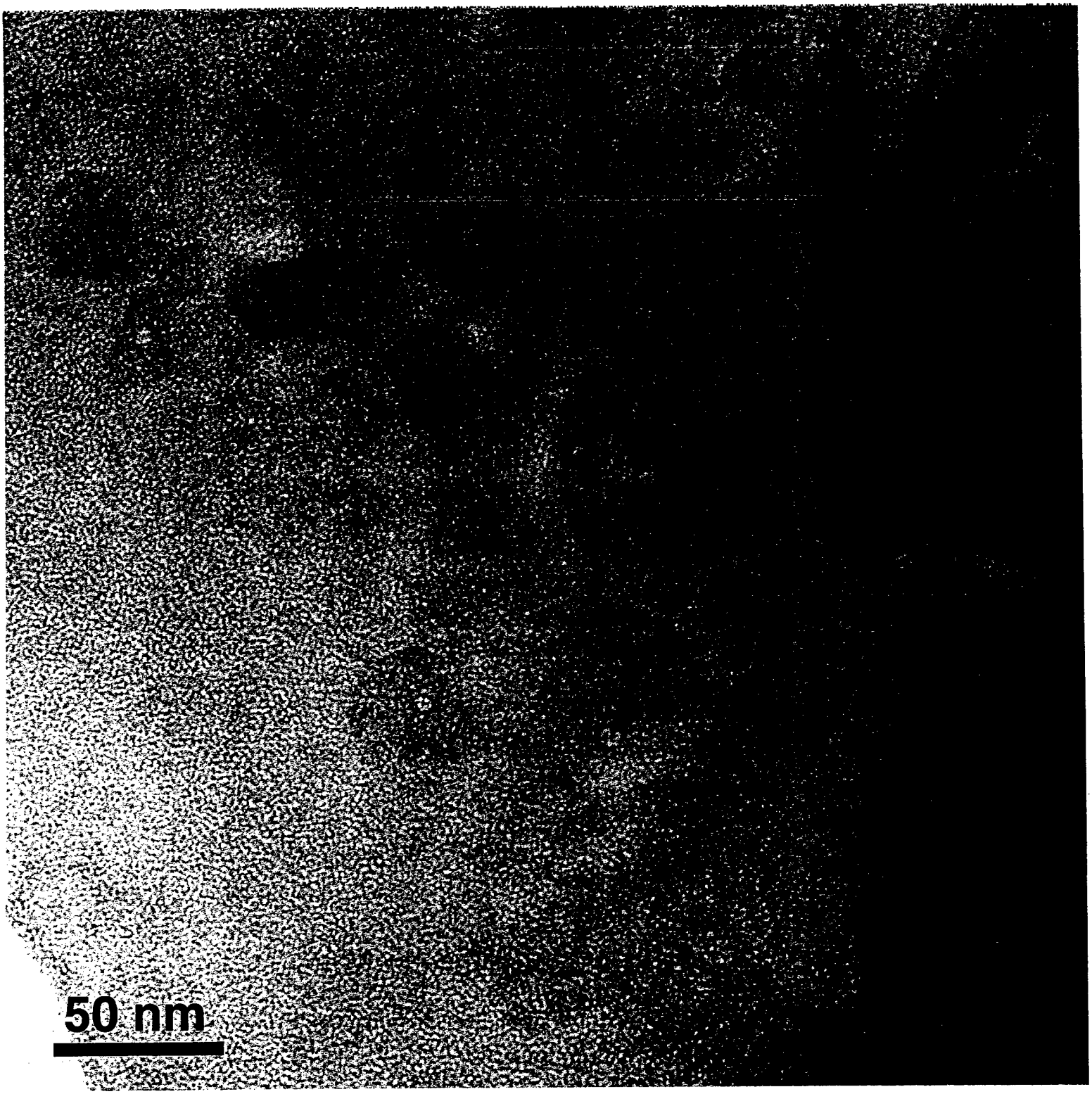

Quenched
YAG
YAG crystallized
in DTA (T=1000°C)
Intensity
20
30
40
50
60
Degrees 2 θ

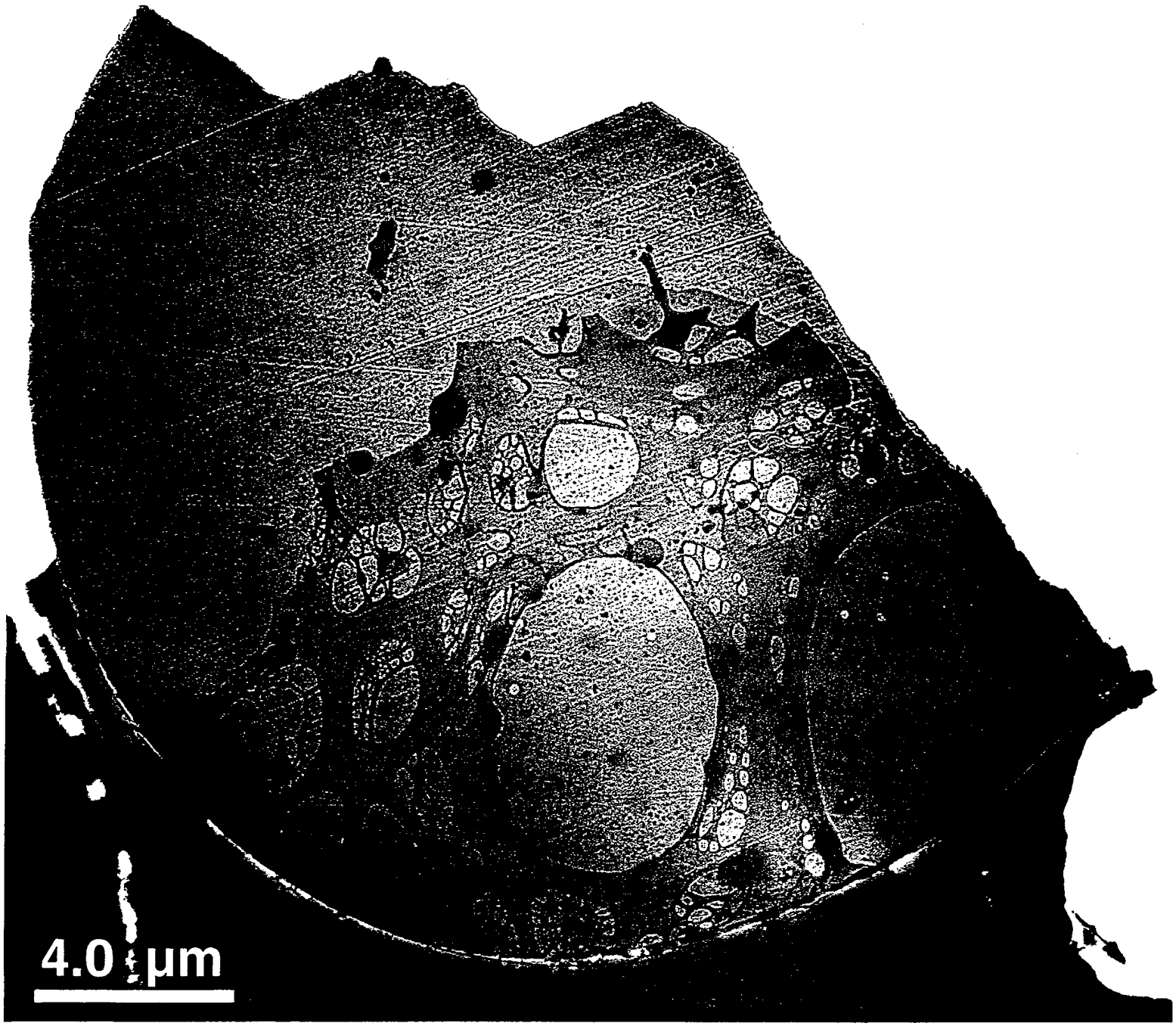

Quenched
YAG
YAG crystallized
in DTA (T=1000°C)
Intensity
20
30
40
50
60
Degrees 2 θ


1
2
[100] Zone axis
600 nm


[112] Zone axis
5.0 µm


400 nm


50 nm


4.0 µm

Crystal structure development during devitrification of amorphous mullite

Bradley R. Johnson, Waltraud M. Kriven
Department of Materials Science and Engineering, University of Illinois at Urbana-Champaign, Urbana, IL 61801

Julius Schneider
Institut für Kristallographie und Angewandte Mineralogie, München, Germany

Abstract

Crystallization kinetics, microstructural changes, and crystal structure development of quenched mullite composition glass ($3Al_2O_3 \cdot 2SiO_2$) were studied during the transition from an amorphous to a crystalline state between 900° and 1400°C. The phenomena observed were characterized using non-isothermal differential scanning calorimetry (DSC), transmission electron microscopy (TEM), energy dispersive spectroscopy (EDS) and powder x-ray diffraction (XRD) with both a standard laboratory diffractometer, as well as with synchrotron radiation. Crystallization of amorphous mullite was observed to occur in two steps. The activation energy for crystallization was 836.9 KJ/mole for the first step and 1,337.5 KJ/mole for the second step. From the amorphous state, the first phase(s) to crystallize were alumina-rich, pseudotetragonal mullite (~ 70 mol% Al_2O_3). These crystals were highly strained and contained numerous nanometer scale inclusions. With increasing temperature, the crystal structure was observed to incorporate increasing amounts of SiO_2, and approach the equilibrium orthorhombic structure. By 1400°C the pseudotetragonal to orthorhombic transition was complete, the strain and the inclusions were eliminated, there was ~ 67% reduction in grain size, and the crystals had attained the composition of the initial, bulk glass (~60 mol% Al_2O_3).

Keywords: Mullite, crystallization, kinetics, microstructure

1. Introduction

Mullite ($3Al_2O_3 \cdot 2SiO_2$) is the only stable compound in the Al_2O_3 - SiO_2 phase diagram at ambient pressures. It occurs in a narrow, temperature-dependent, solid solution range, between 60 - 63 mol% Al_2O_3.[1-3] It is an important structural and refractory ceramic with very good strength and creep properties. It is often used in such application as refractory bricks, furnace liners, and for structural fibers. Considerable work has been done to characterize the composition and structure of mullite.

The composition and crystal structure of mullite varies with the formation temperature. The correlation between the variation in the lattice parameters with the composition of mullite was initially reported by Cameron[4], and subsequently verified and refined by Kriven and Pask,[1] Okada and Otsuka,[3] Ban and Okada,[5] and Fischer et al.[6,7] The equilibrium crystal structure of mullite with a composition of $3Al_2O_3 \cdot 2SiO_2$, (60 mol% Al_2O_3) is orthorhombic, and it belongs to the space group Pbam.[8-11] However, when formed from molecularly mixed precursors, the first mullite crystals formed tend to be Al_2O_3-rich, (~70 mol% Al_2O_3) independent of the bulk composition of the precursors.[12] These crystals have an a-lattice parameter that is very close in size to their b-lattice parameter. This initial crystal structure has sometimes been termed pseudotetragonal mullite.[5,13-15] Another way to describe the structure is to call it the "pseudotetragonal metric"[16] since the crystal symmetry is still orthorhombic even when the a-lattice and b-lattice parameters are equal in length. Although termed pseudotetragonal, there is only a very subtle difference between the pseudotetragonal metric and orthorhombic mullite. This distinction can be observed by close examination of the extent of splitting between the (120) and (210) peaks at approximately 26° 2θ (using Cu Kα radiation). When initially formed, the two peaks overlap for the pseudotetragonal metric, and as the annealing temperature increases, the peaks tend to split apart and become more distinct (d_{120} = 3.428Å, d_{210} = 3.390Å, Powder Diffraction File 15-776)).[14,17] This structural change with increase in temperature was interpreted as incorporation of SiO_2 into the mullite structure, resulting in the reduction of the a-lattice parameter.[3,18]

An anomaly of the gradual compositional and structural change in mullite as it crystallizes, is the variation in the c-lattice parameter. Although the "a" and "b" lattice parameters change linearly with composition, (and hence with temperature as precursors crystallize), the value and the variation of the c-lattice parameter depends on the initial formation temperature. Mullite crystals of a given composition formed at temperatures below 1200°C have c-lattice parameters that are approximately 0.0005 nm shorter than mullite crystals of the same composition that were heated above 1200°C. This variation was first pointed out by Ban and Okada[5,19], but the same trend can be observed in data previously presented by Okada et al.[3,18]

Considerable work has been done regarding the crystallization of amorphous mullite precursors.[20-23] Depending on the degree of homogeneity, two primary crystallization pathways appear to be most prominent. In the case of molecularly mixed precursors (such as a slowly hydrolyzed sol-gel precursor, or an amorphous glass) mullite crystallizes at approximately 1000°C, depending on the heating rate.[18] For inhomogeneously mixed systems (e.g. kaolinite, diphasic precursors, or rapidly hydrolyzed gels) intermediate phases such as spinel ($6Al_2O_3 \cdot SiO_2$) form around 1000°C, and are subsequently converted to mullite around 1200°C.[24-29] For chemically synthesized mullite, the processing conditions play a critical role in

obtaining single-phase, molecularly mixed precursors, and great care is necessary to avoid forming diphasic precursors.[30]

Recently, work has been done to synthesize structural mullite fibers drawn from the melt using containerless methods.[31-33] These amorphous fibers require subsequent thermal processing to crystallize them. The crystallization of quenched, amorphous mullite composition glasses was studied to determine appropriate processing conditions for the crystallization of melt-drawn mullite composition fibers. This work was focused on gaining greater understanding of the crystallization kinetics, microstructural changes, and crystal structure development of amorphous, quenched, mullite composition glass.

2. Experimental Procedures

Materials: Commercially obtained mullite powder (KM 101 mullite powder, Kyoritsu Ceramic Materials Co. LTD., Nagoya, Japan) was supplied to Containerless Research Inc. (Evanston, IL) for processing to synthesize amorphous beads and fibers. The powders were melted in a water-cooled hearth using a CO_2 laser to form a spherical bead.[34] The bead was then levitated in an oxygen atmosphere with an aero-acoustic levitator, and melted again with a CO_2 laser as described in literature elsewhere.[35-38] Melt temperatures were approximately 2200°C as indicated by optical pyrometry. The suspended molten droplet was then rapidly quenched at a rate of approximately 250°C per sec, to form a solid bead about 2 – 3 mm in diameter. The beads were subsequently crushed between two stainless steel plates to form a coarse powder. Final grinding was accomplished with an agate mortar and pestle, to produce a fine powder that was used in thermal analysis, x-ray diffraction, and TEM experiments.

Thermal analysis: Nucleation and crystallization studies of as-received, ground, quenched, mullite composition beads were conducted with a Netzsch STA 409 Simultaneous Thermal Analyzer (Selb, Germany) used in DSC mode. The experiments were done in a flowing atmosphere of 75cc/min of Ar, and covered Pt crucibles to were used to hold the specimen and the reference. Temperature calibration of the instrument was accomplished by observing the melting points of 99.999% gold and silver. The average value of three different melting points was used. A mass of ~15.0 mg was used for the sample and reference material (α-alumina).

Two different types of experiments were used to study the nucleation and crystallization of amorphous, mullite composition glasses. Nucleation experiments were conducted to determine the effects of pre-crystallization heat treatment on the crystallization temperature, T_p (the temperature at the maximum of the crystallization exotherm). This information was necessary to set up conditions for the second set of crystallization experiments. Non-isothermal DSC experiments were done to determine the crystallization kinetics. For nucleation experiments, specimens were heated at 20°C/min to a specified soak (or nucleation) temperature (T_N),

annealed at that temperature for 3 hr, and then heated again at a 10°C/min to a maximum temperature of 1100°C. The variation in crystallization temperature, T_p, during the second heating ramp was observed. This was repeated for a series of different nucleation temperatures (850°C to 940°C). For non-isothermal DSC experiments, specimens were heated at a rate of 20°C/min to 850°C, and held there for 15 min. Above that temperature, ten different heating rates were used (viz. 0.5°, 1.0°, 1.5°, 2.0°, 3.0°, 4.0°, 5.0°, 6.0°, 8.0° and 10.0° C/min) to heat the specimen up to a maximum temperature of 1100°C. Crystallization was observed to occur exothermally during the second heating ramp segment. The variation in T_p with heating rate was used to calculate the kinetics of crystallization.

Electron Microscopy: The microstructure and microchemical composition of mullite at various stages of crystallization was characterized using a TEM (Philips CM12, FEI Company, Hillsboro, OR, USA) equipped with an EDS detector (EDAX, Mahwah, NJ, USA). Selected specimens were also examined with a Vacuum Generators HB 501 scanning transmission electron microscope (STEM) equipped with a 100 kV field emission gun filament and an Oxford Instruments (Oxfordshire, England) Link® EDS system. Several different specimens were chosen after being subjected to various thermal treatments (Table 1). Specimens were prepared from ground, quenched, mullite composition beads as well as from tripod polished,[39,40] and ion milled sliced sections of quenched beads. The specimens were examined by bright field (BF) and dark field (DF) imaging, convergent beam electron diffraction (CBED), selected area diffraction (SAD), and energy dispersive spectroscopy (EDS). Quantitative EDS calculations were based on the Cliff-Lorimer approximation.[41] The camera length constant for the microscope was determined from a specimen of evaporated gold deposited on to holey carbon film. The diffraction patterns for gold and the various specimen images were collected digitally and distances were measured using a free-ware image analysis software package (*MacLispix*) made available by the National Institute of Standards and Testing (NIST).[42] Quantitative particle size measurements were made with the image analysis program *Object-Image*[43] using micrographs taken with a calibrated CCD camera (Gatan Multi-Scan camera, Gatan, Inc., Pleasanton, CA).

X-ray diffraction: Initial x-ray diffraction studies were conducted with a Cu K_α source on a standard laboratory diffractometer, (Giegerflex DMax automated powder diffractometer, Rigaku/USA, Danvers, MA) equipped with a graphite monochromator. The diffractometer was operated at a voltage of 40 kV and a current of 40 mA with a slit system of: 1/2°-1/2°-0.3mm-0.8mm. The data was collected in a theta – 2-theta scanning mode. Spectra were collected from crushed, quenched beads, before and after crystallization in thermal analysis experiments. For crystallized specimens, typically a goniometer speed of 2° 2θ/min was used with a step size of 0.01° 2θ, and the data was summed over 10 scans. For quenched specimens, typically a

goniometer speed of 2° 2θ/min was used with a step size of 0.01° 2θ, and the data was summed over 50 scans.

Detailed crystal structure measurements of annealed powder specimens (M1, M2, M3 and M4, Table 1) were made at the Advanced Photon Source (APS) at the Argonne National Laboratory at the UNICAT beamline E33 (the undulator). Specimens were chosen to represent various stages of mullite crystallization (Table 1). The beam cross section was approx. 2 x 1 mm and the wavelength was 0.75266 Å, as determined by Rietveld refinement of a Si standard (SRM 640b, National Institute of Standards). Specimens were loaded in a capillary tube with a 0.5mm ID, which was rotated at a minimum rate of 60 rpm. The data was collected by step scanning a single slit scintillation counter, versus a constant monitor counting rate. Minimum counting times of about 1 second per step were chosen to achieve at least one revolution of the capillary sample spinner. An angular range of 5.0° - 37° 2θ (8.6276 - 1.1860 Å) was scanned at a step size of 0.008°, yielding 4000 data points per powder diagram.

3. Results and Discussion

3.1. Thermal Analysis

The Johnson-Mehls-Avrami (JMA) equation (Eq. 1) was the basis for modeling non-isothermal DTA experiments. Although this equation was derived for isothermal phase transformations, it has been successfully applied to non-isothermal DTA or DSC experiments under appropriate experimental conditions.[44-48] The key relationship observed is the variation of the crystallization temperature, T_p, with heating rate, α. Since the crystallization exotherm is not a delta function, but rather a curve that occurs over a range of temperatures, it is important to determine the temperature at each heating rate that corresponds to the same degree of crystallization. This is necessary to accurately model the α *vs.* T_p trend. It has been demonstrated that the maximum in the crystallization exotherm corresponds to approximately 55% conversion, independent of the heating rate.[45] Thus the temperature at the exothermic peak (T_p) was chosen as the reference temperature in these studies.

$$x = 1 - \exp\left[-(kt)^n\right] \tag{1}$$

A pre-requisite for using JMA based equations for kinetic analysis of non-isothermal experiments, as pointed out by Ray et al.,[47] is that the specimen must be thoroughly nucleated prior to crystal growth so that crystallization occurs with a constant number of nuclei. This precludes a situation where nucleation and growth occur simultaneously. Experimental conditions where crystallization occurs with a constant number of nuclei is also an important factor for using the equation for the reaction rate, k, (Eq.2). The reaction rate is typically assumed to have an Arrhenius temperature dependence, and to be independent of time. In order to minimize errors when calculating the reaction rate, non-isothermal crystallization experiments should be designed to occur within a narrow temperature range and with a near-zero nucleation rate.[47]

$$k = \nu \exp\left[\frac{-E}{RT}\right] \tag{2}$$

The kinetic model proposed by Bansal and Doremus[44,45] was used to analyze the non-isothermal crystallization data for these experiments. The final result of their derivation is shown in Eq. 3. A plot can then be made of $\ln(\alpha/T_p^2)$ vs. $1/T_p$. This type of plot is sometimes termed a Kissinger plot.[47,49]

$$\ln\left(\frac{T_p^2}{\alpha}\right) = \frac{E}{R}\left(\frac{1}{T_p}\right) + \ln\left(\frac{E}{R\nu}\right) \tag{3}$$

The slope of the line through the data points is used to calculate the activation energy for crystallization, E, and the y-intercept of the line is used to calculate the pre-exponential factor, ν in Eq. 2.

The other variable yet remaining to be calculated from the data is the Avrami exponent, n. The method of Augis and Bennet[50] was used, Eq. 4.

$$n = \frac{2.5}{\Delta T_{FWHM}}\left(\frac{T_p^2}{E/R}\right) \tag{4}$$

The value of the Avrami exponent provides information regarding the morphology of the growing crystals. For conditions where crystallization occurs throughout the bulk of the material with a constant number of nuclei, the value of n indicates the dimensionality of the growing crystals.[47] All of the pertinent variables (n, k, E and ν) for the JMA equation (Eq. 1) were thus computed from the non-isothermal data.

3.1 a Nucleation Studies

Nucleation experiments were carried out to determine necessary annealing conditions to saturate the quenched glass with nuclei. Since the nucleation rate is a function of time and temperature similar to crystal growth,[51] there is a variation of T_p with the soak temperature, T_N. The soak temperature where T_p is the lowest, is where the nucleation rate is a maximum. Annealing the specimens at this temperature would thus saturate them with nuclei and establish appropriate conditions for non-isothermal crystallization studies. This variation is typically pronounced for strong, glass-forming systems, (e.g. Li_2O-Al_2O_3-SiO_2 glasses).[47,48]

Nucleation rate studies on quenched mullite composition glass beads did not show a significant variation of T_p with T_N. The standard for comparison was a specimen heated at a rate of 10.0°C/m from room temperature to 1100°C. There was no significant difference in T_p between the standard sample heated at 10.0°C/min and those subjected to the various annealing treatments. The specimens isothermally held at 930°C and 940°C crystallized during the hold time. The results are listed in Table 2. Thus, it was concluded that the specimens were fully nucleated by the time they reached 850°C, and that further annealing treatments were unnecessary. These findings seemed reasonable, since mullite is a very fragile glass forming material.

3.1 b Crystallization Kinetics

Non-isothermal DSC crystallization experiments with quenched mullite composition specimens were conducted as previously stated. Results for the heating rate, T_p, and the Avrami exponent are listed in Table 3. A Kissinger type plot[49] (Figure 1, based on Eq. 3) was used to calculate the activation energy, *E*, and pre-exponential factor, ν.

A significant change in slope between 3.0°C/min and 4.0°C/min heating rates was observed (Fig. 1). This indicated that more than one kinetic mechanism was involved in the crystallization process. A closer examination of the DSC exotherms at these lower heating rates (e.g. < 6°C/min) revealed that there were two different exothermic events that occurred during crystallization. At heating rates ≤ 3.0°C/min, the first event was dominant, whereas at heating rates ≥ 4.0°C/min, the second event became dominant. Figure 2 is a comparison of the DSC exotherms at 3.0 and 4.0°C/min, showing the two different exothermic events, and the shift in dominance between them. The values for T_p listed in Table 3 were the more prominent of the two. At heating rates above 5.0°C/min, the two peaks overlapped sufficiently so that it was very difficult to differentiate between them. For $\alpha \geq 8.0$°C/min, the increased intensity and overlap of the two events created significant asymmetry in the shape of the crystallization exotherms.

The linear regression correlation coefficient (R^2) for the line fit applied to heating rates ≤ 3.0°C/min on Fig. 1 was 0.994 and the value of R^2 for the line fit applied to heating rates ≥ 4.0°C/min was 0.987. The activation energies for crystallization were 836.9 and 1,337.5 KJ/mole for the first and second events, respectively. The values of the Avrami exponent, *n*, in Table 3 were calculated based on Eq. 4. The combined average value of *n*, was 2.6, which indicates three dimensional crystal growth. (The values of n for α = 8.0 and 10.0 °C/min were not included in the average due to the significant asymmetry in the shape of the crystallization exotherm.) The values for ν ($4.5E+32s^{-1}$, and $5.27E+53s^{-1}$ for events one and two, respectively) were rather large. Since mullite is a fragile glass former, and these values were determined from the extrapolated value of the y-intercept from Fig. 1 using Eq. 3, there may be a reasonable margin of error in the computed values of ν. Nonetheless, they do reflect the rapidity at which amorphous mullite composition glasses crystallize.

The activation energy for mullite crystallization has been reported to be precursor dependent.[23] Nonetheless, the calculated activation energies for mullite crystallization in this system lie within the range of values reported in the literature, e.g. ~ 850 - 1300 KJ/mol.[20,22,23,52,53] Additionally, the phenomena of two over-lapping crystallization exotherms for isothermal crystallization of sol-gel derived precursors was reported by Tkalcec et. al[20], and a 3-stage crystallization sequence in alumino-silicate fibers was reported by Takie et al.[53] The two mullite crystallization activation energies reported here, (836.9 KJ/mol, and 1,337.5 KJ/mol) correlate very well with the two activation energies for first stage crystallization of a 49 mass% Al_2O_3 fiber reported by Takei et. al.[53] (E_a^N for nucleation was 864 KJ/mol and E_a^{NG} for nucleation and growth was 1288 KJ/mol). Their three stage crystallization sequence (Stage 1 = 900°-1000°C, Stage 2 = 1000°-1200°C, and Stage 3 = 1200°-1400°C) was determined by quantitative XRD analysis of alumino-silicate fibers crystallized after various thermal treatments. Thus, it was satisfying to note that the non-isothermal DSC derived kinetic data reported here, for the crystallization of quenched mullite composition glass (at temperatures below 1000°C), was similar to that determined by quantitative XRD analysis, for their Stage 1 crystallization of alumino-silicate fibers.

The two different exothermic events observed during crystallization were probably the result of two slightly different composition mullite phases crystallizing. The shift in the prominence of the two exothermic events indicates the possibility of competing crystallization mechanisms between the two compositions. Microstructural characterization and Rietveld analysis were conducted to corroborate the existence of multiple phases in mullite crystallized at low temperatures. Those findings are discussed below.

3.2. Microstructure

3.2 a As-received and nucleated specimens (Q and N)

Specimens Q and N were used to characterize the as-received mullite beads, and to examine the microstructure of mullite just prior to crystallization. Figure 3 is a TEM bright field (BF) (A) and a STEM BF (B) micrograph of a polished, thin section from an as-received, quenched mullite bead (specimen Q, Table 1). The contrast observed in the specimen was typical of phase-separated, amorphous materials. Chemical analysis of the specimen at various points revealed a wide variation in composition. The chemical composition for the field of view in Fig. 3B was 75.8 mol% Al_2O_3 and 24.2 mol% SiO_2. An EDS line scan showing a variation in the Al/Si ratio within Fig. 3B is shown as an inset image. The observed sub-micron chemical inhomogeneity for the quenched specimens was consistent with reports of a metastable immiscibility gap in the Al_2O_3-SiO_2 phase diagram.[54-57] This apparent phase separation may have been responsible for the two crystallization events observed by DSC.

Figure 4 is a TEM BF micrograph of a quenched, amorphous, melt-drawn mullite fiber that was annealed at 920°C for 3h (specimen N, Table 1). This thermal treatment was the highest annealing temperature that was observed in the DSC, without the onset of complete crystallization (Table 2). The dark regions were examined by selected area diffraction (SAD), and were identified as small crystallites. The SAD pattern of the crystallites is shown in the inset image in Fig. 4A. The pattern was indexed as belonging to the pseudotetragonal metric of mullite. The size of 150 crystallites was measured and the average length of the major and minor axes was 13.4 ± 2.9 nm and 11.5 ± 2.7 nm, respectively (Table 4). A high resolution micrograph of one of the crystallites is shown in Fig. 4B. The d-spacing for the lattice fringes in this crystallite was 3.38Å, which is close the d-spacing for the (120) and (210) lattice planes of orthorhombic mullite (3.428Å, and 3.390Å, respectively). It was only possible to resolve one ring at this d-spacing in the SAD pattern, which is consistent with psuedotetragonal mullite.

3.2 b Pseudotetragonal mullite (M1, M1.5, and M2)

The thermal treatments applied to specimens M1 and M2 were chosen in order to characterize pseudotetragonal mullite after initial formation and just prior to conversion into orthorhombic mullite, respectively.[5,17,19] These specimens correspond to the first and second crystallization stages reported by Takei et. al.[53] Specimen M1.5 was used to compare the effects of sample preparation (powders *vs.* thin film) on microstructure for pseudotetragonal mullite and to examine the microstructure at an intermediate temperature. Figure 5 is a TEM BF micrograph of a crushed, quenched, mullite composition bead that was crystallized isothermally by annealing it at 938°C for 2.5h (specimen M1). The microstructure consisted of a matrix of

angular, crystalline grains (~370 x 260 nm in size) with smaller, ellipsoidal inclusions (average size = 10.0 x 7.8 nm) embedded in them (Table 4). Figure 6 is a higher magnification of another particle from the same specimen. The right portion of Fig. 6A was one of the grains; the smaller, rounded, lighter features were the inclusions. In bright field mode, the grains had a variegated diffraction contrast (Fig 5), where different regions of the grain would go in and out of extinction in a sweeping fashion as it was tilted. Figure 6B is the same area as Fig. 6A, only in a dark field condition. The beam was tilted so that a particular set of lattice planes from the grain were allowed to pass through the objective aperture, thus creating the bright band in Fig. 6B. The dark circular features were the ellipsoidal inclusions.

Figure 7 consists of TEM BF micrographs from a polished thin section of a quenched mullite bead that was heated to 1085°C for 0.5 h (specimen M1.5). EDS analyses were taken at the ten different labeled points in Fig. 7A (beam diameter ~ 70 - 100 nm), and the average composition at each point was 60 ± 1 mol% Al_2O_3, 40 ± 1 mol% SiO_2. Figure 7B is a micrograph from M1.5 at higher magnification showing a grain and a large number of small, ellipsoidal inclusions embedded in it (similar to what was observed in Fig. 6). The inclusions appear as bright spots on the right side of the micrograph, and as dark spots on the left side. When the specimen was observed in an over- and under-focused conditions at higher magnification (at the same angle of tilt), the contrast of the inclusions changed from dark areas with a light fringe to light areas with a dark fringe. This was interpreted as a Fresnel fringe effect due to a density difference between the inclusions and the matrix (inclusion density < matrix density).[41] The inset image is a [001] zone axis SAD pattern taken from another grain in this specimen. Any extra spots in the pattern not belonging to the zone axis were identified to originate from an adjacent or overlapping grain by DF mode, and were not from the inclusions. Qualitatively, the microstructures for M1 and M1.5 appeared very similar, howerver, quantitatively, subtle differences were noted. The average length of the major and minor axes for the small, ellipsoidal inclusions was 9.4 ± 2.5 nm and 7.9 ± 2 nm respectively, and the average size of the major and minor axes for the grains was ~510 nm and 380 nm, respectively (Table 4). Figure 8 is a BF STEM micrograph of M1.5 where an EDS line scan was performed using a much smaller beam diameter than for the EDS analysis in Fig. 7A. The inset graph illustrates the variation in the Al/Si ratio over the scanned line. The smaller diameter beam was able to reveal chemical heterogeneity in this specimen that was not observed in Fig. 7.

Figure 9 is a TEM BF micrograph of a crushed, quenched mullite composition bead that was heated to 1200°C (specimen M2). The inset image is a Kossel-Möllenstedt (KM) micro-diffraction pattern taken from one of the crystals oriented along the [120] zone axis for mullite. The average grain size was 270 x 190 nm. Small inclusions embedded within the grains were also observed, with an average size of 7.9 ± 1.7 x 6.6 ± 1.5 nm (Table 4). The variegated diffraction

contrast observed in specimens M1 and M1.5 was still present. EDS analysis conducted at several different locations on several different particles indicated a nominal composition of 60 ± 2 mol% Al_2O_3, and 40 ± 2 mol% SiO_2.

3.2 c Orthorhombic mullite (M3)

Figure 10 is a TEM BF micrograph of a crushed, quenched mullite composition bead that was heated to 1400°C (M3). This thermal treatment was chosen in order to characterize the microstructure of mullite after conversion to the orthorhombic phase, and prior to the temperature where it begins to exsolve SiO_2.[2,3] This thermal treatment also corresponds to the end of stage 3 crystallization reported by Takei et. al.[53] The average grain size was 100 x 69 nm. A typical, polycrystalline microstructure was observed. The variegated diffraction contrast, and the small inclusions observed at lower temperatures were no longer present.

3.2 d Microstructural observations

The presence of discrete crystallites observed at the very early stages of crystallization (Fig. 4) is evidence that crystallization proceeded via a nucleation and growth mechanism. The large number of crystallites uniformly dispersed throughout the specimen indicates that the material was site saturated, that crystallization occurred with a constant number of nuclei, and that crystallization occurred throughout the bulk of the material (*vs.* just at the surface). These observations were consistent with the results from DSC nucleation experiments.

There were several common features to the microstructures of specimens M1, M1.5 and M2. Although there was a large distribution in grain sizes, they all had fairly equiaxed grains (Fig. 5, 7). The grains showed a variegated diffraction contrast, that in several of the micrographs appeared to originate from the center of the grain (Fig. 7). This suggests that crystallization occurred three dimensionally, and that the crystals grew spherulitically, from a point of origin. Three dimensional crystal growth occurring throughout the bulk of the material is characteristic of an Avrami exponent equal to three. The computed value of n from DSC experiments was 2.6. Thus the observed microstructure was consistent with the kinetic parameters determined by non-isothermal DSC experiments.

The variegated diffraction contrast in M1, M1.5 and M2 was an indication that the crystal lattice of these specimens was distorted, possibly by internal strain. A distorted lattice will cause the incident electron beam to diffract in a wavy manner, as observed in Fig. 5 - 9.[41] Although several of the TEM specimens were made from ground powders, the observed internal strain probably was not an artifact of sample preparation. Specimen M1.5 (Fig. 7, 8) was prepared as a thin foil by tripod polishing and ion milling, and it had the same variegated diffraction contrast as the ground powder specimens M1 and M2 (Fig. 5, 6, and 9). Specimen

M3 (orthorhombic phase, heated to 1400°C, Fig. 10) was another crushed powder specimen, and it did not show variegated diffraction contrast. Additionally, the samples were ground while amorphous, and examined after crystallization. The high temperatures and structural rearrangement that occurred during crystallization should have been sufficient to relieve any residual strain in the material.[58] These observations suggest that pseudotetragonal mullite has a very strained crystal structure.

The other common feature to specimens M1, M1.5 and M2 was that they all contained numerous inclusions, ~7 - 10 nm in size. The exact chemical composition and structure of these inclusions was not conclusively determined. Several different microscopic techniques were used to examine them microstructurally and microchemically, including EDS, SAD, convergent beam electron diffraction (CBED), electron energy loss spectroscopy (EELS), and elemental mapping with an energy filtered TEM. Their small size necessitated a very small diameter electron beam to probe them individually, however the specimens were susceptible to beam damage, making them difficult to analyze. Since they were very similar chemically to the crystal matrix that they were embedded in, it was difficult to differentiate their chemical identity using broader diameter electron beam analyses (e.g. energy filtered elemental mapping). High resolution TEM analysis of the interface between the matrix and the inclusions was also complicated by beam damage.

However, zone axis SAD patterns were obtained from grains containing the inclusions (Fig. 7B). If the inclusions were crystalline, and randomly oriented within the matrix crystal, it would be plausible to see a SAD pattern containing both the zone axis pattern for the matrix crystal along with a ring pattern from the numerous inclusions. Or, if the inclusions were crystalline, and epitaxially related to the matrix, then extra reflections might appear in zone axis SAD patterns. However, neither of these phenomena were observed. Any additional reflections in the SAD pattern that did not belong to the zone axis were identified (by DF) to belong to either a different region from the strained grain (in a different diffracting condition), or from a adjacent or overlapping grain. This evidence would indicate that the inclusions were amorphous.

Additional evidence concerning the identity and structure of the inclusions can be inferred from other experiments. Rietveld analysis of specimens M1 and M2 (discussed later) revealed that the crystals were alumina rich (~ 70 mol% Al_2O_3) based on their lattice parameters, and their spectra showed a broad amorphous hump centered around the 100% peak. TEM EDS analysis with a moderate diameter electron beam (70 - 100 nm) on specimens M1.5 (Fig. 7A) and M2 indicated a composition close to 60 mol% Al_2O_3, whereas STEM EDS analysis using a much smaller probe diameter showed significant compositional variations over a smaller length scale (Fig. 8). The correlation of this information indicates the existence of an amorphous, SiO_2rich phase that is very small and dispersed on a very fine level. It would appear that the inclusions observed in specimens M1, M1.5 and M2 are this phase.

These inclusions may have been the source of strain observed in specimens M1, M1.5 and M2. TEM BF and DF imaging was done of two overlapping grains in specimen M1. The sample was oriented such that two closely spaced reflections (one from each grain) were allowed to pass through the objective aperture (inset, Fig. 11A). This set up a condition where a moiré pattern was formed by the overlapping lattice planes for the two grains.[41] This was seen in the centered dark field (CDF) micrograph by thin wavy lines passing through region where the grains overlapped (Fig. 11A). The moiré pattern was revealed in greater detail by (i) taking the Fourier transform (FFT) of the CDF image (inset, Fig. 11B), (ii) applying a filter to the FFT to remove everything except the periodic features, and then (iii) by taking the inverse Fourier transform of the filtered FFT. The filtered image is shown in Fig. 11B. The average spacing between the fringes was 8.56Å, which was larger than any of lattice parameters for mullite. The regular periodicity of the lines, their presence throughout the region of overlap between the two grains, and the large spacing between them were all evidence that they were moiré fringes created by the overlap of lattice planes from two single crystals. This was confirmed by indexing the two reflections used to create the pattern, calculating their d-spacing, and measuring the angle between them. The two spots were indexed as the (220) and (230) planes of mullite, their d-spacing was d_{220} = 2.704Å, d_{230} = 2.124Å, (using Rietveld refined lattice parameters for this specimen) and the angle between them was 7.85°. The calculated d-spacing for a misfit moiré pattern using the above values was 8.62Å.[41] This compared favorably to the measured fringe spacing of 8.56Å, thus confirming the identity of the moiré pattern. One of the important observations from the moiré pattern was that it was very distorted (wavy lines, dislocations, etc.), and the distortions were spatially correlated to the small inclusions observed in the DF micrograph (bright spots in Fig. 11A). This would suggest that the inclusions created a distortion in the psuedotetragonal mullite lattice. The overlapping effects of the numerous inclusions was thus responsible for the complicated, variegated diffraction contrast observed in bright field micrographs of these specimens.

Table 4 lists the stereological measurements made on several of the specimens. The initial crystallites (~ 13.4 x 11.5 nm ellipsoids) apparently coalesced to form larger, angular grains ~200 x 300 nm. The average grain size for M1.5 was significantly larger than for M1 and M2. This can be explained by the fact that it was crystallized as a monolithic disk ~3mm in diameter, and not as a powder like specimen M1 and M2. Additionally, since the specimen was made by polishing and thinning, it was possible to measure grains over a very large electron transparent region, whereas only selected thin areas from small particles could be measured for specimens M1 and M2. Other researchers performing quantitative XRD analysis of mullite crystallization have reported a steady increase in crystallinity and volume fraction of mullite produced with increasing thermal treatment between 1000° and 1400°C.[12,14,53] Although there was not a

significant variation in grain size observed between specimens M1, M1.5 and M2, there was a significant reduction in the size of the inclusions. From M1 to M1.5, there was a 6% reduction in the size of the inclusions, from M1.5 to M2 a 15% reduction, and from M1 to M2 a 22% reduction in the size of the inclusions. This indicates that with increasing temperature, the inclusions were gradually assimilated into the crystal. This finding is consistent with the interpretation that they are an amorphous, SiO_2-rich phase, since the SiO_2 content of psuedotetragonal mullite has been reported to increase (i.e. decreasing Al_2O_3 concentration) with thermal treatment.[3,5,14] The reported increased volume fraction of mullite crystallized over this temperature range from quantitative XRD studies thus appears to be related to the assimilation of these inclusions into the crystal. This may be microstructural evidence that the pseudotetragonal to orthorhombic transition, during the crystallization of mullite, is diffusion limited, as reported by Li and Thompson[59] and Takei et. al..[53]

Of particular note is the ~ 67% reduction in grain size from M2 (1200°C) to M3 (1400°C). Normally grain size increases as a function of temperature. Grain size reduction may have been the mechanism used to relieve the observed internal strain. A similar phenomena is observed in metallic systems, where highly strained metals have been observed to recrystallize and form smaller grains after being annealed at elevated temperatures.[58] Possible sources of strain were the inclusions as well as the anisotropic change in lattice parameter dimensions for the pseudotetragonal to orthorhombic transition (-.82% for a, 1.6% for b, and -1.5% for c, discussed later).

3.3 XRD

X-ray diffraction measurements of crushed, quenched mullite composition beads were made before and after thermal analysis in a DTA/DSC. This was done to confirm the identity of the exothermic events observed between 940° and 990°C. Figure 12 is a graph of the combined, normalized XRD spectra for quenched mullite composition glass beads before and after thermal analysis. The spectrum for specimen Q was a broad, diffuse hump characteristic of amorphous materials, with a maximum near the 100% peak for crystalline mullite. Additionally, the presence of some crystalline phase was also apparent. The pattern for specimen M2 was highly crystalline. It was similar to the equilibrium mullite structure (PDF 15-1776), except that the 120 and 210 peaks overlapped (i.e. pseudotetragonal). No other phases were observed, and specifically, there was no indication of an Al-Si spinel phase. It was concluded that the exothermic events observed by DSC were due to mullite crystallization since that was the only phase detected by XRD of annealed specimens.

3.4. Synchrotron Powder Diffraction Measurements

Specimens M1, M2, M3 and M4 were chosen for Rietveld analysis using synchrotron radiation XRD data to characterize the crystal structure of mullite after various thermal treatments. One of the objectives was to determine if the multiple crystallization events observed by DSC could be validated by the presence of multiple crystalline phases in pseudotetragonal mullite. The other objective was to ascertain the crystallization pathway for quenched mullite glass by correlating microstructural results with precise crystal structure data.

3.4 a Structure Models

Mullite, a solid solution of Al_2O_3 and SiO_2, may be represented by the following general formula:

$$Al_{4+2x}\ Si_{2-2x}\ O_{10-x} \tag{5}$$

The end members of this general formula are represented by the mineral sillimanite (x = 0) and a hypothetical substance iota-alumina (x = 1). Metastable mullite with a composition of $SiO_2 \cdot Al_2O_3$ (x = 0.40) is often termed "fused mullite", since it is typically formed from the melt, whereas mullite with a composition of $3Al_2O_3 \cdot 2SiO_2$ (x = 0.25), such as the Kyoritsu KM101 mullite used in this study, is typically called "stoichiometric" or stable mullite. In the "average" structure model of mullite, as assigned by Burnham,[60,61] and later confirmed by Saalfeld and Guse[62] and Angel and Prewitt[11], the repartition of the atoms on the respective Wyckoff positions within space group Pbam (no. 55) is given in Table 5. The structures of sillimanite and mullite consist of chains of edge-shared AlO_6 - octahedra running parallel to the c-axis that are interconnected by double chains of AlO_4/SiO_4 tetrahedra that are also parallel to the c-axis. In sillimanite, the regular AlO_4/SiO_4 tetrahedral sequence parallel to the c-axis results in a doubled c-cell. This regularity is lost in mullite, because with increasing x, Si^{4+} cations are replaced by Al^{3+} according to the reaction:

$$2\,Si^{4+} + O^{2-} = 2\,Al^{3+} + V_{\ddot{o}} \tag{6}$$

The AlO_6 - octahedra are built up by Al ions at the 2a sites and oxygen atoms at O_{ab} and O_d sites. Whereas in sillimanite the tetrahedral Al^{3+}/Si^{4+} ions occupy the T positions, in mullite any Al atom in excess of 4 replaces a Si atom at the 4h site, resulting in an oxygen vacancy at the tetrahedral corner sharing position O_c. This leads to a local structural rearrangement shifting the excess Al atom on to a new position T* and the corresponding next neighbor oxygen on to the shifted position O_c*. Figure 13 shows projections of the idealized structures of sillimanite and mullite on to the ab-plane.

The difference between various mullites is known to manifest itself by variations of the cell dimensions and, structurally speaking, essentially by variations of the positions and occupancies of the T* and O* positions. The maximum oxygen deficiency possible by this one parameter disorder model as given by Eq. 5 and Table 5, is reached for x = 2/3, when all Oc atoms have been eliminated. Fischer et al.[6,7] discussed structure models for x > 2/3. Angel et al.[9] further refined this "average" mullite structure by assigning atoms to the T, O_{ab} and O_d positions, and by including anharmonic temperature factors. Angel et al.[9,11] also discuss the incommensurate modulations observed with certain mullites.

3.4 b Single Phase Rietveld Refinement

Table 6. summarizes the results of single phase Rietveld refinements of the "low temperature" (LT) samples M1, M2 and the "high temperature" (HT) samples M3, M4 applying the structure model and the constraints given in Table 5. The last column lists the x-ray single crystal results of Saalfeld & Guse[62] obtained from a 3:2 mullite for comparison. A remarkable qualitative difference between the LT- and HT-data is given by the large high angle line broadening of the LT specimens as shown in Fig. 14. This effect normally is indicative of microstrain in the sample and it may also be responsible for the larger estimated standard deviations (esd's) of the refined LT specimen parameters. The microstrain indicated by line broadening (shown in Fig. 14 for M1 and M2), correlates very well with the evidence of strained crystals as observed by TEM (e.g. variegated diffraction contrast in BF mode in Fig. 5 - 9). This provides further evidence that the structure of pseudotetragonal mullite was highly strained. Evidence that the strain was not an artifact of sample preparation lies in the much broader line widths for the LT specimens as compared to M3, even though they were all prepared the same way. The refined lattice parameters for these specimens may be analyzed with respect to three criteria: (i) Al_2O_3/SiO_2 ratio, (ii) cell dimensions, and (iii) structure.

(i) Al_2O_3/SiO_2 ratio

The most direct indicator of the Al_2O_3/SiO_2 ratio is the mixing parameter x (see Eq. 5 and the line "mullite x" in Table 6) as derived from the refined site occupancies. Due to the low x-ray scattering power of oxygen and the very low scattering contrast of Al3+/Si4+ ions, this parameter is normally not easily refineable from powder data. However, the various site constraints (occupancies of T-, T*-, Oc- and Oc*- sites constrained by only one parameter x, isotropic temperature factors, temperature factors of all O-atoms constrained to be identical) and the high quality of synchrotron powder data reduces the usual number of correlations between occupancies and temperature factors. The mixing parameters of the HT samples

(0.34, 0.33) refine to values somewhat in between the nominal values of x = 0.25 for 3:2 mullite and x = 0.40 for 2:1 mullite, whereas the value x = 0.274 obtained by Saalfeld and Guse[62] is much closer but still above the value for 3:2 mullite. However, the mixing parameters of the LT specimens (0.50,0.58) refine to much higher values, even higher than the x = 0.40 for 2:1 mullite.

To cross-check these results obtained from Rietveld refined intensities constrained by the above structure model, three other indicators of the Al_2O_3 content were evaluated: the linear dependence of the a-lattice parameter on the Al_2O_3 content as observed by Cameron[4] and confirmed by Ban & Okada[5], the linear dependence of the density on the composition x assuming a constant number of cations of Al + Si = 6 (Cameron[4]) per unit cell and the linear dependence of the ratio of the 220 and 111 reflection intensities on x (Ban & Okada[5]). Using the respective regressions :

$$Al_2O_3\,(\text{mole }\%) = 1443\ (\text{length of a axis}) - 1028.06 \qquad (7)$$

$$\text{density} = -.3031*x + 3.247 \qquad (8)$$

$$Al_2O_3\,(\text{mole }\%) = 41.77\ (I_{220}/I_{111}) + 27.6 \qquad (9)$$

the resulting Al_2O_3 contents are shown in Table 7. In converting the mixing parameter x to Al_2O_3 (mole %) the obvious relations

$$Al/Si = (2+x)/(1-x) \quad \text{and} \quad Al_2O_3(\text{mole }\%) = (2+x)/(4-x) \qquad (10)$$

were used. We observe that whereas the HT specimens and the literature data yield fairly consistent Al_2O_3 fractions around 61 mol% (nominal value for 3:2 mullite: 60.0 mol%), the LT samples yield much higher fractions around 70 mol% (nominal value for 2:1 mullite: 66.7 mol%), varying significantly depending on which indicator was used. This was another indication of the anomalous behaviour of the LT specimens (to be discussed in more detail below).

(ii) Cell Dimensions

Fig. 15 compares the Rietveld refined cell dimensions a and c with the lines separating orthorhombic mullite from pseudotetragonal mullite as given by Cameron[4] and Ban et al.[5] The LT specimens M1 and M2 clearly fall into the region of pseudotetragonal mullite and the HT specimens M3 and M4 and the Saalfeld & Guse[62] results into the orthorhombic mullite region. The density calculated from the refined cell dimensions increases by about 1.6% in transforming from the LT to the HT mullites. This seems reasonable in considering that

pseudotetragonal mullite is a metastable transitional phase between the amorphous starting material and the stable stoichiometric 2:1 or 3:2 mullites, and that the transition involves crystallization of the residual amorphous phase. However, this densification is brought about by a non-uniform shrinkage of the unit cell: da/a = -0.82%, db/b = +1.6%, dc/c = -1.5%. As the cell dimensions of the HT specimens closely correspond to equilibrium 3:2 mullite (Ban & Okada,[5]) this would imply a highly macro-strained material for the LT specimens M1 and M2 in addition to the severe micro-strain indicated by the large line broadening mentioned above.

(iii) Structure

Table 6 shows that the refined structural parameters for the HT specimens agree within one estimated standard deviation (except x(T*), 2 esd's). This proves that specimen M3 has regained the structure of the starting material M4. Compared to the single crystal data of Saalfeld & Guse[62] these specimens show a slight increase towards the values of Angel et al.[9,10] obtained for 2:1 mullite.

The refined occupancies demonstrate that the transition from pseudotetragonal mullite to orthorhombic mullite is accompanied by a depopulation of Al-atoms at the T*-site in favor of an increase of Si atoms at the "normal" T-site. The corresponding depopulation of the O_c*-site in favor of an increase of the population at the "normal" O_c-site was also observed (except for sample M2), and is required by the structural model given in Eq. 5 and Table 5.

Significant changes of the positional parameters were observed in the transformation from pseudotetragonal to orthorhombic mullite. This is mostly seen by an increase of the y-coordinates of the T*- and the O*-sites, which may be related to the increase of the b-lattice parameter. A significant decrease of the x-coordinate of the octahedral O_d-oxygen may be related to the decrease of the a-lattice parameter. The other coordinates, in particular those of the T-sites and the O_{ab}-sites, remain essentially constant.

3.4.c Multiphase Rietveld Refinement

Considering the fact that specimens M1, M2 and M3 had undergone various thermal treatments, they should reflect the timewise integrated history of their respective kinetic processes. In addition, as previously mentioned, specimen M2 was an averaged sample, consisting of a mixture of several powders with different thermal treatments, each with an ultimate temperature of 1200°C. Thus, together with the findings of DSC (two exothermic events, Fig. 2) and TEM investigations (7 - 10 nm inclusions embedded in 200 - 500 nm grains) a mixture of more than one mullite phase seemed possible with specimens M1 and M2. The

presence of multiple phases would also help to explain the anomalous line broadening observed in the synchrotron XRD spectra for these specimens. A close inspection of weak high angle reflections revealed line splittings and line shoulders that were averaged over in the single phase Rietveld refinement previously discussed. Figure 16A is an enlarged view of the synchrotron XRD spectra around the 002 reflection for specimen M1(938°C). The data clearly shows the overlap of three different peaks, indicating the presence of three different composition mullite phases. This corroborates the multiple exothermic peaks observed by DSC. The dashed and solid lines show results for the single phase refinement previously discussed and for a three phase refinement, respectively. However, due to the high degree of line overlap a separate refinement of structure, cell and line widths parameters for the whole spectra was not possible. The c-lattice dimension, as taken directly from the data, as well as the a- and b-lattice parameters and the corresponding Al_2O_3 mole fractions as taken from Fischer et al.[6] are given in Table 8. Quantitative analysis via refinement of scale factors yielded the indicated weight fractions. Besides the majority phase (50 wt%) of some 70 mol% Al_2O_3, which is close to the average value obtained with the single phase analysis, a second (40 wt%) fraction of very high Al_2O_3 content (76 mol%) and a third phase (10 wt%) of very low Al_2O_3 content (< 60 mol% Al_2O_3) can clearly be identified. The c-lattice dimension (0.2875 nm) of the latter fraction is lower than observed before in any mullite, which may be related to the phenomenon of anomalously low c cell dimensions in mullites heat treated below 1200°C, as observed by Ban et al..[5,19] Additional shoulders and line broadening at high and low angle tails of reflection 002 (Fig. 16A) suggest further minority phases and also microstrain. Fig. 16B is a plot of synchrotron XRD spectra comparing the 002 reflection region for specimens M1 (938°C), M2 (1200°C) and M3 (1400°C). It is apparent that a weighted distribution of at least 5 to 6 phases could be applied to the 002 peak for specimen M2. The very narrow 002 reflection for specimen M3 shows the final product phase after the tetragonal - orthorhombic transition was completed.

The multiple peaks in M1 and M2 at the low angle side (high c-cell dimension, high Al_2O_3 content), as well as on the high angle side (low c-cell dimension, low Al_2O_3 content), of the final 002 reflection position of sample M3, suggest the following picture of the crystallization sequence: At the beginning two phases of high and low Al_2O_3 content respectively start to crystallize, obviously because of the miscibility gap discussed by Ban et al.[56] and Takei et al..[57] With time and temperature these transform into the final phase as determined by the bulk Al_2O_3 and SiO_2 composition. It should be mentioned that the starting phase with the very high Al_2O_3 content (76 mol%) is very close to the composition of 78 mol%, where Fischer et al.[6] placed the crossover point of the a- and b-cell dimensions, i. e. close to the ideal "tetragonal" mullite. However, even at this composition the structure remains orthorhombic with a symmetrically independent coincidence of a and b. It should also be mentioned, that

according to the one parameter structure model (Eq. 5) and Table 5, the composition x = 2/3, where all of the Oc oxygen atoms are replaced by vacancies, corresponds to only slightly higher Al_2O_3 content of 80 mole %. This suggests that the "tetragonal" mullite with a quasi equal distribution of O_c-vacancies along the a- and b-cell directions has the lowest lattice energy and thus crystallizes first. Only subsequent annealing produces Si/Al exchange coupled with placing O_c oxygens onto their vacant sites. This process seems to occur preferentially along the a-cell direction leading to the inverse change in length of a and b.

Summarizing, we may state that the synchrotron XRD spectra for specimens M1 and M2 reflect integrated time histograms of incomplete mullite crystallization that show the formation of multiple mullite phases. To reduce the observed heavy line overlap, in situ (isothermal) high temperature and high resolution powder diffraction experiments should be performed to follow the structural implications of this crystallization kinetics in more detail.

5. Summary

1. Pseudotetragonal mullite was observed to crystallize directly from $3Al_2O_3 \cdot 2SiO_2$ composition quenched melts without the formation of intermediate phases such as Al-Si spinel. The kinetics for initial crystallization of pseudotetragonal mullite were characterized by DSC as a two-step process, with activation energies of 836.9 KJ/mol and 1,337.5 KJ/mol for the two steps, respectively. The presence of multiple crystalline phases was confirmed by Rietveld analysis of synchrotron XRD data for specimens crystallized at low temperatures. Multiple Rietveld phase fitting (3 phases) was successfully applied to specimen M1.

2. Crystallization of pseudotetragonal mullite occurred via a nucleation and growth process without an induction period. Quenched mullite composition glasses were observed to be site saturated with discrete, ellipsoidal, crystallites (~ 13.5 x 11.5 nm) throughout the bulk after annealing at 920°C for 3h. The crystallites coalesced and grew three-dimensionally with apparent spherulitic grain growth. The computed Avrami exponent, n = 2.6, was consistent with the observed microstructure (n = 3 for three dimensional, bulk, crystal growth). Crystallization was observed to occur extremely quickly at temperatures above 970°C when heated at moderate rates (3.0° to 10.0°C/min).

3. Pseudotetragonal mullite specimens had a microstructure of faceted, angular grains ~200 x 300nm in size with numerous small ~7 x 10 nm inclusions embedded within them. The pseudotetragonal mullite crystals were highly strained as observed by the variegated contrast in BF TEM micrographs and by the broad lines in the synchrotron XRD spectra. The strain was spatially correlated to the embedded inclusions.

4. Rietveld analysis of synchrotron XRD spectra for $3Al_2O_3 \cdot 2SiO_2$ composition mullite glass crystallized at temperatures $\leq$ 1200°C determined that the crystals were pseudotetragonal

with a composition of approx. 70 mol% Al_2O_3 (based on their lattice parameters). Multiple phases were detected. The formation of the Al_2O_3-rich phases was attributed to phase separation as a result of a metastable immiscibility gap. The XRD spectra for these specimens contained a large amorphous hump Since the composition of the glass was 60 mol% Al_2O_3, and crystals contained ~ 70 mol% Al_2O_3, it was inferred that the amorphous phase was SiO_2-rich.

5. Quantitative Rietveld fitting of high angle pseudotetragonal mullite peaks (002) suggested that a "tetragonal" (symmetrically independent coincidence of a and b) mullite, with a quasi-equal distribution of O_c vacancies along the a- and b- cell dimensions, had the lowest free energy, and that it was first phase to crystallize. Subsequent annealing produced Si/Al exchange, coupled with placing oxygens onto vacant O_c sites. This process appeared to occur preferentially along the a-cell direction, leading to the inverse change in the length of a and b as the pseudotetragonal phase converted to the orthorhombic phase.

6. Direct TEM characterization of nm-sized inclusions, embedded in pseudotetragonal mullite crystals, was complicated by their small size, sensitivity to beam damage, and chemical similarity to the matrix. Based on SAD and EDS, it was inferred that they were amorphous and differed in composition from the matrix. Coupled with the existence of an amorphous, SiO_2-rich phase (as deduced from XRD spectra and Rietveld analysis), it was concluded that the inclusions were amorphous and rich in SiO_2.

7. The psuedotetragonal to orthorhombic transition occurred between ~938°C - 1400°C, and appeared to be diffusion limited, as the crystals assimilated the 7 - 10nm, SiO_2-rich inclusions. By 1200°C, there was an approx. 22% reduction in the size of the inclusions, and the composition of the pseudotetragonal mullite crystals was closer to that of the bulk material (based on the $I_{220/111}$ intensity ratio). By 1400°C, the previously observed strain was gone: the variegated contrast observed by TEM in BF mode disappeared as well as the inclusions, and there was a significant reduction in line widths from the synchrotron XRD spectra. At this temperature, equilibrium orthorhombic mullite was formed, the composition was ~ 60mol% Al_2O_3, and a more typical, polycrystalline microstructure was observed.

8. The pseudotetragonal - orthorhombic transition was accompanied by ~ 67% reduction in grain size from 1200°C to 1400°C. The relief of built up internal strain from the embedded inclusions and the anisotropic change in lattice parameters from the phase transition was suggested as the driving force for grain size reduction. The phenomena of recrystallization after annealing highly strained metals was offered as an example of a similar phenomena.

Acknowledgments

The authors would like to gratefully acknowledge Richard Weber and Johan Abadie from Containerless Research Inc. for supplying the quenched mullite beads used in this work, as well as Pankaj Sarin from the University of Illinois and Paul Zschack from the UNICAT facility at the APS facility at ANL for their assistance in collecting the synchrotron radiation data. This project was funded by the U.S. Air Force Office of Scientific Research under Science and Technology Transfer Research (STTR) grants F49620-97-1-0427 and F49620-98-C-0050. Microstructural and crystallographic characterization was performed in part using equipment in the Center for Microanalysis of Materials (in the Materials Research Laboratory) and in the Center for Cement Composite Materials, both located at the University of Illinois at Urbana-Champaign.

References

1. Kriven, W. M.; Pask, J. A., Solid solution range and microstructures of melt-grown mullite, *J. Am. Ceram. Soc.*, **66** [9] 649-654 (1983).
2. Prochazka, S.; Klug, F. J., Infrared-transparent mullite ceramic, *J. Am. Ceram. Soc.*, **66** [12] 874-880 (1983).
3. Okada, K.; Otsuka, N., Change in chemical compostion of mullite formed from $2SiO_2 \cdot 3Al_2O_3$ xerogel during the formation process, *J. Am. Ceram. Soc.*, **70** [10] C245-C247 (1987).
4. Cameron, W. E., Composition and cell dimensions of mullite, *Am. Cer. Soc. Bull.*, **56** [11] 1003-1011 (1977).
5. Ban, T.; Okada, K., Structure refinement of mullite by the Rietveld method and a new method for estimation of chemical composition, *J. Am. Ceram. Soc.*, **75** [1] 227-30 (1992).
6. Fischer, R. X.; Schneider, H.; Schmucker, M., Crystal structure of Al-rich mullite, *Am. Mineral.*, **79** [9-10] 983-990 (1994).
7. Fischer, R. X.; Schneider, H.; Voll, D., Formation of aluminum rich 9:1 mullite and its transformation to low alumina mullite upon heating, *J. Eur. Cer. Soc.*, **16** 109-13 (1996).
8. Rahman, S. H., Crystal chemistry of mullite; pp. 5-82 in *Mullite and Mullite Ceramics,* Edited by H. Schneider; K. Okada and J. Pask. John Wiley and Sons, New York, 1994.
9. Angel, R. J.; McMullan, R. K.; Prewitt, C. T., Substructure and superstructure of mullite by neutron diffraction, *Am. Mineral.*, **76** 332-342 (1991).
10. Angel, R. J.; Prewitt, C. T., Crystal structure of mullite: A re-examination of the average structure, *Am. Mineral.*, **71** 1476-1482 (1986).
11. Angel, R. J.; Prewitt, C. T., The incomensurate structure of mullite by Patterson synthesis, *Acta Cryst.*, **B43** 116-125 (1987).
12. Wang, Y.; Thomson, W. J., Mullite formation from nonstoichiometric slow hydrolyzed single phase gels, *J. Mater. Res.*, **10** [4] 912-917 (1995).

13. Osaka, J., Tetragonal mullite-like phase from co-precipitated gels, *Nature,* **191** 1000-1001 (1961).
14. Li, D. X.; Thomson, W. J., Tetragonal to orthorhombic transformation during mullite formation, *J. Mater. Res.,* **6** [4] 819-824 (1991).
15. Schneider, H.; Rymon-Lipinski, T., Occurrence of pseudotetragonal mullite, *J. Am. Ceram. Soc.,* **71** [3] C162-C164 (1988).
16. Schneider, H.; Fischer, R. X.; Voll, D., Mullite with lattice constants a>b, *J. Am. Ceram. Soc.,* **76** [7] 1879-81 (1993).
17. Petry, M. D.; Tai-Il, M., Effect of thermal exposures on the strengths of Nextel™ 550 and 720 filaments, *J. Am. Ceram. Soc.,* **82** [10] 2801-7 (1999).
18. Okada, K.; Hoshi, Y.; Otsuka, N., Formation reaction of mullite from SiO_2-Al_2O_3 xerogels, *J. Mater. Sci. Lett.,* **5** [12] 1316-1318 (1986).
19. Ban, T.; Okada, K., Analysis of local cation arrangement in mullite using ^{29}Si magic-angle spinning nuclear magnetic resonance spectra, *J. Am. Ceram. Soc.,* **76** [10] 2491-2496 (1993).
20. Tkalcec, E.; Nass, R.; Schmauch, J.; Schmidt, H.; Kurajica, S.; Bezjak, A.; Ivankovic, H., Crystallization kinetics of mullite from single-phase gel determined by isothermal differential scanning calorimetry, *J. Non-Cryst. Solids,* **223** 57-72 (1998).
21. Wei, W.-C.; Halloran, J. W., Phase transformation of diphasic aluminosilicate gels, *J. Am. Ceram. Soc.,* **71** [3] 166-172 (1988).
22. Wei, W.-C.; Halloran, J. W., Transformation kinetics of diphasic aluminosilicate gels, *J. Am. Ceram. Soc.,* **71** [7] 581-587 (1988).
23. Boccaccini, A. R.; Khalil, T. K.; Bucker, M., Activation energy for the mullitization of a diphasic gel obtained from fumed silica and boehmite sol, *Mater. Lett.,* **38** [2] 116-20 (1999).
24. Okada, K.; Otsuka, N.; Osaka, J., Characterization of spinel phase formed in the kaolin-mullite thermal sequence, *J. Am. Ceram. Soc.,* **69** [10] C251-C253 (1986).
25. Okada, K.; Otsuka, N., Characterization of the spinel phase from SiO_2-Al_2O_3 xerogels and the formation process of mullite, *J. Am. Ceram. Soc.,* **69** [9] 652-6 (1986).
26. Hyatt, M. J.; Bansal, N. P., Phase transformations in xerogels of mullite composition, *J. Mater. Sci.,* **25** [6] 2815-2821 (1990).
27. Chakraborty, A. K., Formation of silicon-aluminum spinel, *J. Am. Ceram. Soc.,* **62** [3-4] 120-124 (1979).
28. Chakraborty, A. K., Intermediate Si-Al spinel phase formation in phase transformation of diphasic mullite gel, *J. Mater. Sci.,* **28** [14] 3839-44 (1993).
29. Sujeong, L.; Youn Joong, K.; Hi-Soo, M., Phase transformation sequence from kaolinite to mullite investigated by an energy-filtering transmission electron microscope, *J. Am. Ceram. Soc.,* **82** [10] 2841-8 (1999).
30. Ban, T.; Hayashi, S.; Yasumori, A.; Okada, K., Characterization of low temperature mullitization, *J. Eur. Cer. Soc.,* **16** 127-132 (1996).
31. Zhu, D.; Jilavi, M. H.; Kriven, W. M., Synthesis and characterization of mullite and YAG fibers grown from deeply undercooled melts, *Proceedings of the 1997 21st 1997 21st Annual*

Conference on Composites, Advanced Ceramics, Materials, and Structures-A. Cocoa Beach, FL, USA. 19970112-19970116. Conference Code: 46907., **18** [3] 31-38 (1997).

32. Kriven, W. M.; Jilavi, M. H.; Zhu, D.; Weber, J. K. R.; Cho, B.; Felten, J.; Nordine, P. C., Synthesis and microstructure of mullite fibers grown from deeply undercooled melts; pp. 169-176 in *Ceramic Microstructures: Control at the Atomic Level,* Proceedings of the International Materials Symposium on Ceramic Microstructures '96: Control at the Atomic Level, Edited by A. P. Tomsia and A. M. Glaeser. Plenum Press, New York, 1998.
33. Weber, J. K. R.; Cho, B.; Hixson, A. D.; Abadie, J. G.; Nordine, P. C.; Kriven, W. M.; Johnson, B. R.; Zhu, D., Growth and crystallization of YAG- and mullite-composition glass fibers, *J. Eur. Cer. Soc.,* **19** [13-14] 2543-2550 (1999).
34. Weber, J. K. R.; Felten, J. J.; Nordine, P. C., New method of high purity ceramic synthesis, *Rev. Sci. Inst.,* **78** 31-35 (1996).
35. Weber, J. K. R.; Anderson, C. D.; Krishnan, S.; Nordine, P. C., Solidification behavior of undercooled liquid aluminum oxide, *J. Am. Ceram. Soc.,* **78** 577-582 (1995).
36. Weber, J. K. R.; Hampton, S. S.; Merkley, D. R.; Rey, C. A.; Zatarski, M. M.; Nordine, P. C., Aero-acoustic levitation - a method for containerless liquid-phase processing at high temperatures, *Rev. Sci. Inst.,* **65** [456-465] (1994).
37. Weber, J. K. R.; Nordine, P. C., Containerless liquid-phase processing at high temperatures, *Microgravity Science and Technology,* **VII** 279-282 (1995).
38. Krishnan, S.; Felten, J. J.; Rix, J. E.; Weber, J. K. R., Levitation apparatus for structural studies of high temperature liquids using synchrotron radiation, *Rev. Sci. Inst.,* **68** 3512-18 (1997).
39. Benedict, J.; Anderson, R.; Klepeis, S. J., Recent developments in the use of the tripod polisher for TEM specimen preparation; pp. 121-141 in *Specimen Preparation for Transmission Electron Microscopy of Materials III*, Materials Research Society Symposium Proceedings, Vol. 254. Edited by R. Anderson; B. Tracy and J. Bravman. Materials Research Society, Pittsburgh, PA, 1992.
40. Klepeis, S. J.; Benedict, J. P.; Anderson, R. M., A grinding/polishing tool for TEM sample preparation; pp. 179-184 in *Specimen Preparation for Transmission Electron Microscopy of Materials*, Materials Research Soceity Symposium Proceedings, Vol. 115. Edited by J. C. Bravman; R. M. Anderson and M. L. McDonald. Materials Research Society, Pittsburgh, PA, 1988.
41. Williams, D. B.; Carter, C. B., *Transmission Electron Microscopy a Textbook for Materials Science,* Plenum Press, New York, 1996.
42. Bright, D. S., Program: *Maclispix,* v. 2-99, National Insitute of Standards, Gaithersburg, MD, 1999.
43. Vischer, N., Program: *Object-image,* v. 2.06, University of Amsterdam, Amsterdam, Netherlands, 2000.
44. Bansal, N. P.; Doremus, R. H., Determination of reaction kinetic parameters from variable temperature DSC or DTA, *J. Therm. Anal.,* **29** 115-119 (1984).

45. Bansal, N. P.; Doremus, R. H.; Bruce, A. J.; Moynihan, C. T., Kinetics of crystallization of ZrF_4-BaF_2-LaF_3 glass by differential scanning calorimetry, *J. Am. Ceram. Soc.*, **66** [4] 233-238 (1983).

46. Bansal, N. P.; Hyatt, M. J., Crystallization kinetics of BaO-Al_2O_3-SiO_2 glasses, *J. Mater. Res.*, **4** [5] 1257-1265 (1989).

47. Ray, C. S.; Ray, D. E., Nucleation and crystallization in glasses as determined by DTA; pp. 207-233 in *Nucleation and Crystallization in Liquids and Glasses*, Ceramic Transactions, Vol. 30. Edited by M. C. Weinberg. The American Ceramic Society, Westerville, Ohio, 1993.

48. Cheng, K., Determining crystallization kinetic parameters of Li_2O-Al_2O_3-SiO_2 glass from derivative differential thermal analysis curves, *Mater. Sci. Eng. B.*, **60** [3] 194-199 (1999).

49. Kissinger, H. E., Variation of peak temperature with heating rate in differential thermal analysis, *J. Res. Nat. Bur. Stand.*, **57** [4] 217-221 (1956).

50. Augis, J. A.; Bennet, J. D., Calculation of the Avrami parameters for heterogeneous solid state reactions using a modification of the Kissinger method, *J. Therm. Anal.*, **13** [2] 283-293 (1978).

51. Porter, D. A.; Easterling, K. E., *Phase Transformations in Metals and Alloys,* Chapman and Hall, New York, 1992.

52. Li, D. X.; Thomson, W. J., Kinetic mechanisms for mullite formation from sol-gel precursors, *J. Mater. Res.*, **5** [9] 1963-1969 (1990).

53. Takei, T.; Kameshima, Y.; Yasumori, A.; Okada, K., Crystallization kinetics of mullite in alumina-silica glass fibers, *J. Am. Ceram. Soc.*, **82** [10] 2876-80 (1999).

54. MacDowell, J. F.; Beall, G. H., Immiscibility and crystallization in Al_2O_3-SiO_2 glasses, *J. Am. Ceram. Soc.*, **52** [1] 17-25 (1969).

55. Risbud, S. H.; Pask, J. A., Calculated thermodynamic data and metastable immiscibility in the system SiO_2-Al_2O_3, *J. Am. Ceram. Soc.*, **60** [9-10] 418-424 (1977).

56. Ban, T.; Hayashi, S.; Yasumori, A.; Okada, K., Calculation of metastable immiscibility region in the Al_2O_3-SiO_2 system, *J. Mater. Res.*, **11** [6] 1421-1427 (1996).

57. Takei, T.; Kameshima, Y.; Yasumori, A.; Okada, K., Calculation of metastable immiscibility region in the Al_2O_3-SiO_2 system using molecular dynamics simulation, *J. Mater. Res.*, **15** [1] 186-93 (2000).

58. Vlack, L. H. V., *Materials Science for Engineers,* Addison-Wesley Publishing Co., Reading, MA, 1970.

59. Li, D. X.; Thomson, W. J., Mullite formation kinetics of a single-phase gel, *J. Am. Ceram. Soc.*, **73** [4] 964-969 (1990).

60. Burnham, C. W., Crystal structure of mullite, *Carnegie Inst. Washington Yearbook,* **63** 223-227 (1964).

61. Burnham, C. W., Composition limits of mullite and the sillimanite-mullite solid solution problem, *Carnegie Inst. Washington Yearbook,* **63** [227-228] (1964).

62. Saalfeld, H.; Guse, W., Structure refinement of 3:2 mullite ($3Al_2O_3 \cdot 2SiO_2$), *Neues Jahrb. Mineral. Monatsh,* 145-150 (1981).

List of Tables

Table 1. The designation, thermal history, and description of specimens characterized by various techniques.

Table 2. Variation of crystallization temperature, T_p, with annealing temperature, T_N, for crystallization of quenched mullite composition glass beads.

Table 3. Kinetic data for the crystallization of quenched mullite composition beads from non-isothermal DSC studies.

Table 4. Particle size measurements for quenched mullite composition specimens after various thermal treatments.

Table 5. Wyckoff positions, coordinates and names[10] of the atom sites of the "average" mullite structure, space group Pbam (no.55).

Table 6. Results of Rietveld refinements, space group P b a m

Table 7. Al_2O_3 contents as derived from various indicators: cell dimensions a, b, and c, density Dx, ratio of the integrated intensities of 220 and 111 reflections, Rietveld refined "mullite x" and microprobe (μ--probe).

Table 8. Quantitative 3 phase analysis of specimen M1

List of Figures

Figure 1. Kissinger plot ($\ln(T_p^2/\alpha)$ *vs.* $1/T_p$) for non-isothermal crystallization of quenched mullite beads. Note that there were two different crystallization regimes with a break in the heating rate between 3.0° and 4.0°C/min.

Figure 2. Plot of the DSC exotherms for non-isothermal crystallization of quenched mullite composition glass, at heating rates of 3.0° and 4.0°C/min. Note the asymmetry in both curves, indicating two different exothermic events, and the shift in prominence of the two different events.

Figure 3. TEM BF image (A) and STEM BF image (B) of a polished thin section from an as-received, quenched, mullite composition bead (specimen Q). The contrast variations in (A) were typical of phase-separated, amorphous materials. The overall composition for the field of view in (B) was 75.8 mol% Al_2O_3 and 24.2 mol% SiO_2, as determined by STEM EDS. The graph in (B) shows the variation in the Al/Si Kα ratio from an EDS line scan through the central dark region in the sample. An Al/Si Kα ratio of 2.8 corresponds to 3:2 mullite (60 mol% alumina).

Figure 4. TEM BF images of an amorphous mullite fiber annealed at 920°C for 3h (specimen N). The inset image in (A) is an SAD pattern taken from the crystallites along the edge. The pattern was indexed as the pseudotetragonal metric of mullite. The lattice spacing of the crystallite in (B) was 3.38 Å, which corresponded to the (120)/(210) lattice planes of mullite (3.428 Å, and 3.390 Å, respectively).

Figure 5. TEM BF micrograph of a crushed, quenched, mullite composition bead that was isothermally crystallized at 938°C for 2.5h (specimen M1).

Figure 6. TEM BF (A) and DF (B) micrographs of a ground sample from a quenched mullite composition bead that was isothermally crystallized in a DSC at 938°C for 2.5 h (specimen M1). The darker, matrix region in the BF image (A) appeared as the bright region in the DF image (B), and the light, circular inclusions observed in the BF image appeared dark in the DF image.

Figure 7. TEM BF images (A and B) from a polished thin section of a quenched mullite composition bead heated to 1085°C (specimen M1.5). EDS analyses were made at the points labeled alphabetically, and the composition at each point was 60±1 mol% Al_2O_3, 40±1 mol% SiO_2. The variegated diffraction contrast in the grains was due to lattice strain. Higher magnification of one of the grains (B) revealed small inclusions with and average size of 9.4 x 7.9 nm. The SAD pattern in (B) was taken from the [001] zone axis of a similar grain in the specimen.

Figure 8. STEM BF micrograph of a quenched mullite bead heated to 1085°C (specimen M1.5). The horizontal line in the center of the micrograph was due to beam damage of the specimen

during EDS line profile analysis. The inset graph shows the variation in the Al/Si Kα ratio over the region scanned. This was an indication of chemical inhomogeneity at very small length scales.

Figure 9. TEM bright field image of quenched mullite composition powder after being heated up to 1200°C (specimen M2). The inset image is a Kossel-Möllenstedt microdiffraction pattern for the designated crystal oriented along the [120] zone axis.

Figure 10. TEM bright field image of quenched mullite composition powder after being heated up to 1400°C (specimen M3).

Figure 11. TEM CDF micrograph (A) and corresponding moiré pattern (B) from a crushed, quenched mullite composition bead isothermally crystallized at 938°C for 2.5 h (M1). The micrograph was taken from an area of two overlapping crystals using the (220) reflection from one and the (230) reflection from the other (SAD inset, A). The overlapping lattice fringes from the two crystals created the observed moiré pattern (dark wavy lines). B is a filtered Fourier image of A showing the moiré pattern in greater detail. The inset in B is the fast Fourier transform (FFT) of A. The average fringe spacing in B was 8.56Å; the computed fringe spacing from the SAD pattern was 8.62Å. The distortion in the moiré pattern was an indication of strain in the two crystals, and was spatially correlated to the embedded inclusions in A (bright areas).

Figure 12. Combined, normalized XRD spectra for quenched mullite composition glass beads, before and after crystallization in a DTA. The crystalline pattern belongs to mullite, and verifies that the exothermic events observed by DTA/DSC were due to crystallization of mullite.

Figure 13. Idealized structure of sillimanite (A) and mullite (B) projected along the a-b plane.

Figure 14. Line widths, full width at half maximum, (FWHM) obtained from single phase Rietveld refinements of synchrotron XRD spectra for specimens M1, M2, M3, M4 and from a Si powder standard (SRM 640b, NIST).

Figure 15. Positioning of the refined a and c cell dimensions for specimens M1, M2, M3 and M4 on an orthorhombic - pseudotetragonal mullite diagram.

Figure 16. Detailed sections of measured powder diagrams around the well separated 002 reflection for various spectra.
16a) sample M1: observed data (dots), single phase Rietveld refinement (dashes), 3-phase Rietveld refinement (line)
16b) comparison of data from partly crystallized samples M1, M2 with those of the well crystallized specimen M3.

Tables

Table 1.

The designation, thermal history, and description of specimens characterized by various techniques.

Symbol	Thermal History	Analyses	Form	Details
Q	Quenched glass	DSC, TEM, XRD	Powder, thin film	Glass beads received from CRI.
N	10°C/min, to 920°C, 3h	DSC, TEM	Powder, fiber	Highest annealing temperature observed in DSC without crystallization exotherm.
M1	40°C/min to 938°C, 2.5h	DSC, TEM, Synchrotron.	Powder	Pseudotetragonal mullite formed at a low temperature.
M1.5	10°C/min to 1085°C, 0.5h	TEM	Thin film	Polished thin film specimen of psuedotetragonal mullite
M2	10°C/min to 900-930°C, 3h, various rates to 1200°C	TEM, XRD, Synchrotron	Powder	Pseudotetragonal mullite prior to transition to orthorhombic phase. Mixture of powders.
M3	10°C/min to 1400°C	TEM, Synchrotron	Powder	Orthorhombic phase.
M4	Kyoritsu KM101	XRD, Synchrotron	Powder	Source material.

Table 2.

Variation of crystallization temperature, T_p, with annealing temperature, T_N, for crystallization of quenched mullite composition glass beads.

Nucleation Temp, T_N	**Crystallization Temperature, T_p**
10°C/min Ramp	984.6°C
850°C/3hr	985.5°C
890°C/3hr	984.6°C
900°C/3hr	986.0°C
910°C/3hr	985.9°C
920°C/3hr	987.2°C
930°C/3hr	-
940°C/3hr	-

Table 3.
Kinetic data for the crystallization of quenched mullite composition beads from non-isothermal DSC studies.

α (°C/min)	T_p (°C)	n
0.5	944.160	2.2
1.0	955.500	2.4
1.5	959.400	2.3
2.0	964.770	2.1
3.0	970.700	2.2
4.0	977.200	2.8
5.0	979.400	3.6
6.0	980.300	3.1
8.0	983.400	7.5
10.0	986.100	16.9
E_1 (KJ/mole)	**836.92**	
E_2 (KJ/mole)	**1,337.52**	
ν_1 (s^{-1})	**4.535E+32**	
ν_2 (s^{-1})	**5.266E+53**	

Table 4.

Particle size measurements for quenched mullite composition specimens after various thermal treatments.

Specimen	Major Axis (nm)	Minor Axis (nm)	Ave. Diam. (nm)	Ave. Area (nm^2)	No. of Measurements
N (crystallites)	13.4 ± 2.9	11.5 ± 2.7	12.6 ± 7.9 nm	123.8 ± 49.3	150
M1 (inclusions)	10.0 ± 2.2	7.8 ± 1.9	9.0 ± 5.6 nm	63.0 ± 24.8	150
M1 (grains)*	~ 370	~ 260	-	9.6E+04	40
M1.5 (inclusions)	9.4 ± 2.5	7.9 ± 2	8.8 ± 6.4 nm	61.4 ± 32	150
M1.5 (grains)*	~ 510	~ 380	-	.2.03E+05	50
M2 (inclusions)	7.9 ± 1.7	6.6 ± 1.5	7.3 ± 4.7 nm	42.2 ± 17.43	150
M2 (grains)*	~ 270	~ 190	-	5.2E+04	135
M3 (grains)	100 ± 55	69 ± 38	-	7.68E+03	60

* Broad size distribution

Table 5.
Wyckoff positions, coordinates and names[10] of the atom sites of the "average" mullite structure, space group Pbam (no.55).

Atoms	Al_2	$[Al_2\ Si_{2-2x}]$	Al_{2x}	O_{2-3x}	O_{2x}	O_4	O_4
Wyckoff positions	2a	4h	4h	2d	4h	4h	4g
Coordinates	0, 0, 0	x, y, _	x, y, _	_, 0, _	x, y, _	x, y, _	x, y, 0
Names [10]	Al	T(Si/Al)	T*(Al*)	O_c	O_c*	O_{ab}	O_d

Table 6.
Refined parameters of the 4 mullite samples, and a reference. Space group Pbam.

Sample	M1	M2	M3	M4	Saalfeld & Guse[62]
a [nm]	0.7616(2)	0.7606(1)	0.75454(2)	0.75499(3)	0.7553(1)
b [nm]	0.7678(2)	0.7682(1)	0.76956(2)	0.76883(3)	0.7686(1)
c [nm]	0.28891(4)	0.28871(4)	0.288398(6)	0.288379(9)	0.28864(7)
V [nm^3]	0.16897	0.16870	0.16746	0.16739	0.16756
Density [g/cm^3]	3.10	3.09	3.15	3.16	3.16
R_{WP}	0.049	0.049	0.051	0.032	
R_{Bragg}	0.060	0.063	0.049	0.025	0.027
X(Al)	0.	0.	0.	0.	0.
Y(Al)	0.	0.	0.	0.	0.
Z(Al)	0.	0.	0.	0.	0.
B(Al)	0.9(3)	1.0(3)	0.5(1)	0.5(1)	
Occ.(Al)	1.0	1.0	1.0	1.0	1.0
X(T)	0.148(2)	0.147(2)	0.1480(6)	0.1474(6)	0.1485
Y(T)	0.339(2)	0.340(1)	0.3412(6)	0.3410(6)	0.3411
Z(T)	0.5	0.5	0.5	0.5	0.5
B(T)	1.7(4)	0.8(3)	0.3(1)	0.3(1)	
Occ.(T), Al	0.5	0.5	0.5	0.5	0.5
Occ.(T), Si	0.25(2)	0.21(2)	0.332(7)	0.334(7)	0.363
X(T*)	0.275(4)	0.282(4)	0.275(3)	0.268(3)	0.2621
Y(T*)	0.195(4)	0.194(4)	0.209(2)	0.207(2)	0.2057
Z(T*)	0.5	0.5	0.5	0.5	0.5
B(T*)	0.1(4)	3(1)	1.7(8)	1.2(8)	
Occ. (T*), Al	0.25(2)	0.29(2)	0.168(7)	0.166(7)	0.137
X(Oab)	0.354(2)	0.349(1)	0.3567(6)	0.3566(6)	0.3579
Y(Oab)	0.423(2)	0.422(1)	0.4195(6)	0.4201(6)	0.4221
Z(Oab)	0.5	0.5	0.5	0.5	0.5
B(Oab)	0.2(2)	0.4(2)	0.8(1)	0.8(1)	
Occ.(Oab)	1.0	1.0	1.0	1.0	1.0
X(Od)	0.136(2)	0.133(1)	0.1270(9)	0.1263(9)	0.1265
Y(Od)	0.220(2)	0.222(1)	0.2219(8)	0.2216(8)	0.2201
Z(Od)	0.0	0.0	0.0	0.0	0.0
B(Od)	0.2(2)	0.4(2)	0.8(1)	0.8(1)	
Occ.(Od)	1.0	1.0	1.0	1.0	1.0
X(Oc)	0.5	0.5	0.5	0.5	0.5
Y(Oc)	0.0	0.0	0.0	0.0	0.0
Z(Oc)	0.5	0.5	0.5	0.5	0.5
B(Oc)	0.2(2)	0.4(2)	0.8(1)	0.8(1)	
Occ.(Oc)	0.26(1)	0.58(3)	0.49(1)	0.50(1)	0.590
X(Oc*)	0.442(8)	0.457(6)	0.453(5)	0.451(5)	0.4507
Y(Oc*)	0.039(9)	0.029(8)	0.049(5)	0.048(5)	0.0518
Z(Oc*)	0.5	0.5	0.5	0.5	0.5
B(Oc*)	0.2(2)	0.4(2)	0.8(1)	0.8(1)	
Occ.(Oc*)	0.25(1)	0.29(2)	0.168(7)	0.166(7)	0.137
Mullite x	0.49(4)	0.58(3)	0.34(1)	0.33(1)	0.274

Table 7.
Al_2O_3 contents as derived from various indicators: cell dimensions a, b, and c, density Dx, ratio of the integrated intensities of 220 and 111 reflections, Rietveld refined "mullite x" and microprobe (μ--probe).

Specimen	M1	M2	M3	M4	S & G[62]
mole % (a)	70.9	69.5	60.7	61.4	61.8
mole % (b)	70.9	68.5	60.0	64.6	66.0
mole % (c)					
mole % (Dx)	70.8	72.3	62.8	61.8	61.8
mole % ($I_{220/111}$)	75.2	64.9	62.5	59.9	
mole % (mullite x)	71.4	75.4	63.8	63.6	61.0
mole % (μ-probe)					60.9

Table 8.
Quantitative 3 phase analysis of specimen M1.

Parameter	Phase A	Phase B	Phase C
a [nm]	0.7651	0.7611	0.7562
b [nm]	0.7659	0.7678	0.7692
c[nm]	0.2895	0.2887	0.2875
mole % Al_2O_3	76	70	< 60
weight fraction [%]	40	50	10

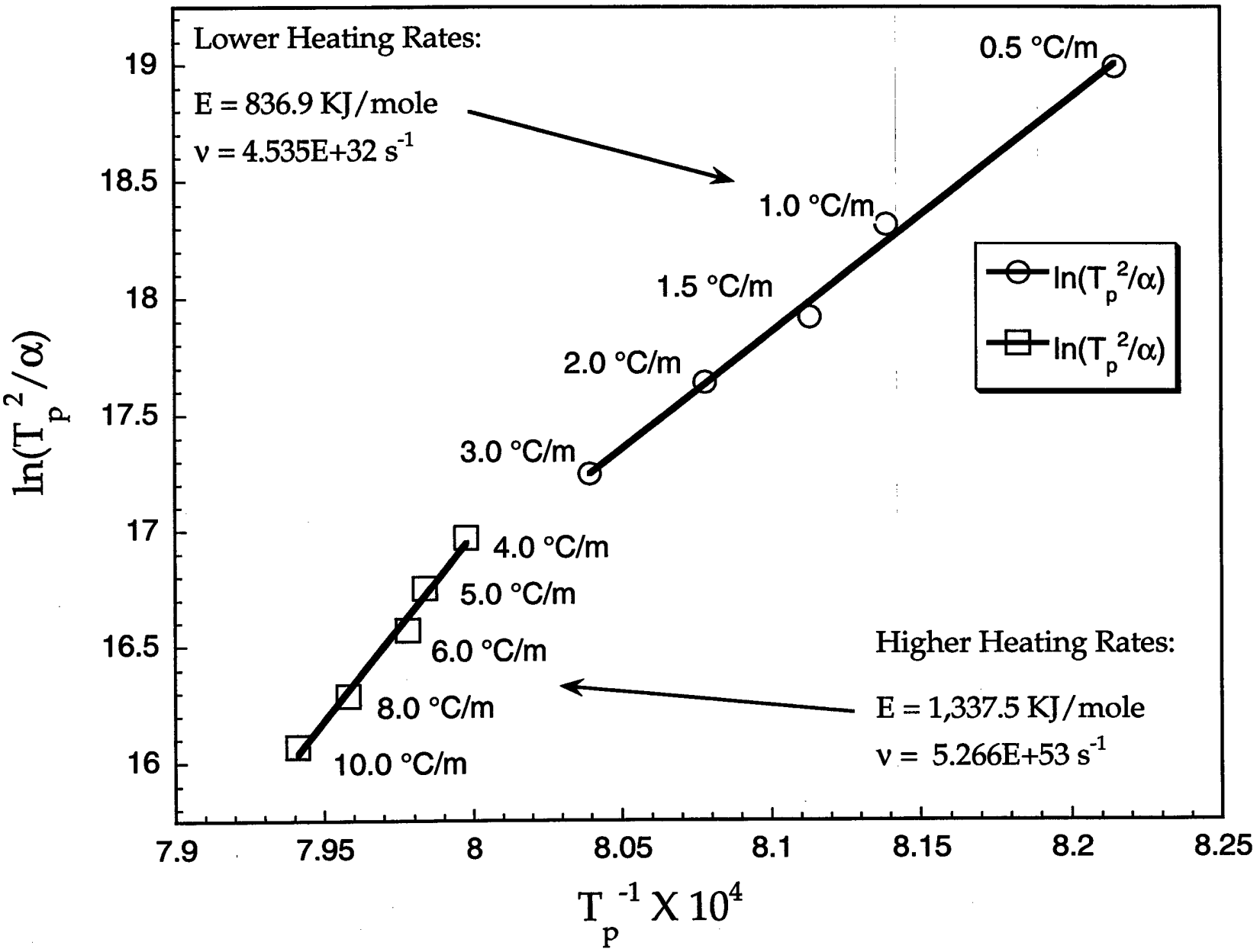


Figure 1. Kissinger plot (ln(Tp2/a) vs. 1/Tp) for non-isothermal crystallization of quenched mullite beads. Note that there were two different crystallization regimes with a break in the heating rate between 3.0° and 4.0°C/min.

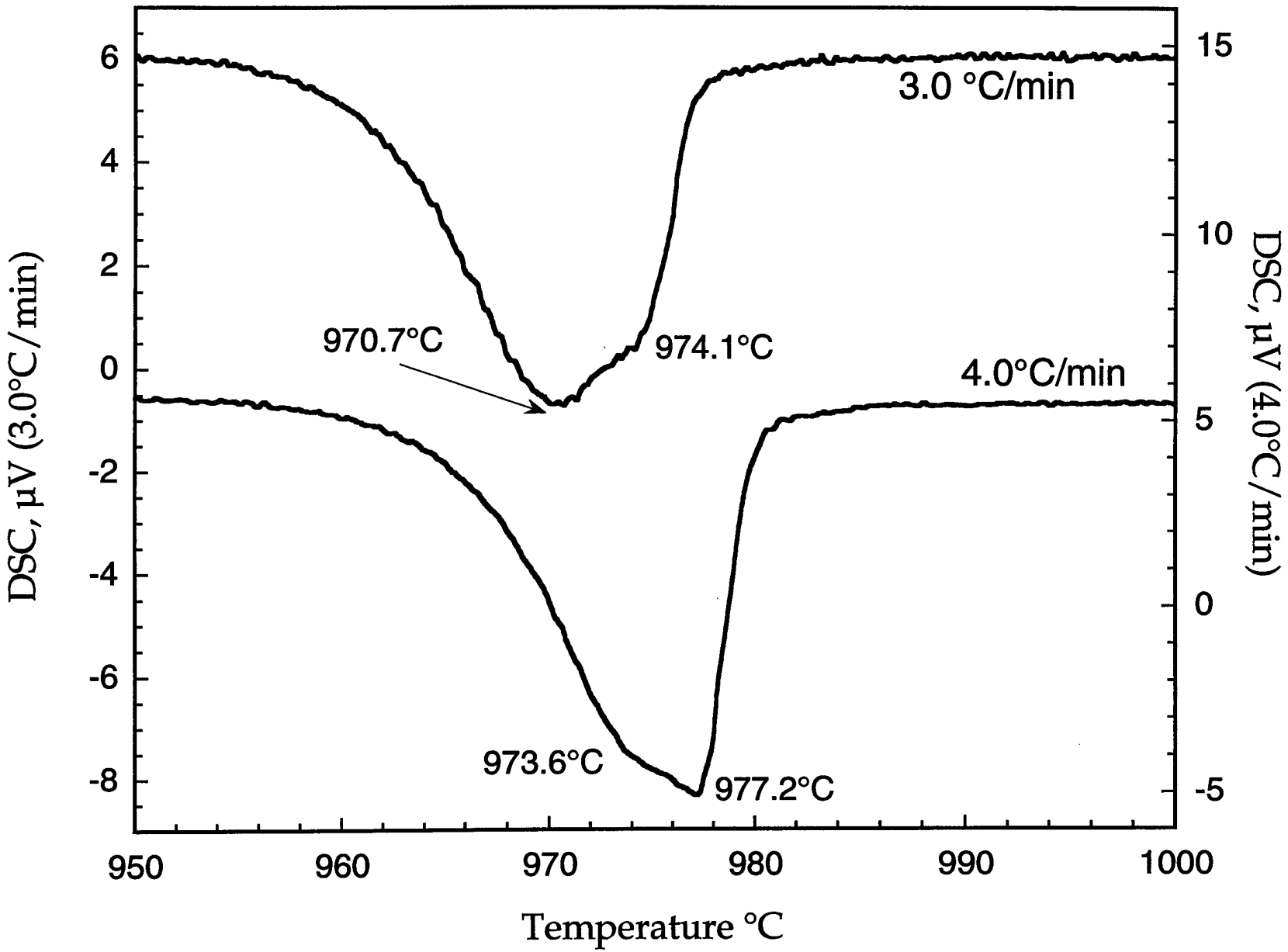


Figure 2. Plot of the DSC exotherms for non-isothermal crystallization of quenched mullite composition glass, at heating rates of 3.0° and 4.0°C/min. Note the asymmetry in both curves, indicating two different exothermic events, and the shift in prominence of the two different events.

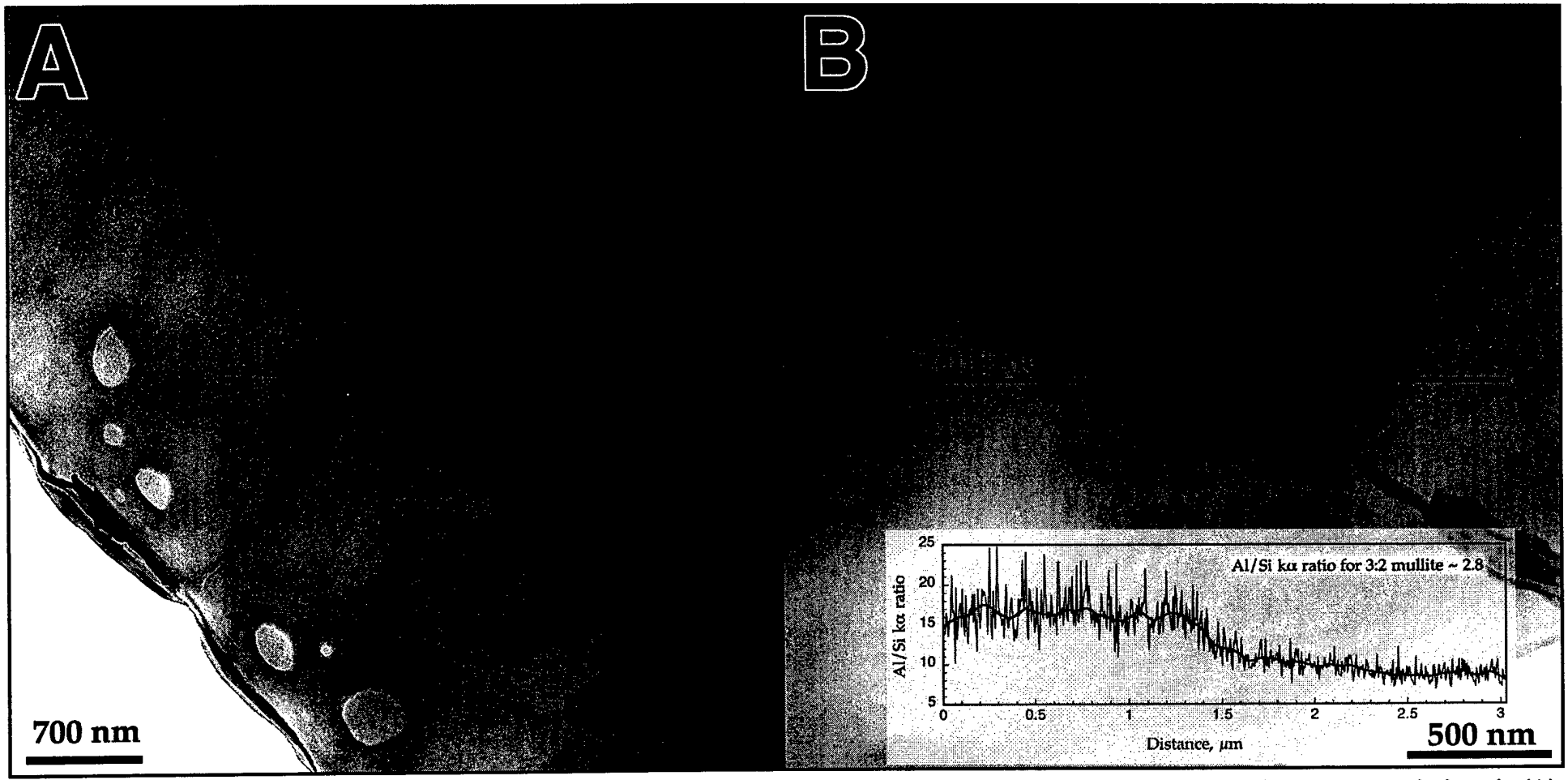


Figure 3. TEM BF image (A) and a STEM BF image (B) of a quenched mullite composition glass bead (specimen Q). The contrast variations in (A) were typical of phase separated, amorphous materials. The entire field of view in (B) had a composition of 75.8 mol% Al_2O_3 and 24.2 mol% SiO_2 as determined by STEM EDS. The graph in (B) shows the variation in Al/Si kα ratio from an EDS line scan through the central dark region in the sample. An Al/Si kα ratio of ~ 2.8 corresponds to 3:2 mullite (60 mole% alumina).

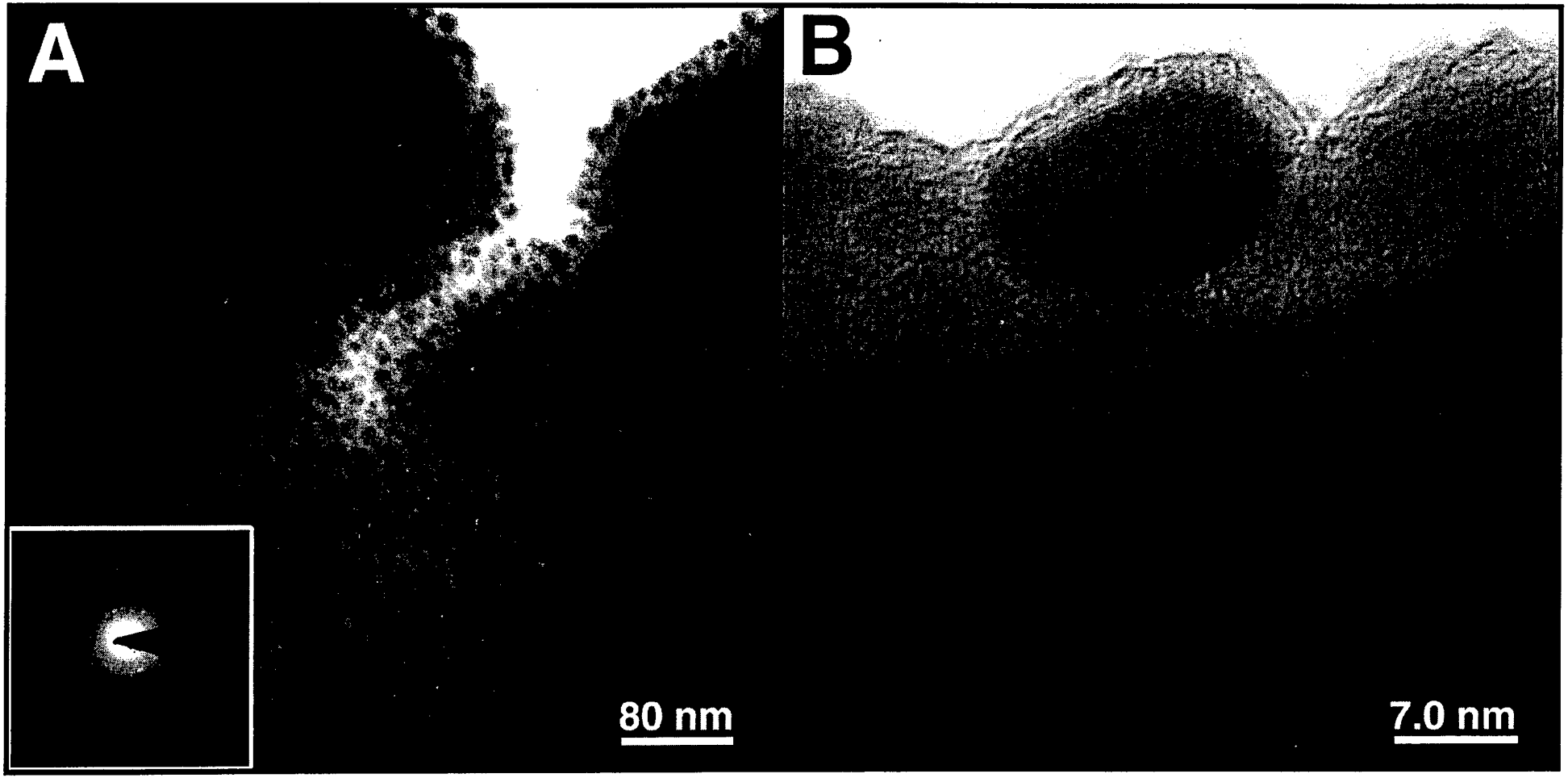


Figure 4. TEM BF images of an amorphous mullite fiber annealed at 920°C for 3h (speicmen N). The inset image in (A) is an SAD pattern taken from the crystallites along the edge. The pattern was indexed as the pseudotetragonal metric of mullite. The lattice spacing of the crystallite in (B) was3.38 Å, which corresponded to the (120)/(210) lattice planes of mullite (3.428 and 3.390 Å, respectively).

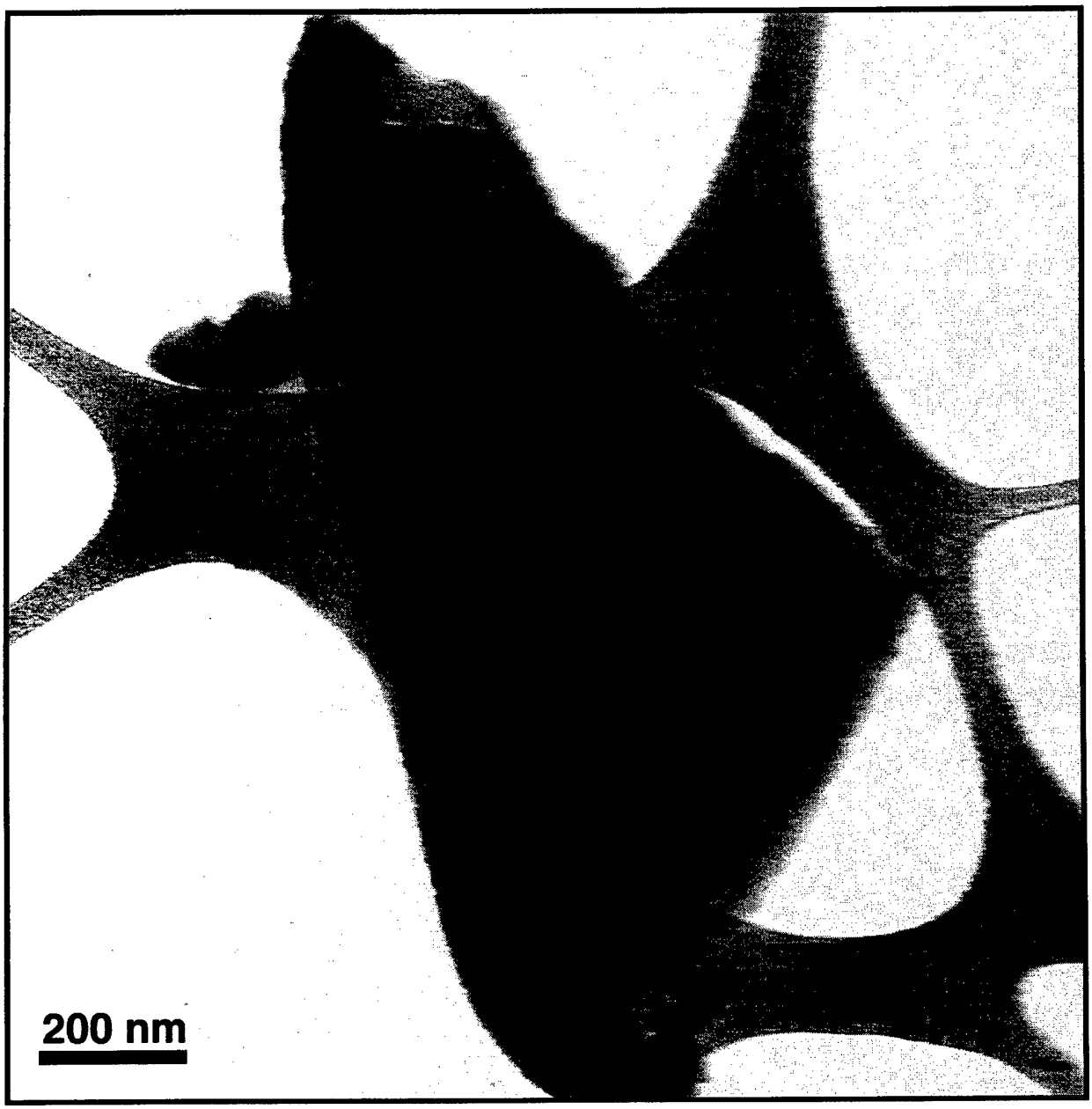


Figure 5. TEM BF micrograph of a crushed, quenched, mullite compositon bead that was isothermally crystallized at 938°C for 2.5h (specimen M1).

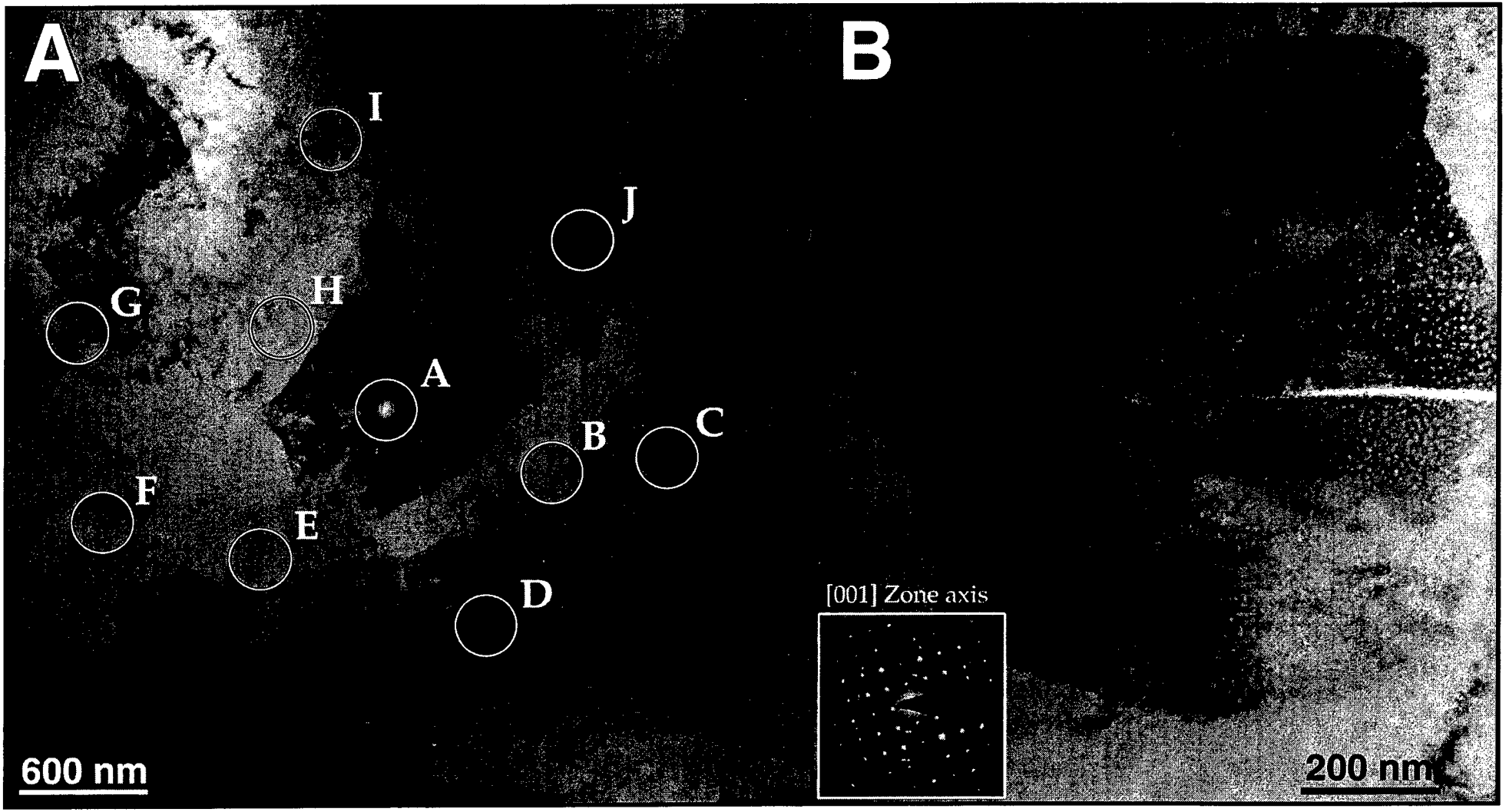


Figure 7. TEM BF images (A and B) from a polished thin section of a quenched mullite composition bead heated to 1085°C (speicmen M1.5). EDS analyses were made at the points labeled alphabetically, and the composition at each point was 60±1 mol% Al_2O_3, 40±1 mol% SiO_2. The variegated diffraction contrast in the grains was due to lattice strain. Higher magnification of one of the grains (B) revealed sm inclusions with and average size of 9.4 x 7.9 nm. The SAD pattern in (B) was from the [001] zone axis of a similar grain.



Figure 8. STEM bright field micrograph of a quenched mullite bead heated to 1085°C (specimen M1.5). The horizontal line in the center of the micrograph was due to beam damage of the specimen during EDS line profile analysis. The inset graph shows the variation in the Al/Si Ka ratio over the region scanned. This was an indication of chemical inhomogeneity at very small length scales.

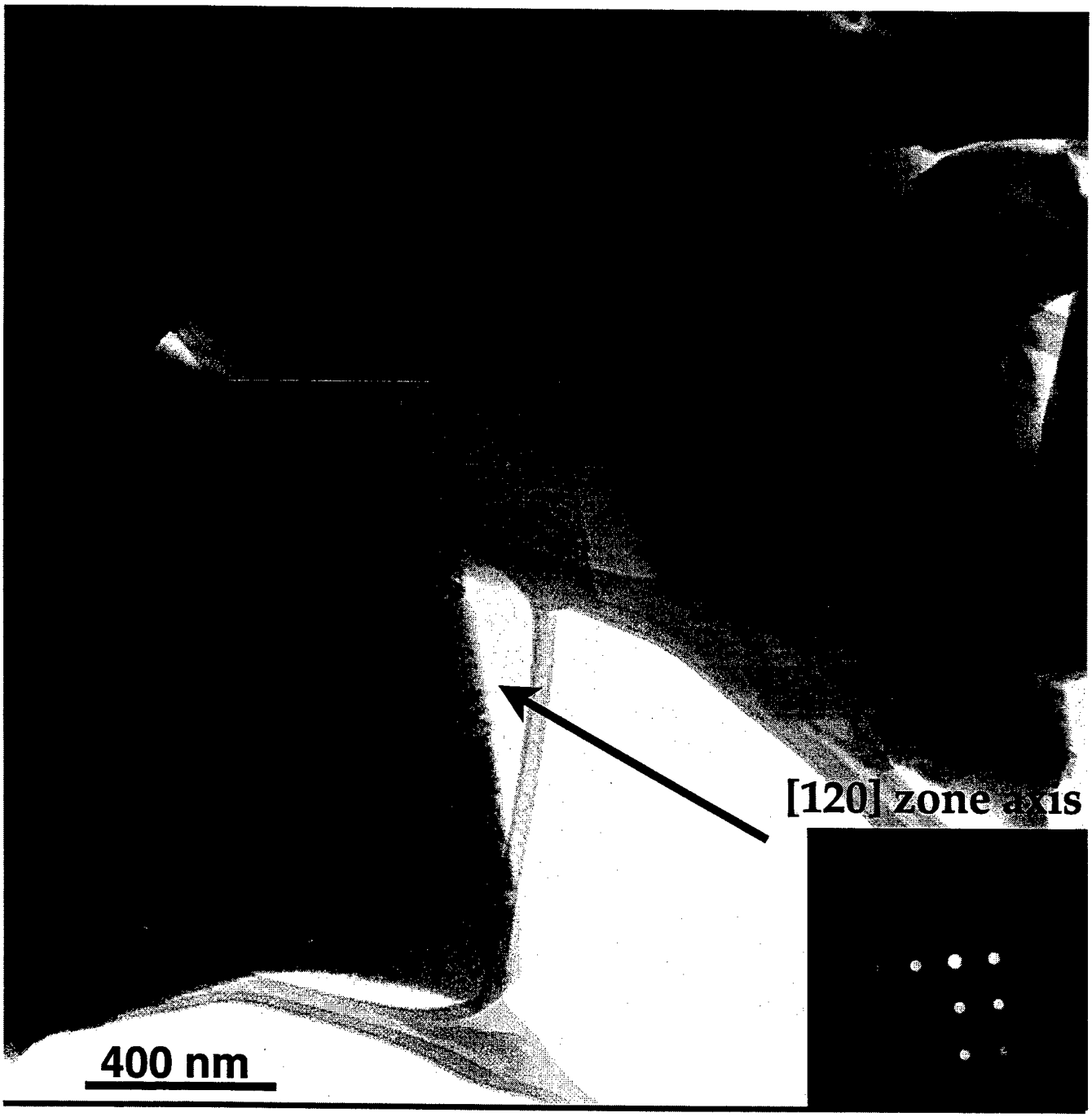


Figure 9. TEM bright field image of quenched mullite composition powder after being heated up to 1200°C (specimen M2). The inset image is a Kossel-Möllenstedt micro-diffraction pattern for the designated crystal oriented along the [120] zone axis.

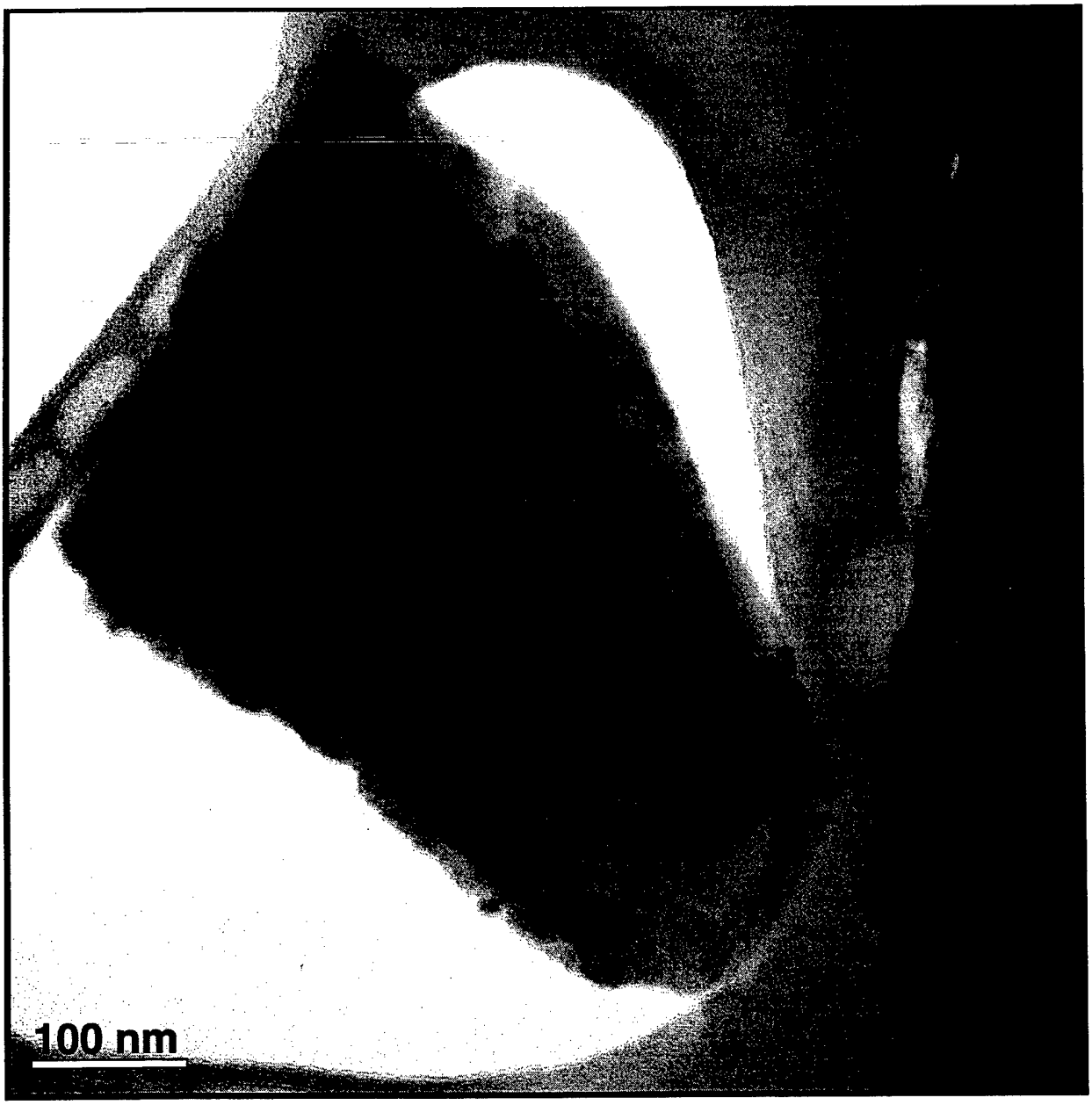


Figure 10. TEM bright field image of quenched mullite composition powder after being heated up to 1400°C (specimen M3).

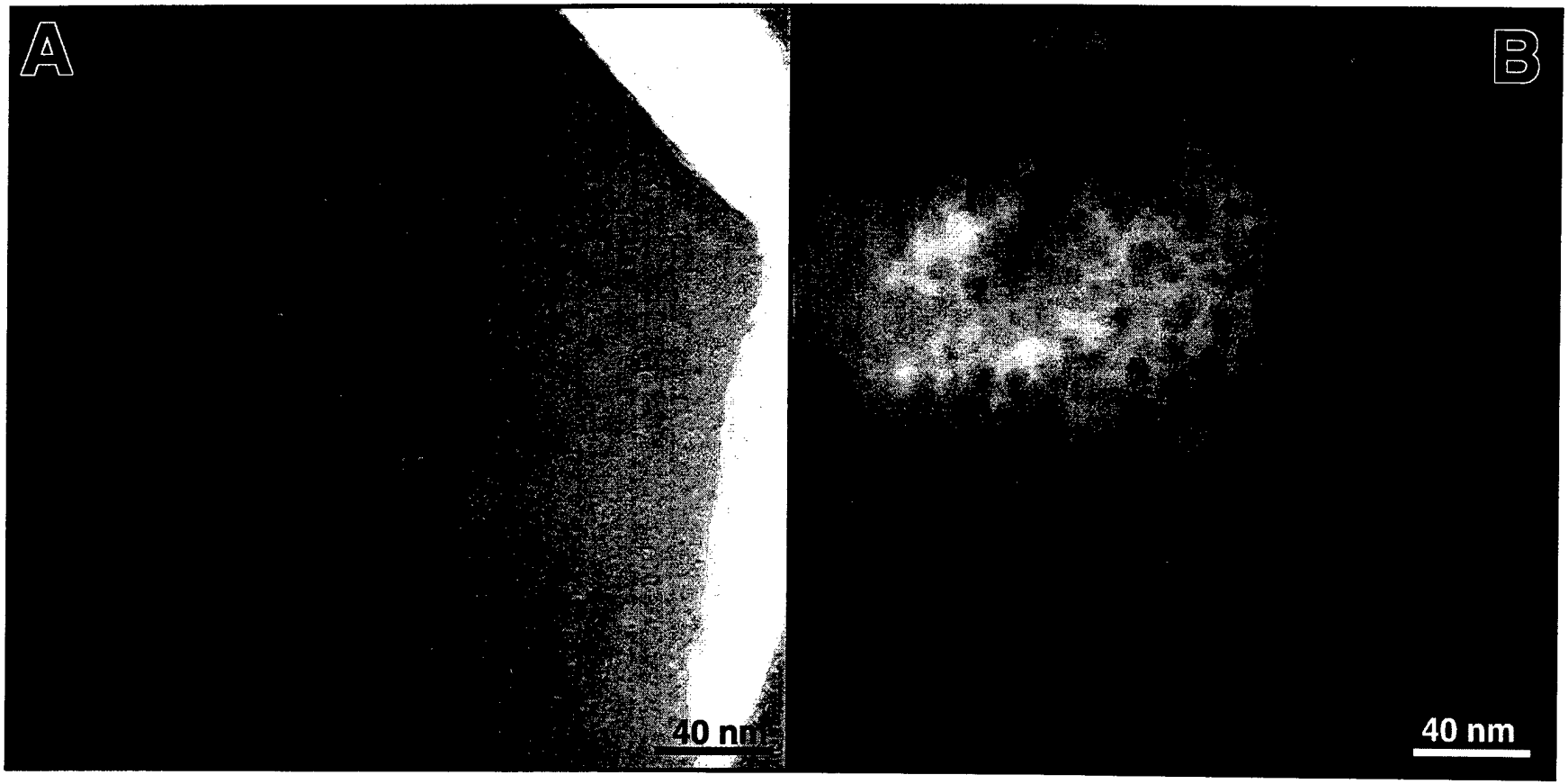


Figure 6. TEM BF (A) and DF (B) micrographs of a ground sample from a quenched mullite composition bead that was isothermally crystallized in a DSC at 938°C for 2.5 h (specimen M1). The darker, matrix region in the BF image (A) appeared as the bright region in the DF image (B), and the light, circular inclusions observed in the BF image appeared dark in the DF image.

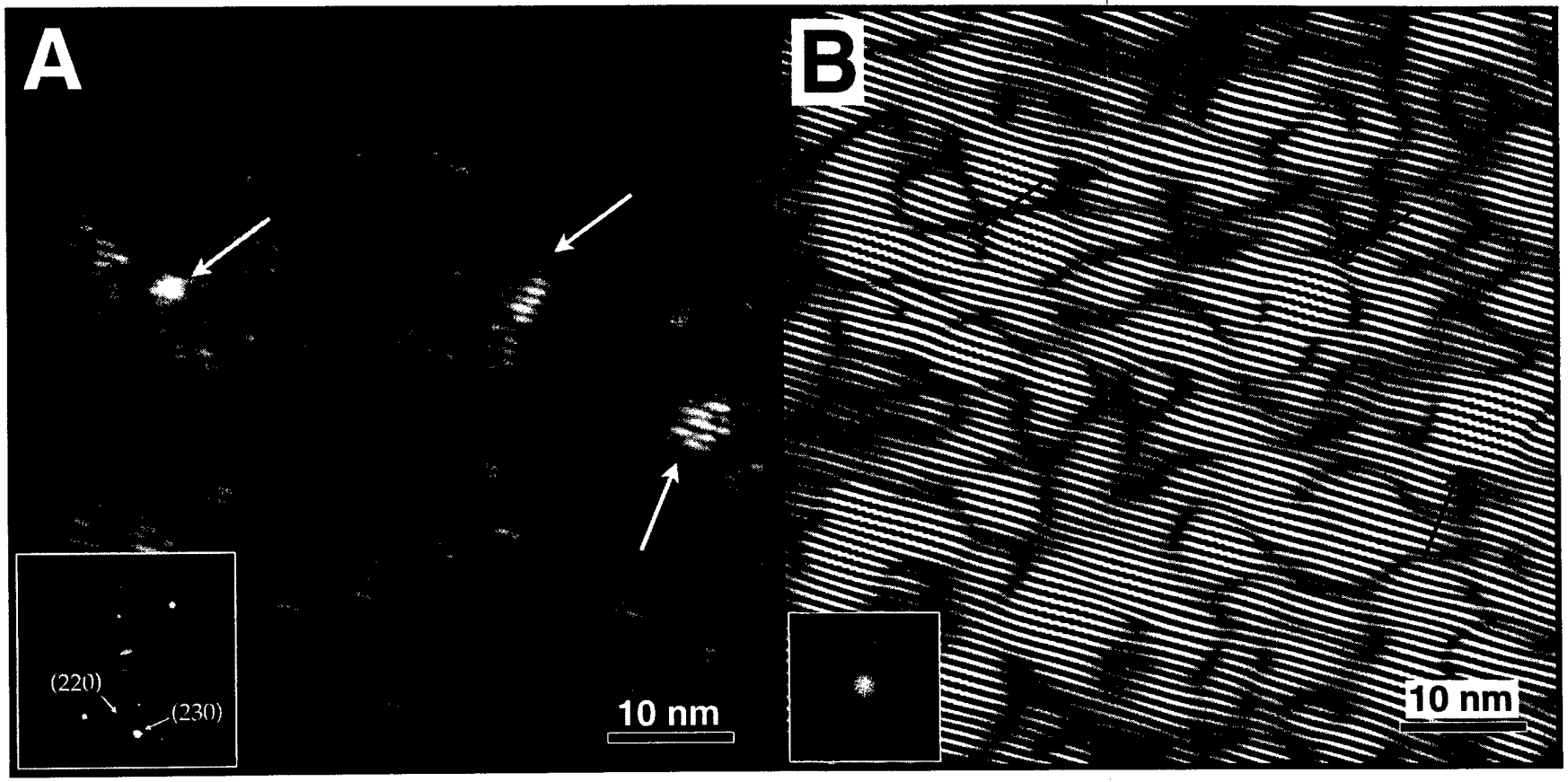


Figure 11. TEM CDF micrograph (A) and corresponding moiré pattern (B) from a crushed, quenched mullite composition bead isothermally crystallized at 938°C for 2.5 h (M1). The micrograph was taken from an area of two overalpping crystals using the (220) reflection from one and the (230) reflection from the other (SAD inset, A). The overlapping lattice fringes from the two crystals created the observed moiré pattern (dark wavy lines). B is a filtered Fourier image of A showing the moiré pattern in greater detail. The inset in B is the fast Fourier transform (FFT) of A. The average fringe spacing was 8.56Å. The distortion in the moiré pattern was an indication of strain in the two crystals, and was spatially correlated to the embedded inclusions in A (bright areas).

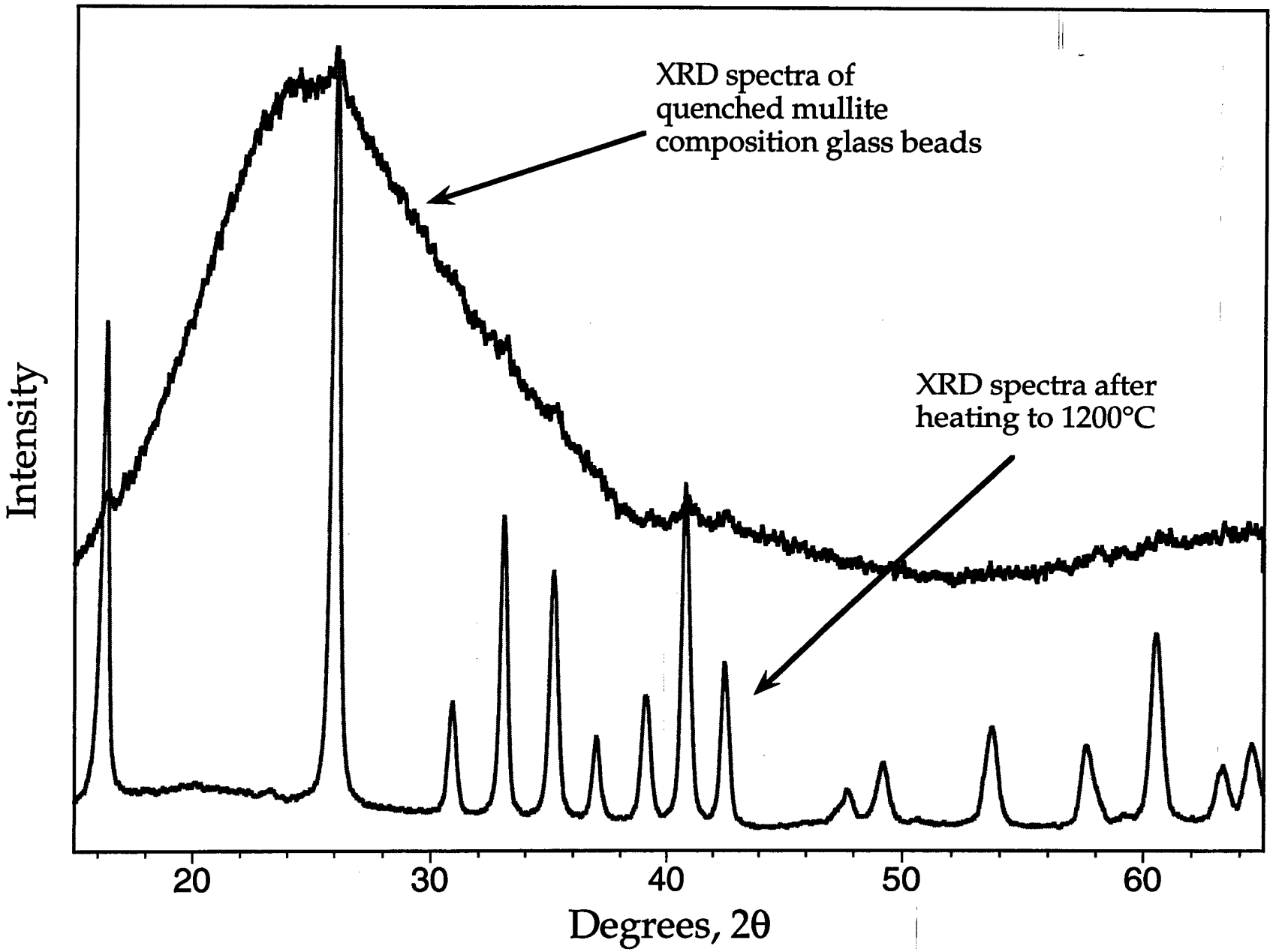


Figure 12. Combined, normalized XRD spectra for quenched mullite composition glass beads, before and after crystallization in a DTA. The crystalline pattern belongs to mullite, and verifies that the exothermic events observed by DTA/DSC were due to crystallization of mullite.

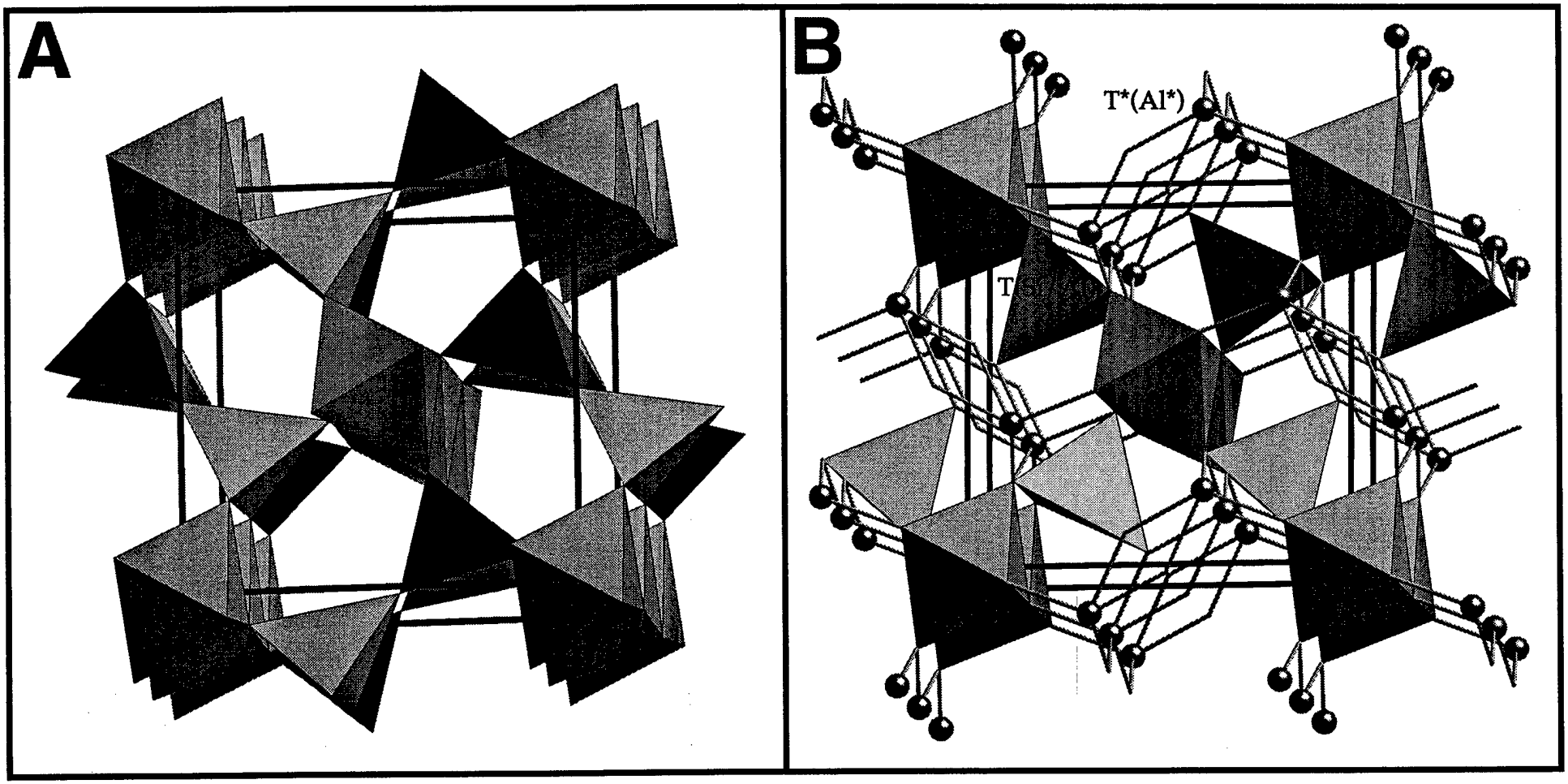


Figure 13. Idealized structure of sillimanite (A) and mullite (B) projected down the a-b plane.

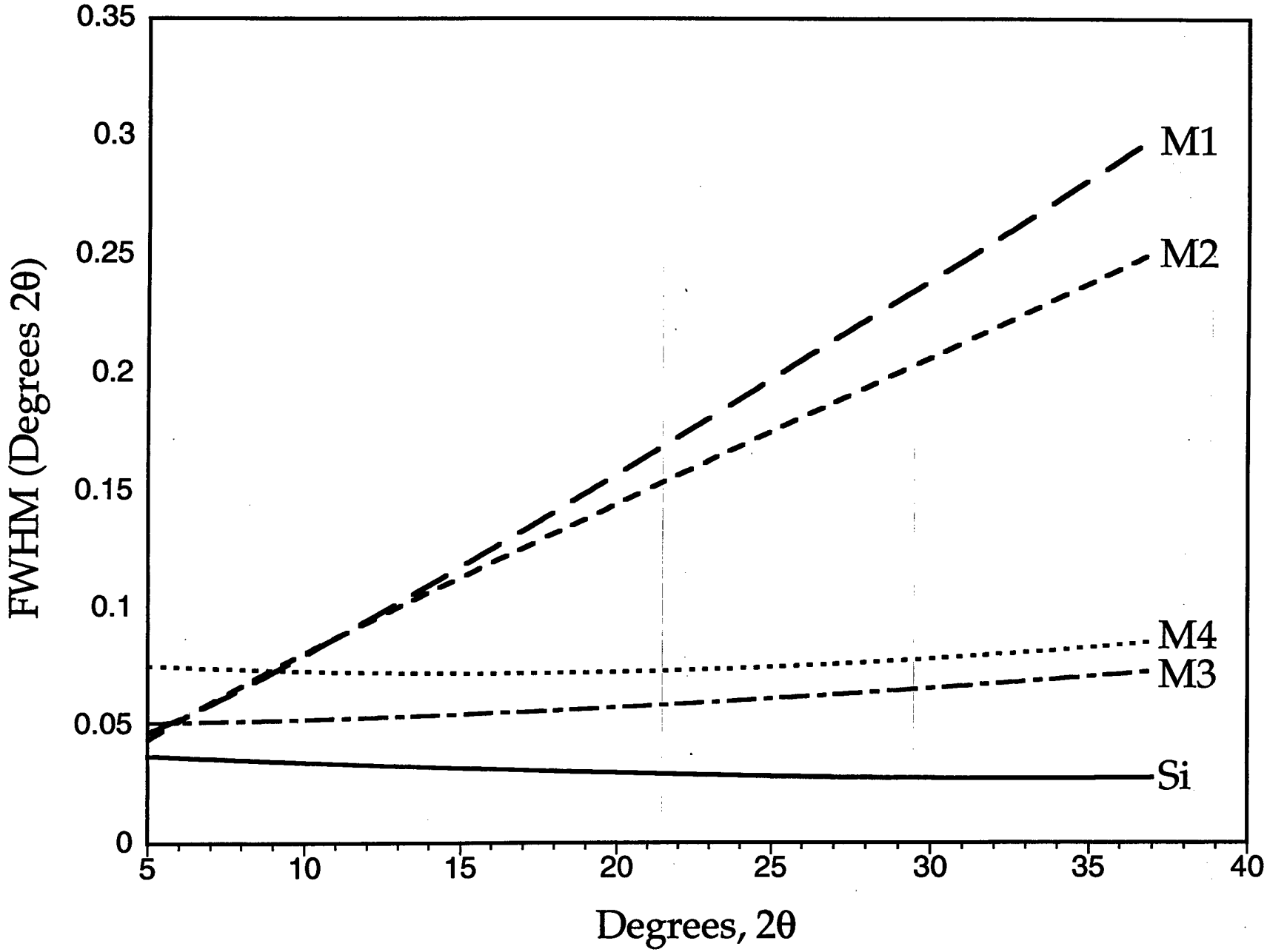


Figure 14. Line widths, full width at half maximum, (FWHM) obtained from single phase Rietveld refinements of synchrotron XRD spectra for specimens M1, M2, M3, M4 and from a Si powder standard (SRM 640b, NIST).

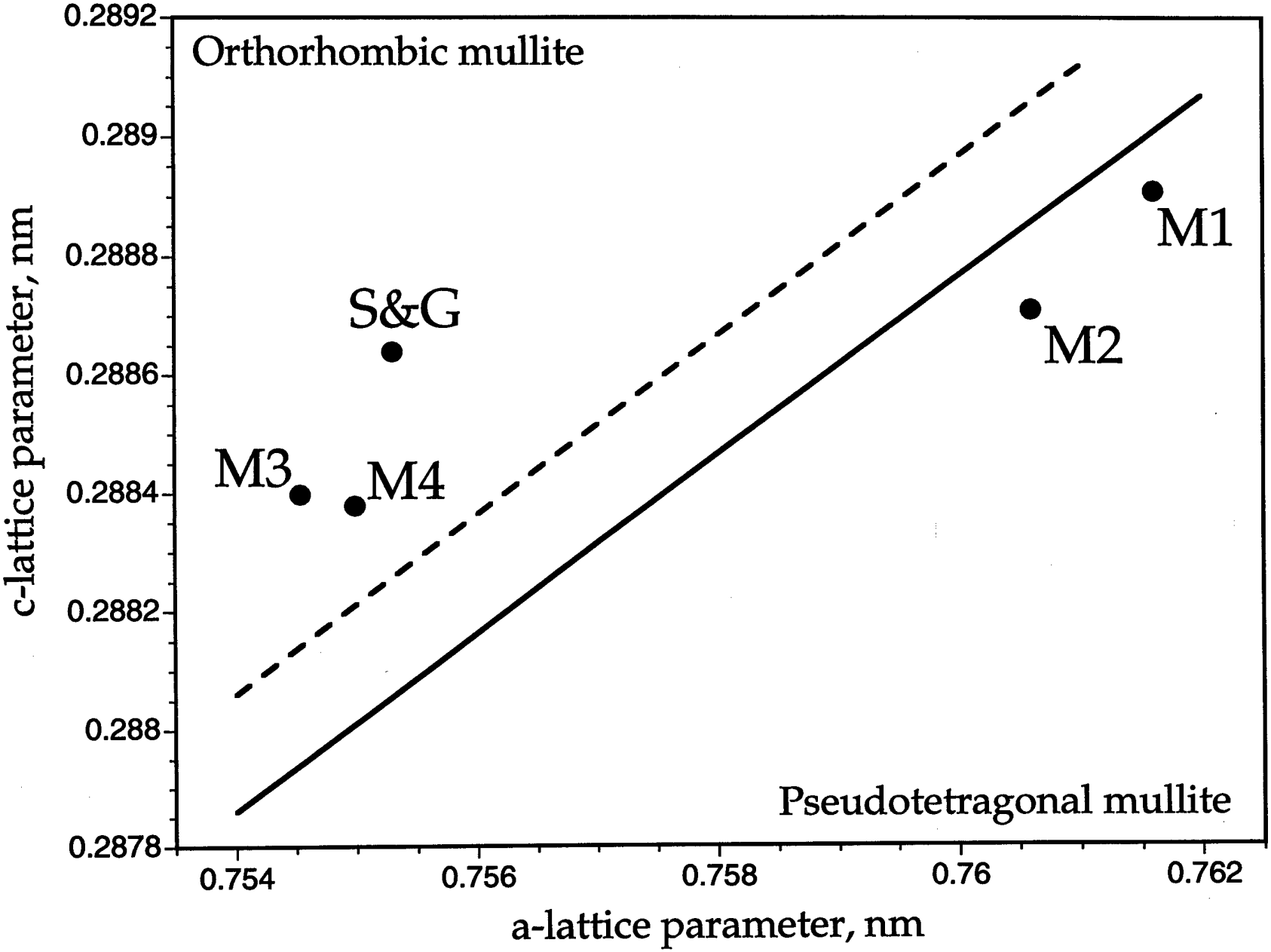


Figure 15. Positioning of the refined a and c cell dimensions for specimens M1, M2, M3 and M4 on an orthorhombic - pseudotetragonal mullite diagram.

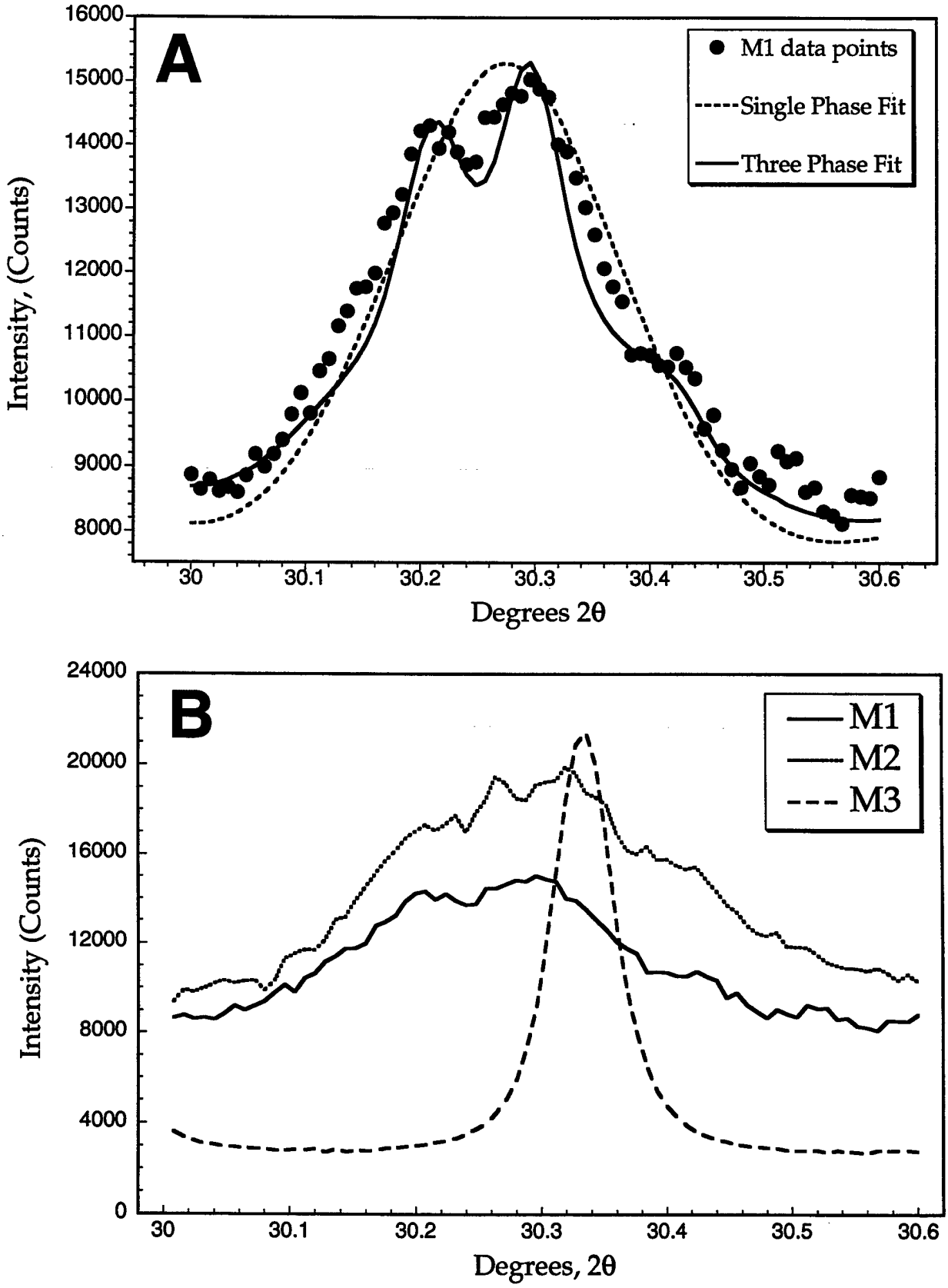


Figure 16. Detailed sections of measured powder diagrams around the well separated 002 reflection for various spectra. 16A, sample M1: observed data (dots), single phase Rietveld refinement (dashes), 3-phase Rietveld refinement (line). 16B, comparison of data from partly crystallized samples M1, M2 with those of the well crystallized specimen M3.

ELECTROPHORETIC DEPOSITION OF OXIDE CERAMICS ON MULLITE FABRIC

Introduction

The electrophoretic technique [1] was used in an attempt to deposit an even layer of oxide coating onto mullite fabric. The mullite fabric served as the deposition electrode in the electrophoretic cell setup while an aluminum plate was used as the counter electrode.

Since mullite is non-conducting, it was first coated with a continuous thin layer of carbon to render it electrically conductive. A polymer-derived pitch was found to be suitable for this purpose. With the proper selection of polymer type and molecular weight range, a pitch of sufficient viscosity at the pyrolysis temperature was obtained that was able to infiltrate the fiber tows through capillary action. This resulted in an even coating of each individual fiber on the woven fabric. In this work, a PEG-derived pitch was used.

Eectrophoretic deposition was carried out using aqueous sols of nanosized alumina and zirconia as model systems. The use of an aqueous system limited the operating voltage to a maximum of 4.5V to prevent the electrolytic decomposition of water into O_2 and H_2 at the anode and cathode, respectively; gaseous product at the deposition electrode would result in a porous deposit that is undesirable.

Experimental

1. Carbon coating of mullite fabric

A polymer:mullite fabric ratio of about 5:1 (weight basis) was used. Thin discs of PEG were hand pressed and placed on sized Nextel 440 (3M Co.) mullite fabric. For soft solid PEGs, the polymer was simply spread over the fabric. In the case of liquid PEGs, the fabric was soaked in the liquid polymer for a period of about 5 minutes. The prepared samples were pyrolysed in an argon atmosphere at 800°C for 1 h.

2. Electrophoretic deposition

The counter electrode was an aluminum plate and a voltage of 4.5 V (dc) was used throughout. The colloidal sols used were Nyacol Zr50/20 (pH 3) ZrO_2 and Nyacol AL20 (pH 4) Al_2O_3 both of which have an average particle size of 50 nm. Based on prior studies, deposition times of 5 and 10 mins were selected for the Al_2O_3 and ZrO_2 experiments, respectively. The EPD samples were dried slowly in a saturated water vapor environment.

3. SEM sample preparation

A low viscosity resin was used to prepare the dried EPD samples for cross-sectional observation under the SEM. All samples were sectioned at the midpoint for a better representation of the deposition process.

Results

While most of the PEGs screened were suitable for use to impart a thin continuous layer of carbon on the mullite fabric, Carbowax PEG 1450 was selected due to the ease of handling. For comparative purposes, Aldrich PEG 200 and ethylene glycol (EG) derived pitch were also used. It was found that PEG 1450 gives a more consistent result in terms

of a percolating pathway for electrical conductivity. In some cases with the other two PEGs, there were isolated areas of non-conductivity.

Optical microscopic (OM) observation of both surfaces of the Al_2O_3-EPD fabric showed the formation of an even, almost continuous, coating layer on the fabric. Crack lines due to drying stresses were observed at certain parts on the coating layer - especially at the tow-tow intersection - but the coating remained essentially intact.

SEM observation of cross-sections of the Al_2O_3-EPD samples indicated an "envelope" of alumina from between 15 - 20 μm encompassing each fiber tow. These "envelopes" were invariably discontinuous at the tow-tow intersection. However, there was no observable evidence of infiltration of the tow and coating of the individual fibers within the tow.

In the ZrO_2-EPD samples, OM examination revealed a brittle "bead-like" texture of the coating layer. The appearance seems to suggest that individual surface fibers were being coated - much like a string of glassy beads. The thickness of this layer was observed to decrease with decreasing carbon chain of the PEG used for coating the fabric. SEM observation indicated no infiltration into the tow as in the case of the alumina sol. However, there were no observable "envelopes" unlike in the previous case. Unevenly distributed discontinuous sections of thick coatings were observed on the surface of the PEG1450 sample. In the other two cases, hardly any zirconia coating layer was observed though OM indicated their presence originally. Moreover, the "extent" of coverage as observed under SEM was much less than that indicated by OM. It is plausible that the brittle glassy zirconia layer may have been removed in the sample preparation process. A better alternative would be to calcine the sample to "bond" the zirconia phase to the mullite fiber prior to sectioning and polishing.

Concluding remarks

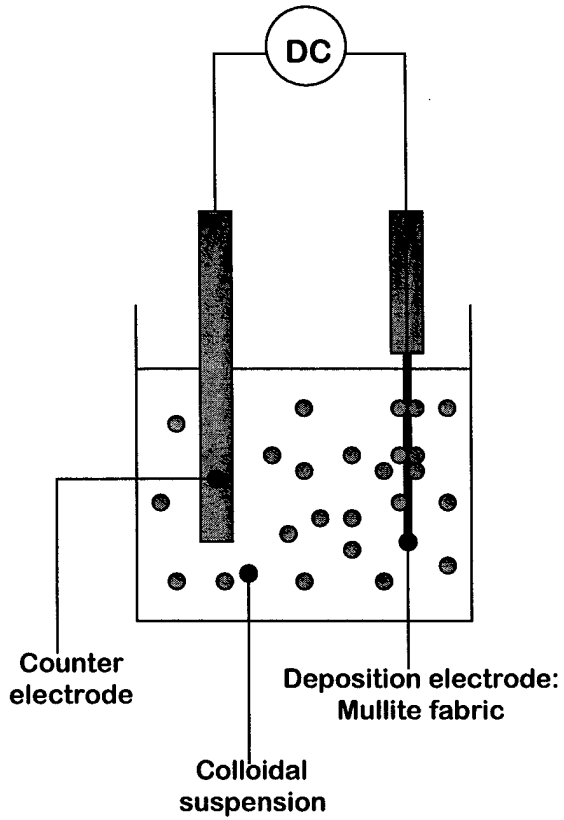
The thickness of the EPD coating layer is dependent on many parameters - deposition voltage, time, concentration of colloidal suspension etc. The voltage in these experiments was deliberately kept low at around 4 V for application using aqueous sols. The PEG-derived pitch appears to be a simple but effective way to impart electrical conductivity to the fabric. It is also apparent that the EPD technique is able to follow the contour of the substrate. However, further work has to be undertaken to effect infiltration into the tow such as (1) using a more open fabric weave; (2) using a higher voltage which would require the use of non-aqueous systems; (3) imparting a higher carbon density combined with (2) and etc.

References

1. Sarkar, P. and Nicholson, P.S., "Electrophoretic deposition (EPD): Mechanisms, kinetics and application to ceramics", *J. Am. Ceram. Soc.*, 79 (1996) 1987
2. Inagaki, M., Miura, H. and Konno, H., "A new simple process for carbon coating of ceramic particles using poly(vinyl chloride)", *J. Eur. Ceram. Soc.*, 18 (1998) 1011

Lay Foong, April 1999

Electrophoretic Deposition



EXPERIMENTAL PARAMETERS:

Deposition electrode	:	C-coated mullite fabric (PEG-derived pitch)
Counter electrode	:	Aluminum
Deposition voltage	:	4.5 V
Deposition time	:	5 to 10 minutes
Deposition material	:	Nyacol ZrO_2 (50nm; pH 3) Nyacol Al_2O_3 (50nm; pH4)

Electrophoretic Deposition

RESULTS

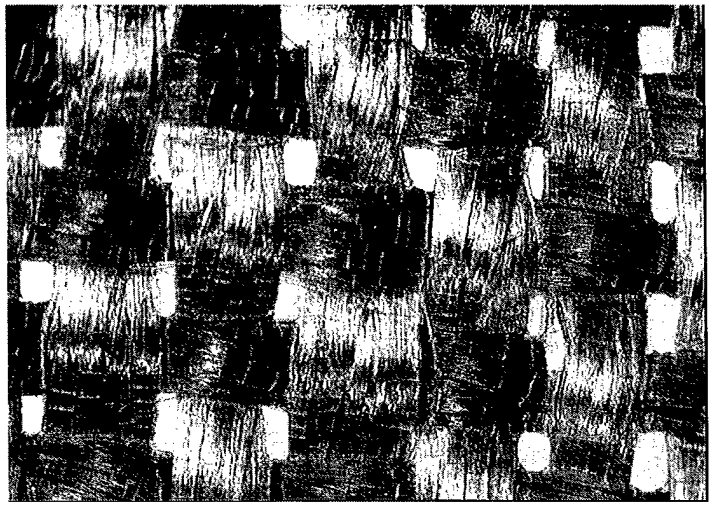
Optical microscope :

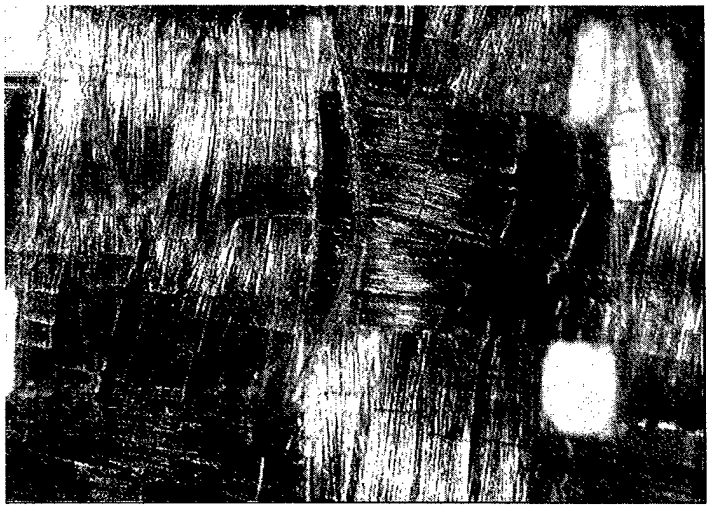
- a coating layer was observed on both the exposed (outer) surfaces
- cracking due to drying stresses

SEM observation (cross sec tion) :

- rather uniform thickness on outer surface
  - follow fabric contour especially obvious in the case of alumina
- lack of infiltration
  - "clogging/plugging" results in surface coating only
  - tight, twisted weave of fabric with tortuous path - "internal" fibers not accessible to sol

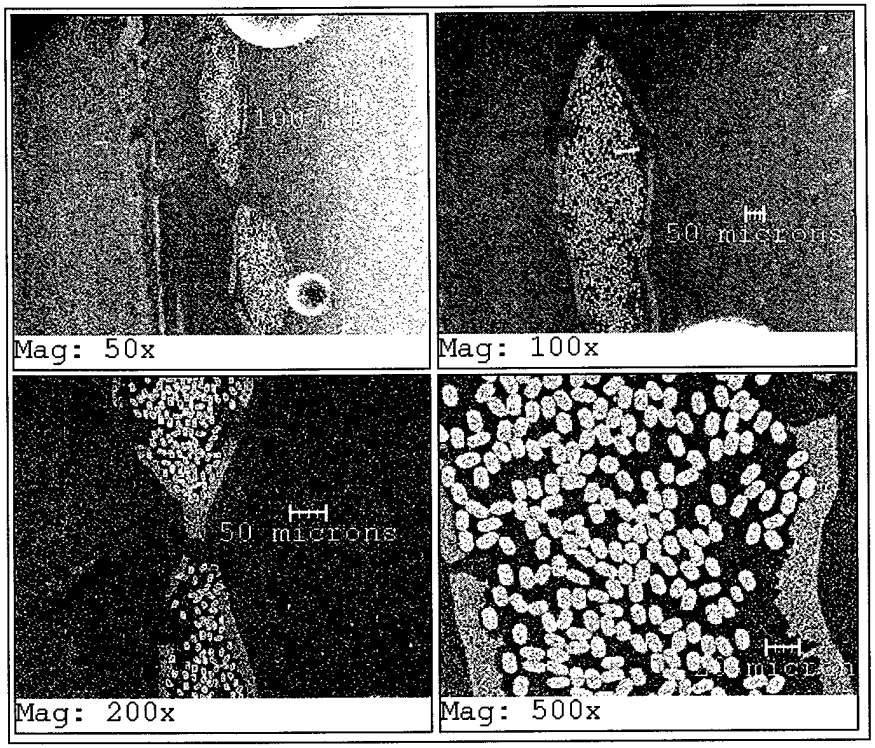
EPD: Alumina on Nextel 440



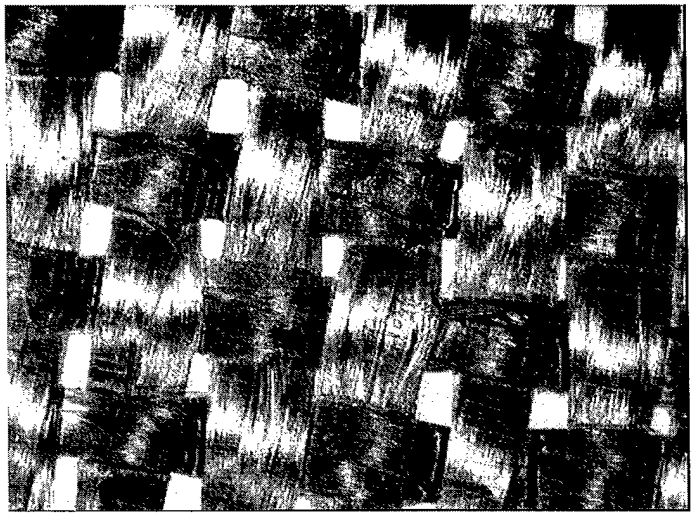


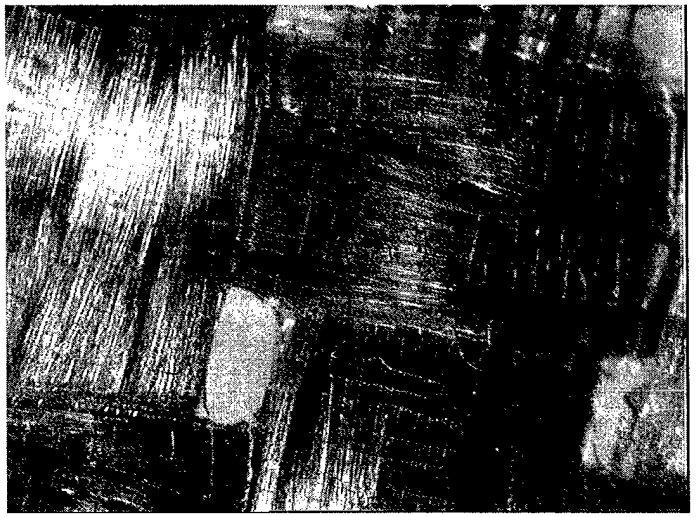
Deposition parameters:

C source	:	Carbowax PEG1450
Material	:	Al_2O_3 (50 nm; pH 4)
Voltage	:	4.5 V
Time	:	5 minutes



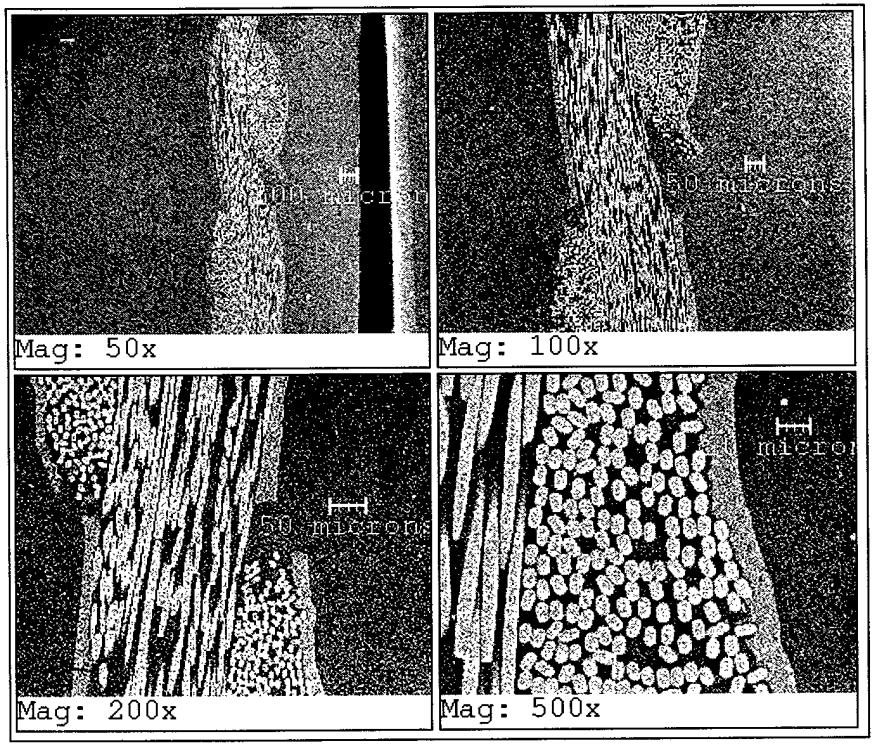
EPD: Alumina on Nextel 440





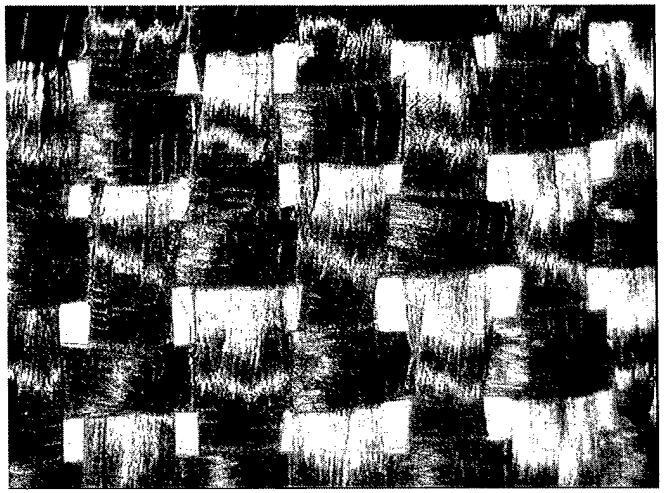
Deposition parameters:

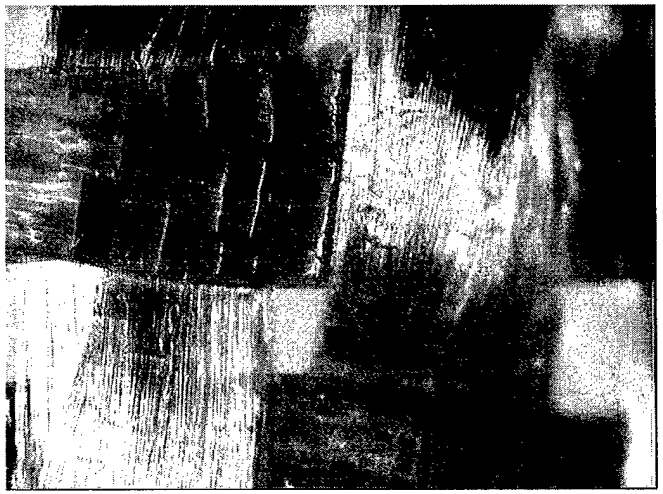
C source	:	Aldrich PEG 200
Material	:	Al_2O_3 (50 nm; pH 4)
Voltage	:	4.5 V
Time	:	5 minutes



University of Illinois at Urbana-Champaign

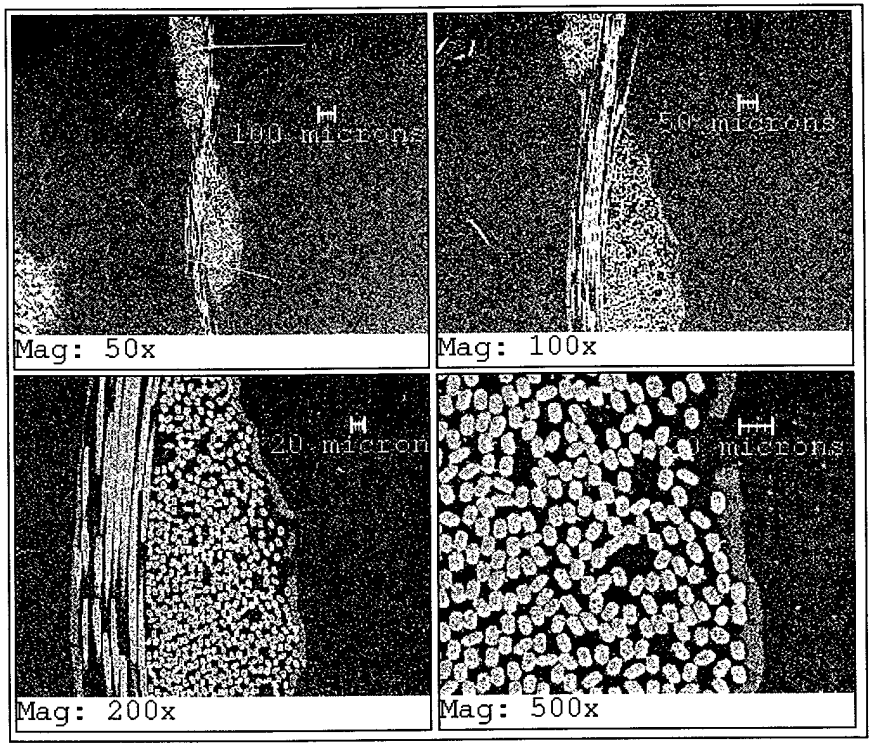
EPD: Alumina on Nextel 440





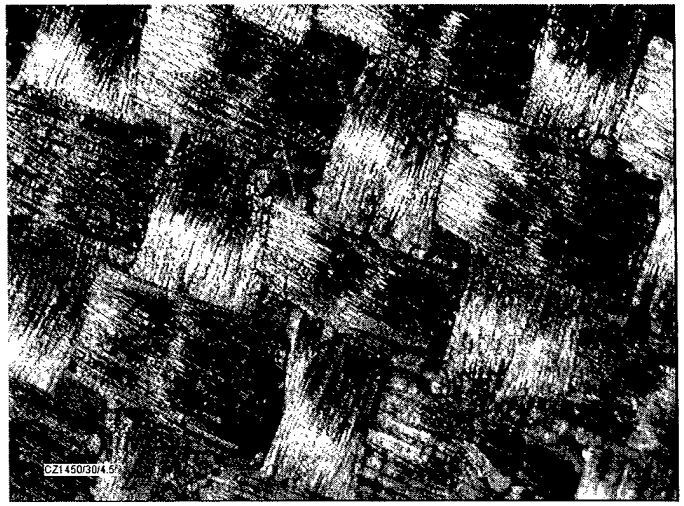
Deposition parameters:

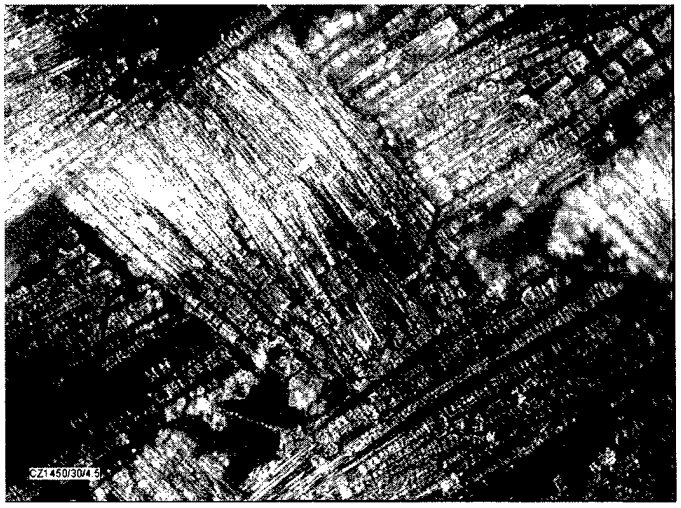
C source	:	Ethylene glycol
Material	:	Al_2O_3 (50 nm; pH 4)
Voltage	:	4.5 V
Time	:	5 minutes



University of Illinois at Urbana-Champaign

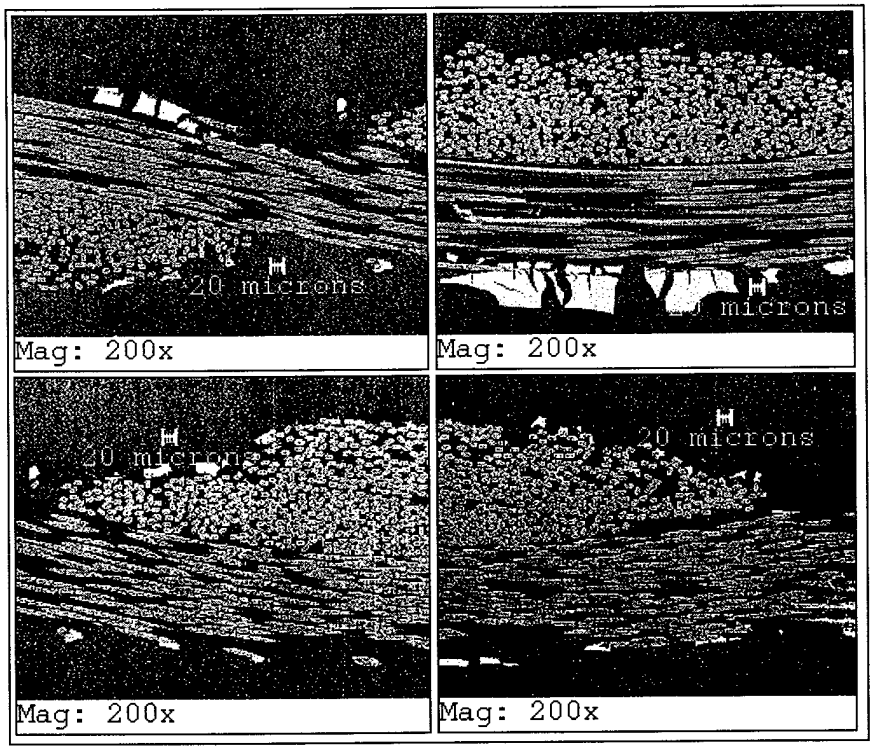
EPD: Zirconia on Nextel 440



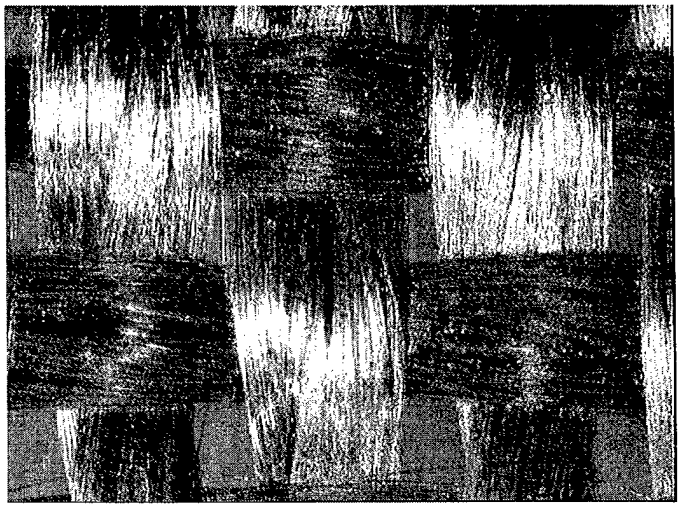


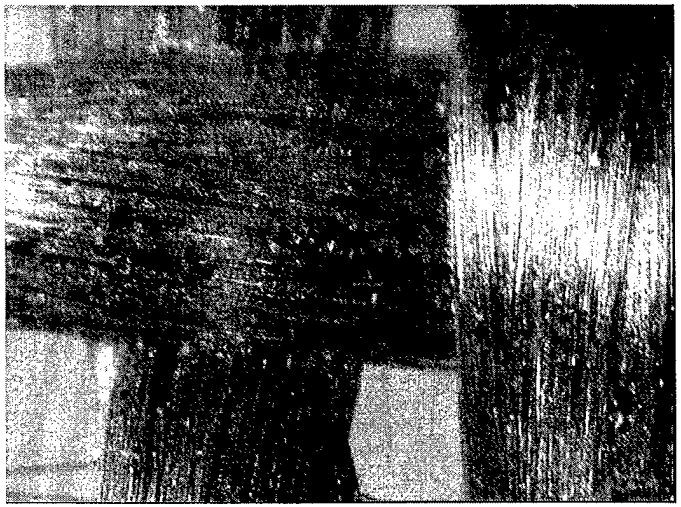
Deposition parameters:

C source	:	Carbowax PEG1450
Material	:	ZrO_2 (50 nm; pH 3)
Voltage	:	4.5 V
Time	:	10 minutes



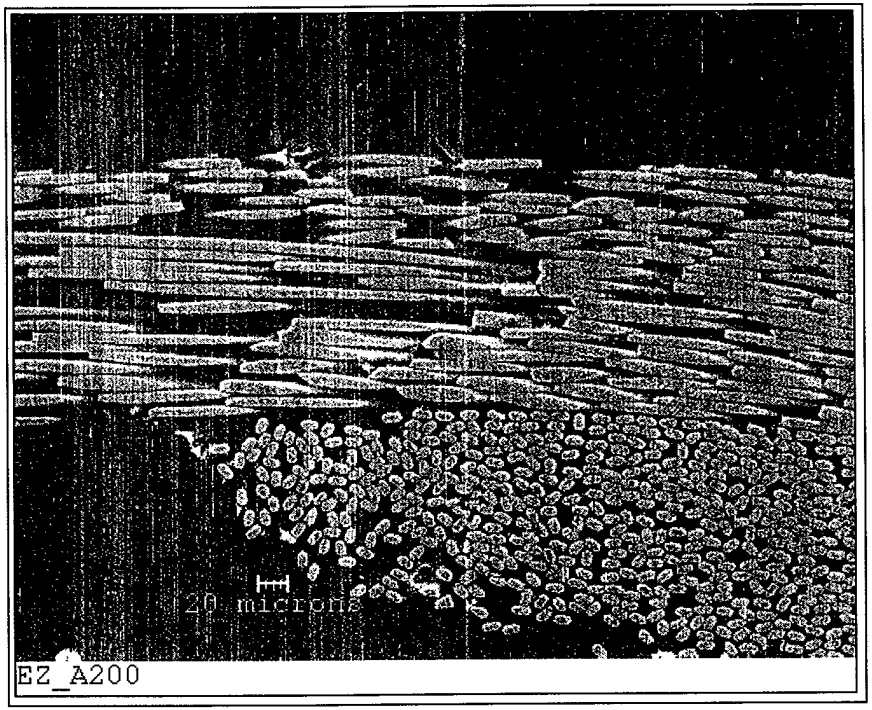
EPD: Zirconia on Nextel 440





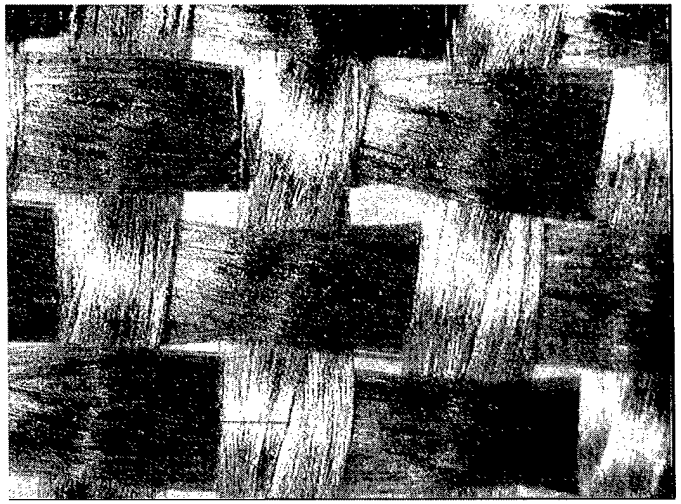
Deposition parameters:

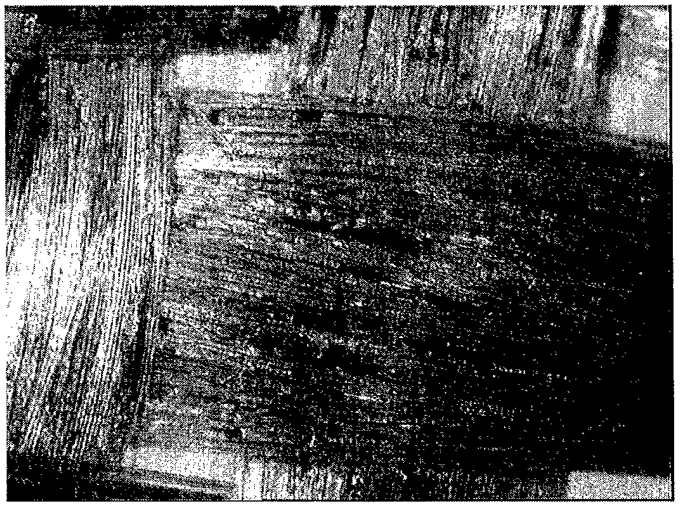
C source	:	Aldrich PEG 200
Material	:	ZrO_2 (50 nm; pH 3)
Voltage	:	4.5 V
Time	:	10 minutes



University of Illinois at Urbana-Champaign

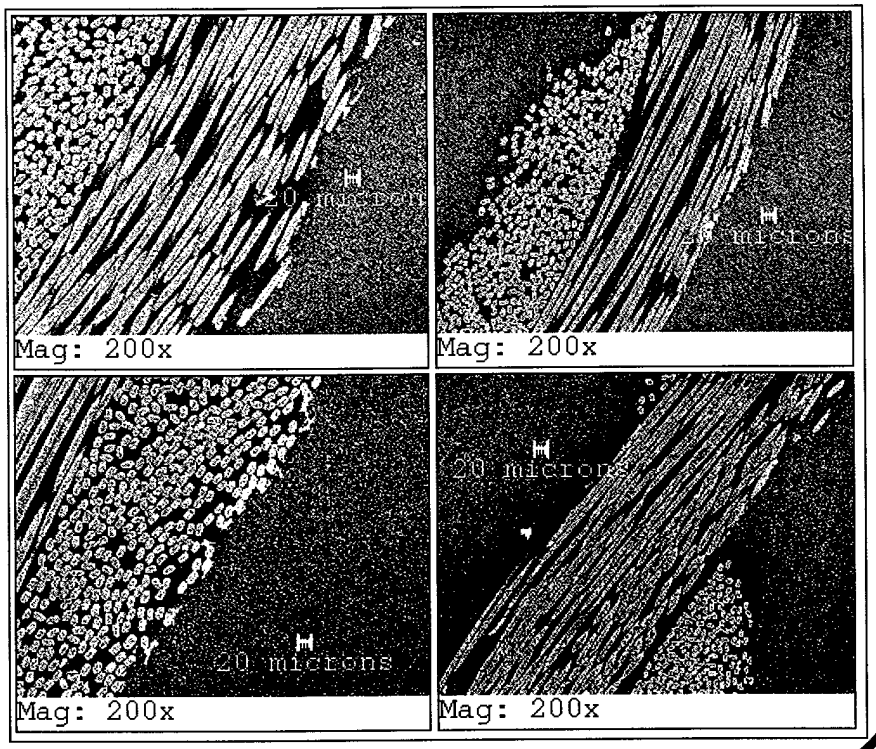
EPD: Zirconia on Nextel 440





Deposition parameters:

C source	:	Ethylene glycol
Material	:	ZrO_2 (50 nm; pH 3)
Voltage	:	4.5 V
Time	:	10 minutes



University of Illinois at Urbana-Champaign

Electrophoretic Deposition

CONCLUSIONS

a PEG-based pitch is suitable to impart a percolating conductive carbon layer onto woven mullite fabric

the tightly woven fabric is not conducive for sol penetration using the EPD technique - only a surface "envelope" was obtainable

Executive Summary

The original aim of this work was to develop a viable, on line, coating technique for oxide fibers and weaves. The coating was to be a chemically compatible, oxide (eg. hexacelsian ($BaAl_2SiO_8$)) which provided a temperature-independent, debonding mechanism based on residual stresses developed at 1590°C, due to a reconstructive phase transformation accompanied by a 5.6% volume contraction. However, the method adopted, the charged liquid beam cluster technique proved to be unfeasible at the current time. Attention was therefore focused on to electrophoretic deposition of oxide sols (alumina, zirconia) onto carbon-coated fibers and weaves of alumina and mullite ($3Al_2O_3 \cdot 2SiO_2$). However drying of films led to extensive microcracking and this method too, was found to be unsuitable. Attention was then turned to support related AFOSR work for which ongoing, but intermittent funding was obtained (STTR stages I and II); viz., (i) the development of mullite and YAG fibers by amorphous crystallization from a frozen, amorphous melt; (ii) the elastic constants of single crystal, mullite and yttria fibers as measured by Brillouin spectroscopy to 1200°C; and (iii) powder synthesis of oxides for matrices or deposition as coatings.

Journal Publications

(In chronolgical order)

1 "Preparation of Portland Cement Components by PVA Solution Polymerization," S.-J. Lee, E. A. Benson and W. M. Kriven, J. Am. Ceram. Soc. **82** [8] 2049-2055 (1999).

2 "Growth and Crystallization of YAG and Mullite-Composition Glass Fibers," J. K. R. Weber, B. Cho, A. D. Hixson, J. G. Abadie, P. C. Nordine, W. M. Kriven, B. R. Johnson and D. Zhu, J. Europ. Ceram. Soc., **19** [13] 2543-2550 (1999).

3 "High Temperature Single Crystal Properties of Mullite" W. M. Kriven, J. Palko, S. Sinogeikin, Jay D. Bass, A. Sayir, G. Brunauer, H. Boysen, F. Frey and J. Schneider, J. Europ. Ceram. Soc., **19** [13] 2529-2541 (1999).

4 "Synthesis of Oxide Powders via Polymeric Steric Entrapment," (invited review paper) W. M. Kriven, S. J. Lee, M. A. Gulgun, M. H. Nguyen and D. K. Kim, in Innovative Processing/Synthesis: Ceramics, Glasses, Composites III. Ceramic Transactions, vol **108,** 99-110 (2000).

5 "Electrosynthesis and Microstructural Characterization of Anodic VO_x Films," J. P. Schreckenbach, D. Butte, G. Marx, B. R. Johnson and W. M. Kriven, J. Mater. Res., **15** [7] 1483-1489 (2000).

6 "The Single Crystal Elasticity of Yttria to High Temperature," J. W. Palko, S. V. Sinogeikin, Ali Sayir, W. M. Kriven and J. D. Bass, J. Appl. Phys., submitted.

7 "Single Crystal Elastic Moduli of Mullite (~$2.5Al_2O_3 \cdot SiO_2$) to High Temperatures by Brillouin Spectroscopy," J. W. Palko, A. Sayir, S. V. Sinogeikin, W. M Kriven and J. D. Bass, J. Am. Ceram. Soc., submitted.

8 "Crystallization Kinetics of Yttrium Aluminum Garnet ($Y_3Al_5O_{12}$)," B. R. Johnson and W. M. Kriven, J. Mater Res., submitted.

9 "Crystal Structure Development during Devitrification of Amorphous Mullite," B. R. Johnson, W. M. Kriven and J. Schneider, J. Europ. Ceram. Soc., submitted.

J. Appl. Physics, submitted, Sept 200

The Single-crystal Elasticity of Yttria (Y_2O_3) to High Temperature

James W. Palko and Waltraud M. Kriven

Department of Materials Science and Engineering, University of Illinois, Urbana, IL 61801

Stanislav V. Sinogeikin and Jay D. Bass

Department of Geology, University of Illinois, Urbana, IL 61801

Ali Sayir

NASA Glenn Research Center, Cleveland, OH 44135

(Recieved

The single-crystal elastic moduli of yttria have been measured by Brillouin spectroscopy up to 1200 °C. The room temperature values obtained are C_{11} = 223.6 ± 0.6 GPa, C_{44} = 74.6 ± 0.5 GPa, and C_{12} = 112.4 ± 1.0 GPa. The resulting bulk and (Voigt-Reuss-Hill) shear moduli are K = 149.5 ± 1.0 GPa and G_{VRH} = 66.3 ± 0.8 GPa, respectively. These agree much more closely with experimental values reported for polycrystalline samples than do previous single-crystal measurements. Linear least squares regressions to the variation of bulk and shear moduli with temperature result in derivatives of dK/dT = -17 ± 2 MPa/°C and dG_{VRH}/dT = -8 ± 2 MPa/°C. Elastic anisotropy was found to remain essentially constant over the temperature range studied.

PACS numbers: 62.20.Dc

I. Introduction

Yttria, or yttrium sesquioxide (Y_2O_3), is a refractory material with a cubic crystal structure.[1] Yttria, in the form of dense polycrystalline ceramics, has been considered for use in nuclear applications[2] and has gained interest relatively recently for use in infrared optics.[1,3,4] Due to yttria's optical isotropy (resulting from its cubic structure), it is possible that, in the future, optical components requiring high quality may be made from single crystals. The single-crystal elastic moduli are valuable for designing such optical components. In particular, the temperature derivatives of elastic moduli allow dimensional changes due to heating under physical constraint, as well as acoustic excitation to be determined. The single-crystal elastic moduli are also useful in understanding the fundamental physics of yttria. Single-crystal yttria fibers suitable for such elasticity measurements have recently been produced using a laser-heated, float zone technique.[5]

The elastic properties of pure and doped polycrystalline yttria have been determined by several authors[6-13] including measurements to high temperatures.[1,2,14] In addition, single-crystal measurements have been reported at room temperature.[15,16] There are, however, significant discrepancies between the bulk and shear moduli reported for dense polycrystalline materials and those calculated from the previously reported single-crystal moduli. The purpose of this study was to obtain accurate values of the single crystal elastic moduli of Y_2O_3 both at room and elevated temperatures.

Brillouin scattering offers a convenient means of measuring the complete set of elastic moduli for single crystals, especially at elevated temperatures. It requires no physical contact with the sample, is capable of measuring along numerous crystallographic directions in a single sample, and requires only small sample volumes. Brillouin scattering

arises from the inelastic scattering of photons from acoustic phonons in the sample. The scattered light is shifted in frequency with respect to the incident light by a factor that is proportional to the velocity of the acoustic waves (Eq. 1).[17]

$$V = \left(\frac{\Delta\omega}{\omega}\right)\left(\frac{c}{2\,n\sin\left(\theta/2\right)}\right) \qquad (1)$$

Here V is the velocity of an acoustic wave, $\Delta\omega$ is the frequency shift of the scattered light, ω is the frequency of the incident light, c is the speed of light, n is the index of refraction of the sample, and θ is the scattering angle. In this study, we employed a special case of symmetric scattering called platelet geometry (Figure 1), which utilizes a sample with flat, parallel faces and equal angles between the face normals and incident/scattered beam directions. The phonon propagation direction q is in the plane of the sample, and the face normals as well as the incident/scattered light rays all lie within a plane.[18] Figure 1 shows a schematic of symmetric platelet scattering. With symmetric platelet scattering geometry, the scattering angle is easily defined, and no knowledge of the index of the refraction of the sample is necessary. As seen in Figure 1, Snell's law allows the replacement of n $\sin(\theta/2)$ with $n_o\sin(\theta_o/2)$ in Eq. 1. This is particularly beneficial for high temperature studies where the variation of index of refraction with temperature is generally unknown and difficult to measure.

The elastic waves may be treated by a continuum mechanical analysis which relates their velocities along a given crystallographic direction to the adiabatic elastic moduli and density of the material via Christoffel's equation (Eq. 2).[19]

$$\left|C_{ijkl}q_jq_l - \rho V^2\delta_{ik}\right| = 0 \qquad (2)$$

C_{ijkl} is the elasticity tensor for the material, ρ is the density, and δ_{ik} is the Krönecker delta function. Since yttria has cubic symmetry, there are only three independent, nonzero components in its elasticity tensor, $C_{11}(=C_{22}=C_{33})$, $C_{12}(=C_{13}=C_{23})$, and $C_{44}(=C_{55}=C_{66})$ (in Voigt notation).[20]

II. Experiment

A. Samples

Samples for this study were taken from single-crystal fibers grown from high purity Y_2O_3 powder by a laser heated float zone (LHFZ) technique.[5,21] This containerless technique uses a scanned CO_2 laser beam (10.6 μm wavelength) that is split and focused at the tip of a polycrystalline source rod to produce a melt which is held between the source and product phases by surface tension. Temperature in the molten region was stabilized using infrared pyrometery, but absolute temperature was not determined because the emissivity of molten yttria is not known.

For preparation of the source rod, high purity (99.999% pure) polycrystalline yttria powder (Alpha Aesar) was used. Since the LHFZ technique is essentially a zone refining

process, the final purity of the yttria crystal is likely even higher. This powder was blended with 5 weight % binder (Methocel 20-231, The Dow Chemical Company, Midland, MI 48674) and glycerin was used as a plasticizer in a water based slurry. The slurry was then degassed overnight with a moderate vacuum (~$70x10^3$ Pa) to achieve a high viscosity paste. This paste was extruded with a custom-made mini-extruder, i.e. a modified hypodermic syringe. The plastic syringe wall was replaced within high wear regions to avoid contamination. At least two extrusions were made to minimize porosity in the paste. The extruded source rod was normally 250 μm in diameter and extruded lengths were 15 to 20 cm long. The rods were furnace dried in air at 200 °C for approximately 1 hour and placed in the LHFZ apparatus without any presintering.

At steady state, the source to fiber diameter ratio is inversely proportional to the square root of the feed rod to pull rod velocity ratio. The fibers used for the Brillouin work had nearly circular cross sections with average diameters slightly less than 500 μm. For fibers grown in this study, the molten zone height was kept constant at approximately one and half times the fiber diameter, and fibers were grown in air.

Octahedral cleavage was apparent in fragments broken from the fibers and showed that the fiber axis coincided closely with the <111> crystal direction. The material was clear except for occasional inclusions that appear to be bubbles. The samples were optically isotropic when examined under cross polarized light. An X-ray analysis was performed on a large fiber sample by four circle diffractometry, in order to verify the single-crystal nature and cubic symmetry of the samples. Precise values of the lattice parameter at all temperatures were calculated from the regression equation of Taylor (Eq. 3),[22]

$$a(T) = (1.06016\ \text{nm})\ (1 + 6.76\text{x}10^{-6}\ T + 1.22\text{x}10^{-9}\ T^2) \qquad (3)$$

where a(T) is the cell edge parameter at a temperature T (in °C). A value of 1.0603 nm (corresponding to 22°C) yielding a theoretical density of 5.033 g/cm^3 (which matches that reported by Tropf and Harris[1]) was used for all room temperature calculations.

Velocity measurements were performed on a single sample. It was ground into a flat plate with a thickness of ~150 μm.[23] Due to breakage during sample preparation, the usable area of the sample faces was around 250 μm x 250 μm. The ground faces corresponded closely to the {100} crystallographic plane. Orientation was accomplished by optical goniometery from cleavage planes, and measurements subsequent to grinding showed the face to be within ~2° of the {100} face.

B. Brillouin Scattering

Illumination of the sample was provided by the 514.5 nm line of an Ar^+ laser at a power of 200 mW or less for the ambient temperature measurements. For high temperature runs, a laser power of up to 400 mW was used to maximize the Brillouin signal since sample heating was not a particular concern. Higher power was necessary for high temperature experiments because of the furnace windows which reduce the intensities of both the incident and scattered beams by partial reflection and introduction of astigmatism into the focusing and collecting optical paths. Scattered light was collected through a slot with an angular acceptance of approximately 5.5° in the scattering plane to lessen broadening of Brillouin peaks. The scattered light was analyzed by a 6-pass,

tandem, Fabry-Perot interferometer. The spectrometer has been described in detail elsewhere.[24,25]

Room temperature measurements were performed with a 90° scattering angle. An Eularian cradle was used to rotate the sample around its face normal to access different phonon directions. The high temperature results of this study were obtained using a compact furnace mounted on the Eularian cradle, allowing multiple phonon directions to be collected without remounting the sample. The construction and operation of this furnace is described elsewhere.[26] An 80° scattering angle was used for the high temperature work. Velocities calculated from the measured Brillouin shifts were used in a linearized inversion algorithm[27] to solve for the elastic moduli.

III. Results and Discussion

Velocities measured at room temperature, in the plane ~(001) (outside the furnace), have a close correspondence to fits from the calculated elastic constants (solid curves Figure 2). This figure gives a sense of the anisotropy in yttria. Longitudinal velocities vary by ~ 4% in this plane, while shear velocities vary by ~ 15%.

The adiabatic elastic constants obtained are given in Table I along with those reported by Aleksandrov et al. (also measured using Brillouin spectroscopy)[15,16] Errors in Table I include contributions due to residuals of the velocity fits as well as uncertainty in sample orientation.[23] There are substantial differences between Aleksandrov's values and those obtained here (C_{11} +1.5%, C_{44} –8%, C_{12} +20%). Table II lists the bulk modulus, K, and shear modulus, G, calculated from the room temperature constants using the Voigt, Reuss, and Voigt-Reuss-Hill averaging schemes (denoted by subscripts V, R, and VRH

respectively) for both this study and for Aleksandrov et al. For comparison, values of K and G (adiabatic) reported previously by several authors for polycrystalline yttria are included in Table II. The values reported by Manning[8] are a Spriggs extrapolation to zero porosity from samples with porosity ranging from 4-22 %, whereas those of Yeheskel[13] and Tropf[1] are uncorrected, and correspond to samples of greater than 99% theoretical density. This fact may account for the differences in bulk modulus.

The values of Aleksandrov et al.[15,16] for K and G_{VRH} are 11% higher and 14% lower, respectively, than those reported here. Clearly, the current measurements agree much more closely with polycrystalline measurements than those of Aleksandrov et al. No details of the quality or properties of the sample are reported in the previous single crystal study,[15] but these aspects may partially account for some of the discrepancies. Another possible explanation is a misorientation of the sample used in the previous study. The differences decrease in the order: $|\Delta C_{12}/C_{12}| > |\Delta C_{44}/C_{44}| > |\Delta C_{11}/C_{11}|$. Ingel and Lewis derived a similar relation of relative magnitudes of deviation for misorientation in Y_2O_3 stabilized ZrO_2 along certain directions.[28] Aleksandrov et al. calculated moduli based on the longitudinal and shear (degernerate) velocities along [100] for which the reported values are 6.75 $\pm$ 0.02 km/s and 3.71 $\pm$ 0.03 km/s, respectively, as well as both shear velocities along [0.5 0.5 $1/\sqrt{2}$] which are reported as 3.43 $\pm$ 0.02 km/s and 3.69 $\pm$ 0.01 km/s.[15] Similar velocities result from Eq. 2 using the elastic moduli determined in this study, if a rotation of ~ 13° around [010] is applied to the coordinates of Aleksandrov et al. (i.e. [100] becomes [0.9744 0 0.2250], and [0.5 0.5 $1/\sqrt{2}$] becomes [0.3281 0.5 0.8015].) The resulting longitudinal and shear velocities along [0.9744 0 0.2250] are 6.726 km/s and 3.745 km/s. (The other shear mode with a velocity of 3.849 km/s is

polarized along [010]. Since the incident and scattered beams were directed along [110] and [-110] (in the original coordinate system),[15] this wave is polarized in the scattering plane and would have zero scattered intensity.[29]) The shear velocities along [0.3281 0.5 0.8015] are 3.710 km/s and 3.454 km/s. Aleksandrov et al. report the accuracy of face orientation as 3 to 5°,[15] but this degree of misorientation cannot account for the differences with the current study.

The variation of the single-crystal elastic moduli with temperature is consistent with a linear trend as shown by Figure 3. Table III lists values for the adiabatic constants determined at elevated temperatures. Errors given again include contributions from residuals in the fit as well as uncertainty in sample orientation.[23] Higher order polynomial fits to these results are not warranted, given the uncertainties in the data. The temperature derivatives of the elastic moduli from the linear fits are listed in Table IV along with those for the bulk modulus and Voigt-Reuss-Hill shear modulus. Errors in the temperature derivatives are based on the 95% confidence intervals for the slope of the linear fit. An error of ±5% is given in temperature itself based on uncertainty in the gain of the amplifier used in measuring temperature. This may contribute to an absolute error in slope, but the internal temperature precision is much better (<3%).[23] Furthermore, the uncertainty in slope is dominated by errors in velocity, not in temperature.

Figures 4 and 5 show the temperature dependence of bulk and shear (Voigt-Reuss-Hill) moduli respectively. Also shown are values measured by Dickson and Anderson using a resonance technique (resulting in adiabatic moduli) on a 0.91 Y_2O_3•0.09 ThO_2 polycrystalline sample.[14] There is a slight offset in bulk modulus, but the rate of softening with temperature is similar for both materials. Linear fits to the data of Dickson and

Anderson[14] yield slopes of -15.3 MPa/ °C and -8.5 MPa/ °C for bulk and shear modulus respectively. The offset in bulk modulus may be due to composition, but no estimate of possible errors is given by Dickson and Anderson[14] so the differences may be insignificant.

Figure 6 shows the Young's modulus for yttria calculated from Eq. 4,

$$E = \frac{9KG_{VRH}}{3K + G_{VRH}} \tag{4}$$

along with the data of Price and Hubbert,[30] Dickson and Anderson,[14] a linear fit to the data of Marlowe and Wilder up to 1000 °C,[2] and a fit suggested by Tropf and Harris[1] (based on data from Price and Hubbert[30]). The fit to the data of Marlowe and Wilder[2] yields a slope of -19.5 MPa/ °C. Tropf and Harris[1] infer a pronounced softening of Y_2O_3 at high temperature and a rapid non-linear decrease in elastic modulus at temperatures greater than 1200 °C. The present results do not support such a high order variation in elastic modulus, at least not within the temperature range of this study. The constants of Dickson and Anderson[14] and Marlowe and Wilder[2] are adiabatic while those of Price and Hubbert[30] are for constant temperature.

Elastic anisotropy for a cubic crystal may be characterized by the factor, A, computed using Eq. 5.

$$A = \frac{2C_{44} + C_{12}}{C_{11}} - 1 \tag{5}$$

The elastic constants measured here yield a value for A of 0.170 ± 0.015, while those of Aleksandrov et al. yield 0.212.[15,16] For comparison the values of A for MgO, BaO, and yttrium aluminum garnet ($Y_3Al_5O_{12}$, YAG) are 0.37, -0.07 and 0.02, respectively.[16]

The anisotropy does not vary significantly over the temperature range measured. There appears to be no systematic trend, and no variations in A within the error of the measurement. This contrasts with the behavior of several other oxides which show marked changes with temperature (Table V).

It is possible that this behavior simply results from a peculiarity of the interactions of Y and O, namely that they do not change substantially with temperature, but it is also possible that the constance of anisotropy with temperature is partially tied to the structure of yttria.

To a rough approximation, the elasticity of a crystal may be described by pair potentials between neighboring atoms and 3-body terms which give a potential energy based on the angle of two bonds attached to a central atom. For the halite structure, these may be related qualitatively to the macroscopic elasticity tensor. The halite structure consists of octahedra whose points are directed along the <100> crystallographic directions.[31] Therefore, tension or compression along <100> directions (C_{11}) corresponds to a change in length of the bonds which are all directed toward the points of the octahedra (i.e. <100> directions). Shear along the <100> directions (C_{44}), however, results in the bending of 3 atom groups. Therefore, to a first approximation, a change with temperature, of only the pair potentials between atoms would result in a change in C_{11} leaving C_{44} unaffected, and vice versa for a change in the 3-body term. Though oversimplified, this analysis suggests that the halite structure would show comparable

changes in its macroscopic moduli and its fundamental atomic interactions (i.e. the relative resistance to bond stretching/compression as compared to 3-body bending).

Yttria also has 6-fold coordinated cations. It's structure (bixbyite), however, is much more complex than that of halite, with 16 formula units per cell, and the coordination polyhedra in yttria are not regular octahedra.[31] They are substantially deformed, and the structure is sometimes described as having cubic coordination for Y^{3+} with O^{2-} ions at opposite corners of the cube missing, essentially a defect fluorite structure.[22,32] Regardless of the description of the structure, the Y-O bonds point in many crystallographic directions. Therefore, unlike compounds with the halite structure, uniaxial forces along any crystallographic direction will involve both stretching/compression of bonds and 3-body bending. Therefore, a change in relative resistance of one of these as compared to the other may produce a much smaller change in the macroscopic moduli and hence the anisotropy.

This hypothesis is supported by the relatively low change in anisotropy with temperature for other crystals with a complex relationship between bond directions and the unit cell. This is seen for YAG in Table V, and applies to several other garnets such as almandine and pyrope.[16] Like yttria, garnets have a complex crystal structure with irregular coordination polyhedra. Spinel also follows this trend with a relatively low value of dA/dT.[16,33] Various III-V compounds with zinc-blende lattices, such as GaAs or GaSb, and elements with diamond cubic lattices, such as diamond and silicon, show very low changes in anisotropy with temperature as well.[16] These structures also experience a combination of bond stretching/compression and 3-body bending, for both uniaxial tension and pure shear along high symmetry directions.

IV. Conclusions

The single-crystal elastic moduli of yttria were measured using Brillouin spectroscopy at room temperature and high temperatures ranging to 1200°C. The room temperature values differed significantly from previous single-crystal measurements,[15,16] but bulk properties calculated from the present study agree much more closely with most literature values reported for polycrystalline yttria.[1,8,9,11,13] This is important since it suggests that the elasticity of polycrystalline yttria ceramics can be accounted for by the elasticity of the Y_2O_3 crystal lattice itself. No second phase or secondary effect is indicated here as may have been suggested by the previous results. Sample misorientation in the previous study is offered as a potential reason for the discrepancy.

All elastic moduli display a modest linear decrease over the temperature range studied. The variation of bulk and shear moduli with temperature correspond closely to those reported for a $91Y_2O_3 \cdot 9ThO_2$ compound.[14] Likewise, the change in Young's modulus with temperature agrees well with measurements on pure polycrystalline yttria.[2] Since accurate determinations of the temperature variation of properties for polycrystalline yttria ceramics have been made previously,[2,14] perhaps the more important addition of this study is the temperature dependence of elastic anisotropy, which was found to remain essentially constant for yttria as compared to significant changes for several other oxides with simpler cubic structures. A possible relation between the elastic anisotropy change with temperature and structure is proposed.

Acknowledgements

The work of J. W. Palko was supported by the Fannie and John Hertz Foundation graduate fellowship. X-ray work was performed by J. McMillan at the Center for Microanalysis of Materials at UIUC. Thanks to D.C. Harris for help in obtaining certain reference matter. This work was partially supported by a United States Air Force Office of Scientific Research AASERT Grant, under contract number F49620-97-1-0427 and NSF grant EAR-96-14416.

References

1 W. J. Tropf and D. C. Harris, Proc. SPIE **1112,** 9 (1989).

2 M. O. Marlowe and D. R. Wilder, J. Am. Ceram. Soc. **48,** 227 (1965).

3 R. L. Gentilman, Proc. SPIE **683,** 2 (1986).

4 W. H. Rhodes, G. C. Wei, and E. A. Trickett, Proc. SPIE **683,** 12 (1986).

5 A. Sayir, S. C. Farmer, P. O. Dikerson, and H. M. Yun, Mat. Res. Soc. Sym. Proc. **365,** 21 (1995).

6 E. K. Keler and A. B. Andreeva, Ogneupory, no.5, 224 (1963)[Refractories, no. 5, 243 (1963)].

7 W. R. Manning and J. Orville Hunter, J. Am. Ceram. Soc. **51,** 537 (1968).

8 W. R. Manning, J. O. Hunter, and J. B. R. Powell, J. Am. Ceram. Soc. **52,** 436 (1969).

9 K. K. Phani and S. K. Niyogi, J. Am. Ceram. Soc. **70,** C362 (1987).

10 G. C. Wei, C. Brecher, M. R. Pascucci, E. A. Trickett, and W. H. Rhodes, Proc. SPIE **929,** 50 (1988).

11 K. Shibata, H. Nakamura, and A. Fujii, Proc. SPIE **1326,** 48 (1990).

12 G. C. Wei, M. R. Pascucci, E. A. Trickett, S. Natansohn, and W. H. Rhodes, Proc. SPIE **1326,** 33 (1990).

13 O. Yeheskel and O. Tevet, J. Am. Ceram. Soc. **82,** 136 (1999).

14 R. W. Dickson and R. C. Anderson, J. Am. Ceram. Soc. **51,** 233 (1968).

15 V. I. Aleksandrov, V. F. Kitaeva, V. V. Osiko, N. N. Sobolev, V. M. Tatarintsev, and I. L. Chistyi, Sb. Kratk. Soobshch. Fiz. AN SSSR Fiz. Inst. P. N. Lebedeva, no. 4, 8 (1976)[Sov. Phys. Lebedev Inst. Rep., no. 4, 7 (1976)].

16 *Elastic, Piezoelectric, Pyroelectric, Piezooptic, Electrooptic Constants, and Nonlinear Dielectric Susceptibilites of Crystals*; *Vol. III/18*, edited by K.-H. Hellwege and O. Madelung (Springer-Verlag, Berlin, 1984).

17 G. B. Benedek and K. Fritsch, Phys. Rev. **149,** 647 (1966).

18 E. S. Zouboulis and M. Grimsditch, J. Appl. Phys. **70,** 772 (1991).

19 L. D. Landau and E. M. Lifshitz, *Theory of Elasticity* (Pergamon Press, London, 1959), p. 104.

20 J. F. Nye, *Physical Properties of Crystals: Their Representation by Tensors and Matrices* (Clarendon Press, Oxford, 1985), p. 114.

21 A. Sayir and S. C. Farmer, Mat. Res. Soc. Sym. Proc. **365,** 11 (1995).

22 D. Taylor, Brit. Ceram. Trans. and J. **83,** 92 (1984).

23 J. Palko, M.S. Thesis, University of Illinois, Urbana-Champaign, 2000.

24 J. D. Bass, J. Geophys. Res. **94,** 7621 (1989).

25 S. V. Sinogeikin, J. D. Bass, and T. Katsura, J. Geophys. Res. **103,** 20 (1998).

26 S. V. Sinogeikin, J. M. Jackson, B. O'Neill, J. W. Palko, and J. D. Bass, Rev. Sci. Instrum. **71,** 201 (2000).

27 D. J. Weidner and H. R. Carleton, J. Geophys. Res. **82,** 1334 (1977).

28 R. P. Ingel and D. Lewis, J. Am. Ceram. Soc. **71,** 261 (1988).

29 R. Vacher and L. Boyer, Phys. Rev. B **6,** 639 (1972).

30 M. W. Price and T. E. Hubbert, "Mechanical and Thermal Properties of Four IR Dome Materials," Southern Research Institute Report No. SRI-EAS-87-1272-6225, 1988 (unpublished see ref. 1).

31 R. W. G. Wyckoff, *Crystal Structures*, Vol. 2, 2 ed. (John Wiley & Sons, New York, 1963), p. 2.

32 M. G. Paton and E. N. Maslen, Acta Crystallogr. **19,** 307 (1965).

33 V. Askarpour, M. H. Manghnani, S. Fassbender, and A. Yoneda, Phys. Chem. Miner. **19,** 511 (1993).

Table I: Room temperature elastic constants of yttria

Modulus	This study	Aleksandrov, et al.[15,16]
C_{11} (GPa)	223.6 ± 0.6	227
C_{44} (GPa)	74.6 ± 0.5	68.6
C_{12} (GPa)	112.4 ± 1.0	138

Table II: Measured and calculated bulk properties of yttria at room conditions

K (GPa)	G_V (GPa)	G_R (GPa)	G_{VRH} (GPa)	$G_{Polycrystal}$ (GPa)	Ref.
149.5 ± 1.0	67.0 ± 0.8	65.6 ± 0.8	66.3 ± 0.8		This Study
167.7	59.0	56.4	57.7		15,16
148.9 ± 3.0				69.2 ± 2.0	13
145				67	1
146.2				69.42	8

Table III: Measured elastic constants for yttria at elevated temperatures

T (°C)	C_{11} (GPa)	C_{44} (GPa)	C_{12} (GPa)	K (GPa)	G_{VRH} (GPa)
22[a]	225.1	74.6	113.6	150.8	66.4
22[b]	222.4	73.7	110.8	148.0	66.0
200	221.1	73.4	110.6	147.5	65.5
400	216.9	72.8	108.0	144.3	64.8
600	212.2	70.4	106.7	141.8	62.7
800[a]	206.2	69.0	102.5	137.1	61.5
800[b]	205.3	67.3	103.2	137.2	60.3
1000	199.1	65.3	99.5	132.7	58.6
1200	193.6	63.7	97.9	129.8	56.8

[a] Experimental run to 800°C. Errors for this run are $\pm$0.7% for C_{11}, $\pm$3.3% for C_{44}, and $\pm$1.9% for C_{12}.

[b] Experimental run from 800°C to 1200°C. Errors for this run are $\pm$0.9% for C_{11}, $\pm$3.4% for C_{44}, and $\pm$3.5% for C_{12}.

Table IV: Fitted temperature derivatives for single-crystal and bulk elastic properties of yttria

Modulus	Temperature Derivative (MPa/ °C)
C_{11}	-26 ± 3
C_{44}	-9 ± 2
C_{12}	-13 ± 2
K	-17 ± 2
G_{VRH}	-8 ± 2

Table V: Comparison of changes in elasticity and anisotropy with temperature for several oxides

All temperature derivatives in (10^{-4}/K)	Y_2O_3 pres. study	MgO [16]	BaO [16]	$Y_3Al_5O_{12}$ (YAG) [16]
$(dC_{11}/dT)/C_{11}$	-1.14 ± 0.13	-2.0	-3.7	-0.9
$(dC_{44}/dT)/C_{44}$	-1.21 ± 0.24	-0.8	-1.16	-0.7
$(dC_{12}/dT)/C_{12}$	-1.11 ± 0.18	0.7	0	-0.52
A	0.170 ± 0.015	0.37	-0.07	0.02
dA/dT	0 ± 0.1	2.1	2.8	0.3

Figure 1: Schematic of symmetric platelet scattering geometry

Figure 2: Room temperature velocities in the {100} plane of yttria.

Figure 3: Single-crystal elastic moduli at high temperature

Figure 4: Variation of the bulk modulus of yttria with temperature

Figure 5: Variation of the shear modulus of yttria with temperature

Figure 6: Variation of the Young's modulus of yttria with temperature.

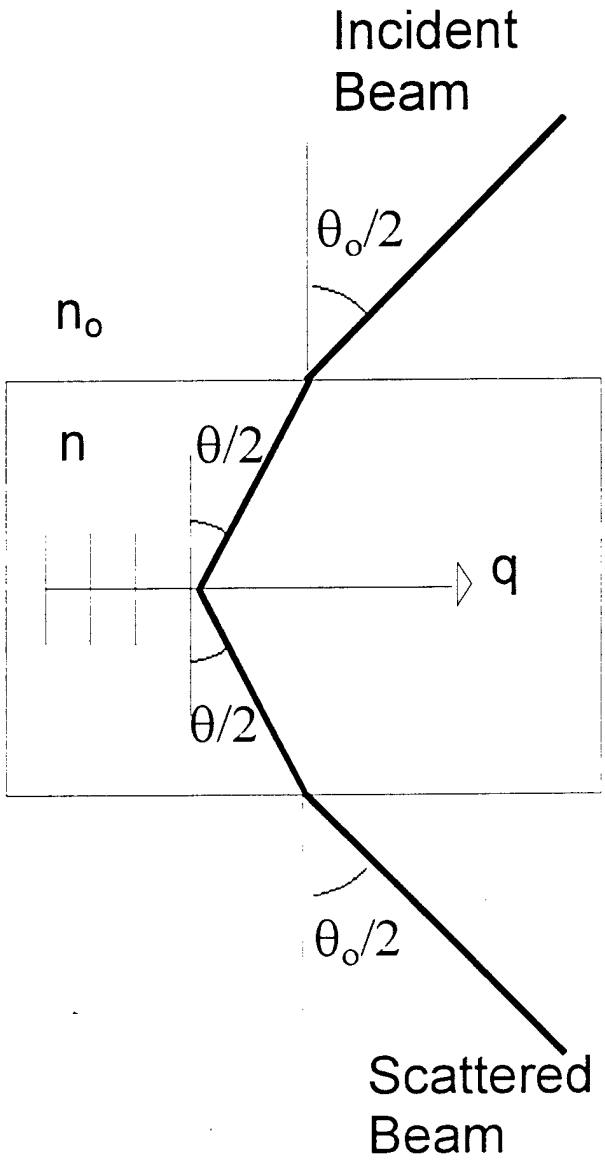


Figure 1 Palko, Kriven, Sinogeikin, Bass, Sayir (2000)

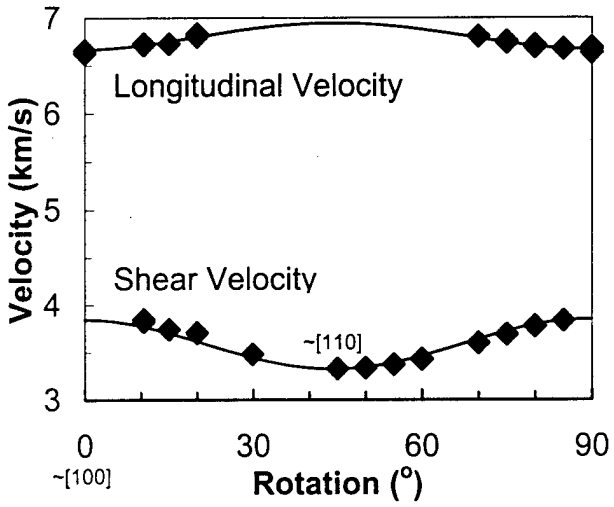


Figure 2 Palko, Kriven, Sinogeikin, Bass, Sayir (2000)

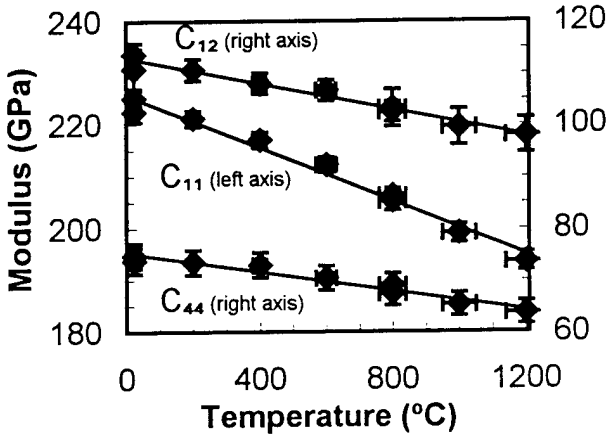


Figure 3 Palko, Kriven, Sinogeikin, Bass, Sayir (2000)

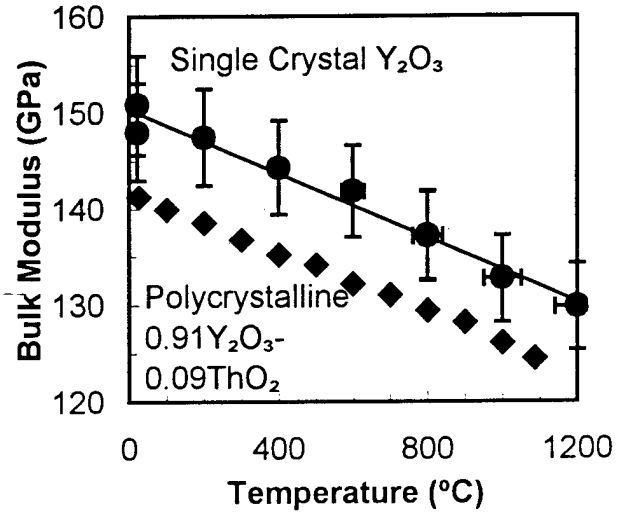


Figure 4 Palko, Kriven, Sinogeikin, Bass, Sayir (2000)

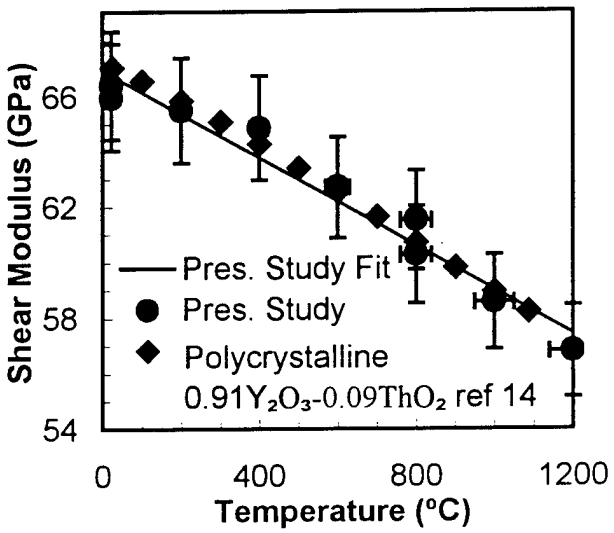


Figure 5 Palko, Kriven, Sinogeikin, Bass, Sayir (2000)

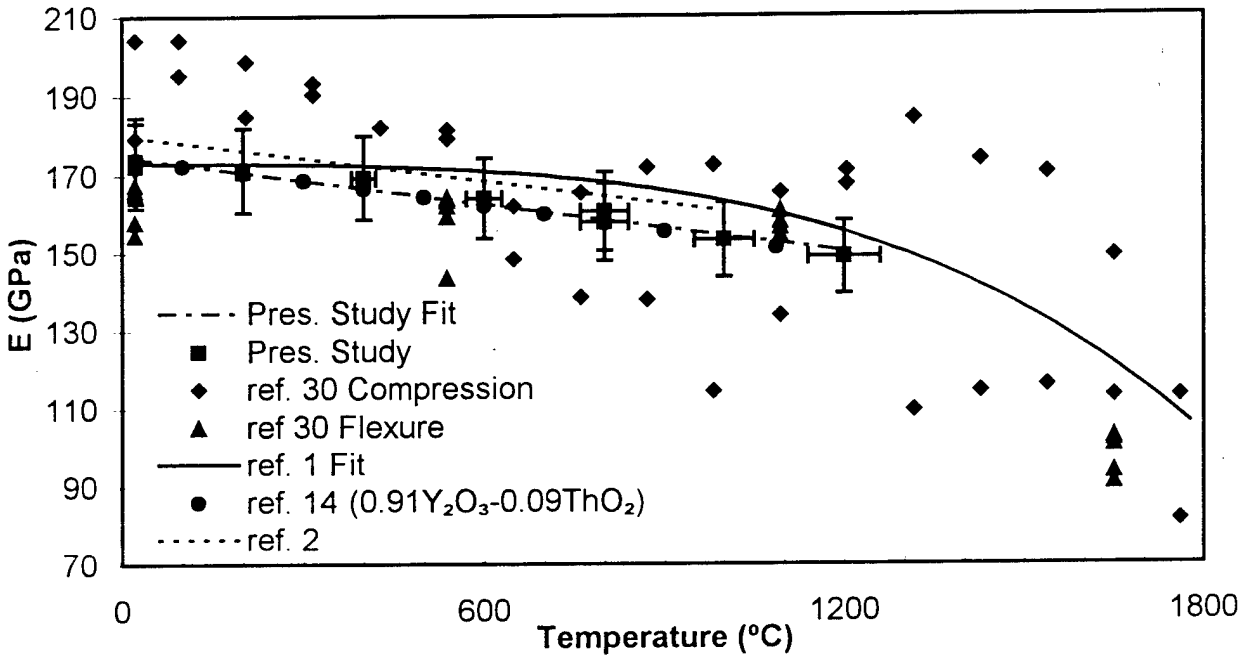


Figure 6 Palko, Kriven, Sinogeikin, Bass, Sayir (2000)

Extended Table I: Room temperature velocities for yttria

Sample Face Normal			Propagation Direction			Vl (m/s)	Vs (m/s)
0.0228	0.0007	0.9997	0.0758	0.9971	-0.0024	6671.0	3834.2
0.0228	0.0007	0.9997	0.1624	0.9867	-0.0044	6688.4	3772.8
0.0228	0.0007	0.9997	0.1624	0.9867	-0.0044	6712.7	3779.8
0.0228	0.0007	0.9997	0.2478	0.9688	-0.0063	6750.8	3689.5
0.0228	0.0007	0.9997	0.2478	0.9688	-0.0063	6735.8	3690.7
0.0228	0.0007	0.9997	0.3313	0.9435	-0.0082	6802.9	3599.3
0.0228	0.0007	0.9997	0.9355	0.3526	-0.0216	6830.0	3711.4
0.0228	0.0007	0.9997	0.9355	0.3526	-0.0216	6802.3	3703.3
0.0228	0.0007	0.9997	0.9627	0.2697	-0.0221	6724.2	3742.8
0.0228	0.0007	0.9997	0.9809	0.1933	-0.0225	6712.0	3823.7
0.0228	0.0007	0.9997	0.9809	0.1933	-0.0225	6728.2	3848.0
0.0228	0.0007	0.9997	0.4900	0.8716	-0.0118		3430.4
0.0228	0.0007	0.9997	0.4900	0.8716	-0.0118		3425.8
0.0228	0.0007	0.9997	0.5641	0.8256	-0.0134		3371.4
0.0228	0.0007	0.9997	0.6339	0.7733	-0.0150		3335.5
0.0228	0.0007	0.9997	0.6989	0.7151	-0.0164		3327.4
0.0228	0.0007	0.9997	0.8610	0.5083	-0.0200		3480.1
0.0228	0.0007	0.9997	0.9997	0.0113	-0.0228	6629.4	
0.0228	0.0007	0.9997	0.9997	0.0113	-0.0228	6658.3	
0.0228	0.0007	0.9997	-0.0113	0.9999	-0.0004	6686.1	

Extended Table I (Continued)

Sample Face Normal			Propagation Direction			Vl (m/s)	Vs (m/s)
0.0228	0.0007	0.9997	-0.0113	0.9999	-0.0004	6665.2	
0.0228	0.0007	0.9997	-0.0113	0.9999	-0.0004	6629.4	

Extended Table II: Velocities used in calculation of constants for yttria to 800 degrees Celsius

Sample Face Normal			**Propagation Direction**			**Vl (m/s)**	**Vs (m/s)**
Room temperature (~20 degrees Celsius)							
0.0228	0.0007	0.9997	0.0053	1.0000	-0.0008	6678.5	0.0
0.0228	0.0007	0.9997	0.0053	1.0000	-0.0008	6679.6	0.0
0.0228	0.0007	0.9997	0.1788	0.9839	-0.0047	6722.2	3792.3
0.0228	0.0007	0.9997	0.1788	0.9839	-0.0047	6730.1	3783.3
0.0228	0.0007	0.9997	0.3469	0.9379	-0.0085	6835.5	3619.6
0.0228	0.0007	0.9997	0.3469	0.9379	-0.0085	6806.3	3615.1
0.0228	0.0007	0.9997	0.4430	0.8965	-0.0107	0.0	3495.1
0.0228	0.0007	0.9997	0.5044	0.8634	-0.0121	0.0	3442.4
0.0228	0.0007	0.9997	0.5044	0.8634	-0.0121	0.0	3435.7
0.0228	0.0007	0.9997	0.5320	0.8466	-0.0127	0.0	3417.7
0.0228	0.0007	0.9997	0.5919	0.8059	-0.0140	0.0	3370.7
0.0228	0.0007	0.9997	0.6598	0.7512	-0.0155	0.0	3344.9
0.0228	0.0007	0.9997	0.6982	0.7157	-0.0164	0.0	3335.9
0.0228	0.0007	0.9997	0.7106	0.7034	-0.0167	0.0	3338.1
0.0228	0.0007	0.9997	0.7106	0.7034	-0.0167	0.0	3341.5
0.0228	0.0007	0.9997	0.7228	0.6909	-0.0169	0.0	3331.4
0.0228	0.0007	0.9997	0.7802	0.6252	-0.0182	0.0	3350.5
0.0228	0.0007	0.9997	0.8317	0.5548	-0.0193	0.0	3399.8

Extended Table II (Continued)

Sample Face Normal			Propagation Direction			Vl (m/s)	Vs (m/s)
Temperature = 200 degrees Celsius							
0.0228	0.0007	0.9997	0.0053	1.0000	-0.0008	6631.4	0.0
0.0228	0.0007	0.9997	0.0053	1.0000	-0.0008	6628.0	0.0
0.0228	0.0007	0.9997	0.1788	0.9839	-0.0047	6692.0	3754.1
0.0228	0.0007	0.9997	0.1788	0.9839	-0.0047	6695.3	3759.7
0.0228	0.0007	0.9997	0.3469	0.9379	-0.0085	6753.6	3614.0
0.0228	0.0007	0.9997	0.3469	0.9379	-0.0085	6760.4	3611.7
0.0228	0.0007	0.9997	0.5044	0.8634	-0.0121	0.0	3431.2
0.0228	0.0007	0.9997	0.5044	0.8634	-0.0121	0.0	3436.8
0.0228	0.0007	0.9997	0.7106	0.7034	-0.0167	0.0	3319.1
0.0228	0.0007	0.9997	0.7106	0.7034	-0.0167	0.0	3319.1
Temperature = 400 degrees Celsius							
0.0228	0.0007	0.9997	0.0053	1.0000	-0.0008	6594.4	0.0
0.0228	0.0007	0.9997	0.0053	1.0000	-0.0008	6591.0	0.0
0.0228	0.0007	0.9997	0.1788	0.9839	-0.0047	6634.8	3754.1
0.0228	0.0007	0.9997	0.1788	0.9839	-0.0047	6640.4	3760.9
0.0228	0.0007	0.9997	0.3469	0.9379	-0.0085	6720.0	3590.4
0.0228	0.0007	0.9997	0.3469	0.9379	-0.0085	6699.8	3591.5
0.0228	0.0007	0.9997	0.5044	0.8634	-0.0121	0.0	3430.1
0.0228	0.0007	0.9997	0.5044	0.8634	-0.0121	0.0	3426.7

Extended Table II (Continued)

Sample Face Normal			Propagation Direction			Vl (m/s)	Vs (m/s)
Temperature = 400 degrees Celsius							
0.0228	0.0007	0.9997	0.7106	0.7034	-0.0167	0.0	3302.3
0.0228	0.0007	0.9997	0.7106	0.7034	-0.0167	0.0	3301.1
Temperature = 600 degrees Celsius							
0.0228	0.0007	0.9997	0.0053	1.0000	-0.0008	6526.0	0.0
0.0228	0.0007	0.9997	0.0053	1.0000	-0.0008	6526.0	0.0
0.0228	0.0007	0.9997	0.1788	0.9839	-0.0047	6581.0	3695.8
0.0228	0.0007	0.9997	0.1788	0.9839	-0.0047	6579.8	3702.6
0.0228	0.0007	0.9997	0.3469	0.9379	-0.0085	6658.3	3540.0
0.0228	0.0007	0.9997	0.3469	0.9379	-0.0085	6656.1	3553.4
0.0228	0.0007	0.9997	0.5044	0.8634	-0.0121	0.0	3365.0
0.0228	0.0007	0.9997	0.5044	0.8634	-0.0121	0.0	3368.4
0.0228	0.0007	0.9997	0.7106	0.7034	-0.0167	0.0	3273.1
0.0228	0.0007	0.9997	0.7106	0.7034	-0.0167	0.0	3260.8
Temperature = 800 degrees Celsius							
0.0228	0.0007	0.9997	0.0053	1.0000	-0.0008	6456.5	0.0
0.0228	0.0007	0.9997	0.0053	1.0000	-0.0008	6457.6	0.0
0.0228	0.0007	0.9997	0.1788	0.9839	-0.0047	6494.6	3682.4
0.0228	0.0007	0.9997	0.1788	0.9839	-0.0047	6495.7	3661.1
0.0228	0.0007	0.9997	0.3469	0.9379	-0.0085	6586.6	3524.3

Extended Table II (Continued)

Sample Face Normal			**Propagation Direction**			**Vl (m/s)**	**Vs (m/s)**
Temperature = 800 degrees Celsius							
0.0228	0.0007	0.9997	0.3469	0.9379	-0.0085	6575.3	3510.8
0.0228	0.0007	0.9997	0.5044	0.8634	-0.0121	0.0	3358.3
0.0228	0.0007	0.9997	0.5044	0.8634	-0.0121	0.0	3358.3
0.0228	0.0007	0.9997	0.7106	0.7034	-0.0167	0.0	3238.3
0.0228	0.0007	0.9997	0.7106	0.7034	-0.0167	0.0	3238.3

Extended Table III: Velocities used in calculation of constants for yttria to 1200 degrees Celsius

Sample Face Normal			Propagation Direction			Vl (m/s)	Vs (m/s)
Room temperature (~20 degrees Celsius)							
0.0228	0.0007	0.9997	-0.3506	0.9365	0.0074	0.0	3598.6
0.0228	0.0007	0.9997	-0.0092	1.0000	-0.0005	6640.5	0.0
0.0228	0.0007	0.9997	-0.0092	1.0000	-0.0005	6655.0	0.0
0.0228	0.0007	0.9997	0.1645	0.9864	-0.0044	6648.3	3811.4
0.0228	0.0007	0.9997	0.1645	0.9864	-0.0044	6673.0	3815.8
0.0228	0.0007	0.9997	0.3332	0.9428	-0.0082	6776.0	3653.4
0.0228	0.0007	0.9997	0.3332	0.9428	-0.0082	6781.6	3641.1
0.0228	0.0007	0.9997	0.4141	0.9102	-0.0101	0.0	3537.0
0.0228	0.0007	0.9997	0.4919	0.8706	-0.0118	0.0	3431.7
0.0228	0.0007	0.9997	0.4919	0.8706	-0.0118	0.0	3470.9
0.0228	0.0007	0.9997	0.4919	0.8706	-0.0118	0.0	3465.3
0.0228	0.0007	0.9997	0.5658	0.8244	-0.0135	0.0	3381.3
0.0228	0.0007	0.9997	0.6355	0.7719	-0.0150	0.0	3360.0
0.0228	0.0007	0.9997	0.7004	0.7136	-0.0164	0.0	3323.0
0.0228	0.0007	0.9997	0.7004	0.7136	-0.0164	0.0	3332.0
0.0228	0.0007	0.9997	0.7599	0.6498	-0.0178	0.0	3329.8
0.0228	0.0007	0.9997	0.8136	0.5811	-0.0189	0.0	3382.4
0.0228	0.0007	0.9997	0.8611	0.5080	-0.0200	0.0	3470.9

Extended Table III (Continued)

Sample Face Normal			Propagation Direction			Vl (m/s)	Vs (m/s)
Temperature = 800 degrees Celsius							
0.0228	0.0007	0.9997	-0.0092	1.0000	-0.0005	6449.0	0.0
0.0228	0.0007	0.9997	-0.0092	1.0000	-0.0005	6434.4	0.0
0.0228	0.0007	0.9997	0.1645	0.9864	-0.0044	6455.7	3660.2
0.0228	0.0007	0.9997	0.1645	0.9864	-0.0044	6473.6	3675.8
0.0228	0.0007	0.9997	0.3332	0.9428	-0.0082	6580.0	3493.3
0.0228	0.0007	0.9997	0.3332	0.9428	-0.0082	6547.5	3485.4
0.0228	0.0007	0.9997	0.4919	0.8706	-0.0118	0.0	3334.2
0.0228	0.0007	0.9997	0.4919	0.8706	-0.0118	0.0	3344.3
0.0228	0.0007	0.9997	0.7004	0.7136	-0.0164	0.0	3215.5
0.0228	0.0007	0.9997	0.7004	0.7136	-0.0164	0.0	3218.9
Temperature = 1000 degrees Celsius							
0.0228	0.0007	0.9997	-0.0092	1.0000	-0.0005	6372.8	0.0
0.0228	0.0007	0.9997	-0.0092	1.0000	-0.0005	6356.0	0.0
0 0228	0.0007	0.9997	0.1645	0.9864	-0.0044	6399.7	3631.0
0.0228	0.0007	0.9997	0.1645	0.9864	-0.0044	6389.6	3615.4
0.0228	0.0007	0.9997	0.3332	0.9428	-0.0082	6473.6	3457.4
0.0228	0.0007	0.9997	0.3332	0.9428	-0.0082	6452.3	3459.7
0 0228	0.0007	0.9997	0.4919	0.8706	-0.0118	0.0	3292.8
0.0228	0.0007	0.9997	0.4919	0.8706	-0.0118	0.0	3287.2

Extended Table III (Continued)

Sample Face Normal			Propagation Direction			Vl (m/s)	Vs (m/s)
Temperature = 1000 degrees Celsius							
0.0228	0.0007	0.9997	0.7004	0.7136	-0.0164	0.0	3194.2
0.0228	0.0007	0.9997	0.7004	0.7136	-0.0164	0.0	3185.3
Temperature = 1200 degrees Celsius							
0.0228	0.0007	0.9997	-0.0092	1.0000	-0.0005	6311.2	0.0
0.0228	0.0007	0.9997	-0.0092	1.0000	-0.0005	6259.7	0.0
0.0228	0.0007	0.9997	0.1645	0.9864	-0.0044	6315.7	3563.8
0.0228	0.0007	0.9997	0.1645	0.9864	-0.0044	6328.0	3560.5
0.0228	0.0007	0.9997	0.3332	0.9428	-0.0082	6424.3	3404.8
0.0228	0.0007	0.9997	0.3332	0.9428	-0.0082	6394.1	3414.9
0.0228	0.0007	0.9997	0.4919	0.8706	-0.0118	0.0	3233.4
0.0228	0.0007	0.9997	0.4919	0.8706	-0.0118	0.0	3244.6
0.0228	0.0007	0.9997	0.7004	0.7136	-0.0164	0.0	3138.2
0.0228	0.0007	0.9997	0.7004	0.7136	-0.0164	0.0	3148.3

J. Am. Ceram. Soc., submitted Dec 2000

Single Crystal Elastic Moduli of Mullite (~$2.5Al_2O_3 \cdot SiO_2$) to High Temperatures by Brillouin Spectroscopy

James W. Palko[a], Ali Sayir[b], Stanislav V. Sinogeikin[c], Waltraud M. Kriven[a,**], Jay D. Bass[c]

a – Department of Materials Science and Engineering, University of Illinois, Urbana, Illinois

b – NASA Glenn Research Center, Cleveland, Ohio

c – Department of Geology, University of Illinois, Urbana, Illinois

Abstract

The complete elastic tensor of mullite has been determined by brillouin spectroscopy at room temperature and elevated temperatures up to 1200 °C. Equivalent, isotropic moduli (bulk, shear, and Young's) have been calculated. The room temperature values obtained by Voigt-Reuss-Hill averaging are (in GPa): $K_{VRH} = 173.5 \pm 6.9$, $G_{VRH} = 88.0 \pm 3.5$, $E_{VRH} = 225.9 \pm 9.0$. All moduli show relatively gradual decreases with temperature. The temperature derivatives obtained for the equivalent, isotropoic moduli are (in MPa/K): $dK_{VRH}/dT = -17.5 \pm 2.5$, $dG_{VRH}/dT = -8.8 \pm 1.4$, $dE_{VRH}/dT = -22.6 \pm 2.8$. Substantial differences between bulk properties calculated from the single crystal measurements in this study and the properties reported in literature for polycrystalline sintered mullite are identified, indicating the importance of factors such as microstructure, intergranular phases, and composition to the elasticity of mullite ceramics.

** - Fellow American Ceramic Society

I. Introduction

Mullite is found in many common ceramics. More recently it has gained favor for use in advanced materials such as structural ceramic matrix composites as both a matrix and reinforcing phase. It has such desirable qualities as high temperature stability and oxidation resistance that make it ideal for use in applications such as gas turbine engines.[1]

Because of the long-term use of mullite and its technological importance,[2] many measurements have been made of its mechanical properties, including measurements of its elastic properties at ambient and elevated temperatures.[3-9] These have all concentrated, however, on bulk polycrystalline properties, and there are great discrepancies in the measured values.

Recently, mullite has become available in single-crystal or highly textured polycrystalline fiber form by use of a laser-heated float zone technique.[10] Such samples allow measurement of the single-crystal elastic properties of mullite. These single crystal measurements provide useful property data for the design of components using large single crystals (e.g. single crystal reinforcing fibers). They also yield information as to what degree the elastic properties of mullite ceramics are a result of the intrinsic properties of the mullite crystal as compared to characteristics that may depend on processing such as microstructure and intergranular phases, which are common in sintered mullite. Therefore, a detailed understanding of the single crystal elastic properties of mullite is extremely useful for a fundamental understanding of the mechanical properties of complex, alumino-silicate ceramics. Such single crystal measurements are made in this study using Brillioun scattering.

Recently, we have reported a full single crystal elastic tensor for mullite at room temperature and selected constants (C_{11}, C_{33}, C_{44}, C_{55}) to 1400°C using brillouin spectroscopy.[11]

This work gives a more accurate room temperature tensor than the previous work (due to a refinement of the sample crystal orientations) as well as the temperature dependence of the full tensor to 1200 °C also with improved accuracy.

II. Theory

Brillouin scattering is the inelastic scattering of light from acoustic waves, allowing the determination of the wave speed. It provides an ideal probe of the elastic properties of the single crystal mullite samples available (especially at high temperatures), requiring only small sample volumes (e.g. 100 x 100 x 50 μm) and no physical contact with the sample. It is capable of measuring the phonon velocities along many propagation directions in a single sample. Brillouin scattered light is shifted in frequency with respect to the incident light by a factor that is proportional to the velocity of the acoustic waves (Eq. 1).[12]

$$V = \left(\frac{\Delta\omega}{\omega}\right)\left(\frac{c}{2\,n\sin\left(\frac{\theta}{2}\right)}\right) \qquad (1)$$

Here V is the velocity of the acoustic wave, $\Delta\omega$ is the frequency shift of the scattered light, ω is the frequency of the incident light, c is the speed of light, n is the index of refraction of the sample, and θ is the scattering angle.

For this study, platelet geometry is used such that the sample has flat, parallel faces, the phonon propagates in the plane of the sample, and the face normals, incident, and scattered light rays all lie within a plane[13]. Figure 1 gives a schematic of the platelet scattering geometry. With

the symmetric platelet geometry, the scattering angle is easily defined, and no knowledge of the index of the refraction of the sample is necessary. This is particularly beneficial for high temperature studies where the variation of index of refraction with temperature is generally unknown and difficult to measure.

The elastic waves probed may be treated by a continuum mechanical analysis which relates their velocities along a given crystallographic direction to the elastic moduli and density of the material via Christoffel's equation (Eq. 2)[14].

$$\left|C_{ijkl}q_j q_l - \rho V^2 \delta_{ik}\right| = 0 \qquad (2)$$

C is the elasticity tensor for the material, q is a unit vector along the path of phonon propagation, ρ is the density, and δ is the Krönecker delta function. Since mullite is orthorhombic, 9 independent elastic constants (C_{11}, C_{22}, C_{33}, C_{44}, C_{55}, C_{66}, C_{12}, C_{13}, C_{23}) are required to describe its elastic tensor (in Voigt notation).

III. Experimental Procedure

(1) Brillouin Scattering System

For this study, an Ar^+ laser with a wavelength of 514.5 nm is used to illuminate the sample. Scattered light is analyzed by a 6-pass tandem Fabry-Perot interferometer. Figure 2 is a schematic of the system used to collect Brillouin spectra. The operation of the interferometer has been detailed elsewhere[15,16].

Room temperature work is performed with a 90° scattering angle. An Eularian cradle is used to rotate the sample around its face normal to access different phonon directions. The high temperature results of this study are obtained using a compact furnace mounted on the Eularian cradle, allowing multiple phonon directions to be collected without remounting the sample. The construction and operation of this furnace is described elsewhere.[17] An 80° scattering angle is used for the high temperature work.

(2) Samples

Samples are taken from a fiber grown using the laser-heated, float zone method[10]. Figure 3 shows side and cross sectional views of a representative mullite fiber. A definite growth face is apparent, forming a sawtooth pattern. X-ray analysis shows this to be the (010) face. Cleavage is occasionally observed along this plane, as is observed in natural mullite and sillimanite samples[18]. The fiber has a roughly elliptical cross section minus the growth facet. The roughness on the surface in Figure 3 (b) is due to the diamond saw cutting process. The fiber is for the most part optically clear, with occasional white streaks across its width, apparently consisting of bubbles or occlusions. These white streaks often coincide with the points of the sawtooth pattern along the fiber edge.

The fiber shows uniform extinction under cross polarized light when the polarization direction is nearly aligned or perpendicular to the fiber axis, regardless of rotation about this axis. When ground with parallel faces, some variation in interference color is noted occurring in bands across some samples. This may be a result of a slight change in index of refraction due to compositional variations (or possibly slight variations in thickness). Extinction is somewhat less uniform in cross sections of the fiber.

The composition of the mullite was determined with an electron microprobe (wavelength dispersive) by Dr. Ian Steele using natural kyanite as a standard. The average composition is listed in Table I along with unit cell parameters determined by X-ray diffraction for the mullite sample. The error quoted for composition is the standard deviation of values measured at 10 μm intervals along the length of a fiber section and 5 μm intervals across its width. Density is determined using Eq. 3 for the chemical formula of the unit cell.[19]

$$Al_2(Al_{2+2x}Si_{2-2x})O_{10-x} \qquad (3)$$

x is the average number of oxygen vacancies per unit cell. It is related to the Al_2O_3/SiO_2 molar ratio, $n(Al_2O_3/SiO_2)$ by Eq. 4.

$$x = \frac{2n(Al_2O_3/SiO_2) - 2}{2n(Al_2O_3/SiO_2) + 1} \qquad (4)$$

Initial X-ray diffraction analysis was performed by Ms. Joyce McMillian using a four-circle diffractometer. The X-ray analysis shows that the sample is actually a very highly textured polycrystal, as seen in Figure 4. This analysis verifies that the crystallites have orthorhombic symmetry with slightly varying orientations defined by small rotations about the c axis, which is coincident with the fiber axis. All the crystallites found lie within 5° of each other and the majority lie within 2°. There is no resolvable splitting in the c axis peaks. Lattice parameters for the sample are calculated by fitting the major peak for each scan. A total of six peaks are used in the calculation: (040),(400), $(00\bar{2})$,$(40\bar{2})$, $(04\bar{2})$,$(22\bar{2})$. The errors quoted encompass all cell

parameters calculated with five of the six peaks (i.e. the maximum and minimum values from six calculations with five peaks). The calculated unit cell angles deviate slightly from 90° (α = 90.4174°, β = 90.2971°, γ = 89.8230°), probably due to the small peaks in close proximity resulting from the highly oriented polycrystalline nature of the sample and large sample size. For the purpose of calculating the cell volume, the interaxial angles were fixed to $\alpha = \beta = \chi$ = 90°.

Separate platelets with approximate face normals of ~[0 1 0], ~[0 0 1], and ~[0.9744 0.2250 0] for velocity measurements were ground using a series of diamond and SiC abrasives ranging from 30 to 1 μm. (Normals and planes are given in an equidistant Cartesian coordinate system, not the orthorhombic lattice of mullite.) Machine grinding was used for some of the coarser steps and the finer polishing was completed by hand. Glass was placed around the sample as a sacrificial material to minimize rounding of the sample faces, which was less than 1.5° for the entire included angle of the face (usually < 1°). Nonparallelness between the faces was less than 0.5°, and the faces produced had a mirror finish with very few scratches visible at 40x magnification. Final dimensions of the samples taken lengthwise from the fiber, ~(100) and ~(010), were approximately 3 mm x 0.4 mm x 0.25 – 0.1 mm. Cross sectional samples, ~(001), had approximate diameters of 0.4 mm and thicknesses of 0.15 –0.1 mm. The orientations of the sample platelets were determined after grinding using X-ray precession photography.[20]

IV. Results

(1) Room Temperature Elasticity

158 separate velocities were measured at room temperature along 37 different crystallographic directions in three different planes(Figures 5, 6, and 7). From these velocities a full set of 9 elastic moduli, listed in Table II, have been determined using a linearized least-squares inversion procedure. This algorithm calculates velocities based on an intial set of preliminary C_{ij}'s (Eq. 2) along the same phonon propagation directions as those measured and then varies the elastic moduli so as to minimize the misfit between the calculated and measured velocities[21]. Velocities calculated from the moduli obtained appear as solid curves in Figures 5, 6, and 7. We note that the final best-fit solution is highly insensitive to the starting guess for the C_{ij}'s. Equivalent, isotropic moduli have been calculated using the Voigt, Reuss, and Voigt-Reuss-Hill averaging schemes (denoted by V, R, and VRH subscripts) and are listed in Table II.

The errors in Table II refer purely to the statistical error in the fit. Deviations from the nominal sample normals (~[0 1 0], ~[0 0 1], ~[0.9744 0.2250 0]) are less than ~4° for all samples. The higher symmetry sample normals are retained to simplify calculation of moduli and error analysis. The error resulting from misorientation of the sample (including rotation about the sample plane normal) is estimated to be less than $\pm$ 2% of the calculated moduli, and the uncertainty in density, on which the moduli are directly proportional, is $\pm$ 0.7%.

(2) High Temperature Elasticity

For high temperature moduli determinations, velocities were collected from each sample plane at 200 °C increments to 1200 °C. Figures 8, 9, and 10 show the calculated elastic longitudinal (e.g. C_{11}), shear (e.g. C_{44}), and cross (e.g. C_{12}) moduli along with best fit, least squares regression lines. High temperature constants are calculated at each temperature from 16 velocities collected along 9 directions (3 in each sample plane; one along each projection of the principle axes and one 45° between them). Linear temperature dependencies are suggested for

all single crystal moduli, with the possible exception of C_{23} which shows a large scatter with temperature. Linear decreases in E_{VRH}, G_{VRH}, and K_{VRH} are also indicated (Figures 11, 12, 13).

The high temperature constants are calculated directly from Christofel's equation assuming the same sample face normals as the room temperature calculations. C_{12} and C_{13} are determined from a weighted average of a single shear and longitudinal acoustic modes based on the sensitivity of the moduli to the specific velocity. [20] C_{23} is calculated only from the longitudinal mode due to difficulty in assigning a specific shear mode. This may account for some of the scatter in the data. A volume coefficient of thermal expansion of 15.8×10^{-6} /°C is used for the calculation of density at high temperature as obtained from the sum of linear expansion coefficients of the lattice parameters given by Schneider and Eberhard [22]. The temperature derivatives of the single crystal moduli and Voigt-Reuss-Hill average moduli are given in Table III. Errors quoted refer to the 95% confidence intervals for the slope of the linear fit.

V. Discussion

(1) Room Temperature Elasticity

The single-crystal moduli, for the most part, fall within the error bars of those previously reported.[11] The one significant discrepancy is C_{23} which was previously reported as 135 GPa based an orientation resulting from the symmetry of the velocity data itself. The current reorientation represents a change of 13° for one plane which affects C_{23}. The current value (142.3 GPa) is ~5% higher and is considered the more accurate. The other constants are clearly affected much less by this reorientation.

Sillimanite, Al_2SiO_5, which has a very similar crystal structure to mullite [23], shows similar elastic behavior. The relative magnitudes of the moduli by value is the same for both crystals, except for the exchange of C_{13} and C_{66}. Andalusite shows the same order in longitudinal constants when its a and b axes are exchanged, which is the transformation required to bring its structure into closest correspondence with mullite[23]. The bulk properties calculated for mullite and sillimanite (Table II) are similar, while andalusite has a smaller bulk modulus but larger shear and Young's moduli.

Bulk values calculated here for mullite agree well with the recent measurements of a polycrystalline mullite sample by Ledbetter et al.[9], as well as the polycrystalline Young's modulus measurements of Pentry [6]. There are, however, considerable differences among the values of elastic moduli reported for polycrystalline mullite (Table IV), and certain authors [7,8] have reported values that exceed even the Voigt bounds of the respective moduli calculated here. These should set an upper limit on the possible values for a polycrystalline aggregate of mullite. The discrepancy may be due to intergranular phases. Compositional differences may also play a role. The polycrystalline studies were performed on mullite samples with a lower alumina content ($3\ Al_2O_3 \bullet 2\ SiO_2$).

(2) High Temperature Elasticity

Comparisons with temperature derivatives of polycrystalline elastic properties given in the literature show significant differences (Table V). The derivative obtained for Young's modulus in this study is more negative than -8 MPa/°C as seen in the data of Wachtman for temperatures below 600°C[4]. (Note that the scale in Figure 11 for the literature data is twice as fine than for the current data, while in Figure 12 it is twice as coarse.) Ledbetter also reports a more gradual decrease in Young's modulus (-11 MPa/°C)[9]. These differences could result from

a glassy phase in the polycrystalline body. Silica glass is known to stiffen with temperature[24]. A similar effect may occur with an intergranular glass phase, thereby mitigating the reduction in stiffness of the mullite grains. The temperature derivative of the shear modulus from the present study, however, is much smaller than -30 MPa/°C which is suggested by a linear fit to Wygant's data.[3] This may be due to a low melting (or more rapidly softening) intergranular phase. Ledbetter reports an extremely gradual -3.3 MPa/°C temperature derivative of shear modulus as well as a bulk modulus temperature derivative of -20 MPa/°C[9]. All values from Ledbetter are for room temperature and are corrected to zero porosity. The temperature behavior of mullite ceramics is clearly affected, and possibly dominated, by properties other than those intrinsic to the crystalline mullite itself.

VI. Conclusions

The full elastic tensor of mullite has been determined at room and elevated temperatures to 1200 °C. Room temperature values show close correspondence with structural analogs, sillimanite and andalusite. Bulk elastic properties calculated from the single crystal moduli agree well with some measurements on polycrystalline mullite[6,9], but there are substantial differences with much published data. In particular some authors report values[7,8] that exceed the maximum possible limit (Voigt bound) for average moduli calculated here, suggesting that intergranular phases and composition may play a very large role in determining the elastic properties of nominally pure mullite ceramics.

High temperature measurements were made in 200 °C intervals to 1200°C. A relatively gradual linear decrease was noted in all moduli with temperature. The temperature derivatives of bulk properties calculated from the single crystal moduli do not correspond well with much of

the data in literature, again suggesting that intergranular phases are important in the elasticity of mullite ceramics. Phases having behavior at high temperature much different than mullite, such as stiffening or rapid softening with temperature, are suggested by this data.

Acknowledgments:

The work of J. W. Palko was supported by the Fannie and John Hertz Foundation graduate fellowship. X-ray work was performed by J. McMillan at the Center for Microanalysis of Materials at UIUC. Electron microprobe analysis was conducted by Dr. I. Steele at the University of Chicago. This work was partially supported by a United States Air Force Office of Scientific Research AASERT Grant, under contract number F49620-97-1-0427 and NSF grant EAR-96-14416.

References

1 U. Steinhauser, W. Braue, J. Gootring, B. Kanka, and H. Schneider, "A New Concept for Thermal Protection of All-Mullite Composites in Combustion Chambers," J. Europ. Ceram. Soc **20** 651-658 (2000).

2 A. J. Skoog and R. E. Moore, "Refractory of the Past for the Future: Mullite and Its Use as a Bonding Phase," Am. Ceram. Soc. Bull. **67** [7] 1180-1185 (1988).

3 J. F. Wygant, "Elastic and Flow Properties of Dense, Pure Oxide Refractories," J. Am. Ceram. Soc. **34** [12] 374-380 (1951).

4 J. B. Wachtman and D. G. Lam, "Young's Modulus of Various Refractory Materials as a Function of Temperature," J. Am. Ceram. Soc. **42** [5] 254-260 (1959).

5 J. E. Fenstermacher and F. A. Hummel, "High-Temperature Mechanical Properties of Ceramic Materials: IV Sintered Mullite Bodies," J. Am. Ceram. Soc. **44** [6 June] 284-289 (1961).

6 R. A. Pentry, D. P. H. Hasselman, and R. M. Spriggs, "Young's Modulus of High-Density Polycrystalline Mullite," J. Am. Ceram. Soc. **55** 169-170 (1972).

7 M. G. M. U. Ismail, Z. Nakai, and S. Shigeyuki, "Microstructure and Mechanical Properties of Mullite Prepared by the Sol-Gel Method," Comm. Am. Ceram. Soc. **70** [1] C7-8 (1987).

8 W. H. Kelly, A. N. Palazotto, R. Ruh, J. K. Heuer, and A. Zangvil, "Thermal Shock Resistance of Mullite and Mullite-ZrO_2-SiC Whisker Composites," Ceram. Engr. & Sci. Proc. **18** [3] 195-203 (1997).

9 H. Ledbetter, S. Kim, D. Balzar, S. Crudele, and W. Kriven, "Elastic Properties of Mullite," J. Am. Ceram. Soc. **81** [4] 1025-1028 (1998).

10 A. Sayir and S. C. Farmer, "Directionally Solidified Mullite Fibers," Mat. Res. Soc. Sym. Proc. **365** 11-20 (1995).

11 W. M. Kriven, J. W. Palko, S. Sinogeikin, J. D. Bass, A. Sayir, G. Brunauer, H. Boysen, F. Frey, and J. Schneider, "High Temperature Single Crystal Properties of Mullite," J. Europ. Ceram. Soc. **19** 2529-2541 (1999).

12 G. B. Benedek and K. Fritsch, "Brillouin Scattering in Cubic Crystals," Phys. Rev. **149** [2] 647-662 (1966).

13 E. S. Zouboulis and M. Grimsditch, "Refractive Index and Elastic Properties of Single-crystal Corundum (α-Al_2O_3) up to 2100 K," J. Appl. Phys. **70** [2] 772-776 (1991).

14 L. D. Landau and E. M. Lifshitz, *Theory of Elasticity* (Pergamon Press, London, 1959), p. 104.

15 J. D. Bass, "Elasticity of Grossular and Spessartite Garnets by Brillouin Spectroscopy," J. Geophys. Res. **94** 7621-7628 (1989).

16 S. V. Sinogeikin, J. D. Bass, and T. Katsura, "Sound Velocities and Elastic Properties of Fe-bearing Wadsleyite and Ringwoodite," J. Geophys. Res. **103** [B9] 20,819-825 (1998).

17 S. V. Sinogeikin, J. M. Jackson, B. O'Neill, J. W. Palko, and J. D. Bass, "Compact High-Temperature Cell for Brillouin Scattering Measurements," Rev. Sci. Instrum. **71** [1] 201-206 (2000).

18 W. D. Nesse, *Introduction to Optical Mineralogy* (Oxford University Press, New York, 1986), p. 170-171.

19 W. M. Kriven and J. A. Pask, "Solid Solution Range and Microstructure of Melt-Grown Mullite," J. Am. Ceram. Soc. **66** [9] 649-654 (1983).

20 J. Palko, M.S. Thesis, University of Illinois, Urbana-Champaign, 2000.

21 D. J. Weidner and H. R. Carleton, "Elasticity of Coesite," J. Geophys. Res. **82** [8] 1334-1346 (1977).

22 H. Schneider and E. Eberhard, "Thermal Expansion of Mullite," J. Am. Ceram. Soc. **73** [7] 2073-2076 (1990).

23 H. Schneider, K. Okada, and J. A. Pask, *Mullite and Mullite Ceramics* (John Wiley & Sons, Chichester, 1994), p. 1-8.

24 J. D. Bass, "Elasticity of Minerals, Glasses, and Melts"; pp. 45-63 in *Mineral Physics and Crystallography: A Handbook of Physical Constants*. edited by T. J. Ahrens (American Geophysical Union, Washington, DC, 1995).

25 M. T. Vaughan and D. J. Weidner, "The Relationship of Elasticity and Crystal Structure in Andalusite and Sillimanite," Phys. Chem. Miner. **3** 1-12 (1978).

26 M. I. Osendi, B. A. Bender, and D. Lewis, III, "Microstructure and Mechanical Properties of Mullite-Silicon Carbide Composites," J. Am. Ceram. Soc. **72** [6] 1049-1054 (1989).

Figure 1: Schematic of platelet scattering geometry

Figure 2: Schematic of Brillouin scattering system.

Figure 3: Optical micrographs of mullite sample (a) lengthwise and (b) in cross section

Figure 4: X-ray scan rotating sample around fiber axis with fixed 2θ

Figure 5: Room temperature velocities versus rotation in ~(100) plane

Figure 6: Room temperature velocities versus rotation in ~(010) plane

Figure 7: Room temperature velocities versus rotation in ~(001) plane

Figure 8: Single-crystal longitudinal moduli versus temperature

Figure 9: Single-crystal shear moduli versus temperature

Figure 10: Single-crystal cross moduli versus temperature

Figure 11: Young's modulus of mullite versus temperature

Figure 12: Shear modulus of mullite versus temperature

Figure 13: Bulk modulus of mullite versus temperature

Table I: Properties of mullite sample at room temperature

a (nm)	0.758 ± 0.001
b (nm)	0.767 ± 0.001
c (nm)	0.289 ± 0.001
Cell Volume (nm^3)	0.168 ± 0.001
Molar Al_2O_3/SiO_2 ratio	2.5 ± 0.1
Theoretical Density (g/cm^3)	3.11 ± 0.02

Table II: Room temperature moduli of mullite, andalusite, and sillimanite

Constant	Mullite	Sillimanite[25]	Andalusite[25]
C_{11} (GPa)	281.9 ± 0.7	287.3	233.4
C_{22} (GPa)	244.2 ± 0.9	231.9	289.0
C_{33} (GPa)	363.6 ± 1.0	388.4	380.1
C_{44} (GPa)	111.7 ± 0.6	122.4	99.5
C_{55} (GPa)	78.2 ± 0.5	80.7	87.8
C_{66} (GPa)	79.2 ± 0.5	89.3	112.3
C_{12} (GPa)	105.1 ± 1.0	94.7	81.4
C_{13} (GPa)	100.3 ± 1.3	83.4	116.2
C_{23} (GPa)	142.3 ± 1.6	158.6	97.7
K_V (GPa)	176.1	175.1	165.9
K_R (GPa)	171.0	166.4	158.0
K_{VRH} (GPa)	173.5	170.8	162.0
G_V (GPa)	90.0	95.1	100.4
G_R (GPa)	86.1	87.8	97.7
G_{VRH} (GPa)	88.0	91.5	99.1
E_V (GPa)	230.6	241.6	250.6
E_R (GPa)	221.2	224.0	243.0
E_{VRH} (GPa)	225.9	232.8	246.8

Table III: Fitted temperature derivatives for mullite to 1200°C

Modulus	**Temperature derivative (MPa/°C)**
C_{11}	-29.2 ± 3.2
C_{22}	-29.7 ± 1.6
C_{33}	-28.6 ± 4.2
C_{44}	-7.9 ± 1.1
C_{55}	-6.5 ± 0.9
C_{66}	-10.1 ± 0.9
C_{12}	-16.1 ± 0.5
C_{13}	-6.8 ± 1.4
C_{23}	-8.1 ± 10.5
K_{VRH}	-17.5 ± 2.5
G_{VRH}	-8.8 ± 1.4
E_{VRH}	-22.6 ± 2.8

Table IV: Bulk properties of polycrystalline mullite reported in literature

E (GPa)	**ν**	**G (GPa)**	**K (GPa)**	**Density**	**Ref.**
225.9		88.0	173.5	3110 kg/m^3	Pres. Study (VRH Avr)
		59			3
143.0				2780 kg/m^3	4
124					5
223.4 ± 5.5				Corrected to 100% (Spriggs)	6
224.1 ± 5.5				Corrected to 100% (Hasselman)	"
246				>98% (3150 kg/m^3)	7
194	0.276	76.0	144.3	95%	26
252	0.266	99.5	179.5		8
227.5	0.280	88.9	172.4	99.6%	9
229.1	0.280	89.5	173.9	Corrected to 100%	"

Table V: Comparison of temperature derivatives with literature values

dK/dT (MPa/K)	**dG/dT(MPa/K)**	**dE/dT (MPa/K)**	**Ref.**	**Notes**
-17.5 $\pm$ 2.5	-8.8 $\pm$ 1.4	-22.6 $\pm$ 2.8	Pres. Study	VRH average
				20 – 1200 °C
		-8	4	20 – 600 °C
-20	-3.3	-11	9	
	-30		3	

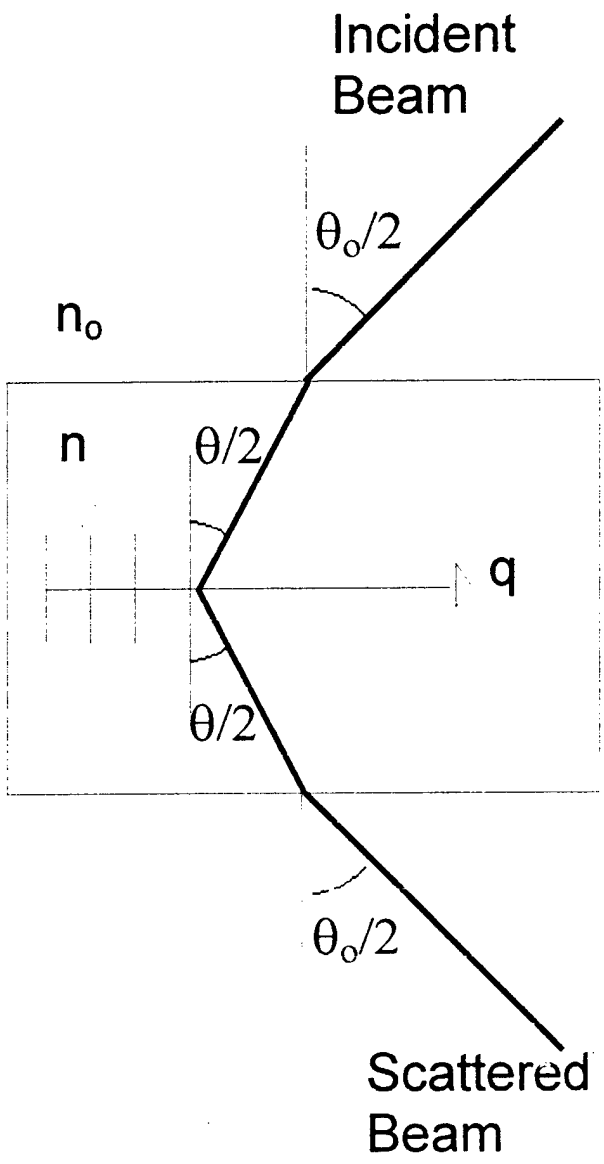


Figure 1: Schematic of platelet scattering geometry

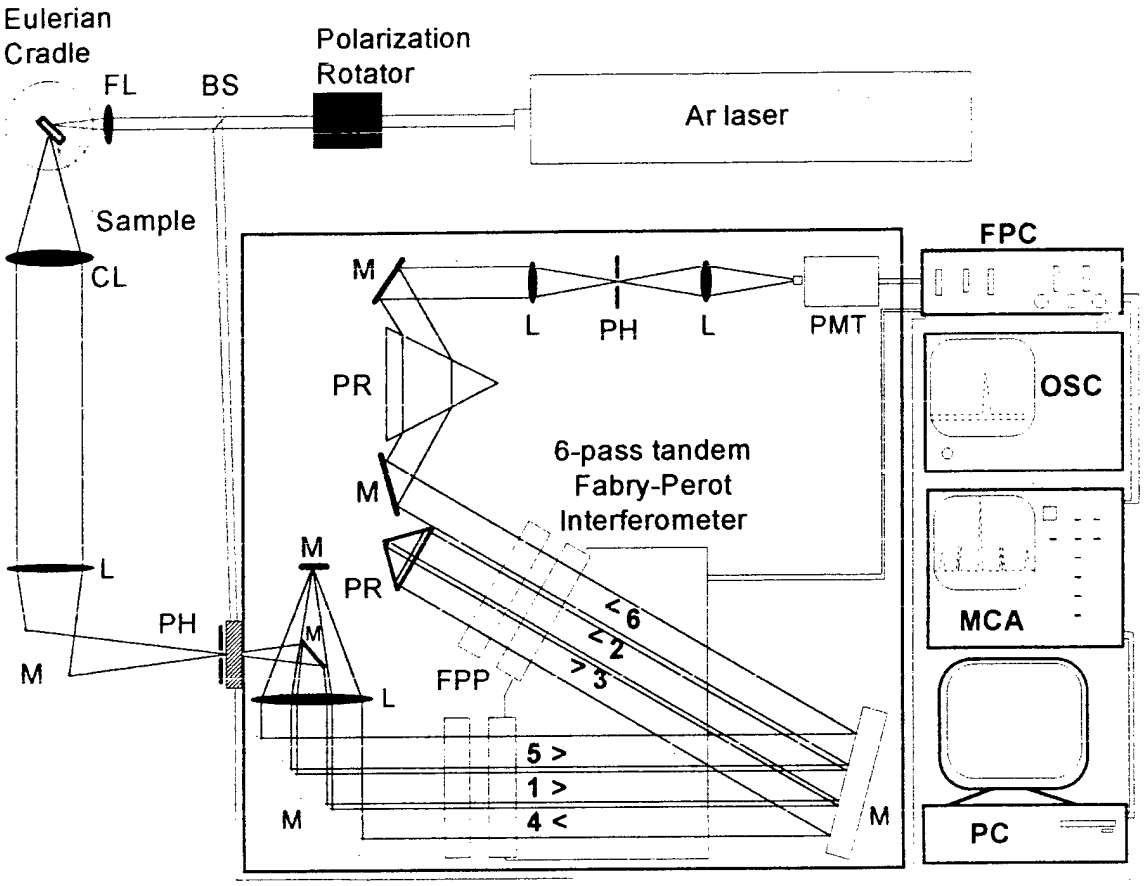


Figure 2: Schematic of the Brillouin spectroscopy system (BS = beam splitter, M = mirror, L = lens, FL = focusing lens, CL = collecting lens, PH = pinhole, PR = prism, FPC = Fabry-Perot controller, OSC = oscilloscope, MCA = multichannel analyzer, PC = Personal Computer, FPP = Fabry Perot Plates)

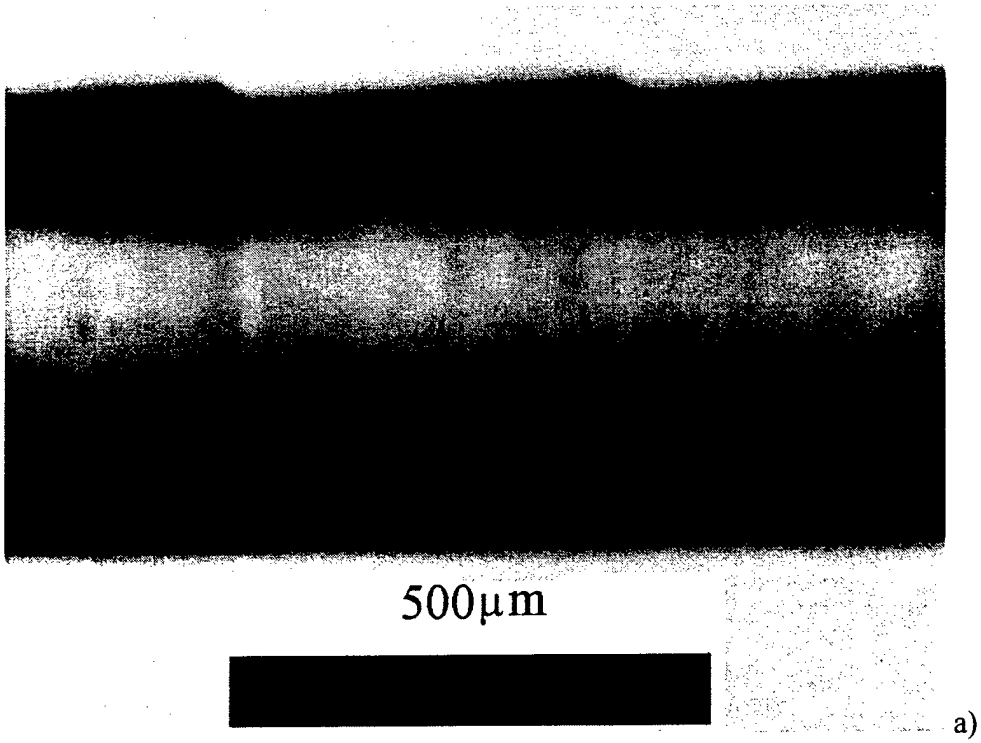


Figure 3: Optical micrographs of mullite sample (a) lengthwise and (b) in cross section

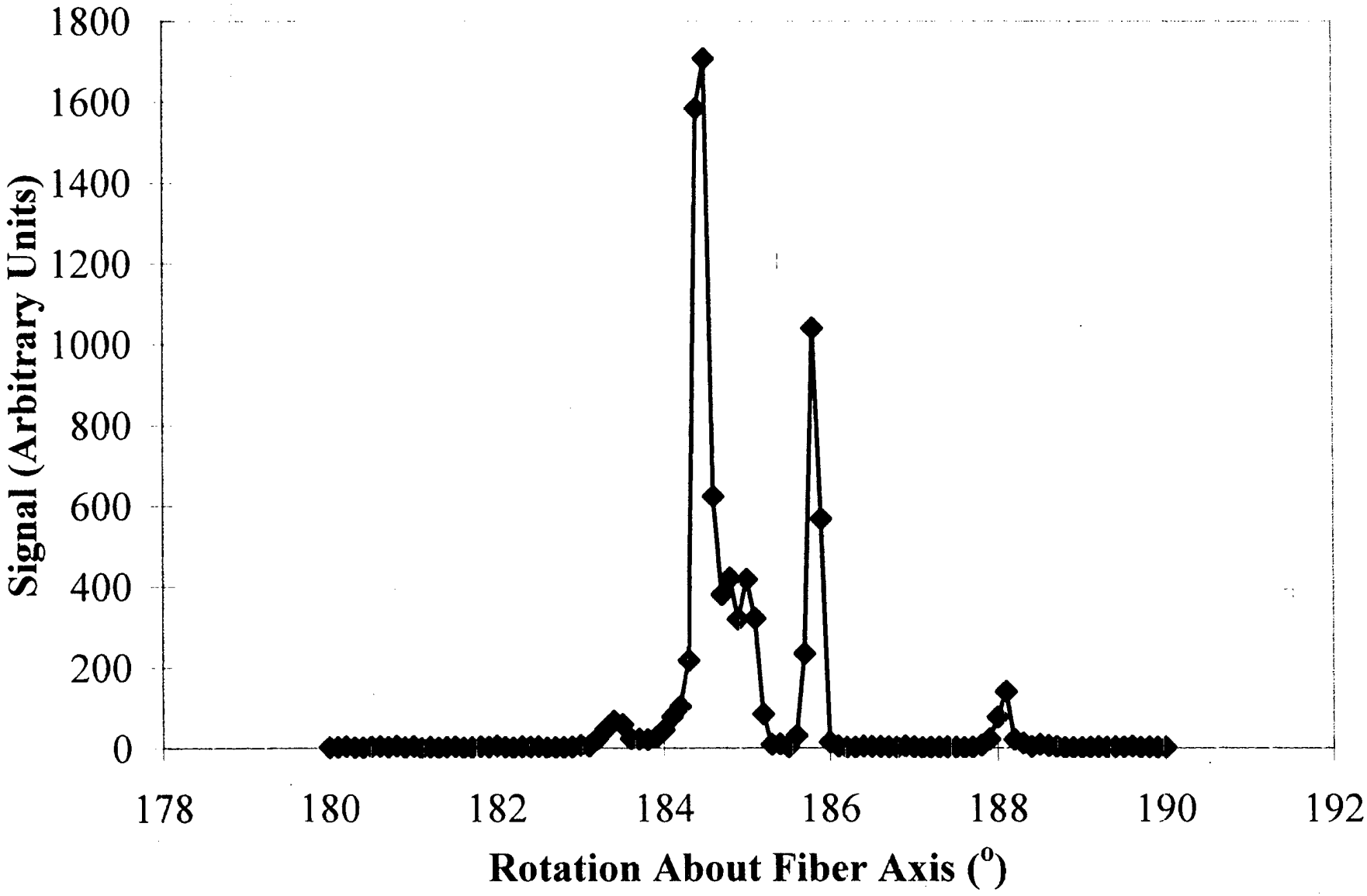


Figure 4: X-ray scan rotating sample around fiber axis with fixed 2θ

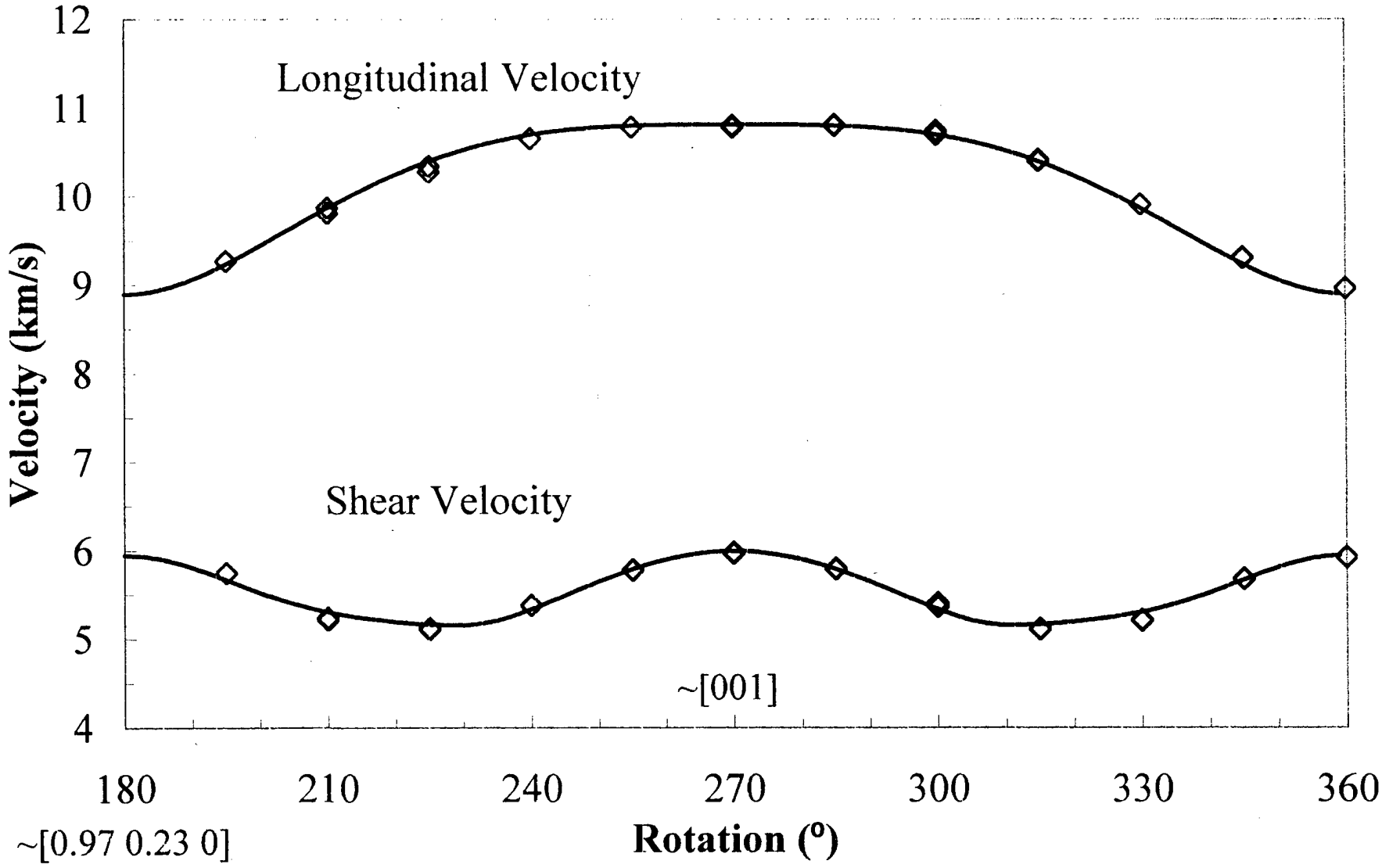


Figure 5: Room temperature velocities versus rotation in ~(100) plane

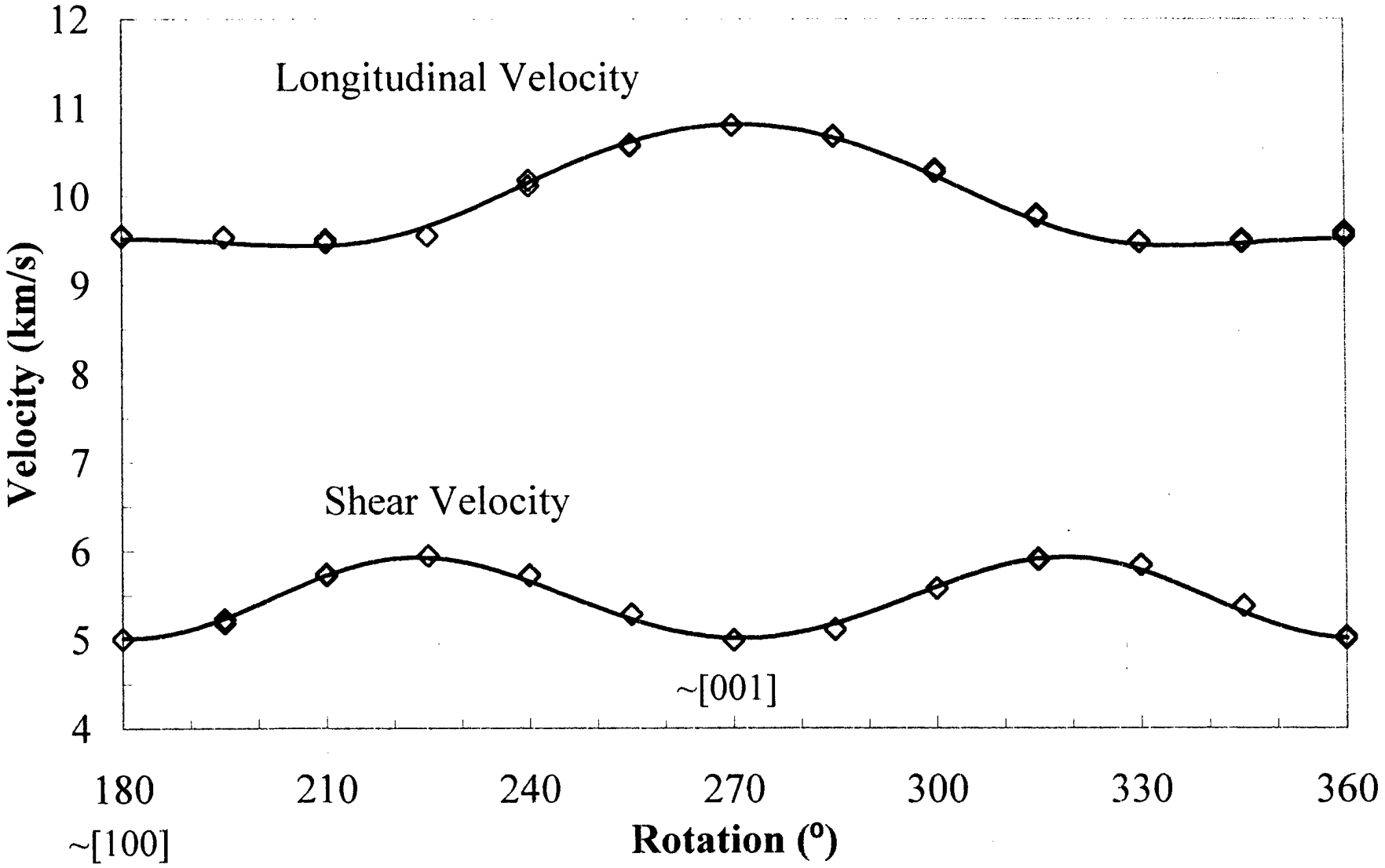


Figure 6: Room temperature velocities versus rotation in ~(010) plane

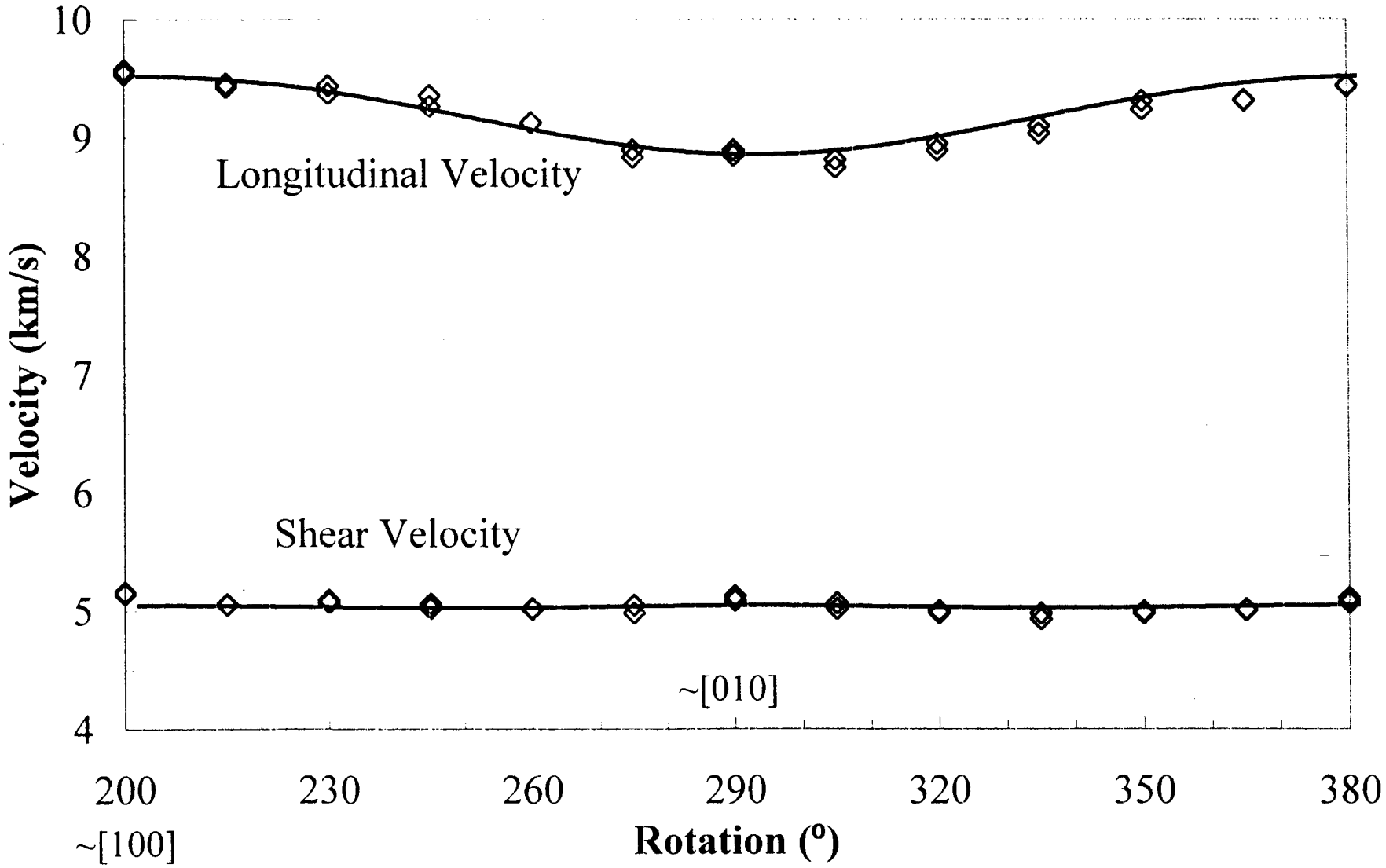


Figure 7: Room temperature velocities versus rotation in ~(001) plane

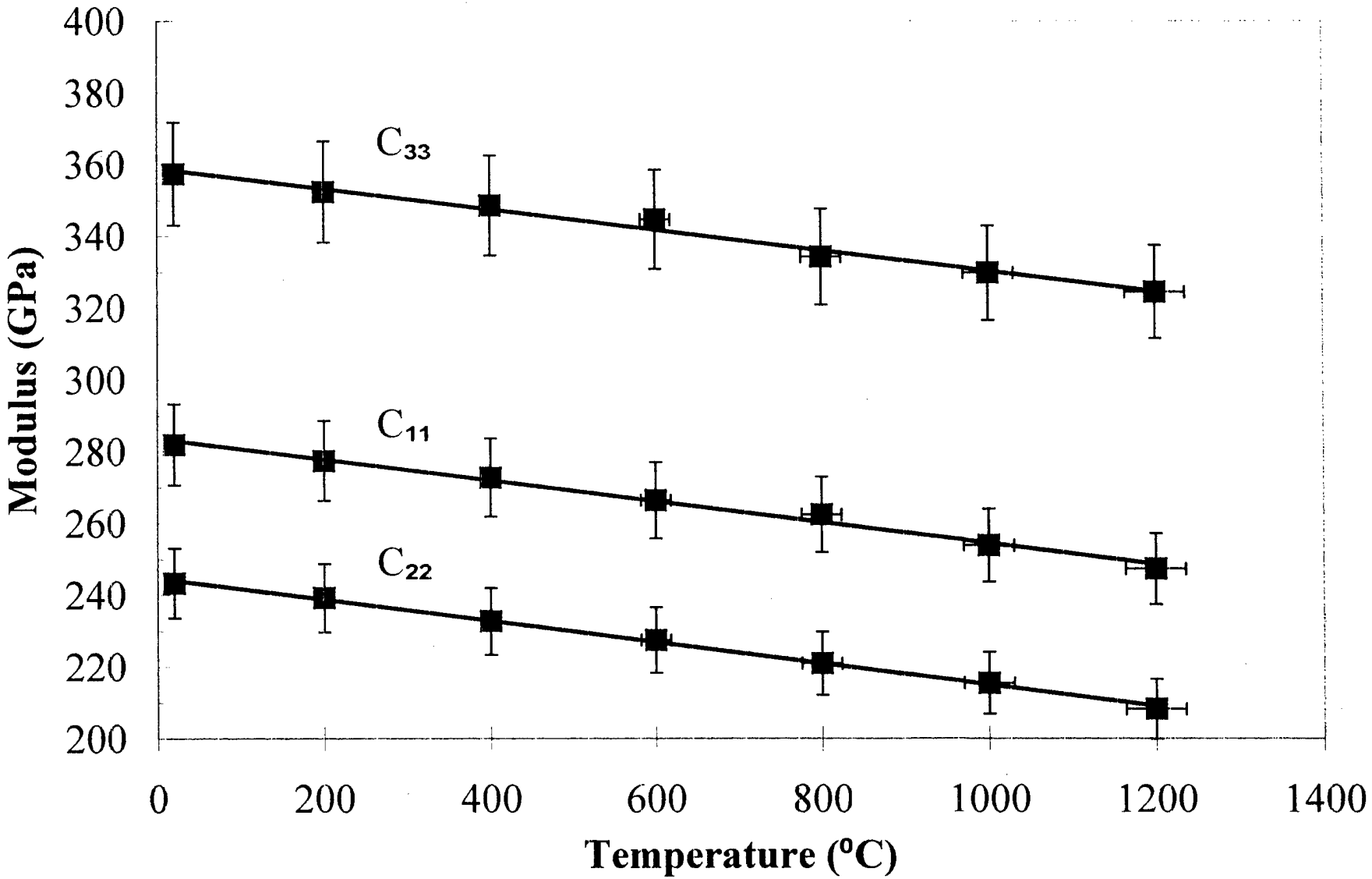


Figure 8: Single-crystal longitudinal moduli versus temperature

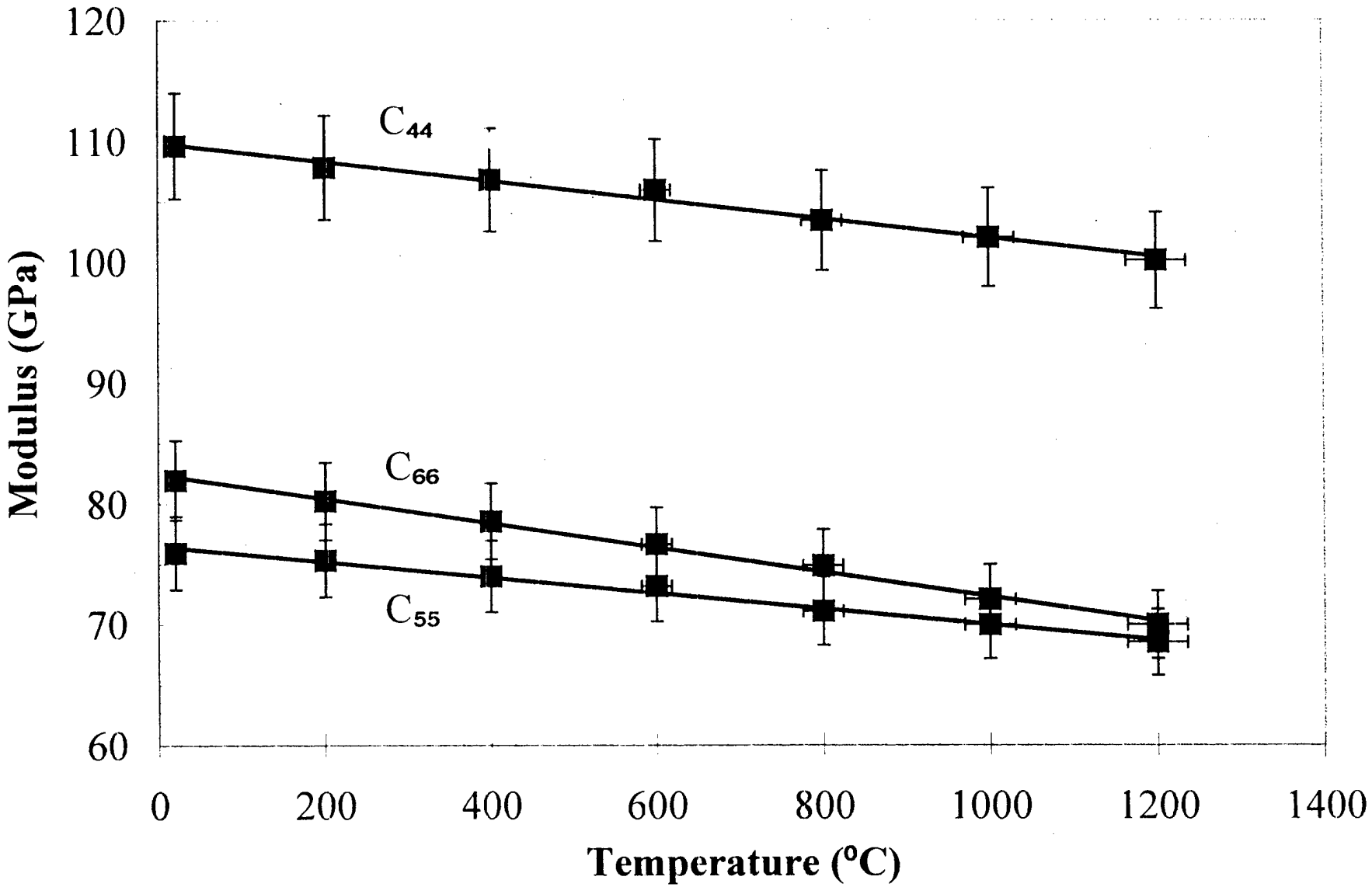


Figure 9: Single-crystal shear moduli versus temperature

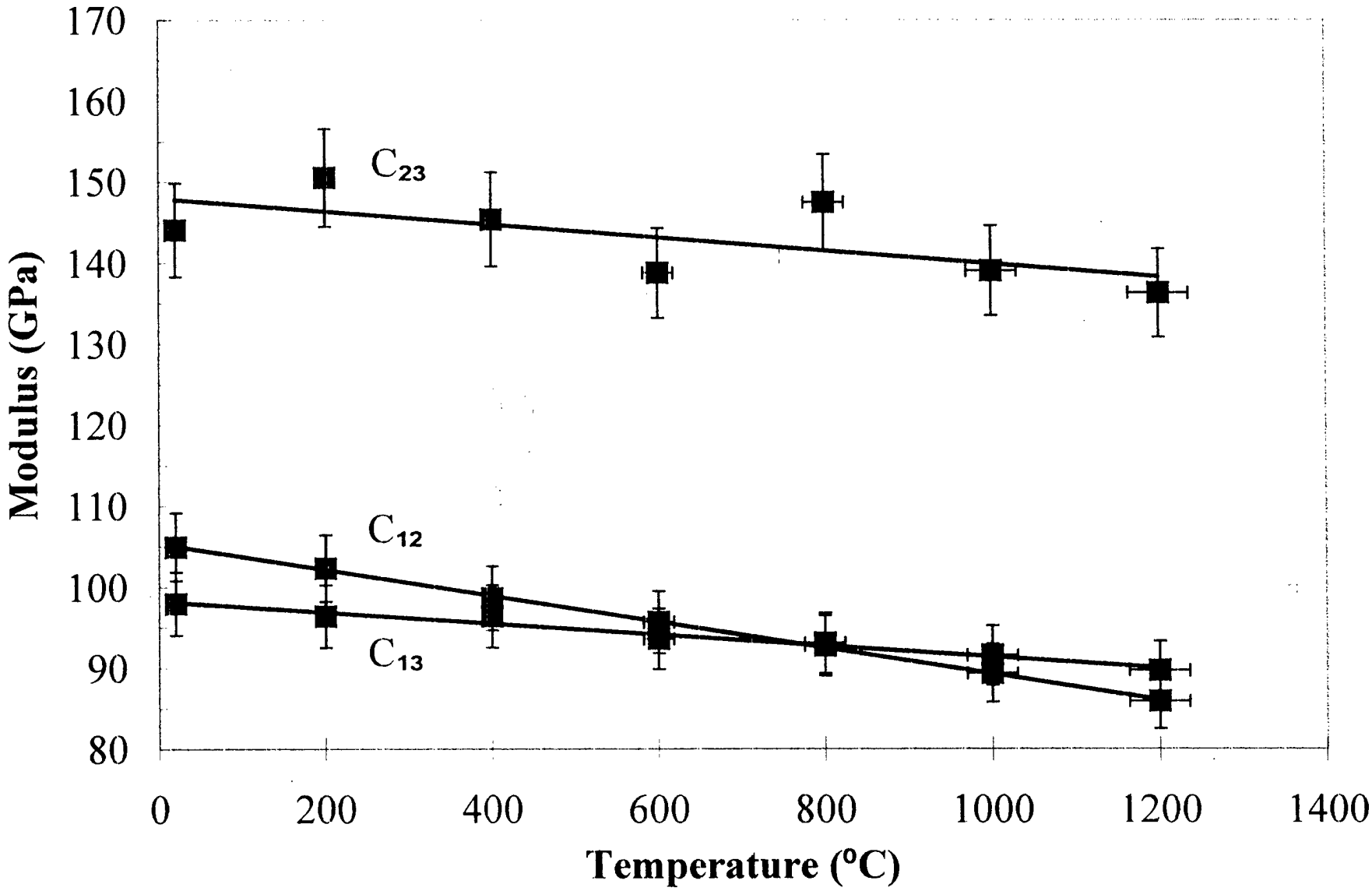


Figure 10: Single-crystal cross moduli versus temperature

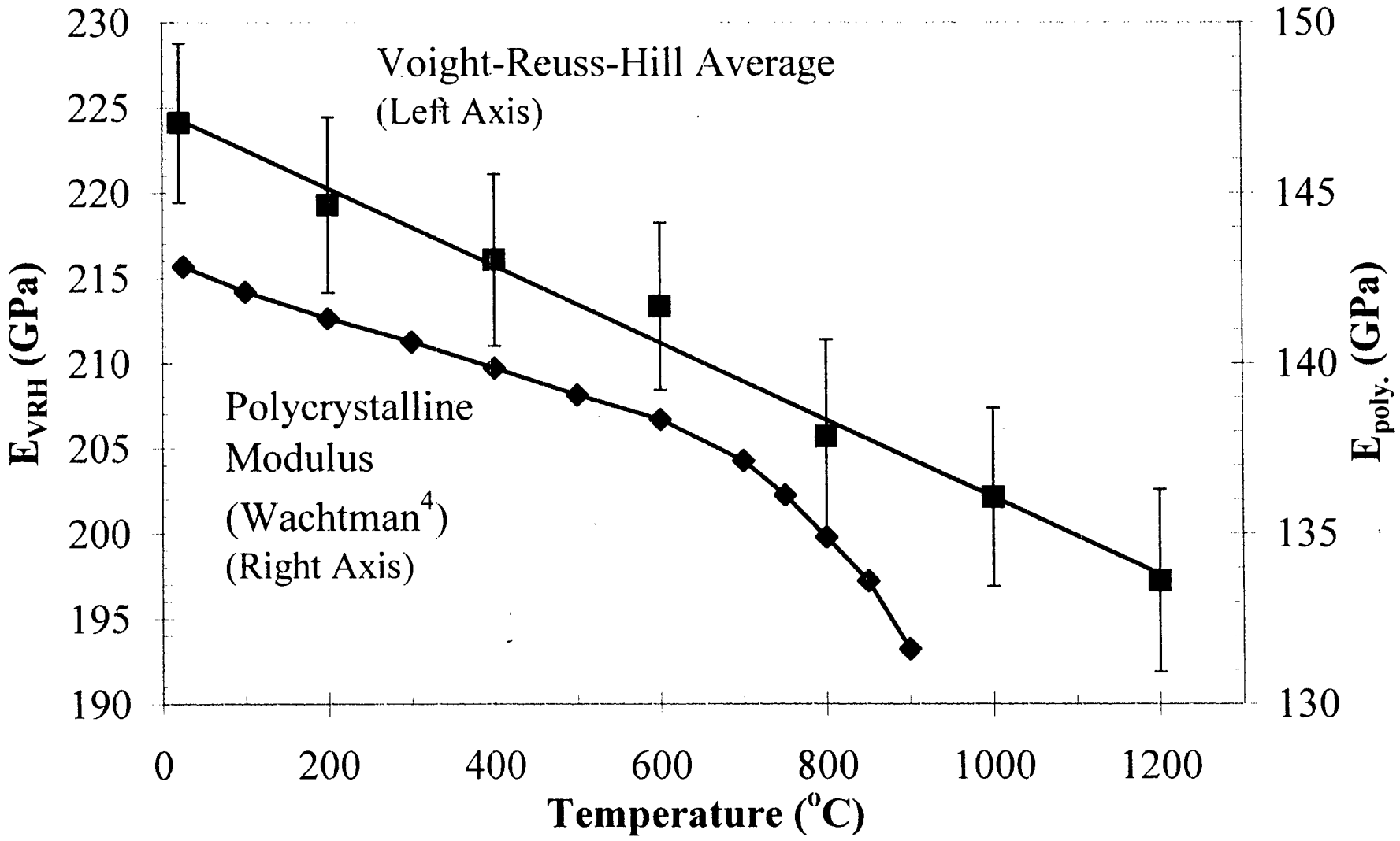


Figure 11: Young's modulus of mullite versus temperature

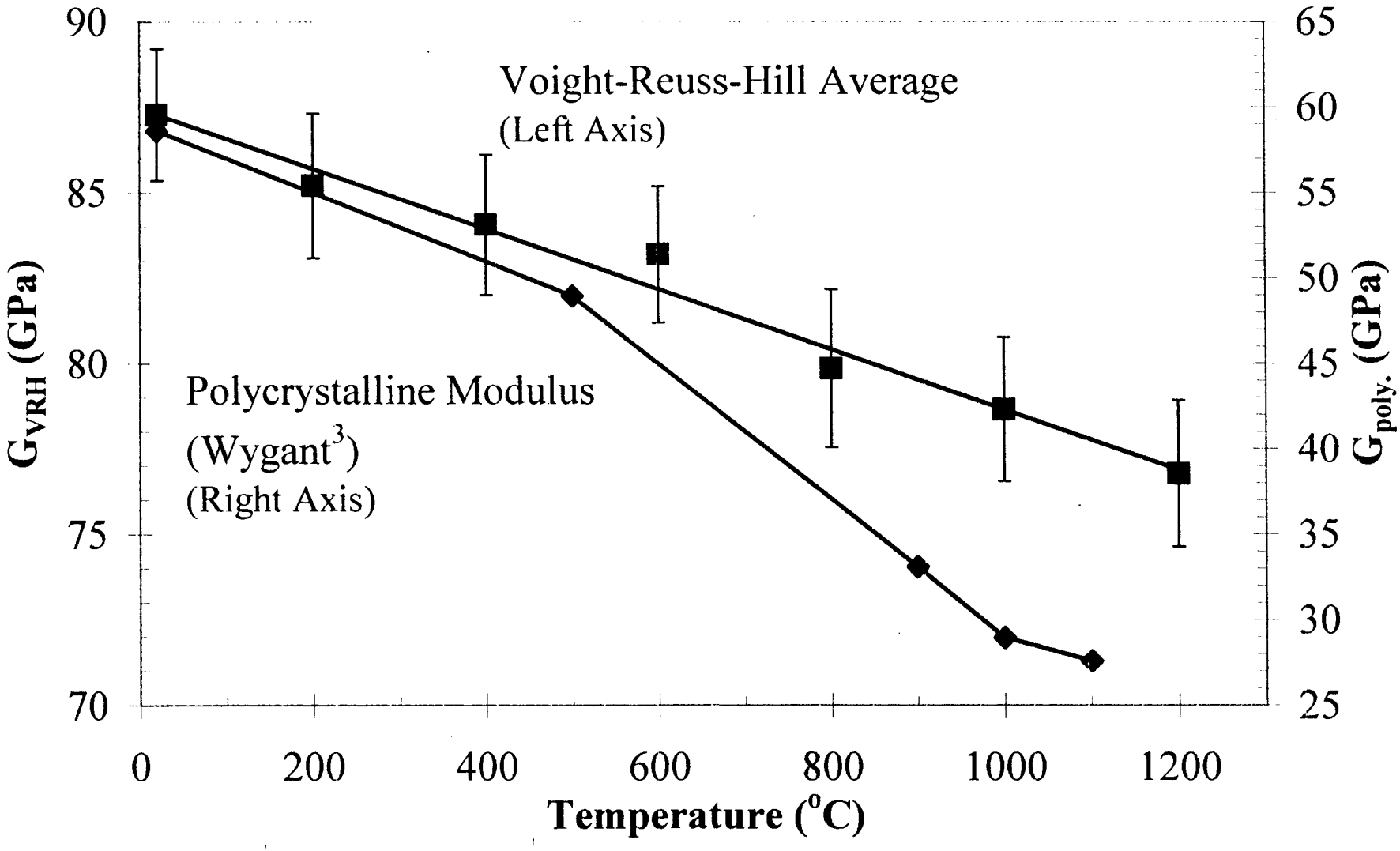


Figure 12: Shear modulus of mullite versus temperature

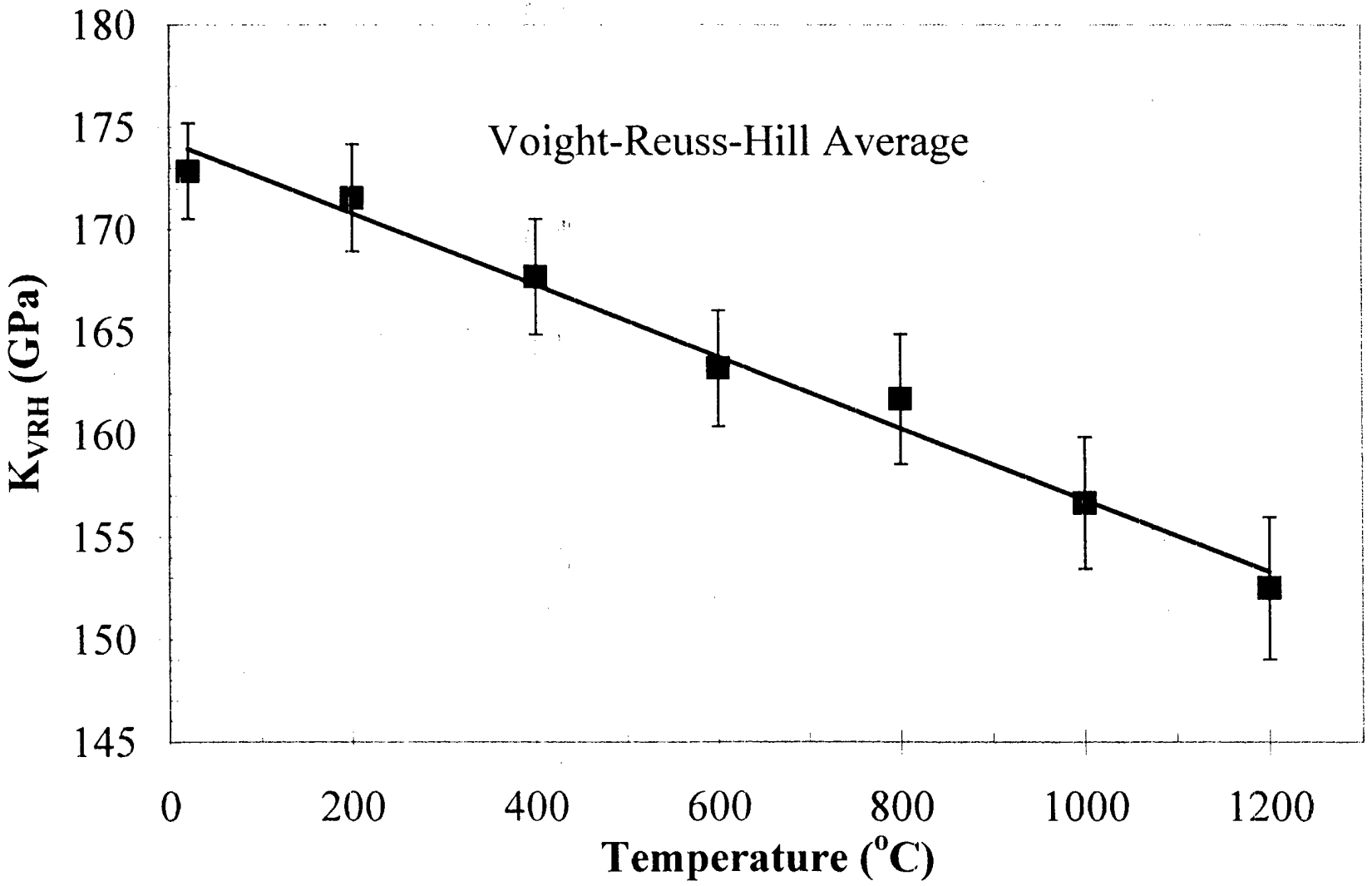


Figure 13: Bulk modulus of mullite versus temperature

J. Mat. Res., submitted, Nov 2000

Crystallization kinetics of yttrium aluminum garnet ($Y_3Al_5O_{12}$)

Bradley R. Johnson and Waltraud M. Kriven
Department of Materials Science and Engineering, University of Illinois at Urbana-Champaign, 1304 W. Green Street, Urbana, IL 61801, USA

The crystallization behavior of solid, amorphous, yttrium aluminum garnet (YAG) was studied using isothermal differential thermal analysis (DTA), X-ray diffraction (XRD) and transmission electron microscopy (TEM). The activation energy for crystallization was 437 KJ/mole and the measured Avrami exponent was 2.74, which corresponded to a three dimensional crystal growth mechanism with a constant number of nuclei. Time – temperature – transformation (T-T-T) curves were developed from the data to predict crystallization rates as a function of temperature. The crystallization pathway for YAG in this system is compared to others reported in the literature.

I. INTRODUCTION:

Yttrium aluminum garnet ($Y_3Al_5O_{12}$, "YAG") is an important ceramic material used in structural refractory applications as well as in optical applications such as laser materials (e.g. when doped with rare-earth cations, such as neodymium). Single crystal YAG is also one of the most creep resistant ceramic oxides known.[1,2] Its low creep, coupled with its very high melting temperature (1940°C[3]) makes it particularly attractive for structural applications, and it is currently under investigation for potential use as structural fibers.[4-11]

One route of structural fiber development under investigation is to use containerless methods to pull amorphous fibers from highly under-cooled melts, and to subsequently crystallize them.[4,12,13] Some of the advantages of this process are that fibers can be drawn from typically fragile, glass-forming materials, as well as from compositions which are difficult to access due to their incongruent melting behavior (e.g. mullite). To successfully crystallize such fibers with a controlled microstructure, a thorough understanding of the crystallization kinetics of quenched YAG-composition glasses is necessary.

Although YAG is a significant and well-studied engineering material, both for structural and optical applications, not much data is available concerning its crystallization kinetics. This is primarily due to the fact that YAG is a very fragile glass-forming substance, and its primary use is in its crystalline form.[14,15] Additionally crystallization studies are complicated by its very high melting temperature, making cooling studies from a molten state very difficult using standard thermal analysis techniques. Consequently, it was decided to use rapidly quenched YAG specimens to study the kinetics of crystallization from the amorphous state, and subsequently to use this information for controlled crystallization of amorphous YAG fibers.

II. EXPERIMENTAL PROCEDURES

YAG powder was chemically synthesized via a complex polymerization method as described elsewhere.[16-18] The precursors were yttrium nitrate hexahydrate,

$Y(NO_3)_3 \bullet 6H_2O$ (Alfa Aesar, Ward Hill, MA) and aluminum nitrate nonahydrate, $Al(NO_3)_3 \bullet 9H_2O$ (Aldrich, Milwaukee, WI). They were dissolved in a 5 wt% solution of 78% hydrolyzed polyvinyl alcohol PVA (Gohsenol KH-17s, MW = 106,000, Nippon Gohsei, Inc., Osaka, Japan). The chemically synthesized powders were subsequently melted in a water cooled hearth using a CO_2 laser to form a pellet.[19] The pellet was then levitated in an oxygen atmosphere with an aero-acoustic levitator, and melted again by a CO_2 laser as described in literature elsewhere.[20-23] Melt temperatures were approximately 2200°C as indicated by optical pyrometry. The suspended molten droplet was then rapidly quenched to form an amorphous YAG bead approximately 2 – 3 mm in diameter. The beads were initially crushed between two stainless steel plates to form a coarse powder. Fine grinding was done using an agate mortar and pestle. The powdered material was used for isothermal DTA experiments as well as for XRD analysis.

Isothermal DTA experiments were carried out using a Dupont 910 DTA modified by Innovative Thermal Systems (Atlanta, GA) with updated signal processing electronics and a computer controlled digital data acquisition system. The sample mass consisted of 50 mg of crushed quenched powder, while 45 mg of α-Al_2O_3 was used as the reference (to approximately match the thermal mass of the sample). Platinum crucibles were used for both sample and reference. The experiments were done with a flowing atmosphere of Ar (60 cc/min) and an initial heating rate of 40°C/min up to the desired hold temperature. The DTA thermocouples were calibrated with the melting point of gold and silver using alumina crucibles. Eight different hold temperatures were used between 840°C and 875°C at 5° increments. Hold times varied from three hours to 45 minutes, as the hold temperature was increased.

X-ray diffraction analysis was done with a DMax Automated Powder diffractometer, (Rigaku/USA, Danvers, MA) equipped with a graphite monochromator, emitting Cu K_α radiation. The operating voltage was 40 kV with a current of 40 mA and the diffractometer was operated in theta – 2-theta mode. Spectra were collected for crystallized specimens using a goniometer speed of 5° 2θ/min, with a step size of 0.01° 2θ, and summing over 5 scans. For quenched specimens, a goniometer speed of 2° 2θ/min, with a step size of 0.02° 2θ was used, and a minimum of 30 scans were summed.

Microstructural analysis of quenched YAG beads was done using a Philips CM12 (FEI company, Hillsboro, OR, USA) transmission electron microscope with a LaB_6 filament, equipped with a Gatan (Pleasanton, CA, USA) multi-scan CCD camera and an EDAX (Mahwah, NJ, USA) energy dispersive spectrometer (EDS). TEM specimens were prepared by slicing sections from the quenched beads with a diamond wafer saw (Buehler Isomet® low speed saw, Lake Bluff, IL) and mechanically thinning the sections by tripod polishing[24,25] (Model 590W, South Bay Technologies, San Clemente, CA) with diamond lapping films. Final thinning was done using an ion mill (Gatan 600 DuoMill, Pleasanton, CA, USA). The specimens were examined by bright field (BF) imaging, convergent beam electron diffraction (CBED), selected area diffraction (SAD), and energy dispersive spectroscopy (EDS). The camera length constant for the microscope was determined using a specimen of evaporated gold on a holey carbon film. The diffraction patterns for gold and the various specimen images were collected digitally and distances were measured using a free-ware image analysis software package made available by the National Institute of Standards and Testing (NIST).[26]

III. THEORETICAL ANALYSIS

Data analysis was conducted with the raw isothermal data to determine the parameters which best described the kinetics of the amorphous to crystalline transformation. Several different models were examined and tested,[27] but the model which best described the data was the Johnson – Mehls – Avrami equation[28]:

$$x = 1 - \exp\left[-(kt)^n\right] \tag{1}$$

where x is the fraction transformed, k is the reaction rate, t is time and n is the Avrami exponent which describes the geometry of the crystal growth front. The reaction rate, k, is itself an Arrhenius expression as follows:

$$k = \nu \exp\left[\frac{-E}{RT}\right] \tag{2}$$

where ν is the pre-exponential factor (in units of inverse time), E is the activation energy, R is the gas constant, and T is temperature.

Typically, the isothermal DTA or DSC data described by the JMA equation is analyzed through a series of data reduction steps and least squares fitting of Arrhenius plots. First, Eq. (1) is re-arranged as follows:

$$\ln\left(-\ln(1-x)\right) = n\ln(k) + n\ln(t) \tag{3}$$

Plots are generated of ln[-ln(1-x)] vs. ln(t) for each hold temperature and values of k and n are found from least squares fitting of the data. Next, values for the activation energy and pre-exponential factor are determined by re-arranging Equation 2 as follows:

$$\ln(k) = \ln(\nu) - \frac{E}{RT} \tag{4}$$

A plot is then generated of ln(k) vs. $1/T$ and a least squares fit is applied to the data points to determine the activation energy, E, and the pre-exponential factor ν from the slope and y-intercept of the line, respectively.

However, with the advent of digital data acquisition and sophisticated data analysis and plotting software packages[29] it is possible to analyze the raw data directly without going through the previously described data reduction processes. This is facilitated by the fact that the raw data from a DTA or DSC plot is proportional to the first derivative of the JMA equation[27] (Eq. (5)):

$$\frac{dx}{dt} = nk^n t^{n-1} \exp\left[-(kt)^n\right] \tag{5}$$

By including a proportionality constant, a curve fit can be directly applied to the raw data and numerically optimized to simultaneously determine the optimum values of n and k at each hold temperature. This was the procedure used for this analysis. This method has the advantage of being more accurate and more sensitive to subtle features

of the kinetic process. The equation used for curve fitting raw isothermal exotherms is shown in equation 6:

$$y = Ank\left[kt_0^{(n-1)}\right]\exp\left[-(kt_0)^n\right] \tag{6}$$

where A is a proportionality factor, n and k are as previously defined, and t_0 is the start time of the exotherm.

All of the pertinent variables (n, k, E and ν) for the JMA equation (Eq. 1) were thus computed from the isothermal exotherms. Time – temperature – transformation (T-T-T) curves were then calculated by re-arranging the JMA equation (Eq. 1) and analytically calculating the temperature required for a fixed fraction of conversion as a function of time:

$$T = \frac{E}{R}\left[\frac{1}{\ln(\nu t) - \frac{1}{n}\ln(-\ln(1-x))}\right] \tag{7}$$

IV. RESULTS

A. Thermal Analysis

A composite plot of isothermal DTA exotherms for the crystallization of quenched YAG beads is shown in Fig. 1. Numerical curve fitting was done to the raw data to determine the kinetic parameters of the crystallization transformation using Eq. 6. An example curve fit of the raw data and the optimized kinetic parameters (e.g. n and k) for an exotherm at a hold temperature of 855°C is shown in Fig. 2. This type of optimization was performed at each temperature and the calculated values for n and k are listed in Table I. Using the values for k and T in Table I, a plot was generated of reaction rate *vs.* temperature (Fig. 3). The equation for the reaction rate (Eq. 2) was used to fit the data and it was numerically optimized to find the best values for the pre-exponential factor, ν and the activation energy, E. The result of this curve fit for the isothermal crystallization of YAG is shown in Fig. 3.

These parameters were used in the JMA equation (Eq. 1) to calculate a T-T-T curve (Eq. 7) for the isothermal crystallization of amorphous YAG, Fig. 4. Superimposed on the plot are raw data points which show the time required for 1% and 99% crystallization. These times were measured from a plot where the integrated area under the crystallization exotherm was normalized to one.

B. X-ray Diffraction

X-ray diffraction analysis was done of the quenched YAG – composition glass powders both before and after crystallization in the DTA. A combined plot of the XRD spectra before and after crystallization with the same vertical axis is shown in Fig. 5. Figure 6 is the same two spectra in a plot normalized with respect to the 100% peak for each.

C. Microstructural Characterization

The microstructure of quenched YAG composition glass beads was examined using transmission electron microscopy (TEM). Measured d-spacings from SAD micrographs were compared to those published in the Powder Diffraction Files, PDF®, of the International Center for Diffraction Data (ICDD®, formerly known as the Joint Committee on Powder Diffraction Standards, JCPDS). Typical bright field images of a quenched YAG composition glass are shown in Figs. 7 through 10. The labeled points in Fig. 7 indicate regions where EDS analysis and microdiffraction were taken. The inset images in Fig. 7 and 8 are CBED patterns which identify the designated regions as being YAG crystals. The specimen had several dark regions. Some of these were crystalline (as noted) but not all of them. EDS spectra were taken for light regions, dark regions and crystalline regions. Standardless quantitative analysis was done using the Cliff-Lorimer approximation.[30] All regions had essentially the same composition (63 ± 1 mol % Al_2O_3 and 37 ± 1 mol % Y_2O_3. The stoichiometric composition for YAG is 62.5 mol % Al_2O_3 and 37.5 mol % Y_2O_3.

Additional analysis on other areas of the specimen showed the presence of nanocrystals being formed from the amorphous matrix. Figure 9 is a bright field image of a region with nanocrystals of YAG embedded in an amorphous matrix. The inset image is an SAD pattern corresponding to YAG which was taken from a similar area close to the BF image in Fig. 9. Figure 10 is a higher magnification BF image showing the transition from amorphous to crystalline YAG regions. Figure 11 is a TEM bright field image of the cross-section from a quenched YAG – composition fiber which was pulled from a levitated, sub-cooled liquid. Only a couple of isolated nanocrystals of YAG were found in this specimen. The darker contrast areas on the specimen were from the holey carbon support film and the glue used to hold the specimen on to the film.

V. DISCUSSION:

A. Review of YAG Synthesis

In order to put the present work in perspective and to provide better understanding of the mechanisms of crystallization in the yttrium aluminate system, a selected review is provided of YAG synthesis from chemical routes. Several different crystallization pathways and mechanisms have been proposed by other researchers who have investigated YAG synthesis via various chemical processing routes. A summary of these crystallization pathways is shown in Table II. Yamaguchi et al.[31,32] used an alkoxy-derived stoichiometric precursor for synthesizing "YAP" ($YAlO_3$), "YAM" ($Y_4Al_2O_9$) and YAG. For YAG and YAP composition precursors, the formation of an intermediate hexagonal $YAlO_3$ (PDF 16-219) phase was observed at approximately 800° - 890°C . For $Y_3Al_5O_{12}$ composition precursors, the hexagonal $YAlO_3$ phase converted to YAG and was single phase by 1050°C. For $YAlO_3$ precursors, the crystallization pathway was more complicated. Hexagonal $YAlO_3$ crystallized between 870° and 900°C and transformed into a cubic solid solution phase ($Y_3AlY(AlO_4)_3$) with a garnet structure similar to YAG (PDF 33-40) from 1000° - 1060°C. The cubic $YAlO_3$ phase (PDF 38-222) then decomposed to a YAG + YAM mixture between 1080 – 1200°C which subsequently underwent a solid state reaction to form single phase orthorhombic YAP by 1650°C. It was hypothesized that when hexagonal $YAlO_3$ was formed from $Y_3Al_5O_{12}$ precursors, the excess alumina (which must exist to maintain stoichiometry)

was accommodated into the hexagonal $YAlO_3$ structure. This conclusion was based on yttrium aluminate synthesis results over a range of compositions. Thus, Yamaguchi et al.[31,32] suggested that this phase, (hexagonal $YAlO_3$), exists in a solid solution range between 50 and 62.5 mol% Al_2O_3.

Vietch[33] used a stoichiometric mixture of aluminum and yttrium nitrates dissolved in glycerol and malonic acid as a precursor solution for YAG synthesis. The precursors were heated up and YAG formation was studied using XRD, Fourier transform infrared spectroscopy (FTIR) and DTA. Again, the hexagonal form of $YAlO_3$ (PDF 16-219) was reported to formed as an intermediate at 850°C and was eventually converted to single phase YAG by 1100°C. Since crystalline alumina was not observed by XRD when hexagonal $YAlO_3$ formed from YAG precursors, it was assumed to exist in an amorphous state.

Hay[34] studied the crystallization of YAG via an extensive TEM analysis of diphasic $Y_3Al_5O_{12}$ composition sol-gel derived films (from aluminum and yttrium isopropoxides). In this system, hydrated Y_2O_3 and Al_2O_3 particles formed first as the sol-gel films were heated, consequently mixing was not on an atomic level (as was the case in this study and some of the others mentioned). TEM analysis was done on films using a hot stage as well as by subjecting them to various heat treatments and then examining them at room temperature. XRD spectra were collected of bulk specimens heated to various temperatures to complement the study of phase evolution. It is interesting to note that the pattern for the 800°C heat treated diphasic sol had a general profile similar to what is reported here for quenched YAG composition beads.

The diphasic nature of the films (colloidal mixture of hydrated Y_2O_3 and Al_2O_3 particles) resulted in a complicated crystallization pathway with the formation of several intermediate, metastable phases (e.g. $Y_4Al_2O_9$, ϕ-Al_2O_3, and a garnet form of $YAlO_3$ (PDF 38-222)) before YAG finally crystallized. Hay[34] postulated that the nucleation of YAM ($Y_4Al_2O_9$) before YAG, was due to lower yttria mobility combined with influence of strain energy effects (due to the different volume changes associated with forming the various yttrium aluminates). The nucleation of YAG from the parent material was reported to be site saturated and crystal growth occurred by consumption of the parent phases. Crystallization was described as being a cellular transformation with spherulitic growth and with a constant number of nuclei. Crystal growth was essentially two dimensional due to very thin film thickness in comparison to spherulite size. The reported activation energy for YAG formation in this system was 280 KJ/mol. This was thought to be related to YAG-YAM boundary diffusion or surface diffusion due to the microstructural and microchemical phase composition of the parent intermediate phases.

Hess et al.[35] studied the formation of YAG, YAP and YAM via combustion synthesis of aqueous glycine-nitrate solutions with stoichiometric yttrium-to-aluminum cation ratios. This process produced X-ray amorphous powders which were crystallized by subsequent heat treatments. The general shape of the X-ray spectra for the amorphous precursors was similar to Hay's 800°C pattern[34] and to that shown here for quenched YAG-composition beads. Hess et al.[35] suggested that the two broad humps in their spectra might be due to the presence of microcrystalline Y_2O_3. Two possible crystallization pathways for YAG formation from $Y_3Al_5O_{12}$ precursors were proposed, depending on heat treatment. At temperatures of 800°C or less, YAG crystallized directly from the amorphous precursors. At higher temperatures, hexagonal YAP formed as a metastable intermediate product. Hess et al.[35] commented on the previous work of Veitch[33] and Yamaguchi[31,32] and provided evidence to show

that the transition from hexagonal $YAlO_3$ to YAG occurred by the diffusion of amorphous alumina (a separate phase, not in solid solution) into hexagonal $YAlO_3$ followed by a structural transformation into the garnet structure. It was also observed that the fuel concentration used during combustion synthesis of $Y_3Al_5O_{12}$ precursors affected the phases formed during subsequent crystallization. Specimens formed with higher fuel concentrations and subsequently crystallized produced samples containing hexagonal YAP along with YAG, whereas lower fuel concentrations produced only YAG. Since the fuel concentration could possibly affect the ultimate temperature reached during combustion synthesis, these results may be related to the metastable formation of YAP + alumina during the solidification of $Y_3Al_5O_{12}$ melts heated above 2000°C as reported by Le Floch et al.[36]

Liu et al.[37] used a metallo-organic synthesis route (based on isobutyrate) for forming YAG, and reported the direct formation of the garnet structure at 910°C with no intermediate phases. They heated up precursors to various temperatures and used Diffuse Reflectance Infrared Fourier Transform Spectroscopy (DRIFTS) and XRD to characterize phase development. The XRD spectra at 800°C appeared similar to those reported here (for quenched beads), and by Hay[34] and Hess.[35] Liu et al.[37] concluded that there was short-range order or nucleation which existed between 500° and 900°C in their system, and that the local environment was possibly YAG, but that diffusion rates were too slow at these temperatures to allow large scale crystallization. Based on similar XRD spectra profiles, and microstructural evidence by TEM of the quenched YAG specimens examined here and in sol-gel films with $Y_3Al_5O_{12}$ composition examined by Hay,[34] it is possible that there might be nanoscale YAG crystals beginning to form in the metalloorganic precursors studied by Liu.

Nguyen et al.[16,18] reported the synthesis of YAG via a polymeric solution route using metal nitrates (similar to Veitch[33]) and polyvinyl alcohol (PVA). Phase formation as a function of temperature was examined using XRD, simultaneous differential thermal analysis and thermogravimetric analysis (DTA/TGA), Fourier transform infrared spectroscopy (FTIR) and nuclear magnetic resonance (NMR). They reported the direct crystallization of YAG at 940°C, which is similar to the 910°C crystallization temperature reported by Liu[37] for the metallo-organic system they used. The XRD spectra for the PVA YAG precursors heat treated to 800° - 900°C was again similar to that reported here for quenched $Y_3Al_5O_{12}$ composition beads.

B. Thermal Analysis

The results for isothermal analysis are presented in Figs. 1 through 4. As expected, there was a decrease in duration and an increase in intensity of the crystallization exotherms as the hold temperature was increased. The best mathematical model found to characterize the data was the JMA equation (Eq. 1). The raw data from the crystallization exotherms were modeled using the first derivative of this equation, and the curve fits produced matched the experimental data very well; typical R^2-values were 0.99 or better. The overall activation energy for crystallization in the temperature range studied (840° - 875°C) was 437 KJ/mole and the value of the pre-exponential term for the reaction rate was 6.33×10^{16} (Fig. 3). The average Avrami exponent for this data set was 2.74 (Table 1). This data was used to generate a T-T-T curve (Fig. 4) to show how the rate of crystallization varied as a function of time and temperature. The exotherm observed by DTA was confirmed to be crystallization of YAG, based on TEM and XRD data. The small YAG crystals initially present in the

quenched YAG-composition beads most likely acted as sites for crystal growth, thus eliminating the activation barrier for homogeneous nucleation. The morphology of the crystals observed indicated that the geometry of crystallization was three-dimensional. Therefore, the kinetic phenomena observed by isothermal DTA was most likely three-dimensional crystal growth, with a constant number of nucleation sites (pre-existent crystals).

C. XRD

X-ray diffraction spectra of crushed quenched YAG-composition beads before and after crystallization in the DTA were consistent with SAD analysis in the TEM. The spectra for the quenched glass beads showed two diffuse humps, a pronounced one between 25° and 35° 2 theta, and a more diffuse hump between 35° and 65°. Both had several identifiable peaks super-imposed on them. The appearance of the spectra was similar to that shown by several other researchers working with chemically synthesized YAG.[18,34,35,37] The diffuse humps are considered to be due to short range ordering in the material (2.4 - 4.0 Å, and 1.4 – 2.4 Å). Most of the peaks present corresponded to YAG (PDF 33-40). Additionally, there were some peaks which corresponded to a hexagonal form of $YAlO_3$, (PDF 16-219) and an orthorhombic form of $Y_4Al_2O_9$ (PDF 14-475) as well as a few remaining peaks which could have correspond to Y_2O_3 and Al_2O_3. Several of these phases were reported by other researchers to be intermediate phases which formed during chemical synthesis of YAG.[31-35] The multi-phase nature of the quenched specimens was reasonable considering the poor glass-forming tendency of the alumina-yttria system and the slower quench rate the beads had in comparison to the fibers.

During specimen preparation, the quenched glass beads were crushed and ground to form a fine powder. Minkova et al.[38] reported results from XRD studies on highly strained YAG (e.g. ground by planetary ball milling). It was found that single-phase YAG was transformed into a mixture of the garnet phase (PDF 33-40), and a tetragonal phase $Y_3Al_5O_{12}$ (PDF 9-310).[39] Consequently, the XRD spectra for quenched YAG beads (Figs. 5 and 6) were examined for the presence of tetragonal $Y_3Al_5O_{12}$. The peak position and intensities for tetragonal $Y_3Al_5O_{12}$ did not match the data very well, and it was concluded that this phase was not present in the specimen.

The metastable formation of $YAlO_3$ + α-Al_2O_3 crystals from undercooled $Y_3Al_5O_{12}$ melts has been reported by other investigators.[3,36,40,41] Lin et al.[42] explained that this phenomenon was due to the relatively small difference in free energy of formation between YAG and $YAlO_3$ + α-Al_2O_3, (472.49 vs. 440.35 KJ/mol, respectively) and that though YAG is thermodynamically more stable, kinetic factors favor the formation of $YAlO_3$ + α-Al_2O_3.[42] Cockayne[41] offered an explanation based on the relative complexity of the respective unit cells. (YAG has 160 atoms per unit cell whereas $YAlO_3$ and Al_2O_3 have 20 atoms and 10 atoms per unit cell, respectively.) Cockayne postulated that, with increased undercooling and subsequent increased melt viscosity, it might be energetically more favorable to form $YAlO_3$ + α-Al_2O_3 instead of YAG, because of the smaller critically-sized nuclei involved.[41] Gervais et al.[40] performed high temperature DTA studies on the melting and solidification of $Y_3Al_5O_{12}$ and other rare-earth garnets. They reported the existence of a critical temperature for the molten liquid, T_{clg} (T_{clg} = 2000°C for YAG). When YAG composition liquids were heated above a critical temperature, T_{clg}, $YAlO_3$ + α-Al_2O_3 formed upon cooling, and when heated below T_{clg}, $Y_3Al_5O_{12}$ formed during solidification. Le Floch et al.[36] also studied the solidification behavior of rare-earth garnets using high temperature DTA. Additionally, they

investigated phase formation in quenched $Y_3Al_5O_{12}$ melts heated to 1980° - 2400°C using laser-heated containerless methods (a similar process as used in this study). Both the DTA studies and the containerless cooling studies of $Y_3Al_5O_{12}$ melts confirmed the existence of a critical melt temperature of 2000°C (below which YAG would crystallize, and above which $YAlO_3$ + α - Al_2O_3 formed). Based on their quench studies of containerless, laser-heated $Y_3Al_5O_{12}$ melts, they reported another molten temperature regime where solidification of $Y_3Al_5O_{12}$ melts heated above 2400°C resulted in the formation of a metastable, cubic garnet-type structure, with lattice parameters slightly larger than those of equilibrium YAG (1.2041 nm vs. 1.12010 nm).

Subsequent work by that same group (Gervais et al.[43]) refined their understanding of solidification of molten YAG. It was found that above 2000°C, the critical factor which determined the phase formed during solidification of levitated molten $Y_3Al_5O_{12}$ was the cooling rate. Starting from a temperature of 2100°C, three different solids could be formed: YAP + α-Al_2O_3, YAG or glass (in the order of increasing cooling rate). The postulated mechanisms responsible for this behavior were the combined effects of difficult YAG nucleation and varying diffusion rates in the sub-cooled liquids. At relatively low cooling rates, YAP + α-Al_2O_3 solidified at approximately 1375°C. At this cooling rate and solidification temperature, the explanation was that the homogeneous nucleation rate of YAG was extremely low while relatively high diffusion rates (due to the low melt viscosity) allowed the melt to partition into a metastable mixture of YAP + α-Al_2O_3 upon solidification. At faster cooling rates, YAG solidified from the melt at approximately 1025°C. This result was given as evidence of a high barrier to homogeneous nucleation. Gervais et al.[43] stated that the complexity of the unit cell (160 atoms) might be the reason why such high undercoolings (~920°C) were necessary for YAG crystallizaton. It was also suggested that at this temperature range (~900°C below T_{mp}), long-range diffusion in the melt would be fairly limited, possibly even comparable to the growth rate of the solid-liquid interface, thus precluding the phase separation observed at higher temperatures and lower cooling rates. At extremely fast quench rates (with over 1000°C undercooling) amorphous solid glasses formed which crystallized into single-phase YAG upon subsequent heat treatment. These results are identical to what is reported here.

Weber et al.[44] studied the structure of sub-cooled liquid $Y_3Al_5O_{12}$ using containerless methods. Though the maximum temperature for these melts was not stated, it was probably in excess of 2000°C. They reported that the primary structural units in the melt from ~ 1435° - 1900°C were AlO_4^{5-} tetrahedra and YO_6^{9-} octahedra. These units were most likely linked by corner - and edge - shared oxygen atoms in a variety of configurations in order to fulfill stoichiometry constraints. The existence of these smaller structural units in the sub-cooled liquid would seem to explain the variability of solids formed from the melt depending on the cooling rate and support the solidification model proposed by Gervais et al.[43]

With all of the above data in mind, it would seem that YAG (T_{mp} = 1940°C) nuclei can exist in the melt up to about 2000°C, thus facilitating YAG crystallization upon cooling from melts heated below that temperature (Gervais[40] and Le Floch[36]). However, it appears that above 2000°C, the majority of these nuclei are broken down into smaller embryonic units (Weber[44]). These embryonic units apparently tend to phase separate metastably into $YAlO_3$ + Al_2O_3 when the melt cools slowly and there is only a small amount of sub-cooling. At these temperatures the diffusion rates are relatively high and viscosity is low, thus facilitating phase separation. When the melt is cooled at

higher rates and solidification occurs at lower temperatures, the higher viscosity and lower diffusion rates prevent the embryonic units from phase separating. At these temperatures, the degree of undercooling (~900°C < T_{mp}) is sufficient for homogeneous YAG nucleation to be energetically favorable. At even higher cooling rates, these embryonic units are quenched into an amorphous solid with only short-range ordering. This amorphous solid is reported to have two different structural states with different densities, hardnesses and degrees of ordering, yet with the same composition.[45]

The presence of a mixture of YAG, $YAlO_3$ and Al_2O_3 crystals in the quenched beads of this study (heated to approximately 2200°C) correlates well with the data reported by Le Floch[36] and Gervais.[43] And, the presence of YAG crystals (thermodynamically more stable) explains why YAG crystallized so readily in these DTA experiments instead of $YAlO_3$ + Al_2O_3.

The XRD spectra collected after the powder was crystallized in the DTA was highly crystalline and corresponded to YAG. This confirms that the exothermic event observed by DTA was in fact a crystallization exotherm. One of the interesting differences between the XRD spectra before and after crystallization was the difference in the location of the 100% peak. For the quenched glass bead sample, the maximum in the broad diffuse hump was near 31.15° 2θ (~2.87 Å), whereas after crystallization the 100% peak (YAG) was at 33.45° 2θ (~2.68 Å).

D. Microstructure:

In TEM, Bright field (BF) and diffraction analysis (SAD and CBED) of quenched YAG-composition beads showed that the material was primarily amorphous, but that there was also a substantial number of crystals present. The crystals found could be divided into two groups by size. The larger crystals had a length scale in the micron range and the smaller crystals had a length scale in the range of tens of nanometers. The population and density of these crystals appeared to be random. In contrast, there were barely any crystals found in the amorphous YAG-composition fiber pulled from sub-cooled levitated droplets (Fig 11). The difference in microstructure was most likely a function of cooling rates. The quenched beads had an estimated cooling rate of ≥ 250°C/s while the amorphous fiber had an estimated cooling rate of ≥ 2500°C/min. The presence of crystals in the quenched beads is evidence of the poor glass-forming tendencies of YAG.

In addition to crystalline regions, there were other regions where there was enhanced contrast in the BF mode which was not due to crystallinity. Extensive EDS analysis showed no significant compositional variation between the three different regions (crystalline, light amorphous, and dark amorphous). The contrast difference observed between the two regions may be due to differences in density or thickness, or both (if the denser region had a different thinning rate then it would be thicker and also result in a darker appearance in the BF mode). There have been reports in the literature of polyamorphism in quenched YAG-composition glasses.[15,45,46] "Polyamorphism" is a term used to describe a material where there are two different amorphous phases with identical composition but different short-range order structures, with one phase typically being denser than the other.[47] The observed contrast in the amorphous regions may be the result of this phenomenon.

VI. SUMMARY

Even though rapidly quenched at approximately 250°C/s, the YAG composition glass beads were populated by crystals of YAG whose size was in the nanoscale, as well as in the micron range. These crystals most likely acted as seeds for crystal growth during subsequent studies on crystallization kinetics. In addition to crystals, there were also amorphous regions of different contrast (yet with the same composition) as observed by bright field imaging and EDS in the TEM. These regions may have been due to polyamorphism. XRD spectra of specimens heated in the DTA confirmed that the exotherm observed was for crystallization of YAG. The DTA exotherms were successfully analyzed by curve fitting the first derivative of the JMA equation to the raw data. The activation energy for crystallization was 437 KJ/mole and the Avrami exponent was 2.74. The material crystallized directly into stoichiometric YAG at temperatures as low as 840°C; no intermediate phases were observed. Crystallization most likely occurred with a constant number of sites and crystal growth was three-dimensional. Isothermal crystallization data was used to generate a TTT curve to describe crystallization as a function of time and temperature. This data set may be useful for fabricating structural YAG fibers from amorphous pre-cursors.

ACKNOWLEDGEMENTS

The authors would like to gratefully acknowledge Richard Weber and Johan Abadie from Containerless Research Inc. for supplying the quenched YAG beads used in this work. This project was funded by the U.S. Air Force Office of Scientific Research under Science and Technology Transfer Research (STTR) grants F49620 -97-1-0427 and F49620-98-C-0050. Microstructural and crystallographic characterization was performed, in part using equipment in the Center for Microanalysis of Materials (in the Materials Research Laboratory), and in the Center for Cement Composite Materials, both located at the University of Illinois at Urbana-Champaign.

REFERENCES

1. G. S. Corman, J. Mater. Sci. Lett. **12**, 379 (1993).
2. S. Karato, X. Wang, and K. Fujino, J. Mater. Sci. **29**, 6458 (1994).
3. J. L. Caslavsky and D. J. Viechnicki, J. Mater. Sci. **15**, 1709 (1980).
4. J. K. R. Weber, B. Cho, A. D. Hixson, J. G. Abadie, P. C. Nordine, W. M. Kriven, and B. R. Johnson, J. Eur. Cer. Soc. **19** (8), 2543 (1999).
5. P. A. Doleman and E. G. Butler, Key Eng. Mater. **127-131**, 193 (1997).
6. B. H. King and J. W. Halloran, J. Am. Ceram. Soc. **78** (8), 2141 (1995).
7. G. N. Morscher, K. C. Chen, and K. S. Mazdiyasni, Cer. Eng. and Sci. Proc. **15** (4), 181 (1994).
8. L. Yin, Z. Zhi-Fan, J. Halloran, and R. M. Laine, J. Am. Ceram. Soc. **81** (3), 629 (1998).
9. D. Popovich, J. L. Lombardi, and B. H. King, Cer. Eng. and Sci. Proc. **18** (3), 65 (1997).
10. W. R. Blumenthal and S. T. Taylor, Act. Mater. **45** (7), 3071 (1997).
11. W. R. Blumenthal and D. S. Phillips, J. Am. Ceram. Soc. **79** (4), 1047 (1996).

12. W. M. Kriven, M. H. Jilavi, D. Zhu, J. K. R. Weber, B. Cho, and J. Felten, in *Ceramic Microstructure: Control at the Atomic Level,* edited by A. P. Tomsia and A. Glaeser 1998), p. 169.
13. J. K. R. Weber, J. J. Felten, B. Cho, and P. C. Nordine, Nature **393**, 469 (1998).
14. C. A. Angel, Science **267**, 1924 (1995).
15. J. K. R. Weber, J. G. Abadie, A. D. Hixson, P. C. Nordine, and G. A. Jerman, J. Am. Ceram. Soc., In press (Accepted Feb 2000).
16. M. H. Nguyen, "A New Polymer Route to the Synthesis of Mixed Oxide Ceramics," MS Thesis, University of Illinois at Urbana-Champaign, 1997.
17. M. A. Gülgün, M. H. Nguyen, and W. M. Kriven, J. Am. Ceram. Soc. **82** (3), 556 (1999).
18. M. H. Nguyen, S.-J. Lee, and W. M. Kriven, J. Mater. Res. **14** (8), 3417 (1999).
19. J. K. R. Weber, J. J. Felten, and P. C. Nordine, Rev. Sci. Inst. **78**, 31 (1996).
20. S. Krishnan, J. J. Felten, J. E. Rix, and J. K. R. Weber, Rev. Sci. Inst. **68**, 3512 (1997).
21. J. K. R. Weber, C. D. Anderson, S. Krishnan, and P. C. Nordine, J. Am. Ceram. Soc. **78**, 577 (1995).
22. J. K. R. Weber, S. S. Hampton, D. R. Merkley, C. A. Rey, M. M. Zatarski, and P. C. Nordine, Rev. Sci. Inst. **65** (456-465) (1994).
23. J. K. R. Weber and P. C. Nordine, Microgravity Science and Technology **VII**, 279 (1995).
24. J. Benedict, R. Anderson, and S. J. Klepeis, in *Specimen Preparation for Transmission Electron Microscopy of Materials III,* edited by R. Anderson, B. Tracy and J. Bravman (Materials Research Society Symposium Proceedings **254**, Pittsburgh, PA, 1992), p. 121.
25. S. J. Klepeis, J. P. Benedict, and R. M. Anderson, in *Specimen Preparation for Transmission Electron Microscopy of Materials,* edited by J. C. Bravman, R. M. Anderson and M. L. McDonald (Materials Research Soceity Symposium Proceedings **115**, Pittsburgh, PA, 1988), p. 179.
26. D. S. Bright, MacLispix (National Insitute of Standards, Gaithersburg, MD, 1999).
27. A. K. Galwey and M. E. Brown, in *Handbook of Thermal Analysis and Calorimetry, Vol. 1: Principles and Practice,* edited by M. E. Brown (Elsevier Science, Amsterdam, 1998), Vol. 1, p. 147.
28. D. A. Porter and K. E. Easterling, *Phase Transformations in Metals and Alloys* (Chapman and Hall, New York, 1992).
29. Kaleidagraph (Synergy Software, Perkiomen, PA, 1998).
30. D. B. Williams and C. B. Carter, *Transmission Electron Microscopy a Textbook for Materials Science* (Plenum Press, New York, 1996).
31. O. Yamaguchi, K. Takeoka, and A. Hayashida, J. Mater. Sci. Lett. **10**, 101 (1990).
32. O. Yamaguchi, K. Takeoka, K. Hirota, H. Takano, and A. Hayashida, J. Mater. Sci. **27**, 1261 (1992).
33. C. D. Veitch, J. Mater. Sci. **26**, 6527 (1991).
34. R. S. Hay, J. Mater. Res. **8** (3), 578 (1993).
35. N. J. Hess, G. D. Maupin, L. A. Chick, D. S. Sunberg, D. E. McCreedy, and T. R. Armstrong, J. Mater. Sci. **29**, 1873 (1994).
36. S. Le Floch, J. C. Rifflet, J. Coutures, M. Gervais, and J. P. Coutures, Mater. Sci. Eng. A. **A173**, 185 (1993).
37. Y. Liu, Z.-F. Zhang, B. King, J. Halloran, and R. M. Laine, J. Am. Ceram. Soc. **79** (2), 385 (1996).

38. N. Minkova, D. Todorovsky, and G. Furdinova, Mater. Chem. Phys. **38**, 383 (1994).
39. H. S. Yoder and M. L. Kieth, Amer. Mineral. **36** (7, 8), 519 (1951).
40. M. Gervais, S. Le Floch, J. C. Rifflet, J. Coutures, and J. P. Coutures, J. Am. Ceram. Soc. **75** (11), 3166 (1992).
41. B. Cockayne, J. Less-Com. Metals **114**, 199 (1985).
42. I.-C. Lin, A. Navrotsky, J. K. R. Weber, and P. C. Nordine, J. Non-Cryst. Solids **243**, 273 (1999).
43. M. Gervais, S. Le Floch, N. Gautier, D. Massiot, and J. P. Coutures, Mater. Sci. Eng. B. **B45**, 108 (1997).
44. J. K. R. Weber, S. Krishnan, S. Ansell, A. D. Hixson, and P. C. Nordine, Phys. Rev. Let. **84** (16), 3622 (2000).
45. S. Aasland and P. F. McMillan, Nature **369** (6482), 633 (1994).
46. P. F. McMillan, C. Ho, S. Aasland, A. Yeganeh-Haeri, and R. Weber, in *Structure and Dynamics of Glasses and Glass Formers*, edited by C. A. Angell, K. L. Ngai, J. Kieffer et al. (Materials Research Society Symposium Proceedings **455**, Pittsburgh, PA, 1997), p. 377.
47. C. A. Angell, J. Shao, and M. Grabow, in *Non Equilibrium Phenomena in Supercooled Fluids, Glasses and Amorphous Materials*, edited by M. Giordano, D. Leporini and M. P. Tosi Singapore, 1996), p. 50.

LIST OF TABLES

TABLE I. List of Avrami exponent and reaction rate values as a function of temperature for isothermal crystallization of quenched YAG composition beads.

Temperature (°C)	n	k (s^{-1})
840°	2.615	1.98E-04
845°	2.616	2.45E-04
850°	2.744	3.01E-04
855°	2.653	3.88E-04
860°	2.813	4.43E-04
865°	2.909	5.14E-04
870°	2.785	7.09E-04
875°	2.780	8.27E-04
Avg.	**2.739**	

TABLE II. Crystallization pathways for YAG synthesis via different precursors.

Precursors	Pathway	
Alkoxy precursors	$YAlO_3$ (hex)→ $YAlO_3$(ortho) → YAG (800°C) (950°C) (1050°C)	Yamaguchi et al.[31,32]
Organometallic (nitrates)	$YAlO_3$ (hex) → YAG (850°C) (1100°C)	Vietch[33]
Glycine-nitrate	$YAlO_3$ (hex) → YAG (~875°C) (~1050°C)	Hess et al.[35]
Diphasic sol-gel	$\theta - Al_2O_3 + Y_2O_3 \rightarrow \theta - Al_2O_3 + YAM \rightarrow$ (500°C) (800°C) $\theta - Al_2O_3 + YAlO_3$ (garnet) → YAG (~800 – 1100°C) (900 - 1050°C)	Hay[34]
Y & Al Isobutyrate	$5Al(O_2CiPr)_3{:}3Y(O_2CiPr)_3$ → YAG (910°C)	Liu et al.[37]
PVA + Y & Al nitrates	Sterically entraped Al^{+3} and Y^{+3} cations → YAG (900°C)	Nguyen et al.[18]
Solidification of molten YAG	$YAG_L \rightarrow YAP + \alpha\text{-}Al_2O_3$: Slow cool, 1375°C [upon re-heating, melts as a metastable eutectic] $YAG_L \rightarrow$ YAG : Faster cool, 1025°C $YAG_L \rightarrow$ amorphous $Y_3Al_5O_{12}$: Quench, < 900°C	Gervais et al.[40,43] LeFloch et al.[36]
Solidification of molten YAG and re-crystallization	$YAG_L \rightarrow$ amorphous + YAG + others amorphous $Y_3Al_5O_{12}$ + mixture of phases → YAG (900°C)	This study

LIST OF FIGURES

Figure 1. Combined plot of DTA exotherms (μV vs. time for various temperatures) for isothermal crystallization of quenched YAG composition glass beads.

Figure 2. Example of an optimized curve fit directly applied to a DTA exotherm for crystallization of quenched YAG composition glass.

Figure 3. Plot of reaction rate vs. temperature with a curve fit applied to determine the optimum values for the activation energy and pre-exponential factor for crystallization of quenched YAG composition glass.

Figure 4. Time-temperature-transformation curve for isothermal crystallization of quenched YAG.

Figure 5. XRD spectra for quenched YAG composition glass, before and after crystallization in a DTA.

Figure 6. Normalized XRD spectra for quenched YAG composition glass, before and after crystallization via DTA.

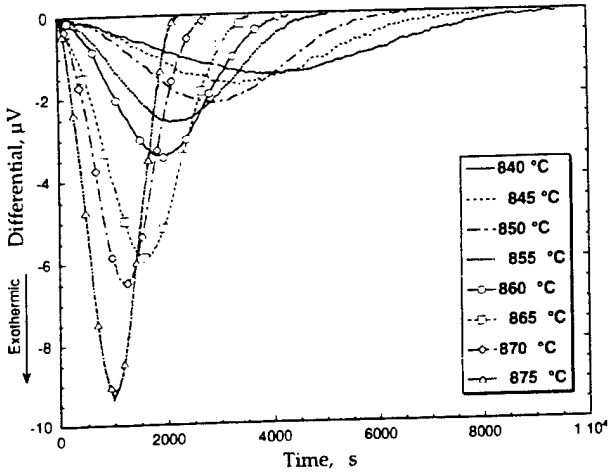
Figure 7. TEM bright field image of a quenched YAG composition glass bead. Regions 1 and 2 designate areas of EDS analysis and microdiffraction. The inset image is a CBED pattern taken from region 2 showing it crystallinity. The lighter area near region 1 was amorphous.

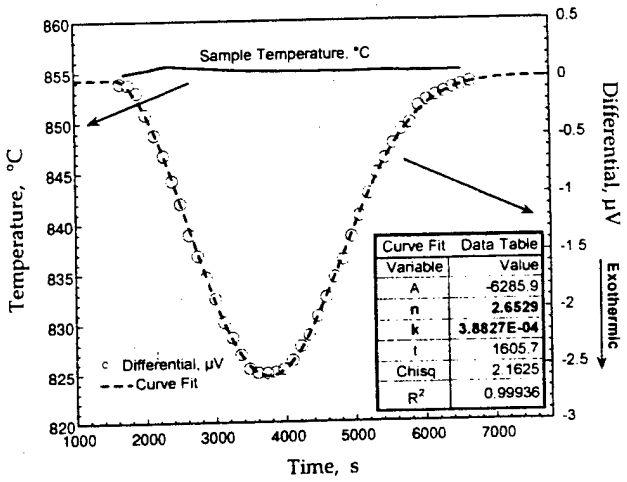
Figure 8. TEM bright field image of a diffraction YAG crystal in a quenched YAG composition glass. The adjacent region is amorphous and shows a contrast mechanism which is not due to diffraction effects. The inset image is a CBED pattern from the diffracting crystal.

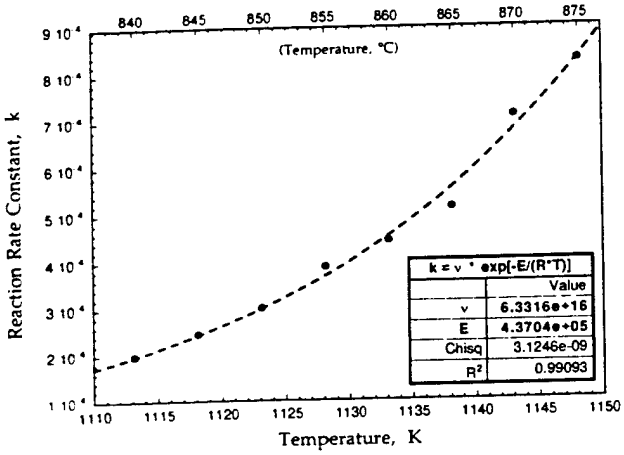
Figure 9. TEM bright field image of a quenched YAG composition glass bead showing nanocrystals of YAG. The inset image is an SAD pattern taken from similar nanocrystals in an adjacent area. The SAD pattern was indexed to be YAG.

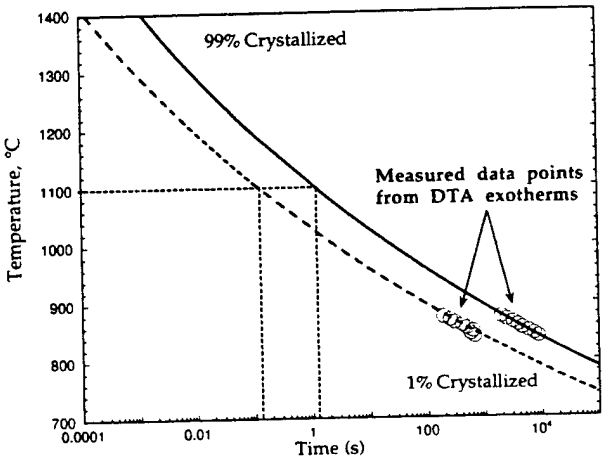
Figure 10. TEM bright field image of a quenched YAG-composition glass bead showing YAG crystals growing out of the amorphous matrix.

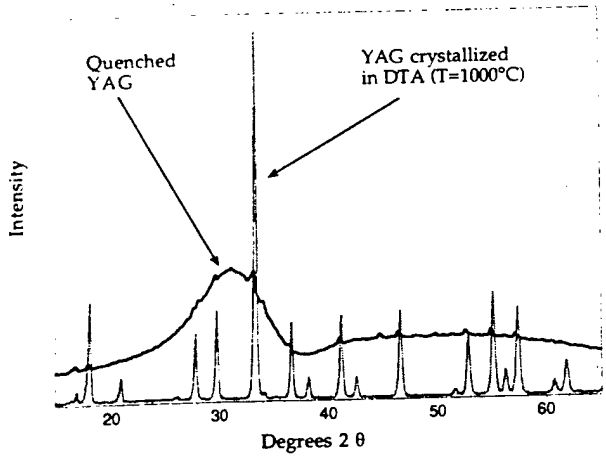
Figure 11. TEM bright field image of a cross sectioned amorphous YAG composition fiber which was pulled from a levitated, molten droplet using containerless methods. The web or lace-like features on most of the lower part of the specimen is the holey carbon film that the fiber was resting on. The dark region around the lower half of the circumference is the epoxy used to glue the fibers together.

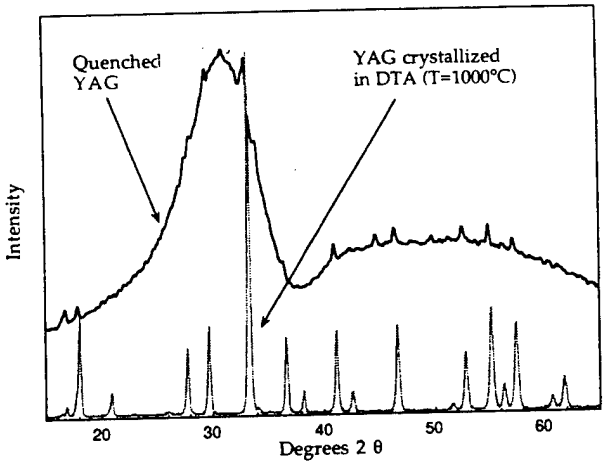

Differential, µV
Exothermic
Time, s
840 °C
845 °C
850 °C
855 °C
860 °C
865 °C
870 °C
875 °C

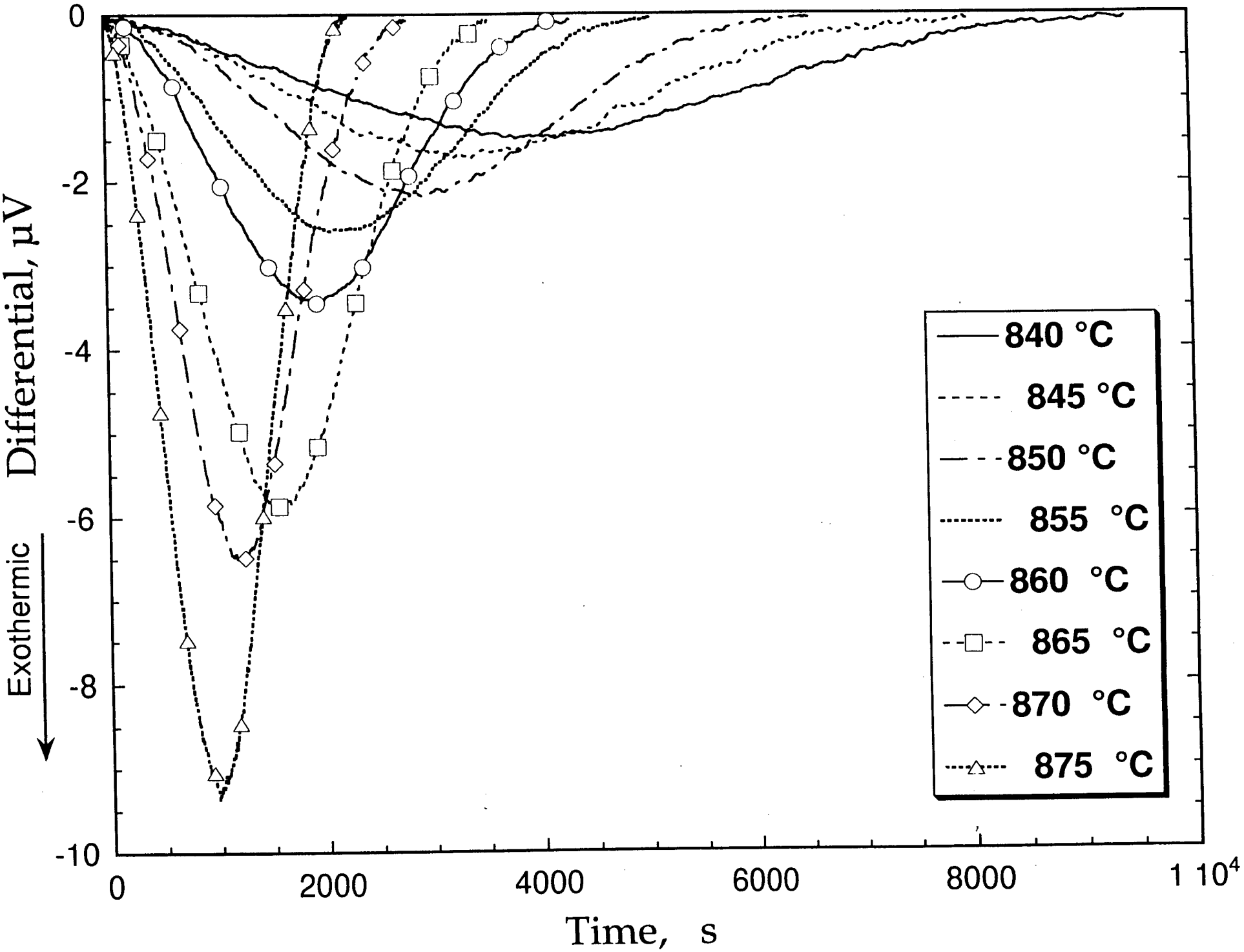

Sample Temperature, °C
Temperature, °C
Differential, µV
Exothermic
Time, s
c Differential, µV
Curve Fit
Curve Fit Data Table
Variable Value
A -6285.9
n 2.6529
k 3.8827E-04
t 1605.7
Chisq 2.1625
R² 0.99936

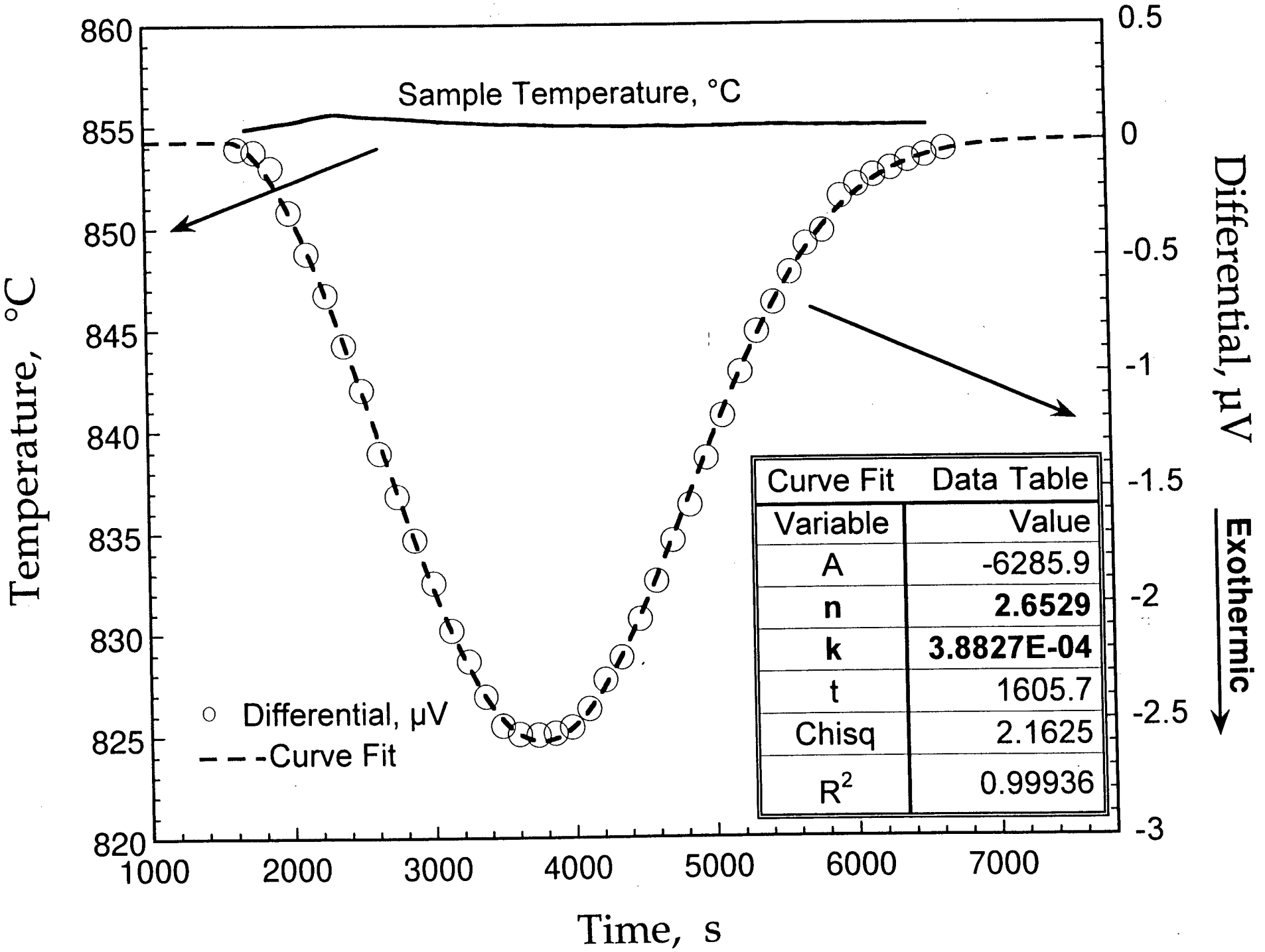

(Temperature, °C)
Reaction Rate Constant, k
Temperature, K
k = v * exp[-E/(R*T)]
Value
v 6.3316e+16
E 4.3704e+05
Chisq 3.1246e-09
R² 0.99093

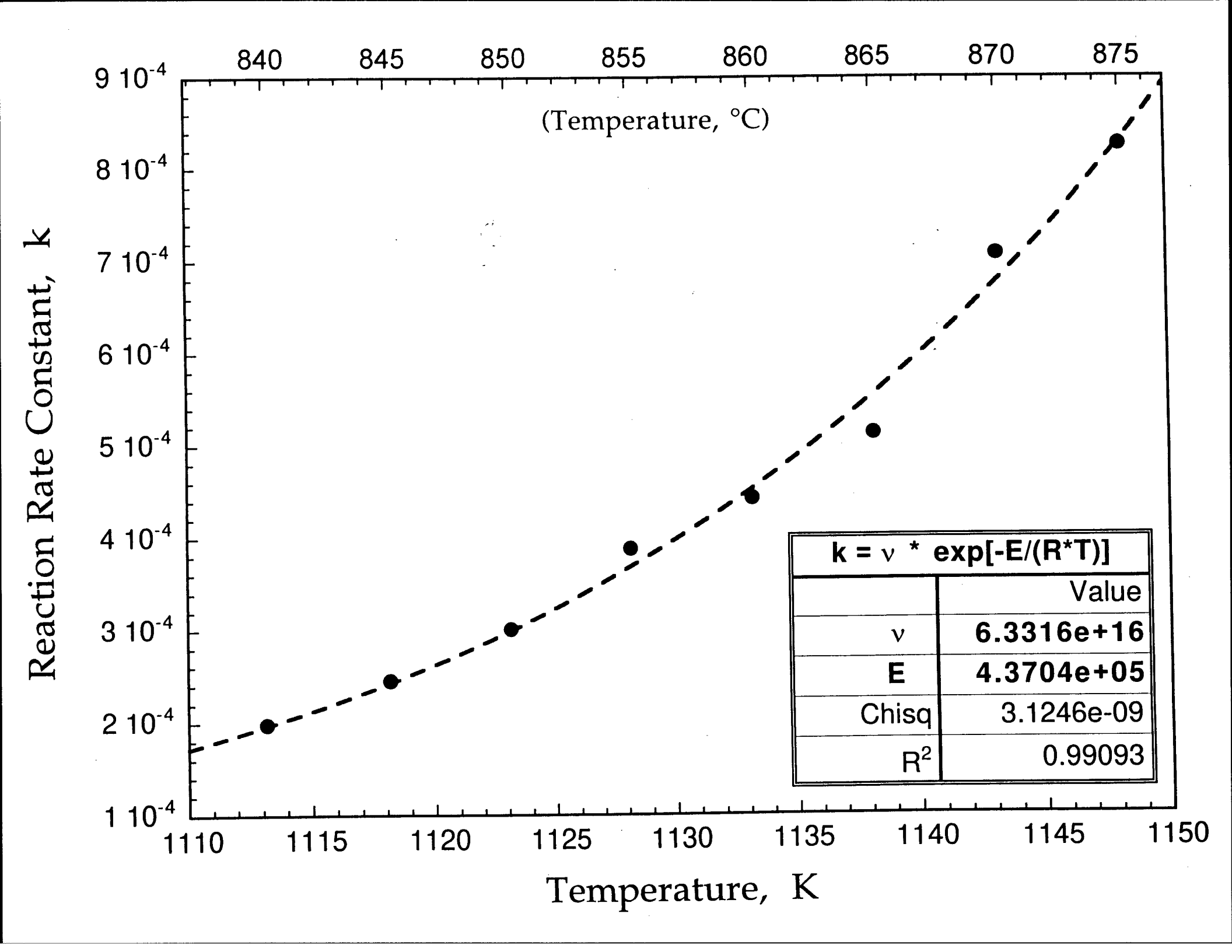

99% Crystallized
Measured data points from DTA exotherms
1% Crystallized
Temperature, °C
Time (s)

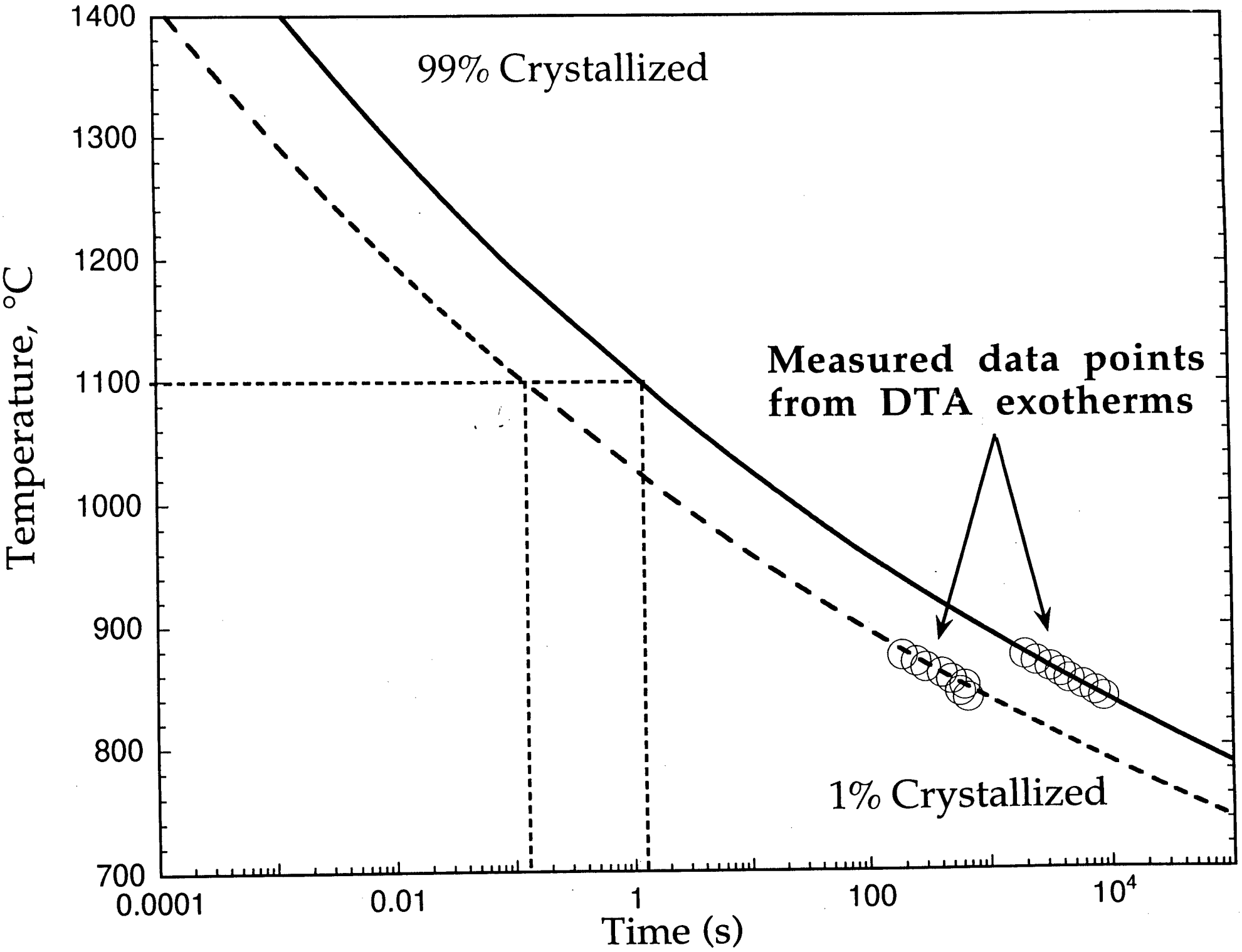

Quenched YAG
YAG crystallized in DTA (T=1000°C)
Intensity
Degrees 2 θ

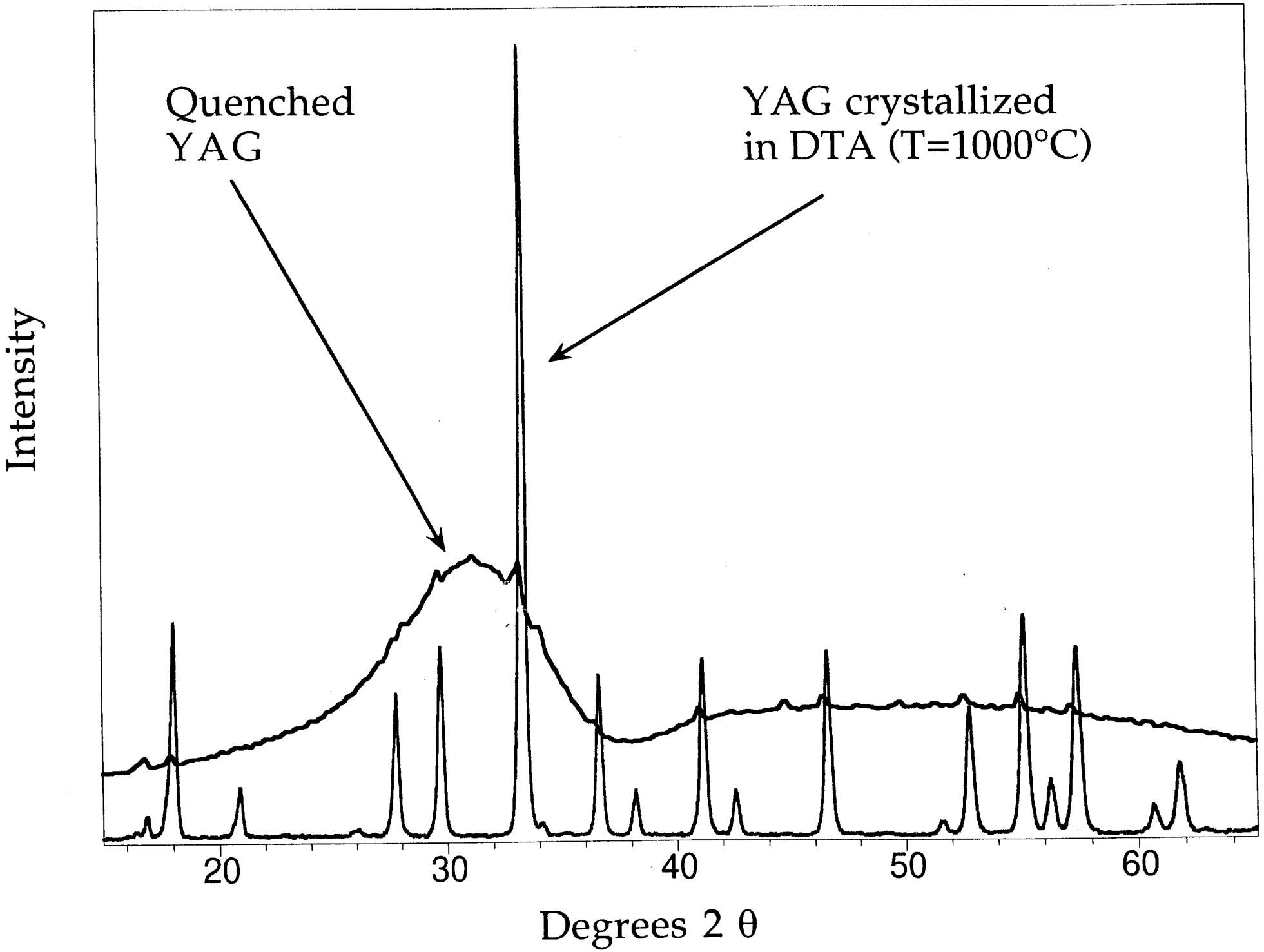

Quenched YAG
YAG crystallized in DTA (T=1000°C)
Intensity
Degrees 2 θ

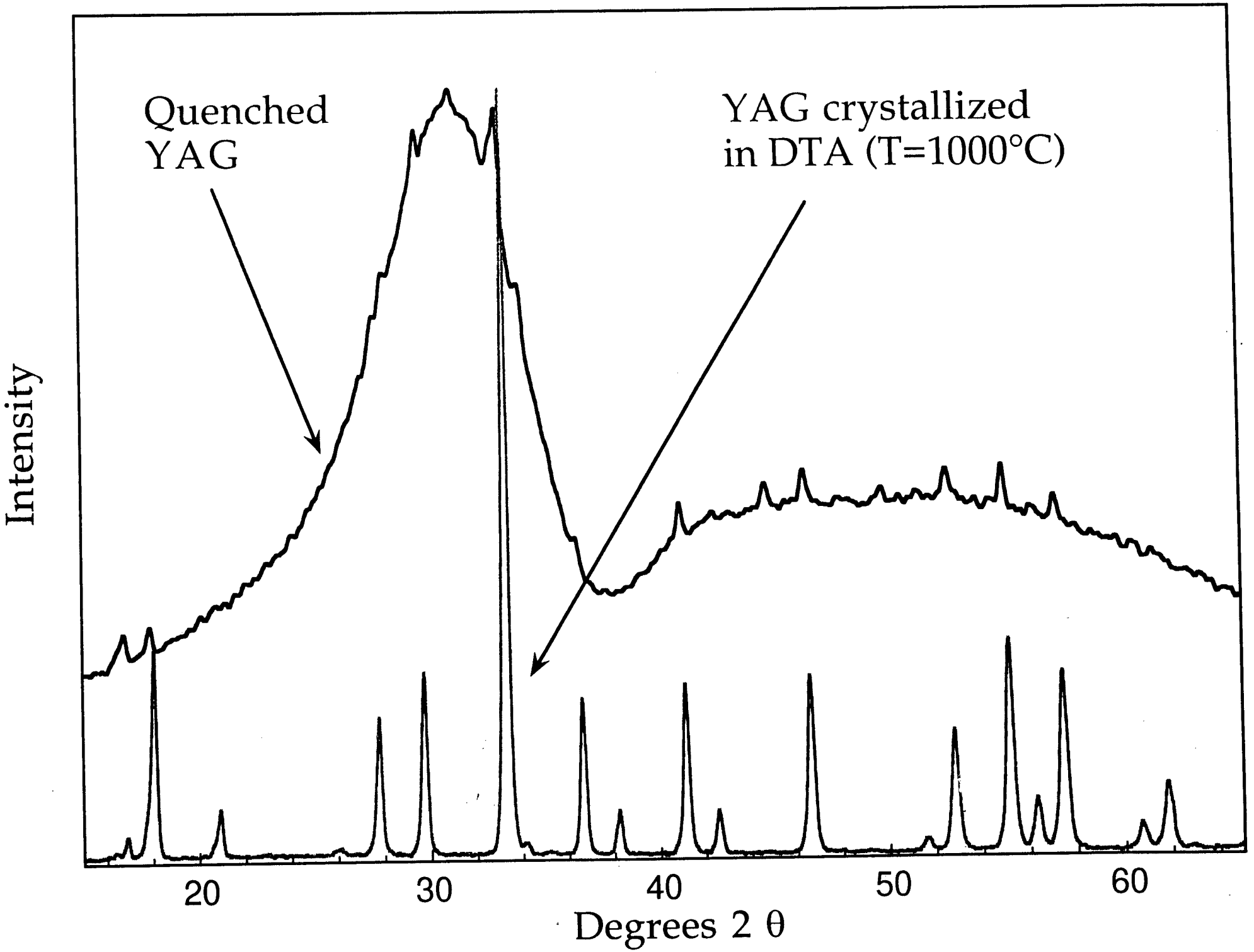

0
-2
-4
-6
-8
-10
Differential, μV
Exothermic
0
2000
4000
6000
8000
1 10^4
Time, s
840 °C
845 °C
850 °C
855 °C
860 °C
865 °C
870 °C
875 °C

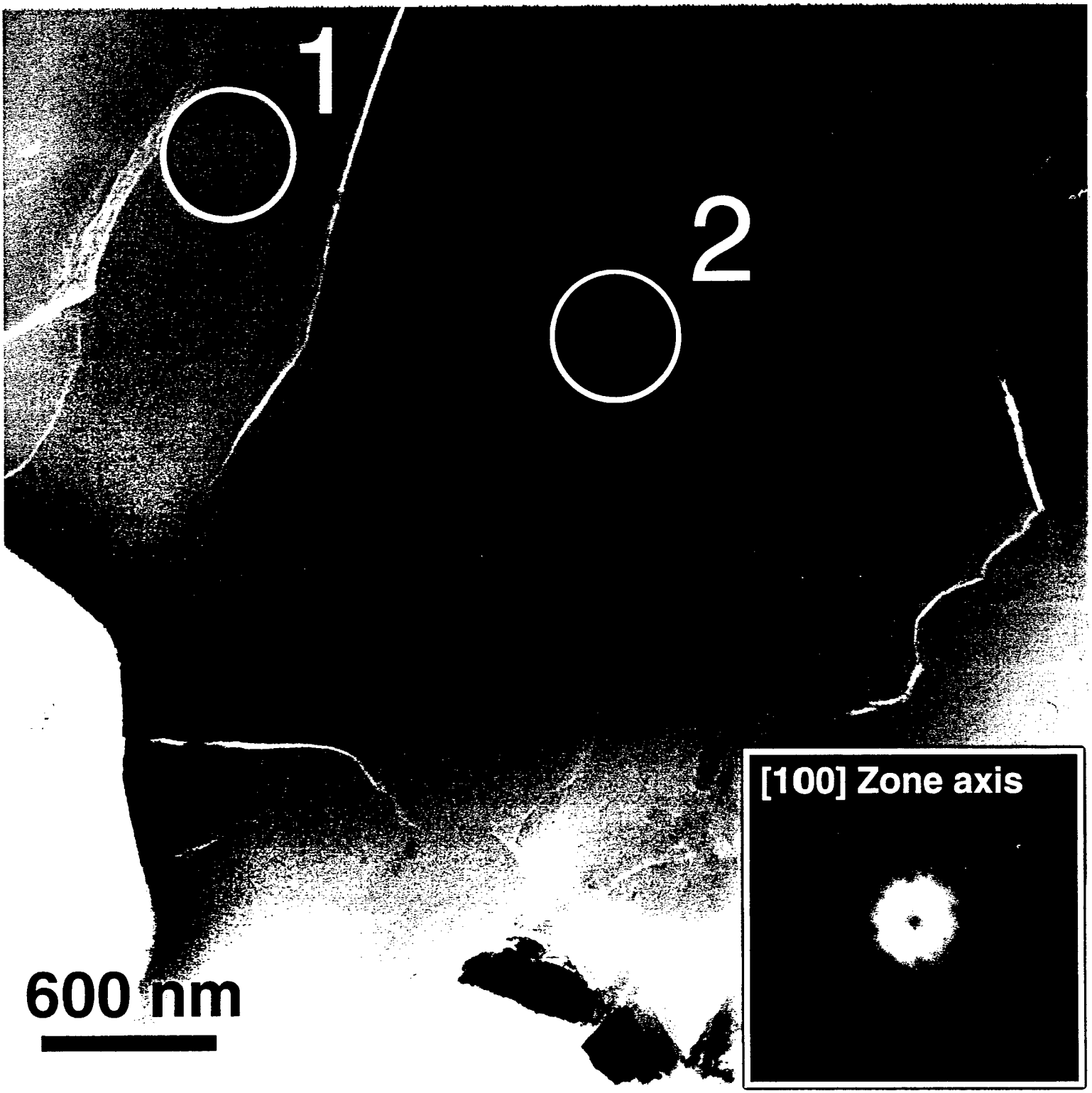

Sample Temperature, °C
Temperature, °C
Differential, µV
Exothermic
Time, s
Differential, µV
Curve Fit
860
855
850
845
840
835
830
825
820
0.5
0
-0.5
-1
-1.5
-2
-2.5
-3
1000
2000
3000
4000
5000
6000
7000
Curve Fit Data Table
Variable Value
A -6285.9
n 2.6529
k 3.8827E-04
t 1605.7
Chisq 2.1625
R2 0.99936

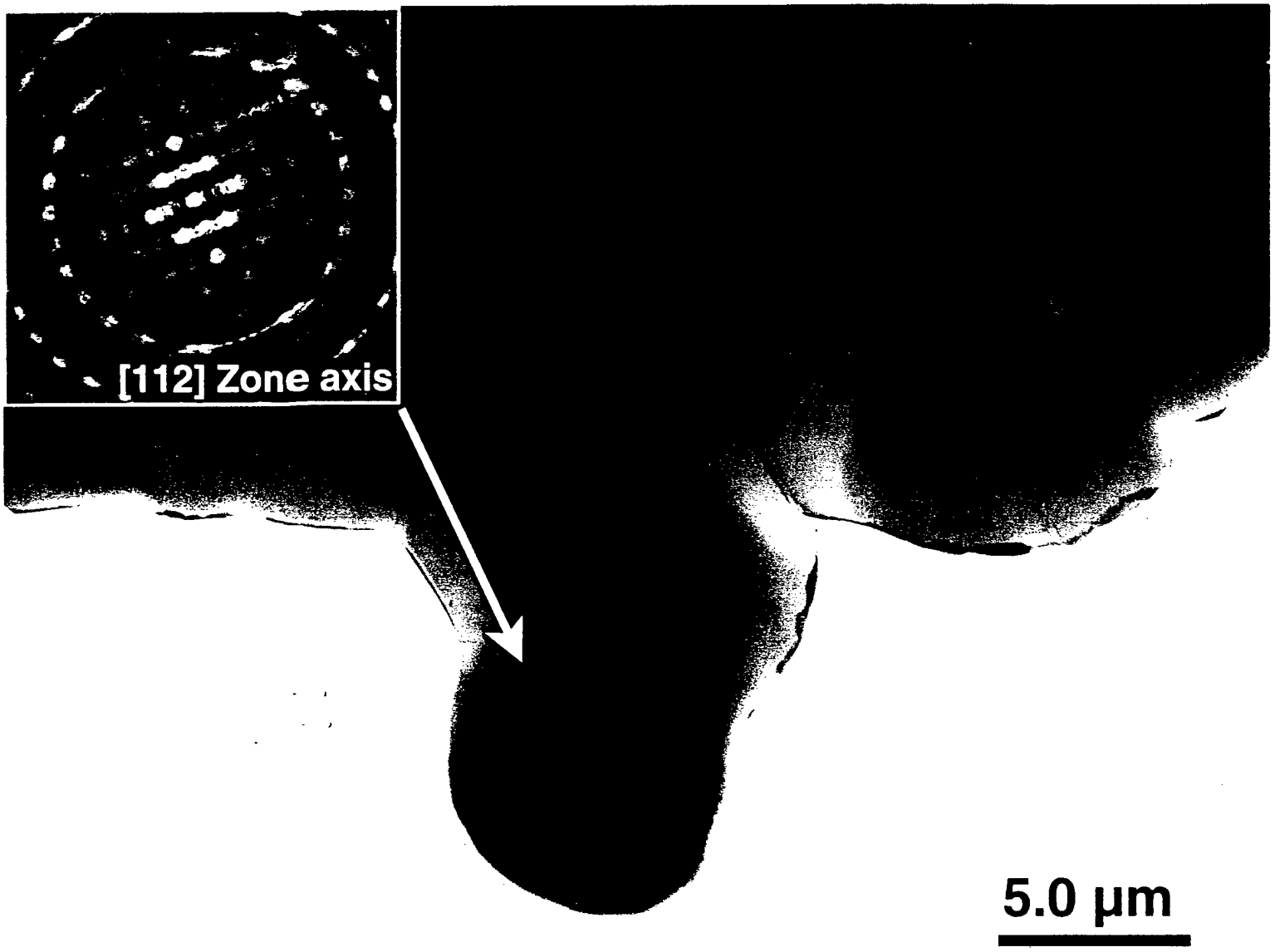

840
845
850
855
860
865
870
875
(Temperature, °C)
9 10-4
8 10-4
7 10-4
6 10-4
5 10-4
4 10-4
3 10-4
2 10-4
1 10-4
Reaction Rate Constant, k
1110
1115
1120
1125
1130
1135
1140
1145
1150
Temperature, K
k = ν * exp[-E/(R*T)]
Value
ν
6.3316e+16
E
4.3704e+05
Chisq
3.1246e-09
R2
0.99093

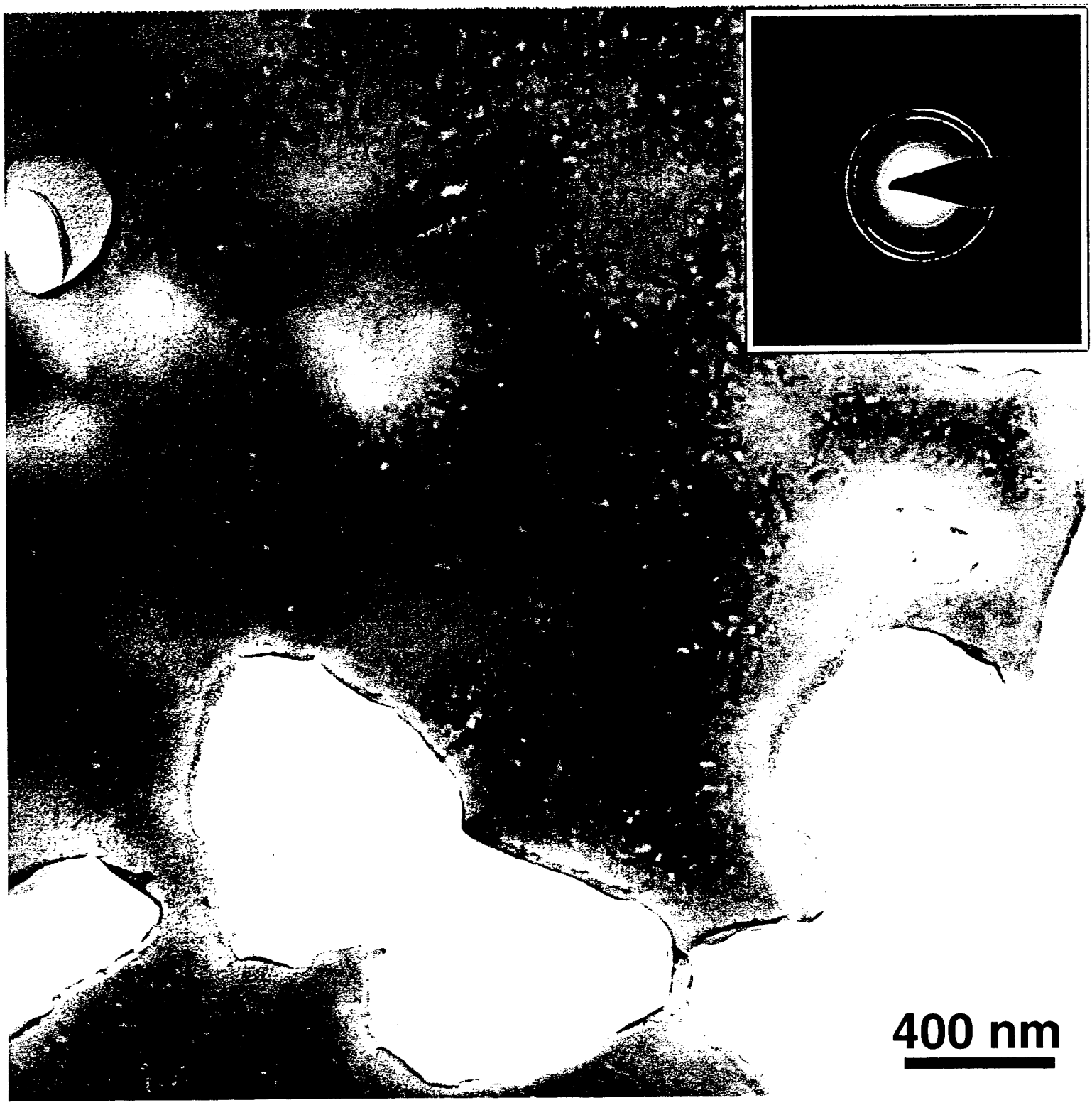

99% Crystallized
Measured data points
from DTA exotherms
1% Crystallized
Temperature, °C
Time (s)
1400
1300
1200
1100
1000
900
800
700
0.0001
0.01
1
100
10^4

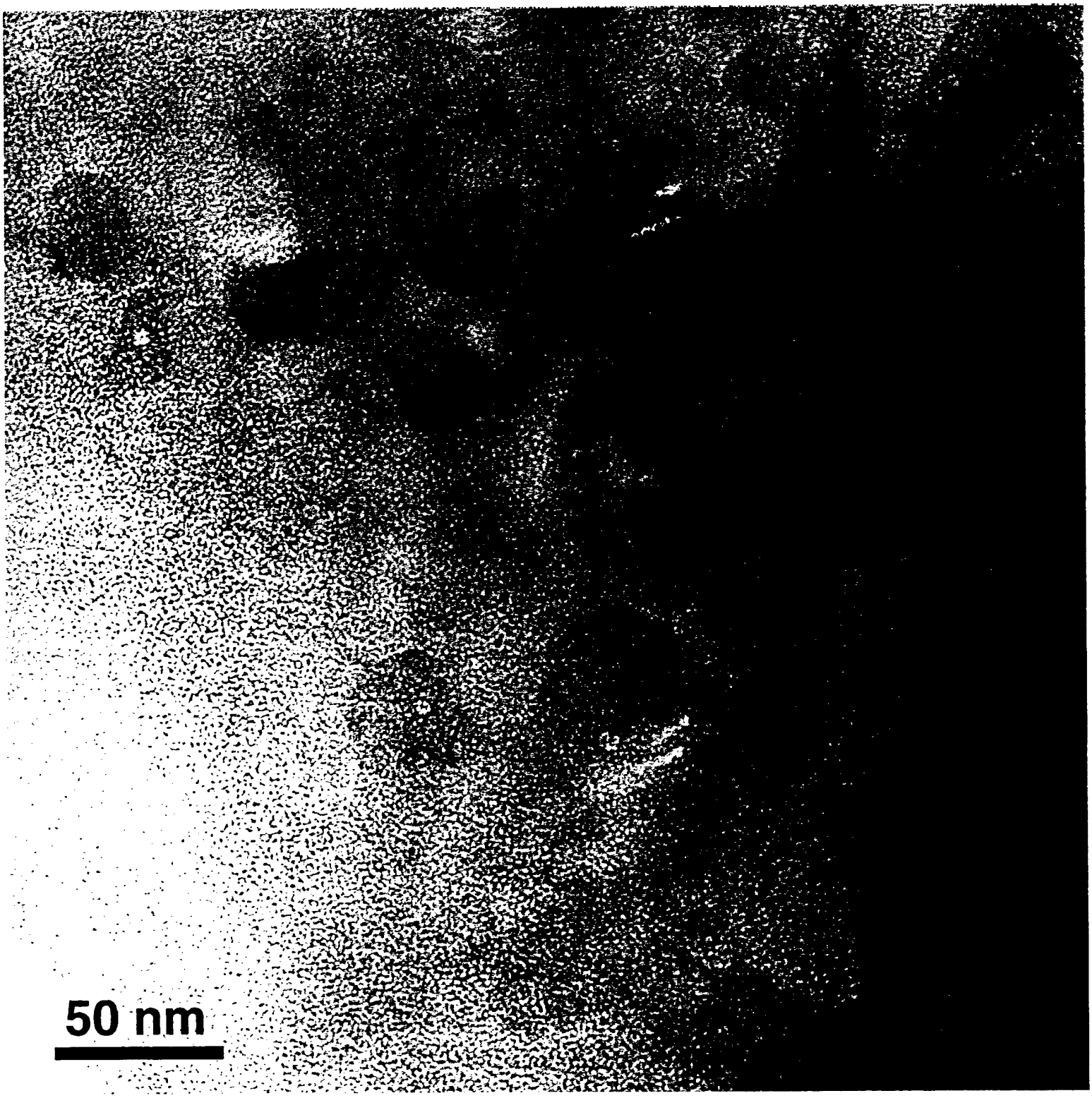

Quenched
YAG
YAG crystallized
in DTA (T=1000°C)
Intensity
20
30
40
50
60
Degrees 2 θ

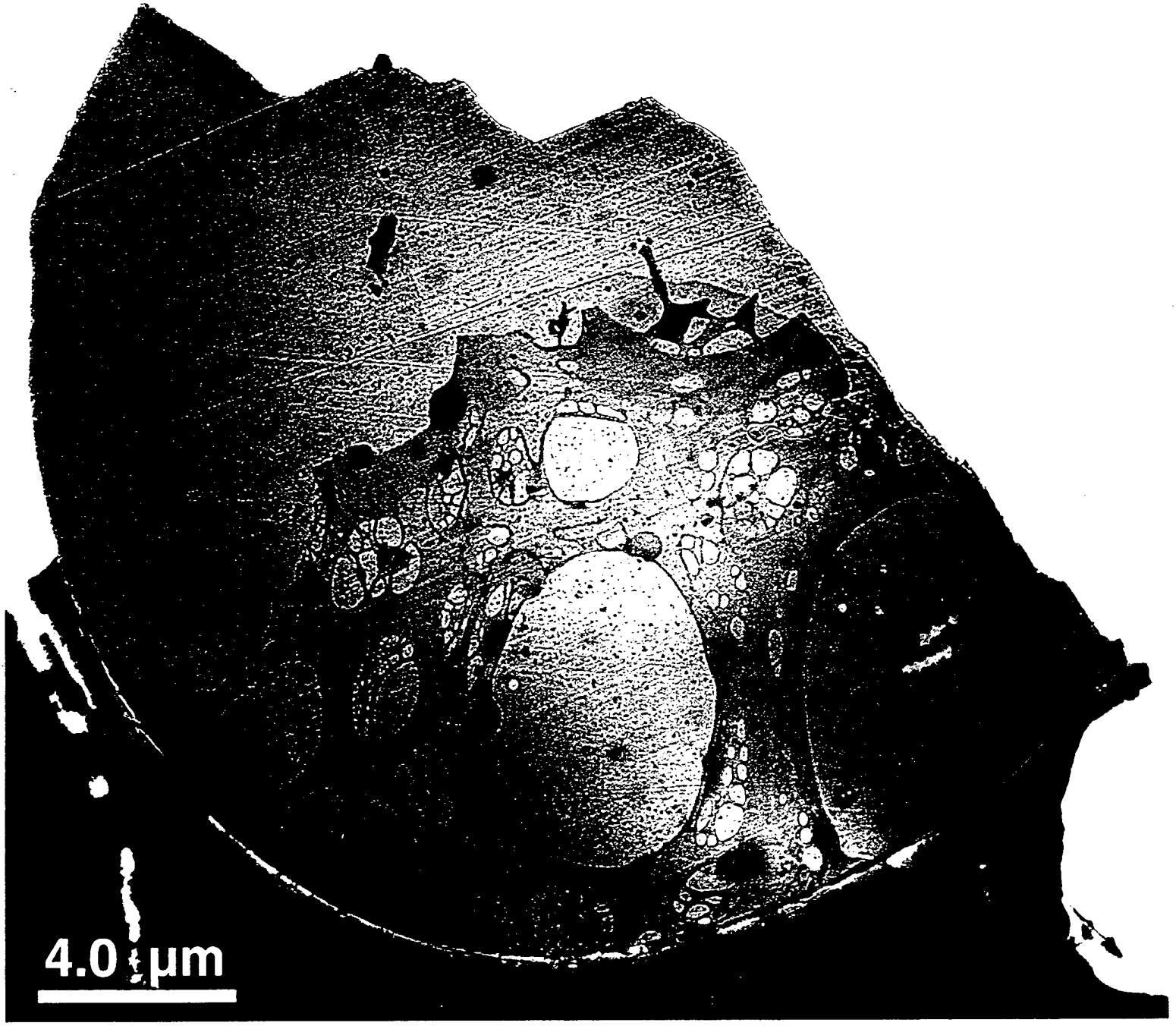

Quenched
YAG
YAG crystallized
in DTA (T=1000°C)
Intensity
20
30
40
50
60
Degrees 2 θ


1
2
600 nm
[100] Zone axis


[112] Zone axis
5.0 µm


400 nm


50 nm


4.0 µm

Crystal structure development during devitrification of amorphous mullite

Bradley R. Johnson, Waltraud M. Kriven
Department of Materials Science and Engineering, University of Illinois at Urbana-Champaign, Urbana, IL 61801

Julius Schneider
Institut für Kristallographie und Angewandte Mineralogie, München, Germany

Abstract

Crystallization kinetics, microstructural changes, and crystal structure development of quenched mullite composition glass ($3Al_2O_3 \cdot 2SiO_2$) were studied during the transition from an amorphous to a crystalline state between 900° and 1400°C. The phenomena observed were characterized using non-isothermal differential scanning calorimetry (DSC), transmission electron microscopy (TEM), energy dispersive spectroscopy (EDS) and powder x-ray diffraction (XRD) with both a standard laboratory diffractometer, as well as with synchrotron radiation. Crystallization of amorphous mullite was observed to occur in two steps. The activation energy for crystallization was 836.9 KJ/mole for the first step and 1,337.5 KJ/mole for the second step. From the amorphous state, the first phase(s) to crystallize were alumina-rich, pseudotetragonal mullite (~ 70 mol% Al_2O_3). These crystals were highly strained and contained numerous nanometer scale inclusions. With increasing temperature, the crystal structure was observed to incorporate increasing amounts of SiO_2, and approach the equilibrium orthorhombic structure. By 1400°C the pseudotetragonal to orthorhombic transition was complete, the strain and the inclusions were eliminated, there was ~ 67% reduction in grain size, and the crystals had attained the composition of the initial, bulk glass (~60 mol% Al_2O_3).

Keywords: Mullite, crystallization, kinetics, microstructure

1. Introduction

Mullite ($3Al_2O_3 \cdot 2SiO_2$) is the only stable compound in the Al_2O_3 - SiO_2 phase diagram at ambient pressures. It occurs in a narrow, temperature-dependent, solid solution range, between 60 - 63 mol% Al_2O_3.[1-3] It is an important structural and refractory ceramic with very good strength and creep properties. It is often used in such application as refractory bricks, furnace liners, and for structural fibers. Considerable work has been done to characterize the composition and structure of mullite.

The composition and crystal structure of mullite varies with the formation temperature. The correlation between the variation in the lattice parameters with the composition of mullite was initially reported by Cameron[4], and subsequently verified and refined by Kriven and Pask,[1] Okada and Otsuka,[3] Ban and Okada,[5] and Fischer et al.[6,7] The equilibrium crystal structure of mullite with a composition of $3Al_2O_3 \cdot 2SiO_2$, (60 mol% Al_2O_3) is orthorhombic, and it belongs to the space group Pbam.[8-11] However, when formed from molecularly mixed precursors, the first mullite crystals formed tend to be Al_2O_3-rich, (~70 mol% Al_2O_3) independent of the bulk composition of the precursors.[12] These crystals have an a-lattice parameter that is very close in size to their b-lattice parameter. This initial crystal structure has sometimes been termed pseudotetragonal mullite.[5,13-15] Another way to describe the structure is to call it the "pseudotetragonal metric"[16] since the crystal symmetry is still orthorhombic even when the a-lattice and b-lattice parameters are equal in length. Although termed pseudotetragonal, there is only a very subtle difference between the pseudotetragonal metric and orthorhombic mullite. This distinction can be observed by close examination of the extent of splitting between the (120) and (210) peaks at approximately 26° 2θ (using Cu Kα radiation). When initially formed, the two peaks overlap for the pseudotetragonal metric, and as the annealing temperature increases, the peaks tend to split apart and become more distinct (d_{120} = 3.428Å, d_{210} = 3.390Å, Powder Diffraction File 15-776)).[14,17] This structural change with increase in temperature was interpreted as incorporation of SiO_2 into the mullite structure, resulting in the reduction of the a-lattice parameter.[3,18]

An anomaly of the gradual compositional and structural change in mullite as it crystallizes, is the variation in the c-lattice parameter. Although the "a" and "b" lattice parameters change linearly with composition, (and hence with temperature as precursors crystallize), the value and the variation of the c-lattice parameter depends on the initial formation temperature. Mullite crystals of a given composition formed at temperatures below 1200°C have c-lattice parameters that are approximately 0.0005 nm shorter than mullite crystals of the same composition that were heated above 1200°C. This variation was first pointed out by Ban and Okada[5,19], but the same trend can be observed in data previously presented by Okada et al.[3,18]

Considerable work has been done regarding the crystallization of amorphous mullite precursors.[20-23] Depending on the degree of homogeneity, two primary crystallization pathways appear to be most prominent. In the case of molecularly mixed precursors (such as a slowly hydrolyzed sol-gel precursor, or an amorphous glass) mullite crystallizes at approximately 1000°C, depending on the heating rate.[18] For inhomogeneously mixed systems (e.g. kaolinite, diphasic precursors, or rapidly hydrolyzed gels) intermediate phases such as spinel ($6Al_2O_3 \cdot SiO_2$) form around 1000°C, and are subsequently converted to mullite around 1200°C.[24-29] For chemically synthesized mullite, the processing conditions play a critical role in

obtaining single-phase, molecularly mixed precursors, and great care is necessary to avoid forming diphasic precursors.[30]

Recently, work has been done to synthesize structural mullite fibers drawn from the melt using containerless methods.[31-33] These amorphous fibers require subsequent thermal processing to crystallize them. The crystallization of quenched, amorphous mullite composition glasses was studied to determine appropriate processing conditions for the crystallization of melt-drawn mullite composition fibers. This work was focused on gaining greater understanding of the crystallization kinetics, microstructural changes, and crystal structure development of amorphous, quenched, mullite composition glass.

2. Experimental Procedures

Materials: Commercially obtained mullite powder (KM 101 mullite powder, Kyoritsu Ceramic Materials Co. LTD., Nagoya, Japan) was supplied to Containerless Research Inc. (Evanston, IL) for processing to synthesize amorphous beads and fibers. The powders were melted in a water-cooled hearth using a CO_2 laser to form a spherical bead.[34] The bead was then levitated in an oxygen atmosphere with an aero-acoustic levitator, and melted again with a CO_2 laser as described in literature elsewhere.[35-38] Melt temperatures were approximately 2200°C as indicated by optical pyrometry. The suspended molten droplet was then rapidly quenched at a rate of approximately 250°C per sec, to form a solid bead about 2 – 3 mm in diameter. The beads were subsequently crushed between two stainless steel plates to form a coarse powder. Final grinding was accomplished with an agate mortar and pestle, to produce a fine powder that was used in thermal analysis, x-ray diffraction, and TEM experiments.

Thermal analysis: Nucleation and crystallization studies of as-received, ground, quenched, mullite composition beads were conducted with a Netzsch STA 409 Simultaneous Thermal Analyzer (Selb, Germany) used in DSC mode. The experiments were done in a flowing atmosphere of 75cc/min of Ar, and covered Pt crucibles to were used to hold the specimen and the reference. Temperature calibration of the instrument was accomplished by observing the melting points of 99.999% gold and silver. The average value of three different melting points was used. A mass of ~15.0 mg was used for the sample and reference material (α-alumina).

Two different types of experiments were used to study the nucleation and crystallization of amorphous, mullite composition glasses. Nucleation experiments were conducted to determine the effects of pre-crystallization heat treatment on the crystallization temperature, T_p (the temperature at the maximum of the crystallization exotherm). This information was necessary to set up conditions for the second set of crystallization experiments. Non-isothermal DSC experiments were done to determine the crystallization kinetics. For nucleation experiments, specimens were heated at 20°C/min to a specified soak (or nucleation) temperature (T_N),

annealed at that temperature for 3 hr. and then heated again at a 10°C/min to a maximum temperature of 1100°C. The variation in crystallization temperature, T_p, during the second heating ramp was observed. This was repeated for a series of different nucleation temperatures (850°C to 940°C). For non-isothermal DSC experiments, specimens were heated at a rate of 20°C/min to 850°C, and held there for 15 min. Above that temperature, ten different heating rates were used (viz. 0.5°, 1.0°, 1.5°, 2.0°, 3.0°, 4.0°, 5.0°, 6.0°, 8.0° and 10.0° C/min) to heat the specimen up to a maximum temperature of 1100°C. Crystallization was observed to occur exothermally during the second heating ramp segment. The variation in T_p with heating rate was used to calculate the kinetics of crystallization.

Electron Microscopy: The microstructure and microchemical composition of mullite at various stages of crystallization was characterized using a TEM (Philips CM12, FEI Company, Hillsboro, OR, USA) equipped with an EDS detector (EDAX, Mahwah, NJ, USA). Selected specimens were also examined with a Vacuum Generators HB 501 scanning transmission electron microscope (STEM) equipped with a 100 kV field emission gun filament and an Oxford Instruments (Oxfordshire, England) Link® EDS system. Several different specimens were chosen after being subjected to various thermal treatments (Table 1). Specimens were prepared from ground, quenched, mullite composition beads as well as from tripod polished,[39,40] and ion milled sliced sections of quenched beads. The specimens were examined by bright field (BF) and dark field (DF) imaging, convergent beam electron diffraction (CBED), selected area diffraction (SAD), and energy dispersive spectroscopy (EDS). Quantitative EDS calculations were based on the Cliff-Lorimer approximation.[41] The camera length constant for the microscope was determined from a specimen of evaporated gold deposited on to holey carbon film. The diffraction patterns for gold and the various specimen images were collected digitally and distances were measured using a free-ware image analysis software package (*MacLispix*) made available by the National Institute of Standards and Testing (NIST).[42] Quantitative particle size measurements were made with the image analysis program *Object-Image*[43] using micrographs taken with a calibrated CCD camera (Gatan Multi-Scan camera, Gatan, Inc., Pleasanton, CA).

X-ray diffraction: Initial x-ray diffraction studies were conducted with a Cu K_α source on a standard laboratory diffractometer, (Giegerflex DMax automated powder diffractometer, Rigaku/USA, Danvers, MA) equipped with a graphite monochromator. The diffractometer was operated at a voltage of 40 kV and a current of 40 mA with a slit system of: 1/2°-1/2°-0.3mm-0.8mm. The data was collected in a theta – 2-theta scanning mode. Spectra were collected from crushed, quenched beads, before and after crystallization in thermal analysis experiments. For crystallized specimens, typically a goniometer speed of 2° 2θ/min was used with a step size of 0.01° 2θ, and the data was summed over 10 scans. For quenched specimens, typically a

goniometer speed of 2° 2θ/min was used with a step size of 0.01° 2θ, and the data was summed over 50 scans.

Detailed crystal structure measurements of annealed powder specimens (M1, M2, M3 and M4, Table 1) were made at the Advanced Photon Source (APS) at the Argonne National Laboratory at the UNICAT beamline E33 (the undulator). Specimens were chosen to represent various stages of mullite crystallization (Table 1). The beam cross section was approx. 2 x 1 mm and the wavelength was 0.75266 Å, as determined by Rietveld refinement of a Si standard (SRM 640b, National Institute of Standards). Specimens were loaded in a capillary tube with a 0.5mm ID, which was rotated at a minimum rate of 60 rpm. The data was collected by step scanning a single slit scintillation counter, versus a constant monitor counting rate. Minimum counting times of about 1 second per step were chosen to achieve at least one revolution of the capillary sample spinner. An angular range of 5.0° - 37° 2θ (8.6276 - 1.1860 Å) was scanned at a step size of 0.008°, yielding 4000 data points per powder diagram.

3. Results and Discussion

3.1. Thermal Analysis

The Johnson-Mehls-Avrami (JMA) equation (Eq. 1) was the basis for modeling non-isothermal DTA experiments. Although this equation was derived for isothermal phase transformations, it has been successfully applied to non-isothermal DTA or DSC experiments under appropriate experimental conditions.[44-48] The key relationship observed is the variation of the crystallization temperature, T_p, with heating rate, α. Since the crystallization exotherm is not a delta function, but rather a curve that occurs over a range of temperatures, it is important to determine the temperature at each heating rate that corresponds to the same degree of crystallization. This is necessary to accurately model the α *vs.* T_p trend. It has been demonstrated that the maximum in the crystallization exotherm corresponds to approximately 55% conversion, independent of the heating rate.[45] Thus the temperature at the exothermic peak (T_p) was chosen as the reference temperature in these studies.

$$x = 1 - \exp\left[-(kt)^n\right] \tag{1}$$

A pre-requisite for using JMA based equations for kinetic analysis of non-isothermal experiments, as pointed out by Ray et al.,[47] is that the specimen must be thoroughly nucleated prior to crystal growth so that crystallization occurs with a constant number of nuclei. This precludes a situation where nucleation and growth occur simultaneously. Experimental conditions where crystallization occurs with a constant number of nuclei is also an important factor for using the equation for the reaction rate, k, (Eq.2). The reaction rate is typically assumed to have an Arrhenius temperature dependence, and to be independent of time. In order to minimize errors when calculating the reaction rate, non-isothermal crystallization experiments should be designed to occur within a narrow temperature range and with a near-zero nucleation rate.[47]

$$k = \nu \exp\left[\frac{-E}{RT}\right] \tag{2}$$

The kinetic model proposed by Bansal and Doremus[44,45] was used to analyze the non-isothermal crystallization data for these experiments. The final result of their derivation is shown in Eq. 3. A plot can then be made of $\ln(\alpha/T_p^2)$ vs. $1/T_p$. This type of plot is sometimes termed a Kissinger plot.[47,49]

$$\ln\left(\frac{T_p^2}{\alpha}\right) = \frac{E}{R}\left(\frac{1}{T_p}\right) + \ln\left(\frac{E}{R\nu}\right) \tag{3}$$

The slope of the line through the data points is used to calculate the activation energy for crystallization, E, and the y-intercept of the line is used to calculate the pre-exponential factor, ν in Eq. 2.

The other variable yet remaining to be calculated from the data is the Avrami exponent, n. The method of Augis and Bennet[50] was used, Eq. 4.

$$n = \frac{2.5}{\Delta T_{FWHM}}\left(\frac{T_p^2}{E}_R\right) \tag{4}$$

The value of the Avrami exponent provides information regarding the morphology of the growing crystals. For conditions where crystallization occurs throughout the bulk of the material with a constant number of nuclei, the value of n indicates the dimensionality of the growing crystals.[47] All of the pertinent variables (n, k, E and ν) for the JMA equation (Eq. 1) were thus computed from the non-isothermal data.

3.1 a Nucleation Studies

Nucleation experiments were carried out to determine necessary annealing conditions to saturate the quenched glass with nuclei. Since the nucleation rate is a function of time and temperature similar to crystal growth,[51] there is a variation of T_p with the soak temperature, T_N. The soak temperature where T_p is the lowest, is where the nucleation rate is a maximum. Annealing the specimens at this temperature would thus saturate them with nuclei and establish appropriate conditions for non-isothermal crystallization studies. This variation is typically pronounced for strong, glass-forming systems, (e.g. Li_2O-Al_2O_3-SiO_2 glasses).[47,48]

Nucleation rate studies on quenched mullite composition glass beads did not show a significant variation of T_p with T_N. The standard for comparison was a specimen heated at a rate of 10.0°C/m from room temperature to 1100°C. There was no significant difference in T_p between the standard sample heated at 10.0°C/min and those subjected to the various annealing treatments. The specimens isothermally held at 930°C and 940°C crystallized during the hold time. The results are listed in Table 2. Thus, it was concluded that the specimens were fully nucleated by the time they reached 850°C, and that further annealing treatments were unnecessary. These findings seemed reasonable, since mullite is a very fragile glass forming material.

3.1 b Crystallization Kinetics

Non-isothermal DSC crystallization experiments with quenched mullite composition specimens were conducted as previously stated. Results for the heating rate, T_p, and the Avrami exponent are listed in Table 3. A Kissinger type plot[49] (Figure 1, based on Eq. 3) was used to calculate the activation energy, E, and pre-exponential factor, ν.

A significant change in slope between 3.0°C/min and 4.0°C/min heating rates was observed (Fig. 1). This indicated that more than one kinetic mechanism was involved in the crystallization process. A closer examination of the DSC exotherms at these lower heating rates (e.g. < 6°C/min) revealed that there were two different exothermic events that occurred during crystallization. At heating rates ≤ 3.0°C/min, the first event was dominant, whereas at heating rates ≥ 4.0°C/min, the second event became dominant. Figure 2 is a comparison of the DSC exotherms at 3.0 and 4.0°C/min, showing the two different exothermic events, and the shift in dominance between them. The values for T_p listed in Table 3 were the more prominent of the two. At heating rates above 5.0°C/min, the two peaks overlapped sufficiently so that it was very difficult to differentiate between them. For $\alpha \geq 8.0$°C/min, the increased intensity and overlap of the two events created significant asymmetry in the shape of the crystallization exotherms.

The linear regression correlation coefficient (R^2) for the line fit applied to heating rates ≤ 3.0°C/min on Fig. 1 was 0.994 and the value of R^2 for the line fit applied to heating rates ≥ 4.0°C/min was 0.987. The activation energies for crystallization were 836.9 and 1,337.5 KJ/mole for the first and second events, respectively. The values of the Avrami exponent, *n*, in Table 3 were calculated based on Eq. 4. The combined average value of *n*, was 2.6, which indicates three dimensional crystal growth. (The values of n for α = 8.0 and 10.0 °C/min were not included in the average due to the significant asymmetry in the shape of the crystallization exotherm.) The values for ν (4.5E+32s^{-1}, and 5.27E+53s^{-1} for events one and two, respectively) were rather large. Since mullite is a fragile glass former, and these values were determined from the extrapolated value of the y-intercept from Fig. 1 using Eq. 3, there may be a reasonable margin of error in the computed values of ν. Nonetheless, they do reflect the rapidity at which amorphous mullite composition glasses crystallize.

The activation energy for mullite crystallization has been reported to be precursor dependent.[23] Nonetheless, the calculated activation energies for mullite crystallization in this system lie within the range of values reported in the literature, e.g. ~ 850 - 1300 KJ/mol.[20,22,23,52,53] Additionally, the phenomena of two over-lapping crystallization exotherms for isothermal crystallization of sol-gel derived precursors was reported by Tkalcec et. al[20], and a 3-stage crystallization sequence in alumino-silicate fibers was reported by Takie et al.[53] The two mullite crystallization activation energies reported here, (836.9 KJ/mol, and 1,337.5 KJ/mol) correlate very well with the two activation energies for first stage crystallization of a 49 mass% Al_2O_3 fiber reported by Takei et. al.[53] (E_a^N for nucleation was 864 KJ/mol and E_a^{NG} for nucleation and growth was 1288 KJ/mol). Their three stage crystallization sequence (Stage 1 = 900°-1000°C, Stage 2 = 1000°-1200°C, and Stage 3 = 1200°-1400°C) was determined by quantitative XRD analysis of alumino-silicate fibers crystallized after various thermal treatments. Thus, it was satisfying to note that the non-isothermal DSC derived kinetic data reported here, for the crystallization of quenched mullite composition glass (at temperatures below 1000°C), was similar to that determined by quantitative XRD analysis, for their Stage 1 crystallization of alumino-silicate fibers.

The two different exothermic events observed during crystallization were probably the result of two slightly different composition mullite phases crystallizing. The shift in the prominence of the two exothermic events indicates the possibility of competing crystallization mechanisms between the two compositions. Microstructural characterization and Rietveld analysis were conducted to corroborate the existence of multiple phases in mullite crystallized at low temperatures. Those findings are discussed below.

3.2. Microstructure

3.2 a As-received and nucleated specimens (Q and N)

Specimens Q and N were used to characterize the as-received mullite beads, and to examine the microstructure of mullite just prior to crystallization. Figure 3 is a TEM bright field (BF) (A) and a STEM BF (B) micrograph of a polished, thin section from an as-received, quenched mullite bead (specimen Q, Table 1). The contrast observed in the specimen was typical of phase-separated, amorphous materials. Chemical analysis of the specimen at various points revealed a wide variation in composition. The chemical composition for the field of view in Fig. 3B was 75.8 mol% Al_2O_3 and 24.2 mol% SiO_2. An EDS line scan showing a variation in the Al/Si ratio within Fig. 3B is shown as an inset image. The observed sub-micron chemical inhomogeneity for the quenched specimens was consistent with reports of a metastable immiscibility gap in the Al_2O_3-SiO_2 phase diagram.[54-57] This apparent phase separation may have been responsible for the two crystallization events observed by DSC.

Figure 4 is a TEM BF micrograph of a quenched, amorphous, melt-drawn mullite fiber that was annealed at 920°C for 3h (specimen N, Table 1). This thermal treatment was the highest annealing temperature that was observed in the DSC, without the onset of complete crystallization (Table 2). The dark regions were examined by selected area diffraction (SAD), and were identified as small crystallites. The SAD pattern of the crystallites is shown in the inset image in Fig. 4A. The pattern was indexed as belonging to the pseudotetragonal metric of mullite. The size of 150 crystallites was measured and the average length of the major and minor axes was 13.4 ± 2.9 nm and 11.5 ± 2.7 nm, respectively (Table 4). A high resolution micrograph of one of the crystallites is shown in Fig. 4B. The d-spacing for the lattice fringes in this crystallite was 3.38Å, which is close the d-spacing for the (120) and (210) lattice planes of orthorhombic mullite (3.428Å, and 3.390Å, respectively). It was only possible to resolve one ring at this d-spacing in the SAD pattern, which is consistent with psuedotetragonal mullite.

3.2 b Pseudotetragonal mullite (M1, M1.5, and M2)

The thermal treatments applied to specimens M1 and M2 were chosen in order to characterize pseudotetragonal mullite after initial formation and just prior to conversion into orthorhombic mullite, respectively.[5,17,19] These specimens correspond to the first and second crystallization stages reported by Takei et. al.[53] Specimen M1.5 was used to compare the effects of sample preparation (powders *vs.* thin film) on microstructure for pseudotetragonal mullite and to examine the microstructure at an intermediate temperature. Figure 5 is a TEM BF micrograph of a crushed, quenched, mullite composition bead that was crystallized isothermally by annealing it at 938°C for 2.5h (specimen M1). The microstructure consisted of a matrix of

angular, crystalline grains (~370 x 260 nm in size) with smaller, ellipsoidal inclusions (average size = 10.0 x 7.8 nm) embedded in them (Table 4). Figure 6 is a higher magnification of another particle from the same specimen. The right portion of Fig. 6A was one of the grains; the smaller, rounded, lighter features were the inclusions. In bright field mode, the grains had a variegated diffraction contrast (Fig 5), where different regions of the grain would go in and out of extinction in a sweeping fashion as it was tilted. Figure 6B is the same area as Fig. 6A, only in a dark field condition. The beam was tilted so that a particular set of lattice planes from the grain were allowed to pass through the objective aperture, thus creating the bright band in Fig. 6B. The dark circular features were the ellipsoidal inclusions.

Figure 7 consists of TEM BF micrographs from a polished thin section of a quenched mullite bead that was heated to 1085°C for 0.5 h (specimen M1.5). EDS analyses were taken at the ten different labeled points in Fig. 7A (beam diameter ~ 70 - 100 nm), and the average composition at each point was 60 ± 1 mol% Al_2O_3, 40 ± 1 mol% SiO_2. Figure 7B is a micrograph from M1.5 at higher magnification showing a grain and a large number of small, ellipsoidal inclusions embedded in it (similar to what was observed in Fig. 6). The inclusions appear as bright spots on the right side of the micrograph, and as dark spots on the left side. When the specimen was observed in an over- and under-focused conditions at higher magnification (at the same angle of tilt), the contrast of the inclusions changed from dark areas with a light fringe to light areas with a dark fringe. This was interpreted as a Fresnel fringe effect due to a density difference between the inclusions and the matrix (inclusion density < matrix density).[41] The inset image is a [001] zone axis SAD pattern taken from another grain in this specimen. Any extra spots in the pattern not belonging to the zone axis were identified to originate from an adjacent or overlapping grain by DF mode, and were not from the inclusions. Qualitatively, the microstructures for M1 and M1.5 appeared very similar, howerver, quantitatively, subtle differences were noted. The average length of the major and minor axes for the small, ellipsoidal inclusions was 9.4 ± 2.5 nm and 7.9 ± 2 nm respectively, and the average size of the major and minor axes for the grains was ~510 nm and 380 nm, respectively (Table 4). Figure 8 is a BF STEM micrograph of M1.5 where an EDS line scan was performed using a much smaller beam diameter than for the EDS analysis in Fig. 7A. The inset graph illustrates the variation in the Al/Si ratio over the scanned line. The smaller diameter beam was able to reveal chemical heterogeneity in this specimen that was not observed in Fig. 7.

Figure 9 is a TEM BF micrograph of a crushed, quenched mullite composition bead that was heated to 1200°C (specimen M2). The inset image is a Kossel-Möllenstedt (KM) micro-diffraction pattern taken from one of the crystals oriented along the [120] zone axis for mullite. The average grain size was 270 x 190 nm. Small inclusions embedded within the grains were also observed, with an average size of 7.9 ± 1.7 x 6.6 ± 1.5 nm (Table 4). The variegated diffraction

contrast observed in specimens M1 and M1.5 was still present. EDS analysis conducted at several different locations on several different particles indicated a nominal composition of 60 ± 2 mol% Al_2O_3, and 40 ± 2 mol% SiO_2.

3.2 c Orthorhombic mullite (M3)

Figure 10 is a TEM BF micrograph of a crushed, quenched mullite composition bead that was heated to 1400°C (M3). This thermal treatment was chosen in order to characterize the microstructure of mullite after conversion to the orthorhombic phase, and prior to the temperature where it begins to exsolve SiO_2.[2,3] This thermal treatment also corresponds to the end of stage 3 crystallization reported by Takei et. al.[53] The average grain size was 100 x 69 nm. A typical, polycrystalline microstructure was observed. The variegated diffraction contrast, and the small inclusions observed at lower temperatures were no longer present.

3.2 d Microstructural observations

The presence of discrete crystallites observed at the very early stages of crystallization (Fig. 4) is evidence that crystallization proceeded via a nucleation and growth mechanism. The large number of crystallites uniformly dispersed throughout the specimen indicates that the material was site saturated, that crystallization occurred with a constant number of nuclei, and that crystallization occurred throughout the bulk of the material (*vs.* just at the surface). These observations were consistent with the results from DSC nucleation experiments.

There were several common features to the microstructures of specimens M1, M1.5 and M2. Although there was a large distribution in grain sizes, they all had fairly equiaxed grains (Fig. 5, 7). The grains showed a variegated diffraction contrast, that in several of the micrographs appeared to originate from the center of the grain (Fig. 7). This suggests that crystallization occurred three dimensionally, and that the crystals grew spherulitically, from a point of origin. Three dimensional crystal growth occurring throughout the bulk of the material is characteristic of an Avrami exponent equal to three. The computed value of n from DSC experiments was 2.6. Thus the observed microstructure was consistent with the kinetic parameters determined by non-isothermal DSC experiments.

The variegated diffraction contrast in M1, M1.5 and M2 was an indication that the crystal lattice of these specimens was distorted, possibly by internal strain. A distorted lattice will cause the incident electron beam to diffract in a wavy manner, as observed in Fig. 5 - 9.[41] Although several of the TEM specimens were made from ground powders, the observed internal strain probably was not an artifact of sample preparation. Specimen M1.5 (Fig. 7, 8) was prepared as a thin foil by tripod polishing and ion milling, and it had the same variegated diffraction contrast as the ground powder specimens M1 and M2 (Fig. 5, 6, and 9). Specimen

M3 (orthorhombic phase, heated to 1400°C, Fig. 10) was another crushed powder specimen, and it did not show variegated diffraction contrast. Additionally, the samples were ground while amorphous, and examined after crystallization. The high temperatures and structural rearrangement that occurred during crystallization should have been sufficient to relieve any residual strain in the material.[58] These observations suggest that pseudotetragonal mullite has a very strained crystal structure.

The other common feature to specimens M1, M1.5 and M2 was that they all contained numerous inclusions, ~7 - 10 nm in size. The exact chemical composition and structure of these inclusions was not conclusively determined. Several different microscopic techniques were used to examine them microstructurally and microchemically, including EDS, SAD, convergent beam electron diffraction (CBED), electron energy loss spectroscopy (EELS), and elemental mapping with an energy filtered TEM. Their small size necessitated a very small diameter electron beam to probe them individually, however the specimens were susceptible to beam damage, making them difficult to analyze. Since they were very similar chemically to the crystal matrix that they were embedded in, it was difficult to differentiate their chemical identity using broader diameter electron beam analyses (e.g. energy filtered elemental mapping). High resolution TEM analysis of the interface between the matrix and the inclusions was also complicated by beam damage.

However, zone axis SAD patterns were obtained from grains containing the inclusions (Fig. 7B). If the inclusions were crystalline, and randomly oriented within the matrix crystal, it would be plausible to see a SAD pattern containing both the zone axis pattern for the matrix crystal along with a ring pattern from the numerous inclusions. Or, if the inclusions were crystalline, and epitaxially related to the matrix, then extra reflections might appear in zone axis SAD patterns. However, neither of these phenomena were observed. Any additional reflections in the SAD pattern that did not belong to the zone axis were identified (by DF) to belong to either a different region from the strained grain (in a different diffracting condition), or from a adjacent or overlapping grain. This evidence would indicate that the inclusions were amorphous.

Additional evidence concerning the identity and structure of the inclusions can be inferred from other experiments. Rietveld analysis of specimens M1 and M2 (discussed later) revealed that the crystals were alumina rich (~ 70 mol% Al_2O_3) based on their lattice parameters, and their spectra showed a broad amorphous hump centered around the 100% peak. TEM EDS analysis with a moderate diameter electron beam (70 - 100 nm) on specimens M1.5 (Fig. 7A) and M2 indicated a composition close to 60 mol% Al_2O_3, whereas STEM EDS analysis using a much smaller probe diameter showed significant compositional variations over a smaller length scale (Fig. 8). The correlation of this information indicates the existence of an amorphous, SiO_2-rich phase that is very small and dispersed on a very fine level. It would appear that the inclusions observed in specimens M1, M1.5 and M2 are this phase.

These inclusions may have been the source of strain observed in specimens M1, M1.5 and M2. TEM BF and DF imaging was done of two overlapping grains in specimen M1. The sample was oriented such that two closely spaced reflections (one from each grain) were allowed to pass through the objective aperture (inset, Fig. 11A). This set up a condition where a moiré pattern was formed by the overlapping lattice planes for the two grains.[41] This was seen in the centered dark field (CDF) micrograph by thin wavy lines passing through region where the grains overlapped (Fig. 11A). The moiré pattern was revealed in greater detail by (i) taking the Fourier transform (FFT) of the CDF image (inset, Fig. 11B), (ii) applying a filter to the FFT to remove everything except the periodic features, and then (iii) by taking the inverse Fourier transform of the filtered FFT. The filtered image is shown in Fig. 11B. The average spacing between the fringes was 8.56Å, which was larger than any of lattice parameters for mullite. The regular periodicity of the lines, their presence throughout the region of overlap between the two grains, and the large spacing between them were all evidence that they were moiré fringes created by the overlap of lattice planes from two single crystals. This was confirmed by indexing the two reflections used to create the pattern, calculating their d-spacing, and measuring the angle between them. The two spots were indexed as the (220) and (230) planes of mullite, their d-spacing was d_{220} = 2.704Å, d_{230} = 2.124Å, (using Rietveld refined lattice parameters for this specimen) and the angle between them was 7.85°. The calculated d-spacing for a misfit moiré pattern using the above values was 8.62Å.[41] This compared favorably to the measured fringe spacing of 8.56Å, thus confirming the identity of the moiré pattern. One of the important observations from the moiré pattern was that it was very distorted (wavy lines, dislocations, etc.), and the distortions were spatially correlated to the small inclusions observed in the DF micrograph (bright spots in Fig. 11A). This would suggest that the inclusions created a distortion in the psuedotetragonal mullite lattice. The overlapping effects of the numerous inclusions was thus responsible for the complicated, variegated diffraction contrast observed in bright field micrographs of these specimens.

Table 4 lists the stereological measurements made on several of the specimens. The initial crystallites (~ 13.4 x 11.5 nm ellipsoids) apparently coalesced to form larger, angular grains ~200 x 300 nm. The average grain size for M1.5 was significantly larger than for M1 and M2. This can be explained by the fact that it was crystallized as a monolithic disk ~3mm in diameter, and not as a powder like specimen M1 and M2. Additionally, since the specimen was made by polishing and thinning, it was possible to measure grains over a very large electron transparent region, whereas only selected thin areas from small particles could be measured for specimens M1 and M2. Other researchers performing quantitative XRD analysis of mullite crystallization have reported a steady increase in crystallinity and volume fraction of mullite produced with increasing thermal treatment between 1000° and 1400°C.[12,14,53] Although there was not a

significant variation in grain size observed between specimens M1, M1.5 and M2, there was a significant reduction in the size of the inclusions. From M1 to M1.5, there was a 6% reduction in the size of the inclusions, from M1.5 to M2 a 15% reduction, and from M1 to M2 a 22% reduction in the size of the inclusions. This indicates that with increasing temperature, the inclusions were gradually assimilated into the crystal. This finding is consistent with the interpretation that they are an amorphous, SiO_2-rich phase, since the SiO_2 content of psuedotetragonal mullite has been reported to increase (i.e. decreasing Al_2O_3 concentration) with thermal treatment.[3,5,14] The reported increased volume fraction of mullite crystallized over this temperature range from quantitative XRD studies thus appears to be related to the assimilation of these inclusions into the crystal. This may be microstructural evidence that the pseudotetragonal to orthorhombic transition, during the crystallization of mullite, is diffusion limited, as reported by Li and Thompson[59] and Takei et. al..[53]

Of particular note is the ~ 67% reduction in grain size from M2 (1200°C) to M3 (1400°C). Normally grain size increases as a function of temperature. Grain size reduction may have been the mechanism used to relieve the observed internal strain. A similar phenomena is observed in metallic systems, where highly strained metals have been observed to recrystallize and form smaller grains after being annealed at elevated temperatures.[58] Possible sources of strain were the inclusions as well as the anisotropic change in lattice parameter dimensions for the pseudotetragonal to orthorhombic transition (-.82% for a, 1.6% for b, and -1.5% for c, discussed later).

3.3 XRD

X-ray diffraction measurements of crushed, quenched mullite composition beads were made before and after thermal analysis in a DTA/DSC. This was done to confirm the identity of the exothermic events observed between 940° and 990°C. Figure 12 is a graph of the combined, normalized XRD spectra for quenched mullite composition glass beads before and after thermal analysis. The spectrum for specimen Q was a broad, diffuse hump characteristic of amorphous materials, with a maximum near the 100% peak for crystalline mullite. Additionally, the presence of some crystalline phase was also apparent. The pattern for specimen M2 was highly crystalline. It was similar to the equilibrium mullite structure (PDF 15-1776), except that the 120 and 210 peaks overlapped (i.e. pseudotetragonal). No other phases were observed, and specifically, there was no indication of an Al-Si spinel phase. It was concluded that the exothermic events observed by DSC were due to mullite crystallization since that was the only phase detected by XRD of annealed specimens.

3.4. Synchrotron Powder Diffraction Measurements

Specimens M1, M2, M3 and M4 were chosen for Rietveld analysis using synchrotron radiation XRD data to characterize the crystal structure of mullite after various thermal treatments. One of the objectives was to determine if the multiple crystallization events observed by DSC could be validated by the presence of multiple crystalline phases in pseudotetragonal mullite. The other objective was to ascertain the crystallization pathway for quenched mullite glass by correlating microstructural results with precise crystal structure data.

3.4 a Structure Models

Mullite, a solid solution of Al_2O_3 and SiO_2, may be represented by the following general formula:

$$Al_{4+2x}\ Si_{2-2x}\ O_{10-x} \tag{5}$$

The end members of this general formula are represented by the mineral sillimanite (x = 0) and a hypothetical substance iota-alumina (x = 1). Metastable mullite with a composition of $SiO_2 \cdot Al_2O_3$ (x = 0.40) is often termed "fused mullite", since it is typically formed from the melt, whereas mullite with a composition of $3Al_2O_3 \cdot 2SiO_2$ (x = 0.25), such as the Kyoritsu KM101 mullite used in this study, is typically called "stoichiometric" or stable mullite. In the "average" structure model of mullite, as assigned by Burnham,[60,61] and later confirmed by Saalfeld and Guse[62] and Angel and Prewitt[11], the repartition of the atoms on the respective Wyckoff positions within space group Pbam (no. 55) is given in Table 5. The structures of sillimanite and mullite consist of chains of edge-shared AlO_6 - octahedra running parallel to the c-axis that are interconnected by double chains of AlO_4/SiO_4 tetrahedra that are also parallel to the c-axis. In sillimanite, the regular AlO_4/SiO_4 tetrahedral sequence parallel to the c-axis results in a doubled c-cell. This regularity is lost in mullite, because with increasing x, Si^{4+} cations are replaced by Al^{3+} according to the reaction:

$$2\,Si^{4+} + O^{2-} = 2\,Al^{3+} + V_{\ddot{o}} \tag{6}$$

The AlO_6 - octahedra are built up by Al ions at the 2a sites and oxygen atoms at O_{ab} and O_d sites. Whereas in sillimanite the tetrahedral Al^{3+}/Si^{4+} ions occupy the T positions, in mullite any Al atom in excess of 4 replaces a Si atom at the 4h site, resulting in an oxygen vacancy at the tetrahedral corner sharing position O_c. This leads to a local structural rearrangement shifting the excess Al atom on to a new position T* and the corresponding next neighbor oxygen on to the shifted position O_c*. Figure 13 shows projections of the idealized structures of sillimanite and mullite on to the ab-plane.

The difference between various mullites is known to manifest itself by variations of the cell dimensions and, structurally speaking, essentially by variations of the positions and occupancies of the T* and O* positions. The maximum oxygen deficiency possible by this one parameter disorder model as given by Eq. 5 and Table 5, is reached for x = 2/3, when all Oc atoms have been eliminated. Fischer et al.[6,7] discussed structure models for x > 2/3. Angel et al.[9] further refined this "average" mullite structure by assigning atoms to the T, O_{ab} and O_d positions, and by including anharmonic temperature factors. Angel et al.[9,11] also discuss the incommensurate modulations observed with certain mullites.

3.4 b Single Phase Rietveld Refinement

Table 6. summarizes the results of single phase Rietveld refinements of the "low temperature" (LT) samples M1, M2 and the "high temperature" (HT) samples M3, M4 applying the structure model and the constraints given in Table 5. The last column lists the x-ray single crystal results of Saalfeld & Guse[62] obtained from a 3:2 mullite for comparison. A remarkable qualitative difference between the LT- and HT-data is given by the large high angle line broadening of the LT specimens as shown in Fig. 14. This effect normally is indicative of microstrain in the sample and it may also be responsible for the larger estimated standard deviations (esd's) of the refined LT specimen parameters. The microstrain indicated by line broadening (shown in Fig. 14 for M1 and M2), correlates very well with the evidence of strained crystals as observed by TEM (e.g. variegated diffraction contrast in BF mode in Fig. 5 - 9). This provides further evidence that the structure of pseudotetragonal mullite was highly strained. Evidence that the strain was not an artifact of sample preparation lies in the much broader line widths for the LT specimens as compared to M3, even though they were all prepared the same way. The refined lattice parameters for these specimens may be analyzed with respect to three criteria: (i) Al_2O_3/SiO_2 ratio, (ii) cell dimensions, and (iii) structure.

(i) Al_2O_3/SiO_2 ratio

The most direct indicator of the Al_2O_3/SiO_2 ratio is the mixing parameter x (see Eq. 5 and the line "mullite x" in Table 6) as derived from the refined site occupancies. Due to the low x-ray scattering power of oxygen and the very low scattering contrast of Al3+/Si4+ ions, this parameter is normally not easily refineable from powder data. However, the various site constraints (occupancies of T-, T*-, Oc- and Oc*- sites constrained by only one parameter x, isotropic temperature factors, temperature factors of all O-atoms constrained to be identical) and the high quality of synchrotron powder data reduces the usual number of correlations between occupancies and temperature factors. The mixing parameters of the HT samples

(0.34, 0.33) refine to values somewhat in between the nominal values of x = 0.25 for 3:2 mullite and x = 0.40 for 2:1 mullite, whereas the value x = 0.274 obtained by Saalfeld and Guse[62] is much closer but still above the value for 3:2 mullite. However, the mixing parameters of the LT specimens (0.50,0.58) refine to much higher values, even higher than the x = 0.40 for 2:1 mullite.

To cross-check these results obtained from Rietveld refined intensities constrained by the above structure model, three other indicators of the Al_2O_3 content were evaluated: the linear dependence of the a-lattice parameter on the Al_2O_3 content as observed by Cameron[4] and confirmed by Ban & Okada[5], the linear dependence of the density on the composition x assuming a constant number of cations of Al + Si = 6 (Cameron[4]) per unit cell and the linear dependence of the ratio of the 220 and 111 reflection intensities on x (Ban & Okada[5]). Using the respective regressions :

$$Al_2O_3\,(\text{mole }\%) = 1443\ (\text{length of a axis}) - 1028.06 \qquad (7)$$

$$\text{density} = -.3031*x + 3.247 \qquad (8)$$

$$Al_2O_3\,(\text{mole }\%) = 41.77\ (I_{220}/I_{111}) + 27.6 \qquad (9)$$

the resulting Al_2O_3 contents are shown in Table 7. In converting the mixing parameter x to Al_2O_3 (mole %) the obvious relations

$$Al/Si = (2+x)/(1-x) \quad \text{and} \quad Al_2O_3(\text{mole }\%) = (2+x)/(4-x) \qquad (10)$$

were used. We observe that whereas the HT specimens and the literature data yield fairly consistent Al_2O_3 fractions around 61 mol% (nominal value for 3:2 mullite: 60.0 mol%), the LT samples yield much higher fractions around 70 mol% (nominal value for 2:1 mullite: 66.7 mol%), varying significantly depending on which indicator was used. This was another indication of the anomalous behaviour of the LT specimens (to be discussed in more detail below).

(ii) Cell Dimensions

Fig. 15 compares the Rietveld refined cell dimensions a and c with the lines separating orthorhombic mullite from pseudotetragonal mullite as given by Cameron[4] and Ban et al.[5] The LT specimens M1 and M2 clearly fall into the region of pseudotetragonal mullite and the HT specimens M3 and M4 and the Saalfeld & Guse[62] results into the orthorhombic mullite region. The density calculated from the refined cell dimensions increases by about 1.6% in transforming from the LT to the HT mullites. This seems reasonable in considering that

pseudotetragonal mullite is a metastable transitional phase between the amorphous starting material and the stable stoichiometric 2:1 or 3:2 mullites, and that the transition involves crystallization of the residual amorphous phase. However, this densification is brought about by a non-uniform shrinkage of the unit cell: da/a = -0.82%, db/b = +1.6%, dc/c = -1.5%. As the cell dimensions of the HT specimens closely correspond to equilibrium 3:2 mullite (Ban & Okada,[5]) this would imply a highly macro-strained material for the LT specimens M1 and M2 in addition to the severe micro-strain indicated by the large line broadening mentioned above.

(iii) Structure

Table 6 shows that the refined structural parameters for the HT specimens agree within one estimated standard deviation (except x(T*), 2 esd's). This proves that specimen M3 has regained the structure of the starting material M4. Compared to the single crystal data of Saalfeld & Guse[62] these specimens show a slight increase towards the values of Angel et al.[9,10] obtained for 2:1 mullite.

The refined occupancies demonstrate that the transition from pseudotetragonal mullite to orthorhombic mullite is accompanied by a depopulation of Al-atoms at the T*-site in favor of an increase of Si atoms at the "normal" T-site. The corresponding depopulation of the O_c*-site in favor of an increase of the population at the "normal" O_c-site was also observed (except for sample M2), and is required by the structural model given in Eq. 5 and Table 5.

Significant changes of the positional parameters were observed in the transformation from pseudotetragonal to orthorhombic mullite. This is mostly seen by an increase of the y-coordinates of the T*- and the O*-sites, which may be related to the increase of the b-lattice parameter. A significant decrease of the x-coordinate of the octahedral O_d-oxygen may be related to the decrease of the a-lattice parameter. The other coordinates, in particular those of the T-sites and the O_{ab}-sites, remain essentially constant.

3.4.c Multiphase Rietveld Refinement

Considering the fact that specimens M1, M2 and M3 had undergone various thermal treatments, they should reflect the timewise integrated history of their respective kinetic processes. In addition, as previously mentioned, specimen M2 was an averaged sample, consisting of a mixture of several powders with different thermal treatments, each with an ultimate temperature of 1200°C. Thus, together with the findings of DSC (two exothermic events, Fig. 2) and TEM investigations (7 - 10 nm inclusions embedded in 200 - 500 nm grains) a mixture of more than one mullite phase seemed possible with specimens M1 and M2. The

presence of multiple phases would also help to explain the anomalous line broadening observed in the synchrotron XRD spectra for these specimens. A close inspection of weak high angle reflections revealed line splittings and line shoulders that were averaged over in the single phase Rietveld refinement previously discussed. Figure 16A is an enlarged view of the synchrotron XRD spectra around the 002 reflection for specimen M1(938°C). The data clearly shows the overlap of three different peaks, indicating the presence of three different composition mullite phases. This corroborates the multiple exothermic peaks observed by DSC. The dashed and solid lines show results for the single phase refinement previously discussed and for a three phase refinement, respectively. However, due to the high degree of line overlap a separate refinement of structure, cell and line widths parameters for the whole spectra was not possible. The c-lattice dimension, as taken directly from the data, as well as the a- and b-lattice parameters and the corresponding Al_2O_3 mole fractions as taken from Fischer et al.[6] are given in Table 8. Quantitative analysis via refinement of scale factors yielded the indicated weight fractions. Besides the majority phase (50 wt%) of some 70 mol% Al_2O_3, which is close to the average value obtained with the single phase analysis, a second (40 wt%) fraction of very high Al_2O_3 content (76 mol%) and a third phase (10 wt%) of very low Al_2O_3 content (< 60 mol% Al_2O_3) can clearly be identified. The c-lattice dimension (0.2875 nm) of the latter fraction is lower than observed before in any mullite, which may be related to the phenomenon of anomalously low c cell dimensions in mullites heat treated below 1200°C, as observed by Ban et al..[5,19] Additional shoulders and line broadening at high and low angle tails of reflection 002 (Fig. 16A) suggest further minority phases and also microstrain. Fig. 16B is a plot of synchrotron XRD spectra comparing the 002 reflection region for specimens M1 (938°C), M2 (1200°C) and M3 (1400°C). It is apparent that a weighted distribution of at least 5 to 6 phases could be applied to the 002 peak for specimen M2. The very narrow 002 reflection for specimen M3 shows the final product phase after the tetragonal - orthorhombic transition was completed.

The multiple peaks in M1 and M2 at the low angle side (high c-cell dimension, high Al_2O_3 content), as well as on the high angle side (low c-cell dimension, low Al_2O_3 content), of the final 002 reflection position of sample M3, suggest the following picture of the crystallization sequence: At the beginning two phases of high and low Al_2O_3 content respectively start to crystallize, obviously because of the miscibility gap discussed by Ban et al.[56] and Takei et al..[57] With time and temperature these transform into the final phase as determined by the bulk Al_2O_3 and SiO_2 composition. It should be mentioned that the starting phase with the very high Al_2O_3 content (76 mol%) is very close to the composition of 78 mol%, where Fischer et al.[6] placed the crossover point of the a- and b-cell dimensions, i. e. close to the ideal "tetragonal" mullite. However, even at this composition the structure remains orthorhombic with a symmetrically independent coincidence of a and b. It should also be mentioned, that

according to the one parameter structure model (Eq. 5) and Table 5, the composition x = 2/3, where all of the Oc oxygen atoms are replaced by vacancies, corresponds to only slightly higher Al_2O_3 content of 80 mole %. This suggests that the "tetragonal" mullite with a quasi equal distribution of O_c-vacancies along the a- and b-cell directions has the lowest lattice energy and thus crystallizes first. Only subsequent annealing produces Si/Al exchange coupled with placing O_c oxygens onto their vacant sites. This process seems to occur preferentially along the a-cell direction leading to the inverse change in length of a and b.

Summarizing, we may state that the synchrotron XRD spectra for specimens M1 and M2 reflect integrated time histograms of incomplete mullite crystallization that show the formation of multiple mullite phases. To reduce the observed heavy line overlap, in situ (isothermal) high temperature and high resolution powder diffraction experiments should be performed to follow the structural implications of this crystallization kinetics in more detail.

5. Summary

1. Pseudotetragonal mullite was observed to crystallize directly from $3Al_2O_3 \cdot 2SiO_2$ composition quenched melts without the formation of intermediate phases such as Al-Si spinel. The kinetics for initial crystallization of pseudotetragonal mullite were characterized by DSC as a two-step process, with activation energies of 836.9 KJ/mol and 1,337.5 KJ/mol for the two steps, respectively. The presence of multiple crystalline phases was confirmed by Rietveld analysis of synchrotron XRD data for specimens crystallized at low temperatures. Multiple Rietveld phase fitting (3 phases) was successfully applied to specimen M1.

2. Crystallization of pseudotetragonal mullite occurred via a nucleation and growth process without an induction period. Quenched mullite composition glasses were observed to be site saturated with discrete, ellipsoidal, crystallites (~ 13.5 x 11.5 nm) throughout the bulk after annealing at 920°C for 3h. The crystallites coalesced and grew three-dimensionally with apparent spherulitic grain growth. The computed Avrami exponent, n = 2.6, was consistent with the observed microstructure (n = 3 for three dimensional, bulk, crystal growth). Crystallization was observed to occur extremely quickly at temperatures above 970°C when heated at moderate rates (3.0° to 10.0°C/min).

3. Pseudotetragonal mullite specimens had a microstructure of faceted, angular grains ~200 x 300nm in size with numerous small ~7 x 10 nm inclusions embedded within them. The pseudotetragonal mullite crystals were highly strained as observed by the variegated contrast in BF TEM micrographs and by the broad lines in the synchrotron XRD spectra. The strain was spatially correlated to the embedded inclusions.

4. Rietveld analysis of synchrotron XRD spectra for $3Al_2O_3 \cdot 2SiO_2$ composition mullite glass crystallized at temperatures $\leq$ 1200°C determined that the crystals were pseudotetragonal

with a composition of approx. 70 mol% Al_2O_3 (based on their lattice parameters). Multiple phases were detected. The formation of the Al_2O_3-rich phases was attributed to phase separation as a result of a metastable immiscibility gap. The XRD spectra for these specimens contained a large amorphous hump Since the composition of the glass was 60 mol% Al_2O_3, and crystals contained ~ 70 mol% Al_2O_3, it was inferred that the amorphous phase was SiO_2-rich.

5. Quantitative Rietveld fitting of high angle pseudotetragonal mullite peaks (002) suggested that a "tetragonal" (symmetrically independent coincidence of a and b) mullite, with a quasi-equal distribution of O_c vacancies along the a- and b- cell dimensions, had the lowest free energy, and that it was first phase to crystallize. Subsequent annealing produced Si/Al exchange, coupled with placing oxygens onto vacant O_c sites. This process appeared to occur preferentially along the a-cell direction, leading to the inverse change in the length of a and b as the pseudotetragonal phase converted to the orthorhombic phase.

6. Direct TEM characterization of nm-sized inclusions, embedded in pseudotetragonal mullite crystals, was complicated by their small size, sensitivity to beam damage, and chemical similarity to the matrix. Based on SAD and EDS, it was inferred that they were amorphous and differed in composition from the matrix. Coupled with the existence of an amorphous, SiO_2-rich phase (as deduced from XRD spectra and Rietveld analysis), it was concluded that the inclusions were amorphous and rich in SiO_2.

7. The psuedotetragonal to orthorhombic transition occurred between ~938°C - 1400°C, and appeared to be diffusion limited, as the crystals assimilated the 7 - 10nm, SiO_2-rich inclusions. By 1200°C, there was an approx. 22% reduction in the size of the inclusions, and the composition of the pseudotetragonal mullite crystals was closer to that of the bulk material (based on the $I_{220/111}$ intensity ratio). By 1400°C, the previously observed strain was gone: the variegated contrast observed by TEM in BF mode disappeared as well as the inclusions, and there was a significant reduction in line widths from the synchrotron XRD spectra. At this temperature, equilibrium orthorhombic mullite was formed, the composition was ~ 60mol% Al_2O_3, and a more typical, polycrystalline microstructure was observed.

8. The pseudotetragonal - orthorhombic transition was accompanied by ~ 67% reduction in grain size from 1200°C to 1400°C. The relief of built up internal strain from the embedded inclusions and the anisotropic change in lattice parameters from the phase transition was suggested as the driving force for grain size reduction. The phenomena of recrystallization after annealing highly strained metals was offered as an example of a similar phenomena.

Acknowledgments

The authors would like to gratefully acknowledge Richard Weber and Johan Abadie from Containerless Research Inc. for supplying the quenched mullite beads used in this work, as well as Pankaj Sarin from the University of Illinois and Paul Zschack from the UNICAT facility at the APS facility at ANL for their assistance in collecting the synchrotron radiation data. This project was funded by the U.S. Air Force Office of Scientific Research under Science and Technology Transfer Research (STTR) grants F49620-97-1-0427 and F49620-98-C-0050. Microstructural and crystallographic characterization was performed in part using equipment in the Center for Microanalysis of Materials (in the Materials Research Laboratory) and in the Center for Cement Composite Materials, both located at the University of Illinois at Urbana-Champaign.

References

1. Kriven, W. M.; Pask, J. A., Solid solution range and microstructures of melt-grown mullite, *J. Am. Ceram. Soc.*, **66** [9] 649-654 (1983).
2. Prochazka, S.; Klug, F. J., Infrared-transparent mullite ceramic, *J. Am. Ceram. Soc.*, **66** [12] 874-880 (1983).
3. Okada, K.; Otsuka, N., Change in chemical compostion of mullite formed from $2SiO_2 \cdot 3Al_2O_3$ xerogel during the formation process, *J. Am. Ceram. Soc.*, **70** [10] C245-C247 (1987).
4. Cameron, W. E., Composition and cell dimensions of mullite, *Am. Cer. Soc. Bull.*, **56** [11] 1003-1011 (1977).
5. Ban, T.; Okada, K., Structure refinement of mullite by the Rietveld method and a new method for estimation of chemical composition, *J. Am. Ceram. Soc.*, **75** [1] 227-30 (1992).
6. Fischer, R. X.; Schneider, H.; Schmucker, M., Crystal structure of Al-rich mullite, *Am. Mineral.*, **79** [9-10] 983-990 (1994).
7. Fischer, R. X.; Schneider, H.; Voll, D., Formation of aluminum rich 9:1 mullite and its transformation to low alumina mullite upon heating, *J. Eur. Cer. Soc.*, **16** 109-13 (1996).
8. Rahman, S. H., Crystal chemistry of mullite; pp. 5-82 in *Mullite and Mullite Ceramics*. Edited by H. Schneider; K. Okada and J. Pask. John Wiley and Sons, New York, 1994.
9. Angel, R. J.; McMullan, R. K.; Prewitt, C. T., Substructure and superstructure of mullite by neutron diffraction, *Am. Mineral.*, **76** 332-342 (1991).
10. Angel, R. J.; Prewitt, C. T., Crystal structure of mullite: A re-examination of the average structure, *Am. Mineral.*, **71** 1476-1482 (1986).
11. Angel, R. J.; Prewitt, C. T., The incomensurate structure of mullite by Patterson synthesis, *Acta Cryst.*, **B43** 116-125 (1987).
12. Wang, Y.; Thomson, W. J., Mullite formation from nonstoichiometric slow hydrolyzed single phase gels, *J. Mater. Res.*, **10** [4] 912-917 (1995).

13. Osaka, J., Tetragonal mullite-like phase from co-precipitated gels, *Nature*. **191** 1000-1001 (1961).

14. Li, D. X.; Thomson, W. J., Tetragonal to orthorhombic transformation during mullite formation, *J. Mater. Res.*, **6** [4] 819-824 (1991).

15. Schneider, H.; Rymon-Lipinski, T., Occurrence of pseudotetragonal mullite, *J. Am. Ceram. Soc.*, **71** [3] C162-C164 (1988).

16. Schneider, H.; Fischer, R. X.; Voll, D., Mullite with lattice constants a>b, *J. Am. Ceram. Soc.*, **76** [7] 1879-81 (1993).

17. Petry, M. D.; Tai-Il, M., Effect of thermal exposures on the strengths of Nextel™ 550 and 720 filaments, *J. Am. Ceram. Soc.*, **82** [10] 2801-7 (1999).

18. Okada, K.; Hoshi, Y.; Otsuka, N., Formation reaction of mullite from SiO_2-Al_2O_3 xerogels, *J. Mater. Sci. Lett.*, **5** [12] 1316-1318 (1986).

19. Ban, T.; Okada, K., Analysis of local cation arrangement in mullite using ^{29}Si magic-angle spinning nuclear magnetic resonance spectra, *J. Am. Ceram. Soc.*, **76** [10] 2491-2496 (1993).

20. Tkalcec, E.; Nass, R.; Schmauch, J.; Schmidt, H.; Kurajica, S.; Bezjak, A.; Ivankovic, H., Crystallization kinetics of mullite from single-phase gel determined by isothermal differential scanning calorimetry, *J. Non-Cryst. Solids*, **223** 57-72 (1998).

21. Wei, W.-C.; Halloran, J. W., Phase transformation of diphasic aluminosilicate gels, *J. Am. Ceram. Soc.*, **71** [3] 166-172 (1988).

22. Wei, W.-C.; Halloran, J. W., Transformation kinetics of diphasic aluminosilicate gels, *J. Am. Ceram. Soc.*, **71** [7] 581-587 (1988).

23. Boccaccini, A. R.; Khalil, T. K.; Bucker, M., Activation energy for the mullitization of a diphasic gel obtained from fumed silica and boehmite sol, *Mater. Lett.*, **38** [2] 116-20 (1999).

24. Okada, K.; Otsuka, N.; Osaka, J., Characterization of spinel phase formed in the kaolin-mullite thermal sequence, *J. Am. Ceram. Soc.*, **69** [10] C251-C253 (1986).

25. Okada, K.; Otsuka, N., Characterization of the spinel phase from SiO_2-Al_2O_3 xerogels and the formation process of mullite, *J. Am. Ceram. Soc.*, **69** [9] 652-6 (1986).

26. Hyatt, M. J.; Bansal, N. P., Phase transformations in xerogels of mullite composition, *J. Mater. Sci.*, **25** [6] 2815-2821 (1990).

27. Chakraborty, A. K., Formation of silicon-aluminum spinel, *J. Am. Ceram. Soc.*, **62** [3-4] 120-124 (1979).

28. Chakraborty, A. K., Intermediate Si-Al spinel phase formation in phase transformation of diphasic mullite gel, *J. Mater. Sci.*, **28** [14] 3839-44 (1993).

29. Sujeong, L.; Youn Joong, K.; Hi-Soo, M., Phase transformation sequence from kaolinite to mullite investigated by an energy-filtering transmission electron microscope, *J. Am. Ceram. Soc.*, **82** [10] 2841-8 (1999).

30. Ban, T.; Hayashi, S.; Yasumori, A.; Okada, K., Characterization of low temperature mullitization, *J. Eur. Cer. Soc.*, **16** 127-132 (1996).

31. Zhu, D.; Jilavi, M. H.; Kriven, W. M., Synthesis and characterization of mullite and YAG fibers grown from deeply undercooled melts, *Proceedings of the 1997 21st 1997 21st Annual*

Conference on Composites, Advanced Ceramics, Materials, and Structures-A. Cocoa Beach, FL, USA, 19970112-19970116. Conference Code: 46907., **18** [3] 31-38 (1997).

32. Kriven, W. M.; Jilavi, M. H.; Zhu, D.; Weber, J. K. R.; Cho, B.; Felten, J.; Nordine, P. C., Synthesis and microstructure of mullite fibers grown from deeply undercooled melts; pp. 169-176 in *Ceramic Microstructures: Control at the Atomic Level*, Proceedings of the International Materials Symposium on Ceramic Microstructures '96: Control at the Atomic Level, Edited by A. P. Tomsia and A. M. Glaeser. Plenum Press, New York, 1998.

33. Weber, J. K. R.; Cho, B.; Hixson, A. D.; Abadie, J. G.; Nordine, P. C.; Kriven, W. M.; Johnson, B. R.; Zhu, D., Growth and crystallization of YAG- and mullite-composition glass fibers, *J. Eur. Cer. Soc.*, **19** [13-14] 2543-2550 (1999).

34. Weber, J. K. R.; Felten, J. J.; Nordine, P. C., New method of high purity ceramic synthesis, *Rev. Sci. Inst.*, **78** 31-35 (1996).

35. Weber, J. K. R.; Anderson, C. D.; Krishnan, S.; Nordine, P. C., Solidification behavior of undercooled liquid aluminum oxide, *J. Am. Ceram. Soc.*, **78** 577-582 (1995).

36. Weber, J. K. R.; Hampton, S. S.; Merkley, D. R.; Rey, C. A.; Zatarski, M. M.; Nordine, P. C., Aero-acoustic levitation - a method for containerless liquid-phase processing at high temperatures, *Rev. Sci. Inst.*, **65** [456-465] (1994).

37. Weber, J. K. R.; Nordine, P. C., Containerless liquid-phase processing at high temperatures, *Microgravity Science and Technology*, **VII** 279-282 (1995).

38. Krishnan, S.; Felten, J. J.; Rix, J. E.; Weber, J. K. R., Levitation apparatus for structural studies of high temperature liquids using synchrotron radiation, *Rev. Sci. Inst.*, **68** 3512-18 (1997).

39. Benedict, J.; Anderson, R.; Klepeis, S. J., Recent developments in the use of the tripod polisher for TEM specimen preparation; pp. 121-141 in *Specimen Preparation for Transmission Electron Microscopy of Materials III*, Materials Research Society Symposium Proceedings, Vol. 254, Edited by R. Anderson; B. Tracy and J. Bravman. Materials Research Society, Pittsburgh, PA, 1992.

40. Klepeis, S. J.; Benedict, J. P.; Anderson, R. M., A grinding/polishing tool for TEM sample preparation; pp. 179-184 in *Specimen Preparation for Transmission Electron Microscopy of Materials*, Materials Research Soceity Symposium Proceedings, Vol. 115. Edited by J. C. Bravman; R. M. Anderson and M. L. McDonald. Materials Research Society, Pittsburgh, PA, 1988.

41. Williams, D. B.; Carter, C. B., *Transmission Electron Microscopy a Textbook for Materials Science*, Plenum Press, New York, 1996.

42. Bright, D. S., Program: *Maclispix*, v. 2-99, National Insitute of Standards, Gaithersburg, MD, 1999.

43. Vischer, N., Program: *Object-image*, v. 2.06, University of Amsterdam, Amsterdam, Netherlands, 2000.

44. Bansal, N. P.; Doremus, R. H., Determination of reaction kinetic parameters from variable temperature DSC or DTA, *J. Therm. Anal.*, **29** 115-119 (1984).

45. Bansal, N. P.; Doremus, R. H.; Bruce, A. J.; Moynihan, C. T., Kinetics of crystallization of ZrF_4-BaF_2-LaF_3 glass by differential scanning calorimetry, *J. Am. Ceram. Soc.*, **66** [4] 233-238 (1983).

46. Bansal, N. P.; Hyatt, M. J., Crystallization kinetics of BaO-Al_2O_3-SiO_2 glasses, *J. Mater. Res.*, **4** [5] 1257-1265 (1989).

47. Ray, C. S.; Ray, D. E., Nucleation and crystallization in glasses as determined by DTA; pp. 207-233 in *Nucleation and Crystallization in Liquids and Glasses*, Ceramic Transactions, Vol. 30. Edited by M. C. Weinberg. The American Ceramic Society, Westerville, Ohio, 1993.

48. Cheng, K., Determining crystallization kinetic parameters of Li_2O-Al_2O_3-SiO_2 glass from derivative differential thermal analysis curves, *Mater. Sci. Eng. B.*, **60** [3] 194-199 (1999).

49. Kissinger, H. E., Variation of peak temperature with heating rate in differential thermal analysis, *J. Res. Nat. Bur. Stand.*, **57** [4] 217-221 (1956).

50. Augis, J. A.; Bennet, J. D., Calculation of the Avrami parameters for heterogeneous solid state reactions using a modification of the Kissinger method, *J. Therm. Anal.*, **13** [2] 283-293 (1978).

51. Porter, D. A.; Easterling, K. E., *Phase Transformations in Metals and Alloys*. Chapman and Hall, New York, 1992.

52. Li, D. X.; Thomson, W. J., Kinetic mechanisms for mullite formation from sol-gel precursors, *J. Mater. Res.*, **5** [9] 1963-1969 (1990).

53. Takei, T.; Kameshima, Y.; Yasumori, A.; Okada, K., Crystallization kinetics of mullite in alumina-silica glass fibers, *J. Am. Ceram. Soc.*, **82** [10] 2876-80 (1999).

54. MacDowell, J. F.; Beall, G. H., Immiscibility and crystallization in Al_2O_3-SiO_2 glasses, *J. Am. Ceram. Soc.*, **52** [1] 17-25 (1969).

55. Risbud, S. H.; Pask, J. A., Calculated thermodynamic data and metastable immiscibility in the system SiO_2-Al_2O_3, *J. Am. Ceram. Soc.*, **60** [9-10] 418-424 (1977).

56. Ban, T.; Hayashi, S.; Yasumori, A.; Okada, K., Calculation of metastable immiscibility region in the Al_2O_3-SiO_2 system, *J. Mater. Res.*, **11** [6] 1421-1427 (1996).

57. Takei, T.; Kameshima, Y.; Yasumori, A.; Okada, K., Calculation of metastable immiscibility region in the Al_2O_3-SiO_2 system using molecular dynamics simulation, *J. Mater. Res.*, **15** [1] 186-93 (2000).

58. Vlack, L. H. V., *Materials Science for Engineers*. Addison-Wesley Publishing Co., Reading, MA, 1970.

59. Li, D. X.; Thomson, W. J., Mullite formation kinetics of a single-phase gel, *J. Am. Ceram. Soc.*, **73** [4] 964-969 (1990).

60. Burnham, C. W., Crystal structure of mullite, *Carnegie Inst. Washington Yearbook*, **63** 223-227 (1964).

61. Burnham, C. W., Composition limits of mullite and the sillimanite-mullite solid solution problem, *Carnegie Inst. Washington Yearbook*, **63** [227-228] (1964).

62. Saalfeld, H.; Guse, W., Structure refinement of 3:2 mullite ($3Al_2O_3 \cdot 2SiO_2$), *Neues Jahrb. Mineral. Monatsh*, 145-150 (1981).

List of Tables

Table 1. The designation, thermal history, and description of specimens characterized by various techniques.

Table 2. Variation of crystallization temperature, T_p, with annealing temperature, T_N, for crystallization of quenched mullite composition glass beads.

Table 3. Kinetic data for the crystallization of quenched mullite composition beads from non-isothermal DSC studies.

Table 4. Particle size measurements for quenched mullite composition specimens after various thermal treatments.

Table 5. Wyckoff positions, coordinates and names[10] of the atom sites of the "average" mullite structure, space group Pbam (no.55).

Table 6. Results of Rietveld refinements, space group P b a m

Table 7. Al_2O_3 contents as derived from various indicators: cell dimensions a, b, and c, density Dx, ratio of the integrated intensities of 220 and 111 reflections, Rietveld refined "mullite x" and microprobe (μ--probe).

Table 8. Quantitative 3 phase analysis of specimen M1

List of Figures

Figure 1. Kissinger plot ($\ln(T_p^2/\alpha)$ *vs.* $1/T_p$) for non-isothermal crystallization of quenched mullite beads. Note that there were two different crystallization regimes with a break in the heating rate between 3.0° and 4.0°C/min.

Figure 2. Plot of the DSC exotherms for non-isothermal crystallization of quenched mullite composition glass, at heating rates of 3.0° and 4.0°C/min. Note the asymmetry in both curves, indicating two different exothermic events, and the shift in prominence of the two different events.

Figure 3. TEM BF image (A) and STEM BF image (B) of a polished thin section from an as-received, quenched, mullite composition bead (specimen Q). The contrast variations in (A) were typical of phase-separated, amorphous materials. The overall composition for the field of view in (B) was 75.8 mol% Al_2O_3 and 24.2 mol% SiO_2, as determined by STEM EDS. The graph in (B) shows the variation in the Al/Si Kα ratio from an EDS line scan through the central dark region in the sample. An Al/Si Kα ratio of 2.8 corresponds to 3:2 mullite (60 mol% alumina).

Figure 4. TEM BF images of an amorphous mullite fiber annealed at 920°C for 3h (specimen N). The inset image in (A) is an SAD pattern taken from the crystallites along the edge. The pattern was indexed as the pseudotetragonal metric of mullite. The lattice spacing of the crystallite in (B) was 3.38 Å, which corresponded to the (120)/(210) lattice planes of mullite (3.428 Å, and 3.390 Å, respectively).

Figure 5. TEM BF micrograph of a crushed, quenched, mullite composition bead that was isothermally crystallized at 938°C for 2.5h (specimen M1).

Figure 6. TEM BF (A) and DF (B) micrographs of a ground sample from a quenched mullite composition bead that was isothermally crystallized in a DSC at 938°C for 2.5 h (specimen M1). The darker, matrix region in the BF image (A) appeared as the bright region in the DF image (B), and the light, circular inclusions observed in the BF image appeared dark in the DF image.

Figure 7. TEM BF images (A and B) from a polished thin section of a quenched mullite composition bead heated to 1085°C (specimen M1.5). EDS analyses were made at the points labeled alphabetically, and the composition at each point was 60±1 mol% Al_2O_3, 40±1 mol% SiO_2. The variegated diffraction contrast in the grains was due to lattice strain. Higher magnification of one of the grains (B) revealed small inclusions with and average size of 9.4 x 7.9 nm. The SAD pattern in (B) was taken from the [001] zone axis of a similar grain in the specimen.

Figure 8. STEM BF micrograph of a quenched mullite bead heated to 1085°C (specimen M1.5). The horizontal line in the center of the micrograph was due to beam damage of the specimen

during EDS line profile analysis. The inset graph shows the variation in the Al/Si Kα ratio over the region scanned. This was an indication of chemical inhomogeneity at very small length scales.

Figure 9. TEM bright field image of quenched mullite composition powder after being heated up to 1200°C (specimen M2). The inset image is a Kossel-Möllenstedt microdiffraction pattern for the designated crystal oriented along the [120] zone axis.

Figure 10. TEM bright field image of quenched mullite composition powder after being heated up to 1400°C (specimen M3).

Figure 11. TEM CDF micrograph (A) and corresponding moiré pattern (B) from a crushed, quenched mullite composition bead isothermally crystallized at 938°C for 2.5 h (M1). The micrograph was taken from an area of two overlapping crystals using the (220) reflection from one and the (230) reflection from the other (SAD inset, A). The overlapping lattice fringes from the two crystals created the observed moiré pattern (dark wavy lines). B is a filtered Fourier image of A showing the moiré pattern in greater detail. The inset in B is the fast Fourier transform (FFT) of A. The average fringe spacing in B was 8.56Å; the computed fringe spacing from the SAD pattern was 8.62Å. The distortion in the moiré pattern was an indication of strain in the two crystals, and was spatially correlated to the embedded inclusions in A (bright areas).

Figure 12. Combined, normalized XRD spectra for quenched mullite composition glass beads, before and after crystallization in a DTA. The crystalline pattern belongs to mullite, and verifies that the exothermic events observed by DTA/DSC were due to crystallization of mullite.

Figure 13. Idealized structure of sillimanite (A) and mullite (B) projected along the a-b plane.

Figure 14. Line widths, full width at half maximum, (FWHM) obtained from single phase Rietveld refinements of synchrotron XRD spectra for specimens M1, M2, M3, M4 and from a Si powder standard (SRM 640b, NIST).

Figure 15. Positioning of the refined a and c cell dimensions for specimens M1, M2, M3 and M4 on an orthorhombic - pseudotetragonal mullite diagram.

Figure 16. Detailed sections of measured powder diagrams around the well separated 002 reflection for various spectra.
16a) sample M1: observed data (dots), single phase Rietveld refinement (dashes), 3-phase Rietveld refinement (line)
16b) comparison of data from partly crystallized samples M1, M2 with those of the well crystallized specimen M3.

Tables

Table 1.

The designation, thermal history, and description of specimens characterized by various techniques.

Symbol	Thermal History	Analyses	Form	Details
Q	Quenched glass	DSC, TEM, XRD	Powder, thin film	Glass beads received from CRI.
N	10°C/min, to 920°C, 3h	DSC, TEM	Powder, fiber	Highest annealing temperature observed in DSC without crystallization exotherm.
M1	40°C/min to 938°C, 2.5h	DSC, TEM, Synchrotron.	Powder	Pseudotetragonal mullite formed at a low temperature.
M1.5	10°C/min to 1085°C, 0.5h	TEM	Thin film	Polished thin film specimen of psuedotetragonal mullite
M2	10°C/min to 900-930°C, 3h, various rates to 1200°C	TEM, XRD, Synchrotron	Powder	Pseudotetragonal mullite prior to transition to orthorhombic phase. Mixture of powders.
M3	10°C/min to 1400°C	TEM, Synchrotron	Powder	Orthorhombic phase.
M4	Kyoritsu KM101	XRD, Synchrotron	Powder	Source material.

Table 2.

Variation of crystallization temperature, T_p, with annealing temperature, T_N, for crystallization of quenched mullite composition glass beads.

Nucleation Temp, T_N	**Crystallization Temperature, T_p**
10°C/min Ramp	984.6°C
850°C/3hr	985.5°C
890°C/3hr	984.6°C
900°C/3hr	986.0°C
910°C/3hr	985.9°C
920°C/3hr	987.2°C
930°C/3hr	-
940°C/3hr	-

Table 3.
Kinetic data for the crystallization of quenched mullite composition beads from non-isothermal DSC studies.

α (°C/min)	T_p (°C)	n
0.5	944.160	2.2
1.0	955.500	2.4
1.5	959.400	2.3
2.0	964.770	2.1
3.0	970.700	2.2
4.0	977.200	2.8
5.0	979.400	3.6
6.0	980.300	3.1
8.0	983.400	7.5
10.0	986.100	16.9
E_1 (KJ/mole)	836.92	
E_2 (KJ/mole)	1,337.52	
ν_1 (s^{-1})	4.535E+32	
ν_2 (s^{-1})	5.266E+53	

Table 4.

Particle size measurements for quenched mullite composition specimens after various thermal treatments.

Specimen	Major Axis (nm)	Minor Axis (nm)	Ave. Diam. (nm)	Ave. Area (nm^2)	No. of Measurements
N (crystallites)	13.4 ± 2.9	11.5 ± 2.7	12.6 ± 7.9 nm	123.8 ± 49.3	150
M1 (inclusions)	10.0 ± 2.2	7.8 ± 1.9	9.0 ± 5.6 nm	63.0 ± 24.8	150
M1 (grains)*	~ 370	~ 260	-	9.6E+04	40
M1.5 (inclusions)	9.4 ± 2.5	7.9 ± 2	8.8 ± 6.4 nm	61.4 ± 32	150
M1.5 (grains)*	~ 510	~ 380	-	.2.03E+05	50
M2 (inclusions)	7.9 ± 1.7	6.6 ± 1.5	7.3 ± 4.7 nm	42.2 ± 17.43	150
M2 (grains)*	~ 270	~ 190	-	5.2E+04	135
M3 (grains)	100 ± 55	69 ± 38	-	7.68E+03	60

* Broad size distribution

Table 5.

Wyckoff positions, coordinates and names[10] of the atom sites of the "average" mullite structure, space group Pbam (no.55).

Atoms	Al_2	$[Al_2\ Si_{2-2x}]$	Al_{2x}	O_{2-3x}	O_{2x}	O_4	O_4
Wyckoff positions	2a	4h	4h	2d	4h	4h	4g
Coordinates	0, 0, 0	x, y, _	x, y, _	_, 0, _	x, y, _	x, y, _	x, y, 0
Names [10]	Al	T(Si/Al)	T*(Al*)	O_c	O_c*	O_{ab}	O_d

Table 6.
Refined parameters of the 4 mullite samples, and a reference. Space group Pbam.

Sample	M1	M2	M3	M4	Saalfeld & Guse[62]
a [nm]	0.7616(2)	0.7606(1)	0.75454(2)	0.75499(3)	0.7553(1)
b [nm]	0.7678(2)	0.7682(1)	0.76956(2)	0.76883(3)	0.7686(1)
c [nm]	0.28891(4)	0.28871(4)	0.288398(6)	0.288379(9)	0.28864(7)
V [nm^3]	0.16897	0.16870	0.16746	0.16739	0.16756
Density [g/cm^3]	3.10	3.09	3.15	3.16	3.16
R_{WP}	0.049	0.049	0.051	0.032	
R_{Bragg}	0.060	0.063	0.049	0.025	0.027
X(Al)	0.	0.	0.	0.	0.
Y(Al)	0.	0.	0.	0.	0.
Z(Al)	0.	0.	0.	0.	0.
B(Al)	0.9(3)	1.0(3)	0.5(1)	0.5(1)	
Occ.(Al)	1.0	1.0	1.0	1.0	1.0
X(T)	0.148(2)	0.147(2)	0.1480(6)	0.1474(6)	0.1485
Y(T)	0.339(2)	0.340(1)	0.3412(6)	0.3410(6)	0.3411
Z(T)	0.5	0.5	0.5	0.5	0.5
B(T)	1.7(4)	0.8(3)	0.3(1)	0.3(1)	
Occ.(T), Al	0.5	0.5	0.5	0.5	0.5
Occ.(T), Si	0.25(2)	0.21(2)	0.332(7)	0.334(7)	0.363
X(T*)	0.275(4)	0.282(4)	0.275(3)	0.268(3)	0.2621
Y(T*)	0.195(4)	0.194(4)	0.209(2)	0.207(2)	0.2057
Z(T*)	0.5	0.5	0.5	0.5	0.5
B(T*)	0.1(4)	3(1)	1.7(8)	1.2(8)	
Occ.(T*), Al	0.25(2)	0.29(2)	0.168(7)	0.166(7)	0.137
X(Oab)	0.354(2)	0.349(1)	0.3567(6)	0.3566(6)	0.3579
Y(Oab)	0.423(2)	0.422(1)	0.4195(6)	0.4201(6)	0.4221
Z(Oab)	0.5	0.5	0.5	0.5	0.5
B(Oab)	0.2(2)	0.4(2)	0.8(1)	0.8(1)	
Occ.(Oab)	1.0	1.0	1.0	1.0	1.0
X(Od)	0.136(2)	0.133(1)	0.1270(9)	0.1263(9)	0.1265
Y(Od)	0.220(2)	0.222(1)	0.2219(8)	0.2216(8)	0.2201
Z(Od)	0.0	0.0	0.0	0.0	0.0
B(Od)	0.2(2)	0.4(2)	0.8(1)	0.8(1)	
Occ.(Od)	1.0	1.0	1.0	1.0	1.0
X(Oc)	0.5	0.5	0.5	0.5	0.5
Y(Oc)	0.0	0.0	0.0	0.0	0.0
Z(Oc)	0.5	0.5	0.5	0.5	0.5
B(Oc)	0.2(2)	0.4(2)	0.8(1)	0.8(1)	
Occ.(Oc)	0.26(1)	0.58(3)	0.49(1)	0.50(1)	0.590
X(Oc*)	0.442(8)	0.457(6)	0.453(5)	0.451(5)	0.4507
Y(Oc*)	0.039(9)	0.029(8)	0.049(5)	0.048(5)	0.0518
Z(Oc*)	0.5	0.5	0.5	0.5	0.5
B(Oc*)	0.2(2)	0.4(2)	0.8(1)	0.8(1)	
Occ.(Oc*)	0.25(1)	0.29(2)	0.168(7)	0.166(7)	0.137
Mullite x	0.49(4)	0.58(3)	0.34(1)	0.33(1)	0.274

Table 7.
Al_2O_3 contents as derived from various indicators: cell dimensions a, b, and c, density Dx, ratio of the integrated intensities of 220 and 111 reflections, Rietveld refined "mullite x" and microprobe (μ--probe).

Specimen	M1	M2	M3	M4	S & G[62]
mole % (a)	70.9	69.5	60.7	61.4	61.8
mole % (b)	70.9	68.5	60.0	64.6	66.0
mole % (c)					
mole % (Dx)	70.8	72.3	62.8	61.8	61.8
mole % ($I_{220/111}$)	75.2	64.9	62.5	59.9	
mole % (mullite x)	71.4	75.4	63.8	63.6	61.0
mole % (μ-probe)					60.9

Table 8.
Quantitative 3 phase analysis of specimen M1.

Parameter	Phase A	Phase B	Phase C
a [nm]	0.7651	0.7611	0.7562
b [nm]	0.7659	0.7678	0.7692
c[nm]	0.2895	0.2887	0.2875
mole % Al_2O_3	76	70	< 60
weight fraction [%]	40	50	10

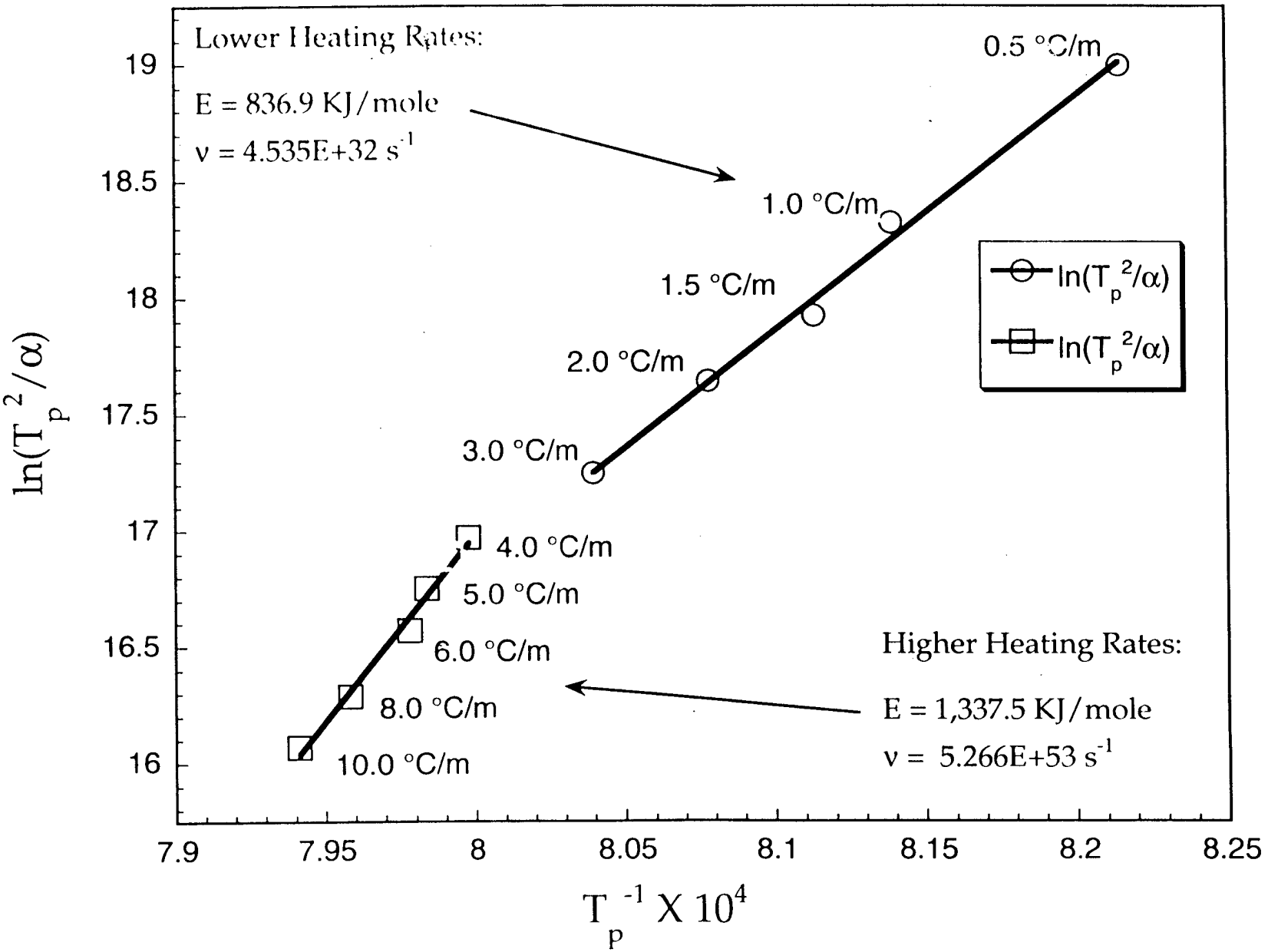


Figure 1. Kissinger plot (ln(Tp2/a) vs. 1/Tp) for non-isothermal crystallization of quenched mullite beads. Note that there were two different crystallization regimes with a break in the heating rate between 3.0° and 4.0°C/min.

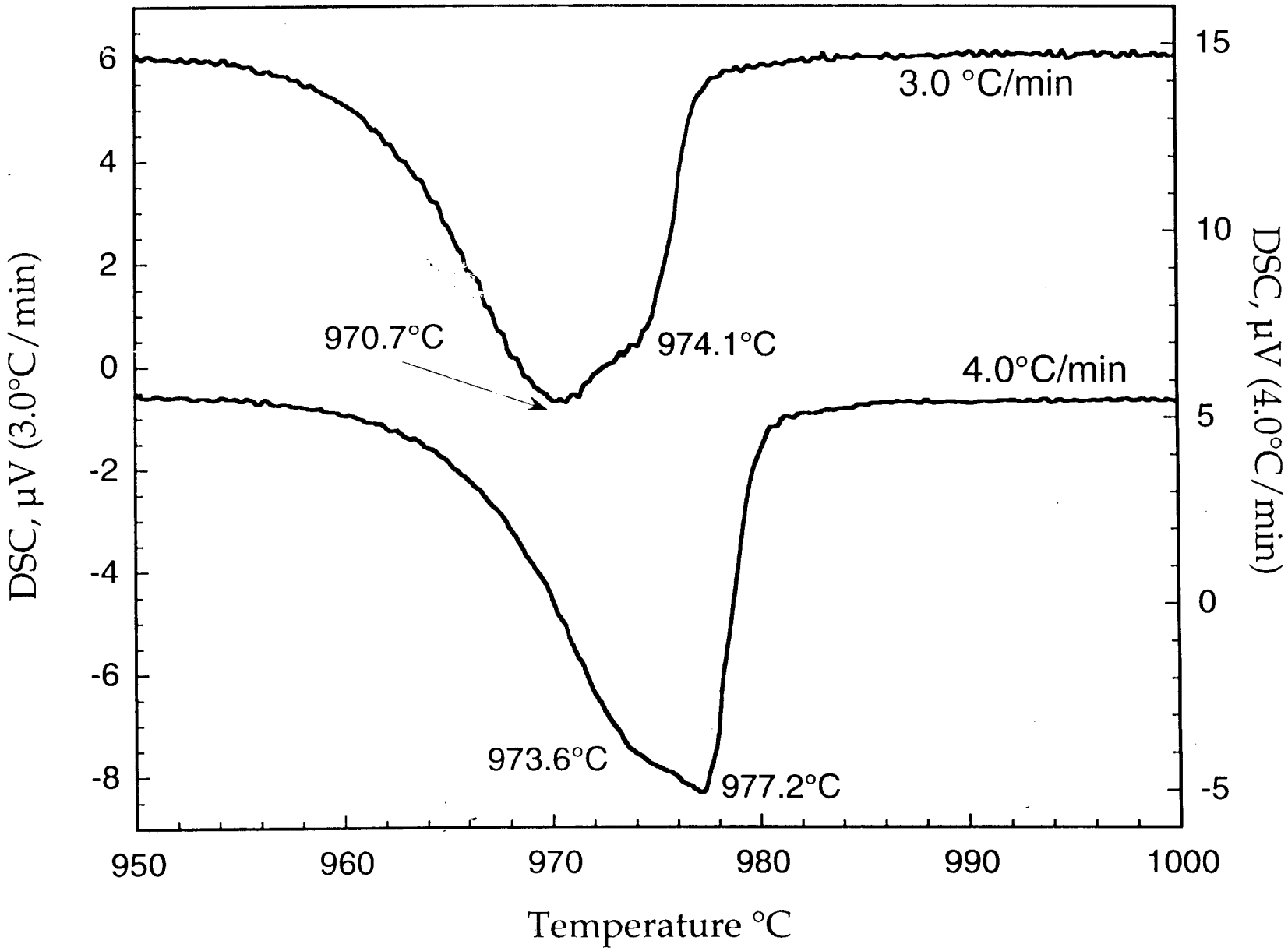


Figure 2. Plot of the DSC exotherms for non-isothermal crystallization of quenched mullite composition glass, at heating rates of 3.0° and 4.0°C/min. Note the asymmetry in both curves, indicating two different exothermic events, and the shift in prominence of the two different events.

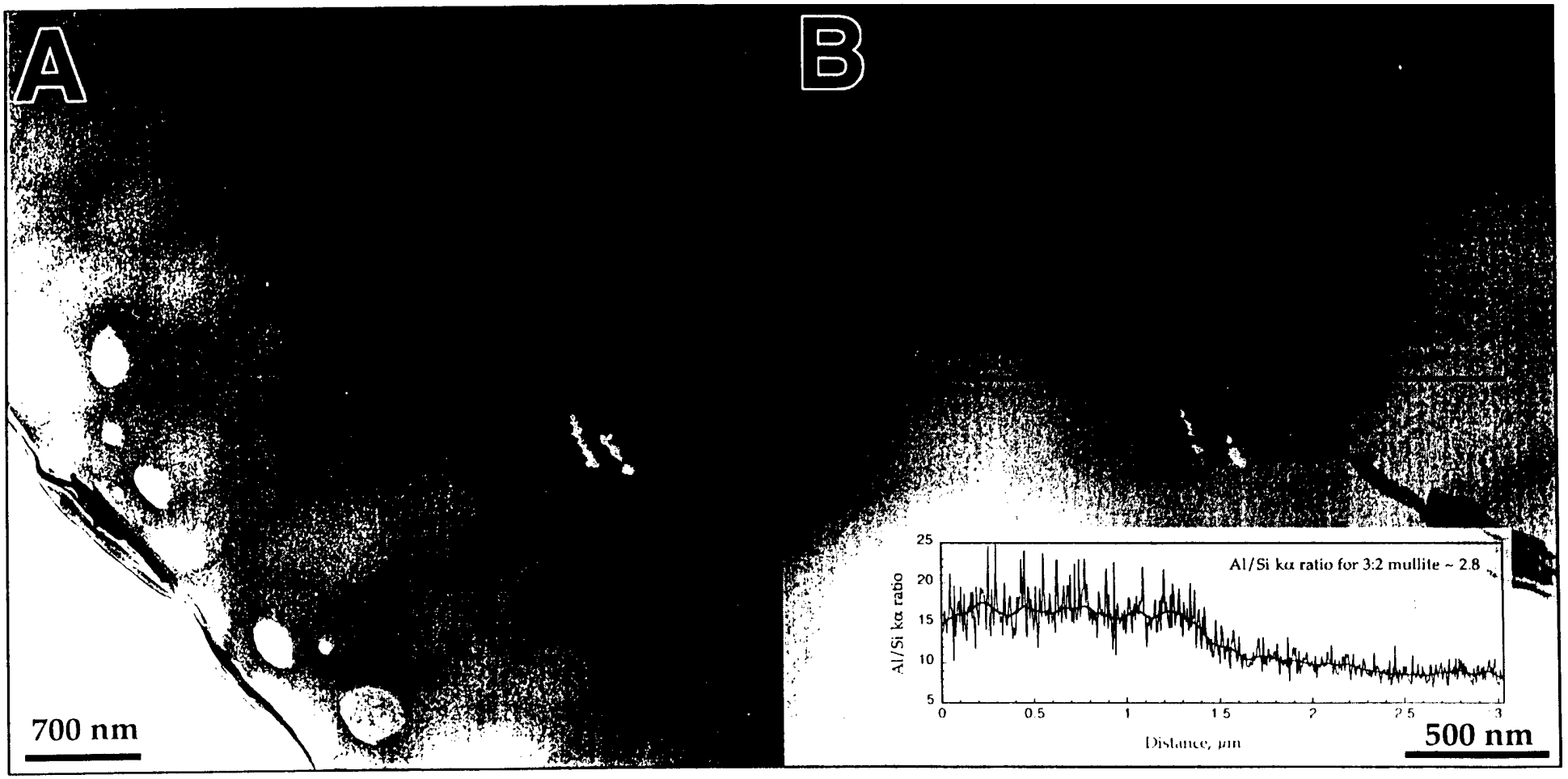


Figure 3. TEM BF image (A) and a STEM BF image (B) of a quenched mullite composition glass bead (specimen Q). The contrast variations in (A) were typical of phase separated, amorphous materials. The entire field of view in (B) had a composition of 75.8 mol% Al_2O_3 and 24.2 mol% SiO_2 as determined by STEM EDS. The graph in (B) shows the variation in Al/Si kα ratio from an EDS line scan through the central dark region in the sample. An Al/Si kα ratio of ~ 2.8 corresponds to 3:2 mullite (60 mole% alumina).

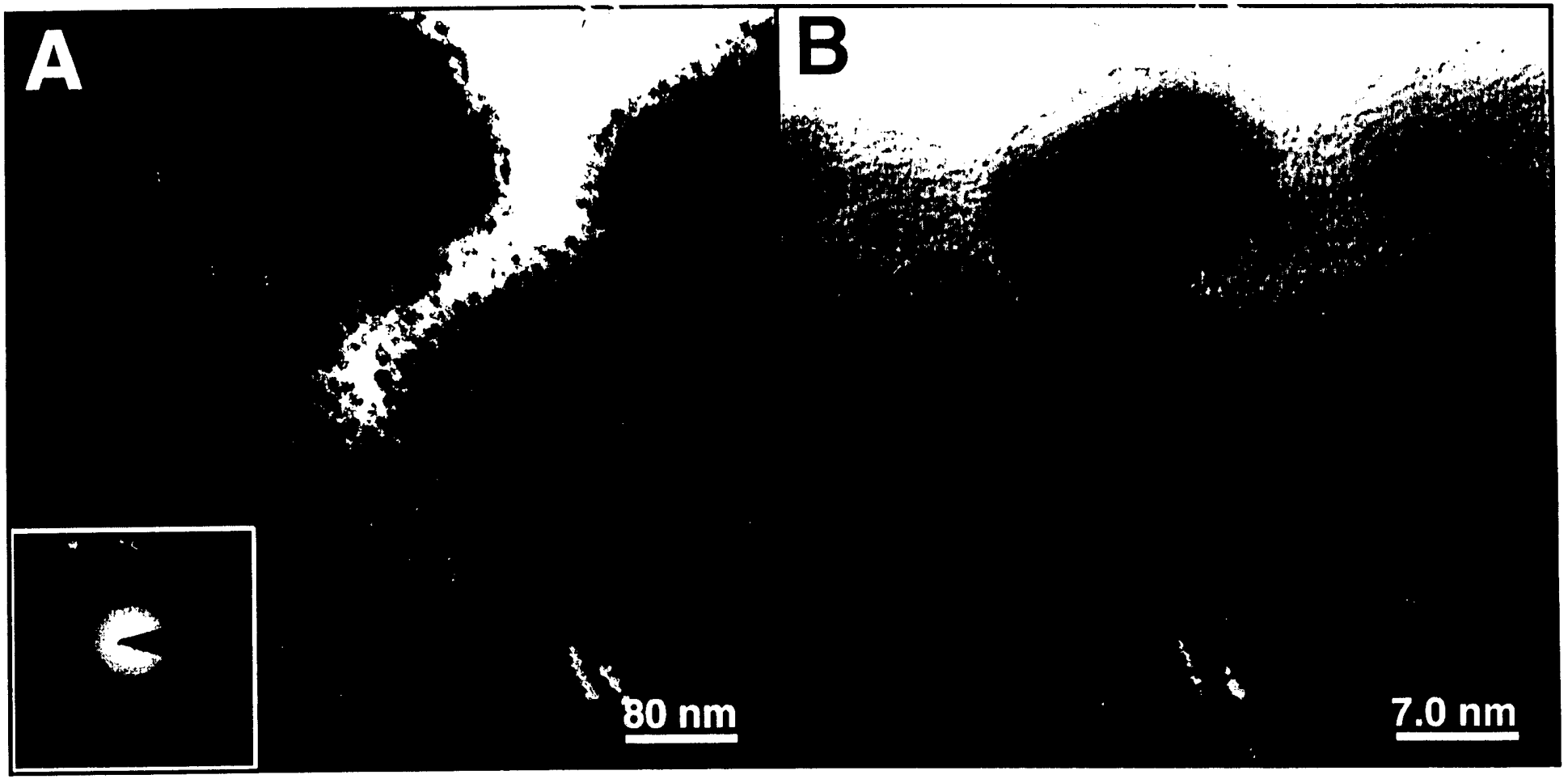


Figure 4. TEM BF images of an amorphous mullite fiber annealed at 920°C for 3h (speicmen N). The inset image in (A) is an SAD pattern taken from the crystallites along the edge. The pattern was indexed as the pseudotetragonal metric of mullite. The lattice spacing of the crystallite in (B) was3.38 Å, which corresponded to the (120)/(210) lattice planes of mullite (3.428 and 3.390 Å, respectively).

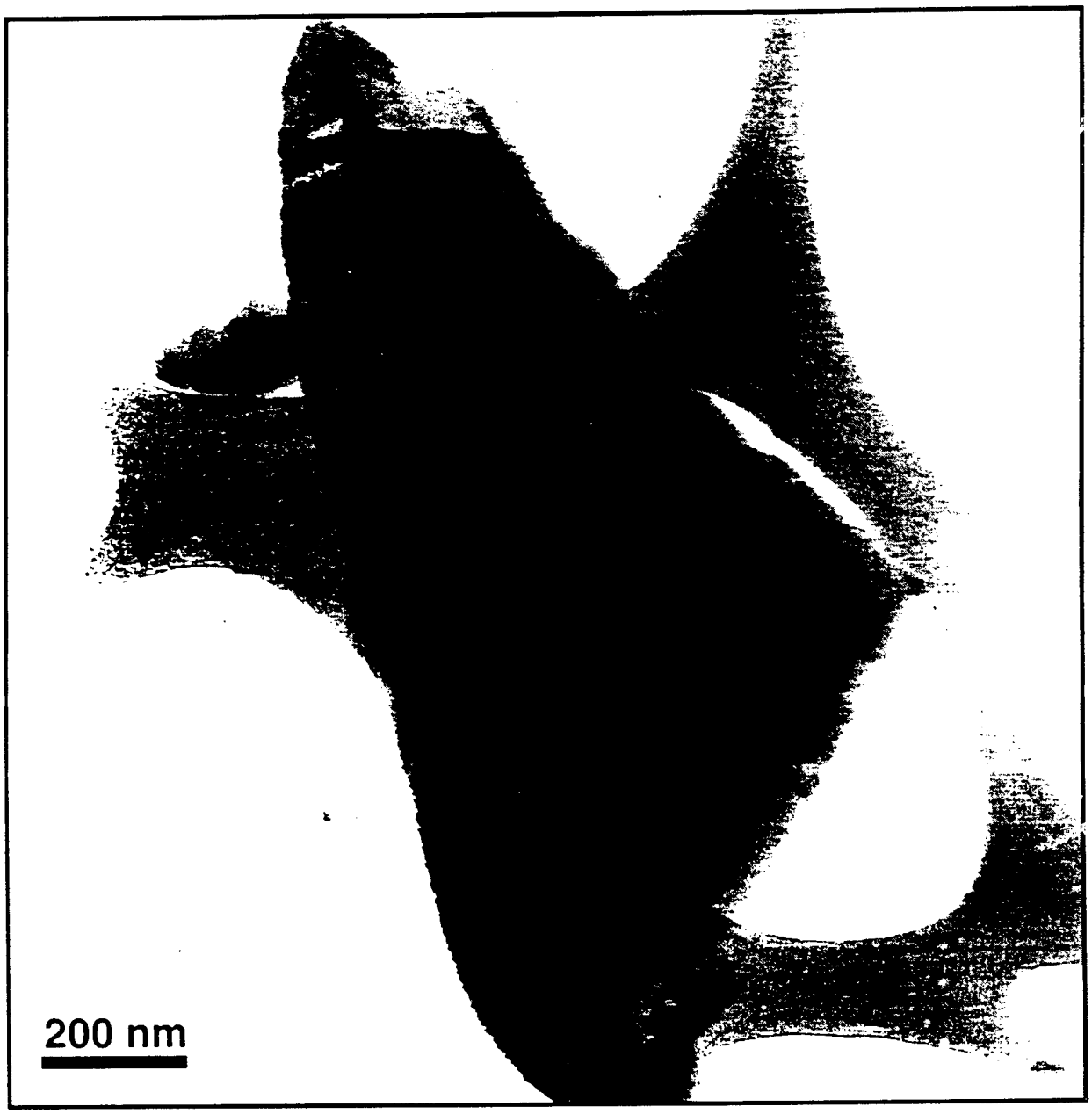


Figure 5. TEM BF micrograph of a crushed, quenched, mullite compositon bead that was isothermally crystallized at 938°C for 2.5h (specimen M1).

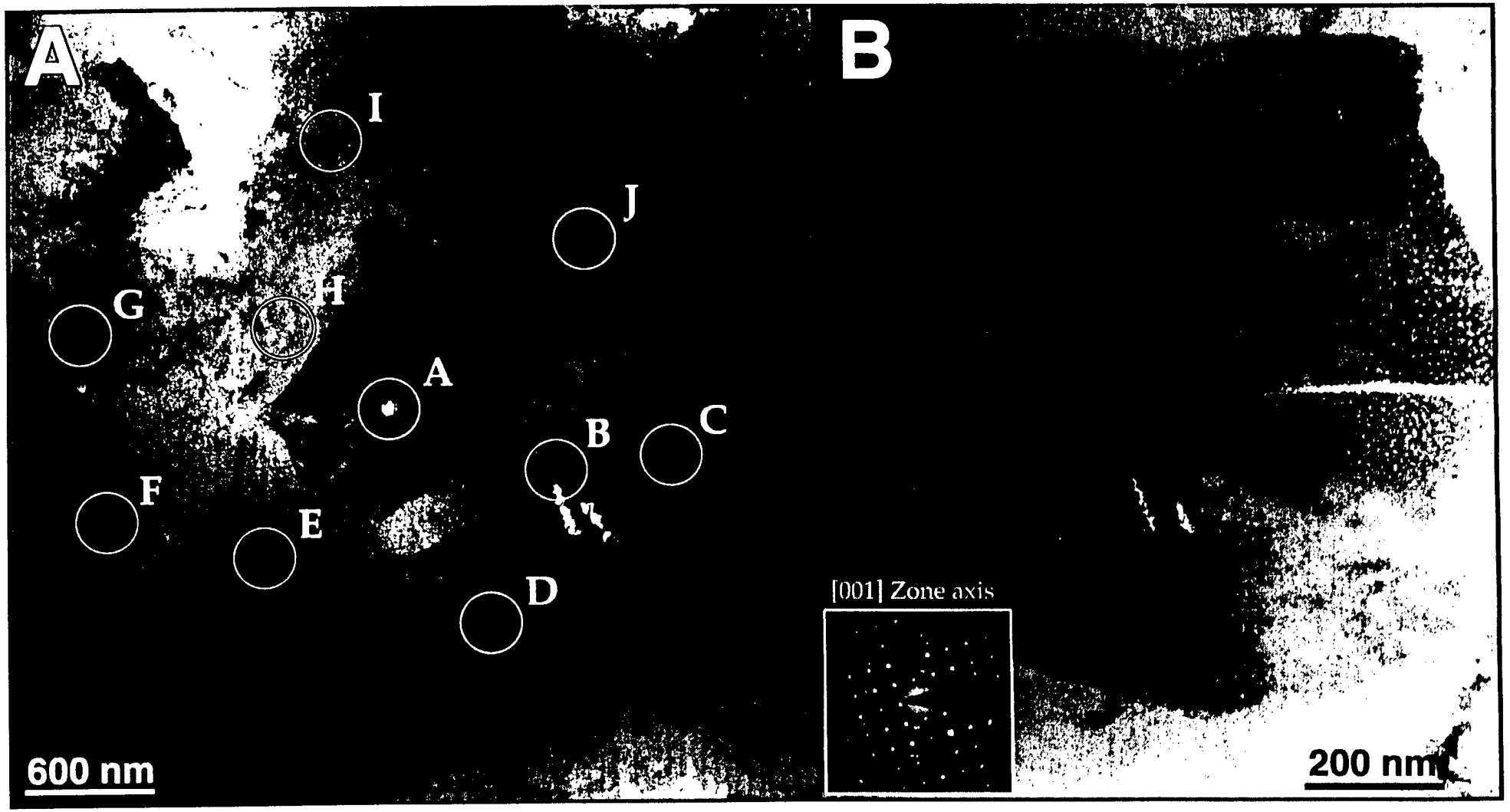


Figure 7. TEM BF images (A and B) from a polished thin section of a quenched mullite composition bead heated to 1085°C (speicmen M1.5). EDS analyses were made at the points labeled alphabetically, and the composition at each point was 60±1 mol% Al_2O_3, 40±1 mol% SiO_2. The variegated diffraction contrast in the grains was due to lattice strain. Higher magnification of one of the grains (B) revealed sm inclusions with and average size of 9.4 x 7.9 nm. The SAD pattern in (B) was from the [001] zone axis of a similar grain.

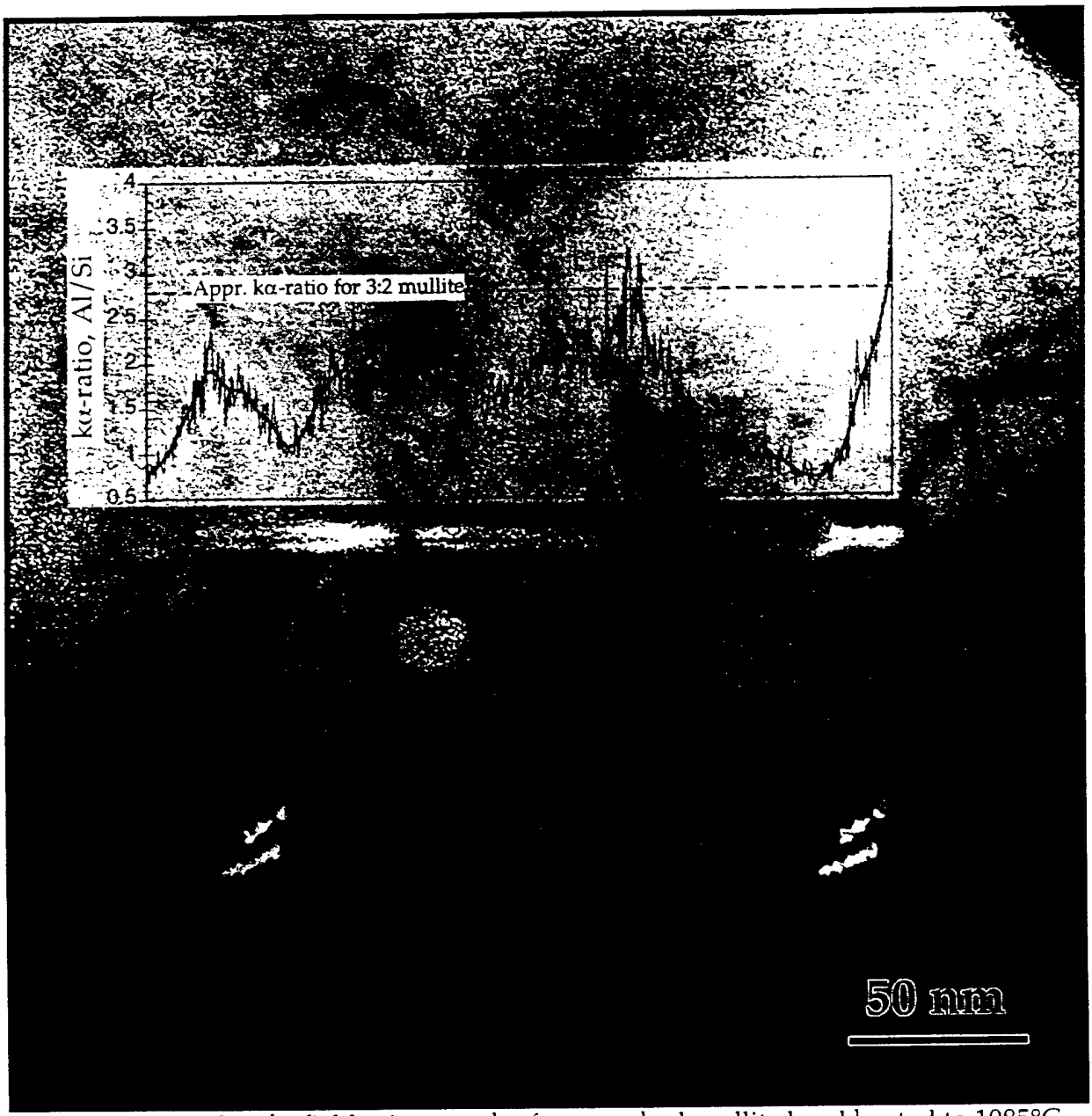


Figure 8. STEM bright field micrograph of a quenched mullite bead heated to 1085°C (specimen M1.5). The horizontal line in the center of the micrograph was due to beam damage of the specimen during EDS line profile analysis. The inset graph shows the variation in the Al/Si Ka ratio over the region scanned. This was an indication of chemical inhomogeneity at very small length scales.

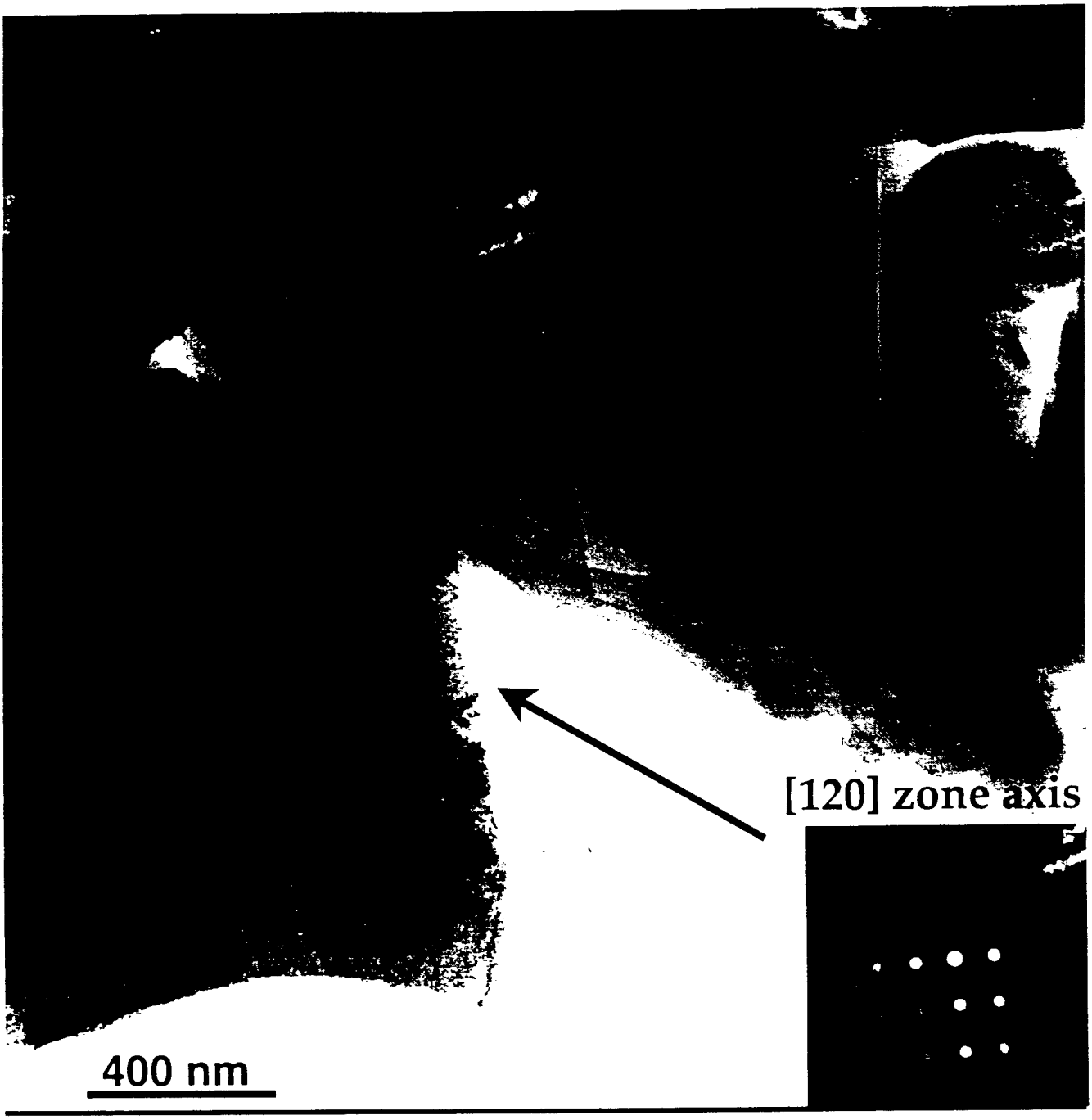


Figure 9. TEM bright field image of quenched mullite composition powder after being heated up to 1200°C (specimen M2). The inset image is a Kossel-Möllenstedt micro-diffraction pattern for the designated crystal oriented along the [120] zone axis.

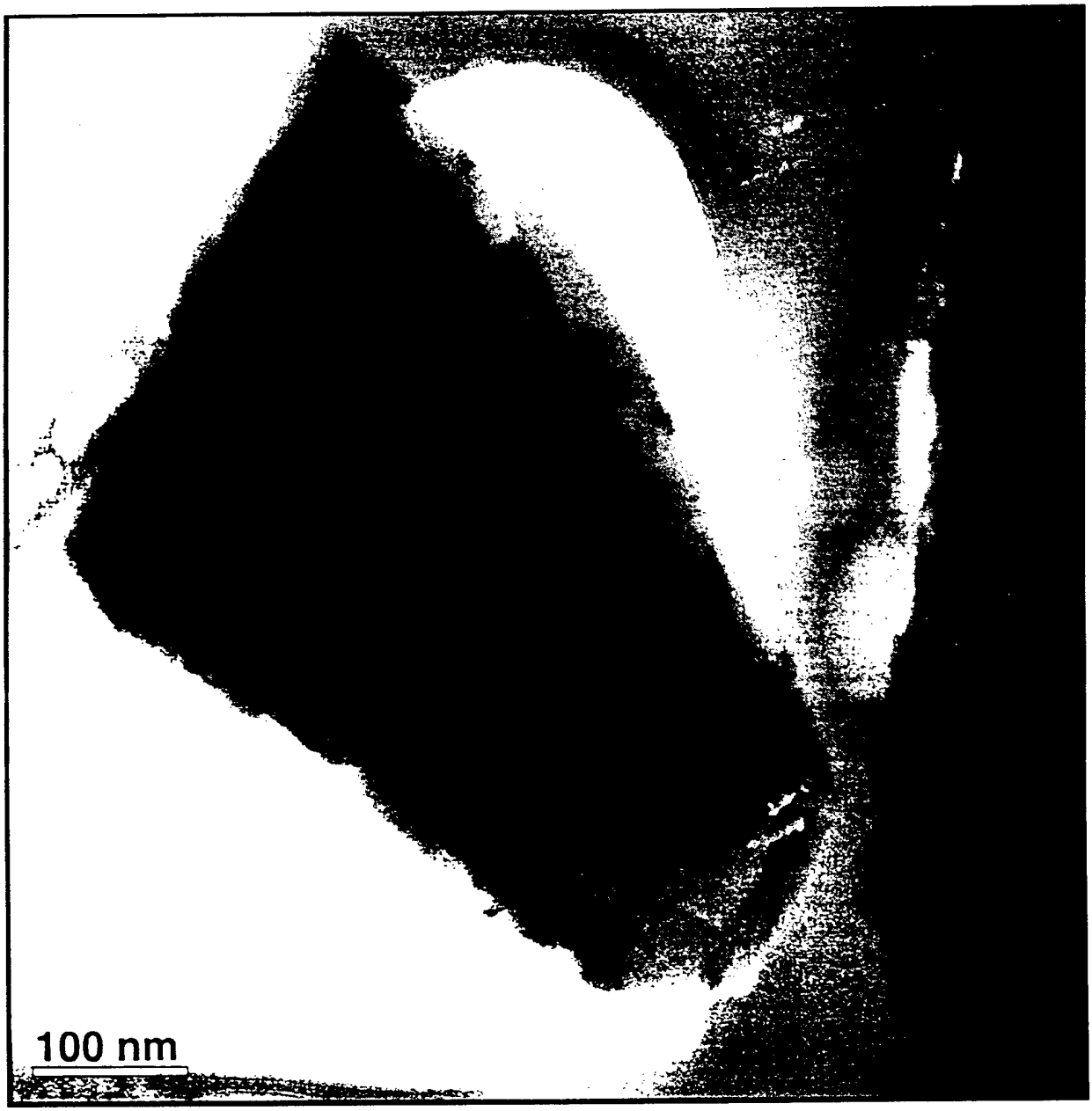


Figure 10. TEM bright field image of quenched mullite composition powder after being heated up to 1400°C (specimen M3).

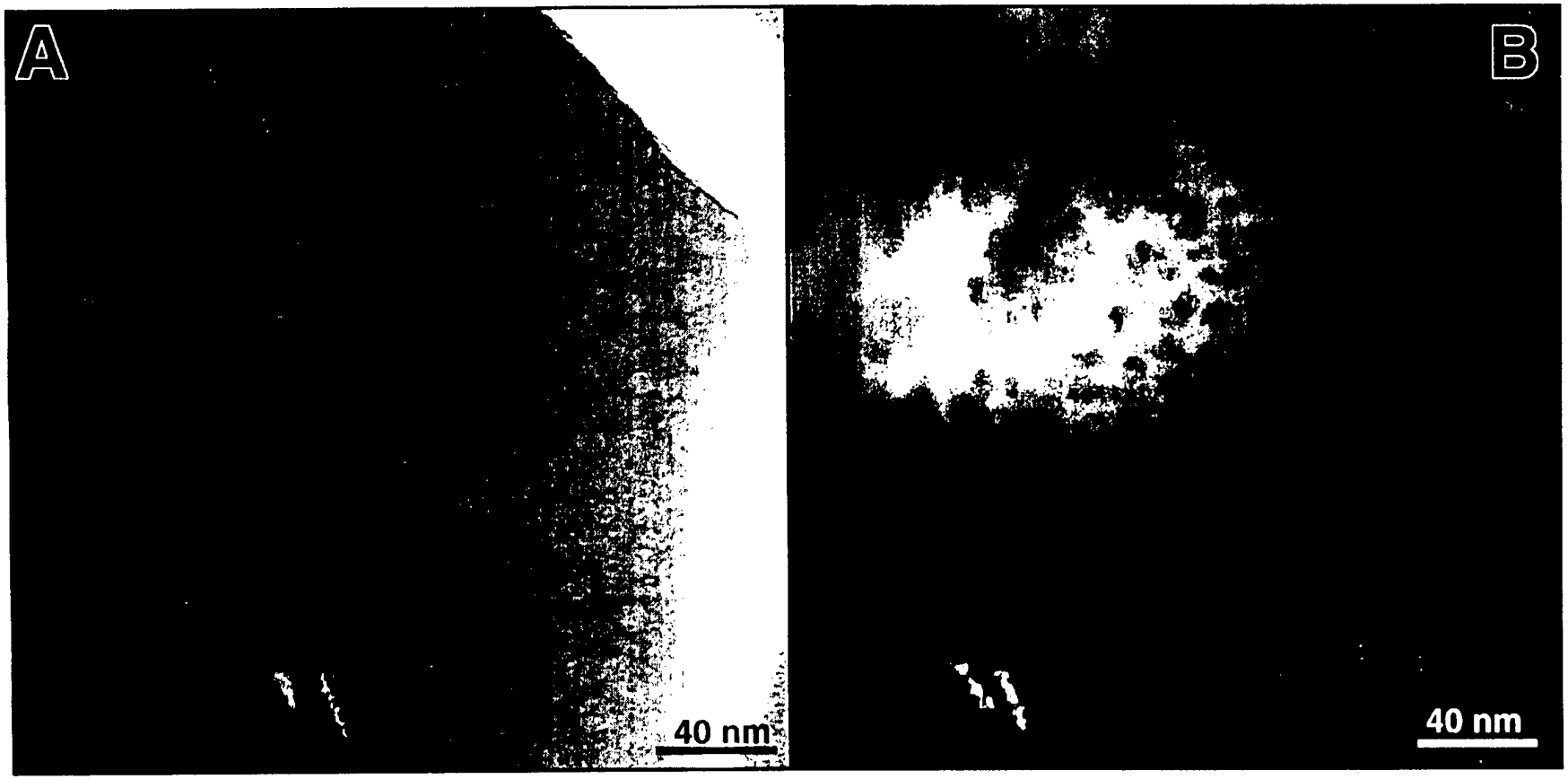


Figure 6. TEM BF (A) and DF (B) micrographs of a ground sample from a quenched mullite composition bead that was isothermally crystallized in a DSC at 938°C for 2.5 h (specimen M1). The darker, matrix region in the BF image (A) appeared as the bright region in the DF image (B), and the light, circular inclusions observed in the BF image appeared dark in the DF image.

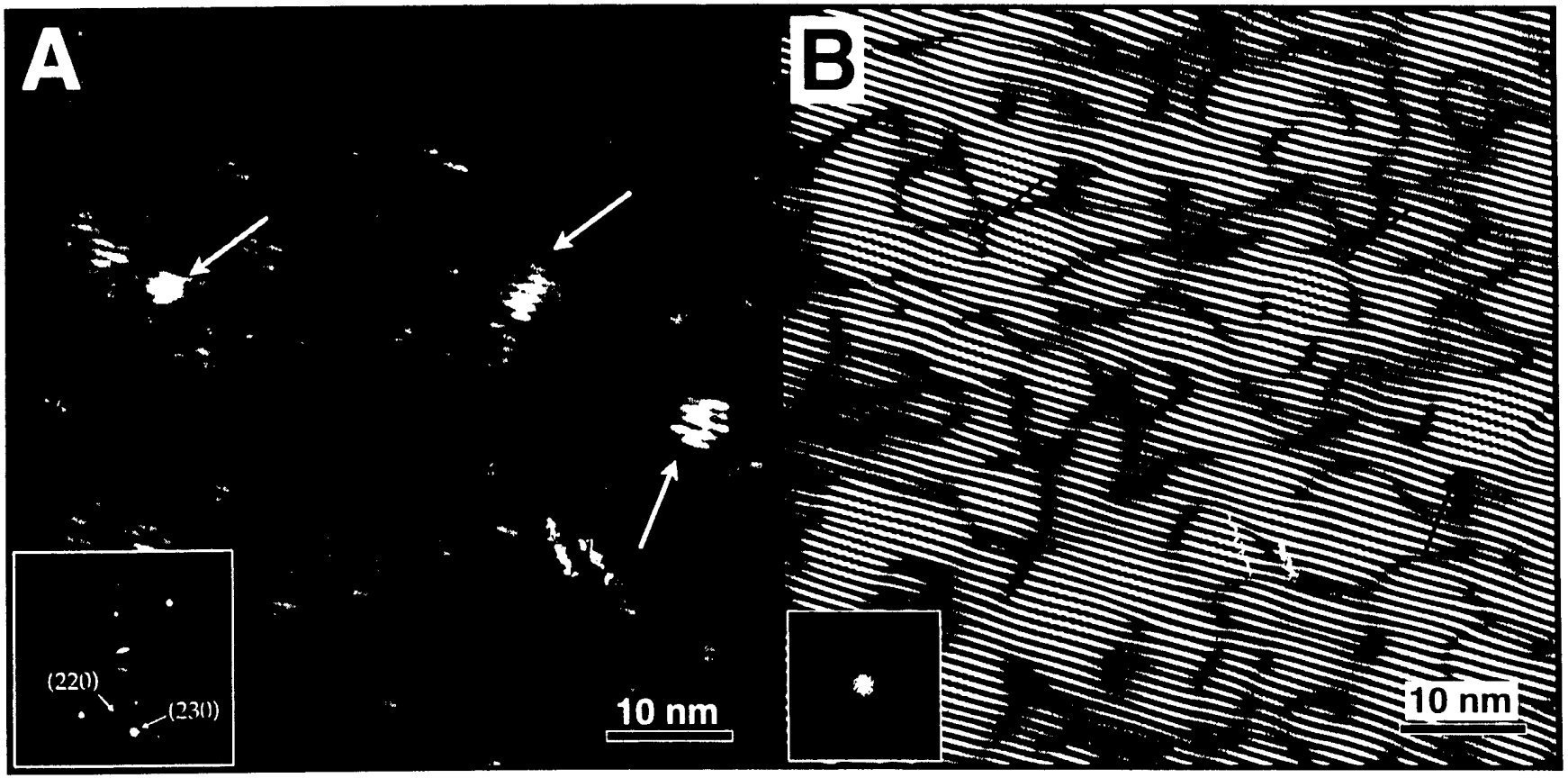


Figure 11. TEM CDF micrograph (A) and corresponding moiré pattern (B) from a crushed, quenched mullite composition bead isothermally crystallized at 938°C for 2.5 h (M1). The micrograph was taken from an area of two overalpping crystals using the (220) reflection from one and the (230) reflection from the other (SAD inset, A). The overlapping lattice fringes from the two crystals created the observed moiré pattern (dark wavy lines). B is a filtered Fourier image of A showing the moiré pattern in greater detail. The inset in B is the fast Fourier transform (FFT) of A. The average fringe spacing was 8.56Å. The distortion in the moiré pattern was an indication of strain in the two crystals, and was spatially correlated to the embedded inclusions in A (bright areas).

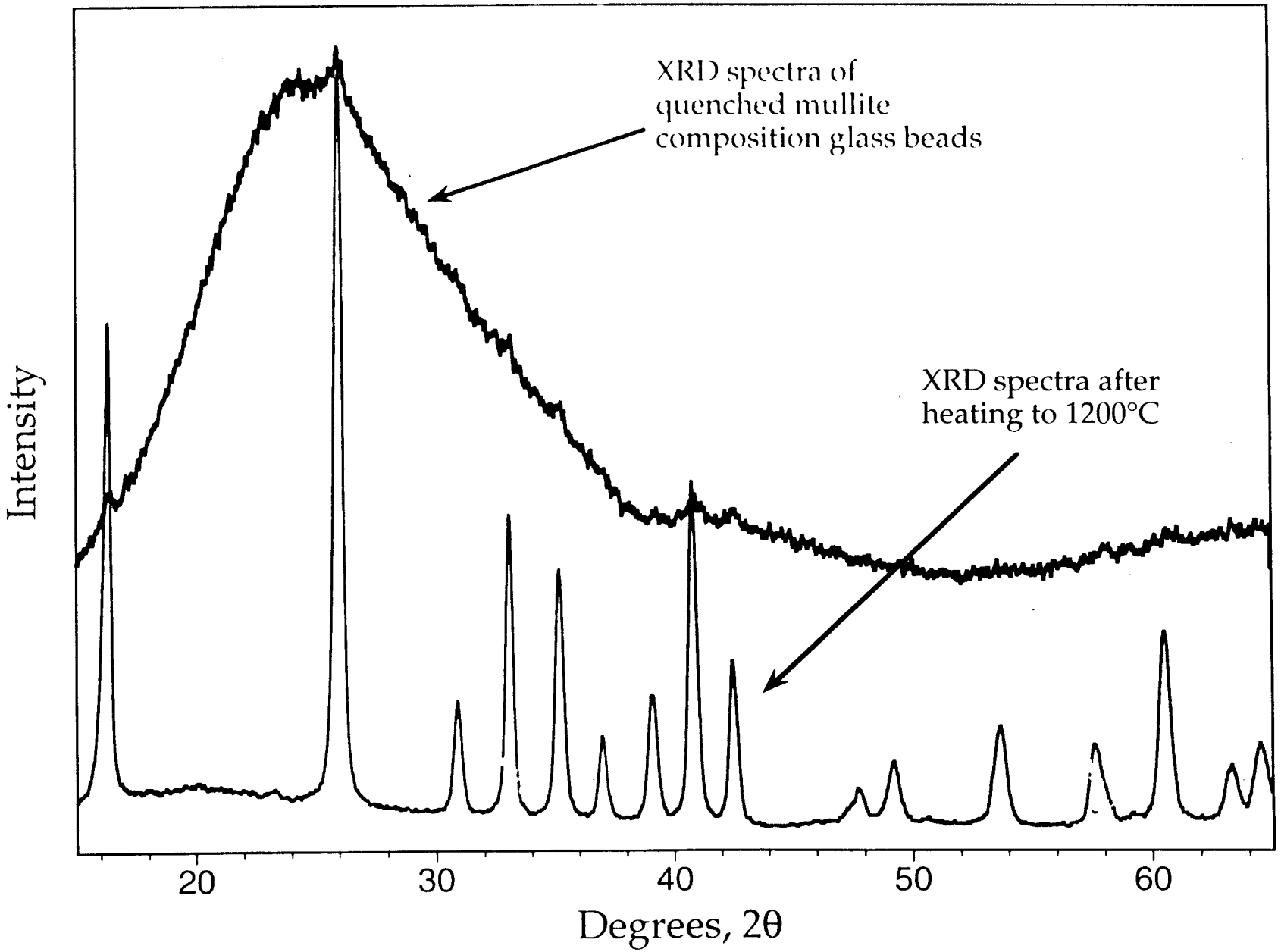


Figure 12. Combined, normalized XRD spectra for quenched mullite composition glass beads, before and after crystallization in a DTA. The crystalline pattern belongs to mullite, and verifies that the exothermic events observed by DTA/DSC were due to crystallization of mullite.

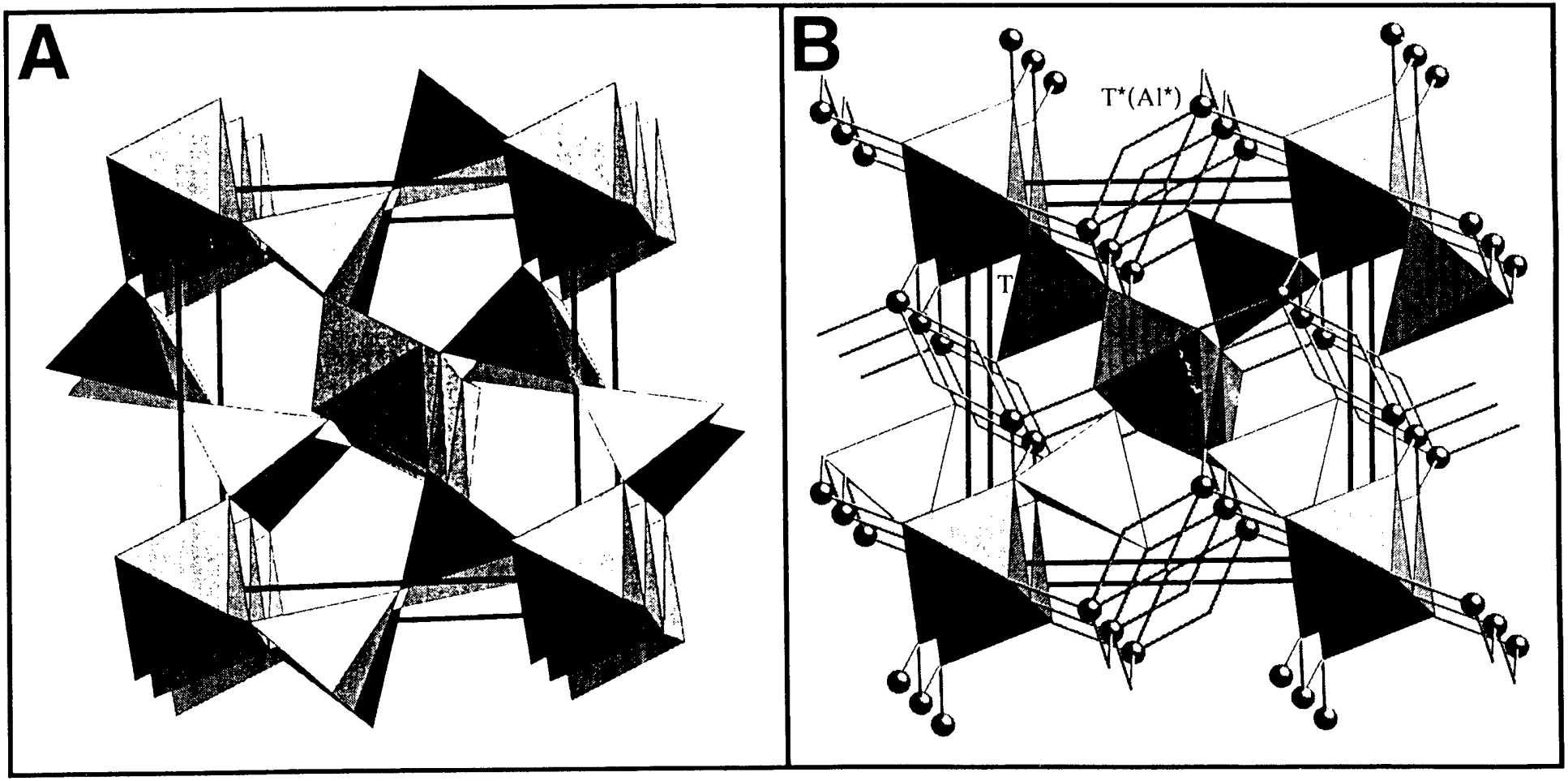


Figure 13. Idealized structure of sillimanite (A) and mullite (B) projected down the a-b plane.

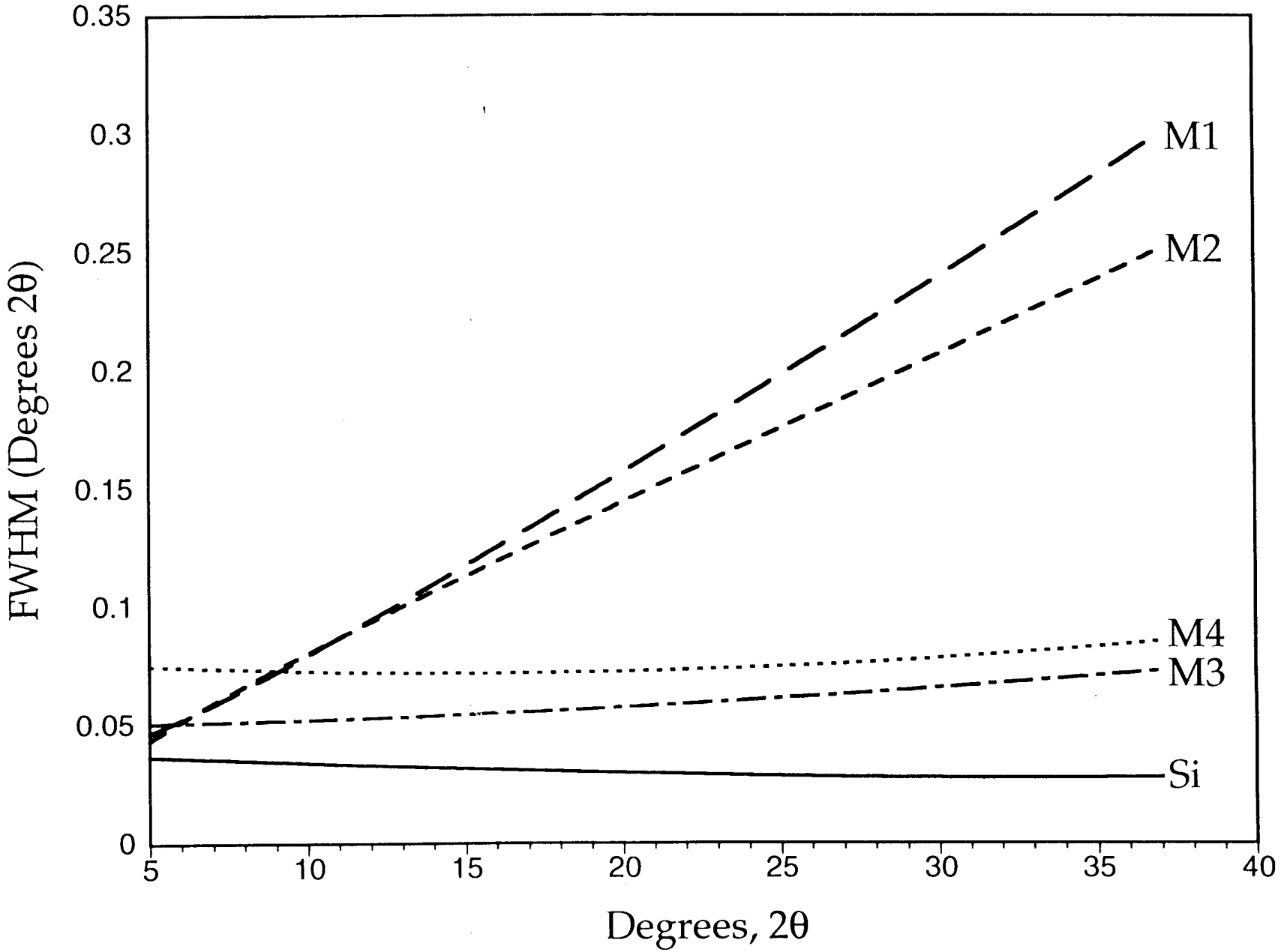


Figure 14. Line widths, full width at half maximum, (FWHM) obtained from single phase Rietveld refinements of synchrotron XRD spectra for specimens M1, M2, M3, M4 and from a Si powder standard (SRM 640b, NIST).

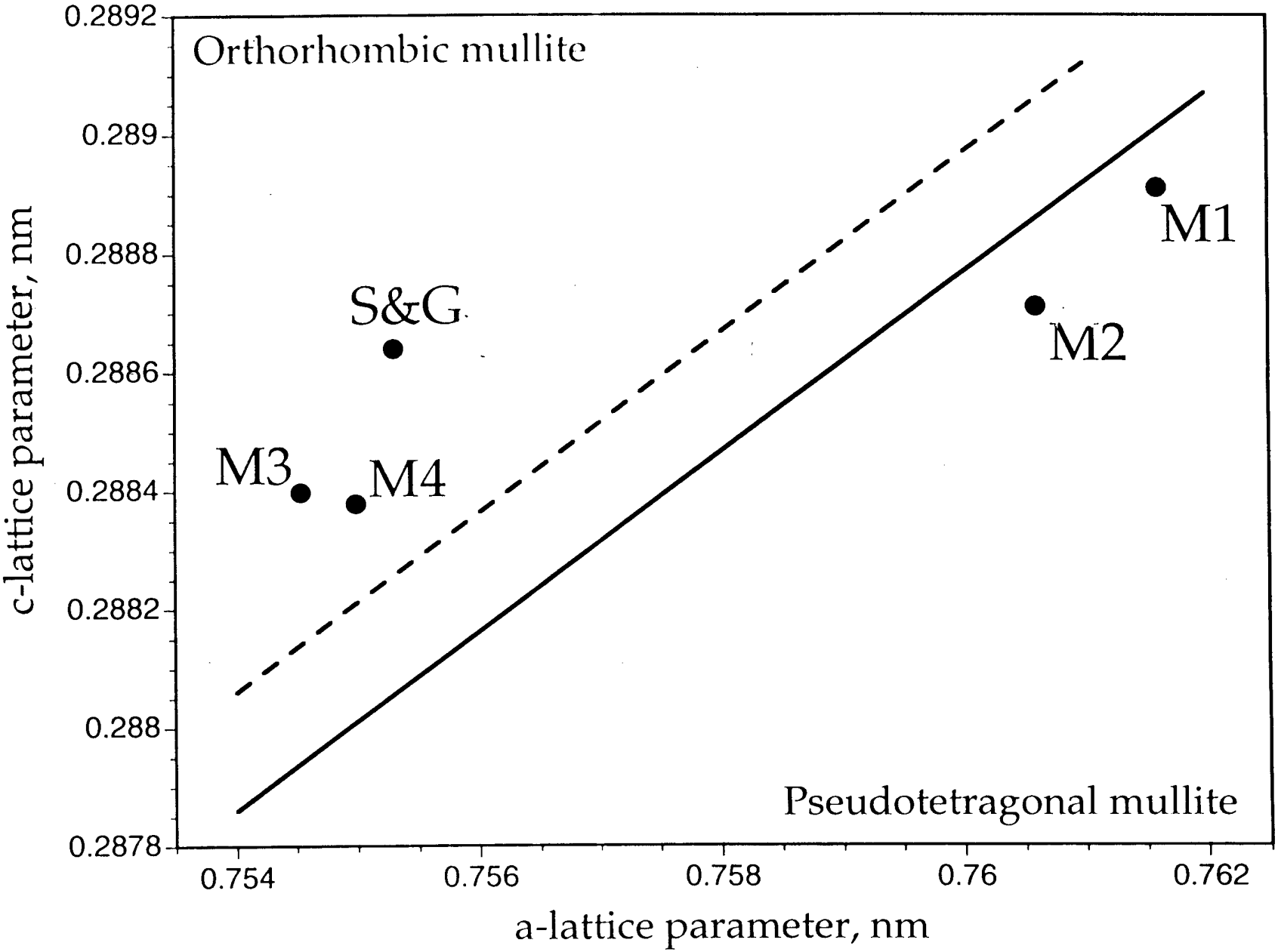
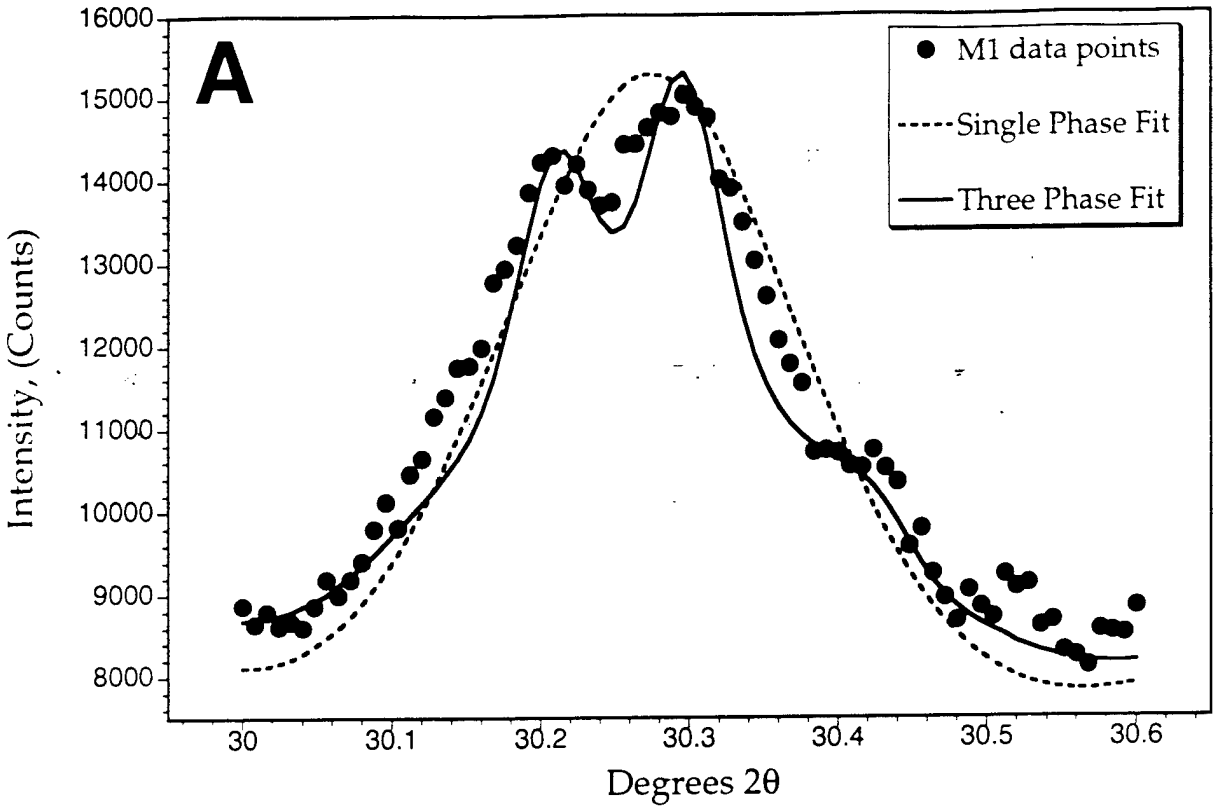


Figure 15. Positioning of the refined a and c cell dimensions for specimens M1, M2, M3 and M4 on an orthorhombic - pseudotetragonal mullite diagram.



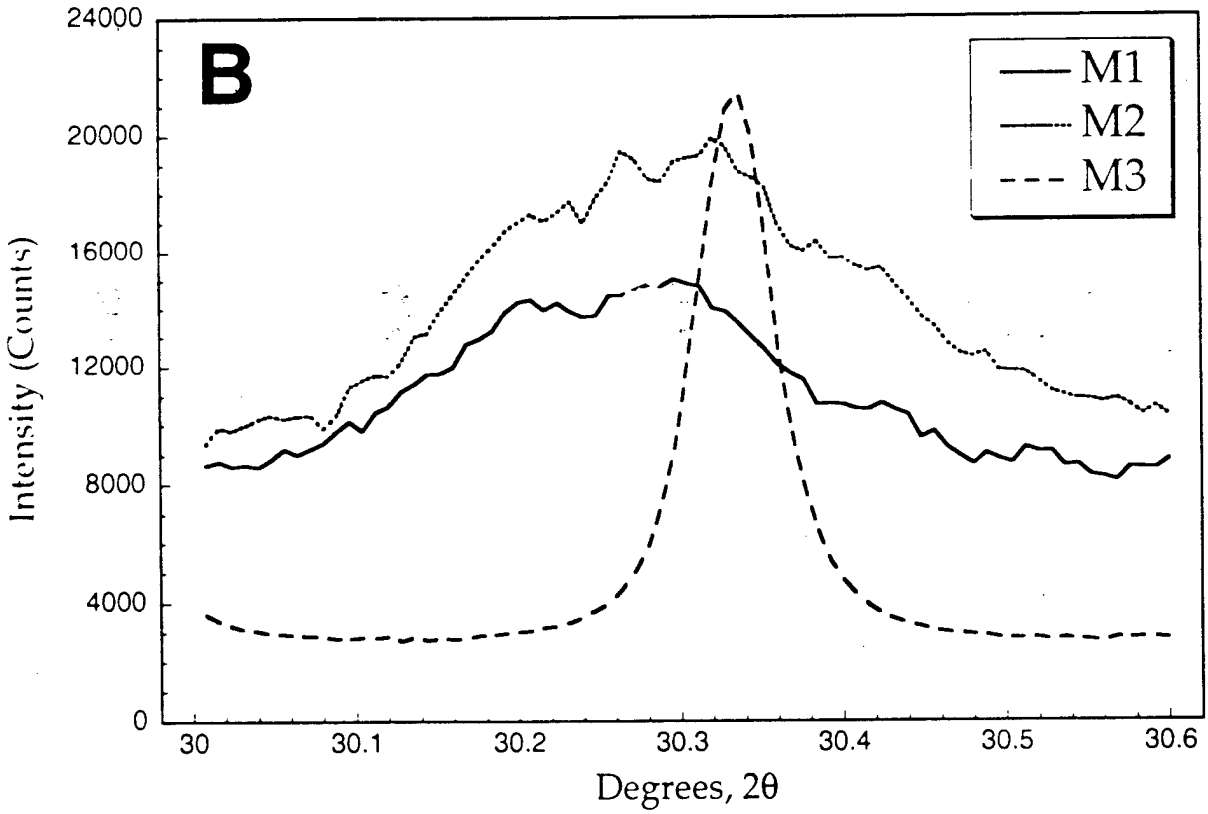


Figure 16. Detailed sections of measured powder diagrams around the well separated 002 reflection for various spectra. 16A, sample M1: observed data (dots), single phase Rietveld refinement (dashes), 3-phase Rietveld refinement (line). 16B, comparison of data from partly crystallized samples M1, M2 with those of the well crystallized specimen M3.

ELECTROPHORETIC DEPOSITION OF OXIDE CERAMICS ON MULLITE FABRIC

Introduction

The electrophoretic technique [1] was used in an attempt to deposit an even layer of oxide coating onto mullite fabric. The mullite fabric served as the deposition electrode in the electrophoretic cell setup while an aluminum plate was used as the counter electrode.

Since mullite is non-conducting, it was first coated with a continuous thin layer of carbon to render it electrically conductive. A polymer-derived pitch was found to be suitable for this purpose. With the proper selection of polymer type and molecular weight range, a pitch of sufficient viscosity at the pyrolysis temperature was obtained that was able to infiltrate the fiber tows through capillary action. This resulted in an even coating of each individual fiber on the woven fabric. In this work, a PEG-derived pitch was used.

Eectrophoretic deposition was carried out using aqueous sols of nanosized alumina and zirconia as model systems. The use of an aqueous system limited the operating voltage to a maximum of 4.5V to prevent the electrolytic decomposition of water into O_2 and H_2 at the anode and cathode, respectively; gaseous product at the deposition electrode would result in a porous deposit that is undesirable.

Experimental

1. Carbon coating of mullite fabric

A polymer:mullite fabric ratio of about 5:1 (weight basis) was used. Thin discs of PEG were hand pressed and placed on sized Nextel 440 (3M Co.) mullite fabric. For soft solid PEGs, the polymer was simply spread over the fabric. In the case of liquid PEGs, the fabric was soaked in the liquid polymer for a period of about 5 minutes. The prepared samples were pyrolysed in an argon atmosphere at 800°C for 1 h.

2. Electrophoretic deposition

The counter electrode was an aluminum plate and a voltage of 4.5 V (dc) was used throughout. The colloidal sols used were Nyacol Zr50/20 (pH 3) ZrO_2 and Nyacol AL20 (pH 4) Al_2O_3 both of which have an average particle size of 50 nm. Based on prior studies, deposition times of 5 and 10 mins were selected for the Al_2O_3 and ZrO_2 experiments, respectively. The EPD samples were dried slowly in a saturated water vapor environment.

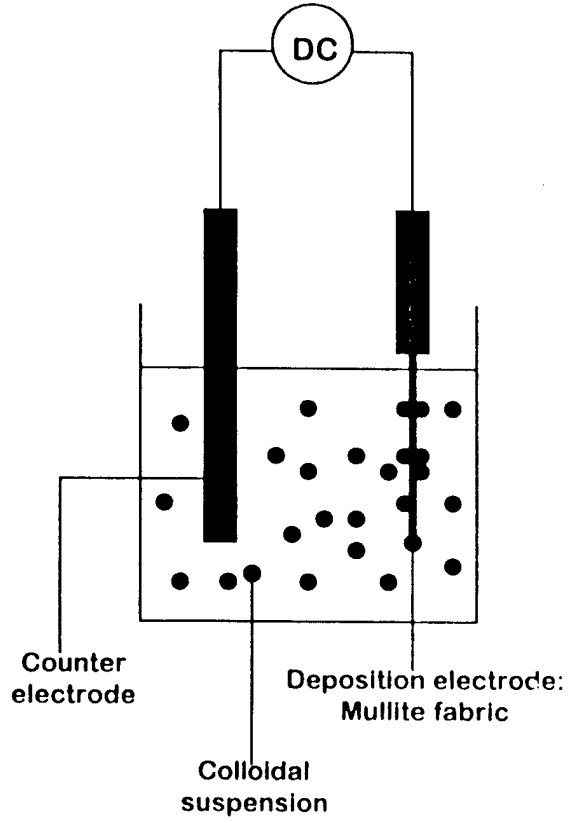
3. SEM sample preparation

A low viscosity resin was used to prepare the dried EPD samples for cross-sectional observation under the SEM. All samples were sectioned at the midpoint for a better representation of the deposition process.

Results

While most of the PEGs screened were suitable for use to impart a thin continuous layer of carbon on the mullite fabric, Carbowax PEG 1450 was selected due to the ease of handling. For comparative purposes, Aldrich PEG 200 and ethylene glycol (EG) derived pitch were also used. It was found that PEG 1450 gives a more consistent result in terms

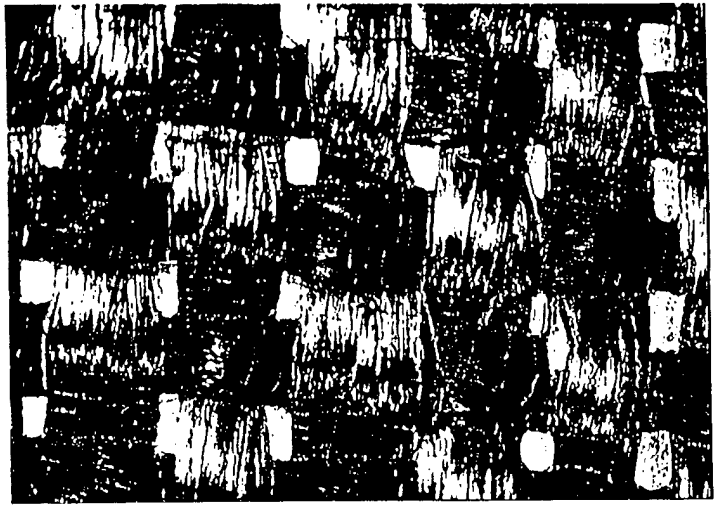
Electrophoretic Deposition



EXPERIMENTAL PARAMETERS:

Deposition electrode	:	C-coated mullite fabric (PEG-derived pitch)
Counter electrode	:	Aluminum
Deposition voltage	:	4.5 V
Deposition time	:	5 to 10 minutes
Deposition material	:	Nyacol ZrO_2 (50nm; pH 3) Nyacol Al_2O_3 (50nm; pH4)

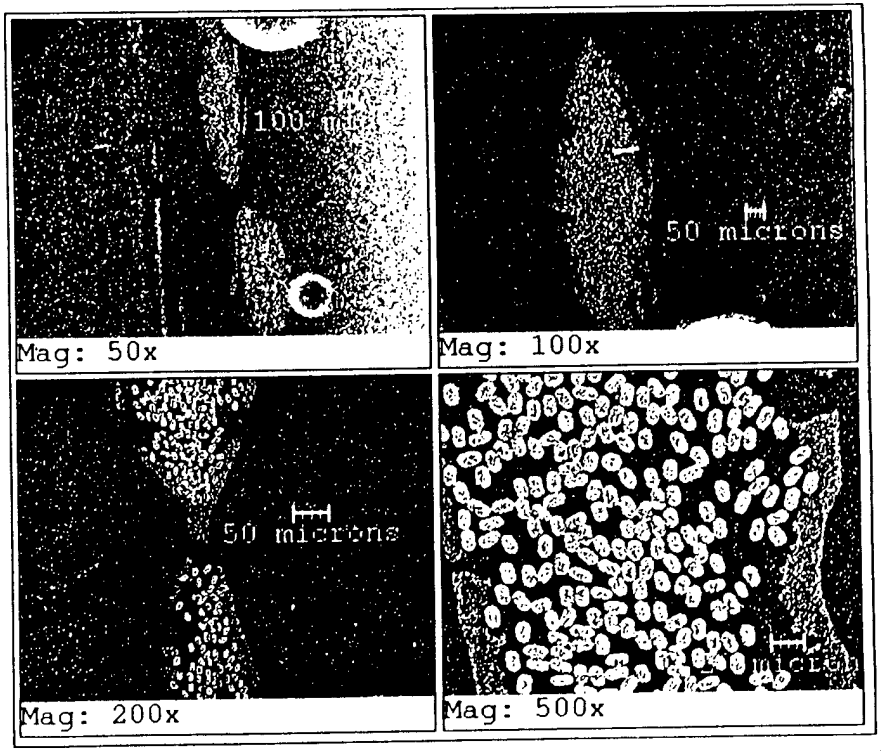
EPD: Alumina on Nextel 440



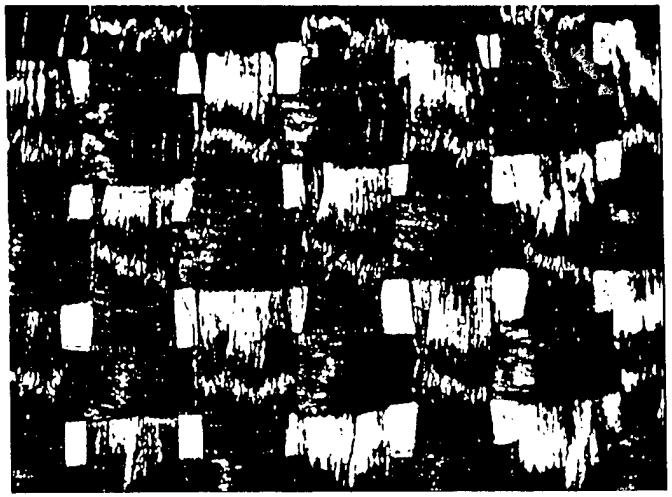


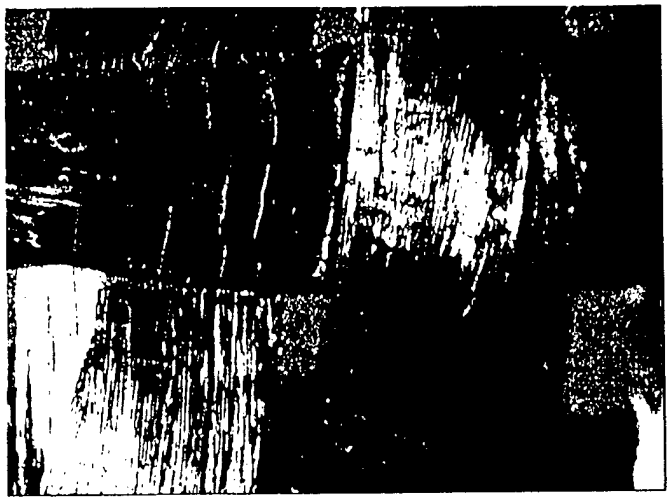
Deposition parameters:

C source	:	Carbowax PEG1450
Material	:	Al_2O_3 (50 nm; pH 4)
Voltage	:	4.5 V
Time	:	5 minutes



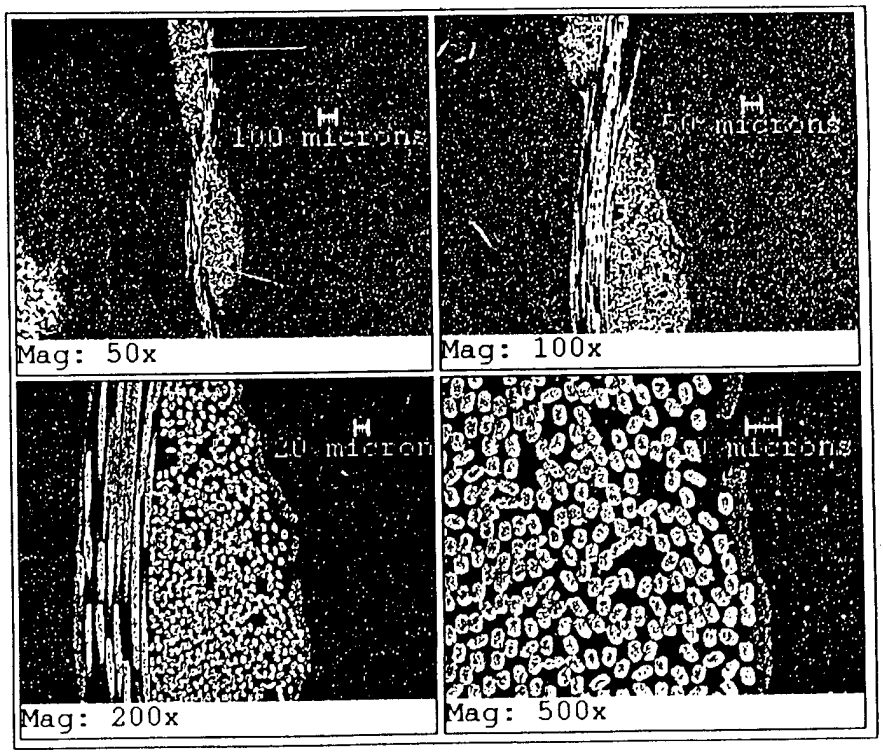
EPD: Alumina on Nextel 440





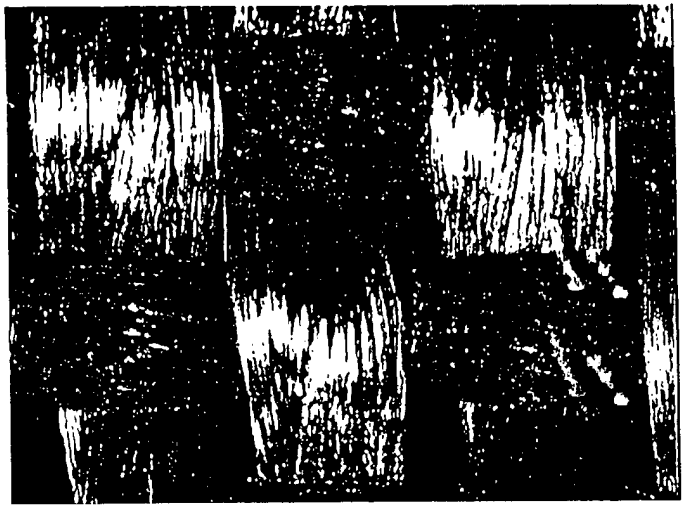
Deposition parameters:

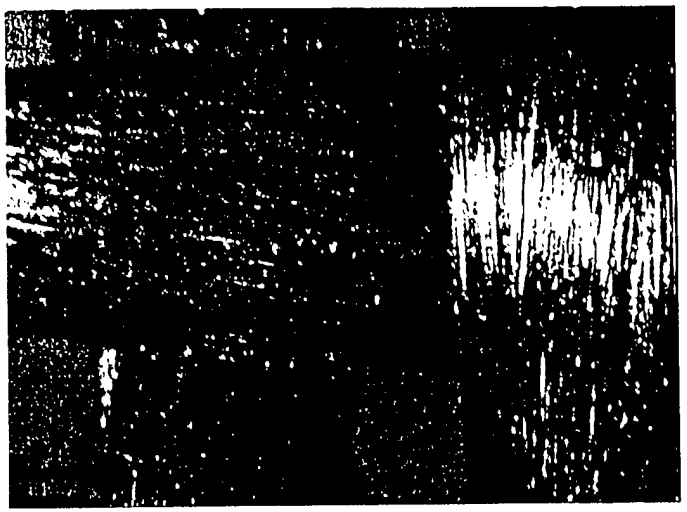
C source	:	Ethylene glycol
Material	:	Al_2O_3 (50 nm; pH 4)
Voltage	:	4.5 V
Time	:	5 minutes



University of Illinois at Urbana-Champaign

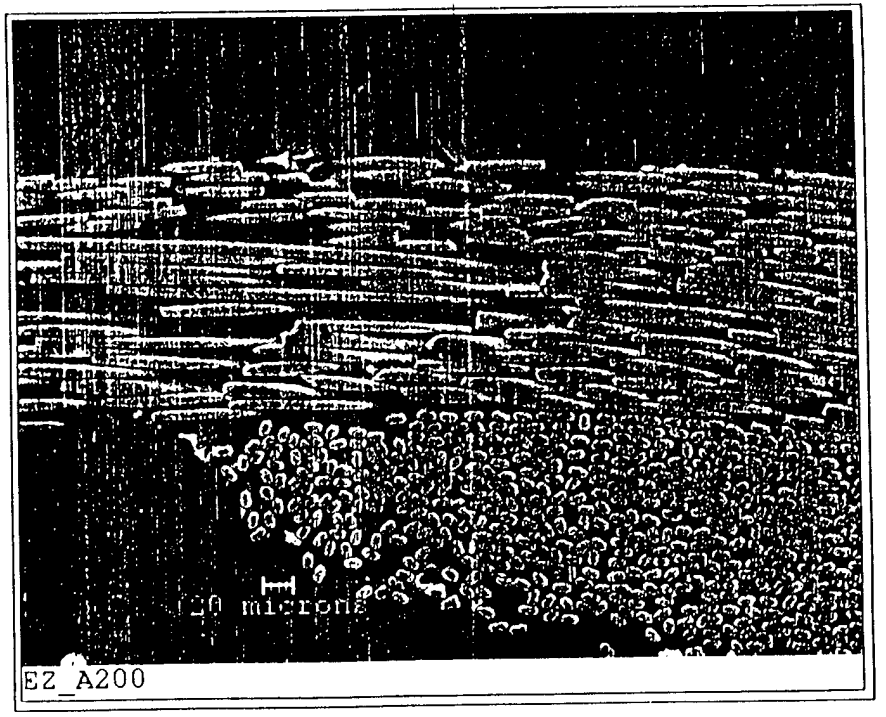
EPD: Zirconia on Nextel 440





Deposition parameters:

C source	:	Aldrich PEG 200
Material	:	ZrO_2 (50 nm; pH 3)
Voltage	:	4.5 V
Time	:	10 minutes



University of Illinois at Urbana-Champaign

Electrophoretic Deposition

CONCLUSIONS

a PEG-based pitch is suitable to impart a percolating conductive carbon layer onto woven mullite fabric

the tightly woven fabric is not conducive for sol penetration using the EPD technique - only a surface "envelope" was obtainable

Executive Summary

The original aim of this work was to develop a viable, on line, coating technique for oxide fibers and weaves. The coating was to be a chemically compatible, oxide (eg. hexacelsian ($BaAl_2SiO_8$)) which provided a temperature-independent, debonding mechanism based on residual stresses developed at 1590°C, due to a reconstructive phase transformation accompanied by a 5.6% volume contraction. However, the method adopted, the charged liquid beam cluster technique proved to be unfeasible at the current time. Attention was therefore focused on to electrophoretic deposition of oxide sols (alumina, zirconia) onto carbon-coated fibers and weaves of alumina and mullite ($3Al_2O_3 \cdot 2SiO_2$). However drying of films led to extensive microcracking and this method too, was found to be unsuitable. Attention was then turned to support related AFOSR work for which ongoing, but intermittent funding was obtained (STTR stages I and II); viz., (i) the development of mullite and YAG fibers by amorphous crystallization from a frozen, amorphous melt; (ii) the elastic constants of single crystal, mullite and yttria fibers as measured by Brillouin spectroscopy to 1200°C; and (iii) powder synthesis of oxides for matrices or deposition as coatings.

Journal Publications

(In chronolgical order)

1 "Preparation of Portland Cement Components by PVA Solution Polymerization," S.-J. Lee, E. A. Benson and W. M. Kriven, J. Am. Ceram. Soc. **82** [8] 2049-2055 (1999).

2 "Growth and Crystallization of YAG and Mullite-Composition Glass Fibers," J. K. R. Weber, B. Cho, A. D. Hixson, J. G. Abadie, P. C. Nordine, W. M. Kriven, B. R. Johnson and D. Zhu, J. Europ. Ceram. Soc., **19** [13] 2543-2550 (1999).

3 "High Temperature Single Crystal Properties of Mullite" W. M. Kriven, J. Palko, S. Sinogeikin, Jay D. Bass, A. Sayir, G. Brunauer, H. Boysen, F. Frey and J. Schneider, J. Europ. Ceram. Soc., **19** [13] 2529-2541 (1999).

4 "Synthesis of Oxide Powders via Polymeric Steric Entrapment," (invited review paper) W. M. Kriven, S. J. Lee, M. A. Gulgun, M. H. Nguyen and D. K. Kim, in Innovative Processing/Synthesis: Ceramics, Glasses, Composites III. Ceramic Transactions, vol **108,** 99-110 (2000).

5 "Electrosynthesis and Microstructural Characterization of Anodic VO_x Films," J. P. Schreckenbach, D. Butte, G. Marx, B. R. Johnson and W. M. Kriven, J. Mater. Res., **15** [7] 1483-1489 (2000).

6 "The Single Crystal Elasticity of Yttria to High Temperature," J. W. Palko, S. V. Sinogeikin, Ali Sayir, W. M. Kriven and J. D. Bass, J. Appl. Phys., submitted.

7 "Single Crystal Elastic Moduli of Mullite (~$2.5Al_2O_3 \cdot SiO_2$) to High Temperatures by Brillouin Spectroscopy," J. W. Palko, A. Sayir, S. V. Sinogeikin, W. M Kriven and J. D. Bass, J. Am. Ceram. Soc., submitted.

8 "Crystallization Kinetics of Yttrium Aluminum Garnet ($Y_3Al_5O_{12}$)," B. R. Johnson and W. M. Kriven, J. Mater Res., submitted.

9 "Crystal Structure Development during Devitrification of Amorphous Mullite," B. R. Johnson, W. M. Kriven and J. Schneider, J. Europ. Ceram. Soc., submitted.

J. Appl. Physics, submitted, Sept 200

The Single-crystal Elasticity of Yttria (Y_2O_3) to High Temperature

James W. Palko and Waltraud M. Kriven

Department of Materials Science and Engineering, University of Illinois, Urbana, IL 61801

Stanislav V. Sinogeikin and Jay D. Bass

Department of Geology, University of Illinois, Urbana, IL 61801

Ali Sayir

NASA Glenn Research Center, Cleveland, OH 44135

(Recieved

The single-crystal elastic moduli of yttria have been measured by Brillouin spectroscopy up to 1200 °C. The room temperature values obtained are C_{11} = 223.6 ± 0.6 GPa, C_{44} = 74.6 ± 0.5 GPa, and C_{12} = 112.4 ± 1.0 GPa. The resulting bulk and (Voigt-Reuss-Hill) shear moduli are K = 149.5 ± 1.0 GPa and G_{VRH} = 66.3 ± 0.8 GPa, respectively. These agree much more closely with experimental values reported for polycrystalline samples than do previous single-crystal measurements. Linear least squares regressions to the variation of bulk and shear moduli with temperature result in derivatives of dK/dT = -17 ± 2 MPa/°C and dG_{VRH}/dT = -8 ± 2 MPa/°C. Elastic anisotropy was found to remain essentially constant over the temperature range studied.

PACS numbers: 62.20.Dc

I. Introduction

Yttria, or yttrium sesquioxide (Y_2O_3), is a refractory material with a cubic crystal structure.[1] Yttria, in the form of dense polycrystalline ceramics, has been considered for use in nuclear applications[2] and has gained interest relatively recently for use in infrared optics.[1,3,4] Due to yttria's optical isotropy (resulting from its cubic structure), it is possible that, in the future, optical components requiring high quality may be made from single crystals. The single-crystal elastic moduli are valuable for designing such optical components. In particular, the temperature derivatives of elastic moduli allow dimensional changes due to heating under physical constraint, as well as acoustic excitation to be determined. The single-crystal elastic moduli are also useful in understanding the fundamental physics of yttria. Single-crystal yttria fibers suitable for such elasticity measurements have recently been produced using a laser-heated, float zone technique.[5]

The elastic properties of pure and doped polycrystalline yttria have been determined by several authors[6-13] including measurements to high temperatures.[1,2,14] In addition, single-crystal measurements have been reported at room temperature.[15,16] There are, however, significant discrepancies between the bulk and shear moduli reported for dense polycrystalline materials and those calculated from the previously reported single-crystal moduli. The purpose of this study was to obtain accurate values of the single crystal elastic moduli of Y_2O_3 both at room and elevated temperatures.

Brillouin scattering offers a convenient means of measuring the complete set of elastic moduli for single crystals, especially at elevated temperatures. It requires no physical contact with the sample, is capable of measuring along numerous crystallographic directions in a single sample, and requires only small sample volumes. Brillouin scattering

arises from the inelastic scattering of photons from acoustic phonons in the sample. The scattered light is shifted in frequency with respect to the incident light by a factor that is proportional to the velocity of the acoustic waves (Eq. 1).[17]

$$V = \left(\frac{\Delta\omega}{\omega}\right)\left(\frac{c}{2\, n \sin\left(\theta/2\right)}\right) \qquad (1)$$

Here V is the velocity of an acoustic wave, $\Delta\omega$ is the frequency shift of the scattered light, ω is the frequency of the incident light, c is the speed of light, n is the index of refraction of the sample, and θ is the scattering angle. In this study, we employed a special case of symmetric scattering called platelet geometry (Figure 1), which utilizes a sample with flat, parallel faces and equal angles between the face normals and incident/scattered beam directions. The phonon propagation direction q is in the plane of the sample, and the face normals as well as the incident/scattered light rays all lie within a plane.[18] Figure 1 shows a schematic of symmetric platelet scattering. With symmetric platelet scattering geometry, the scattering angle is easily defined, and no knowledge of the index of the refraction of the sample is necessary. As seen in Figure 1, Snell's law allows the replacement of $n \sin(\theta/2)$ with $n_o \sin(\theta_o/2)$ in Eq. 1. This is particularly beneficial for high temperature studies where the variation of index of refraction with temperature is generally unknown and difficult to measure.

The elastic waves may be treated by a continuum mechanical analysis which relates their velocities along a given crystallographic direction to the adiabatic elastic moduli and density of the material via Christoffel's equation (Eq. 2).[19]

$$\left|C_{ijkl}q_jq_l - \rho V^2\delta_{ik}\right| = 0 \qquad (2)$$

C_{ijkl} is the elasticity tensor for the material, ρ is the density, and δ_{ik} is the Krönecker delta function. Since yttria has cubic symmetry, there are only three independent, nonzero components in its elasticity tensor, $C_{11}(=C_{22}=C_{33})$, $C_{12}(=C_{13}=C_{23})$, and $C_{44}(=C_{55}=C_{66})$ (in Voigt notation).[20]

II Experiment

A Samples

Samples for this study were taken from single-crystal fibers grown from high purity Y_2O_3 powder by a laser heated float zone (LHFZ) technique.[5,21] This containerless technique uses a scanned CO_2 laser beam (10.6 μm wavelength) that is split and focused at the tip of a polycrystalline source rod to produce a melt which is held between the source and product phases by surface tension. Temperature in the molten region was stabilized using infrared pyrometery, but absolute temperature was not determined because the emissivity of molten yttria is not known.

For preparation of the source rod, high purity (99.999% pure) polycrystalline yttria powder (Alpha Aesar) was used. Since the LHFZ technique is essentially a zone refining

process, the final purity of the yttria crystal is likely even higher. This powder was blended with 5 weight % binder (Methocel 20-231, The Dow Chemical Company, Midland, MI 48674) and glycerin was used as a plasticizer in a water based slurry. The slurry was then degassed overnight with a moderate vacuum (~70×10^3 Pa) to achieve a high viscosity paste. This paste was extruded with a custom-made mini-extruder, i.e. a modified hypodermic syringe. The plastic syringe wall was replaced within high wear regions to avoid contamination. At least two extrusions were made to minimize porosity in the paste. The extruded source rod was normally 250 μm in diameter and extruded lengths were 15 to 20 cm long. The rods were furnace dried in air at 200 °C for approximately 1 hour and placed in the LHFZ apparatus without any presintering.

At steady state, the source to fiber diameter ratio is inversely proportional to the square root of the feed rod to pull rod velocity ratio. The fibers used for the Brillouin work had nearly circular cross sections with average diameters slightly less than 500 μm. For fibers grown in this study, the molten zone height was kept constant at approximately one and half times the fiber diameter, and fibers were grown in air.

Octahedral cleavage was apparent in fragments broken from the fibers and showed that the fiber axis coincided closely with the <111> crystal direction. The material was clear except for occasional inclusions that appear to be bubbles. The samples were optically isotropic when examined under cross polarized light. An X-ray analysis was performed on a large fiber sample by four circle diffractometry, in order to verify the single-crystal nature and cubic symmetry of the samples. Precise values of the lattice parameter at all temperatures were calculated from the regression equation of Taylor (Eq. 3).[22]

$$a(T) = (1.06016\ \text{nm})\,(1 + 6.76\times10^{-6}\,T + 1.22\times10^{-9}\,T^2) \qquad (3)$$

where a(T) is the cell edge parameter at a temperature T (in °C). A value of 1.0603 nm (corresponding to 22°C) yielding a theoretical density of 5.033 g/cm^3 (which matches that reported by Tropf and Harris[1]) was used for all room temperature calculations.

Velocity measurements were performed on a single sample. It was ground into a flat plate with a thickness of ~150 μm.[23] Due to breakage during sample preparation, the usable area of the sample faces was around 250 μm x 250 μm. The ground faces corresponded closely to the {100} crystallographic plane. Orientation was accomplished by optical goniometery from cleavage planes, and measurements subsequent to grinding showed the face to be within ~2° of the {100} face.

B Brillouin Scattering

Illumination of the sample was provided by the 514.5 nm line of an Ar$^+$ laser at a power of 200 mW or less for the ambient temperature measurements. For high temperature runs, a laser power of up to 400 mW was used to maximize the Brillouin signal since sample heating was not a particular concern. Higher power was necessary for high temperature experiments because of the furnace windows which reduce the intensities of both the incident and scattered beams by partial reflection and introduction of astigmatism into the focusing and collecting optical paths. Scattered light was collected through a slot with an angular acceptance of approximately 5.5° in the scattering plane to lessen broadening of Brillouin peaks. The scattered light was analyzed by a 6-pass,

tandem, Fabry-Perot interferometer. The spectrometer has been described in detail elsewhere.[24,25]

Room temperature measurements were performed with a 90° scattering angle. An Eularian cradle was used to rotate the sample around its face normal to access different phonon directions. The high temperature results of this study were obtained using a compact furnace mounted on the Eularian cradle, allowing multiple phonon directions to be collected without remounting the sample. The construction and operation of this furnace is described elsewhere.[26] An 80° scattering angle was used for the high temperature work. Velocities calculated from the measured Brillouin shifts were used in a linearized inversion algorithm[27] to solve for the elastic moduli.

III Results and Discussion

Velocities measured at room temperature, in the plane ~(001) (outside the furnace), have a close correspondence to fits from the calculated elastic constants (solid curves Figure 2) This figure gives a sense of the anisotropy in yttria Longitudinal velocities vary by ~ 4% in this plane, while shear velocities vary by ~ 15%

The adiabatic elastic constants obtained are given in Table I along with those reported by Aleksandrov et al (also measured using Brillouin spectroscopy)[15,16] Errors in Table I include contributions due to residuals of the velocity fits as well as uncertainty in sample orientation.[23] There are substantial differences between Aleksandrov's values and those obtained here (C_{11} +1.5%, C_{44} −8%, C_{12} +20%). Table II lists the bulk modulus, K, and shear modulus, G, calculated from the room temperature constants using the Voigt, Reuss, and Voigt-Reuss-Hill averaging schemes (denoted by subscripts V, R, and VRH

respectively) for both this study and for Aleksandrov et al. For comparison, values of K and G (adiabatic) reported previously by several authors for polycrystalline yttria are included in Table II. The values reported by Manning[8] are a Spriggs extrapolation to zero porosity from samples with porosity ranging from 4-22 %, whereas those of Yeheskel[13] and Tropf[1] are uncorrected, and correspond to samples of greater than 99% theoretical density. This fact may account for the differences in bulk modulus.

The values of Aleksandrov et al.[15,16] for K and G_{VRH} are 11% higher and 14% lower, respectively, than those reported here. Clearly, the current measurements agree much more closely with polycrystalline measurements than those of Aleksandrov et al. No details of the quality or properties of the sample are reported in the previous single crystal study,[15] but these aspects may partially account for some of the discrepancies. Another possible explanation is a misorientation of the sample used in the previous study. The differences decrease in the order: $|\Delta C_{12}/C_{12}| > |\Delta C_{44}/C_{44}| > |\Delta C_{11}/C_{11}|$. Ingel and Lewis derived a similar relation of relative magnitudes of deviation for misorientation in Y_2O_3 stabilized ZrO_2 along certain directions.[28] Aleksandrov et al. calculated moduli based on the longitudinal and shear (degernerate) velocities along [100] for which the reported values are 6.75 ± 0.02 km/s and 3.71 ± 0.03 km/s, respectively, as well as both shear velocities along [0.5 0.5 1/√2] which are reported as 3.43 ± 0.02 km/s and 3.69 ± 0.01 km/s.[15] Similar velocities result from Eq. 2 using the elastic moduli determined in this study, if a rotation of ~ 13° around [010] is applied to the coordinates of Aleksandrov et al. (i.e. [100] becomes [0.9744 0 0.2250], and [0.5 0.5 1/√2] becomes [0.3281 0.5 0.8015]). The resulting longitudinal and shear velocities along [0.9744 0 0.2250] are 6.726 km/s and 3.745 km/s. (The other shear mode with a velocity of 3.849 km/s is

polarized along [010]. Since the incident and scattered beams were directed along [110] and [-110] (in the original coordinate system),[15] this wave is polarized in the scattering plane and would have zero scattered intensity.[29]) The shear velocities along [0.3281 0.5 0.8015] are 3.710 km/s and 3.454 km/s. Aleksandrov et al. report the accuracy of face orientation as 3 to 5°,[15] but this degree of misorientation cannot account for the differences with the current study.

The variation of the single-crystal elastic moduli with temperature is consistent with a linear trend as shown by Figure 3. Table III lists values for the adiabatic constants determined at elevated temperatures. Errors given again include contributions from residuals in the fit as well as uncertainty in sample orientation.[23] Higher order polynomial fits to these results are not warranted, given the uncertainties in the data. The temperature derivatives of the elastic moduli from the linear fits are listed in Table IV along with those for the bulk modulus and Voigt-Reuss-Hill shear modulus. Errors in the temperature derivatives are based on the 95% confidence intervals for the slope of the linear fit. An error of ±5% is given in temperature itself based on uncertainty in the gain of the amplifier used in measuring temperature. This may contribute to an absolute error in slope, but the internal temperature precision is much better (<3%).[23] Furthermore, the uncertainty in slope is dominated by errors in velocity, not in temperature.

Figures 4 and 5 show the temperature dependence of bulk and shear (Voïgt-Reuss-Hill) moduli respectively. Also shown are values measured by Dickson and Anderson using a resonance technique (resulting in adiabatic moduli) on a 0.91 Y_2O_3•0.09 ThO_2 polycrystalline sample.[14] There is a slight offset in bulk modulus, but the rate of softening with temperature is similar for both materials. Linear fits to the data of Dickson and

Anderson[14] yield slopes of -15.3 MPa/ °C and -8.5 MPa/ °C for bulk and shear modulus respectively. The offset in bulk modulus may be due to composition, but no estimate of possible errors is given by Dickson and Anderson[14] so the differences may be insignificant.

Figure 6 shows the Young's modulus for yttria calculated from Eq. 4,

$$E = \frac{9KG_{VRH}}{3K + G_{VRH}} \tag{4}$$

along with the data of Price and Hubbert,[30] Dickson and Anderson,[14] a linear fit to the data of Marlowe and Wilder up to 1000 °C,[2] and a fit suggested by Tropf and Harris[1] (based on data from Price and Hubbert[30]). The fit to the data of Marlowe and Wilder[2] yields a slope of -19.5 MPa/ °C. Tropf and Harris[1] infer a pronounced softening of Y_2O_3 at high temperature and a rapid non-linear decrease in elastic modulus at temperatures greater than 1200 °C. The present results do not support such a high order variation in elastic modulus, at least not within the temperature range of this study. The constants of Dickson and Anderson[14] and Marlowe and Wilder[2] are adiabatic while those of Price and Hubbert[30] are for constant temperature.

Elastic anisotropy for a cubic crystal may be characterized by the factor, A, computed using Eq. 5.

$$A = \frac{2C_{44} + C_{12}}{C_{11}} - 1 \tag{5}$$

The elastic constants measured here yield a value for A of 0.170 ± 0.015, while those of Aleksandrov et al. yield 0.212.[15,16] For comparison the values of A for MgO, BaO, and yttrium aluminum garnet ($Y_3Al_5O_{12}$, YAG) are 0.37, -0.07 and 0.02, respectively.[16]

The anisotropy does not vary significantly over the temperature range measured. There appears to be no systematic trend, and no variations in A within the error of the measurement. This contrasts with the behavior of several other oxides which show marked changes with temperature (Table V).

It is possible that this behavior simply results from a peculiarity of the interactions of Y and O, namely that they do not change substantially with temperature, but it is also possible that the constance of anisotropy with temperature is partially tied to the structure of yttria.

To a rough approximation, the elasticity of a crystal may be described by pair potentials between neighboring atoms and 3-body terms which give a potential energy based on the angle of two bonds attached to a central atom. For the halite structure, these may be related qualitatively to the macroscopic elasticity tensor. The halite structure consists of octahedra whose points are directed along the <100> crystallographic directions.[31] Therefore, tension or compression along <100> directions (C_{11}) corresponds to a change in length of the bonds which are all directed toward the points of the octahedra (i.e. <100> directions). Shear along the <100> directions (C_{44}), however, results in the bending of 3 atom groups. Therefore, to a first approximation, a change with temperature, of only the pair potentials between atoms would result in a change in C_{11} leaving C_{44} unaffected, and vice versa for a change in the 3-body term. Though oversimplified, this analysis suggests that the halite structure would show comparable

changes in its macroscopic moduli and its fundamental atomic interactions (i.e. the relative resistance to bond stretching/compression as compared to 3-body bending)

Yttria also has 6-fold coordinated cations. It's structure (bixbyite), however, is much more complex than that of halite, with 16 formula units per cell, and the coordination polyhedra in yttria are not regular octahedra.[31] They are substantially deformed, and the structure is sometimes described as having cubic coordination for Y^{3+} with O^{2-} ions at opposite corners of the cube missing, essentially a defect fluorite structure.[22,32] Regardless of the description of the structure, the Y-O bonds point in many crystallographic directions. Therefore, unlike compounds with the halite structure, uniaxial forces along any crystallographic direction will involve both stretching/compression of bonds and 3-body bending. Therefore, a change in relative resistance of one of these as compared to the other may produce a much smaller change in the macroscopic moduli and hence the anisotropy

This hypothesis is supported by the relatively low change in anisotropy with temperature for other crystals with a complex relationship between bond directions and the unit cell. This is seen for YAG in Table V, and applies to several other garnets such as almandine and pyrope.[16] Like yttria, garnets have a complex crystal structure with irregular coordination polyhedra. Spinel also follows this trend with a relatively low value of dA/dT.[16,33] Various III-V compounds with zinc-blende lattices, such as GaAs or GaSb, and elements with diamond cubic lattices, such as diamond and silicon, show very low changes in anisotropy with temperature as well.[16] These structures also experience a combination of bond stretching/compression and 3-body bending, for both uniaxial tension and pure shear along high symmetry directions.

IV. Conclusions

The single-crystal elastic moduli of yttria were measured using Brillouin spectroscopy at room temperature and high temperatures ranging to 1200°C. The room temperature values differed significantly from previous single-crystal measurements,[15,16] but bulk properties calculated from the present study agree much more closely with most literature values reported for polycrystalline yttria.[1,8,9,11,13] This is important since it suggests that the elasticity of polycrystalline yttria ceramics can be accounted for by the elasticity of the Y_2O_3 crystal lattice itself. No second phase or secondary effect is indicated here as may have been suggested by the previous results. Sample misorientation in the previous study is offered as a potential reason for the discrepancy.

All elastic moduli display a modest linear decrease over the temperature range studied. The variation of bulk and shear moduli with temperature correspond closely to those reported for a $91Y_2O_3 \cdot 9ThO_2$ compound.[14] Likewise, the change in Young's modulus with temperature agrees well with measurements on pure polycrystalline yttria.[2] Since accurate determinations of the temperature variation of properties for polycrystalline yttria ceramics have been made previously,[2,14] perhaps the more important addition of this study is the temperature dependence of elastic anisotropy, which was found to remain essentially constant for yttria as compared to significant changes for several other oxides with simpler cubic structures. A possible relation between the elastic anisotropy change with temperature and structure is proposed.

Acknowledgements

The work of J. W. Palko was supported by the Fannie and John Hertz Foundation graduate fellowship. X-ray work was performed by J. McMillan at the Center for Microanalysis of Materials at UIUC. Thanks to D.C. Harris for help in obtaining certain reference matter. This work was partially supported by a United States Air Force Office of Scientific Research AASERT Grant, under contract number F49620-97-1-0427 and NSF grant EAR-96-14416.

References

1 W. J. Tropf and D. C. Harris, Proc. SPIE **1112,** 9 (1989).

2 M. O. Marlowe and D. R. Wilder, J. Am. Ceram. Soc. **48,** 227 (1965).

3 R. L. Gentilman, Proc. SPIE **683,** 2 (1986).

4 W. H. Rhodes, G. C. Wei, and E. A. Trickett, Proc. SPIE **683,** 12 (1986).

5 A. Sayir, S. C. Farmer, P. O. Dikerson, and H. M. Yun, Mat. Res. Soc. Sym. Proc. **365,** 21 (1995).

6 E. K. Keler and A. B. Andreeva, Ogneupory, no.5, 224 (1963)[Refractories, no. 5, 243 (1963)]

7 W. R. Manning and J. Orville Hunter, J. Am. Ceram. Soc. **51,** 537 (1968).

8 W. R. Manning, J. O. Hunter, and J. B. R. Powell, J. Am. Ceram. Soc. **52,** 436 (1969)

9 K. K. Phani and S. K. Niyogi, J. Am. Ceram. Soc. **70,** C362 (1987)

10 G. C. Wei, C. Brecher, M. R. Pascucci, E. A. Trickett, and W. H. Rhodes, Proc. SPIE **929,** 50 (1988)

11 K. Shibata, H. Nakamura, and A. Fujii, Proc. SPIE **1326,** 48 (1990)

12 G. C. Wei, M. R. Pascucci, E. A. Trickett, S. Natansohn, and W. H. Rhodes, Proc. SPIE **1326,** 33 (1990).

13 O. Yeheskel and O. Tevet, J. Am. Ceram. Soc. **82,** 136 (1999).

14 R. W. Dickson and R. C. Anderson, J. Am. Ceram. Soc. **51,** 233 (1968).

15 V. I. Aleksandrov, V. F. Kitaeva, V. V. Osiko, N. N. Sobolev, V. M. Tatarintsev, and I. L. Chistyi, Sb. Kratk. Soobshch. Fiz. AN SSSR Fiz. Inst. P. N. Lebedeva, no. 4, 8 (1976)[Sov. Phys. Lebedev Inst. Rep., no. 4, 7 (1976)].

16 *Elastic, Piezoelectric, Pyroelectric, Piezooptic, Electrooptic Constants, and Nonlinear Dielectric Susceptibilites of Crystals*; *Vol. III 18*, edited by K.-H. Hellwege and O. Madelung (Springer-Verlag, Berlin, 1984).

17 G. B. Benedek and K. Fritsch, Phys. Rev. **149,** 647 (1966).

18 E. S. Zouboulis and M. Grimsditch, J. Appl. Phys. **70,** 772 (1991).

19 L. D. Landau and E. M. Lifshitz, *Theory of Elasticity* (Pergamon Press, London, 1959), p. 104

20 J. F. Nye, *Physical Properties of Crystals: Their Representation by Tensors and Matrices* (Clarendon Press, Oxford, 1985), p. 114.

21 A. Sayir and S. C. Farmer, Mat. Res. Soc. Sym. Proc. **365,** 11 (1995)

22 D. Taylor, Brit. Ceram. Trans. and J. **83,** 92 (1984)

23 J. Palko, M.S. Thesis, University of Illinois, Urbana-Champaign, 2000

24 J. D. Bass, J. Geophys. Res. **94,** 7621 (1989)

25 S. V. Sinogeikin, J. D. Bass, and T. Katsura, J. Geophys. Res. **103,** 20 (1998)

26 S. V. Sinogeikin, J. M. Jackson, B. O'Neill, J. W. Palko, and J. D. Bass, Rev. Sci. Instrum. **71,** 201 (2000).

27 D. J. Weidner and H. R. Carleton, J. Geophys. Res. **82,** 1334 (1977).

28 R. P. Ingel and D. Lewis, J. Am. Ceram. Soc. **71,** 261 (1988).

29 R. Vacher and L. Boyer, Phys. Rev. B **6,** 639 (1972).

30 M. W. Price and T. E. Hubbert, "Mechanical and Thermal Properties of Four IR Dome Materials," Southern Research Institute Report No. SRI-EAS-87-1272-6225, 1988 (unpublished see ref. 1).

31 R. W. G. Wyckoff, *Crystal Structures*, Vol. 2, 2 ed. (John Wiley & Sons, New York, 1963), p. 2.

32 M. G. Paton and E. N. Maslen, Acta Crystallogr. **19,** 307 (1965).

33 V. Askarpour, M. H. Manghnani, S. Fassbender, and A. Yoneda, Phys. Chem. Miner. **19,** 511 (1993).

Table I: Room temperature elastic constants of yttria

Modulus	This study	Aleksandrov, et al.[15,16]
C_{11} (GPa)	223.6 ± 0.6	227
C_{44} (GPa)	74.6 ± 0.5	68.6
C_{12} (GPa)	112.4 ± 1.0	138

Table II: Measured and calculated bulk properties of yttria at room conditions

K (GPa)	G_V (GPa)	G_R (GPa)	G_{VRH} (GPa)	$G_{Polycrystal}$ (GPa)	Ref.
149.5 ± 1.0	67.0 ± 0.8	65.6 ± 0.8	66.3 ± 0.8		This Study
167.7	59.0	56.4	57.7		15,16
148.9 ± 3.0				69.2 ± 2.0	13
145				67	1
146.2				69.42	8

Table III: Measured elastic constants for yttria at elevated temperatures

T (°C)	C_{11} (GPa)	C_{44} (GPa)	C_{12} (GPa)	K (GPa)	G_{VRH} (GPa)
22[a]	225.1	74.6	113.6	150.8	66.4
22[b]	222.4	73.7	110.8	148.0	66.0
200	221.1	73.4	110.6	147.5	65.5
400	216.9	72.8	108.0	144.3	64.8
600	212.2	70.4	106.7	141.8	62.7
800[a]	206.2	69.0	102.5	137.1	61.5
800[b]	205.3	67.3	103.2	137.2	60.3
1000	199.1	65.3	99.5	132.7	58.6
1200	193.6	63.7	97.9	129.8	56.8

[a] Experimental run to 800°C. Errors for this run are ±0.7% for C_{11}, ±3.3% for C_{44}, and ±1.9% for C_{12}.

[b] Experimental run from 800°C to 1200°C. Errors for this run are ±0.9% for C_{11}, ±3.4% for C_{44}, and ±3.5% for C_{12}.

Table IV: Fitted temperature derivatives for single-crystal and bulk elastic properties of yttria

Modulus	Temperature Derivative (MPa/ °C)
C_{11}	-26 ± 3
C_{44}	-9 ± 2
C_{12}	-13 ± 2
K	-17 ± 2
G_{VRH}	-8 ± 2

Table V: Comparison of changes in elasticity and anisotropy with temperature for several oxides

All temperature derivatives in (10^{-4}/K)	Y_2O_3 pres. study	MgO [16]	BaO [16]	$Y_3Al_5O_{12}$ (YAG) [16]
$(dC_{11}/dT)/C_{11}$	-1.14 ± 0.13	-2.0	-3.7	-0.9
$(dC_{44}/dT)/C_{44}$	-1.21 ± 0.24	-0.8	-1.16	-0.7
$(dC_{12}/dT)/C_{12}$	-1.11 ± 0.18	0.7	0	-0.52
A	0.170 ± 0.015	0.37	-0.07	0.02
dA/dT	0 ± 0.1	2.1	2.8	0.3

Figure 1: Schematic of symmetric platelet scattering geometry

Figure 2: Room temperature velocities in the {100} plane of yttria.

Figure 3: Single-crystal elastic moduli at high temperature

Figure 4: Variation of the bulk modulus of yttria with temperature

Figure 5: Variation of the shear modulus of yttria with temperature

Figure 6: Variation of the Young's modulus of yttria with temperature.

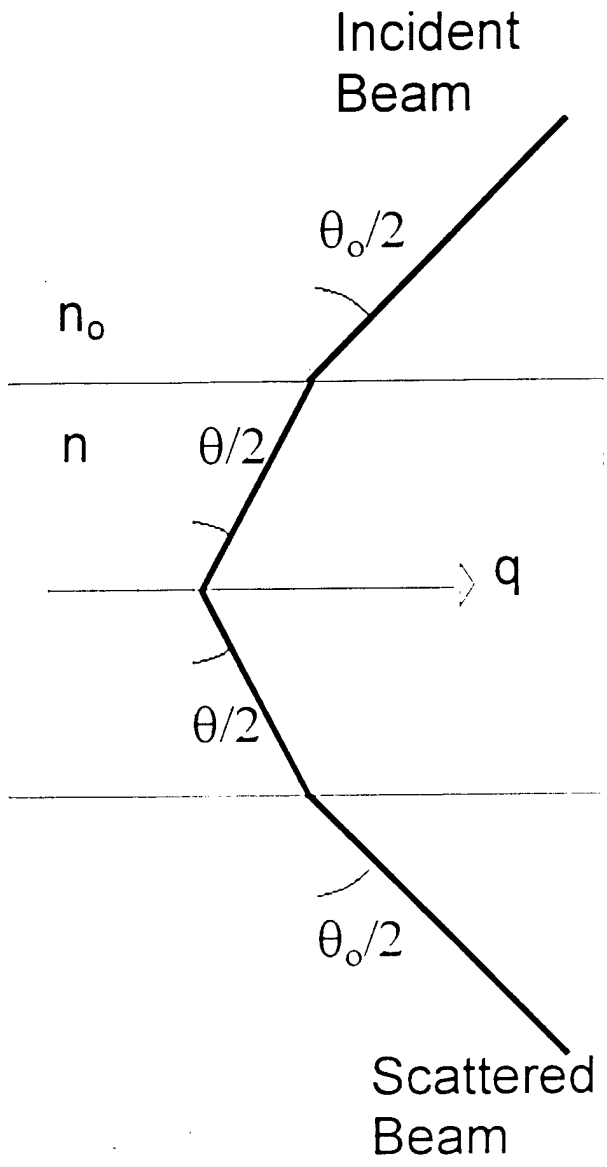


Figure 1 Palko, Kriven, Sinogeikin, Bass, Sayir (2000)

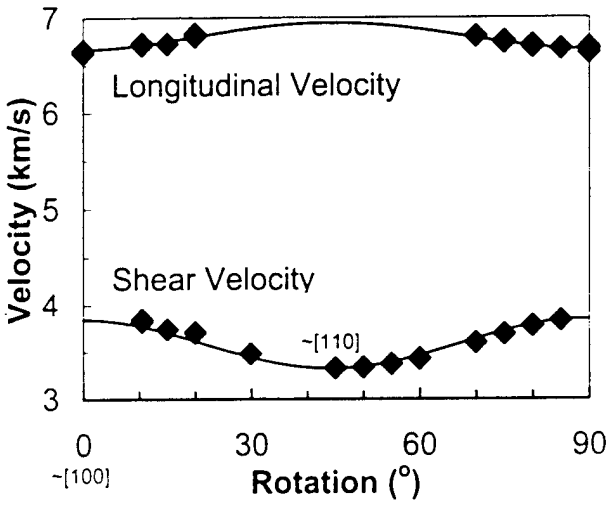


Figure 2 Palko, Kriven, Sinogeikin, Bass, Sayir (2000)

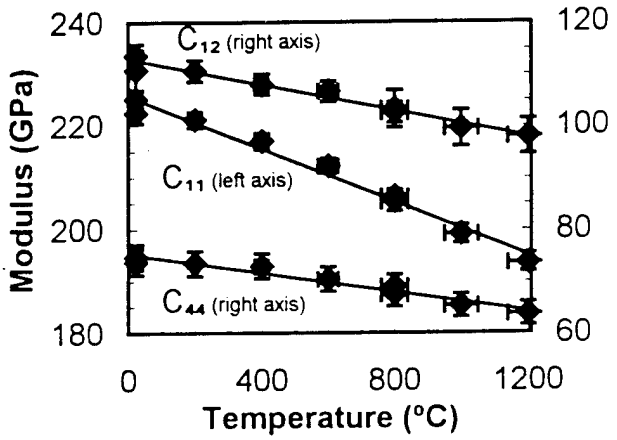


Figure 3 Palko, Kriven, Sinogeikin, Bass, Sayir (2000)

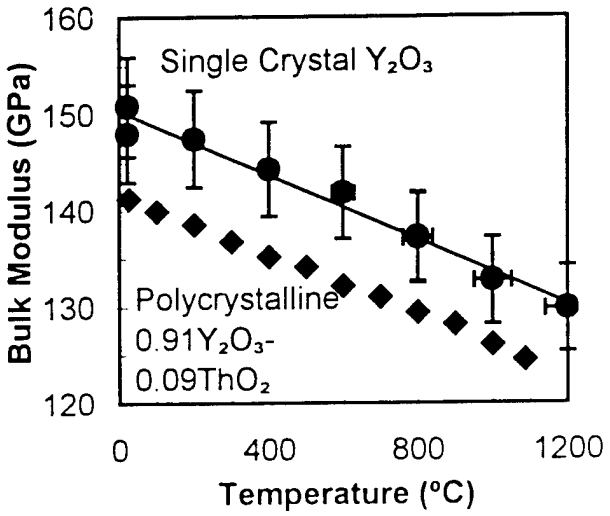


Figure 4 Palko, Kriven, Sinogeikin, Bass, Sayir (2000)

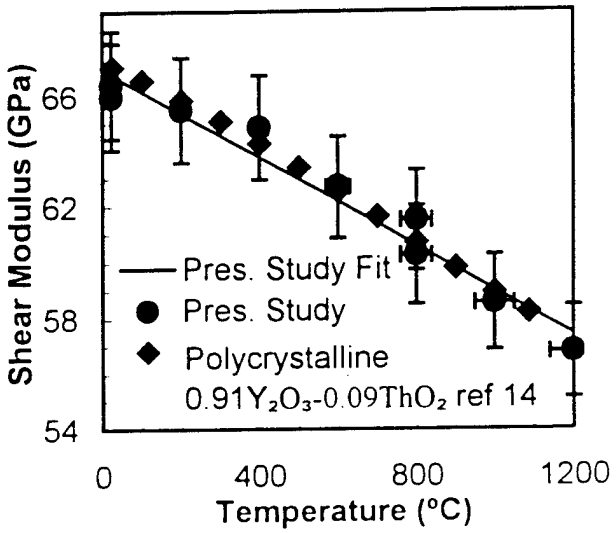


Figure 5 Palko, Kriven, Sinogeikin, Bass, Sayir (2000)

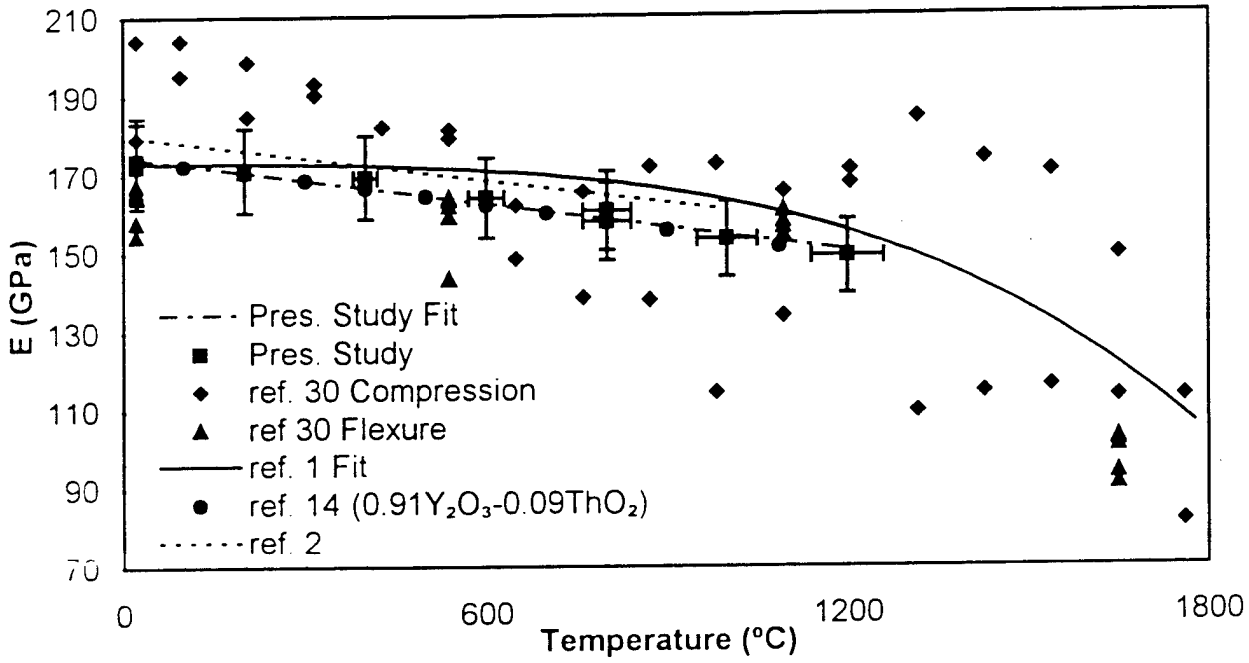


Figure 6 Palko, Kriven, Sinogeikin, Bass, Sayir (2000)

Extended Table I: Room temperature velocities for yttria

Sample Face Normal			Propagation Direction			Vl (m/s)	Vs (m/s)
0.0228	0.0007	0.9997	0.0758	0.9971	-0.0024	6671.0	3834.2
0.0228	0.0007	0.9997	0.1624	0.9867	-0.0044	6688.4	3772.8
0.0228	0.0007	0.9997	0.1624	0.9867	-0.0044	6712.7	3779.8
0.0228	0.0007	0.9997	0.2478	0.9688	-0.0063	6750.8	3689.5
0.0228	0.0007	0.9997	0.2478	0.9688	-0.0063	6735.8	3690.7
0.0228	0.0007	0.9997	0.3313	0.9435	-0.0082	6802.9	3599.3
0.0228	0.0007	0.9997	0.9355	0.3526	-0.0216	6830.0	3711.4
0.0228	0.0007	0.9997	0.9355	0.3526	-0.0216	6802.3	3703.3
0.0228	0.0007	0.9997	0.9627	0.2697	-0.0221	6724.2	3742.8
0.0228	0.0007	0.9997	0.9809	0.1933	-0.0225	6712.0	3823.7
0.0228	0.0007	0.9997	0.9809	0.1933	-0.0225	6728.2	3848.0
0.0228	0.0007	0.9997	0.4900	0.8716	-0.0118		3430.4
0.0228	0.0007	0.9997	0.4900	0.8716	-0.0118		3425.8
0.0228	0.0007	0.9997	0.5641	0.8256	-0.0134		3371.4
0.0228	0.0007	0.9997	0.6339	0.7733	-0.0150		3335.5
0.0228	0.0007	0.9997	0.6989	0.7151	-0.0164		3327.4
0.0228	0.0007	0.9997	0.8610	0.5083	-0.0200		3480.1
0.0228	0.0007	0.9997	0.9997	0.0113	-0.0228	6629.4	
0.0228	0.0007	0.9997	0.9997	0.0113	-0.0228	6658.3	
0.0228	0.0007	0.9997	-0.0113	0.9999	-0.0004	6686.1	

Extended Table I (Continued)

Sample Face Normal			Propagation Direction			Vl (m/s)	Vs (m/s)
0.0228	0.0007	0.9997	-0.0113	0.9999	-0.0004	6665.2	
0.0228	0.0007	0.9997	-0.0113	0.9999	-0.0004	6629.4	

Extended Table II Velocities used in calculation of constants for yttria to 800 degrees Celsius

Sample Face Normal			Propagation Direction			Vl (m/s)	Vs (m/s)
Room temperature (~20 degrees Celsius)							
0.0228	0.0007	0.9997	0.0053	1.0000	-0.0008	6678.5	0.0
0.0228	0.0007	0.9997	0.0053	1.0000	-0.0008	6679.6	0.0
0.0228	0.0007	0.9997	0.1788	0.9839	-0.0047	6722.2	3792.3
0.0228	0.0007	0.9997	0.1788	0.9839	-0.0047	6730.1	3783.3
0.0228	0.0007	0.9997	0.3469	0.9379	-0.0085	6835.5	3619.6
0.0228	0.0007	0.9997	0.3469	0.9379	-0.0085	6806.3	3615.1
0.0228	0.0007	0.9997	0.4430	0.8965	-0.0107	0.0	3495.1
0.0228	0.0007	0.9997	0.5044	0.8634	-0.0121	0.0	3442.4
0.0228	0.0007	0.9997	0.5044	0.8634	-0.0121	0.0	3435.7
0.0228	0.0007	0.9997	0.5320	0.8466	-0.0127	0.0	3417.7
0.0228	0.0007	0.9997	0.5919	0.8059	-0.0140	0.0	3370.7
0.0228	0.0007	0.9997	0.6598	0.7512	-0.0155	0.0	3344.9
0.0228	0.0007	0.9997	0.6982	0.7157	-0.0164	0.0	3335.9
0.0228	0.0007	0.9997	0.7106	0.7034	-0.0167	0.0	3338.1
0.0228	0.0007	0.9997	0.7106	0.7034	-0.0167	0.0	3341.5
0.0228	0.0007	0.9997	0.7228	0.6909	-0.0169	0.0	3331.4
0.0228	0.0007	0.9997	0.7802	0.6252	-0.0182	0.0	3350.5
0.0228	0.0007	0.9997	0.8317	0.5548	-0.0193	0.0	3399.8

Extended Table II (Continued)

Sample Face Normal			Propagation Direction			Vl (m/s)	Vs (m/s)
Temperature = 200 degrees Celsius							
0.0228	0.0007	0.9997	0.0053	1.0000	-0.0008	6631.4	0.0
0.0228	0.0007	0.9997	0.0053	1.0000	-0.0008	6628.0	0.0
0.0228	0.0007	0.9997	0.1788	0.9839	-0.0047	6692.0	3754.1
0.0228	0.0007	0.9997	0.1788	0.9839	-0.0047	6695.3	3759.7
0.0228	0.0007	0.9997	0.3469	0.9379	-0.0085	6753.6	3614.0
0.0228	0.0007	0.9997	0.3469	0.9379	-0.0085	6760.4	3611.7
0.0228	0.0007	0.9997	0.5044	0.8634	-0.0121	0.0	3431.2
0.0228	0.0007	0.9997	0.5044	0.8634	-0.0121	0.0	3436.8
0.0228	0.0007	0.9997	0.7106	0.7034	-0.0167	0.0	3319.1
0.0228	0.0007	0.9997	0.7106	0.7034	-0.0167	0.0	3319.1
Temperature = 400 degrees Celsius							
0.0228	0.0007	0.9997	0.0053	1.0000	-0.0008	6594.4	0.0
0.0228	0.0007	0.9997	0.0053	1.0000	-0.0008	6591.0	0.0
0.0228	0.0007	0.9997	0.1788	0.9839	-0.0047	6634.8	3754.1
0.0228	0.0007	0.9997	0.1788	0.9839	-0.0047	6640.4	3760.9
0.0228	0.0007	0.9997	0.3469	0.9379	-0.0085	6720.0	3590.4
0.0228	0.0007	0.9997	0.3469	0.9379	-0.0085	6699.8	3591.5
0.0228	0.0007	0.9997	0.5044	0.8634	-0.0121	0.0	3430.1
0.0228	0.0007	0.9997	0.5044	0.8634	-0.0121	0.0	3426.7

Extended Table II (Continued)

Sample Face Normal			Propagation Direction			Vl (m/s)	Vs (m/s)
Temperature = 400 degrees Celsius							
0.0228	0.0007	0.9997	0.7106	0.7034	-0.0167	0.0	3302.3
0.0228	0.0007	0.9997	0.7106	0.7034	-0.0167	0.0	3301.1
Temperature = 600 degrees Celsius							
0.0228	0.0007	0.9997	0.0053	1.0000	-0.0008	6526.0	0.0
0.0228	0.0007	0.9997	0.0053	1.0000	-0.0008	6526.0	0.0
0.0228	0.0007	0.9997	0.1788	0.9839	-0.0047	6581.0	3695.8
0.0228	0.0007	0.9997	0.1788	0.9839	-0.0047	6579.8	3702.6
0.0228	0.0007	0.9997	0.3469	0.9379	-0.0085	6658.3	3540.0
0.0228	0.0007	0.9997	0.3469	0.9379	-0.0085	6656.1	3553.4
0.0228	0.0007	0.9997	0.5044	0.8634	-0.0121	0.0	3365.0
0.0228	0.0007	0.9997	0.5044	0.8634	-0.0121	0.0	3368.4
0.0228	0.0007	0.9997	0.7106	0.7034	-0.0167	0.0	3273.1
0.0228	0.0007	0.9997	0.7106	0.7034	-0.0167	0.0	3260.8
Temperature = 800 degrees Celsius							
0.0228	0.0007	0.9997	0.0053	1.0000	-0.0008	6456.5	0.0
0.0228	0.0007	0.9997	0.0053	1.0000	-0.0008	6457.6	0.0
0.0228	0.0007	0.9997	0.1788	0.9839	-0.0047	6494.6	3682.4
0.0228	0.0007	0.9997	0.1788	0.9839	-0.0047	6495.7	3661.1
0.0228	0.0007	0.9997	0.3469	0.9379	-0.0085	6586.6	3524.3

Extended Table II (Continued)

Sample Face Normal			Propagation Direction			Vl (m/s)	Vs (m/s)
Temperature = 800 degrees Celsius							
0.0228	0.0007	0.9997	0.3469	0.9379	-0.0085	6575.3	3510.8
0.0228	0.0007	0.9997	0.5044	0.8634	-0.0121	0.0	3358.3
0.0228	0.0007	0.9997	0.5044	0.8634	-0.0121	0.0	3358.3
0.0228	0.0007	0.9997	0.7106	0.7034	-0.0167	0.0	3238.3
0.0228	0.0007	0.9997	0.7106	0.7034	-0.0167	0.0	3238.3

Extended Table III. Velocities used in calculation of constants for yttria to 1200 degrees Celsius

Sample Face Normal			Propagation Direction			Vl (m/s)	Vs (m/s)
Room temperature (~20 degrees Celsius)							
0.0228	0.0007	0.9997	-0.3506	0.9365	0.0074	0.0	3598.6
0.0228	0.0007	0.9997	-0.0092	1.0000	-0.0005	6640.5	0.0
0.0228	0.0007	0.9997	-0.0092	1.0000	-0.0005	6655.0	0.0
0.0228	0.0007	0.9997	0.1645	0.9864	-0.0044	6648.3	3811.4
0.0228	0.0007	0.9997	0.1645	0.9864	-0.0044	6673.0	3815.8
0.0228	0.0007	0.9997	0.3332	0.9428	-0.0082	6776.0	3653.4
0.0228	0.0007	0.9997	0.3332	0.9428	-0.0082	6781.6	3641.1
0.0228	0.0007	0.9997	0.4141	0.9102	-0.0101	0.0	3537.0
0.0228	0.0007	0.9997	0.4919	0.8706	-0.0118	0.0	3431.7
0.0228	0.0007	0.9997	0.4919	0.8706	-0.0118	0.0	3470.9
0.0228	0.0007	0.9997	0.4919	0.8706	-0.0118	0.0	3465.3
0.0228	0.0007	0.9997	0.5658	0.8244	-0.0135	0.0	3381.3
0.0228	0.0007	0.9997	0.6355	0.7719	-0.0150	0.0	3360.0
0.0228	0.0007	0.9997	0.7004	0.7136	-0.0164	0.0	3323.0
0.0228	0.0007	0.9997	0.7004	0.7136	-0.0164	0.0	3332.0
0.0228	0.0007	0.9997	0.7599	0.6498	-0.0178	0.0	3329.8
0.0228	0.0007	0.9997	0.8136	0.5811	-0.0189	0.0	3382.4
0.0228	0.0007	0.9997	0.8611	0.5080	-0.0200	0.0	3470.9

Extended Table III (Continued)

Sample Face Normal			Propagation Direction			Vl (m/s)	Vs (m/s)
Temperature = 800 degrees Celsius							
0.0228	0.0007	0.9997	-0.0092	1.0000	-0.0005	6449.0	0.0
0.0228	0.0007	0.9997	-0.0092	1.0000	-0.0005	6434.4	0.0
0.0228	0.0007	0.9997	0.1645	0.9864	-0.0044	6455.7	3660.2
0.0228	0.0007	0.9997	0.1645	0.9864	-0.0044	6473.6	3675.8
0.0228	0.0007	0.9997	0.3332	0.9428	-0.0082	6580.0	3493.3
0.0228	0.0007	0.9997	0.3332	0.9428	-0.0082	6547.5	3485.4
0.0228	0.0007	0.9997	0.4919	0.8706	-0.0118	0.0	3334.2
0.0228	0.0007	0.9997	0.4919	0.8706	-0.0118	0.0	3344.3
0.0228	0.0007	0.9997	0.7004	0.7136	-0.0164	0.0	3215.5
0.0228	0.0007	0.9997	0.7004	0.7136	-0.0164	0.0	3218.9
Temperature = 1000 degrees Celsius							
0.0228	0.0007	0.9997	0.0092	1.0000	-0.0005	6372.8	0.0
0.0228	0.0007	0.9997	-0.0092	1.0000	-0.0005	6356.0	0.0
0.0228	0.0007	0.9997	0.1645	0.9864	-0.0044	6399.7	3631.0
0.0228	0.0007	0.9997	0.1645	0.9864	-0.0044	6389.6	3615.4
0.0228	0.0007	0.9997	0.3332	0.9428	-0.0082	6473.6	3457.4
0.0228	0.0007	0.9997	0.3332	0.9428	-0.0082	6452.3	3459.7
0.0228	0.0007	0.9997	0.4919	0.8706	-0.0118	0.0	3292.8
0.0228	0.0007	0.9997	0.4919	0.8706	-0.0118	0.0	3287.2

Extended Table III (Continued)

Sample Face Normal			Propagation Direction			Vl (m/s)	Vs (m/s)
Temperature = 1000 degrees Celsius							
0.0228	0.0007	0.9997	0.7004	0.7136	-0.0164	0.0	3194.2
0.0228	0.0007	0.9997	0.7004	0.7136	-0.0164	0.0	3185.3
Temperature = 1200 degrees Celsius							
0.0228	0.0007	0.9997	-0.0092	1.0000	-0.0005	6311.2	0.0
0.0228	0.0007	0.9997	-0.0092	1.0000	-0.0005	6259.7	0.0
0.0228	0.0007	0.9997	0.1645	0.9864	-0.0044	6315.7	3563.8
0.0228	0.0007	0.9997	0.1645	0.9864	-0.0044	6328.0	3560.5
0.0228	0.0007	0.9997	0.3332	0.9428	-0.0082	6424.3	3404.8
0.0228	0.0007	0.9997	0.3332	0.9428	-0.0082	6394.1	3414.9
0.0228	0.0007	0.9997	0.4919	0.8706	-0.0118	0.0	3233.4
0.0228	0.0007	0.9997	0.4919	0.8706	-0.0118	0.0	3244.6
0.0228	0.0007	0.9997	0.7004	0.7136	-0.0164	0.0	3138.2
0.0228	0.0007	0.9997	0.7004	0.7136	-0.0164	0.0	3148.3

Journal of the European Ceramic Society 19 (1999) 2529–2541
© 1999 Elsevier Science Ltd
Printed in Great Britain. All rights reserved
PII: S0955-2219(99)00124-7
0955-2219/99/$ - see front matter

High Temperature Single Crystal Properties of Mullite

W. M. Kriven,[a]* J. W. Palko,[a] S. Sinogeikin,[b] J. D. Bass,[b] A. Sayir,[c] G. Brunauer,[d] H. Boysen,[d] F. Frey[d] and J. Schneider[d]

[a]Department of Materials Science and Engineering, University of Illinois at Urbana-Champaign, Urbana, IL, USA
[b]Department of Geology, University of Illinois at Urbana-Champaign, Urbana, IL, USA
[c]NASA Glenn Research Center, Cleveland, OH, USA
[d]Institut für Kristallographie und Angewandte Mineralogie, Ludwig Maximilians Universität, München, Germany

Abstract

Extensive neutron diffraction and Rietveld studies of dense, hot pressed mullite ($3Al_2O_3{\cdot}2SiO_2$) have been conducted up to 1650 °C in air, yielding a complete set of lattice parameters and axial thermal expansion coefficients. Unconstrained powders of the same stoichiometric composition were also analyzed by X-ray diffraction and Rietveld techniques up to 900 °C in air, from which lattice parameters and thermal expansion coefficients were obtained. An earlier reported structural discontinuity was confirmed by XRD to lie in the temperature range 425 to 450 °C. Single-crystalline mullite fibers of composition $2{\cdot}5Al_2O_3{\cdot}SiO_2$ were grown from the melt by a laser-heated, float zone method. A partial set of the single-crystal elastic moduli were determined from various sections of fiber, by Brillouin spectroscopy, from room temperature up to 1400 °C. They indicated a roughly 10% reduction in stiffness over that temperature range. © *1999 Elsevier Science Ltd. All rights reserved.*

Keywords: elastic modulus, fibers, X-ray methods, thermal expansion, mullite.

1 Introduction

In the design of oxidation resistant, high temperature ceramic composites, it is wise to know the intrinsic properties of the component materials, independent of their structural configuration in the composite. Detailed theoretical predictions of composite behavior, particularly at elevated temperatures, would rely heavily on a knowledge of single crystal properties. Furthermore, since the fabrication and mechanical evaluation of composites is a difficult, time consuming and costly procedure, any data on the intrinsic properties of a component material is extremely valuable in accelerating the design, modelling and development of high temperature composites.

Mullite, of nominal composition ($3Al_2O_3{\cdot}2SiO_2$), is a highly attractive candidate for oxide composites.[1] As a matrix it is a widespread 'workhorse' refractory material, having very good creep resistance and chemical stability up to 1600 °C. The current, widely accepted phase diagram indicates that the equilibrium phase grown by solid state reaction has a narrow solid solution range around the $3Al_2O_3{\cdot}2SiO_2$ (abbreviated 3:2) composition.[2] However, when grown from the melt, mullite crystallizes in $2Al_2O_3{\cdot}SiO_2$ or 2:1 composition.[2] The solid solution range can further be extended to $3Al_2O_3{\cdot}SiO_2$ or 3:1 composition by rapid cooling in a closed container, in the absence of alumina nuclei.[2,3]

Currently, steady progress is being made in the production of mullite fibers. Directionally solidified mullite fibers can be grown by a laser heated, float-zone method.[4] They appear to consist of columns of single crystals with [c] axes parallel to the fiber direction. Polycrystalline mullite–alumina fibers (Nextel 720, from 3M Company, St. Paul, MN) have also been fabricated by a sol–gel process from an 85 wt Al_2O_3–15 wt. SiO_2 composition, which subsequently converts on firing at 1350 °C to 59 vol% mullite and 41 vol% Al_2O_3.[5] The microstructure is extremely fine grained with ~0·5 μm mullite grains containing < 100 nm largely intragranular alumina grains. This microstructure is unstable above 1300 °C however, due to grain growth and drastic loss of mechanical strength from an initial 2·4 MPa.[6,7] More recently, homogeneous, aluminosilicate, glass fibers (of mullite composition) and amorphous yttrium aluminate fibers (of $Y_3Al_5O_{12}$ or 'YAG' composition) have been pulled from deeply undercooled melts via a

*To whom correspondence should be addressed. Fax: +1-217-333-2736.

containerless processing technique.[8,9] The high tensile strengths of the aluminosilicate glass fibers (~6 GPa) however, are again drastically reduced to 1 GPa at best, due to uncontrolled random crystallization to mullite or YAG, on annealing above 1100 °C. Work is therefore in progress to develop textured or single crystal fibers from the amorphous solid precursors.

1.1 Crystallographic measurements

Measurements of the thermal expansion of various mullite compositions are mainly reported for temperatures up to 900 °C and are either based on dilatometric measurements or on X-ray diffraction.[10-14] For higher temperatures reliable data are rare.[13] It has to be kept in mind that the former, i.e. the dilatometric method provides results which are always of both structural and microstructural origin and therefore, an average, which is hard to interpret on an atomic length scale. X-ray diffraction allows, at least in principle, a separation of both aspects via an evaluation of the positions of the reflections in a diffraction pattern and by a line profile analysis. The X-ray method has its limits if the sample material is coarse grained, which is sometimes unavoidable, and because of absorption effects. In particular in the high temperature regime around and above 1000 °C, the X-ray diffraction method becomes additionally tedious for experimental reasons.

An alternative diffraction method uses neutrons. In the case of mullite neutron diffraction, results are not affected by absorption and the relatively large sample volume allows for good statistics, even in the case of coarse grained samples. Moreover, the oxygens have a relatively high scattering power for neutrons so that oxygen related structural details can be studied in oxide compounds more reliably. We performed in-situ neutron diffraction experiments with the 3:2 mullite described above up to a temperature of 1650 °C. The overall aim of the investigation was a full structure refinement of mullite at high temperatures. Only the thermal expansion results of neutron diffraction measurements will be given here, since full information will be published in a forthcoming paper.[15]

1.2 Elastic constant measurements

1.2.1 Bulk properties

The bulk elastic properties of mullite have been measured on sintered compacts of relatively pure, raw materials.[16,17] More recent work on hot pressed stoichiometric 3:2 mullite, which was hydrothermally grown without any glassy phase, indicated an unusual decrease in Poisson's ratio with increasing temperature up to room temperature.[18] This was attributed to the incommensurate modulation in the mullite crystal structure. Early high temperature measurements[16] of relatively pure raw materials indicate a drop in elastic modulus for both 3:2 and 2:1 mullite above 600 °C, strongly suggesting the presence of intergranular glass. With the availability of highly textured, polycrystalline fibers,[4] it was decided to measure the elastic moduli of mullite up to temperatures of 1400 °C.

1.2.2 Single crystal properties

The complete elasticity tensor can be measured by the Brillouin light scattering technique.[19] This technique presents several advantages over other methods, the most important being that only very small samples are required, no contact is needed with the sample, and it is suitable for low-symmetry crystals. The sample size is limited only by the spot size of the laser used as the excitation source, making Brillouin scattering well-suited for measurements on the thin mullite fibers used in this study. Also, only optical access to the sample is required for Brillouin measurements, which allows much flexibility in furnace design.

Brillouin scattering involves the inelastic scattering of light from phonons in a crystal. If V is the velocity of the phonon, ϕ and ϕ' are the incident and scattered angles, respectively, and ν and ν' are the frequencies of the incident and scattered photons, respectively, then the equation relating phonon velocity to the frequency shift of the scattered photon, $\Delta\nu = \nu' - \nu$, is

$$V = \left(\frac{\Delta\nu}{\nu}\right)\left(\frac{c}{2n\sin\phi}\right) \tag{1}$$

for the case of symmetric scattering where ϕ and ϕ' are very nearly equal. c is the speed of light in vacuum and n is the refractive index for the direction of photon propagation. In this experiment we use a 'platelet geometry',[20] which allows $n\sin\phi$ to be replaced by $n_o\sin\theta_o$, where n_o is the index of the surrounding medium, and θ_o the incidence angle of the laser light. Platelet geometry allows access to all phonon directions in the plane of the sample.

The velocities of acoustic phonons are determined entirely by the elastic moduli and density of the material. The velocity in eqn (1) for plane monochromatic waves must satisfy Christoffel's equation [eqn (2)].[21]

$$\left|C_{iklm}q_iq_m - \rho V^2\delta_{kl}\right| = 0 \tag{2}$$

where q_i and q_m are unit vectors in the phonon propagation direction, ρ is the density, and C_{ijkl} is the elastic tensor.

1.3 Objective

In anticipation of the successful growth of single crystal or aligned textured fibers of mullite, the work described here was undertaken. The goal of a mullite matrix reinforced with mullite fibers coated by a suitable debonding oxide interphase would be well served by a precise knowledge of crystallographic lattice parameters as a function of temperature up to 1600 °C, as well as axial and volumetric thermal expansion coefficients. These data would enable the residual stresses arising during high temperature cycling to be estimated. Since dense mullite composites could be used as shingles to line an aircraft combustion chamber, for example, (Ref. 22 and H. Schneider, German Aerospace Center, pers. comm.) the thermal expansion of dense, hot pressed, polycrystalline mullite samples were measured, rather than of loose powders, as is customary in crystallographic measurements by X-ray or neutron diffraction. In addition, 3:2 mullite powder would be studied by X-ray diffraction up to 900 °C, and the data would be analyzed by Rietveld methods.

To complement the crystallographic data, and enable better modelling of the high temperature behavior of a mullite-containing composite, single crystal elastic moduli for orthorhombic mullite would be determined experimentally. Brillouin spectroscopic measurements would be made both at room temperature, and up to 1400 °C. Information gathered from this work would then indicate the feasibility and limits of using mullite fiber-reinforced composites in a load-bearing structural application, at high temperature in an oxidizing environment.

2 Experimental Procedures

2.1 Sample fabrication

For diffraction studies, hydrothermally grown, stoichiometric 3:2 mullite powder (Kyoritsu Ceramic Materials Co. Ltd., Tsukisan-cho 2-41, Minato-ku, Nagoya 455-91, Japan) was used as a starting material. For X-ray diffractometry, the powder of average particle size 0·3 μm was inserted into 0·3 mm diameter quartz capillaries which were kept in rotation during the measurements at all temperatures to reduce preferred orientation effects. For neutron diffraction, a polycrystalline mullite ceramic specimen was prepared by hot pressing to full density under vacuum, at 1600 °C and 34 MPa for 1 h, in a 3 inch bore graphite die with graphite spacers and plungers.[18,23]

For elastic constant measurements, mullite fibers of ~500 μm diameter were grown from starting compositions close to the 3:2 composition from high purity CERAC® pure (99·99% pure, 325 mesh) polycrystalline alumina powder (Ceralox Corp., Tucson, AZ 08576) and 99·99% pure SiO_2 from Alpha Products. The extruded mixture was made into a feeder rod in a laser heated, floating zone apparatus which was a fully automated, computer-controlled fiber processing facility at the NASA Glenn Research Center. The fiber pulling technique is fully described elsewhere.[4]

2.2 X-ray diffractometry

The X-ray powder diffraction experiments were performed on a focussing STOE-STADIP diffractometer equipped with a curved Ge(111) monochromator to produce strictly monochromatic MoKα_1 radiation. Data were collected using an overlapping stepscan mode of a linear position sensitive detector of about 5° acceptance angle and 0·02° channel width yielding 1500 data points in the 2θ-range from 5·5 to 35·5°. Each scan was repeated four times to monitor the stability of the intensity and the scans were then added together for better averaging. The resulting minimum half-width was 0·09° in 2θ. For measurements at elevated temperatures the computer controlled STOE furnace 0·65·1 was employed. The heating element consists of a current heated graphite tube holding the sample capillary vertically to the scattering plane. Bores in the graphite tube permitted unobstructed pathways for both the primary beam as well as for the scattered radiation. The temperature measured by a thermocouple in the graphite tube was kept constant to within 0·2°.

2.3 Neutron diffraction

The experiments were carried out at the powder diffractometer MANI at the FRM reactor facility in Munich and at the instrument D2B of the HFR ILL in Grenoble. The diffraction patterns were recorded with a wavelength of 0·1594 nm. A mirror furnace was used which operated at ambient conditions in air. The neutron mirror furnace is based on light focussed by two rotational ellipsoids.[24] Two different experiments were carried out. The first one started with a $0{\cdot}8\times1\times1\ cm^3$ sample cut from freshly hot pressed material which had a dark color. Due to a malfunction of the temperature control system at about 1100 °C, the heating procedure was interrupted. After the break, the heating sequence was continued up to 1650 °C. As a by-product we observed a colour change of the sample from dark to white. In the second experiment the 'same' (white, i.e. non-pristine) sample was used. Here an uninterrupted heating (room temperature to 1650 °C) and cooling cycle down to 650 °C was employed.

2.4 Elastic constants measurements

Three platelet-shaped samples were cut from a single mullite fiber produced by the laser-heated float zone method.[4] The platelets were ground nominally parallel to (010), (100), and (001) planes. The former two were oriented lengthwise with respect to the fiber, whereas the later was a cross section.

An Ar^- laser at a power of < 200 mW was used for ambient temperature measurements. At high temperature, up to 400 mW were used to maximize the Brillouin signal, since sample heating was not a concern. Light scattered at 90° from the incident beam, was analyzed by a 6 pass, tandem Fabry–Perot interferometer and photomultiplier tube (PMT).[25] Figure 1 shows a representative spectrum in which Stokes and anti-Stokes Brillouin peaks occur symmetrically about the strong Rayleigh peak. The peaks labeled 'ghost' are the adjacent orders of Rayleigh scattered light which are reduced in amplitude by $> 10^3$ by the tandem interferometer. The distance from the Rayleigh peak to the Brillouin peaks is taken to be the frequency shift for that mode.

A set of elastic constants were obtained by a least-squares procedure which minimized misfit between measured velocities and those calculated from the elastic constants.[26] For the high temperature measurements, elastic moduli were calculated directly from Christoffel's equation[21] using the average velocity for each temperature and direction.

3 Results

3.1 X-ray diffraction

Rietveld refinement was performed for all data sets to extract the temperature dependence of the cell dimensions. The refinement was performed in space group *Pbam*, and published room temperature atom coordinates[27] were used as starting values. The resulting cell dimensions and the corresponding cell volumes are given in Table 1 and are shown Fig. 2(a)–(d). About 2 wt% of Al_2O_3 was detected as a minority phase, which could be neglected for the purpose of a cell parameter Rietveld refinement.

The cell dimensions of our X-ray data compared very well with previous data[14] obtained by the Guinier technique. Our cell parameters *b* and *c* deviated only by about 1 to 2 estimated standard deviations (e.s.d.s), whereas *a* deviated by about 6 e.s.d.s. The discontinuities of cell parameters *a* and *b* between 400°C and 500°C seen by Schneider *et al.*[14] were also found with this sample. The temperature range for the discontinuity could be narrowed down to between 425 and 450 °C. The discontinuity of *a* was found to be more pronounced than that of *b*, which was again in good agreement with previous literature.[14] All cell dimensions showed a marked lower thermal expansion between room temperature and 100 °C. Neglecting the (small) discontinuities around 435 °C, a linear thermal expansion may be fitted to the data from 100 up to 700 °C (presented in Table 2).

Above 700 °C, both *a* and *b* displayed a marked increase in thermal expansion and *c* showed a discontinuity. Cooling down from 900 °C to room temperature, both *a* and *b* adopted higher cell dimensions whereas *c* had a lower cell dimension, as compared to the values before the high temperature cycle.

3.2 Neutron diffraction

The measured data were analysed by the Rietveld technique using an extended version[28] of the program of Thomas and Bendall.[29] This meant that complete structure refinements were carried out for

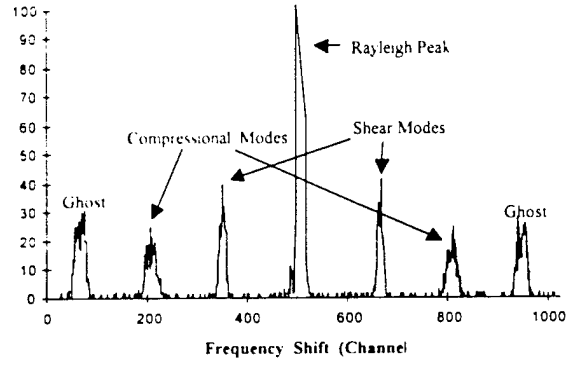


Fig. 1. A typical Brillouin spectrum, depicting the main Rayleigh peak symmetrically surrounded by Stokes and anti-Stokes peaks. The 'ghost' peaks are adjacent orders of Rayleigh scattered light which have been reduced by $> 10^3$ by the tandem Fabry–Perot interferometer.

Table 1. Cell dimensions of 3:2 Kyoritsu mullite powder as determined by X-ray diffraction and Rietvald analysis

Temperature (°C)	*a* (Å)	*b* (Å)	*c* (Å)	*Volume* (Å^3)
29	7·5501(8)	7·6894(8)	2·8837	167·41
100	7·75506	7·6913	2·8845	167.51
200	7·5530	7·6958(9)	2·8858	167·74
300	7·5559	7·6995	2·8872	167·97
400	7·5579	7·7045	2·886	168·20
425	7·75588	7·7056	2·8889	168·27
450	7·5600(9)	7·7061	2·8893(3)	168·33(4)
475	7·5605	7·7073	2·8895	168·38
500	7·5613	7·7087	2·8898	168·44
600	7·5649(10)	7·7126(10)	2·8912	168·68
700	7·5668	7·7167	2·8927	168·91
800	7·5703	7·7221	2·8945	169·21
900	7·5742	7·7295(11)	2·8958	169·53
29	7·5508	7·6914	2·8830	167·43

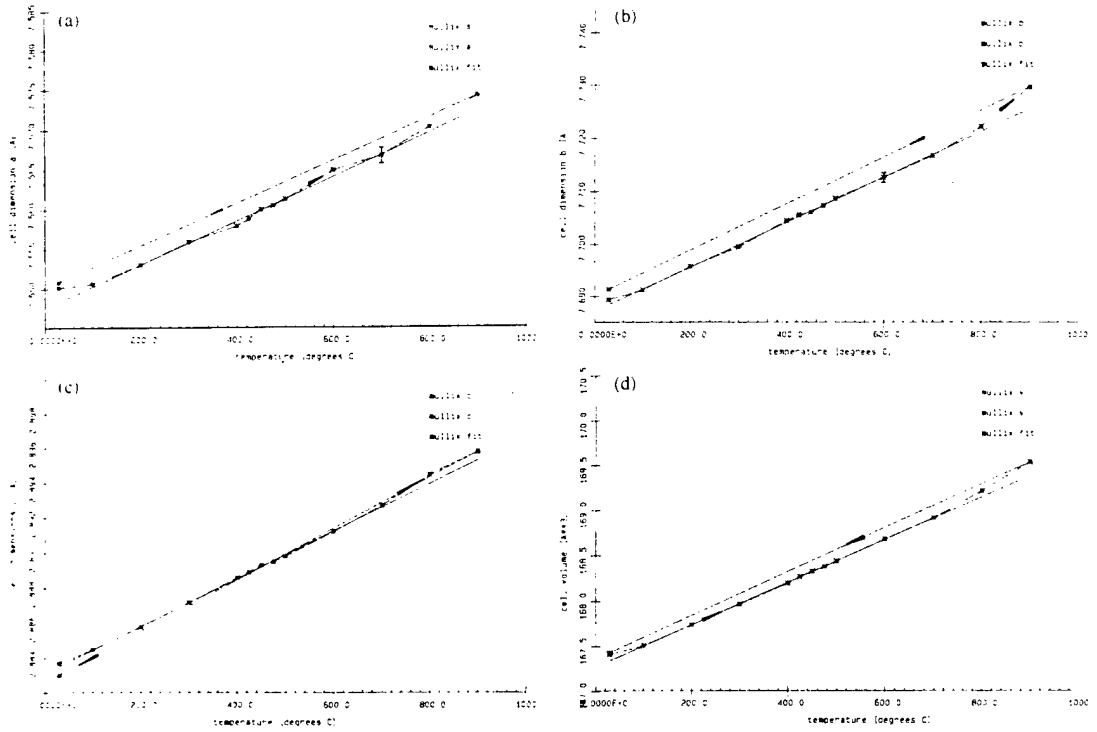


Fig. 2. Cell dimensions measured up to 900 °C by X-ray diffraction and Rietveld analysis, of stoichiometric $3Al_2O_3{\cdot}2SiO_2$ mullite powder. (a) a, (b) b, (c) c, (d) unit cell volume.

Table 2. Linear thermal expansion coefficients and volume expansion of 3:2 Kyoritsu mullite powder as determined by X-ray diffraction and Rietvald analysis

Cell dimension A	*Linear thermal expansion* α (10^{-6}/K) (100–700 °C)
a	3·7(2)
b	5·5(2)
c	4·7(2)
Volume = 1·4(1)·10^{-5} Å^3	

each temperature point. The refinements were carried out within the orthorhombic space group *Pbam*. It is beyond the scope of this paper to discuss the structural changes in any detail. These are the subject of the forthcoming paper.[15] The lattice constants comprised three out of 48 refinable parameters which showed, as usual, only small correlations with the set of remaining structural parameters, such as atomic positions, fractional site occupations and atomic displacement parameters, as well as instrumental parameters related to the shape of the reflections.

Results for the lattice constants are given in Tables 3 and 4, and are shown in Fig. 3(a) (d) as a function of temperature. The lines are only a guide to the eyes and refer to the different parts of the experiment as explained in the experimental procedures (Section 2.3). The agreement factors (precisely, the weighted profile R-factors R_{wp}) between observed and fitted data were around 12%, while the goodness-of-fit values ranged between 1·2 and 1·8. Fig. 3(d) shows the behaviour of the cell volume which is simply given by the product of a, b, and c in the orthorhombic crystal system. From these lattice parameters, the thermal expansion coefficients may be evaluated. In our case of the point group *mmm*, we had only three independent coefficients $\alpha_{ii}(i = 1, 2, 3)$ which may be evaluated from a, b, c by $\alpha_{11} = \frac{\Delta a}{(a\Delta T)}$, $\alpha_{22} = \frac{\Delta \beta}{(\beta \Delta T)}$, $\alpha_{33} = \frac{\Delta c}{(c\Delta T)}$, where T denotes the temperature. These values are included in Table 3. An average lattice expansion coefficient is defined by $\alpha = \frac{(\alpha_{11}+\alpha_{22}+\alpha_{33})}{3}$ and may be compared with values determined by macroscopic methods. One should keep in mind that here a is a structure-related coefficient and not affected by microstructural effects which are governed by the grain-microstructure in the sample. However, structural disorder, for example, produced by vacancies, do affect the α_{ii} or α. These remarks need to be considered when comparing published data for the thermal expansion of mullite.

3.3 Elastic constants determination

Optical microscopy of the laser heated, float zone mullite fibers[4] indicated a 'bamboo-like' columnar structure with a slightly elliptical cross section,

Table 3. (a) Lattice parameters a, b, c, thermal expansion coefficients α_{ii}, and the average thermal expansion $\alpha = (\alpha_{11} + \alpha_{22} + \alpha_{33})/3$ for hot pressed, as-received (grey) 3:2 mullite, as determined by neutron diffraction

Temperature (°K)	a (Å)	α_{11} (10^{-6} K^{-1})	b (Å)	α_{22} (10^{-6} K^{-1})	c (Å)	α_{33} (10^{-6} K^{-1})	α (10^{-6} K^{-1})
298	7·54350(9)	4·05	7·69404(8)	5·65	2·8841(4)	5·70	5·13
723	7·55654(9)	8·14	7·71365(8)	12·41	2·89116(4)	9·81	10·12
923	7·56887(11)	2·09	7·73285(11)	1·00	2·89685(4)	3·09	2·06
1023	7·57045(8)	6·86	7·73362(8)	9·73	2·89774(3)	8·34	8·31
1123	7·57565(9)	6·12	7·74115(9)	8·55	2·90019(4)	7·87	7·51
1173	7·57796(11)	6·25	7·74446(11)	8·49	2·90133(4)	9·00	7·91
1223	7·58033(11)	6·89	7·74775(11)	9·48	2·90264(4)	9·26	8·54
1273	7·58295(10)	6·34	7·75156(9)	10·16	2·90398(4)	7·41	7·97
1373	7·58776(12)		7·75944(11)		2·90613(5)		
(b) Corresponding data after cooling to room temperature and continued heating of air-annealed, (white) 3:2 mullite specimen							
923	7·56337(29)	4·45	7·71767(25)	6·14	2·89381(10)	5·63	5·80
1373	7·57854(25)	4·47	7·73904(23)	6·48	2·90115(9)	5·86	5·60
1473	7·58193(27)	4·59	7·74406(24)	6·47	2·90285(9)	5·40	5·49
1573	7·58541(29)	4·44	7·74907(26)	6·34	2·90442(10)	4·92	5·29
1673	7·58878(23)	5·83	7·75399(20)	9·50	2·90585(8)	6·50	7·28
1773	7·59320(15)	4·83	7·76137(13)	7·45	2·90774(5)	5·49	5·92
1823	7·59504(34)	12·33	7·76426(30)	13·13	2·90854(11)	10·14	11·87
1873	7·59973(22)	3·60	7·76936(20)	10·54	2·91002(7)	3·95	6·03
1923	7·60109(42)		7·77346(38)		2·91059(14)		

Table 4. Neutron diffraction data after second heating of hot pressed, air-annealed (white) 3:2 Kyoritsu mullite specimen

Temperature K	a (Å)	b (Å)	c (Å)
298	7·54736(13)	7·69337(12)	2·88481(5)
723	7·55767(14)	7·70975(12)	2·89021(5)
923	7·56341(14)	7·71862(13)	2·893127(5)
1273	7·57392(15)	7·73401(14)	2·89833(5)
1573	7·58386(12)	7·74743(11)	2·90361(4)
1723	7·58963(18)	7·75566(16)	2·90619(6)
1773	7·59028(19)	7·75657(17)	2·90656(6)
1823	7·59353(20)	7·76253(18)	2·90804(7)
1873	7·59682(23)	7·76810(20)	2·90937(8)
1923	7·60026(25)	7·77305(22)	2·91057(8)
1823	7·59239(21)	7·76147(19)	2·90764(7)
1773	7·58933(20)	7·75694(17)	2·90645(7)
1573	7·58085(17)	7·74428(15)	2·90238(6)
923	7·56138(14)	7·71624(12)	2·89307(5)

reminiscent of an egg shape, with a facet at the bottom of the vertical 'egg'. The fiber was for the most part optically clear, with occasional white streaks across its width, consisting of bubbles or occlusions. These white streaks often coincided with joins of the 'bamboo segments'. The fiber showed uniform extinction along its length under cross polarized light, regardless of rotation about this axis. Extinction was less uniform in cross section, indicating that the fiber was somewhat polycrystalline. Separate X-ray diffraction measurements taken on a four circle diffractometer verified that the fiber consisted of multiple crystallites oriented in very nearly the same direction along the fiber axis. The X-ray data showed that the c axis was virtually coincident with the fiber axis for all the constituent crystallites. However the crystallites had slightly varying rotations about the c axis. All the crystallites lay within 5° of each other, where of those, the majority lay within 2° of each other. Lattice parameters for the sample were calculated by fitting the major peak for each reflection (Table 5). The calculated unit cell angles deviated slightly from 90° due to the small peaks close by, but this deviation was ignored in the calculation of cell volume.

Compositional analysis was made by wavelength dispersive spectroscopy (WDS) in an electron microprobe, and it indicated a mullite composition of $2{\cdot}5Al_2O_3{\cdot}SiO_2$, with a standard deviation of $\pm 0{\cdot}10$ in the molar ratio.

Using the formula $Al_{4-2x}Si_{2-2x}O_{10-x}$ from literature[30] for unit cell composition yielded an average theoretical density of 3·10 g cm^3 at room temperature, which lay between the 2:1 and 3:1 compositional extremes. The densities for high temperature were determined from thermal expansions calculated with a quadratic curve fit to the relative cell volume as measured by neutron diffraction presented in Section 3.2 above, using only the aged sample data.

Figures 4(a)–(c) show the ambient temperature velocities measured for the (010), (100), and (001) platelets, respectively, and velocities calculated from the fitted elastic moduli. Rotation of the sample with respect to its crystal axes was determined by optical extinction under cross-polarized light. The elastic moduli obtained are listed in Table 6. They are considered to be accurate to

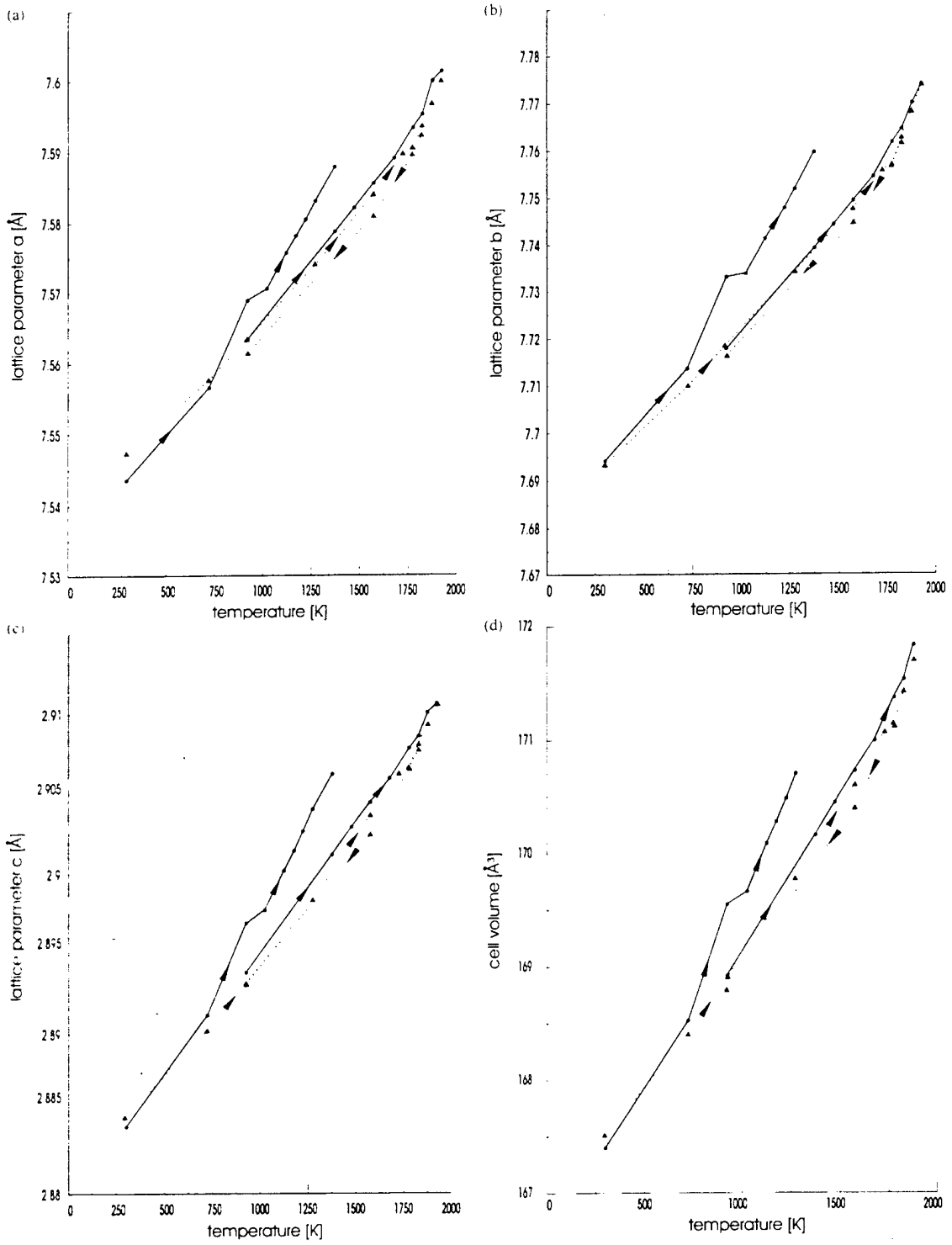


Fig. 3. Lattice parameters a,b,c and cell volume ($=a\times b\times c$) of mullite [(a) to (d), respectively], as a function of temperature. Full circles relate to the first experiment on grey mullite, triangles to the second experiment on annealed white mullite. Error bars are smaller than the symbols. The uncertainty of temperature was about ± 10 K. Solid and dotted lines are only guides to the eyes.

within ± 3% which accounts for uncertainty in the calculated density, as well as possible misorientation of the crystals.

Velocity measurements were made along two directions in both the a–c and b–c crystallographic planes up to 1400 °C, in increments of 200 °C [Fig. 5(a) and (b)]. In these preliminary experiments, nominal temperatures are cited as read directly from the furnace temperature controller. However, even an error of 20°C yields an ~0·2% error in the

Table 5. Lattice parameters measured by X-ray diffractometry for mullite fiber grown by the laser-heated, float-zone method

a (Å)	7·58(1)
b (Å)	7·68(1)
c (Å)	2·90(1)
Cell volume (Å^3)	169(1)
Theoretical density (g cm^{-3})	3·10

Cij's. The moduli C_{11}, C_{33}, C_{44}, and C_{55} were calculated for each temperature [Figs. 6(a) and (b)].

The orientation of the sample at high temperature in a given crystallographic plane was determined from the longitudinal to shear velocity ratio $\left(\frac{l}{t}\right)$. Uncertainties in sample orientation and the thermal expansion increased the error of the high temperature elastic constants. At this point it is difficult to assign a formal uncertainty to the high temperature measurements due to the sparse preliminary data set, but current measurements in progress will allow a more rigorous assessment in the high temperature moduli.[31]

4 Discussions

4.1 X-ray diffraction

The fact that our data also showed the discontinuities of the lattice parameters a and b around 425 °C supports the general validity of this effect in mullite. Explanations were given in terms of the complex dependencies between thermal expansion and structural arrangement of mullite and the related phases andalusite and sillimanite. A relation to domains originating from oxygen vacancies was also discussed by Schneider *et al.*[14] The somewhat larger deviation of our cell parameter a may be related to the fact that this cell direction seems to be more sensitive to sample dependent variations, possibly oxygen vacancies and their related macrostrains. These effects may also be responsible for the heating cycle induced widening and flattening of the unit cell observed with our sample but not with the sample of Schneider *et al.*[14] A full multiphase Rietveld refinement including minority phases will be performed in the future in order to extract more accurate intensities to resolve structural details at the discontinuities mentioned above.

4.2 Neutron diffraction

Figure 3 reveals a striking result in that the behavior of the lattice constants of the pristine (grey) sample material differed appreciably from that of the pre-heated sample. This difference became remarkable at temperatures of about 700 °C. Above this temperature the material exhibited a different, i.e. stronger expansion as compared to the pre-heated sample (see below). This behavior was reflected by all three lattice constants. Note that after the first heating of the sample the colour changed to white. If the hypothesis is correct that the dark colour (of the pristine material) were due to a considerable amount of oxygen vacancies, this different expansion behavior would relate to a strongly disordered mullite structure. After annihilation of these vacancies we should then have a 'normal' expansion. This is evidenced by the coincidence of the values measured in two subsequent experiments and further supported by the full structural analysis.[15] Generally the thermal expansion was most pronounced in the b-direction and the lowest values occurred along the a-axis. The mean expansion coefficient (of the non-pristine, grey sample) was around $5{\cdot}5\times10^{-6}$ (K^{-1}) for temperatures up to 1550 °C. Except for the generally different expansion of the fresh (grey) sample, we observed an additional anomaly at around 700 °C. We refrain from further discussion because this observation is based only on one single temperature measurement, and must be supported by further detailed measurements. We do mention it, however, because some 'anomalies' are reported earlier for temperatures matching this temperature regime.[14] A second 'anomaly' might be in the high temperature regime between 1550 and 1600 °C (cf. Fig. 3 and Tables 3 and 4). Once again, this effect must be substantiated by further experiments. Comparing the two different runs with the heated sample there were only small differences, and, if any, a small hysteris on completing a full heating cooling cycle (cf. Fig. 3). We are not completely sure whether these small differences or 'hysteresis' are substantial or not, because we cannot fully exclude aging effects of the sample undergoing one or more heating cycles in air.

4.3 Elastic constants

Because of fiber microstructure, the elastic moduli probably represent an average over numerous crystallites. Since the crystallites have different rotations about their c axes, this effect is most important in the (001) plane. This plane shows relatively low anisotropy in phonon velocity, which is most likely real, since velocities are averaged over a range of orientations less than 5°. The low anisotropy in the (001) plane can be correlated to the crystal structure. Mullite may be considered as cross-linked, (edge-shared) chains of Al^{3+} octahedra and tetrahedral (corner-shared) chains containing alternating Si^{4+} and Al^{3+} cations, running parallel to the c axis.[32] Longitudinal and transverse vibrations polarized in this plane represent deformations of the voids and cross-linking bonds

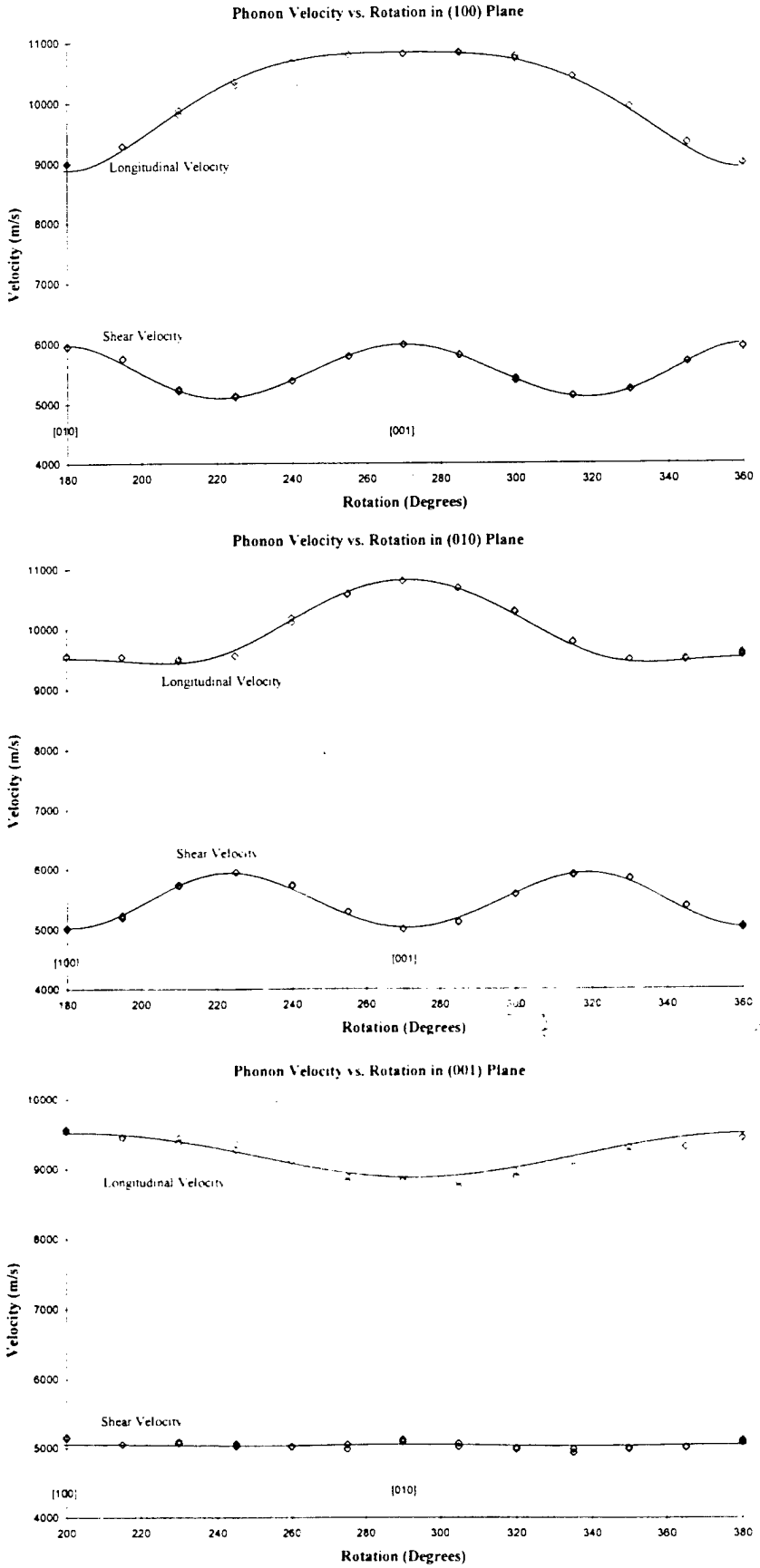


Fig. 4. Measured and fitted phonon velocities of mullite fiber in the (a) (100), (b) (010), and (c) (001) planes.

Table 6. Single crystal, room temperature, elastic moduli of mullite fiber grown by the laser heated, float-zone method

C_{11} (GPa)	280
C_{22} (GPa)	245
C_{33} (GPa)	362
C_{44} (GPa)	111
C_{55} (GPa)	78·1
C_{66} (GPa)	79·0
C_{12} (GPa)	105
C_{13} (GPa)	99·2
C_{23} (GPa)	135

between these chains regardless of directions. In the (100) and (010) planes, the nature of the deformations change from being normal to the polyhedral chains to being parallel to them, as the propagation direction approaches [001] for a longitudinal wave and vice versa for a shear wave polarized in the plane of rotation. This accounts for the higher anisotropy in these planes, since the polyhedral chains are relatively stiff along their length. This is evident from the substantially higher value of C_{33} as compared to C_{11} and C_{22}. Similar correlations have been shown for sillimanite and andalusite[33] which share structural similarities with mullite. The mullite sample measured did not contain a substantial amount of glassy phase as was thought to exist in the impure sample measured in previous work.[16,17] This accounts for the lack of marked decrease in moduli above 600 °C. Further work is in progress to completely specify the elastic tensor of mullite to 1400 °C.[31]

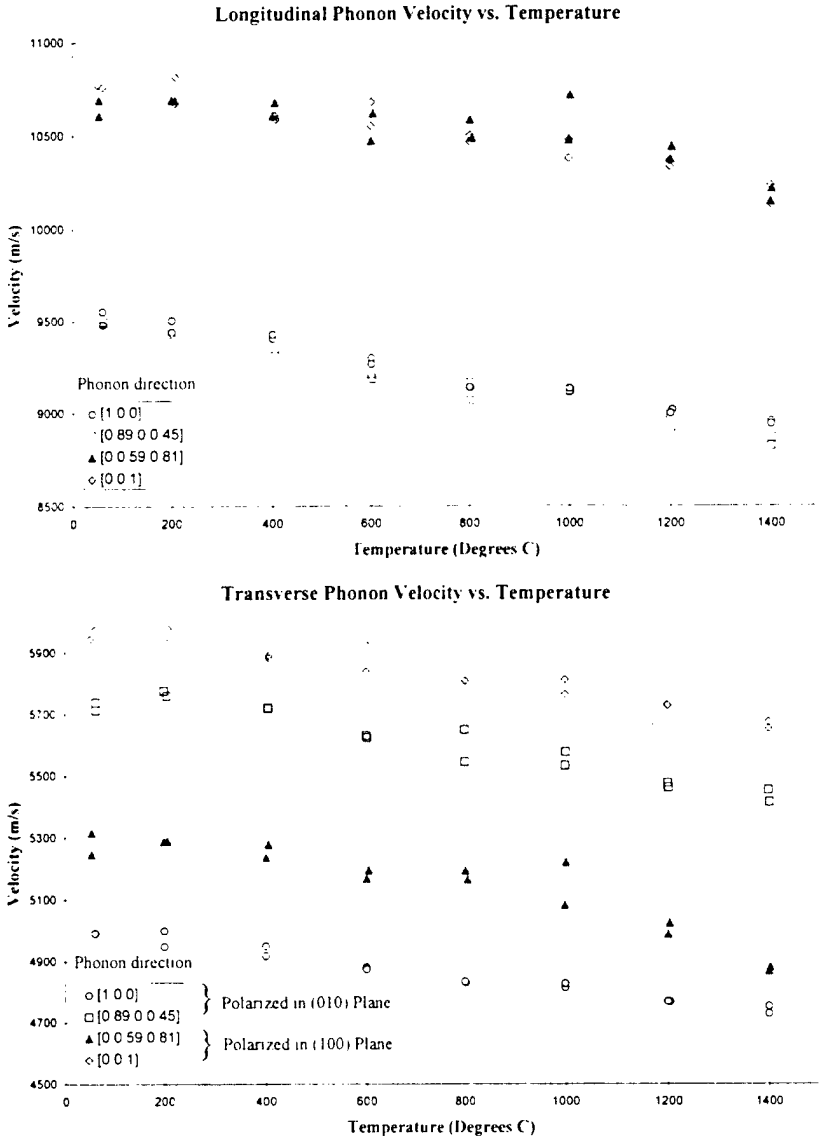


Fig. 5. Measured phonon velocities versus temperature for selected crystallographic directions. (a) longitudinal waves; (b) transverse waves.

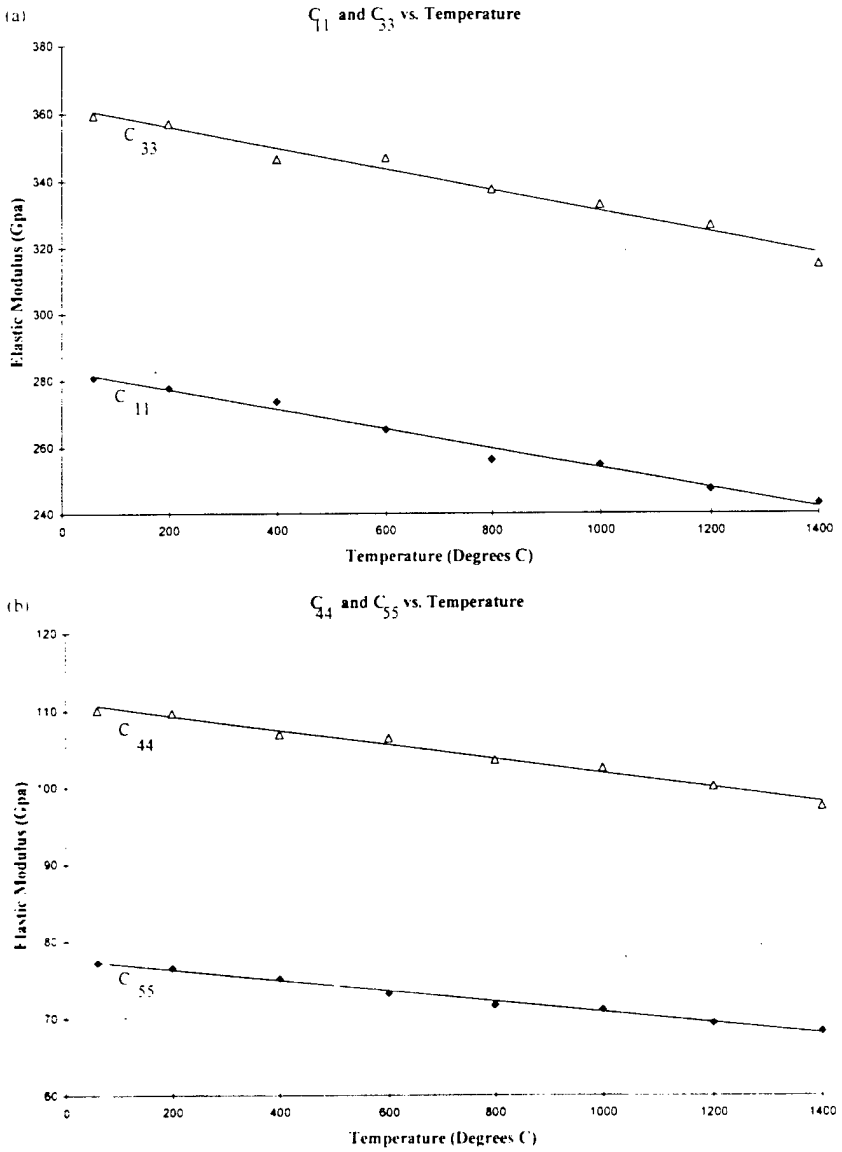


Fig. 6. Variation of selected elastic moduli with temperature

5 Conclusions

In this work, the lattice parameters and thermal expansion coefficients for stoichiometric mullite ($3Al_2O_3{\cdot}2SiO_2$) powder were measured by X-ray diffractometry up to 900 °C. The data was analyzed by the Rietveld technique, and the strutural discontinuity reported by Schneider *et al.*[12] was confirmed. The temperature range of its occurrence was narrowed to between 425 and 450 °C.

A dense, hot pressed sample of the same mullite made from hydrothermally grown, stoichiometric $3Al_2O_3{\cdot}2SiO_2$ powder was examined by high temperature neutron diffraction and Rietveld analysis. Specimens were cycled from room temperature to 1650 °C, yielding a complete set of axial lattice parameters and thermal expansion coefficients.

In addition, the as-hot pressed, grey mullite (thought to be oxygen deficient due to hot pressing in a graphite die under vacuum) exhibited higher lattice parameters than did those of the (presumably) fully oxidized, white mullite specimen examined in subsequent heating cycles after effectively annealing in air. This observation suggests that the highly incommensurately modulated structure is highly sensitive to oxygen vacancies, and this is the subject of further ongoing work.

Cameron and others[3,33,34] define the position of satellite reflections as being determind by structural vacancies needed to accommodate composition. Thus it follows that additional vacancies will be expected to strongly impact this feature. This observation may have general ramifications in that it suggests that lattice parameters and properties of

oxygen deficient oxide ceramics may differ from those of fully oxygenated, stoichiometric oxides.

The single crystal elastic constants were measured for a melt-grown, orthorhombic, mullite fiber. The complete set of nine elastic moduli were obtained at room temperature, while incomplete measurements up to 1400 °C indicated roughly a 10% drop in stiffness at elevated temperatures.

Acknowledgements

W. M. Kriven gratefully acknowledges the Institut für Kristallographie und Angewandte Mineralogie, in München, Germany, for hosting her sabbatical leave of six months in 1997. The work of J. W. Palko was supported in the United States, by a Fannie and John Hertz Foundation graduate Fellowship. The X-ray work in conjunction with the elastic constant measurements was carried out at the Center for Microanalysis of Materials at UIUC. The WDS electron microprobe analysis was conducted by Dr. I. Steele at the University of Chicago. This work was partially supported by a United States Air Force Office of Scientific Research AASERT Grant, under Contract number F49620-97-1-0427.

References

1. Schneider, H., Okada, K. and Pask, J. A., *Mullite and Mullite Ceramics*. John Wiley, Chichester, UK, 1994.
2. Aksay, I. A. and Pask, J. A., Stable and metastable equilibria in the system SiO_2–Al_2O_3. *J. Am. Ceram. Soc.*, 1975, **58**(1–12), 507–512.
3. Kriven, W. M. and Pask, J. A., Solid solution range and microstructures of melt-grown mullite. *J. Am. Ceram. Soc.*, 1983, **66**(9), 649–654.
4. Sayir, A. and Farmer, S. C. Directionally solidified mullite fibers. In *Ceramic Matrix Composites—Advanced High Temperature Structural Materials. Mat. Res. Soc. Symp. Proc.*, Vol. 365, 1995, pp. 11–20.
5. Wilson, D. M., Lieder, S. L. and Lueneburg, D. C., Microstructure and high temperature properties of NEXTEL 720 fibers. *Cer. Eng. Sci. Proc.*, 1995, **16**, 1005–1012.
6. Goring, J. and Schneider, H., Creep and subcritical crack growth of Nextel 720 alumino silicate fibers as-received and after heat treatment at 1300°C. *Cer. Eng. Sci. Proc.*, 1997, **18**(3), 95–102.
7. Schneider, H., Göring, J., Schmücker, M. and Flucht, F., Thermal stability of Nextel 720 alumino silicate fibers. In *Ceramic Microstructure Control at the Atomic Level*, ed. A. P. Tomsia and A. Glaeser. Plenum Press, New York, 1998, pp. 721–730.
8. Kriven, W. M., Jilavi, M. H., Zhu, D., Weber, J. K. R., Cho, B., Felten, J. and Nordine, P. C., Synthesis and microstructure of mullite fibers grown from deeply undercooled melts. In *Ceramic Microstructure Control at the Atomic Level*, ed. A. Glaeser and A. P. Tomsia. Plenum Press, New York, 1998, pp. 169–176.
9. Weber, J. K. R., Cho, B., Hixon, A. D. Abadie, J. G., Nordine, P. C., Kriven, W. M., Johnson, B. R. and Zhu, D., Growth and crystallization of YAG and mullite-composition glass fibers. *J. Euro. Ceram. Soc.*, 1999, **19**(13–14) this issue.
10. Oehlschlegel, G., Kockel, A. and Biedl, A., Anisotrope Mischkristallbildung einiger Verbindungen des ternären Systems BaO–Al_2O_3–SiO_2. Teil II. Messungen an Strukturen mit zweidimensionaler Verknüpfung von $(Si,Al)O_4$-Tetrahederen und Modellvorstellungen von deren Wärmedehnungsanisotropie (Anisotropic mixed crystal formation of a compoundfrom the ternary system BaO–Al_2O_3–SiO_2. Part II. Measurement of structures with two dimensional joining of $(Si,Al)O_4$-tetrahedra and proposed model of their thermal expansion anisotropy). *Glastech. Ber.*, 1974, **47**, 31–41 (in German).
11. Winter, S. and Ghose, S., Thermal expansion and high-temperature crystal chemistry of Al_2SiO_5 polymorphs. *Am. Mineral.*, 1979, **64**, 573–586.
12. Schneider, H. and Eberhard, E., Thermal expansion of mullite. *J. Am. Ceram. Soc.*, 1990, **73**, 2073–2076.
13. Margalit, J., Thermal expansion of mullite up to 1500 °C. Ph.D. thesis, Verlag Mainz, Wissenschaftsverlag, Aachen, Germany, 1993 (in German).
14. Schneider, H., Rodewald, K. and Eberhard, E., Thermal expansion discontinuities of mullite. *J. Amer. Ceram. Soc.*, 1993, **76**, 2896–2898.
15. Brunauer, G., Boysen, H., Frey, F., Hansen, T. and Kriven, W. M., High temperature crystal structure of a 3:2 mullite from neutron diffraction data. In preparation.
16. Fenstermacher, J. E. and Hummel, F. A., High temperature mechanical properties of ceramic materials: IV, sintered mullite bodies. *J. Am. Ceram. Soc.*, 1961, **44**(6), 284–289.
17. Davis, R. F. and Pask, J. A., Mullite. In *High Temperature Oxides*, Vol. 4., ed. A. M. Alper. Academic Press, New York, 1971, pp. 37–76.
18. Ledbetter, H., Kim, S., Crudele, S. D. and Kriven, W. M., Elastic properties of mullite. *J. Am. Ceram. Soc.*, 1998, **81**(4), 1025–1028.
19. Sanderock, J. R., Trends in Brillouin scattering: studies of opaque materials, supported films, and central modes. In *Topics in Applied Physics 51, Light Scattering in Solids III: Recent Results*, ed. G. Guntherodt, M. Cardona. Springer-Verlag, New York, 1982, pp. 173–206.
20. Zouboulis, E. S. and Grimsditch, M., Refractive index and elastic properties of MgO up to 1900 K. *J. Geophysical Res.*, 1991, **96**, 4167–4170.
21. Landau, L. D. and Lifshitz, E. M., *Theory of Elasticity. A Course of Theoretical Physics*, Vol. 7. Pergammon Press, London, 1959.
22. Proc. Int'l. Workshop on Oxide Oxide Composites, Irsee, Bavaria, Germany, 22–24 June 1998. *J. Euro. Ceram. Soc.*, in press.
23. Crudele, S. D., Processing and characterization of alumina platelet-reinforced mullite composites. M.S. thesis, University of Illinois at Urbana-Champaign, 1989.
24. Lorenz, G., Neder, R. B., Marxreiter, J., Frey, F. and Schneider, J., A mirror furnace for neutron diffraction up to 2300 K. *J. Appl. Crystallogr.*, 1993, **26**, 632–635.
25. Sinogeikin, S. V., Bass, J. D. and Katsura, T., Sound velocities and elastic properties of Fe-bearing wadsleyite and ringwoodite. *J. Geophys. Res.*, in press.
26. Weidner, D. J. and Carleton, H. R., Elasticity of coesite. *J. Geophysical Res.*, 1977, **82**(8), 1334–1346.
27. Balzar, D. and Ledbetter, H., Crystal structure and compressibility of 3:2 mullite. *Am. Mineralogist*, 1993, **78**, 1192–1196.
28. Boysen, H., Anharmonic thermal parameters, disorder and phase transition. In *Accuracy in Powder Diffraction II*, ed. E. Prince and J. K. Stalick. NIST, Washington, DC, 1992, pp. 165–174.
29. Thomas, M. W. and Bendall, P. J., A suite of programs for total profile refinement of number of powder diffraction patterns. *Acta Crystallogr.*, 1978, **A34**, 351.

30. Rahman, S. H., Real crystal structure of mullite. In *Mullite and Mullite Ceramics*. John Wiley, Chichester, UK, 1994, pp. 4–31.
31. Palko, J. E., Kriven, W. M., Sinogeikin, S., Bass, J. D. and Sayir, A., Single crystal elastic moduli of mullite. In preparation.
32. Vaughn, M. T. and Weidner, D. J., The relationship of elasticity and crystal structure in andalusite and sillimanite. *J. Phys. Chem. Minerals*, 1978, **3**, 1–12.
33. Cameron, W. E., Composition and cell dimensions of mullite. *Ceram. Bull.* 1977, **56**(11), 1003–1007, 1011.
34. Cameron, W. E., *Amer. Miner.*, 1977, **62**, 747–755.

journal

J. Am. Ceram. Soc., 82 [8] 2049–55 (1999)

Preparation of Portland Cement Components by Poly(vinyl alcohol) Solution Polymerization

Sang-Jin Lee,* Elizabeth A. Benson,† and Waltraud M. Kriven*

Department of Materials Science and Engineering, University of Illinois at Urbana-Champaign, Urbana, Illinois 61801

The four components of portland cement—dicalcium silicate, C_2S (Ca_2SiO_4); tricalcium silicate, C_3S (Ca_3SiO_5); tricalcium aluminate, C_3A ($Ca_3Al_2O_6$); and tetracalcium aluminate iron oxide, C_4AF ($Ca_4Al_2Fe_3O_{10}$)—were formed using a solution–polymerization route based on poly(vinyl alcohol) (PVA) as the polymer carrier. The powders were characterized using X-ray diffraction techniques, BET specific surface area measurements, and scanning electron microscopy. This method produced relatively pure, synthetic cement components of submicrometer or nanometer crystallite dimensions, high specific surface areas, as well as extremely high reactivity at relatively low calcining temperatures. The PVA content and its degree of polymerization had a significant influence on the homogeneity of the final powders. Two types of degree of polymerization (DP) PVA were used. Lower crystallization temperatures and smaller particle size powders were obtained from the low-DP-type PVA at optimum content.

I. Introduction

CERAMIC processing has been using chemical synthesis routes in more recent years.[1–15] Methods based on soft-solution processing provide powders with desired properties, such as high purity and homogeneity. In particular, polymer–metal cation complexes are interesting because of their ability to produce well-characterized materials for various industrial purposes and practical uses. In recent years, a new technique has been developed in powder synthesis processing, viz., the use of a poly(vinyl alcohol) (PVA) as a polymeric carrier in a mixed metal cation solution. By using the PVA process, ceramic powders are synthesized much more easily than in other chemical synthesis routes.[1–7] Initially, Gülgün *et al.*[2,3] synthesized compounds, such as calcium aluminate, CA ($CaAl_2O_4$), and yttrium aluminate garnet, YAG ($Y_3Al_5O_{12}$), phases, using the PVA technique. Unlike the Pechini-resin process,[8,12–15] which involves chelation and polymerization, the PVA process involves primarily steric entrapment of cations into the polymer network.[3,5–7] The PVA ensures the homogenous distribution of the metal ions in its polymeric network structure and inhibits their segregation and/or precipitation from the solution.[2,3,5–7] Water is able to diffuse through the polymer and stretch it because of the acetate clusters. In the solution, the long chain polymer prevents contact between cations and limits their agglomeration and precipitation. A schematic representation of the cationic entrapment mechanism is shown in Fig. 1. The amount of polymer and its molecular length can affect the distribution of cations. The optimum amount and chain length of PVA result in a pure, highly reactive, and homogenous powder at the molecular level. It is speculated that weak hydrogen bonding promotes homogeneous entrapment between the –(OH) hydroxyl groups and cations that are solvated by water molecules. The PVA process also produces carbonaceous material that gives heat through its combustion, so that fine and single-phase powders can be formed at a relatively low external temperature.[1–7]

Some of the portland cement components have been made by other chemical synthesis routes. Kralj *et al.*[16] were able to produce C_2S (Ca_2SiO_4) in a CO_2 atmosphere at 950°C, but this required repeated firings of up to four times, with grinding in between each firing to complete the reaction. Roy *et al.*[9] also experimented with C_2S and C_3S (Ca_3SiO_5) to form the materials by a chemical process using nitrate salts and an aqueous sol of SiO_2. They used both the spray-dry technique and gel preparation methods, and obtained BET specific surface area values of 12.94 m^2/g for C_2S and 12.87 m^2/g for C_3S.

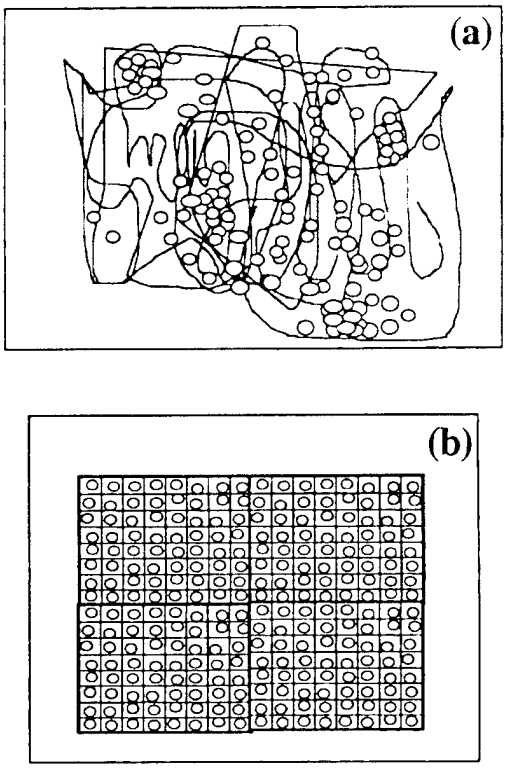


Fig. 1. Schematic representation of cationic entrapment with (a) non-optimal amount of polymer and (b) optimal amount of polymer.

G. W. Scherer—contributing editor

Manuscript No. 189964. Received August 10, 1998; approved December 28, 1998.
Funded in part by the Air Force Institute of Technology at Wright-Patterson AFB, OH, by the Graduate Studies Program at the U.S. Air Force Academy, CO, through a scholarship to the graduate school at the University of Illinois at Urbana-Champaign, and by the Air Force Office of Scientific Research AASERT Program under Grant No. F49620-97-1-0427

*Member, American Ceramic Society.
†Now at Goodfellow AFB, TX.

In this study, the four components of portland cement—dicalcium silicate, C_2S (Ca_2SiO_4); tricalcium silicate, C_3S (Ca_3SiO_5); tricalcium aluminate, C_3A ($Ca_3Al_2O_6$); and tetracalcium aluminate iron oxide; C_4AF ($Ca_4Al_2Fe_3O_{10}$)—were made by a solution–polymerization process using PVA. By using this method, it was possible to control chemical and physical characteristics, to synthesize powders at lower temperatures, to eliminate grinding–refiring steps as mentioned above, and to produce a high powder yield.[7] Optimum synthesis conditions, such as PVA content, degree of polymerization of the PVA, and calcination temperature, were determined for each component. The powders were characterized by microstructural examination (XRD, SEM) and specific surface areas were measured by nitrogen gas adsorption (BET). The powders prepared by this new application can make pure, synthetic, cement components of nanometer or submicrometer crystallite dimensions, high specific surface area, and extremely high reactivity at relatively low calcination temperatures, in comparison with conventional methods.[17] It is then possible to explore the realm of advanced cementitious materials and composites and its interdisciplinary interface with ceramic synthesis and processing. Once the hydraulicity of each component is determined as a function of the powder characteristics, it is possible to optimize various compositions for specific applications, such as enhanced setting speed, higher strength, and other desirable characteristics.[18–20]

II. Experimental Procedure

(1) Powder Processing

The nitrate salts were in the form of cation sources, with the exception of SiO_2, which was supplied as a colloidal SiO_2 product (25% SiO_2 sol; Ludox SK, DuPont, Wilmington, DE). The chemical reagents and product manufacturers are listed in Table I. These cation sources were dissolved in stoichiometric proportions in deionized (DI) water. To improve the process of dissolving the Ludox SK, the pH of the solution was adjusted by addition of nitric acid. Once the cation sources were completely dissolved, the 5 wt% PVA (Airvol Series; Air Products and Chemicals, Inc., Allentown, PA) was dissolved in DI water and added. The degree of polymerization (DP) of the PVA was varied in these experiments. High-DP PVA was made from Airvol 540S, with a DP value of 1625 (monomers/polymer), and low-DP PVA was made with Airvol 205S with a DP of 428 (monomers/polymer). The high DP PVA had a molecular weight of 153 000, and the low DP PVA had a molecular weight of 40 000. The proportions of the PVA to cation sources in the solution were adjusted in such a way that there were 4, 8, or 12 times more positively charged valences from the cations than from the potentially negatively charged –(OH) functional groups of the polymers. The polymeric long chains have hydroxyl groups in solution. Hence, one PVA monomer, which had one hydroxyl –(OH) functional group, could be used as a unit for calculation of PVA content.

In this experiment, the effect of PVA content and its degree of polymerization on powder preparation is studied. Therefore, the exact relative amount of PVA to cations in the solution can be calculated with reference to a monomeric unit of PVA. For example, in the case of the 4:1 PVA ratio in C_2S, the total positively charged valences are eight. Thus, two PVA monomers are used per one C_2S molecule. Water is evaporated by continuous stirring during heating on a hot plate. The resulting gel-type precursors are completely dried after several hours at 100°C. The organic/inorganic precursors are then ground and kept in a dessicator because of their hydrophilic characteristics. Each of the ground precursors are calcined or crystallized at various temperatures in an air atmosphere in a box furnace. Each of the four components are calcined at a heating rate of 3°C/min. Crystallized C_3S and C_3A powders are milled using an attritor mill (Szegvari Attritor System Type B, Model 3576, Union Process, Akron, OH) to examine the effects of milling on the surface area. The powders are attritor milled at 240 rpms for 1 h. Approximately 700 g of ZrO_2 milling media 5 mm in diameter are mixed with 100 mL of methyl alcohol in a 600 mL jar.

(2) Characterization

(A) X-ray Diffraction Analysis: The crystallization behavior of each of the calcined powders was studied as a function of temperature and holding time at elevated temperatures using an X-ray diffractometer (Dmax automated powder diffractometer, Rigaku/USA, Danvers, MA) with CuK_α radiation (40 kV, 40 mA). All XRD data were obtained at room temperature, after the powder had been cooled. A scanning speed of 10°/min with a sampling interval of 0.02° over a range of 10°–70° for C_2S, C_3S, and C_3A was used. For C_4AF, the range varied from 30° to 40°.

In C_3A, the relative volume ratios of C_3A and residual CaO phases were determined by integrating the X-ray peak areas of (440) of C_3A and (200) of CaO using the equation

$$V_{C3A} = \frac{I(440)_{C3A}}{I(200)_{CaO} + I(440)_{C3A}} \times 100$$

where V_{C3A} is the volume fraction of C_3A, and $I(440)_{C3A}$ and $I(200)_{CaO}$ the 100% peak intensities of C_3A and CaO, respectively.

(B) Specific Surface Area Measurement: The specific surface area of the crystallized powders and attrition-milled powders were obtained by five-point BET analysis from nitrogen-gas adsorption (Model ASAP 2400, Micromeritics, Norcross, GA). All samples for testing were kept in a dry oven to prevent hydration of the powders.

(C) Microstructure Characterization: The morphologies of calcined, crystallized, and/or attrition-milled powders were examined by scanning electron microscopy (SEM; model

Table I. Powder Preparation and Processing Variables

Component	Chemical agents	pH adjustment	Solution color	Burnout temperature (°C)	Properties of organic/inorganic precursor
C_2S	Calcium nitrate† + Ludox SK	Nitric acid (pH 2)	Transparent	3°C/min, 1 h hold at 700°C	White precursor, fairly coarse texture, hydrophilic
C_3S	Calcium nitrate + Ludox SK	Nitric acid (pH 2)	Transparent	3°C/min, 1 h hold at 700°C	White precursor, coarse texture, hydrophilic
C_3A	Calcium nitrate + aluminum nitrate‡		Transparent	3°C/min, 1 h hold at 700°C	Yellow precursor, soft and porous texture, hydrophilic,
C_4AF	Calcium nitrate + aluminum nitrate + iron nitrate§		Transparent	3°C/min, 1 h hold at 700°C	Red/brown precursor, soft and porous texture, hydrophilic

†$Ca(NO_3)_2 \cdot 4H_2O$ (reagent grade, Aldrich Chemical Co., Milwaukee, WI). ‡$Al(NO_3)_2 \cdot 9H_2O$ (reagent grade; Aldrich Chemical Co.). §$Fe(NO_3)_3 \cdot 9H_2O$ (reagent grade; ALFA Aesor Chemical Co., Ward Hill, MA)

Table II. Crystallization Behavior from High-DP PVA

Temperature (°C)	C_2S (4:1)*	C_3S (8:1)*	C_3A (8:1)*	C_4AF (8:1)*
600	Amorphous	Amorphous	Amorphous	Amorphous
700	Amorphous + α_L'-Ca_2SiO_4	Amorphous	$Ca_3Al_2O_6$ < CaO	$Ca_4Al_2Fe_3O_{10}$
800	α_L'-Ca_2SiO_4 + CaO < β-Ca_2SiO_4	β-Ca_2SiO_4 + CaO + Ca_3SiO_5	$Ca_3Al_2O_6$ < CaO	$Ca_4Al_2Fe_3O_{10}$
900	α_L'-Ca_2SiO_4 + [CaO] < β-Ca_2SiO_4	β-Ca_2SiO_4 + CaO + Ca_3SiO_5	$Ca_3Al_2O_6$ > CaO	$Ca_4Al_2Fe_3O_{10}$
1000	β-Ca_2SiO_4 + [CaO]	Ca_3SiO_5 + CaO	$Ca_3Al_2O_6$ > CaO	$Ca_4Al_2Fe_3O_{10}$
1100	β-Ca_2SiO_4 + [CaO]	Ca_3SiO_5 + CaO	$Ca_3Al_2O_6$ + [CaO]	$Ca_4Al_2Fe_3O_{10}$
1200	β-Ca_2SiO_4	Ca_3SiO_5 + CaO	$Ca_3Al_2O_6$ + [CaO]	$Ca_4Al_2Fe_3O_{10}$
1300	γ-Ca_2SiO_4	Ca_3SiO_5 + CaO	$Ca_3Al_2O_6$	$Ca_4Al_2Fe_3O_{10}$
1400	γ-Ca_2SiO_4	Ca_3SiO_5 + [CaO]	$Ca_3Al_2O_6$	$Ca_4Al_2Fe_3O_{10}$

*( ) indicates optimum PVA content in terms of ratio of cation valences to -(OH) functional groups for lowest crystallization temperature; [ ] indicates much smaller amounts relative to other phases present.

Table III. Crystallization Behavior from Low-DP PVA

Temperature (°C)	C_2S (4:1)*	C_3S (4:1)*	C_3A (4:1)*	C_4AF (4:1)*
600	Amorphous + α_L'-Ca_2SiO_4	Amorphous	$Ca_3Al_2O_6$ < CaO	$Ca_4Al_2Fe_3O_{10}$
700	α_L'-Ca_2SiO_4 + CaO < β-Ca_2SiO_4	Ca_3SiO_5 + CaO	$Ca_3Al_2O_6$ > CaO	$Ca_4Al_2Fe_3O_{10}$
800	α_L'-Ca_2SiO_4 + [CaO] < β-Ca_2SiO_4	Ca_3SiO_5 + CaO	$Ca_3Al_2O_6$ > CaO	$Ca_4Al_2Fe_3O_{10}$
900	β-Ca_2SiO_4 + [CaO]	Ca_3SiO_5 + CaO	$Ca_3Al_2O_6$ + [CaO]	$Ca_4Al_2Fe_3O_{10}$
1000	β-Ca_2SiO_4 + [CaO]	Ca_3SiO_5 + CaO	$Ca_3Al_2O_6$ + [CaO]	$Ca_4Al_2Fe_3O_{10}$
1100	β-Ca_2SiO_4	Ca_3SiO_5 + CaO	$Ca_3Al_2O_6$	$Ca_4Al_2Fe_3O_{10}$
1200	γ-Ca_2SiO_4	Ca_3SiO_5 + CaO	$Ca_3Al_2O_6$	$Ca_4Al_2Fe_3O_{10}$
1300	γ-Ca_2SiO_4	Ca_3SiO_5 + CaO	$Ca_3Al_2O_6$	$Ca_4Al_2Fe_3O_{10}$
1400	γ-Ca_2SiO_4	Ca_3SiO_5 + [CaO]	$Ca_3Al_2O_6$	$Ca_4Al_2Fe_3O_{10}$

*( ) indicates optimum PVA content in terms of ratio of cation valences to -(OH) functional groups for lowest crystallization temperature; [ ] indicates much smaller amounts relative to other phases present.

S530, Hitachi, Tokyo, Japan). For the SEM specimens, each powder was completely dried, attached to an aluminum stub, and gold sputter coated.

III. Results and Discussion

The optimum pH values for C_2S and C_3S for forming transparent solutions and stoichiometric powders are listed in Table I. For each of the four components, the binder was completely burned out by 700°C. With respect to the characteristics of the dried precursors, both C_3A and C_4AF resembled an aerogel formed by foaming during the stirring and solution-drying process. The foam mainly resulted from elimination of NO_x gases from the $Al(NO_3)_3$ source.

(1) Crystallization Behavior

Tables II and III summarize the XRD data acquired for each of the four powders for high- and low-DP PVA, respectively. The effect of DP was particularly evident in the 700°C calcining range for C_2S and C_3S. In the high-DP route, the amorphous phase was still present, while, with the low-DP PVA, the calcined powders were crystallized. In the case of single-phase C_3A (>95 vol%), the powder prepared via low-DP PVA crystallized at 1000°C for 1 h. In comparison, 1100°C for 3 h conditions were necessary to crystallize relatively pure C_3A made by the high-DP PVA. C_4AF showed no apparent changes in its crystalline behavior.

The effect of DP of the PVA may be attributed to the following considerations. The low-DP PVA had smaller polymer chain lengths than did the high-DP PVA; therefore, it could make the range of distances between cations in the solution shorter.[5] This is especially important in the synthesis of C_3A and C_3S, because the concentration of Ca^{2+} ions is much higher than that of Al^{3+} or Si^{4+} ions, respectively. This can lead to unreacted CaO phase, even at high temperatures. For the compound to be synthesized at low temperatures, the Ca^{2+} ions and Al^{3+} or Si^{4+} ions must be homogeneously dispersed within a short range, rather than long range, of each other to promote reaction. The chain length of the lower-DP PVA is small enough for this mixing to occur in the steric entrapment mechanism. Furthermore, the higher amount of PVA (4:1 ratio) added to the solution aids in this mixing process. The low-DP PVA distributes the metal ions homogeneously, so that, after binder burnout, the network shrinks, enabling C_3A or C_3S to be formed more readily. The cations are sterically entrapped

Table IV. BET Specific Surface Area of Each Crystallized Compound at Optimum PVA Content

Conditions	C_2S	C_3S	C_3A	C_4AF
High-DP PVA method				
Crystallization temperature (°C)	900	1400	1100	700
Holding time (h)	1	2	3	1
BET specific surface area (m^2/g)	12.9	0.9	2.3	9.1
Low-DP PVA method				
Crystallization temperature (°C)	800	1400	1000	700
Holding time (h)	1	1	1	1
BET specific surface area (m^2/g)	22.1	0.8	4.2	17.1
BET specific surface area (m^2/g) (after attrition milling for 1 h)		50	18.9	

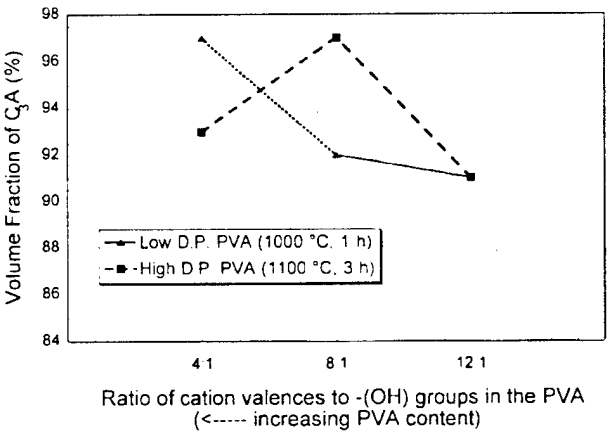


Fig. 2. Volume fraction of C_3A powder synthesized as a function of the ratio of cation valences to -(OH) groups in the PVA polymer.

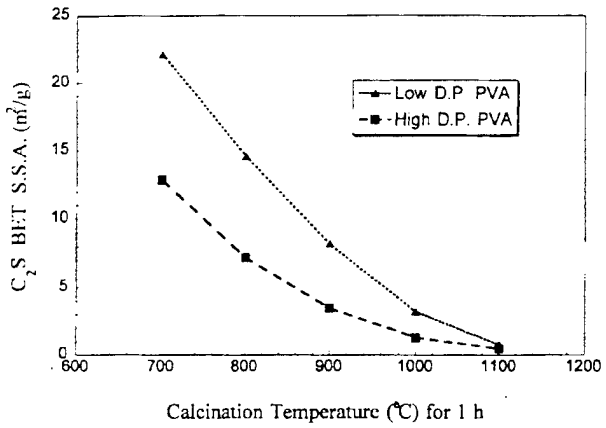


Fig. 3. Decrease in BET specific surface area for C_2S powders with increasing calcining temperature for 1 h holding time at each temperature.

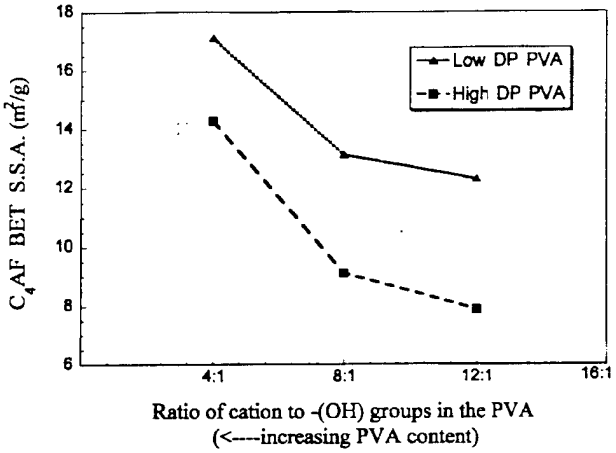


Fig. 4. Variation of BET specific surface areas for C_4AF as a function of the ratio of cation valences to –(OH) groups in the PVA polymer.

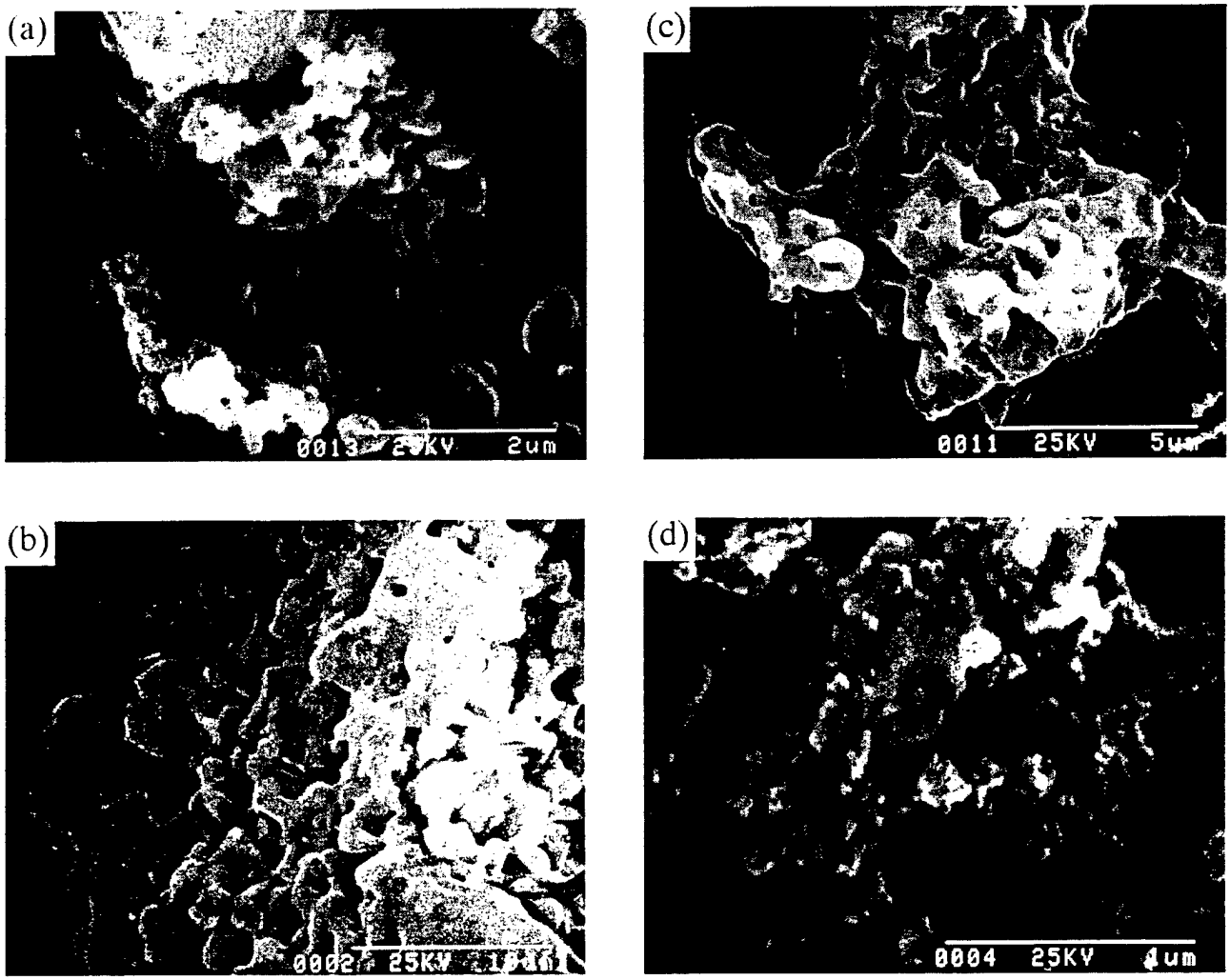


Fig. 5. Morphologies of crystalline powders for the four components of portland cement made by the high degree of polymerization PVA process at optimum PVA content (Table II): (a) C_2S powder as-calcined at 900°C for 1 h, (b) C_3S powder as-calcined at 1400°C for 2 h, (c) C_3A powder as-calcined at 1100°C for 3 h, and (d) C_4AF powder as-calcined at 700°C for 1 h.

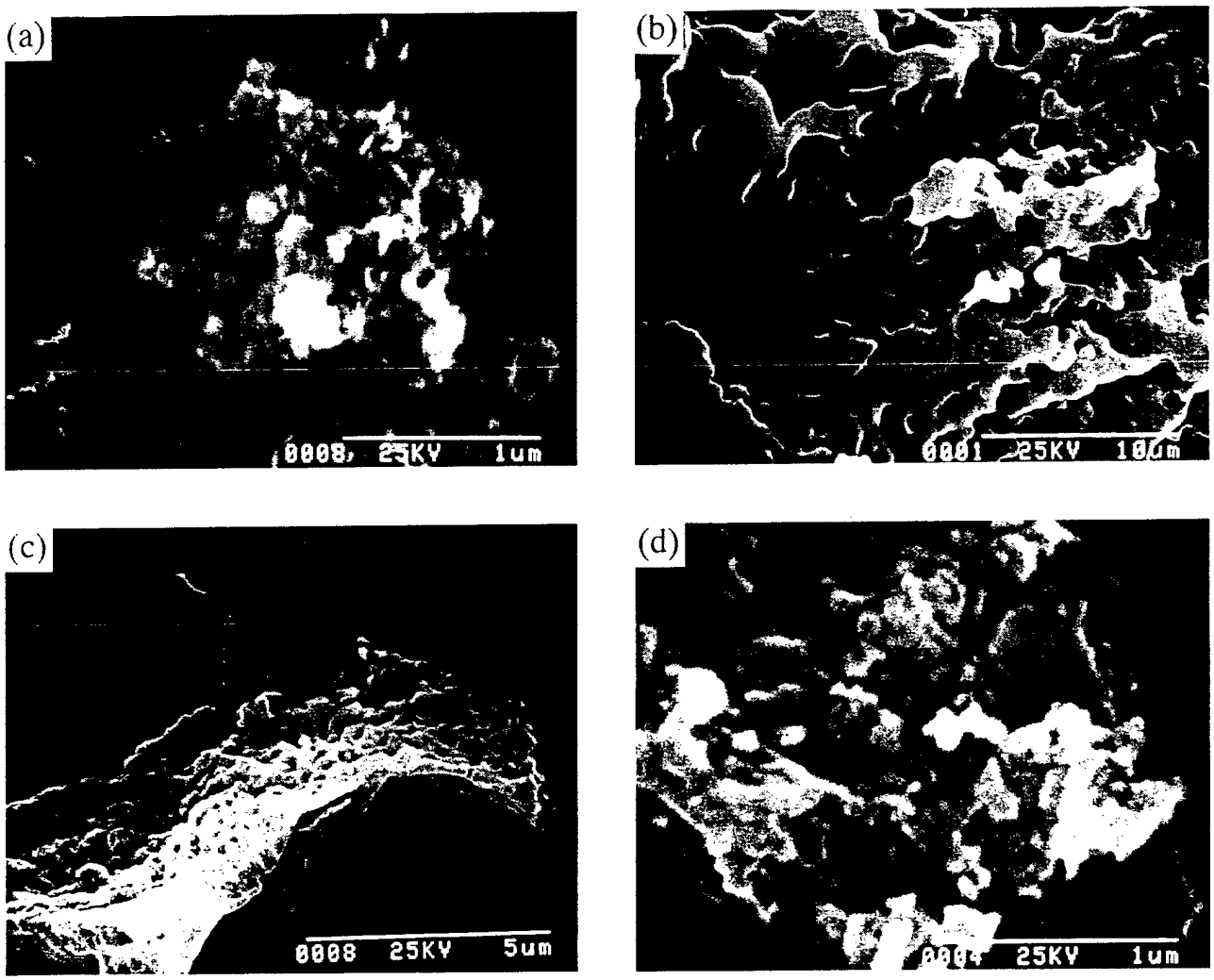


Fig. 6. Morphologies of crystalline powders for the four components of portland cement made by the low-DP PVA process at optimum PVA content (Table III): (a) C_2S powder as-calcined at 800°C for 1 h, (b) C_3S powder as-calcined at 1400°C for 1 h, (c) C_3A powder as-calcined at 1000°C for 1 h, and (d) C_4AF powder as-calcined at 700°C for 1 h.

within short range of each other and form organic precursor complexes.[3,5] Thus, as high a temperature is not required to form the compound.

Figure 2 shows the effect of PVA content on the crystallization of C_3A. The volume fraction of C_3A was determined by comparing the ratio of the integrated area of the 100% intensity peak for CaO with the 100% intensity peak for C_3A. In the low-DP PVA process, the volume fraction of C_3A increased with increased PVA. The best result was obtained with low-DP PVA in a 4:1 ratio. This implies that, in the low-DP PVA system, the higher content of PVA did not make a significant difference in the distance between cations, but rather it improved the homogeneity of the distribution of cations. In the higher-DP PVA system, the 8:1 ratio showed the highest volume fraction of C_3A. This might be attributed to the high-DP PVA chain lengths being longer than the low-DP PVA ones, so that, in the 4:1 case, the cations could not get close enough to one another to form a compound. The solution had a high viscosity with inhomogeneities caused by the entanglements of the long-chain PVA molecules in excess amount. Once this ratio was changed to 8:1, the results improved dramatically, because the metal ions could get close enough to one another to form C_3A.

Because PVA is not an expensive chemical, it may be more economical overall to use more PVA in conjunction with the lower-DP PVA, so as to achieve the best results possible, rather than calcining at 100°C higher and for 2 h longer by using the high-DP PVA. The 12:1 case is the most undesirable for both the low- and high-DP PVA, because there is simply not a high enough PVA content to make a homogeneous mixture. Agglomeration can also occur at the 12:1 PVA ratio, and, hence, the specific surface area is decreased.[5,6]

(2) BET Specific Surface Area

Table IV summarizes the BET specific surface area of each powder at the optimum crystallization conditions that have the lowest crystallization temperature. Except in the case of C_3S, the surface area increases with the use of the low-DP PVA. This may be attributed to lower crystallization and, hence, decreased sintering between particles. The higher the specific surface area, the faster the hydration, which decreases the setting time in cements.[19] Attrition milling for 1 h can also dramatically increase the specific surface area, because of the breaking up of the presintered, coarse, powder agglomerates. By attrition milling, an extra step has been added to the formation of these high-specific-surface-area powders, as well as an extra expense. However, after only 1 h of milling, the surface area is increased by >50 times in the case of C_3S and by >4 times for C_3A. C_3S is known for its ability to hydrate rapidly, to be responsible for the initial set, and to provide early

strength to portland cement.[19] These characteristics are important, because C_3S typically makes up >50% of the material.[19] Therefore, setting time can be decreased by an even greater amount, because C_3S (with a specific surface area of 50 m^2/g) hydrates faster, while providing the same strength to the cement.

A comparison is made between the low- and high-DP PVA, with reference to how the surface area changes with temperature increases. Figure 3 illustrates this behavior for C_2S, as a representative case study for each of the components of portland cement. It shows that, as the calcining temperature increases, the specific surface area decreases. This occurs in the powders made by both the low- and high-DP PVA methods. The powder made with the low-DP PVA exhibits a more negative slope than does the high-DP PVA powder. This implies that the powder made by the low-DP PVA method should have enhanced reactivity, finer particle size, and faster sintering.

Figure 4 shows the effect of PVA content on the BET specific surface area. This experiment was conducted with C_4AF calcined at 700°C, with both the low- and high-DP PVA solutions. The data remained consistent with the results from Fig. 3, in that the low-DP PVA produced powders with higher surface areas. Furthermore, Fig. 4 illustrates that the more PVA used, the higher the surface areas in the powders made from both the low- and high-DP PVA. For systems in which not enough polymer was used, agglomeration could occur. One explanation for this could be that, upon burnout, the agglomerated cation precursors lost most of the organics in the outer region. Because of the intense heat evolved from the oxidative process, organic components remained within the shell. Further application of heat caused the organics to decompose into gases and expand. The less-agglomerated particles lost most or all of the organics with the application of heat. In the case of agglomeration, during the slow decomposition of organics, the agglomerated cations were oxidized. Thus, a large powder particle-size distribution was observed. To maximize powder properties, a balance was, therefore, needed between cations and the amount of polymer.

(3) Powder Morphology

Figures 5 and 6 illustrate the morphologies of crystalline powders calcined at the lowest crystallization temperature for each compound. In the powders prepared by the high-DP PVA method (Fig. 5), particle necking resulting from sintering was observed, except in the C_4AF powder, which crystallized at low temperatures. Presintering resulted from the exceedingly high specific surface area and, hence, enhanced reactivity of the C_3A and C_3S powders, which needed a relatively high crystallization temperature to completely react all the CaO. The C_4AF powder showed a particle size distribution in the range from 50 to 400 nm.

In general, the powders derived from the low-DP PVA were more reactive than powders prepared from the high-DP PVA. For example, in the case of C_3A, the microstructure was more dense with smaller individual particle sizes (Fig. 6(c)), in comparison with the C_3A derived from the high-DP PVA (Fig. 5(c)), despite a lower crystallization temperature for the low-DP PVA method. This suggests that the low-DP PVA method was more effective in making fine and reactive powders than the high-DP PVA method. C_3S prepared from the low-DP PVA showed the same tendency as did the C_3A powder (Figs. 6(b) and 5(b)). The C_2S powder in the low-DP PVA route was crystallized before the onset of sintering. It was possible to retain a small particle size (~100 nm) without particle necking at a low crystallization temperature of 700°C (Figs. 6(a) and 5(a)). Agglomerates ~1.5 μm in size were observed. C_4AF powder derived from the low-DP PVA process exhibited nearly the same result as that obtained from the high-DP PVA system (Figs. 6(d) and 5(d)).

The morphologies of the attritor-milled C_3S and C_3A powders are seen in Fig. 7. Before attrition-milling, C_3S and C_3A powders showed quite a dense morphology because of sintering. However, attritor milling for 1 h was effective in breaking up the porous necked particles. This was clearly demonstrated for the C_3S and C_3A powders (Figs. 5(b) and 7(a) and Figs. 6(c) and 7(b), respectively). In both cases, attritor milling resulted in significant increases in specific surface area (Table IV) and, hence, reactivity.

IV. Conclusion

The four component powders of portland cement have been synthesized by the PVA solution–polymerization route. The length and amount of PVA polymer chains affected the homogeneity and distance between metal ions in the organic/inorganic precursor during the steric entrapment mechanism. More-reactive powders having higher specific surface areas were obtained by a low DP of the PVA. A ratio of 4:1 cation valences to hydroxyl functional groups produced optimum powder characteristics. The low crystallization temperature and high specific surface area of the chemically synthesized powders could economize the process of making specialty portland cement, enhance setting speed, increase strength, and lead to other desirable characteristics. The low specific surface area of the coarse, sintered powder could be improved to a higher specific surface area by an effective attrition-milling process.

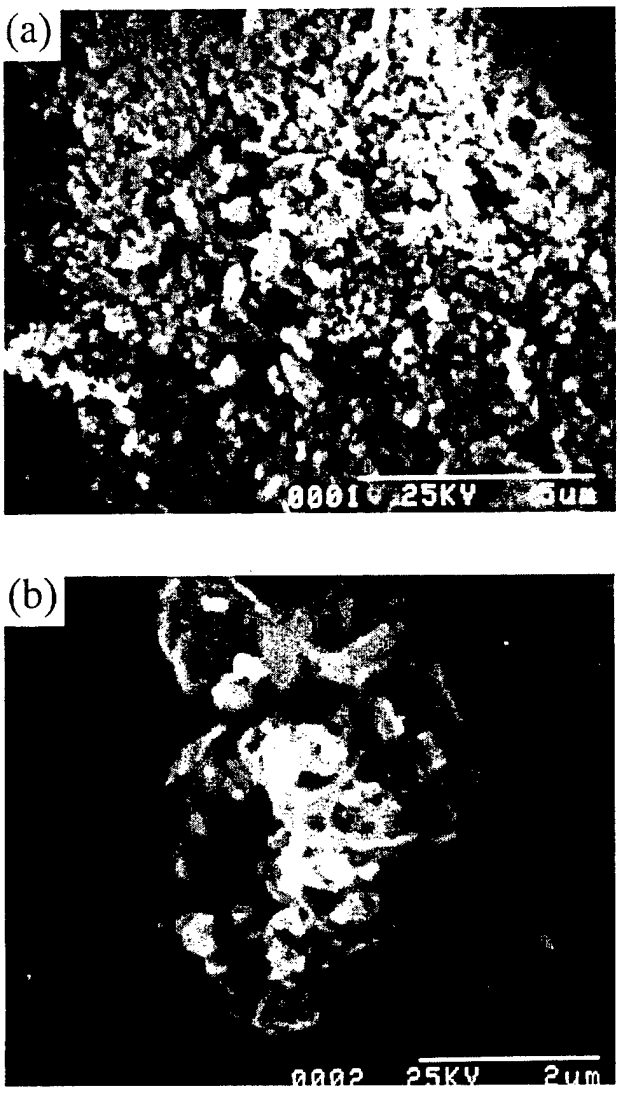


Fig. 7. Micrographs of 1 h attritor-milled crystalline powders for (a) C_3S prepared by the high-DP PVA method and (b) C_3A made by the low-DP PVA method (see also Table IV).

Acknowledgments: Use of the facilities at the Center for Advanced Cement-Based Materials at University of Illinois at Urbana-Champaign is acknowledged.

References

[1]P. Praminik and A. Pathak, "A New Chemical Route for the Preparation of Fine Particles of Mixed Oxide Systems," *Mater. Sci. Bull.*, **17** [6] 967–75 (1994).

[2]M. A. Gülgün and W. M. Kriven, "A Simple Solution–Polymerization Route for Oxide Powder Synthesis"; pp. 57–66 in Ceramic Transactions, Vol. 62, *Science, Technology, and Commercialization of Powder Synthesis and Shape Forming*. Edited by J. J. Kingsley, C. H. Schilling, and J. H. Adair. American Ceramic Society, Westerville, OH, 1995.

[3]M. A. Gülgün, M. H. Nguyen, and W. M. Kriven, "Polymerized Organic–Inorganic Synthesis of Mixed Oxides," *J. Am. Ceram. Soc.*, **82**, [3] 556–60 (1999).

[4]D. A. Fumo, M. R. Morelli, and A. M. Segadaes, "Combustion Synthesis of Calcium Aluminates," *Mater. Res. Bull.*, **31** [10] 1243–55 (1996).

[5]M. H. Nguyen, S. J. Lee, and W. M. Kriven, "Synthesis of Oxide Powders via a Polymeric Steric Entrapment Precursor Route," *J. Mater. Res.*, **14** [8] (1999), in press.

[6]M. H. Nguyen, "A New Polymer Route to the Synthesis of Mixed Oxide Ceramics"; M.S. Thesis, University of Illinois at Urbana-Champaign, IL, 1997.

[7]S. J. Lee and W. M. Kriven, "Crystallization and Densification of Nano-Size, Amorphous Cordierite Powder Prepared by a PVA Solution–Polymerization Route," *J. Am. Ceram. Soc.*, **81** [10] 2605–12 (1998).

[8]I. Nettleship, J. L. Shull, and W. M. Kriven, "Chemical Preparation and Phase Stability of Ca_2SiO_4 and Sr_2SiO_4 Powders," *J. Eur. Ceram. Soc.*, **2**, 291–98 (1993).

[9]D. M. Roy and S. O. Oyefesobi, "Preparation of Very Reactive Ca_2SiO_4 Powder," *J. Am. Ceram. Soc.*, **60**, 178–80 (1977).

[10]P. A. Lessing, "Mixed-Cation Oxide Powders via Polymeric Precursors," *Am. Ceram. Soc. Bull.*, **68** [5] 1002–1007 (1989).

[11]L.-W. Tai, H. U. Anderson, and P. A. Lessing, "Mixed-Cation Oxide Powders via Resin Intermediates Derived from a Water-Soluble Polymer," *J. Am. Ceram. Soc.*, **75** [12] 3490–94 (1992).

[12]M. A. Gülgün, O. O. Popoola, and W. M. Kriven, "Chemical Synthesis and Characterization of Calcium Aluminate Powders," *J. Am. Ceram. Soc.*, **77** [2] 531–39 (1994).

[13]M. Pechini, "Method of Preparing Lead and Alkaline-Earth Titanates and Niobates and Coating Method Using the Same to Form a Capacitor," U.S. Pat. No., 3 330 697, July 11, 1967.

[14]D. Budd and D. A. Payne, "Preparation of Strontium Titanate Ceramics and Internal Boundary Layer Capacitors by the Pechini Method," *Mater. Res. Soc. Symp. Proc.*, **32**, 239 (1984).

[15]L.-W. Tai and P. A. Lessing, "Modified Resin-Intermediate Processing of Perovskite Powders: Part I. Optimization of Polymeric Precursors," *J. Mater. Res.*, **7** [2] 502–10 (1992).

[16]D. Kralj, B. Matkovic, R. Taylor, J. F. Young, and C. J. Chan, "Preparation of Dicalcium Silicate at 950°C," *J. Am. Ceram. Soc.*, **69** [8] C-170–C-172 (1986).

[17]M. Rivera, I. Odler, and S. Abdul-Maula, "Formation of Portland Clinker—Studies on Synthetic Raw Meals," *Adv. Cem. Res.*, **1** [1] 52–57 (1987).

[18]I. Odler and H. Koster, "Investigations on the Structure of Fully Hydrated Portland Cement and Tricalcium Silicate Pastes,' *Cem. Concr. Res.*, **21** [6] 975–82 (1991).

[19]Portland Cement Association, "Portland Cement: Past and Present Characteristics," *Concr. Technol. Today*, **17** [2] 1–4 (1996).

[20]M. V. Munoz, F. G. Garcia, M. G. Rodriguez, M. C. G. Vilchez, and S. Hudson, "Influence of the Mineralogical Composition, Specific Surface Area and Strains," *Cem. Conc. Res.*, **25** [5] 1103–10 (1995). □

Journal of the European Ceramic Society 19 (1999) 2543–2550
© 1999 Elsevier Science Ltd
Printed in Great Britain. All rights reserved
PII: S0955-2219(99)00120-X
0955-2219/99/$ - see front matter

Growth and Crystallization of YAG- and Mullite-composition Glass Fibers

J. K. R. Weber,[a]* B. Cho,[a] A. D. Hixson,[a] J. G. Abadie,[a] P. C. Nordine,[a] W. M. Kriven,[b] B. R. Johnson[b] and D. Zhu[b]

[a]Containerless Research, Inc., 906 University Place, Evanston, IL 60201, USA
[b]Department of Materials Science and Engineering, University of Illinois Urbana-Champaign, Urbana, IL 61801, USA

Abstract

This paper describes a new process to synthesize crystalline oxide fibers for high temperature structural applications. Strong and chemically homogeneous precursor fibers of 5–40 μm diameter were made at rates of up to 1·6 m s^{-1} by glass fiber pulling techniques from undercooled molten oxides. The precursor fibers were heat treated at temperatures up to 1873 K to make crystalline fibers with controlled grain size and properties. Tensile strengths of the precursor fibers were up to 5–6 GPa (900 ksi) for YAG- ($Y_3Al_5O_{12}$) and mullite- ($Al_6Si_2O_{13}$) compositions. Research to optimize fiber compositions and crystallization processes, and to scale up precursor fiber production is discussed. © *1999 Elsevier Science Ltd. All rights reserved.*

Keywords: YAG, glass fibers, fibers, strength, mullite.

1 Introduction

Current technology for fiber synthesis is limited in the composition of materials from which fibers can be formed, the quality and diameters of the fibers that can be obtained, and the compatibility with coating and matrix materials that may be used in composites.[1–5] The relatively high cost of oxide fibers available for composite materials also makes research and development very expensive.[6]

It was recently shown that glass fibers can be drawn from molten oxides which are deeply undercooled to increase the melt viscosity.[7,8] By working with deeply undercooled melts, the new technique allows glass fibers to be made from materials which form 'fragile' liquids and have very low viscosity — less than 0·1 Pa s — at temperatures close to the equilibrium melting point.[9,10] Oxides of interest for high temperature structural applications such as mullite[7] ($Al_6Si_2O_{13}$) and yttrium aluminum garnet or YAG[8] ($Y_3Al_5O_{12}$) can be drawn into glass fibers in this way. Also, the high mutual solubility of many molten oxides would allow a uniform distribution of dopants or additives to be incorporated in the fibers.

Results presented later show that crystallization of mullite- and YAG-composition glass begins to occur at approximately 1200 K when the glass is heated at a rate of 2·5 K min^{-1}. The temperature at the onset of crystallization increases about 20 K when the heating rate is increased to 40 K min^{-1}. Containerless processing experiments on molten oxides achieve deep undercooling and spontaneous crystallization of the metastable liquid at somewhat higher temperatures, leading to crystal growth rates of 5–10 cm s^{-1}.[11] Since the glass fiber heating rate can be increased to several 1000 K s^{-1} by rapidly inserting the fiber into a hot furnace, crystallization can be performed over a wide range of temperatures up to the softening point of the glass fiber. The wide temperature range available for crystallization allowed control of crystal nucleation and growth rates, hence the morphology and properties of the product can be controlled and optimized.

2 Experimental

The approach to synthesis of crystalline oxide fibers comprised two steps: (i) pull glass fibers from the undercooled molten oxides, and (ii) crystallize the glass fibers by heat treatment. Table 1 presents the compositions which were investigated. Materials were synthesized from 99·999% pure elemental oxide powders (Cerac, Inc., Milwaukee, WI),

*To whom correspondence should be addressed. e-mail: weber@containerless.com

Table 1. Compositions of oxide materials investigated in fiber processing research

Aluminium oxide (mol%)	*Yttrium oxide (mol%)*	*Comment*
62·5	37·5	From crushed single crystal and mixed powders
63·5	36·5	From mixed alumina and yttria powder
62·5	36·5	+ 1 mol% Nd_2O_3
62·5	36·5	+ 1 mol% Er_2O_3
Aluminium oxide (mol%)	*Silicon dioxide (mol%)*	
60	40	From Kyoritsu mullite
58	42	From mixed alumina and silica powder
62	38	From mixed alumina and silica powder
59	40	+ 1 mol% Y_2O_3
55	40	+ 5 mol% Y_2O_3
60	39	+ 1 mol% TiO_2
60	35	+ 5 mol% TiO_2
60	39	+ 1 mol% ZrO_2
60	35	+ 5 mol% ZrO_2

Kyoritsu mullite[12] ($Al_6Si_2O_{13}$) or crushed single crystal YAG ($Y_3Al_5O_{12}$). Powder mixtures were formed into spheroids by laser hearth melting.[13] Effects of substituting cations in the mullite and YAG compositions were also investigated.

2.1 Formation of undercooled melts

In order to obtain the viscosity required to support fiber pulling, the molten oxides were undercooled below the liquidus temperature. Nucleation of the undercooled liquid was avoided by using containerless melting in an Aero-Acoustic Levitator[14] or Conical Nozzle Levitator[15] which completely eliminated contact with a solid container. In this way, the liquids could be deeply undercooled and/or cooled to form glass by reducing the heating power.

Preliminary levitation, melting and cooling experiments were performed to establish conditions under which specimens formed glass. Glass formation showed that a large increase in viscosity occurred below the melting point and that conditions which permit fiber pulling could be achieved. Material was levitated in pure argon, oxygen, or air and heated with a continuous-wave CO_2 laser beam. An automatic optical pyrometer measured the apparent temperature of the specimen at rates up to 100 Hz. Rapid cooling of the liquid was obtained by blocking the laser heating beam, and either glass formation or nucleation of crystalline materials were observed as the liquid cooled. The heat released upon nucleation and rapid crystallization of the liquid produced a rapid temperature rise (recalescence) followed by cooling of the solid material. Glass formation resulted in smooth cooling to room temperature without any discontinuity in the measured temperatures.

2.2 Fiber synthesis

The apparatus and procedure used to make most of the fibers from levitated melts is described in Ref. 8. The levitated samples were completely melted and the heating laser beam was blocked so that the drop undercooled. Fibers were pulled from the drop by rapidly introducing and withdrawing a 100 μm diameter tungsten wire stinger at a preselected temperature. Fiber pulling was performed under transient cooling conditions at pulling rates of 50–160 cm s^{-1}. Batches of 10–20 fibers up to 50 cm in length were pulled from each composition.

2.3 Crystallization

X-ray diffraction analysis confirmed that the bulk glass synthesized in the containerless experiments and the as-pulled fibers were free of detectable crystalline phases. Differential thermal analysis (DTA) experiments were performed on crushed bulk glass at heating rates from 2·5 to 40 K s^{-1} in a Netzsch STA 409 Simultaneous Thermal Analyzer.

Bulk glasses were formed from pure mullite compositions and with substituted titanium, yttrium or zirconium. The glass was annealed at 1473 K for 3 h and examined by X-ray diffraction.

Fibers were crystallized by heat treatment at temperatures above the onset temperature for crystallization and below the melting point of the crystalline solid. All of the heat treatment experiments were performed in air. Two heat treatment methods were used.

In the first method, several fibers were placed in a furnace at ambient temperature and heated at a rate of about 10 K min^{-1} to preselected maximum temperatures of 1273–1473 K. The fibers were held at the process temperature for periods of 1–4 h, and then cooled at a rate of approximately 20 K min^{-1}.

In the second method, fibers were mounted on a ceramic lance and rapidly heated by inserting the lance into a tube furnace which was preheated to temperatures of 1373–1873 K. The fibers were held in the furnace for 5–30 s and then rapidly removed and cooled to ambient temperature.

2.4 Characterization

The as-pulled glass fibers were first inspected with a 5× hand lens and their length was measured. In identifying the optimum temperature range and pulling rate for each composition, some fibers were formed that showed defects, variations in fiber diameter, and opaque regions. These fibers were not evaluated further.

Long fiber sections which showed no visible defects were identified using a video microscope

inspection technique. Fibers were mounted on a computer-controlled translation stage and scanned under the field of view of the 175× microscope. A video record of the image was reviewed to select sections of the fiber for property testing and crystallization experiments.

The strength of uniform-diameter glass fibers was measured using a fixture developed for high-modulus, single-filament materials. The fiber diameters were 5–40 μm and the gauge length was fixed at 23 mm, 580–4600 times the fiber diameter. Tests were performed in an Instron 1205 tensile testing machine equipped with a high sensitivity load cell and operated under computer control. Tensile tests were performed using a cross-head speed of 5 $\mu m\ s^{-1}$. Diameter measurements were obtained with an optical microscope prior to tensile testing.

Bend tests were performed on the crystalline fibers to determine the minimum bend radii at which fracture occurred.

Transmission electron microscopy (TEM) was used to examine selected fibers. A new technique for mounting small cross sections of monofilaments for TEM examination was developed. Specimens were made by bonding several 0·5 mm lengths of fiber into a zirconia disk which had an inside diameter of 140 μm and an outside diameter of 2·5 mm. Fiber sections were placed into the mount and set in epoxy resin. The resulting disks were polished and thinned to approximately 1–2 μm using a tripod polisher and diamond lapping film. Polished disks were mounted on a copper grid and thinned in a Gatan 600 Duo Mill ion mill with a liquid nitrogen cooled stage. TEM analysis was performed in Philips EM420 and CM12 microscopes.

3 Results

The following sections present the results of glass fiber synthesis experiments, characterization of the glass fibers, and investigation of crystallization of the glass fibers.

3.1 Fiber synthesis

Fibers could be pulled from mullite-composition melts in the apparent temperature range from 1600–1750 K, 425–575 K below the mullite liquidus temperature. The longest and best quality fibers were obtained at temperatures of about 1700 K. YAG-composition glass fibers were pulled in the apparent temperature range from 1600–1660 K, approximately 600 K below the equilibrium melting point of YAG.

X-ray diffraction studies of mullite-composition materials containing titanium, yttrium or zirconium showed that crystalline material was formed by annealing bulk glass at 1473 K for 3 h. Compositions containing 1–5 mol% titanium and 1 mol% yttrium or zirconium were single phase, had the mullite structure, and had unit cell dimensions that were slightly larger than the values for high purity mullite. The material with 5 mol% yttrium showed a higher background spectrum indicating the presence of amorphous phases. The material with 5 mol% zirconium contained mullite and zirconium silicate ($ZrSiO_4$).

The following guidelines were established for the fiber pulling process.

1. Material needs to be completely melted so that no residual nuclei remain in the liquid. This can be accomplished by superheating the levitated drops 50–100 K above the liquidus temperature.
2. Molten alumina–silica materials have a greater glass forming tendency in an oxygen atmosphere than in argon.
3. Molten alumina–yttria materials have a greater glass forming tendency in an argon atmosphere than in oxygen.[8]
4. Substitution of up 5 mol% yttrium for aluminum and up to 5 mol% zirconium or 1 mol% titanium for silicon in the mullite composition enhances glass formation and improves the quality of fibers pulled from the undercooled melt.
5. Addition of excess alumina or substitution of neodymium oxide for yttrium oxide in the YAG-composition enhances glass formation and improves the quality of fibers pulled from the undercooled melt.

The influence of dopants was significant at concentrations of 1 mol% and considerable at 5 mol%. Longer and more uniform diameter mullite-composition fibers could be pulled from the melts which contained substituted yttrium. Zirconium substitution decreased the temperature range for fiber pulling and increased the quality of the fibers. Fibers less than 5 cm long were obtained from these compositions. Material with 5 mol% titanium substituted for aluminum produced short and brittle fibers, with large diameter variations, which often fractured when they were bent slightly.

3.2 Glass fiber properties

Process conditions that resulted in defect-free sections of fiber with uniform diameters, smooth surfaces and no visible changes in appearance along the fiber over lengths of 5–30 cm were identified. Even the best fibers had defects near their ends, since the fiber pulling occurred in a transient process in which significant changes in the liquid temperature occurred as the fiber was pulled.

Figure 1 presents video microscope images of mullite- and YAG-composition glass fibers. Test

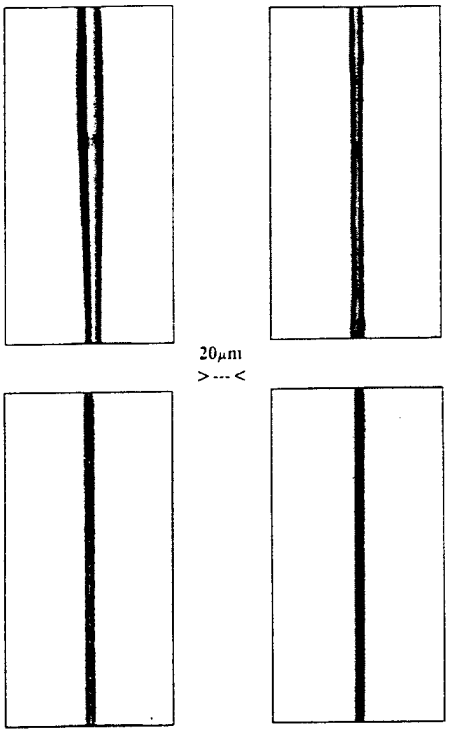


Fig. 1. Video microscope images of glass fibers. Left: mullite-composition; right: YAG-composition with 1 mol% Nd_2O_3 substituted for Y_2O_3. The top figures show characteristic defects. In mullite, regions with smoothly increasing diameter occurred along the length of the fiber. In YAG defects were localized regions where the fiber diameter changed over a distance of a few micrometers. The lower pictures show smooth sections of the fiber with uniform diameters. The scale is marked on the figure.

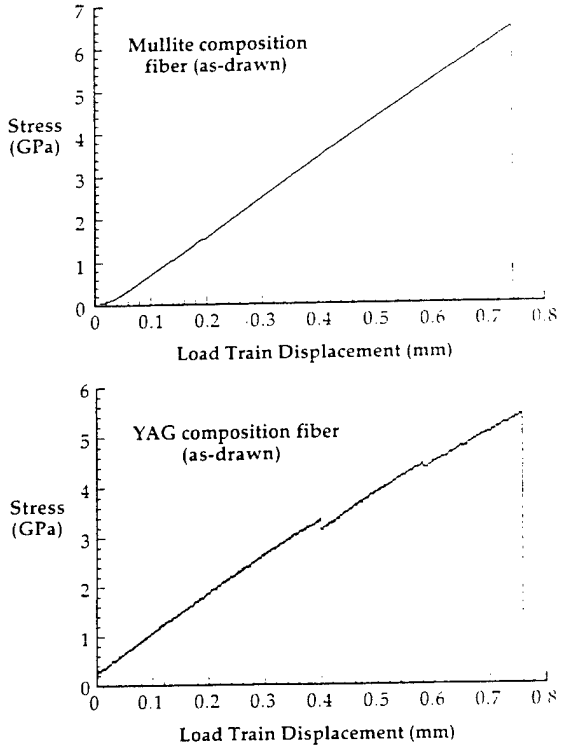


Fig. 2. Typical plots of stress versus load train displacement for selected glass fibers. Above: mullite-composition; below YAG-composition with 1 mol% neodymia substituted for yttria.

specimens were cut from uniform-diameter sections of the fibers for mechanical property testing, crystallization experiments and examination by SEM.

Figure 2 presents selected stress versus elongation plots for the glass fibers. The measurements recorded total cross-head displacement, including the load-train compliance and any movement between the fiber and the mounting, so that modulus cannot be derived from the results. Average tensile fracture strengths were $5{\cdot}6 \pm 0{\cdot}7$ GPa for the mullite-composition glass fibers and $5{\cdot}0 \pm 0{\cdot}3$ GPa for the YAG-composition fibers (with 1 mol% neodymia substituted for yttria). Both YAG- and mullite-composition glass fibers had reproducible mechanical properties. Smooth and uniform diameter mullite-composition glass fibers occasionally fractured at a stress on the order of 2 GPa. Slight movement of the fiber in the mount resulted in 'steps' in the stress-elongation plot for some fibers — see Fig. 2 for example.

3.3 Transmission electron microscopy

Figures 3 and 4 show TEM images from a mullite-composition fiber which had a tensile fracture strength of about 2 GPa, considerably less than the $5{\cdot}6 \pm 0{\cdot}7$ GPa which was obtained on other fibers. Figure 3(A) and 3(B) show regions of the fiber which contained crystallites (the dark areas) which were in the diffracting condition. The crystallites were equiaxed, had dimensions on the order of 20–50 nm, and were distributed throughout the fiber section. Figure 4(A) shows a crystallite which is approximately 75 nm across. Fig. 4(B) is the corresponding convergent beam electron diffraction pattern from this region. The diffraction pattern confirms that crystalline regions were present in the fiber. Additional TEM analysis using selected area diffraction confirmed that the crystalline material was mullite.

3.4 Crystallization

The DTA experiments performed at the slowest heating rates of $2{\cdot}5$ K min^{-1} indicated the onset of bulk glass crystallization at approximately 1233 K for mullite-composition glass and at 1188 K for YAG-composition glass. The data showed that the onset temperature increased with the heating rate and the rate of crystallization increased with temperature.

Rates of crystallization of the undercooled melt determined by observing recalescence were 3·5–15 cm s^{-1} at apparent temperatures of 1500–1800 K for the mullite composition and 1·4–6 cm s^{-1} at

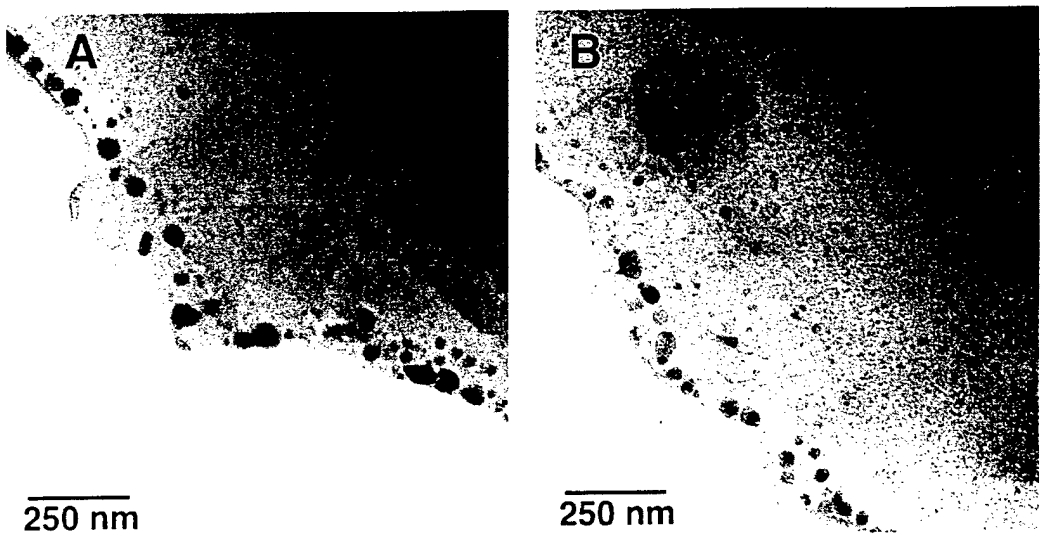


Fig. 3. (A) and (B) Bright field TEM images of an as-drawn mullite-composition glass fiber which fractured at low tensile stress. The dark areas are crystallites which were present in the fiber section.

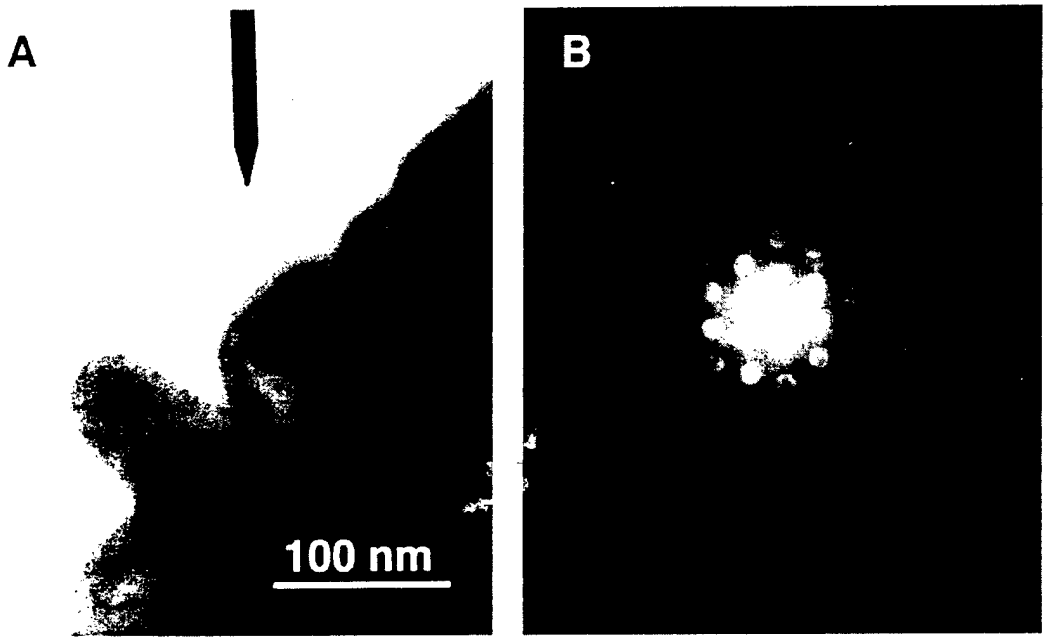


Fig. 4. (A) Bright field image of section containing a crystallite. (B) convergent beam electron diffraction image of the crystallized region.

1400–1900 K for molten YAG. The experiments with undercooled melts also demonstrated that nucleation of crystals occurs at a negligible rate in the melt at apparent temperatures above 1500 K for the mullite composition and above 1400 K for the YAG-composition.

The SEM micrographs in Figs. 5 and 6 show fibers crystallized under rapid heating conditions. Figure 5 shows longitudinal views of YAG and mullite fibers after rapid heating of the glass fibers to 1573 and 1873 K for 30 s. Figure 4 is of etched sections of mullite fibers crystallized by rapid heating to 1373 and 1673 K for 30 s followed by cooling to ambient temperature in air. The figures indicate that the grain size was rather large for the crystalline YAG fibers, on the order of 5–10 μm. Porosity is also visible in the YAG fibers. The mullite-composition glass fibers crystallized to produce dense crystalline material with grain sizes in the range 0·5–1 μm.

3.5 Properties of crystalline fibers

Crystallization of the glass fibers produced stresses that resulted in curved crystalline fibers. Some of the fibers were curled with several bends of variable radius from 2–10 mm, these were not tested.

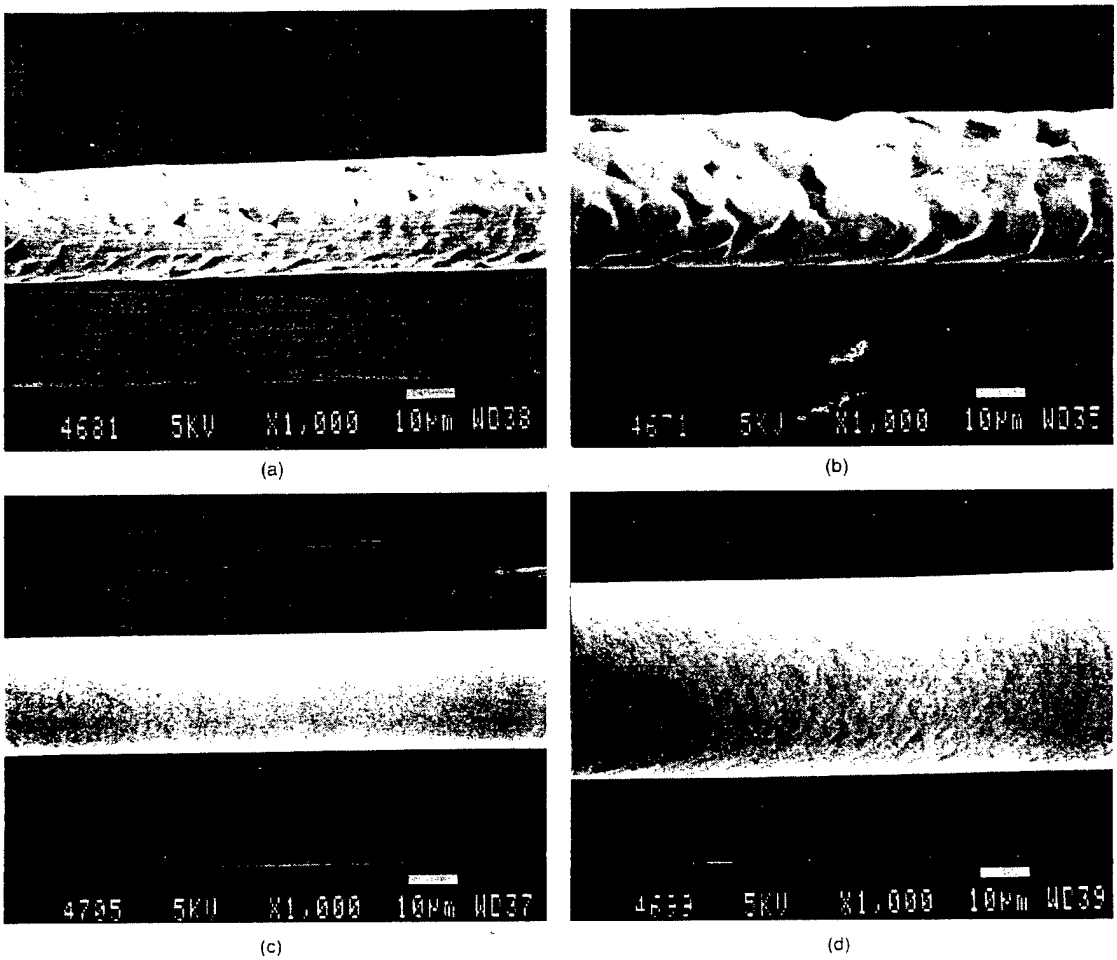


Fig. 5. SEM pictures of longitudinal views of YAG (top) and mullite (bottom) composition fibers which were crystallized by rapid heating to (left) 1573 K and (right) 1873 K and soaking for 30 s.

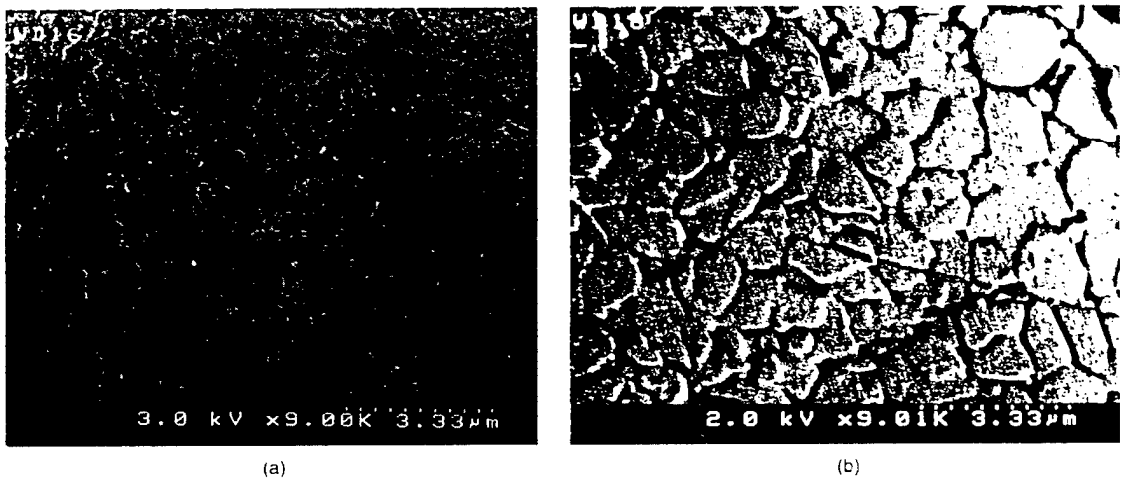


Fig. 6. SEM images of etched cross-sections of mullite fibers processed at (left) 1623 K and (right) 1873 K for 30 s.

Reproducible tensile testing of the crystallized fibers was not possible with the Instron tensile testing machine.

The tensile strength of crystallized mullite fibers was estimated by bending the fibers between the anvils of a vernier caliper. Short sections of crystallized fiber could be bent to a radius of approximately 2 mm. The minimum radius to which a fiber bent without fracture was used to calculate the tensile strain in the outer part of the curved region.

Thus for a fiber of 10 μm radius, a minimum bend radius of 2 mm corresponds to a strain of 0·5%. Using a modulus of elasticity of 360 GPa for mullite,[16] a tensile strength of 1·8 GPa is deduced.

4 Discussion

The intrinsic properties of crystalline oxides present many opportunities for application in high temperature technology. The realization of these applications would be enhanced if ceramic materials, including fibers for ceramic–ceramic composites, can be made with properties approaching the intrinsic values.

The glass fibers pulled from undercooled melts have highly reproducible properties and can be formed at high rates. The fiber pulling process creates uniform property fibers with smooth surfaces which are defined by surface tension of the liquid acting in the region where the fiber is drawn from the molten liquid. The fibers contain minimal flaws and exhibit high and reproducible values of the tensile fracture strength. TEM analysis of glass fibers which had high tensile strength indicated that they were free from crystallinity.[7] TEM analysis of mullite-composition glass fibers with decreased mechanical properties revealed that they contained nanocrystalline regions. The process by which nanocrystals are formed in some of the fibers has not been identified.

The fiber making process also allows selected additives and dopants to be added to the fibers and control of fiber diameter through changes in the fiber pulling conditions. These fibers are thus considered to be suitable precursors for investigating the production of ceramic oxide fibers by controlled crystallization of the glass.

The results demonstrate that high mechanical properties can be achieved in short sections of the crystalline fibers, as seen in the elongation results from bend tests. X-ray diffraction analysis of crystallized glass indicated that at least 1 mol% of cations can be substituted in the mullite crystal lattice and that they change the lattice parameter. Continuing work is emphasizing the study of dopant effects and control of the thermal processing on the microstructure and properties of the crystalline fibers.

The extremely rapid heat transfer that occurs from a hot ambient gas to the thin fibers allows heating rates of several thousand K s^{-1} when a fiber is inserted into a furnace. Since the levitated liquids can be formed into bulk glass at cooling rates of a few hundred K s^{-1}, it appears that the glass fibers can be heated to high temperature without nucleating crystals during the heating step. This observation explains the grain sizes observed in fibers that were rapidly heated to crystallize at high temperatures. The grain size increases with temperature, indicating that growth was enhanced relative to nucleation at the higher process temperatures.

5 Conclusions

The process of forming glass fibers from undercooled melts greatly expands the range of materials which can be made into fibers. The glass fibers have high strength, reproducible properties, and can be produced with a uniform distribution of additives. The fiber making process is inherently fast and potentially inexpensive and it can provide a source of materials for high temperature structural applications. Ongoing research is directed to scale up glass fiber production and optimize the fiber crystallization process.

Acknowledgements

This research was supported by the US Air Force Office of Scientific Research under an STTR and the US National Science Foundation. Work at University of Illinois at Urbana-Champaign (UIUC) was also supported by the AASERT Program. TEM was performed at the Center for Microanalysis of Materials in the Materials Research Laboratory at the UIUC. Earlier experiments on undercooled melts were supported by NASA. SEM photographs of rapidly crystallized fibers were taken by B.C. as part of his senior year project in Materials Science at Northwestern University under the direction of Professor Vinayak Dravid. We thank Mr William Jellison for assistance in the research.

References

1. Loewenstein, K. L., *The Manufacturing Technology of Continuous Glass Fibers*, 3rd ed. Elsevier, Amsterdam, 1993.
2. Pollock, J. T. A., Filamentary sapphire. *J. Mat. Sci.*, 1979, **7**, 787–792.
3. Haggerty, J. S., Menashi, W. P. and Wenckus, J. F., Apparatus for forming refractory fibers. US Patent 4,012,213, March 1977.
4. Sayir, A. and Farmer, S. C., Directionally solidified mullite fibers. *MRS Symp. Proc.*, 1995, **365**, 11–20.
5. Richards, E. A., Goodbrake, C. J. and Sowman, H. Z. G., Reactions and microstructure development in mullite fibers. *J. Am. Ceram. Soc.*, 1991, **74**, 2404–2409.
6. National Material Advisory Board. *Ceramic Fibers and Coatings — Advanced Materials for the Twenty-first Century*. (NMAB-494). National Academy Press, Washington, DC, 1998.
7. Kriven, W. M., Jilavi, M. H., Zhu, D., Weber, J. K. R., Cho, B., Felten, J. J. and Nordine, P. C., Synthesis and microstructure of mullite fibers grown from deeply

undercooled melts. In *Ceramic Microstructure Control at the Atomic Level*, ed. A. P. Tomsia and A. Glaeser. Plenum, New York, 1996, pp. 169–176.
8. Weber, J. K. R., Felten, J. J., Cho, B. and Nordine, P. C., Glass fibers of pure and erbium or neodymium-doped yttria-alumina compositions. *Nature*, 1998, **393**, 769–771.
9. Angell, C. A., Formation of glasses from liquids and biopolymers. *Science*, 1995, **267**, 1924–1935.
10. Debenedetti, P. G., *Metastable Liquids*. Princeton University Press, Princeton, New Jersey, 1997.
11. Weber, J. K. R., Anderson, C. D., Krishnan, S. and Nordine, P. C., Solidification behavior of undercooled liquid aluminum oxide. *J. Am. Ceram. Soc.*, 1995, **78**, 577–582.
12. Mizuno, M. and Saito, H., Preparation of highly pure fine mullite powder. *J. Am. Ceram. Soc.*, 1989, **72**, 377–382.
13. Weber, J. K. R., Felten, J. J. and Nordine, P. C., New method for high purity ceramic synthesis. *Rev. Sci. Instrum.*, 1996, **67**, 522–524.
14. Weber, J. K. R., Hampton, D. S., Merkley, D. R., Rey, C. A., Zatarski, M. M. and Nordine, P. C., Aero-acoustic levitation—a method for containerless liquid-phase processing at high temperatures. *Rev. Sci. Instrum.*, 1994, **65**, 456–465.
15. Weber, J. K. R. and Nordine, P. C., Containerless liquid-phase processing at high temperatures. *Microgravity Science and Technology*, 1995, **VII**, 279–282.
16. Kriven, W. M., Palko, J. W., Sinogeikin, S., Bass, J. D., Sayir, A., Brunauer, G., Boysen, H., Frey, F. and Schneider, J. High temperature single crystal properties of mullite ($3Al_2O_3{\cdot}2SiO_2$). *J. Eur. Ceram. Soc.*, 1999, **19**(13–14), this issue.

Reprinted from Ceramic Transactions, 108, 2000
Copyright © 2000 by The American Ceramic Society

SYNTHESIS OF OXIDE POWDERS VIA POLYMERIC STERIC ENTRAPMENT

W. M. Kriven, S. J. Lee, M. A. Gülgün, M. H. Nguyen, and D. K. Kim
Department of Materials Science and Engineering
University of Illinois at Urbana-Champaign
Urbana, IL. 61801

ABSTRACT

A new, simple, inorganic-organic polymerization method for synthesis of highly reactive, highly sinterable, oxide powders has been development in our laboratory. The method has been used to fabricate a variety of one, two and three component oxides including alumina, cristobalite, mullite, YAG, xenotime, calcium mono- and tri- aluminates, as well as mono-, di- and tri-calcium silicate, cordierite, leucite, zircon, the components of Portland cement, and various other titanates and phosphates. The polymeric carriers are polyvinyl alcohol (PVA), ethylene glycol (EG) or its polymerized form (PEG). The characteristics of such powders, e.g., specific surface areas, nanocrystallite size, and calcining vs crystallization temperatures are briefly reviewed.

INTRODUCTION

Traditionally, refractory mixed oxide powders are produced by high temperature solid state reactions. However, this route can be very cost ineffective and often leads to a final product with multiple, unwanted phases. Mixed oxide powders thus produced have low surface area and large crystallite size.[1]

Various chemical methods have been developed for the synthesis of pure, single phase mixed oxide powders with controlled powder characteristics.[2-18] Even some of these chemical routes tend to result in other phases along with the desired compound. One of the more successful techniques for single phase mixed oxide powders is the so-called Pechini process.[2] Since its invention in the 1960's, the Pechini method (and slight variations thereof) has been utilized to produce niobates, titanates, zirconates, chromites, ferrites, manganites, aluminates, cobaltites, and silicates.[2-4,6,13,15] The process describes utilization of hydroxycarboxylic acids (i.e. citric and lactic acids) in combination with polyhydroxyl alcohols such as ethylene glycol to form a resin through condensation reactions. The acid acts as a chelating agent which chemically binds the cations that are dissolved in the solution. The polymerization is based on the polyesterfication between the metal-chelate complexes and polyhydroxyl alcohols. Due to the chelating action of the hydroxy carboxylic acids and the polymeric network, the cations have low mobility, so that precipitation is hindered. The result is ceramic powders with better chemical homogeneity and smaller particle size.

To the extent authorized under the laws of the United States of America, all copyright interests in this publication are the property of The American Ceramic Society. Any duplication, reproduction, or republication of this publication or any part thereof, without the express written consent of The American Ceramic Society or fee paid to the Copyright Clearance Center, is prohibited.

In general, it is assumed that chelation, or chemical fixation of the cation by the organic molecule is a pre-requisite for a stable, multi-cation precursor. However, in the calcium aluminate system, our previous studies on Pechini precursors with very high metal ion to polymer end group ratios have shown that the precursors were able to support a higher amount of cations than they could chelate.[3] Thus, it is reasonable to suppose that other mechanisms of cation stabilization beside chelation are operative in these organo-metallic precursors. However, there are very few studies on the chemical synthesis of oxide powders via non-chelating organic precursors.[19-20]

In order to explore the possibility of synthesizing stable precursors from simpler molecules, polyvinyl alcohol (-[CH_2-CHOH]-$_n$, or PVA) and polyethylene glycol (H[O-CH_2-CH_2]-$_n$OH, PEG) were used as polymeric carriers. As seen in Fig. 1(a), PVA has only hydroxyl (-OH) group attached to every second C atom in the carbon backbone of a long-chain molecule. In PEG, (Fig. 1(b)) there are only two functional groups (also hydroxyl) at the two ends of the polymer. Thus, neither of the organics possesses chemical chelating capabilities. In this study, we report on the synthesis of various mixed oxides and phosphates using a relatively simple, long-chain polymer as a carrier for the ceramic precursor. By using the polymer complexation process, ceramic powders are synthesized much more easily than in other chemical synthesis routes.[21-30] The PVA ensures the homogenous distribution of the metal ions in its polymeric network structure and inhibits their segregation and/or precipitation from the solution. Water is able to diffuse through the polymer and stretch it due to the acetate clusters. In the solution, the long chain polymer prevents contact between cations and limits their agglomeration and precipitation. A schematic representation of the cationic entrapment mechanism is shown in Fig. 2. The amount of polymer and its molecular length can affect the distribution of cations. The optimum amount and chain length of PVA result in a pure, highly reactive, and homogenous powder at the molecular level. It is speculated that weak hydrogen bonding promotes homogeneous physical entrapment between the -(OH) hydroxyl groups and cations which are solvated by water molecules. The PVA process also produces carbonaceous material that gives heat through its combustion, so that fine and single phase powders can be formed at a relatively low external temperature. For systems in which not enough polymer is used, agglomeration may occur. Upon burnout, the agglomerated cation precursors lose much of their organics in the outer regions Due to the intense heat evolved from the oxidative process, polymer and organic components remain within the shell. Further application of heat causes the organic to decompose into gases and expand, and makes oxides by combustion synthesis. The less-agglomerated particles have lost most or all of the organics with application of heat. Thus, a large powder particle size distribution is observed. To maximize the powder properties, a balance is needed between the precursors and the amount of polymer. In this study, the polymeric steric entrapment route is introduced and the oxide powders derived from this method are reviewed.

EXPERIMENTAL PROCEDURE

(1) Powder Synthesis

In the PVA process, nitrate salts were in the form of cation sources with the exception of silica which was supplied as a colloidal silica product. Diammonium hydrogen phosphate was used as the source of phosphorus. These cation sources were dissolved in stoichiometric proportions in de-ionized (DI) water. Once the cation sources were completely dissolved, the 5 wt% PVA (Air Products and Chemicals, Inc., Airvol Series, Allentown, PA) was dissolved in DI water and added.

The proportions of the PVA to cation sources in the solution were adjusted in such a way that there were 4, 8, or 12 times more positively charged valences from the cations than from the potentially negatively charged -(OH) functional groups of the polymers. The polymeric long chains have hydroxyl groups in solution. Hence, one PVA monomer, which has one hydroxyl (OH) functional group, can be used as an unit for calculation of PVA content. The exact relative amount of PVA to cations in the solution can be calculated with reference to a monomeric unit of PVA.

Water was evaporated by continuous stirring during heating on a hot plate. The resulting gel-type precursor was completely dried after several hours at 100°C. In titanium oxide compounds, titanium (IV) isopropoxide was dissolved in stoichiometric proportions in liquid-type ethylene glycol. Barium nitrite or nitrate salts were used as the source of Ba and other cations, respectively. The amount of ethylene glycol was calculated using a ratio of total weight of metal ions from cation sources to weight of ethylene glycol. The nitrite or nitrate salts were first added to the ethylene glycol and heated to 80 °C, while mixing, until it was fully dissolved. Then, the titanium (IV) isopropoxide was slowly added, while stirring. The solution was then allowed to gel for 48 h in a drying oven at 50 °C. In the case of the PEG method, a transparent sol was prepared from zirconium 2,4-pentanedionate, which is a water-insoluble chemical, and aluminum nitrate in proportions of 50:50 vol%. After dissolving these reagents in ethanol, the organic carrier, PEG (of M.W.: 2000) was added, and the mixture was stirred and heated at 80 °C. The amount of PEG was calculated using a ratio of total weight of metal ions from cation sources to weight of PEG. As the viscosity increased by evaporation of ethyl alcohol, the sol turned to a syrup-like gel. Subsequently, a vigorous exothermic reaction occurred which, with continuous heating at 80 °C, converted the gel into an expanded, porous solid.

The organic/inorganic precursors in the all cases were then ground and were calcined or crystallized at various temperatures in an air atmosphere in a box furnace. Some powders were milled using an attritor mill to examine the effects of milling on the surface area. The powders were attritor milled at 240 rpms for 1 hour using zirconia milling media (ball diameter : 5mm) and isopropyl alcohol as a solvent for milling.

(2) Characterization

(A) X-ray Diffraction Analysis The crystallization behavior of each of the calcined powders was studied as a function of temperature and holding time at elevated temperatures, using a Rigaku X-ray diffractometer (Dmax automated powder diffractometer, Rigaku/USA, Danvers, MA) with CuK_α radiation (40 kV, 40 mA). All

XRD data was obtained at room temperature, after the powder had been cooled. A scanning speed of 10 °/min with a sampling interval of 0.02°.

(B) Specific Surface Area Measurement: : The specific surface area of the crystallized powders and attrition milled powders were obtained by five-point BET analysis from nitrogen gas adsorption (Model ASAP 2400, Micromeritics, Norcross, GA). All samples for testing were kept in a dry oven to prevent hydration of the powders.

(C) *Microstructure Characterization* : The morphologies of calcined, crystallized, and/or attrition-milled powders were examined by scanning electron microscopy, SEM (Model Hitachi S530, Hitachi, Japan). For the SEM specimens, each powder was completely dried, attached to an aluminum stub, and gold sputter coated.

RESULTS AND DISCUSSION

The organic-inorganic precursors derived from the PVA process resembled an aerogel and were formed by the development of foam during the stirring and solution drying process. The foam was generated during evolution of NO_x gas caused by the decomposition of the nitrates. The expansion of the gel due to the evolving NO_x gas continued until the precursors dried completely. In the EG method, the solution was pale yellow and transparent after all the chemicals were dissolved in ethylene glycol. During the drying process at 50 °C, the transparent gel turned to a yellow-colored solid gel. In PEG method, the syrup-like, precursor gel was quite flammable because of ethyl alcohol solvent and had a vigorous exothermic reaction on continuous heating. After the reaction, the gel changed to a sooty, porous solid having about a 20-fold volume expansion.

The summary of oxide powders prepared by the inorganic-organic polymerization method, and the applied methods and chemical sources for each powder were listed in Table I, and II, respectively. For the chemical sources which are insoluble to water, PVA method was substituted for PEG and EG methods. Most of cases, the calcination temperatures were below 800 °C in an air atmosphere. This means the carrier polymers were easily burnt out by the oxidation process. Once the cations are complexed and/or trapped within the polymer, heat is used to remove the polymer. For systems in which not enough polymer is used, agglomeration may occur. Upon burnout, the agglomerated cation precursors lose much of their organics in the outer regions Due to the intense heat evolved from the oxidative process, polymer and organic components remain within the shell. Further application of heat causes the organic to decompose into gases and expand Thus, a large powder particle size distribution is observed The less-agglomerated particles have lost most or all of the organics with application of heat. To maximize the powder properties, a balance is needed between the precursors and the amount of polymer.[28]

The crystallization temperatures showed a difference for each case. In some powders, the crystallization temperatures were much lower than those of other powders prepared by other chemical synthesis. In particular, titanate compounds derived from the EG method showed low crystallization temperatures close to their calcination temperatures In the case of alumina, the crystalline development was different according to the D.P. (degree of polymerization) of polymer carrier. At high D.P of PVA, gamma phase was detected at 1100 °C. The powders prepared by the inorganic-organic polymerization method had extremely high specific surface

areas. The polymer content and its degree of polymerization affected the surface area and morphology.[27] Some powders such as cordierite, alumina and tricalcium silicate were soft agglomerated and easily break out to fine particles after attrition milling. Despite the production of nano-size particles, the calcium aluminate, barium titanate, and xenotime showed low specific surface areas of 12.0, 5.6, and 12.0 m^2/g, respectively, because the powders contained hard-agglomerated, pre-sintered particles. The SEM and TEM micrographs of the representative porous calcined powder and the nano-size powders are shown in the Fig. 3. The SEM micrograph of barium titanate powder revealed nanosized particles with a narrow particle size distribution. The particles were already presintered, suggesting that the nano-size powder was quite reactive even at low temperatures. The powders after ball milling for 1 h increased their surface area to 15 m^2/g, which resulted from breaking up of the presintered particles.

The comparison between the Pechini resin process and the PVA solution process in the cordierite powder is listed in Table III. A high yield of 59%, which is more than double in comparison with the Pechini resin process, was observed in the PVA solution process. A small weight loss was observed during calcination in the PVA solution process. This loss was consistent with the lesser amount of PVA being used in this process, as PVA has a greater effective work of polymerization. In both cases, infinitesimal residual carbon (below 0.1 wt%) was detected in the calcined powders. The powder derived from the Pechini resin had a narrower particle size distribution of 3-50 μm than did the PVA solution process. The precursor derived from the Pechini resin could be ground easily due to the larger amount of organic carrier involved. The development of crystalline phases for each case showed different behavior. In the amorphous-type cordierite derived from the Pechini resin, the α-cordierite was formed without a sequential formation of crystalline cordierite (amorphous→μ→α). However, the cordierite derived from the PVA solution revealed the intermediate μ-phase crystalline cordierite before the crystallization of α-phase. The formation of μ-cordierite was also observed in the sol-gel powder preparation process.[31] In the synthesis of cordierite, the formation of μ-phase reduced the chances of forming other silicate compounds, such as spinel and cristobalite, or the residual cordierite-type amorphous phase.[31,32]

CONCLUSIONS

A polymerized organic-inorganic complex route was successfully employed to synthesize various monophase, fine and pure, mixed oxide powders. The new technique uses simple long-chain polymers like polyvinyl alcohol (-[CH_2-CHOH]-$_n$, PVA) or polyethylene glycol (H[O-CH_2-CH_2]-$_n$OH, PEG) as the organic carrier for the pre-ceramic gel. The results show that metal ion chelation of the solution polymerization method is not the only mechanism to obtain molecularly homogeneous, stable precursors for complex mixed oxide powders. The cations of the mixed oxide are sterically entrapped in the entangled network of the organic polymers. In particular, this method had a higher powder yield than other chemical

synthesis methods and could be extended to even chemicals that decompose in water, such as titanium isopropoxide.

ACKNOWLEDGEMENT

This work was partially supported by an AFOSR AASERT Grant #F49620-97-1-0427.

REFERENCES

[1]K. Fujii, W. Kondo, and H. Ueno, "Kinetics of Hydration of Monocalcium Aluminate," *J. Am. Ceram. Soc.*, **69**[4] 361-364 (1986).

[2]M. Pechini, "Method of Preparing Lead and Alkaline-Earth Titanates and Niobates and Coating Method Using the Same to Form a Capacitor," U.S. Pat. No. 3 330 697, July 11, 1967.

[3]M.A. Gülgün, O.O. Popoola and W.M. Kriven, "Chemical Synthesis and Characterization of Calcium Aluminate Powders," *J. Am. Ceram. Soc.*, 77[2] 531-539 (1994).

[4]M.A. Gülgün, O.O. Popoola, I. Nettleship, W.M. Kriven and J.F. Young, "Preparation and Hydration Behavior of Pure $CaAl_2O_4$," pp. 199-204 in Advanced Cementitious Systems: Mechanisms and Properties, Proceedings of the Materials Research Society Symposium (Boston, MA, December, 1992). Vol. **245**, edited by F.P. Glasser, P.L. Pratt, T.O. Mason, J.F. Young, and G.J. McCarthy. Materials Research Society, Pittsburgh, PA, (1992).

[5]L.W. Tai and P.A. Lessing, "Modified Resin-Intermediate Processing of Perovskite Powders: Part I. Optimization of Polymeric Precursors," *J. Mater. Res.*, 7[2] 502-510 (1992).

[6]L.W. Tai and P.A. Lessing, "Modified Resin-Intermediate Processing of Perovskite Powders: Part II. Processing for Fine, Nonagglomerated Sr-Doped Lanthanum Chromite Powders," *J. Mater. Res.*, 7[2] 511-519 (1992).

[7]S.C. Zhang, G.L. Messing, W. Huebner and M.M. Coleman, "Synthesis of $Yba_2Cu_3O_{7-x}$ Fibers from an Organic Acid," *J. Mater. Res.*, **5**[9] 1806-1812 (1990).

[8]P.A. Lessing, "Mixed-Cation Oxide Powders via Polymeric Precursors," *Am. Ceram. Soc. Bull.*, **68**[5] 1002-1007 (1989).

[9]L.W. Tai, H.U. Anderson, and P.A. Lessing, "Mixed-Cation Oxide Powders via Resin Intermediates Derived from a Water Soluble Polymer," *J. Am. Ceram. Soc.*, **75**[12] 3490-3494 (1992).

[10]H.U. Anderson, M.J. Pennell and J.P. Guha, "Polymeric Synthesis of Lead Magnesium Niobate Powders," in Advances in Ceramics, Vol. 21: *Ceramic Powders Science*, Am. Ceram. Soc., Westeville, OH (1987), p. 91.

[11]N.G. Eror and H.U. Anderson, "Polymeric Synthesis of Ceramic Materials," *Mater. Res. Soc. Symp. Proc.*, **73**, Materials Research Society, Pittburgh, PA (1986), p. 571.

[12]G. DeWith, "Preparation, Microstructure and Properties of $Y_3Al_5O_{12}$ Ceramics," *Phillips J. Res.*, **42**, 119-130 (1987).

[13]D.R. Messier and G.E. Gazza, "Synthesis of $MgAl_2O_4$ and by Thermal Decomposition of Hydrated Nitrate Mixtures," *Am. Ceram Soc. Bull.*, **51**[9] 692-697 (1972).

[14]L.P. Motozova, E.S. Lukin, T.V. Efimovskaya, A.V. Smolya, I.F. Panteleeva, "Synthesis of Aluminum Yttrium Garnet," *Glass. Ceram.*, **35**, 158 (1978).

[15]O.J. Sordolet, M. Akinc, M. Panchula, Y. Han, M.H. Han, "Synthesis of Yttrium Aluminum Garnet Precursor Powders by Homogeneous Precipitation," *J. Euro Ceram. Soc.*, **14**, 123-130 (1994).

[16]D.M. Roy, R.R. Neurgaonkar, T.P. O'Holleran and R. Roy, "Preparation of Fine Oxide Powders by Evaporative Decomposition of Solutions," *Am. Ceram. Soc. Bull.*, **56**[11] 1023-1024 (1977).

[17]I. Nettleship, J.L. Shull, Jr., and W.M. Kriven, "Chemical Preparation and Phase Stability of Ca_2SiO_4 and Sr_2SiO_4 Powders," *J. Euro. Ceram. Soc.*, **11**, 291-298 (1993).

[18]M. Kakihana, M. Arima, M. Yashima, M. Yoshimura, H. Mazaki, and H. Yasuoka, "Chemical Design for Functional Multi-Component Oxides by Polymerized Complex Method," *Trans. Mat. Res. Soc. Jpn.*, **14A**, *Advanced Materials '93, I A: Ceramics, Powders, Corrosion and Advanced Processing*, edited by N. Mizutani et al., Elsevier Sci., 1994, pp. 801-806.

[19]P. Pramanik and A. Pathak, "A New Chemical Route for the Preparation of Fine Ferrite Powders," *Bull. Mater. Sci.*, **17**[6] 967-975 (1994).

[20]S. Kumar Saha, A. Pathak, and P. Pramanik, "Low-Temperature Preparation of Fine Particles of Mixed Oxide Systems," *J. Mater. Sci. Lettr.*, **14**, 35-37 (1995).

[21]P. Praminik and A. Pathak, "A New Chemical Route for the Preparation of Fine Particles of Mixed Oxide Systems," *Mater. Sci. Bull.* **17**[6] 967-975 (1994).

[22]M.A. Gülgün and W.M. Kriven, "A Simple Solution-Polymerization Route for Oxide Powder Synthesis," pp. 57-66 *Ceramic Transactions*, **62** Edited by J.J. Kingsley, C.H. Schilling and J.H. Adair. American Ceramics Society, Westerville (1995).

[23]D.A. Fumo, M.R. Morelli, and A.M. Segadaes, "Combustion Synthesis of Calcium Aluminates," *Mater. Res. Bull.*, **31**[10] 1243-1255 (1996).

[24]M.H. Nguyen, *A New Polymer Route to the Synthesis of Mixed Oxide Ceramics*, M.S. Thesis, University of Illinois at Urbana-Champaign, 1997.

[25]S.J. Lee and W.M. Kriven, "Crystallization and Densification of Nano-Size, Amorphous Cordierite Powder Prepared by a PVA Solution-Polymerization Route," *J. Am. Ceram. Soc.*, **81**[10] 2605-12 (1998).

[26]S.J. Lee and W.M. Kriven, "A Preparation of Ceramic Powders by Solution Polymerization Route Employing PVA Solution," *Ceram. Eng. & Sci. Proc.* **19**[4] 469-476 (1998).

[27]S.J. Lee, E.A. Benson, and W.M. Kriven, "Preparation of Portland Cement Components by PVA Solution Polymerization," *J. Am. Ceram. Soc.*, **82**[8] 2049-55 (1999).

[28]M.H. Nguyen, S.J. Lee, and W.M. Kriven, "Synthesis of Oxide Powders Via a Polymeric Steric Entrapment Precursor Route," in press *J. Mater. Res.*, **14**[8] (1999).

[29]S.J. Lee, M.D. Biegalski and W.M. Kriven, "Preparation and Properties of Barium Titanate and Barium Orthotitanate Powders Through Ethylene Glycol Polymerization Route," *J. Mater. Res.*, **14**[7] 3001-3006 (1999).

[30]S.J. Lee and W.M. Kriven, "A Submicron-Scale Duplex Zirconia and Alumina Composite by Polymer Complexation Processing," in press *Ceram. Eng. & Sci. Proc.* (1999).

[31]H. Suzuki, K. Ota, and H. Saito, "Preparation of Cordierite Ceramics from Metal Alkoxides (Part I. Preparation and Characterization of the Powder)," *Yogyo-Kyokai-Shi*, **95** [2] 28-31 (1987).

[32]H.Y. Jang and B.C. Lim, "Effect of the Scale of Precursor Mixing on Densification Behaviors and Phase-Transformation Kinetics of Cordierite Gels," *J. Mater. Res.*, **9** [10] 2627-2633 (1994).

Table I. Summary of Oxide Powders Prepared by Inorganic-Organic Polymerization Method (Polymeric carrier : poly vinyl alcohol (PVA), poly ethylene glycol (PEG), ethylene glycol (EG)).

Compound	Heating temperature (°C)		Specific surface area (m^2/g)		Particle size (μm)	
	Calcination	Crystallization	amorphous	crystalline	as-calcined	attrition-milled
Alumina (Al_2O_3)	800	1150	83	6.2*		0.1-0.3†
β-Cristobalite (SiO_2)	800	1100	188			0.3
Mullite ($Al_6Si_2O_{13}$)	800	1300	157			0.1
Zircon ($ZrSiO_4$)	800	1100	81			0.2-0.3
Wollastonite ($CaSiO_3$)	800	800		18	0.7	0.2†
Calcium aluminate ($CaAl_2O_4$)	650	900	12		60 nm (hard aggl.)	
Belite (β-Ca_2SiO_4 or C_2S)	700	800		22.1	0.3-0.4	
Alite (Ca_3SiO_5 or C_3S)	700	1400		0.9§	3.0-5.0	0.2-0.4†
C_3A ($Ca_3Al_2O_6$)	700	1000		4.2	0.5-1.0	
C_4AF ($Ca_4Al_2Fe_2O_{10}$)	700	700		17.1	0.1-0.2	
YAG ($Y_3Al_5O_{12}$)	600	900	56	17		
Leucite ($KAlSi_2O_6$)	750	1000	50	0.2	5.0	0.5
Hexacelsian ($BaAl_2Si_2O_8$)	800	1100	79			0.5
Cordierite ($Mg_2Al_4Si_5O_{18}$)	800	1200	181 (attrition milled)			30 nm

Table I.(Cont.) Summary of Oxide Powders Prepared by Inorganic-Organic Polymerization Method (Polymeric carrier : poly vinyl alcohol (PVA), poly ethylene glycol (PEG), ethylene glycol (EG)).

Compound	Heating temperature (°C)		Specific surface area (m^2/g)		Particle size (μm)	
	Calcination	Crystallization	amorphous	crystalline	as-calcined	attrition-milled
Barium titanate ($BaTiO_3$)	700	700		5.6	0.1 (hard aggl.)	
Barium orthotitanate (Ba_2TiO_4)	700	1000				
Dysprosium titanate (Dy_2TiO_5)	800	800				0.2
Yttrium titanate (Y_2TiO_5)	850	850				
Alumina-zirconia composite (Al_2O_3•ZrO_2)	700	1300				0.5
Nickel aluminate ($NiAl_2O_4$)	800	1000	10	4		
Calcium phosphate (CaP_2O_6)	700	900				
Xenotime (YPO_4)	500	830	12		70 nm (hard aggl.)	
Aluminum phosphate ($AlPO_4$)	800	800	136	87	10†	0.9†
Lithium phosphate ($LiPO_4$)	700	800				

§after attrition milling for 1 h : 50 m^2/g

*after attrition milling for 1 h : 55 m^2/g

†crystalline form

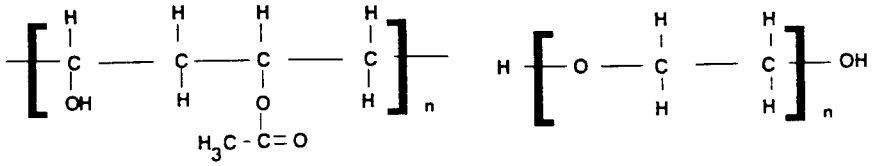
Table II. Polymerization Methods and Chemical Sources for Each Compound.

Polymer carrier	Compound	Chemical source
Polyvinyl alcohol (PVA)	Al_2O_3, SiO_2, $Al_6Si_2O_{13}$, $ZrSiO_4$, $CaAl_2O_4$, $Y_3Al_5O_{12}$, $AlPO_4$, $KAlSi_2O_6$, $BaAl_2Si_2O_8$, $NiAl_2O_4$, $Mg_2Al_4Si_5O_{18}$, CaP_2O_6, $LiPO_4$, $CaSiO_3$, Ca_2SiO_4, Ca_3SiO_5, $Ca_4Al_2Fe_2O_{10}$	nitrate salts (most cases), colloidal silica (for SiO_2), diammonium hydrogen-phosphate
Ethylene glycol (EG)	$BaTiO_3$, Ba_2TiO_4, Dy_2TiO_5, Y_2TiO_5	nitrate salts, barium nitrite, titanium isopropoxide
Polyethylene glycol (PEG)	Al_2O_3•ZrO_2 composite	aluminum nitrate, zirconium 2,4-pentanedionate

Table III. Comparison between Pechini Resin Process and PVA Solution - Polymerization Process in the Synthesis of Cordierite.

Polymeric carrier	†Powder yield (%)	Residual carbon (wt%)	Particle size Distribution (μm)	Phase change
Pechini resin	27	0.07	3-50	amorphous→α
PVA solution	59	0.06	1-100	amorphous→μ →α

†Powder yield = (weight of calcined powder / weight of precursor) × 100



(a) (b)

Fig. 1. Schematic formula for polyvinyl alcohol (PVA) and polyethylene glycol (PEG). (a) PVA and (b) PEG.

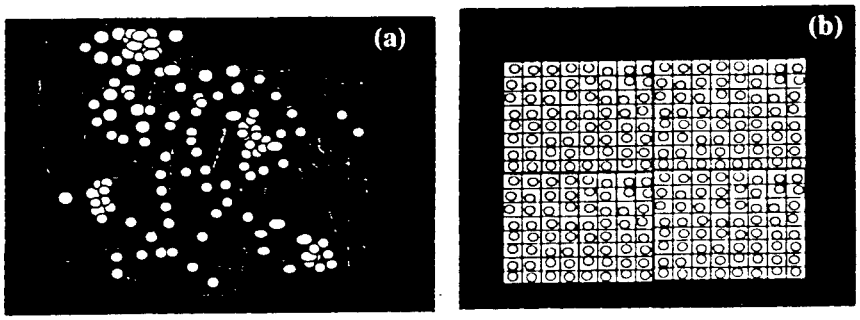


Fig. 2. Schematic of cationic entrapment with (a) small amount of polymer and (b) optimal amount of polymer.
Excess or not enough polymer results in large particle size distributions whereas the optimal amount should give a more uniform distribution.

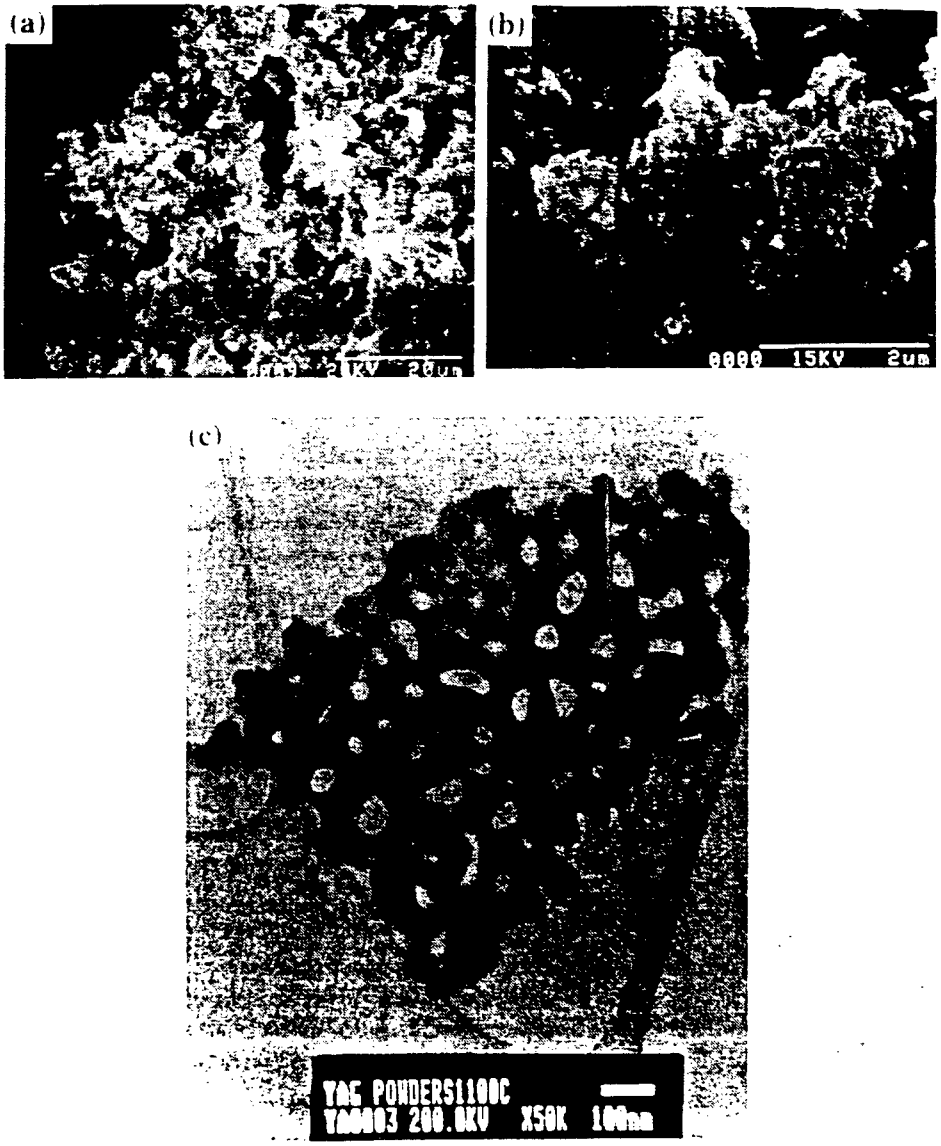


Fig. 3. SEM and TEM micrographs of calcined powders derived from polymeric steric entrapment route (a) monocalcium silicate (SEM), (b) barium titanate (SEM), and (c) YAG (TEM).

Electrosynthesis and microstructural characterization of anodic VO_x films

J.P. Schreckenbach, D. Butte, and G. Marx
Institut für Chemie, Technische Universität Chemnitz, D-09111 Chemnitz, Germany

B.R. Johnson and W.M. Kriven
Department of Materials Science and Engineering, University of Illinois at Urbana-Champaign, Urbana, Illinois 61801

(Received 30 September 1999; accepted 27 March 2000)

Anodic conversion films of vanadium oxides on vanadium were potentiodynamically generated at high voltages in an acetate electrolyte system. The microstructure of the anodic VO_x coatings was characterized by surface and solid-state techniques such as scanning electron microscopy, transmission electron microscopy, Raman spectroscopy, and x-ray photoelectron spectroscopy. An amorphous structure is proposed in which network-forming $[VO_4]$ tetrahedra in various degrees of condensation are connected by distorted $[VO_5]$ and $[VO_6]$ units. Such polyhedra lead to the formation of nanocrystalline phases of stoichiometric and substoichiometric vanadium oxides, which were observed in the amorphous phase.

I. INTRODUCTION

Anodic films on transition metals are of widespread scientific and commercial interest because of their unique physical and chemical properties. They are used in numerous high-technology areas including electronic devices, adhesive bonding, corrosion resistance, or advanced biomaterials.[1–3] Many researchers have studied the structure and growth mechanisms in anodic films, in particular porous alumina on aluminum metal.[1,4] However, the complex structure–property relationships are still not well understood. In comparison with the more widely investigated anodic film-forming metals such as tantalum or aluminum, studies of the structure of anodic conversion films on vanadium, deposited in aqueous and nonaqueous systems, have rarely been published.

There are several different ways to prepare native oxide films on vanadium metal, in addition to anodic deposition. For example, coating techniques such as sol-gel spin coating, flash evaporation, and vacuum or electron beam evaporation are increasingly used for the fabrication of vanadium oxide films, because of their potential applications such as catalysts, electrochromic devices, or high-energy density lithium microbatteries.[5–8]

The first published attempts to prepare anodic vanadium oxides in acetic acid solutions and to identify the anodic conversion films formed were reported by Keil and Salomon.[9] The films were studied by attenuated total reflectance spectra, and the results were characteristic of V_2O_4 structures. Extended investigations of the microstructure and stoichiometry of anodic films on vanadium were published by Arora and Kelly.[10] The anodic films were generated at voltages of 4 and 6 V, respectively. Reflection electron diffraction (REED) examinations of films exhibited very weak diffraction patterns of an unidentified oxide. At voltages higher than 6 V, amorphous films were produced. Hornkjoel,[11] who used chemical analysis and x-ray photoelectron spectroscopy (XPS) to show that the oxide film contained pentavalent vanadium, studied the anodic behavior of vanadium in acid electrolytes.

The reason for the different interpretations of anodic vanadium oxide films is due to the aliovalent nature of vanadium. These result in a large number of different vanadium oxide compounds, many of which have similar crystallographic structures. The most common oxidation states for vanadium are from +2 to +5, where the corresponding oxides are VO and V_2O_5, respectively. Additionally, vanadium has a tendency to polymerize through oxygen links, to form highly stable polymeric V–O–V–O–V linkages.[12] The most prevalent vanadium oxide is V_2O_5, which has an orthorhombic unit cell structure (space group *Pmmn*, No. 59). The coordination of the vanadium ions in V_2O_5 may be considered to be either distorted trigonal bipyramidal, distorted tetragonal pyramidal, or a distorted octahedron with one V–O bond of 279 pm. This structure is usually described as chains of edge-sharing $[VO_5]$ square pyramids.[7,13,14]

The present study was undertaken to characterize the surface morphology and the microstructure of anodic vanadium oxide films prepared by high electrical field anodization. Analysis of the structure and composition of noncrystalline, thin solid films requires the application of various analytical techniques to complement each other

 © 2000 Materials Research Society

and to overcome the limits of each technique. The specimens were investigated by scanning electron microscopy (SEM), transmission electron microscopy (TEM), Raman spectroscopy (RS) and XPS. On the basis of these observations, a possible constitution of the oxide film is proposed.

II. EXPERIMENTAL PROCEDURES

A. Preparation of films

Strips of vanadium metal foil (Aldrich Chemical Co., Milwaukee, WI, 99.7% pure) 0.127 mm thick and approximately 3 cm long by 0.5 cm wide were chosen for anodization. The electrolyte used to deposit anodic coatings on all of the specimens characterized in this investigation consisted of glacial acetic acid, and contained 0.02 mol/l borax ($Na_2B_4O_7$) and 1 mol/l water. Initially, various electrolyte compositions were examined to determine the optimum mixture. The concentration of water used in the electrolyte was varied, up to 5 mol/l. As the water concentration was increased, there was a decrease in the consistency of the coating quality from batch to batch. The experiments were carried out with rectangular vanadium foil as the anode, having a combined surface area of both sides up to 4 cm^2. The specimens were first cleaned in acetone, then electrochemically polished in a mixture of 80% methanol and 20% sulfuric acid for 1 min at 15 V, and finally rinsed in deionized water and dried. The cathode was platinum wire of approximately 0.5 mm in diameter. The electrochemical cell consisted of a beaker-type, round bottomed, three-neck flask. The cathode and anode were placed in the outer necks of the flask. A reflux condenser was connected to the center neck and was used to prevent the escape of acetic acid vapors.

A stabilized power supply unit (Heinzinger PHN 2500-2 pos, Rosenheim, Germany), with a maximum output voltage of 2500 V direct current (dc) and a maximum current output of 2 A was used to power the electrochemical cell. All data recording and excitation of the power supply were computer controlled. The software was capable of both potentiodynamic (varying voltage) and galvanostatic (constant current) operation. The films generated in this investigation were potentiodynamically prepared at sweep rates of 0.1–1 V/s. Time, current, and voltage measurements were made at 0.6 s intervals. Anodic oxide films on vanadium were deposited at voltages up to 480 V, and corresponding current densities, up to 20 mA/cm^2. Films were formed by sweeping once at a given rate from 0 up to the specified voltage. In order to prevent excessive heating and vaporization of the electrolyte, the cell had to be thermostatically controlled to maintain a temperature of 25 °C. After the coating process was completed, the specimens were rinsed in acetone to remove adhering acetic acid residue, dried in air, and stored in inert gas atmosphere.

B. Microstructure characterization

The microstructure of the anodic coating was characterized by SEM (Jeol 840, Peabody, MA and Hitachi S4200, Tokyo, Japan) using secondary electron and backscattered electron imaging modes. Transmission electron microscopy (Philips CM 12, Eindhoven, The Netherlands) and energy dispersive spectroscopy (EDS) were used to determine the microstructure, crystallography, and microchemistry of the anodic films. Powder specimens were made by scraping the oxide coating from the metal foil and grinding the powder dispersed in acetone in an agate mortar and pestle. TEM grids were dipped into the solution and air-dried prior to examination. XPS were recorded on a SPECS SAGE 100 (Berlin, Germany) spectrometer. RS was taken with a DILOR-XY (Jobin, Yvon/Horiba, Lille, France) spectrometer equipped with a nitrogen-cooled ccd camera and an argon ion laser operated at wavelength 514.5 nm.

III. RESULTS

It was found that the water content in acetic acid-based electrolytes had a dominant influence on the growth of anodic films on vanadium. Successful anodic film formation was only possible within a small range of water concentration. When a water-free electrolyte was used, no film formation was observed. Alternatively, when a large amount of water was used (20 mol/l), there was spontaneous electrolytic dissolution of the vanadium metal into complex vanadate ions. Figure 1 shows the current density (i) versus voltage (V) curves obtained during the anodization of vanadium at various water concentrations. During the formation, the films exhibit sharp interference colors ranging from brown to gold and then purple. When using a potential of 100 V and greater, a

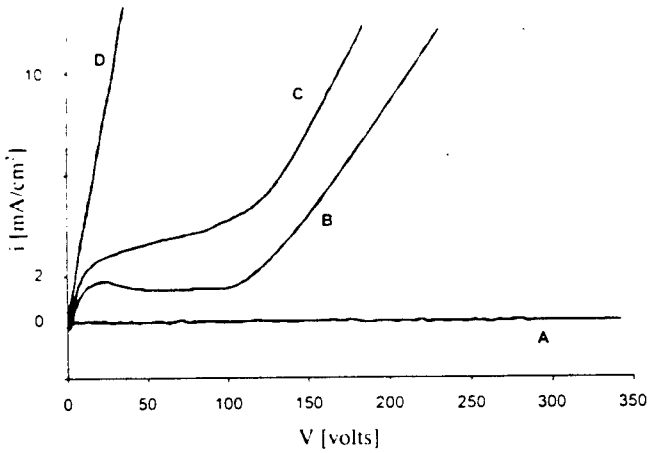


FIG. 1. Potentiodynamic voltage (V) versus current density (i) characteristics (dV/dt = 3 V/s) of the anodization of vanadium for electrolytes: (A) glacial acetic acid, (B) acetic acid + borax + 5 mol/l water, (C) acetic acid + borax + 10 mol/l water, (D) acetic acid + borax + 20 mol/l water.

greenish colored film is formed. The film thickness (d) was determined by infrared-reflectance spectroscopy according to the expression

$$d = \frac{1}{4n(\nu_{max} - \nu_{min})} \quad , \tag{1}$$

with the average refractive index $n = 2.55$ for vanadium oxide and the wave numbers (ν) of the maximum and minimum reflectance between 5000 and 25,000 cm^{-1}, respectively. The corresponding thickness for the interference colored films ranged from 120 nm to about 520 nm for greenish films formed at a voltage of 200 V.

The microstructure of anodic films generated at 80 V is shown in Fig. 2. The surface of these films had a bubbled or domed morphology with pores located in the center of most of the domes. The pore diameters ranged from 100 nm to 1 μm. The domes were thought to be formed by gas bubbles evolved from the metal surface during anodization.

The microstructure of anodic films formed at moderate voltages (150 V) is shown in the SEM micrograph of Fig. 3. An area where this film was ruptured, possibly due to electrochemical dissolution and/or mechanical stress, is seen. At higher magnifications, the surface morphology of these films was similar to those formed at lower deposition voltages.

Figure 4 is a SEM micrograph of a cross-sectioned anodic vanadium oxide film formed at 480 V, dipped in liquid N_2, and fractured. The approximately 5-μm-thick film displayed a dense oxide formation without pore connection to the underlaying metal, which was characteristic of films formed at lower voltages. The film weakly adhered to the metal substrate, and many planar cracks were observed running parallel to the interface. The microstructure was fairly homogeneous and did not possess visible grain boundaries.

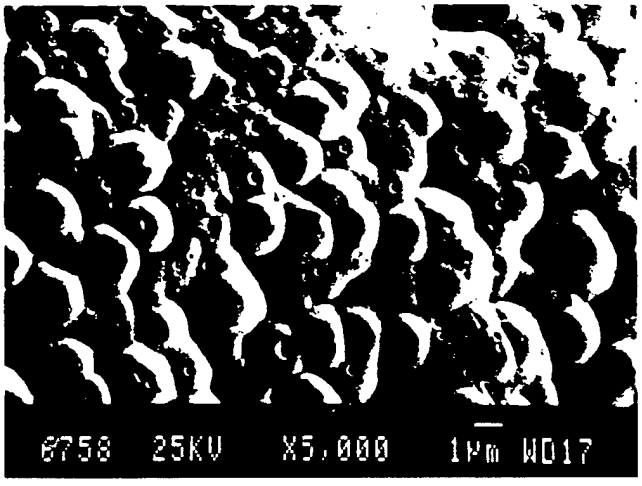


FIG. 2. SEM micrograph showing the morphology of an anodic vanadium oxide film surface deposited at 80 V.

The anodic vanadium oxide coatings were also examined by XPS to determine the oxidation state of vanadium in the coating and, hence, its chemical composition. High-resolution XPS for bare vanadium metal and two different coatings (80 and 480 V) are shown in Fig. 5. There was no significant difference in the XPS spectra for films grown at different voltages. All recorded spectra contained three intense peaks between 535 and 510 eV, corresponding to the core level binding energies of O1*s*, V2$p_{1/2}$, and V2$p_{3/2}$. The O1*s* signal had a binding energy of 530.85 eV and a full width at half-maximum (FWHM) of 1.77 eV, which corresponds to the values for thin V_2O_5 films.[7] Only a small peak asymmetry appeared at about 531.4 eV, which indicated the presence of chemisorbed water. For thin V_2O_5 films, prepared by the

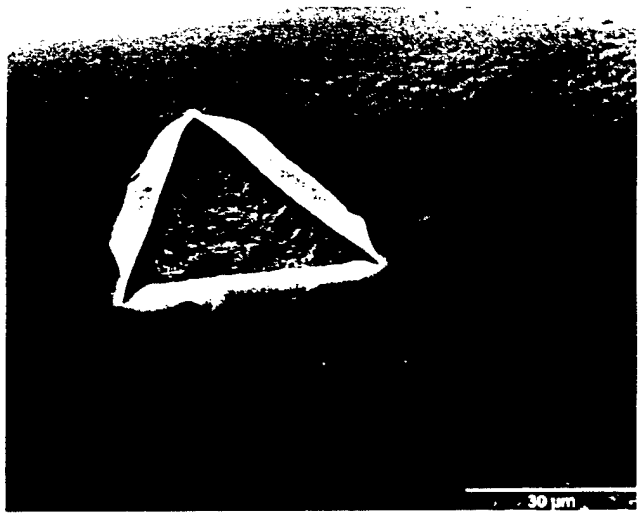


FIG. 3. SEM micrograph of a dissolved region of an outermost vanadium oxide film deposited at 150 V.

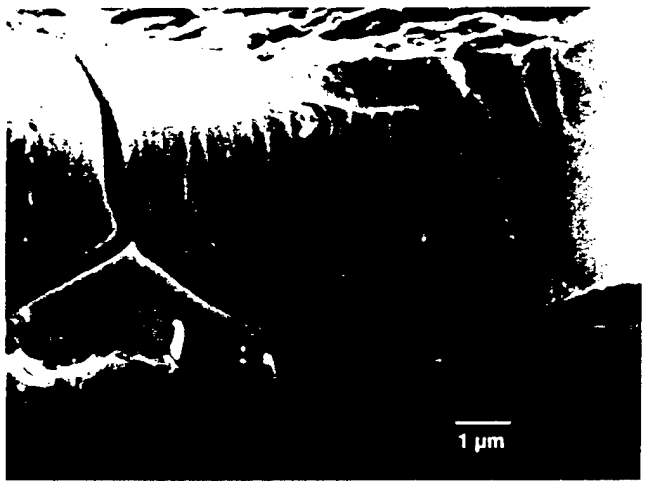


FIG. 4. SEM micrograph of a cross section of a vanadium oxide film deposited at 480 V, dipped in liquid N_2, and fractured. Cracks formed predominantly in the ceramic layer and parallel to the ceramic–metal interface.

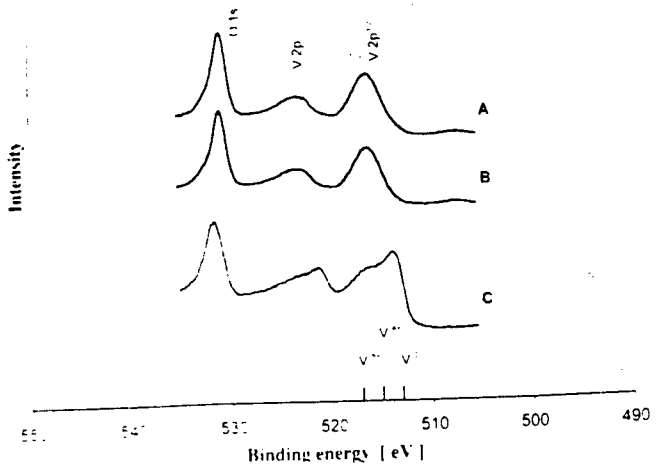


FIG. 5. [illegible] photoelectron spectra: (A) vanadium [illegible] (B) [illegible] oxide film (480 V), (C) uncoated [illegible] transition metal oxide.

sol-gel technique, a peak position for V^{5+} was reported at 516.95 eV.[7] The vanadium binding energy maximum ($V2p_{3/2}$) for our anodic films was observed at 515.86 eV (which was lower than that for pure V^{5+}), and the FWHM (3.6 eV) was too high to assign this E_B value exclusively to V^{5+}. The existence of V^{4+} with E_B = 514.9 eV[7] or the presence of lower mixed valence [illegible] explain this broadened $V2p_{3/2}$ signal. The spectrum for the uncoated vanadium metal (Fig. 5(C)) shows a peak with a binding energy of [illegible] eV for metallic vanadium (V^0). There are also some peaks at lower binding energies, which most likely correspond to the presence of a few monolayers of the native vanadium oxide film.

Electron spin resonance (ESR) measurements on isolated anodic vanadium oxide films indicate an unpaired [illegible] electron.[8] The low-temperature spectra (T = 130 K) exhibited a well-resolved hyperfine structure indicating an electron localization on a single vanadium site (^{51}V nuclear spin $I = 7/2$). The resulting parameters of the g and A values ($g_\parallel = 1.936$, $g_\perp = 1.981$, $A_\parallel = 183.5$, $A_\perp = 71.5$) indicated a distorted $[V^{4+}O_6]$ coordination.[9]

RS further characterized the chemical composition of the anodic film to complement the results obtained by XPS and ESR. The Raman spectra for V_2O_5 and a film grown at 300 V are seen in Fig. 6. Two different spectra were collected from the same film at different laser energy densities. The spectrum for the anodic film using a laser power excitation of 4 mW [Fig. 6(A)] indicates an amorphous structure. The broad Raman bands between 400 and 1000 cm^{-1} correspond to V–O–V stretching and vibrational modes in disordered materials.[5,6,17] The broad Raman intensity at approximately 900 cm^{-1} indicates the existence of $[VO_4]$ tetrahedral structures,[18] and

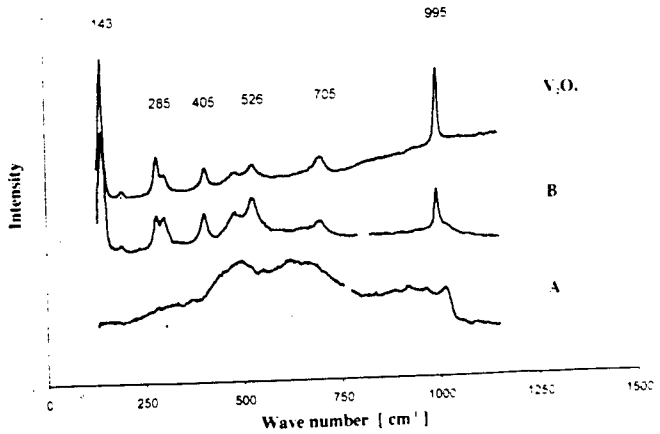


FIG. 6. Raman spectra of vanadium oxide films: (A) anodic VO_x film (4 mW), (B) anodic VO_x film (10 mW), (C) V_2O_5 (reference sample).

the small peak at approximately 1015 cm^{-1} corresponds to the vibration of V=O bonds in isolated $[VO_5]$ trigonal bipyramids.[19]

A drastic modification of the film was observed when the laser power was increased to 10 mW [Fig. 6(B)]. At this power level the film exhibited a well-resolved Raman spectrum characteristic of a crystalline material, and corresponded to that of V_2O_5 [Fig. 6(C)]. Laser-induced alteration of amorphous structures during RS has been previously reported.[20] It can be concluded that the increased laser energy transformed the metastable amorphous structure into microcrystalline V_2O_5 phases. The shift of the vibrational frequency from 1015 cm^{-1} [Fig. 6(A)] to a strong peak at 995 cm^{-1} [Fig. 6(B)] results from an increase of the V=O bond length and is typical for linked $[VO_5]$ units inside the network of the V_2O_5 structure. The strong band at 143 cm^{-1} was assigned to external modes due to the relative motion of long-range ordered vanadium oxide chains.[5,19] Although the spectra for this specimen only had peaks which corresponded to V_2O_5, spectra collected from other specimens[20] indicated the existence of a mixture of vanadium valences, such as was found in the XPS spectra (Fig. 5).

Crystalline phases were not detected by x-ray diffraction (XRD). This result, combined with the Raman spectra collected at low laser powers, indicated that the anodic film was essentially amorphous in nature. Transmission electron microscopy and EDS studies further substantiated and characterized the microstructure and microchemistry of the vanadium oxide films. Powder samples were made by scraping the coating off the vanadium metal and grinding it in an agate mortar and pestle. Several different techniques were tried to make cross-sectional specimens (dimpling, ion milling, tripod polishing, and ultramicrotomy), but due to the softness of the metal, and water solubility of the coating, none of the specimens proved to be satisfactory.

Figure 7(A) is a bright-field (BF) TEM image of a vanadium oxide particle, and Fig. 7(B) is the corresponding selected-area diffraction (SAD) polycrystalline ring pattern. This pattern was indexed as V_2O_5. This particle was mostly amorphous with a couple of small crystalline areas embedded in it. Qualitative EDS analysis of this particle verified that it was a vanadium oxide compound. Figure 8(A) is another SAD pattern from a powdered specimen. This pattern contained both rings and spots and was indexed as the [321] zone axis of orthorhombic V_2O_5. Qualitative EDS analysis of this particle was also performed, and the spectra confirmed it to be a vanadium oxide compound. Figure 8(B) is a SAD polycrystalline powder pattern from a crushed specimen, which contained discrete spots and diffuse rings. This type of pattern indicates a microstructure, which is a mixture of

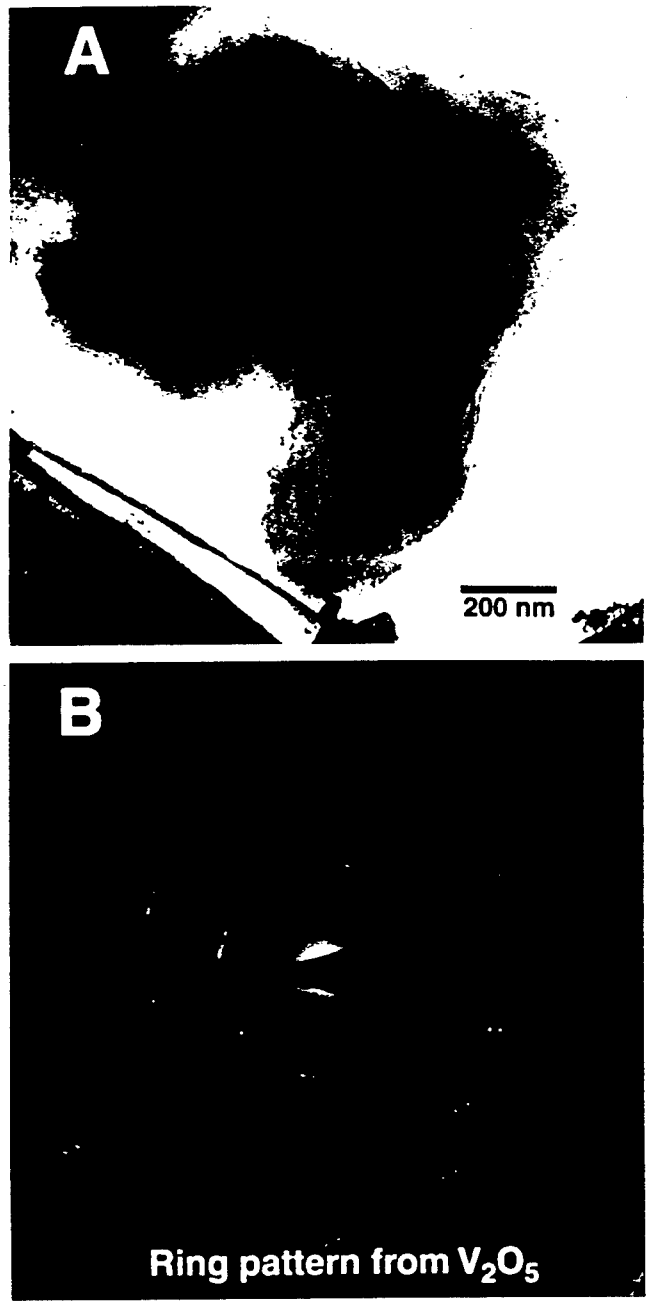


FIG. 7. TEM micrographs of anodic oxide coating on vanadium metal from a powder specimen. (A) is a bright-field TEM image of a vanadium oxide particle, and (B) is the corresponding SAD ring pattern, which identified the particle as containing V_2O_5.

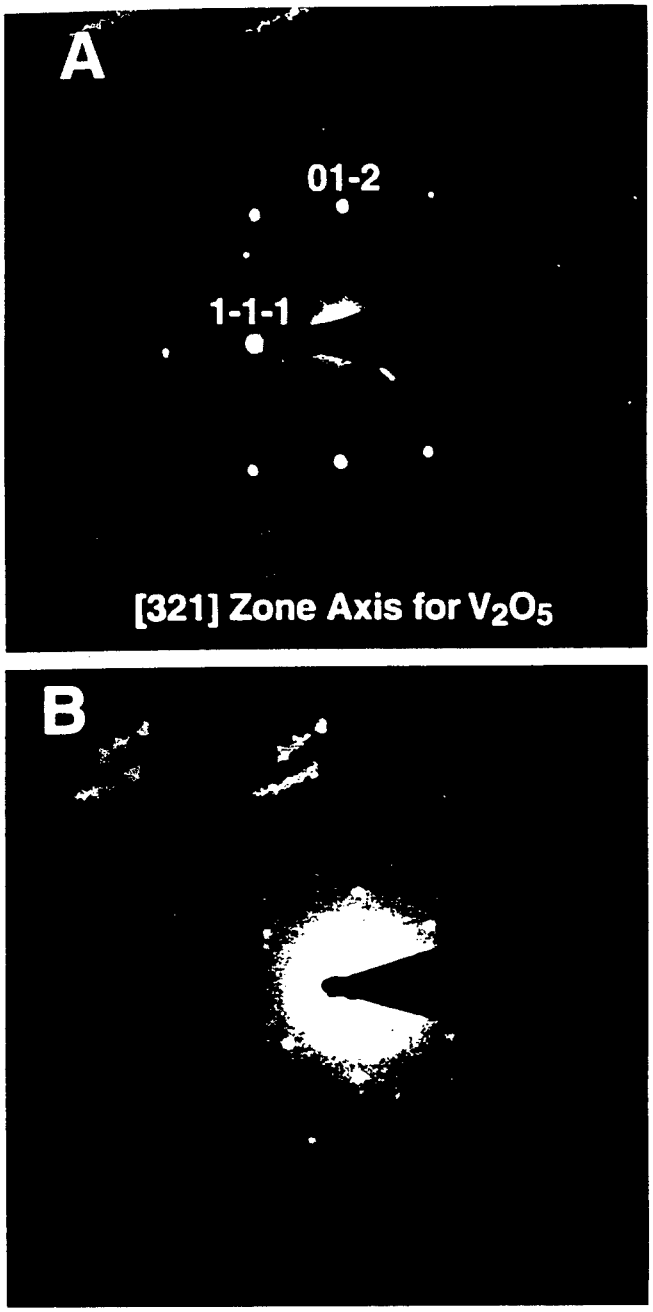


FIG. 8. SAD patterns from anodic vanadium oxide coating from powder specimens. (A) is a combined ring and spot pattern that corresponds to the [321] zone axis of V_2O_5. (B) is a SAD pattern from another region of the specimen, only this pattern contains diffuse rings and spots. This type of pattern is indicative of a mixture of amorphous and crystalline phases.

amorphous and crystalline phases. On the basis of the Raman spectroscopy investigation of the effects of laser-induced crystallization of amorphous anodic films, it is quite possible that this is also occurring under the influence of the electron beam. Crystallization effects or changes of properties during aging and storage of the films for some weeks at room temperature were not observed.

IV. DISCUSSION

Due to the complexity of mixed valence VO_x in the vanadium oxide system, multiphase formation during anodic film deposition is probable. The most common stoichiometric compositions of crystalline oxides are given by the formulae VO, V_2O_3, V_2O_4, and V_2O_5. Furthermore, a homologous series of Magnéli phases exist in the V–O system.[21] These include V_nO_{2n-1} ($4 \leq n \leq 9$) with mixed V^{3+} and V^{4+}, as well as the complex V_nO_{2n+1} phases like V_3O_7, V_4O_9, or V_6O_{13} with V^{4+} and V^{5+} species. According to the general electrochemical reaction

$$xV + yH_2O \rightarrow V_xO_y + 2yH^+ + 2ye^- \quad , \qquad (2)$$

the oxidation of vanadium to the highest valence V^{5+} state is a sequential process. The intermediate generation of low valence states is possible according to the following chemical and electrochemical reactions:

$$V + H_2O \rightarrow V(H_2O)_{ads} \rightarrow V(OH) + H^+ + e \quad , \qquad (3)$$

$$V(OH) \rightarrow V(OH)^{2+} + 2e^- \quad , \qquad (4)$$

$$V(OH)^{2+} + H_2O \rightarrow [V(H_2O)_2]^{3+} \quad , \qquad (5)$$

$$[V(H_2O)_2]^{3+} + H_2O \rightarrow VO^{2+} + 2H_3O^+ + e^- \quad , \qquad (6)$$

$$V(OH)^{2+} + 2H_2O \rightarrow [V(OH)_2]^{2+} + H_3O^+ + e \quad , \qquad (7)$$

$$[V(OH)_2]^{2+} \rightarrow VO_2 + 2H^+ \quad , \qquad (8)$$

$$2VO_2 + H_2O \rightarrow V_2O_5 + 3H^+ + 2e^- \quad . \qquad (9)$$

Under the given conditions V^{3+} compounds are unstable [Eq. (6)], but the oxidation states V^{4+} and V^{5+} can generate stable oxide phases.

The following structural model for the description of anodic vanadium oxide film formation is proposed. It is believed that the primary species formed during the anodization process is a metastable amorphous VO_x phase. The vanadium ions are in tetrahedral coordination with oxygen atoms located at the distance of 175 pm from vanadium and 270 pm apart from each other.[22] These tetrahedra form chains and are connected by $[VO_5]$ square pyramids and highly distorted $[VO_6]$ octahedra, to generate a glassylike, three-dimensional network. Nanocrystalline phases of V_2O_5 units exist in this network. The lack of one-tenth of the oxygen atoms needed to form V_2O_5 during the anodic film growth leads to oxygen vacancies and to substoichiometric compositions of V_4O_9 with an orthorhombic structure.[23] Due to the transformation of corner-linked V–O octahedra into edge-linked structures by the formation of crystallographic shear planes, the V_6O_{13} phase can readily be obtained from V_2O_5.[21] In addition to vanadium oxides[14,22] other transition metal oxides such as titanium or niobium exhibit a structure derived from a translation of the unit cell such that edges or faces of polyhedra are shared instead of corners.[24] These crystallographic shear planes tend to be disordered and are associated with the mixed valence of the transition element. The films also contain paramagnetic V^{4+} ions, which are randomly distributed between the different V–O coordinations.

Figure 9 shows the proposed film architecture. It is an amorphous structure with network forming $[VO_4]$ tetrahedra of different degrees of condensation, connecting nanosize units of crystallographic phases of V_2O_5 and other vanadium suboxides.

V. CONCLUSION

Thin films of vanadium oxides have been grown on vanadium metal using an electrolytic technique at high voltages. Acetic acid with controlled amounts of water constituted the electrolyte. The films ranging from 500 to 5000 nm in thickness were characterized by several complementary techniques including SEM, TEM, EDS, and XPS. A structural chemical model is proposed which involves progressive networking of VO_x polyhedra in a metastable amorphous phase. Predominantly tetra- (V^{4+}) and pentavalent (V^{5+}) oxides are formed in the presence of laser or electron beam energy.

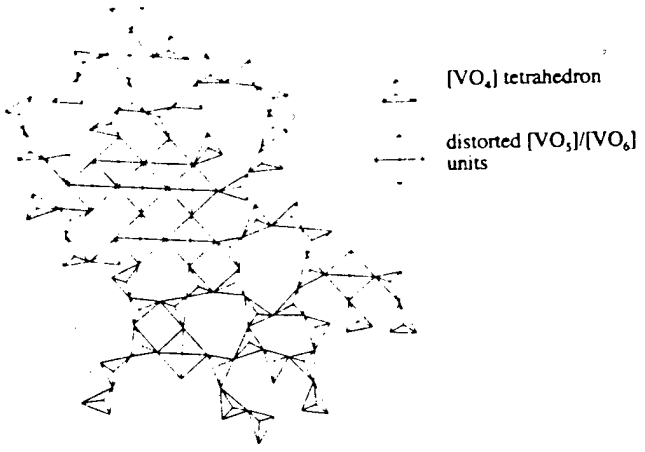


FIG. 9. Proposed chemical structural model of anodic vanadium oxide films. An amorphous $[VO_4]$ tetrahedral network surrounds nanocrystalline regions of $[VO_5]$ and $[VO_6]$ pyramids.

ACKNOWLEDGMENTS

This work was supported by the Deutsche Forschungsgemeinschaft (DFG) of Germany. Thanks are due to Dr. K. Witke for help with Raman spectroscopy. The work of B.R.J. and W.M.K. in the United States was supported by the United States Air Force Office of Scientific Research (AFOSR) under AASERT Grant No. F49620-97-1-0427.

REFERENCES

1. G.E. Thompson, Thin Solid Films **297**, 192 (1997).
2. J.P. Schreckenbach, G. Marx, F. Schlottig, M. Textor, and N.D. Spencer, J. Mater. Sci. Mater. Med. **10**, 1 (1999).
3. J.P. Schreckenbach, F. Schlottig, G. Marx, W.M. Kriven, O.O. [illegible], M.H. [illegible], and S.D. Brown, J. Mater. Res. **14**, 1437 (1999).
4. [illegible], H.S. [illegible], E.E. [illegible], R.M. Metzger, and W.D. Doyle, J. Mater. Sci. Lett. **17**, 295 (1998).
5. [illegible], G.A. Niklasson, and C.G. Bergström, Phys. Status Solidi B **201**, [illegible] (1997).
6. [illegible], J.P. Kincita, and C. Julien, in *Solid-State Ionics IV*, [illegible], G.A. Nazri, J.M. Tarascon, and M. Schreiber (Mater. Res. Soc. Symp. Proc. **369**, Pittsburgh, PA, 1995), p. 649.
7. [illegible], O.M. Hussain, B. Srinivasulu Naidu, C. Julien, and M. [illegible], Mater. Sci. Eng. B **52**, 32 (1998).
8. Y. Chen, K. Xie, and Z.X. Liu, Appl. Surf. Sci. **133**, 221 (1998).
9. R.G. Keil and R.E. Salomon, J. Electrochem. Soc. **115**, 628 (1968).
10. M.R. Arora and R. Kelly, J. Mater. Sci. **12**, 1673 (1977).
11. S. Hornkjoel and I.M. Hornkjoel, Electrochim. Acta **36**, 577 (1991).
12. M. Privman and T. Hepel, J. Electroanal. Chem. **382**, 137 (1995).
13. M. Nabavi, C. Sanchez, and J. Livage, Philos. Mag. B **63**, 941 (1991).
14. J. Haber, M. Witko, and R. Tokarz, Appl. Catal. A **157**, 3 (1997).
15. J. Cui, D. Da, and W. Jiang, Appl. Surf. Sci. **133**, 225 (1998).
16. J.P. Schreckenbach and P. Strauch, Appl. Surf. Sci. **143**, 6 (1999).
17. J.P. Schreckenbach, K. Witke, D. Butte, and G. Marx, Fres. J. Anal. Chem. **363**, 211 (1999).
18. O. Attos, M. Massot, M. Balkanski, E. Haro-Pontatowski, and M. Asomoza, J. Non-Cryst. Solids **210**, 163 (1997).
19. C. Sanchez, J. Livage, and G. Lucazeau, J. Raman Spectrosc. **12**, 68 (1982).
20. K. Witke, D. Klaffke, A. Skopp, and J.P. Schreckenbach, J. Raman Spectrosc. **29**, 411 (1998).
21. H. Oppermann and W. Bruckner, *Vanadiumoxide* (Akademie-Verlag, Berlin, Germany, 1983).
22. A. Mosset, P. Lecante, J. Galy, and J. Livage, Philos. Mag. B **46**, 137 (1982).
23. G. Grymonprez, L. Fiermans, and J. Vennik, Acta Crystallogr. A **33**, 834 (1977).
24. C.N.R. Rao and B. Raveau, *Transition Metal Oxides* (VCH Publishers, New York, 1995).